THE UNIVERSITY *of* EDINBURGH

Deterioration mechanisms of historic cement renders and concrete

Isobel Griffin. MA (Hons)

A thesis submitted to the University of Edinburgh
for the Degree of Doctor of Philosophy

July 2013

Institute for Materials and Processes in the School of Engineering

Contents

ADDITIONAL EXPERIMENTAL DATA INCLUDED ON CD

Declaration

I declare that this thesis has been composed by myself and is all my own work except where otherwise stated and has not been submitted for any other degree or professional qualification.

Isobel Griffin

Acknowledgements

The supervisors for this PhD were Dr Andrea Hamilton and Professor Christopher Hall from the University of Edinburgh, and Dr James Tate from National Museums Scotland, and I am grateful for their support and advice. I would also like to acknowledge the assistance of Dr Tim Stratford, Dr Lorna Eades, Dr Peter Anderson, Dr John Dixon, Dr John Craven, Mike Hall and Henry Hercock at the University of Edinburgh; Agnieszka Klemm at Glasgow Caledonian University; John Hughes at the University of the West of Scotland; Dr Ewan Hyslop and Luis Albornoz-Parra at the British Geological Survey; Dr Maureen Young and Roger Curtis at Historic Scotland; Dr Robyn Pender, Sarah Pinchin and Giles Proctor at English Heritage; Bryan Dickson and William Napier at the National Trust for Scotland; Roz Artiz-Young at the Scottish Lime Centre; Sarah MacKinnon at the Strathclyde Building Preservation Trust; David Anderson at East Lothian Museums; William Revie at Construction Materials Consultants; John Coundon at Petrotech; and Bénédicte Rousset at Conservation Science Consulting. My research was undertaken in partnership with National Museums Scotland, and I received help from many staff within the organization, in particular Suzanna Kirk, Katie Haworth, Stuart Baird, Margaret Wilson and all the staff based at the National Museum of Flight.

This PhD was funded jointly by the Arts and Humanities Research Council and the Engineering and Physical Sciences Research Council as part of the Science and Heritage Programme, and Professor May Cassar and Debbie Williams from the Programme were a further source of support.

Abstract

Since the introduction of Portland cement in the early nineteenth century the number of buildings constructed from concrete or using cement mortars and renders has grown exponentially, and cement is one of the most common building materials in use today. Consequently a significant proportion of the built heritage contains cementitious materials. The relative youth of these buildings means that less research has been undertaken to understand how and why they deteriorate than for traditional buildings, and that the development of appropriate conservation methods and techniques is less advanced.

The primary aim of this research was to understand the causes and mechanisms of some of the types of deterioration commonly found in historic concrete and cement buildings and structures, with reference to the Second World War reinforced concrete and cement-rendered buildings at East Fortune airfield in East Lothian, Scotland. Additional aims were to investigate the efficacy of the building repairs and maintenance regimes undertaken to date, and to make recommendations for the future conservation of the buildings.

East Fortune airfield contains a number of cement-rendered brick masonry buildings and a reinforced concrete air raid shelter. The initial visual survey identified several types of deterioration, from which the blistering and flaking of the render; the cracking and delamination of the render; and the spalling of the concrete in the air raid shelter were selected for further research. The research included time lapse photography, non-destructive testing, environmental monitoring and the physical, chemical and petrographic characterisation of the building materials. Hypotheses regarding the causes of deterioration were tested in the laboratory, for example with linear variable displacement transducer measurements, and modelled using crack propagation theories and models for water transport through porous media.

It is demonstrated that the blistering and flaking of the render is caused by shale aggregate particles, which undergo sufficient expansion during freeze-thaw cycles to crack the surrounding render. This phenomenon is termed ‘pop-outs’ in the concrete literature. The more catastrophic cracking and delamination of the renders is

also due to freeze-thaw cycling, which is shown to cause significant damage provided the moisture content of the render is above a certain threshold level. This type of deterioration has occurred at an accelerated rate for some of the modern render repairs, due to an inadequate understanding of the properties of the original and repair materials. In particular, the properties of the bricks are critical to the performance of the cement renders, and it is found that the sorptivity of historic bricks may vary considerably depending upon the orientation of the brick. Finally, the diagnosis for the air raid shelter is that the corrosion of the steel reinforcements is caused by high levels of chlorides present within the raw materials used to make the pre-cast concrete sections.

The results of the investigations are used to suggest building conservation solutions for this particular site. Furthermore, since the deterioration mechanisms investigated are common for historic cement and concrete, the findings are relevant to many other sites. The over-arching methodology used to investigate the deterioration at the site and the methodologies developed to test particular hypotheses are also applicable for other investigations of historic building materials.

There is much about this research that is innovative and new. The work on render cracking compares the results of dilation tests on cementitious and ceramic materials, which has not been done previously, and the pop-outs diagnosed in the work on render flaking have rarely, if ever, been reported for cement renders. The modelling work undertaken to quantify the stresses produced by the pop-outs and to explain the inclined crack formation patterns is entirely original. The use of petrography to diagnose causes of render failure is described in the literature, but this is one of very few case studies to be written up, and the work on the air raid shelter constitutes the only formal investigation of this type of Stanton shelter.

1.1 Introduction

This work aims to understand the causes and mechanisms of some of the types of deterioration commonly found in historic concrete and cement buildings and structures, with reference to the Second World War reinforced concrete and cement-rendered buildings at East Fortune airfield in East Lothian, Scotland. The relative youth of buildings utilizing Portland cement means that less research has been undertaken to understand how and why they deteriorate than for traditional buildings. Additionally, much of the research undertaken does not relate specifically to historic buildings, and is inappropriate because it does not consider the need in these cases to preserve as much of the original fabric as possible. For example, cement renders are generally considered sacrificial and most research is concentrated on the service life of new renders, while concrete repair standards, such as the relatively new BS EN 1504, are able to make recommendations to stabilise or strengthen a concrete structure with little if any consideration for the visual appearance of the concrete.

The methodology employed was to survey the fieldwork site and identify the key types of deterioration present. A programme of non-destructive testing, physical and chemical characterisation of the building materials and monitoring of the environment at the site was then implemented to gather information about the factors causing and contributing to the deterioration. This was revised as the project progressed because some test methods did not yield useful information, and intermediate findings identified the need for additional measurements. The investigations allowed hypotheses regarding the causes and mechanisms of deterioration to be formed, and laboratory experiments and modelling systems were then devised to test and quantify the hypotheses. The findings allowed recommendations to be made regarding the management of East Fortune airfield and the treatment of individual buildings, and are relevant to other historic buildings containing cementitious materials, which are likely to suffer similar deterioration.

1.2 Thesis preview

The literature review in Chapter 2 begins with an introduction to cement and concrete, covering their chemistry, the history of their use, the ways in which they deteriorate and the theory and practice of their conservation. Methods for

investigating and analysing historic buildings and building materials are then discussed, from non-destructive techniques of recording, assessment and environmental monitoring, through the development of an appropriate sampling strategy, to the petrographic examination and chemical and physical characterization of the samples taken. Reference is made to case studies of historic concrete and cement-rendered buildings describing the investigation and diagnosis of deterioration, because they are useful to put the research undertaken in this thesis into context. The literature on freeze-thaw and expansive aggregates in concrete and cement has also been reviewed, but as this was more in-depth research, undertaken to inform particular experimental work and modelling, it is included within the relevant chapters towards the end of the thesis.

The historic site used as a starting point for this research is introduced in Chapter 3. East Fortune airfield is a military airfield in East Lothian, Scotland, with buildings dating from the First and Second World Wars. The Second World War buildings are now owned by National Museums Scotland and operated as the National Museum of Flight (NMOF), which is a Scheduled Historic Monument. The buildings at NMOF chosen as subjects for this research were cement-rendered brick masonry buildings and a reinforced concrete air raid shelter. A brief history of East Fortune airfield and other military airfields in the UK is included to provide a context for the buildings and their design and construction methods are described. The conservation history of the buildings is mapped out using documentary records and visual evidence. The sampling and testing strategy employed for the research are given at the end of Chapter 3.

The survey work, environmental monitoring and non-destructive testing undertaken at NMOF are detailed in Chapter 4. The site investigations began with a brief visual survey of all 23 cement-rendered brick masonry buildings. This allowed the identification of the main types of deterioration, and the selection of a smaller group of buildings providing good examples of deterioration for further research. The air raid shelter was included within this group because it is the only reinforced concrete building at NMOF. Detailed condition surveys were undertaken in a variety of weather conditions, and comparison of current and historic photographs and time lapse photography over the course of the project allowed the rates of deterioration to

be defined semi-quantitatively. The survey findings were supplemented with non-destructive testing methods, such as infrared thermography and electrical resistivity measurements. A comprehensive environmental monitoring programme which included monitoring of evaporation rates and soil moisture content was also instigated, to relate the deterioration to the environment inside and outside the buildings and the ground conditions.

The results of the non-destructive testing were used to inform a programme of destructive testing. The sampling strategy outlined in Chapter 5 aimed to obtain the maximum amount of information from a minimum number and size of samples. The samples included original and repair renders, original mortar, historic and modern bricks and historic concrete from the air raid shelter, with some samples of historic cementitious materials from other sites for comparison. Following examination at low-magnification, small fragments of the materials were made into thin sections and examined in plane polarized and cross polarized transmitted light. This provided information regarding the chemical composition and physical condition of the building materials, particularly with regards to the workmanship of the original and repair renders and the causes of render deterioration.

Other analysis undertaken to characterize the building materials chemically is described in Chapter 6, and included wet chemistry to establish the binder:aggregate ratios of the renders, determination of the particle size distribution of the aggregates by sieving, ions analysis of aqueous extracts to identify salts and map their distribution and XRD and SEM-EDX to investigate the causes of the render flaking. Key physical properties of the materials were also measured, namely tensile strength, elastic modulus, density, porosity, sorptivity, pore size distribution and drying behaviour.

Chapters 7-11 use the data presented in Chapters 5 and 6 alongside additional experimental work to answer particular questions about the deterioration of the buildings. It had been found that the longevity of the render depended on the strength of the render-brick bond, which in turn was influenced by the sorptivity of the brick. The significant variations in the sorptivity of the bricks tested were considered worthy of additional research, which is described in Chapter 7. The reasons why the render cracks in the first place are discussed in Chapter 8, using linear variable

differential transducer measurements to compare the differential movement of renders and bricks due to freeze-thaw cycling. Chapter 9 follows on from Chapter 8 to investigate why the process of cracking and delamination has been particularly rapid for some of the repair renders.

The other main type of deterioration affecting the cement renders at NMOF was surface blistering and flaking, and the work undertaken to establish its causes is described in Chapter 10. Site observations suggested that the flaking was related to the presence of soft, flaky aggregate particles. These were identified and similar aggregate was sourced from close to NMOF, and used alone and in replica renders for dilation testing with a linear variable differential transducer. Additionally, calculations were undertaken to model the deterioration mechanism, using equations relating to the cracking of concrete due to the volume expansion of corroding reinforcements, which is a comparable process, and crack propagation theory.

The final investigations covered in Chapter 11 focus upon the reinforced concrete air raid shelter, which was in poor condition due to the delamination of large pieces of concrete. The immediate cause of this was clearly the corrosion of the steel reinforcements, but the corrosion and differing rates of deterioration observed required further research. The results are used to make recommendations for the conservation of the shelter, with reference to the relatively new European Standard for concrete repair.

The concluding chapter summarizes the findings regarding the deterioration of the buildings at NMOF and considers their conservation implications. The relevance of the research to other historic concrete and cement-rendered buildings is discussed, and suggestions for further research are made. The over-arching methodology used to investigate the deterioration at the site and the methodologies developed to test particular hypotheses are assessed, and the most useful measurements and experiments are highlighted.

Vast quantities of data were collected at NMOF, and only a small selection has been included in the main body of the thesis, alongside the conclusions drawn from the large datasets. Additional data is available in the appendices and some files have been supplied electronically.

2.1 History of cement manufacture and concrete construction

The Romans and Greeks made hydraulic mortars by combining lime and pozzolanic materials, and this type of mixture 'long retained its position as the only suitable material for work under or exposed to water' [1]. The ability of hydraulic limes to produce similar mortars was recognised by Smeaton in the mid eighteenth century, and natural cements such as Roman cement made by calcining nodules of argillaceous limestone were in use from around the same time. Artificial cements made by calcining a mixture of limestone and clay were developed by Vicat and Frost amongst others, and in 1824 Joseph Aspdin obtained a patent for the artificial cement that came to be known as Portland cement, on account of its colour resemblance to Portland stone. In fact the product obtained by Aspdin was of rather poor quality, and the manufacturing technique was subsequently refined, with higher temperatures being used to make stronger cements.

By the end of the nineteenth century there were a number of companies producing cement in the UK, but the manufacturing process became more standardised when 24 companies joined together in 1900 to form the Associated Portland Cement Manufacturers (1900) Ltd, or APCM. The publication of the first British Standard for Portland cement in 1904 also assisted with standardisation. The use of Portland cement mortars grew in popularity from the mid nineteenth century onwards, and in the twentieth century Portland cement became 'the norm for new construction' and was increasingly also used for repairs on historic buildings, which had originally been constructed with lime mortars and renders [2]. It has been estimated that cement renders now 'account for approximately 62% of facade claddings in Europe' [3].

Ordinary Portland cement (OPC) is prepared by mixing limestone and clay, burning them in a kiln at temperatures above 1260 °C and grinding the resulting clinker to a fine powder. The principal compounds in OPC are alite (tricalcium silicate), belite (dicalcium silicate), aluminate (tricalcium aluminate), ferrite (tetracalcium aluminoferrite) and calcium oxide, present in known proportions. The properties of the cement paste are largely dependent on the alite content, which was increased over the course of the twentieth century to produce stronger cements [4].

Cement paste is produced by adding water to the powder and allowing the resultant mixture to harden. The compounds in the powder hydrate to form a complex range of hydration products, including calcium silicate hydrates (C-S-H), calcium aluminium hydrates (C-A-H), calcium iron aluminium hydrates (C-A-F-H) and calcium hydroxide (CH) [5]. The hardening process can last for months or even years, depending on the initial water content of the mix. A water content of approximately 25% of the mass of the cement is required for the hydration reaction [6], but additional water is required for workability, and this creates a pore network as the cement dries out. Excess calcium hydroxide and other alkaline hydroxides, primarily of sodium and potassium, are present in solution in the pores, resulting in a pH of 12-14 [7].

Portland cement on its own is very prone to shrinkage cracking, and it is generally mixed with sand to make cement mortar, or with both fine and coarse aggregate, such as a sand and gravel mix, to make concrete. The use of concrete again dates back to antiquity, when massive structures including the Basilica of Constantine and the Parthenon were built with concretes made from volcanic tuff or broken brick, lime and pozzolana.

The concrete constructions of the Middle Ages were generally inferior to the work of the Romans, but the introduction of Portland cement generated renewed interest in concrete, and the first all-concrete house was built in the UK in 1835. Although ‘mainstream architecture was hardly touched by the use of concrete until after the end of the nineteenth century’ [8], experimentation with concrete was ongoing through the nineteenth century, with increasing numbers of concrete houses being built as the century drew to a close. Concrete was also becoming a common material for the floors of buildings, allowing architects to achieve long spans, and precast concrete came into use in the 1870s. Early structures often relied on unreinforced concrete, but the potential for increasing the tensile strength of concrete using steel reinforcements was soon recognised, and many patents for systems of reinforcing concrete were filed in the latter half of the nineteenth and early twentieth centuries. The first fully reinforced concrete structure in Britain was Weaver’s Mill in Swansea, erected in 1887.

Concrete was used extensively for building military structures during the First and Second World Wars, as it was relatively cheap and buildings could be erected quickly. Additionally, pre-cast concrete sections for structures such as pill boxes and air raid shelters could be mass-produced. It is observed by Griffin and Tate [9] that 'reinforced concrete in the late nineteenth and early twentieth centuries sometimes suffered from a lack of knowledge of the materials, resulting in design defects such as inadequate depths of concrete cover and undesirably high water-cement ratios'. Inappropriate chemical composition was also an issue, with excessive levels of sulfates and alkali salts for example. However, by the 1930s a substantial body of knowledge had been developed at the Building Research Station and elsewhere, and the Building Research Board appointed a committee to create a Code of Practice for the Use of Reinforced Concrete [10]. This was published in 1933 and covered areas including:

- Aggregate grading and type: the aggregate should be clean and well-graded;
- Water-cement ratio: this was not specified directly, but a 'slump test' to measure the consistency of the concrete was described, and a maximum acceptable value of slump was then specified;
- Depth of concrete cover : this was to be 'not less than half an inch or the diameter of the bar'.

The depth of concrete cover specified was still not sufficient to prevent corrosion of the steel reinforcements, and this was recognised in 1948 when the code was revised, with the depth of cover increased to one inch for external work and some categories of internal work. However, the risk of corrosion arising from the use of calcium chloride to accelerate set was not understood until much later: calcium chloride was used through the twentieth century [11] and was only 'effectively banned' in 1977' [12].

2.2 Deterioration of cement and concrete

There are many causes of damage and deterioration to cement and concrete. The European Standard for the protection and repair of concrete, EN 1504, divides defects into mechanical defects, caused by impact, overload, movement, explosion and vibration; chemical defects, caused by alkali aggregate reaction, aggressive agents and biological activities; and physical defects, caused by freeze-thaw, thermal

effects, salt crystallization, shrinkage, erosion and wear [13]. Some defects arise because of the way the concrete is mixed and placed. For example, if the mix has an excessively high water content, it will undergo considerable shrinkage as it dries out, which may lead to shrinkage cracking, and if the concrete is allowed to reach excessively high temperatures during hydration, this may also cause cracking [14]. Failure to keep the concrete moist during curing may allow it to dry out too quickly, resulting in inadequate hydration of the cement and reduced strength.

Most chemical and physical deterioration mechanisms are exacerbated by the presence of water, and cement renders are particularly vulnerable because they are often the most exposed part of a building. For example, the dissolution of the portlandite present in the cement paste may occur if there are significant quantities of water moving through, particularly if the water is soft water containing dissolved carbon dioxide. Water is also required for the action of aggressive agents such as sulfates, which attack in 'a complex set of processes that cannot be easily divided into physical versus chemical' [15]. The source of the sulfates may be internal – from the cement, aggregates, water or admixtures – or external. External sources include sulfates from ground water, fertilizers and atmospheric SO_3, and sulfate attack from an external source will be visible as a zone of deterioration moving inwards from the exposed surface.

Two examples of internal sulfate attack are the formation of gypsum due to an excess of sulfate present, and delayed ettringite formation, whereby sulfate ions react with mono-sulfoaluminate and calcium hydroxide to form ettringite. Gypsum and ettringite formation are expansive reactions which result in cracking, spalling and delamination. Other forms of sulfate attack include the decomposition of previously formed hydration products, the formation of brucite and magnesium silicate hydrate and the formation of thaumasite. Thaumasite destroys the strength and cohesion of the concrete and turns it into a soft pulp [16].

Expansive reactions involving the aggregate include alkali-silica reaction (ASR), and, less commonly, alkali-carbonate reaction (ACR). ASR may occur if the aggregate contains minerals with high reactivity potential such as greywacke. Reactive silica from the aggregate reacts with the hydroxide ions from the cement paste to form calcium-alkali-silicate gel. Silica gel swells when it absorbs moisture,

and can cause the cracking of concrete and the appearance of white deposits of silica [7]. Although unattractive, it may be harmless, but in its most severe form it can cause 'complete destruction of the concrete structure' [15]. ACR is the reaction between alkalis from the cement or an external source with 'certain dolomitic limestones containing clay' [17]. The alkalis break the dolomite down into brucite and calcite, and this destroys the structure of the rock and allows water to penetrate inside, causing the clay to swell and push apart the aggregate, with subsequent cracking of the concrete.

Freeze-thaw is clearly moisture-dependent, and damages concrete by a similar mechanism to salt crystallization. Aggregates within the concrete may also be affected, resulting in D-cracking. Moisture in the pores expands as it freezes and may cause spalling of the surface or internal cracking, although the severity of the damage depends on the initial moisture content of the concrete, the rate of freezing and whether salts such as calcium chloride and sodium chloride are present [18]. The literature on the mechanism of freeze-thaw damage is discussed in more depth in Chapter 8.

Some types of deterioration are specific to reinforced concrete. Corrosion of the steel reinforcements occurs, whereby the iron ions in the steel go into solution, reacting with hydroxide ions and then with oxygen and water to create solid rust, $Fe_2O_3.H_2O$. The rust layer increases the volume of the reinforcements, which puts pressure on the surrounding concrete and causes it to crack and delaminate. The reinforcements are initially protected by a passive layer on the surface of the steel. However, the passive layer is only stable in an alkaline environment, and breaks down if the surrounding concrete carbonates and the pH drops. Corrosion can then occur, although the rate of corrosion will depend upon the rate at which air and moisture permeate through the concrete. Corrosion is less commonly caused by chloride ions present in the concrete, which attack the passive layer on the reinforcement. A chloride content of above 0.2-0.4% by weight of cement is required for the risk of corrosion to be significant [19]. The chloride ions may be present within the concrete raw materials or may diffuse in over time, for example from the ground water or from wind-born deicing salts, and it may be possible to establish their source by measuring the chloride profile of the concrete. The chloride

distribution will show a profile with depth if the chlorides diffused in, while other distributions suggest that the chlorides were cast in, either as a rapid setting agent or through the use of contaminated water or aggregates.

A thorough understanding of the reasons why cement and concrete deteriorate allows performance criteria to be set for these materials. Concrete is most likely to be resistant to moisture-related deterioration if it has minimal cracking and low porosity and sorptivity, which is achieved by specifying a mix with an appropriate binder:aggregate ratio, a well-graded aggregate and a low initial water content, possibly through the addition of a plasticizer. Alternatively, an air-entraining agent may be added to create a regularly spaced network of pores which protect the concrete against freeze-thaw damage [18]. ASR and ACR may be avoided through the choice of an aggregate with low reactivity potential [7], and the risk of reinforcement corrosion may be reduced by specifying adequate concrete cover and ensuring adequate resistance to chloride ion ingress [20]. Good workmanship is crucial for proper curing, and, in the case of cement renders, to achieve a good bond between the render and the substrate. Additional requirements for renders are lower strength than the substrate to accommodate 'slight movements of the building' [21], and sufficient flexibility to tolerate some movement without cracking.

2.3 Maintenance, repair and conservation of cement and concrete

In comparison to the conservation of traditional building materials such as stone and lime plaster, 'the repair and conservation of historically important concrete is still in its infancy' [22]. The European Standard for the protection and repair of concrete, EN 1504, provides a methodology for repair works, but needs to be applied judiciously 'because it has been developed for general repair situations rather than the conservation of historic structures, and... may therefore suggest inappropriate solutions in some situations' [9]. BS EN 1504 gives six principles for the protection and repair of concrete, such as 'moisture control' and 'concrete restoration', and five principles to protect against reinforcement corrosion, including 'preserving or restoring passivity' and 'cathodic protection' [13]. There is an overlap between maintenance and repair because opinions vary as to how certain treatments should be categorised [23].

The most ubiquitous repair is the patch repair, undertaken to replace small areas of missing or defective concrete or cement render. If patch repairs are necessary because sections of concrete have spalled off due to reinforcement corrosion, it is important to ascertain the extent of the corrosion and address any ongoing corrosion, as the deterioration will otherwise continue. The choice of materials for patching historic buildings is complex, as discussed by Griffin et al. [24]. Polymer-modified mixes are often recommended by the concrete industry, as they produce flexible repairs with good adhesive properties [25], and this approach may seem appropriate if the original materials have caused the concrete to fail. However, mixes containing polymers usually have different hydraulic and mechanical properties to the original materials, which may cause problems at the interface between old and new. A more traditional approach is to replicate the chemical composition of the original render, but this may be difficult because modern cements are typically much stronger and greyer than earlier cements. A third option is therefore to attempt to match the hydraulic and mechanical properties of the original render in its current state, and this may be achieved using cement-lime mixes or hydraulic limes, which are not as strong as modern cement [26]. The choice of materials for filling cracks is similar, and the requirement for flexibility is even more important.

In historic buildings it is often desirable that the patch repairs should provide a good match for the original, and this may be achieved by tinting the repairs, possibly through the selection of a coloured aggregate, or by roughening the surface of the repairs [27]. Live yoghurt or cow dung is sometimes applied to the repair surface to speed up lichen growth, but it is doubtful whether this is actually effective [28].

Concrete repair also frequently involves the use of barrier and impregnation systems. Coatings may be applied to concrete to prevent the ingress of moisture or carbon dioxide, thereby slowing down moisture-related deterioration such as ASR or preventing concrete from carbonating and hence avoiding reinforcement corrosion. Additionally, coloured coatings may be used to tint repairs or to create a uniform finish across a building facade disrupted by patch repairs. The range of coatings is extremely wide, and the choice of coating depends upon its intended purpose. For

example, penetrating sealants such as siloxy silanes may be effective in drying out concrete, but they 'will not stop corrosion, and may accelerate it' [29]. Corrosion inhibitors are relatively new products, which are applied to the concrete surface with the intention that they will diffuse through the concrete to the steel reinforcement and protect the reinforcement from corrosion. Some trials have reported positive results with corrosion inhibitors, but others have not [30], suggesting that the efficacy of the treatment may depend on the circumstances of use.

There are a number of electrochemical techniques available to arrest reinforcement corrosion, namely cathodic protection, electrochemical chloride extraction, also known as desalination, and realkalisation [29]. These techniques introduce an artificial anode and turn the reinforcing steel into a cathode. Electrochemical chloride extraction and realkalisation are short-term techniques involving a temporary anode, whereas cathodic protection requires the installation of a permanent system. Electrochemical techniques can be expensive, but as they involved minimal disruption of the building fabric they offer great potential for the conservation of significant historical structures.

Although treatments for cement renders and concrete are similar, attitudes to render conservation are different because renders are often considered sacrificial, to be replaced when they begin to fail. Gaspar and de Brito [3] undertook field studies in Lisbon, Portugal, and found that the service life of cement renders typically varied from 15 to 35 years, suggesting that it is difficult to try to preserve a cement render indefinitely. However, the value of historic renders is increasingly recognised: it has been stated that 'the surface properties of a render should be preserved as long as possible, especially when this render has an artistic, historic or cultural value' [31].

2.4 Case studies of other historic concrete and cement-rendered buildings

There are some published case studies of work on historic concrete buildings, and they are useful to put this research on the buildings at NMOF into context. Early investigations of historic concrete structures were undertaken in Denmark by Idorn [32], who found the main causes of deterioration to be alkali-aggregate reaction and frost. He described the leaching out of calcium hydroxide and deposition of calcite as a 'common but secondary phenomenon', which tended to occur when concrete had

cracked. Leaching was also found to be a major problem in structures such as 1930s concrete bunkers in Poland surveyed by Katzer [33]; reinforced concrete shells in Estonia investigated by Onton [34] and reinforced concrete bridges and dams surveyed by Thomasen and Searls [35]. Thomasen and Searls additionally reported cracking, softening of the cement paste, organic growth and the exfoliation of concrete layers caused by salts being brought into the concrete by water penetration and then recrystallizing, and concluded that 'most failures are associated with moisture infiltration'.

In historic reinforced concrete buildings the corrosion of the reinforcements is often an issue, and studies have been undertaken to relate the corrosion rate to the strength and composition of the concrete, the depth of carbonation and the external environment [36]. There is less published about historic cement renders, but an infrared thermography survey of the Hill House in Helensburgh, Scotland, found that moisture infiltration through cracks was the primary cause of deterioration [37].

Some case studies describe the initial investigation and diagnosis of deterioration followed by trials and implementation of remedial treatments. Examples include reinforced concrete structures which are suffering deterioration caused by reinforcement corrosion, such as the church of St John and St Mary Magdalene in Goldthorpe dating from 1918 [38], and the 'listening mirrors' built along the Kent coast in the 1930s [30]; and mass concrete structures such as the Tynemouth Coastal Battery [28], which was affected by movement and mechanical damage. Significant concrete buildings may be listed or designated – the church of St John and St Mary Magdalene is Grade II listed, and the listening mirrors and Tynemouth Coastal Battery are Scheduled Monuments – and their repair consequently requires a conservation approach. The case studies describe how 'like-for-like' patch repairs were undertaken, often with analysis of the historic concrete to allow matching of the repair material. Additionally, during the listening mirrors project invisible corrosion inhibitor coatings and a cathodic protection system were trialled, and the cathodic protection system proved particularly effective.

2.5 Recording, documentation and information management

All of the case studies reviewed emphasized the need for thorough documentation of the buildings under investigation and the treatments undertaken, and it is widely accepted that 'recording of the cultural heritage should be seen as a priority and should be undertaken…as a fully integrated part of research and conservation activity' [39]. The need for recording, documentation and information management is recognised in many conservation charters, from the Athens Charter for the Restoration of Historic Monuments (1931) onwards, and is treated most extensively in the 'Principles for the recording of monuments, groups of buildings and sites', produced by ICOMOS in 1996 [40].

Heritage records can take many forms, including reports, other written documents, drawings and photographs. They should include information about a site's 'assets, values, significance, management, condition, maintenance and repairs and the threats and risks to its safekeeping' [39]. The recording of information in a graphic or photographic medium is particularly valuable for conservation planning and to create 'base maps for adding data' from investigations and treatments. Graphic documentation may be undertaken by traditional hand recording, or digitally, where information is produced and stored on a computer, and metric survey techniques such as GPS (Global Positioning System) may be employed to produce scaled graphic documentation [41]. Many guidelines on recording buildings exist, including those produced by English Heritage, Historic Scotland and the Institute for Archaeologists [42, 43, 44]. They specify varying levels of recording depending on the building and any interventions proposed.

The gathering of heritage information should be an ongoing process rather than 'the product of one individual investigation', and so should involve assembling the information existing already and planning for the future acquisition of information, possibly on a rolling programme [43]. Historic documentation is a valuable part of the site record, and will aid in avoiding duplication and informing the strategy for gathering further information. Additionally, if the documentary evidence contains information about the condition of the structure in the past, it can be used to measure the progress of deterioration [45].

2.6 Surveys and non-destructive testing

A crucial part of the information gathered about a historic building is the results of the assessments undertaken, and, as recognized in the European standard for concrete repair BS EN 1504, it is good practice to undertake a thorough assessment of a building to establish the causes and extent of deterioration prior to making recommendations for treatment [46]. The depth of information required varies according to circumstance, and English Heritage differentiates three levels of assessment for concrete buildings: the initial routine survey, involving a full visual inspection, the secondary survey to determine the structural integrity of the building, and the tertiary survey to carry out a more detailed inspection and undertake testing of the concrete, which may involved non-destructive testing and sampling for laboratory testing [47].

The aims of the visual inspection are to obtain information about the materials and method of construction of the building, and the location and extent of defects and deterioration. It may be possible to suggest likely causes of deterioration, either from obvious building defects such as poor drainage, or from characteristics of the deterioration such as cracking patterns [48]. The visual assessment also informs appropriate non-destructive investigations, which are preferred to destructive testing because minimum intervention is a ‘key tenet of conservation philosophy’, and which permit large structures to be assessed ‘rapidly and economically’ [49]. However, the information gained is not necessarily quantitative, and its quality is limited by various uncertainties such as the intrinsic variability of materials. Techniques are therefore often used in combination, either to confirm measurements or improve the interpretation of results [50]. A further issue is that many tests are in fact partially destructive because they involve ‘removal of surface finishes’ or ‘localized surface zone damage’ [48], and this may not be acceptable for historic buildings.

The more common non-destructive tests for concrete are summarised in the International Concrete Repair Institute guidelines and a recent RILEM publication [51, 50], and additional tests are included in other publications [52, 14]. They include techniques for:

- Obtaining information about surface appearance, such as colourimetry and laser scanning;
- Undertaking chemical analysis, such as X-Ray Fluorescence;
- Locating and identifying reinforcements, such as half-cell potential, corrosion rate and electromagnetic cover measurements;
- Identifying sub-surface structural elements and defects, such as hammer surveys, ultrasonic transmission (also known as ultrasonic pulse velocity), ultrasonic echo (also known as pulse echo or impact echo), surface waves methods, impulse response, radiography, radar, thermography, Ground Penetrating Radar and endoscopy;
- Measuring moisture content, such as resistivity, capacitance, thermography and Nuclear Magnetic Resonance (NMR);
- Assessing the mechanical properties of concrete, such as surface hardness tests, 'near-to-surface' tests and ultrasonic methods;
- Measuring mechanical movement, such as strain gauges.

The non-destructive tests used at NMOF were rebound hammer testing, Ultrasonic Pulse Velocity (UPV) testing, infrared thermography and electrical resistivity measurements, and these are discussed in further detail below.

2.6.1 Infrared thermography

Infrared thermography uses a thermographic camera to detect and record the thermal energy output of objects and produce a thermal image of the surface temperature of a building [53]. It may be used in structural surveys to locate concealed construction features, detect services and identify structural defects and areas of high moisture content [49]. The best results are obtained when the structure is heated, either artificially or by the sun, to accentuate the temperature differences between different parts. However, the surface temperature images must be interpreted with caution, because they depend on the circumstances under which a building is heated. For example, voids and high moisture content can make the building fabric appear warmer or colder than adjacent areas [54]. Furthermore, the technique is limited to near-surface effects, and cannot give quantitative values of moisture content.

2.6.2 Moisture measurement techniques

Non-destructive techniques for measuring the moisture content of walls are reviewed by Pinchin [55], and it is concluded that 'there is no single measurement technique that is both non-destructive and able to locate and monitor high levels of moisture accurately within walls'. The main techniques available are resistivity measurements, capacitance measurements and infrared thermography for surface measurements; and resistance tomography, profiled capacitance and microwave readings and portable NMR for profile measurements. Most of these techniques have drawbacks, such as the potential for resistivity measurements to be affected by the presence of soluble salts. However, they are often used in combination to obtain greater accuracy [56], and it is possible to obtain semi-quantitative results by calibrating resistivity equipment on conditioned laboratory samples of a similar material to the structure under investigation [57].

Moisture content may also be measured directly by taking a lump sample or a core and drying it to constant mass [58]. Although this technique is destructive, it may be possible to take samples which are already partially detached from the building, such as delaminating pieces of render, provided that they are still connected hydraulically to the core of the building. Drilled samples may give a moisture profile in depth but care is needed to ensure that the moisture content is not affected by the drilling process [55].

2.6.3 Non-destructive assessment of mechanical properties

Techniques available for assessing the mechanical properties of concrete in situ include surface hardness tests; 'near-to-surface' tests such as internal fracture, pull-out, pull-off, penetration resistance and break-off; and ultrasonic methods. Surface hardness is measured with a rebound or Schmidt hammer, and is covered by BS EN 12504-2:2001. This technique can assess the uniformity of concrete or estimate the compressive strength if a suitable correlation curve is generated by testing a number of core samples with a compressive strength testing machine. The results are influenced by factors including the type and proportion of the cement used, the type of aggregates, the way the concrete was cured and the moisture content of the surface.

The principle of the rebound hammer test is that a piston propelled by a spring strikes a hammer tip in contact with the surface and rebounds back up the shaft. As shown by Basu and Aydin [59]

$$\frac{x_2}{x_1} = \frac{V_2}{V_1} \quad \textbf{(2.1)}$$

where x_1 is the maximum stretch of the spring, x_2 is the maximum rebound position, V_1 is the velocity of the piston when firing and V_2 is the initial rebound velocity of the piston. This ratio expressed in percentage form is called the rebound number R_b

$$R_b = \frac{x_2}{x_1} \times 100 \quad \textbf{(2.2)}$$

Ultrasonic methods may be used to detect variations within the dynamic modulus of elasticity of the concrete, and again can provide semi-quantitative data if the equipment is calibrated. Ultrasonic Pulse Velocity (UPV) testing equipment used on concrete generally consists of two transducers which are placed a fixed distance apart on the surface of the concrete, preferably in a direct or semi-direct arrangement to allow the maximum amount of pulse energy to be transmitted [48]. An ultrasonic pulse passes from the transmitter in one transducer to the receiver in the other, and the travelling time of the pulse is displayed. The velocity V of the pulse travelling in an elastic solid depends upon the density and elastic properties, and provided that the smallest lateral dimension is greater than the pulse wavelength

$$V = \frac{x}{t} \text{ and } V = \sqrt{\frac{E_d}{\rho} \frac{(1-\nu)}{(1+\nu)(1-2\nu)}} \quad \textbf{(2.3 and 2.4)}$$

where x is the distance between the transducers, t is the travelling time of the pulse, E_d is the dynamic modulus of elasticity, ρ is the density and ν is the dynamic Poisson's ratio [48]. Since 'ρ and ν will vary little for mixes with natural aggregates', V is mainly dependent on E_d. The pulse velocity is also affected by the presence of rebars, the moisture content of the concrete and the presence of cracks and voids [60]. UPV is often used in combination with other techniques, for example in the SonReb technique which combines rebound hammer and UPV readings.

2.6.4 Strain measurement

Strain measurement may be undertaken to investigate mechanical movement such as crack growth and static and dynamic fatigues [14]. Several techniques exist to

measure strain within building structures, of which the simplest are mechanical. In the mechanical method described by Bungey and Millard [48], metal studs are attached to the concrete surface a fixed distance apart along the line of strain measurement, and the distance between the studs is measured using a hand-held dial gauge. This method was used at NMOF because it is cheap and simple, but taking readings is labour-intensive and potentially subject to operator error. A similar set-up with electrical resistance strain gauges allows the measurements to be recorded by an electronic data-logger. Other more complex techniques suitable for measuring over small distances include acoustic methods and inductive displacement transducers.

2.7 Sampling

When as much information as possible has been gained from the visual inspection and non-destructive testing, destructive tests may be considered necessary. The number of samples taken should ideally be sufficient to allow 'statistical evaluation techniques to be applied with a high level of confidence' [61], and guidelines for the appropriate size of cores are often given [5]. However, any removal of fabric from a historic building results in 'known and potential' losses [42], and the sampling programme must be planned carefully to obtain the maximum amount of information from a minimum number and size of samples. Leaving historic considerations aside, the taking of large numbers of samples is often not possible in practice because of access restrictions, limited resources and the need to preserve the structural integrity of the building. Any sampling from Scheduled Historic Monuments in the UK requires Scheduled Monument Consent from English Heritage or Historic Scotland.

2.8 Petrographic examination

A considerable amount of petrography was undertaken using the samples from NMOF. The samples taken should initially be examined with the naked eye and at low magnification. Various features such as the size and colour of aggregate particles or inclusions and voids and any evidence of deterioration can be noted, and for renders the presence of separate layers may be visible. The colour of the sample can be measured with a colourimeter or assigned a value using a colour classification system such as the Munsell colour system [62]; and the hardness of the samples can be assessed using a scale such as that developed by Ingham and based on Mohs'

Scale of Hardness [63]. Examination at high magnification may follow, for which samples are generally mounted as thin sections using the techniques developed by geologists for rock samples and described by St.John et al. [64]. It is important that concrete and mortar samples are ground using oil or alcohol rather than water, since water can damage some components of the material.

As there is not a British or European standard for the petrographic examination of concrete, ASTM C856 for concrete or ASTM C1324 for mortar are often followed. Thin section specimens are usually examined in plane polarized or cross polarized transmitted light, and fluorescent dyes may be added to the consolidating resin to highlight pores and cracks when the specimen is viewed using a strong light source and an excitation filter. Additionally, compensator plates may be used to investigate particular optical properties. Highly polished specimens may also be examined in reflected light, which is useful for opaque minerals and cements.

The kind of information which can be obtained from the petrographic examination of concrete thin sections is summarised in a publication by the Concrete Society [65]. The composition of the binder and aggregate are of interest because they may influence the working properties and performance characteristics of the concrete, and petrography can identify the aggregate type, the rocks present within the aggregate, including any potentially deleterious minerals, and other additions such as fly ash. It can establish the type of cement clinker used and the size, distribution and abundance of phases in the cement paste. It is also possible to estimate the original water/cement ratio of the mix. The condition of the concrete can be gauged, and from the study of crack patterns, chemical alteration and secondary mineral deposits, the causes of deterioration may be diagnosed.

2.8.1 Aggregates

The identification of the type of aggregate is usually possible. The aggregate may be natural or artificial, and types of aggregates often found in historic mortars include natural gravel, crushed rock, sharp pit sand and rounded river sand. The aggregate grading may be classified as uniformly graded/very well sorted, moderately well graded/well sorted, well graded/moderately sorted and poorly graded/poorly sorted. The aggregate particle shape and surface texture may be described using a standard chart as given by Fookes et al. [66], and additional terms for surface texture

suggested by the Concrete Society [65] include glassy, smooth, granular, rough, crystalline, honeycombed and porous. Ingham [63] defines terms for classifying the size and abundance of particles, with size ranging from small (<20 μm) to very large (>100 μm) and relative abundance ranging from rare to abundant.

If possible each type of rock present within the aggregate should be identified mineralogically and reference images may be found in standard geological texts [67, 68, 69]. The colour, relative hardness and degree of alteration or weathering of the rocks should be described. It is also suggested that the alkali-reactivity of the aggregate should be classified as low, normal or high, depending on the percentage of mineral constituents with high reactivity potential, and reference tables for the alkali-reactivity classification of various aggregates are available [65]. Other minerals which may affect the durability of the mortar should be identified: for example, pyrite may undergo oxidation reactions to form gypsum, with an accompanying increase in volume which may cause extensive cracking.

2.8.2 Cement matrix and pore network

In thin section the hardened Portland cement matrix of un-carbonated concrete or mortar consists mainly of 'essentially amorphous and isotropic hydrated calcium silicate gel C-S-H…also referred to as 'tobermornite gel'' [63]. Many cement hydrate compounds are too finely crystalline to be visible during petrographic examination, but C-S-H may be identified and portlandite is usually evident, occurring as distinctive brightly coloured crystals when viewed in cross-polarized transmitted light. Residual grains of unhydrated or partially hydrated clinker which appear as clusters of spheres may also be visible. These grains are composed of alite, belite and other clinker constituents, and can be used to identify the cement type. In modern, finely-ground cement they are smaller than 20 μm, whereas in older cement they may be larger than 100 μm. With reinforced concrete it is important to know whether the calcium hydroxide present initially in the binder has carbonated, because this increases the likelihood of corrosion of the steel reinforcements, and the extent of carbonation may be ascertained from the colour of the cement paste. Un-carbonated cement paste appears dark brown, whereas fully carbonated paste contains clumps of calcite crystals, which are extremely birefringent and give the paste a lighter, golden brown colour.

The initial water content of the concrete or mortar can be estimated using petrography, because as the water content increases the hardened cement paste demonstrates higher microporosity, fewer residual unhydrated cement grains and more portlandite crystallites. From assessing these factors it is possible to classify the initial water content as low, medium or high, and if greater accuracy is required the sample can be compared to reference specimens prepared with similar materials.

Petrography also provides information about the voids present in the concrete or mortar, which influence the freeze-thaw resistance of the material. Entrapped air voids incorporated during mixing are often larger than 1 mm and irregularly shaped and distributed, whereas entrained air voids are typically spherical and spaced at regular intervals. The degree of compaction can be obtained from an estimation of the excess voidage, which is the volume percentage of excess entrapped air voids if the specimen is compared to a fully compacted sample of the same concrete. Standard reference photographs have been published by the Concrete Society [70].

2.8.3 Mix proportions

The composition of a material viewed in thin section can be estimated in a number of ways, all of which require some simplifying assumptions to 'reconstruct mathematically the three-dimensional distribution' [18]. This is usually done to investigate the air content and other characteristics of the air void system, but may also be used to estimate mix proportions by volume. The diameters of the air voids within a given two-dimensional space can be recorded, or the space can be intercepted by chords, using the linear traverse method described in ASTM C457/C457M-11 and BS-EN 480-11:2005. The ASTM standard also details the modified point count method, in which the composition of the concrete at a number of regularly distributed points is determined either by a human operator or by computer-assisted image analysis. The use of software is only possible when the phases to be differentiated between have sufficient visual differences.

2.8.4 Workmanship

The composition of the material may be required to check its compliance with the specified mix proportions, and other workmanship issues that can be assessed include the adequacy of mixing and the effectiveness of placing, compaction, curing

and finishing [65]. Inadequate mixing and placing may lead to segregation, whereby the coarse aggregate moves towards the bottom of the form, or the mix water and fines bleed upwards towards the surface, resulting in the formation of highly microporous zones and bleeding channels. Bleeding is exacerbated if moisture loss from the surface is not controlled during the curing process, and low temperatures during curing can lead to reduced concrete strength and durability, while high temperatures can cause thermal cracking and delayed ettringite formation.

2.8.5 Deterioration

If the concrete has deteriorated this is usually visible in the thin section, along with clues as to the causes of deterioration. It is important to establish whether the deterioration is caused by an internal reaction which could affect all of the concrete, or whether it is extrinsic, in which case it should be most severe at the outer surface. Many forms of deterioration involve cracking, and the cause of deterioration may be identified from a description of the cracks. This should include their width, orientation and distribution; whether they occur within the aggregates or the cement paste; the presence and identity of crack infillings; and the appearance of the adjacent cement paste. For example, microcracks generated by drying shrinkage tend to meet at triple junctions in the paste, to run along aggregate surfaces and to initiate from voids, whereas cracks caused by freeze-thaw action or structural movement often run through aggregate particles as well as the cement paste. Cracks caused by corroding reinforcements may contain rust deposits, and cracks caused by internal sulfate attack, including delayed ettringite formation, will be filled with ettringite or gypsum [71].

Petrography is particularly valuable to detect alkali aggregate reactions (AAR), which are manifested externally by map cracking. In thin section the crack patterns are very distinctive, running through aggregate particles and often following the source of the reaction, and alkali-silica gel and signs of reaction in the aggregate particles will also be visible. Other types of deterioration visible may include flaking and scaling of the concrete surface, surface pitting due to ‘pop-outs’ and leaching from the cement matrix. Surface scaling is often caused by salt crystallization, and it may be possible to identify the salts concerned, while pop-outs are cone-shaped holes made by expansive aggregate particles near to the concrete surface. Leaching occurs

if moisture is able to permeate through the concrete, and results in weakening of the cement matrix. It is detected by the depletion of portlandite in the cement matrix and the secondary deposition of portlandite within air voids and cracks, possibly with some leaching and secondary deposition of ettringite. Leaching solutions moving through the concrete can leave calcium carbonate deposits on the surface.

2.8.6 Bricks and render-brick bonds

Petrography may also be used to provide information about the composition and condition of bricks [63]. Under examination bricks typically appear as a matrix of brown fired clay with inclusions such as quartz, feldspar, mica and flint. The colour of the brick relates to the iron and calcium carbonate content of the raw materials and the oxygen levels in the kiln, and is not necessarily uniform. Black areas may result from inclusions of carbonaceous materials which create reducing conditions in the brick. The porosity can vary from 1-50% depending on the clay composition and the firing regime, and is mainly made up of large voids, with low microporosity. Causes of deterioration such as salt crystallization and frost action are usually visible.

For renders applied over bricks the quality of the bond may be assessed. Derluyn et al. [72] found that the appearance of the render-brick interface depended on whether the bricks had been pre-wet. In renders applied to dry bricks, air voids were visible along the edge of the render, resulting from the rapid extraction of water from the render by the bricks. A similar observation was made by Brocken at al. [73] who estimated that only 20-30% of the surface area of the cured mortar was in good contact with the brick.

2.9 Chemical composition

The information about composition obtained using petrography may be complimented by other types of analysis. For example, besides assessing the extent of carbonation of the cement matrix petrographically, a staining technique with phenolphthalein indicator may be used, as described in BS EN 14630:2006. The calcium hydroxide in cement which has not fully carbonated results in a pH above 9, but once all the calcium hydroxide has been converted to calcium carbonate the pH falls below 9. Phenolphthalein turns purple at pH levels above 9. This technique cannot easily show which areas are partially carbonated [74], and more accurate

information about the extent of carbonation can be obtained using a variety of indicators to map pH [75].

Other techniques relating primarily to the chemical composition of binders are given in BS 4551:2005 and summarised elsewhere [4, 76, 77, 78]. For cementitious mortars, the binder:aggregate ratio can be determined by dissolving the binder in a strong acid, usually hydrochloric acid, and drying and weighing the aggregate that remains, providing it does not contain any soluble components such as limestone aggregate or calcareous clays [79]. In order to determine the relative proportions of lime and cement it is also necessary to measure the soluble silica content using a combustion technique or a colorimetric method. The total cement content is calculated from the soluble silica content, and any excess calcium oxide can then be attributed to lime [80]. These methods generate percentages of silica (SiO_2) and calcium oxide (CaO), which must be converted into raw material ratios using various assumptions. A variation on the acid digestion technique involves calculating the carbonate content of the mortar from the volume of carbon dioxide released during acid digestion [81].

Wet chemical analysis may also be used to ascertain the concentrations of other elements and ions, including sulphur trioxide (SO_3), iron oxide (Fe_2O_3), aluminium oxide (Al_2O_3), magnesium oxide (MgO), sulfate ions (SO_4^{2-}) and chloride ions (Cl^-). The presence of chloride ions is of particular interest for reinforced concrete because chloride ions in sufficiently high concentrations cause the corrosion of steel reinforcements. Often a profile of the chlorides with depth is required, in which case a core sample may be cut into slices of known depth from the surface or drilled samples may be taken in fixed increments. Chloride content is usually determined in the laboratory using a titration method, but can also be measured in the field using indicator strips or a field electrode. The acid-soluble chloride content is generally obtained, but there has been some discussion as to whether this is appropriate, given that only the ‘free chlorides’ which are soluble in water can contribute to the corrosion process. However, it is very difficult to measure the water-soluble chloride content reproducibly, so the acid-soluble content is still generally preferred, and since the threshold values required for corrosion to occur are based on total chloride levels, ‘the system is at least self consistent’ [19].

Instrumental techniques provide an alternative to wet chemistry. The water soluble content of common anions and cations can be measured using techniques such as ion chromatography (IC) and inductively coupled plasma – optical emission spectrometry (ICP-OES) [82]. Solid or crushed samples can be investigated using scanning electron microscopy with X-ray analysis (SEM-EDX) and X-ray diffraction (XRD). SEM-EDX allows samples to be viewed at higher magnification than with an optical microscope and is useful for 'characterisation of morphologies and textural and compositional interrelationships of mortar components' [4]. It can also provide elemental analysis at any user-determined point within the mortar. Calculations can be performed using the elemental analysis to identify the minerals present.

SEM-EDX and XRD can provide information about the chemical composition of the aggregate, and other tests for the geometrical properties of the aggregate are given in BS EN 933, which was published in 11 parts between 1996 and 2012. It includes the determination of particle shape, assessment of surface characteristics, assessment of fines and determination of the particle size distribution using the sieving method. To be considered well-graded no more than 30-35% of the aggregate should be retained in any one sieve [83], and this improves the strength and resistance to cracking of the mortar. The shape of the aggregate particles is important because angular particle shapes produce stronger mortars, although they generally make the wet mortar less workable.

The methods of chemical analysis undertaken at NMOF were a simple acid extraction technique to measure the binder:aggregate ratios of the renders; sieving to determine the particle size distribution of the aggregates in the renders; ions analysis of aqueous solutions using IC and ICP-OES; and analysis of solid and crushed samples using SEM-EDX and XRD.

2.10 Strength testing

Besides being used for chemical analysis, the structural and hydraulic properties of the samples may be investigated. The structural properties of most interest in building materials are the compressive strength, tensile strength and modulus of elasticity. Compressive strength is required to predict the behaviour of structural elements, such as concrete walls and columns, while tensile strength may be useful to predict the behaviour of building components subjected to bending and stretching

forces, such as structural beams and buckling renders. The ability of mortars and renders to resist internal forces caused by expansive salts, ice formation and swelling clays is also dependent upon tensile strength. The modulus of elasticity shows to what extent a material is brittle or ductile. Standard test methods include BS EN 12390-3:2009 for the compressive strength of hardened concrete; BS EN 12390-6:2009 for the tensile splitting strength of hardened concrete; BS EN 196-1:2005 for the strength of cement, which covers mortars; and BS EN 772-1:2011 for the compressive strength of clay masonry units. Since BS EN 196-1:2005 is for cement mortars made freshly to specific criteria, it is not really applicable for historic mortars, and the concrete standards are more useful.

Samples of historic concrete or mortar used for strength testing are most likely to be cores, although cubes are also permitted for compressive strength testing. The required dimensions of the samples are specified in EN 12390-1, which states that the cores should have a minimum diameter of three and a half times the maximum size of the aggregate particles and a length to diameter ratio of not less than one. Bricks may be tested whole or cut into smaller pieces. It is often not possible to take cores from historic buildings, particularly for thin render layers, and an alternative may be to measure the flexural strength of a rectangular prism under three-point loading, in accordance with BS EN 12390-5:2009, and use this value to calculate the tensile strength. For concrete the tensile and compressive strengths are closely related and may be represented by formulae of the type

$$f_{ct} = k(f_c)^n \quad \textbf{(2.5)}$$

where f_{ct} and f_c are the tensile and compressive strengths respectively, and k and n are constants. The values of k=0.3 and n=2/3 suggested by Raphael [84] are often used.

The compressive strength of concrete is influenced by the water to cement ratio, the cement to aggregate ratio, properties of the aggregate such as the maximum size, grading, shape and strength of the particles, and the duration and conditions of the curing process [85]. For example, the compressive strength is generally increased by a reduced water to cement ratio or an increased cement to aggregate ratio. It is generally recognised that modern cementitous materials have higher compressive strength than those used historically, because modern Portland cements are higher in tricalcium silicate and more finely ground. Accurate data on the strength of historic

cements is not available because of changes in test methods, but it has been estimated that modern cements are around three times as strong as those used in the 1930s [30]. However, the strength of some historic concretes may have increased as they have aged, as was found for the Hoover dam, constructed in 1931-36 [86]. The compressive strength of modern concrete is typically 42-49 MPa [87].

The tensile strength of historic mortars has been measured to assess how they respond to the dynamic stresses caused by earthquakes or soil movement [88], or to investigate the strength of the bond between two different materials such as a cement render and masonry substrate [89]. The tensile strength of concrete made with modern Portland cement and a range of aggregates has been found to vary from 3.7-4.5 MPa [90], and the value for historic concrete would again be expected to be significantly below this.

The compressive strength of modern clay bricks is comparable to that of modern concrete: values quoted include 56 MPa for an extruded brick [91] and 55 MPa for a grey pressed brick [92]. The method of sampling is important: Krakowiak et al. [91] found that the highest strength was ‘along the axis aligned with the direction of extrusion’ and Zsembery et al. [92] measured considerably higher compressive strength for a whole brick sample than for smaller samples. Historic clay bricks are typically less strong, and in a study of historic bricks in Portugal the maximum compressive strength measured was 21.8 MPa for eighteenth/nineteenth century bricks [93]. Values reported for the modulus of elasticity of building materials include 6165 MPa for cement mortar [94] and 2000-12 700 MPa for clay bricks [91].

The samples from NMOF were subjected to a three-point bending test, from which the tensile strength and modulus of elasticity were calculated.

2.11 Density and porosity

The density and porosity of building materials are usually related. The porosity describes the fraction of pores and voids in the material, and is useful because it gives an indication of the ease with which liquids and gases will permeate through the material. Higher porosity concrete will carbonate more rapidly, because it is easier for carbon dioxide and water to penetrate through the concrete. For cement mortars and concrete, the porosity is increased by a low cement content or high water

to cement ratio [45]. The curing conditions are important, because if the mortar is in contact with an absorbent material, such as brick, this will absorb some of the water and reduce the final porosity [72]**.** The shape and particle size range of the aggregate also affect the porosity of the mortar, since sharp, angular particles and particles with a wide size range can pack most efficiently, resulting in lower porosity [83]. The porosity can be increased by the addition of air-entraining agents, typically industrial soaps and foaming agents, which if used correctly create a system of regularly spaced air voids and improve the freeze-thaw resistance of the material [18].

Density is often measured alongside porosity, and is of particular importance in situations where a lightweight building material is required. The density of cementitious materials can be reduced through the use of lightweight aggregates, such as pumice, expanded clay and glass microspheres, or by adding air-entraining agents to increase the porosity. Autoclaved aerated concrete (AAC) is a special lightweight concrete, in which the reaction between aluminium powder , calcium hydroxide and water produces hydrogen gas and creates very high porosity [95]. Clay bricks may be perforated to reduce their density.

The density of a building material is calculated from the dry mass of the sample and its volume. There are two measures of porosity: the open porosity, which is the total volume of pore space within the material and the effective or capillary porosity, which is the volume of pore space filled by the capillary uptake of water, and hence less than the open porosity [72]. To measure the open porosity the dried sample must be filled with water using a vacuum saturation technique, whereas for effective porosity the sample is stood in a shallow dish of water until it reaches a steady mass. The porosity is calculated from the mass of the water absorbed by the sample, the density of water and the volume of the sample. It has been found that porosity may increase with higher drying temperatures, probably due to internal cracking, and so it is important that the drying temperature is specified [86]. The open porosity may also be obtained using mercury intrusion porosimetry (MIP), but it tends to underestimate the porosity of cementitous materials because the detection limit is above the size of the smaller gel pores [97].

The porosity of a cementitious mortar or concrete containing only cement, aggregate and water is around 25-30%, depending on the mix proportions [98, 99].

For mortars cured in contact with an absorbent material, the porosity may be reduced to as little as 14% [72], and concretes containing super-plasticizers may have porosity as low as 10% [96]. The porosities reported for clay bricks from the eighteenth and nineteenth centuries range from 27% upwards [93, 100], but modern bricks are typically less porous.

The density and open and effective porosities were measured for the NMOF samples.

2.12 Sorptivity

The water suction of building materials is an important property because it controls the rate at which water moves through structures, and the likelihood of moisture-related deterioration occurring. Water suction may be quantified by measuring sorptivity, which is defined as 'the property which expresses the tendency of a material to absorb and transmit water and other liquids by capillarity' [101], and is given by the relationship

$$i(t) = t^{1/2} \int_{\theta_0}^{\theta_s} \phi(\theta) d\theta = St^{1/2} \qquad \textbf{(2.6)}$$

where $i(t)$ is the total volume of liquid taken into the material by capillary absorption at time t, θ_0 and θ_s are the initial and final liquid contents, S is the sorptivity, and ϕ is a function of x and t given by

$$\phi = xt^{-1/2} \qquad \textbf{(2.7)}$$

where x is the location of the wetting front within the material. The sorptivity has been shown to depend upon the properties of the liquid being absorbed, namely surface tension, viscosity and density; the temperature, in that it affects the properties of the liquid being absorbed; and the properties of the absorbent material [101]. The material properties of particular relevance are the porosity and pore size distribution. Sorptivity is generally expected to increase with increasing porosity or average pore size [72], although it is suggested that the capillary pores also 'have a major effect on transport processes' [97]. For bricks the sorptivity may depend on the orientation and location of the sample within the brick, and this is discussed further in Chapter 7.

To calculate sorptivity the mass change of regular samples over time due to the capillary uptake of water or another liquid is required. The sorptivity of a mortar made with three parts sand to one part cement has been reported as 0.34 mm/min^{½} [98], while the sorptivities of clay bricks fall within the range of 0.32-2.72 mm/min^{½}, depending on the composition and method of manufacture [102]. The sorptivity of a substrate material, such as brick, influences the extent of pre-wetting required to achieve a good bond with an applied render: a material with high sorptivity requires extensive pre-wetting, because it will otherwise extract too much water from the render, whereas a virtually impermeable substrate should not be pre-wet at all. Sorptivity was therefore an important parameter to measure for the NMOF samples.

2.13 Pore size distribution

The pore size distribution is worthy of investigation because it influences the sorptivity and the freeze-thaw durability of the material, as discussed further in Chapters 6 and 8. The parameters of interest in discussing pore size distribution are the median pore diameter, which is the diameter for which 50% of the pores is greater and 50% is smaller, and the mode pore diameter, also called the critical pore size or the maximum continuous pore radius. It is the most common pore size within the interconnecting pores, and represents the point at which mercury can penetrate easily through the material. Some materials have a second and larger critical pore size, which 'appears to correspond to the pressure required to break through blockages in the capillary pore network' [97]. A further parameter is the threshold diameter, the diameter above which there is comparatively little mercury intrusion. It has been found that the threshold diameter influences the permeability of cementitious materials more than the total porosity [103]. It is also useful to consider the distribution of pores within different size intervals, and various systems for size classification exist, such as that proposed by Mindess et al. [104].

There are many techniques for measuring pore size distribution, including gas adsorption, nuclear magnetic resonance and stereology. Mercury intrusion porosimetry (MIP) was used for the samples from NMOF and is discussed in further detail here, although it relies upon 'many assumptions that are not necessarily all valid in hardened cement paste' [18].

A mercury intrusion porosimeter forces mercury into the pores of the test material. As the pressure applied increases, so the pores filled become progressively smaller. For a machine working in incremental mode the intruded volume of mercury is recorded at each particular pressure, generating a pressurization curve. The readings of intruded volume can be normalized in a number of ways, for example by dividing by the specimen mass or the specimen bulk volume. The pressure values can be converted into equivalent pore sizes using the equation derived by Washburn in 1921, from Young and Laplace's work on interfacial tension for the rise or depression of liquids in capillaries [97]

$$r_p = \frac{-2\gamma_m \cos\theta}{P} \qquad \textbf{(2.8)}$$

where r_p is the pore radius, γ_m is the surface tension between mercury and the pore wall, θ is the contact angle between mercury and the pore wall and P is the pressure applied on mercury to intrude the pores. This equation assumes a circular cross section for the pores. The surface tension and the contact angle depend on several factors, but are typically taken as 0.485 N/m and 130-140 º respectively.

The curves commonly plotted using the MIP data include the cumulative intruded volume curve (cumulative intrusion in mL/g against pore diameter in microns), the cumulative porosity curve (cumulative porosity in % against pore diameter in microns) and the differential pore size distribution (dV/d(log d) in mL/g). From the cumulative intruded volume curve the total surface area of pores filled by mercury can be calculated as the area under the graph, and the surface area of pores within a particular size interval can be calculated graphically or by numerical methods. The cumulative porosity curve can be used to determine the pore volume within a particular size interval, the median pore diameter and the mode pore diameter, which is the region of steepest slope. The differential pore size distribution curve often shows the mode pore diameter more clearly.

An investigation of the pore size distribution in a render should also consider the pore size distribution in the substrate material. For example, bricks have very different pore systems from mortars, with a higher average pore size and fewer small capillaries, and this can create a resistance at the interface between the two materials [18].

2.14 Drying behaviour

The movement of water through buildings is controlled by the rate at which they dry out as well as the rate at which they absorb water. This property is particularly important in situations where freeze-thaw cycling may occur, because materials which dry out quickly are less prone to being damaged by freeze-thaw, since they quickly reach a moisture content below the threshold required for damage [105]. When a material dries out the drying process occurs in two stages, 'often called the constant drying rate period (stage I) and the falling drying rate period (stage II)' [101]. During stage I water moves in liquid form through the interconnected pores of the material, and evaporates at the surface. The rate of mass loss is constant and should be similar to the rate of evaporation from a free water surface, provided the conditions are the same. Stage I ends when the moisture content of the material reaches the critical saturation level, and thereafter the material enters stage II of the drying process. Water moves through the material by diffusion and the drying rate gradually decreases.

The three key parameters to be measured as discussed by Rousset-Tournier [106] are the initial drying rate, the moisture content at the critical saturation level, given as a percentage of the moisture content at saturation, and the time taken to reach the critical saturation point. If samples of different lengths are being tested, it is useful to compare the time taken to reach the critical saturation point per unit length of the sample. The stage I drying rate depends on the factors which control the rate of evaporation from the pores, such as the temperature, Relative Humidity and rate of air movement. It is generally assumed to be similar for all porous materials, but since evaporation only occurs from small pores at low RH values [18], if the drying rate is measured at high RH it could conceivably be lower for fine-pored materials.

The critical saturation level and the time taken to reach it vary considerably depending on the pore structure of the material. Materials containing large pores, such as some bricks, are generally expected to dry out quickly [98], meaning that a large proportion of the moisture content should be lost during stage I drying, whereas fine-pored materials such as cement mortars appear to remain at high moisture contents for longer.

The drying behaviour was measured for some of the NMOF samples.

2.15 Environmental monitoring

A further key component of the investigations around a particular building may be environmental monitoring, which is relevant because most forms of deterioration are affected by the environment [72] and because knowledge of environmental parameters allows the movement of moisture through structures to be modelled [107]. Temperature and relative humidity (RH) can be monitored very cheaply and easily using stand-alone dataloggers or telemetric monitoring systems, while a weather station allows additional parameters such as absolute pressure, rainfall, wind speed and direction and solar radiation to be monitored. The data has many uses: driving rain may be calculated from the rainfall and wind speed and direction, to establish which elevations of a building are wetted most frequently by rainfall [108] and the growth of algae and fungi on a wall surface may be related to several environmental parameters, including the frequency and intensity of solar radiation [109].

The period of time for which a wall surface remains wet (time of wetness) may be monitored to assist in a diagnosis of the causes of damp, because dampness in an external wall that appears to result from rainwater penetration may in fact be due to condensation occurring for prolonged periods [110]. Time of wetness can be monitored using miniature moisture sensors [111], or the likelihood of condensation occurring may be predicted using the dew point temperature of the air and the surface temperature of the wall surface [112]. The dew point temperature is calculated from the air temperature and RH, using an equation of the form

$$T_{dp} = \frac{\lambda\left[\ln\left(\frac{R}{100}\right)+\left(\frac{\beta T_a}{\lambda+T_a}\right)\right]}{\beta-\left[\ln\left(\frac{R}{100}\right)+\left(\frac{\beta T_a}{\lambda+T_a}\right)\right]} \qquad \textbf{(2.9)}$$

where T_{dp} is the dew point temperature, T_a is the air temperature, R is the relative humidity and β and λ are Magnus parameters given by β=17.62 and λ=243.12 °C [113]. The dew point temperature is subtracted from the measured surface temperature and plotted against time, and if the value approaches zero, there is a strong likelihood of condensation.

Other environmental parameters include the soil moisture content and potential evaporation rate; they are monitored less frequently, but are useful if moisture movement is to be modelled. The potential evaporation rate depends on various environmental parameters, and may be calculated using the Penman-Monteith equation [114]

$$PE = \frac{0.408\Delta R_n + \gamma\left(\frac{900}{T_a + 273}\right)u(e_s - e_a)}{\Delta + \gamma(1 + 0.34u)} \quad \textbf{(2.10)}$$

where PE is the potential evaporation in mm/day, R_n is the net radiation in MJ/m^2/day, T_a is the air temperature in °C, u is the wind speed in m/s, e_s is the saturation vapour pressure in kPa, e_a is the actual vapour pressure in kPa, Δ is the slope of the saturated vapour pressure-temperature curve in kPa/°C and γ is the psychrometric constant in KPa/°C. However, this equation requires various assumptions to be made and several parameters to be measured [115] and an alternative may be to measure the evaporation rate directly using an evaporimeter or atmometer [116].

The environmental parameters monitored for this research as described in Chapter 4 were temperature and relative humidity with a telemetric monitoring system and dataloggers; wind speed, rainfall and other weather parameters with a weather station; internal and external evaporation rates with an evaporimeter; and soil moisture content with a soil moisture sensor.

2.16 Modelling moisture movement through porous building materials

'Comparatively simple mathematical descriptions' of wetting processes can be obtained using a sharp front model, where it is assumed that the wetted region of the material has a uniform and constant water content approaching the saturation water content, and can be represented by a rectangular profile [101]. A sharp front model is used by Hall et al. [107] to show that in a wall where rising damp has stabilized, such that the rate of water absorption at the base of the wall is equivalent to the rate of evaporation from the wall surface, the height of rise h_{ss} may be given by

$$h_{ss} = S\left(\frac{b}{Ne\theta_w}\right)^{1/2} \quad \textbf{(2.11)}$$

where S is the sorptivity of the building material, b is the thickness of the wall, N is the number of surfaces through which evaporation occurs, so that for a two-dimensional model N=1 or N=2, e is the evaporation rate and θ_w is the volume fraction water content of the wetted region. θ_w lies somewhere between the capillary moisture content of the material and the absolute moisture content, often give by f. It is suggested by Hall and Hoff [117] that a value for θ_w of 0.85f should be assumed for short-term processes, but that in walls subject to long-term rising damp, θ_w approaches f. In a structure containing several different materials, an averaged or composite sorptivity may be used.

In the case where a steady height of rise has not been reached and more water is being absorbed than is being lost due to evaporation, it is shown by Hall and Hoff [117] that the height of rise h at time t is given by

$$h^2 = \frac{c}{a}\left[1-\exp\left(-2at\right)\right] \quad \textbf{(2.12)}$$

where $a = e/\theta_w b$ and $c = S^2/2\theta_w^2$. Hence if the wall is initially dry it reaches a steady state of rising damp where $h = h_{ss}$ in a time $t_{95} = 3b\theta_w/2e$. The sharp front model can be modified to take gravitational drainage into account, but it has been demonstrated that gravity has only a minor effect on the rate of rise and the steady state height of rise.

The simplest sharp front model assumes a constant rate of evaporation, whereas in practice the evaporation rate is variable. A sharp front capillary rise model with time-dependent evaporation conditions has been developed by Hall et al. [107], and the results obtained were compared to the results from a full finite-element unsaturated flow model, built on the Buckingham-Richards equation. The calculations for the unsaturated flow model were undertaken with HYDRUS (2D/3D), which is a finite-element program. It was found that the agreement between the two models was good, and that they provided an explanation for phenomena observed in real walls, such as the seasonal rise and fall of the wet front. The use of a simple sharp front model for the buildings at NMOF is described in Chapter 8.

3.1 History of East Fortune airfield

3.1.1 Introduction

East Fortune is a hamlet in East Lothian, Scotland, surrounded by rolling agricultural land and located approximately five miles from the sea. It lies 18 miles to the east of Edinburgh. The establishment and development of the airfield at East Fortune occurred in several short phases, to meet military requirements, and the airfield buildings were erected hurriedly and envisioned as temporary structures.

Despite some losses and the unexceptional nature of the buildings at East Fortune airfield, the site is significant because it constitutes 'the best preserved collection of airfield technical site buildings on probably the most complete Second World War temporary airfield in Britain' [118]. It is generally accepted that 'the identification of...important sites...[constitutes] the most effective method of protecting building types which are otherwise well represented in other, more altered or less significant, contexts' [119]. In 1990 Historic Scotland gave a category B listing to the air control tower, the four hangars and three of the brick masonry buildings: Building 27 (the Parachute Store), Building 28 (the Metal Workshop) and Building 39 (Administration for Hangar 4). The entire East Fortune aerodrome site was then scheduled as a Historic Monument in 1991. These measures protect the site because East Lothian District Council would have to give Listed Building Consent for any major alterations to the listed buildings, and Historic Scotland would have to give Scheduled Monument Consent for all alterations to and developments of the site.

3.1.2 Phases of development

A Royal Naval Air Station was first established at East Fortune in 1915, to house both airships and aircraft. The main buildings in place by the end of the war were three large aeroplane sheds and eight hangars, in addition to three airship hangars and some ancillary buildings to the north of the main site [120]. The station began to wind down from the beginning of 1919, and it was closed in 1920. The airship and aircraft sheds were dismantled, and the land and buildings to the north were sold off to become a sanatorium.

There is little documented about the history of the airfield between the wars. In 1940 the airfield was requisitioned for military use and a rapid programme of building took place, including new taxiways, runways, hangars and technical and domestic buildings, to bring the station up to the specifications of an RAF type A airfield. It functioned as an RAF Operational Training Unit, preparing pilots for night and anti-shipping operations, and at one time over two thousand servicemen and women lived there. More space was required when Mosquito aircraft arrived at the station at the beginning of 1944, and so five blister hangars, a T2 hangar and a fuel store were constructed.

Following the end of the Second World War in 1945 the station became quieter, and the RAF withdrew completely in 1946. The buildings dating from the First World War were returned to the Sanatorium Board, and the other buildings continued to support a small scale commercial airfield until 1961. They were then used for storage by the Ministry of Agriculture, Fisheries and Food. In 1971 National Museums Scotland (NMS) acquired a spitfire aeroplane and stored it in one of the airfield buildings, and the decision to establish a National Museum of Flight (NMOF) was taken thereafter, with a grand opening to the public on 7 July 1975 [121]. NMS introduced the numbering system for the buildings which is referred to in this research.

3.1.3 The present buildings

The buildings remaining within the NMOF site include four hangars, four Nissen huts, 11 brick blast shelters, a reinforced concrete air raid shelter and around 23 cement-rendered brick masonry buildings (Fig. 3.1). To the north of the site just outside the NMOF boundary is the air control tower (Fig. 3.2), and to the south west of the site at Athestaneford Mains there is a cluster of buildings which were constructed for use as an emergency hospital in the event of the main site being attacked, and are now used as farm stores (Fig. 3.3). Not all of the Second World War buildings from the site survive. Black and white photographs show a cluster of buildings at the west end of the site which were demolished at an unknown date (Fig. 3.4), and Building 33 (the Hangar Two Annexe, Fig. 3.5) was only demolished in 1992, being considered in too poor a condition to repair.

The airfield buildings followed the standard designs given in a series of drawings produced by the Ministry of Defence, and were virtually identical to military buildings elsewhere in the UK [122, 123]. The brick masonry buildings belong to the category of 'half-brick huts', so-called because the walls were constructed from a single skin of bricks, and so were effectively half a brick thick. They were generally based on drawing numbers 222/40, 223/40 and 3323/40, where 'huts were built with external brick piers at 10 ft centres', and were erected in spans of 18 ft and 28 ft, chosen to best accommodate furniture. The wall heights varied depending on the function of the building. Drawings were also available for buildings with very specific functions, for example Building 36 at NMOF (the Night Flying Equipment store, Fig. 3.6) is a three-bay garage with double doors, built to drawing number 173831/40.

The air raid shelter at NMOF (Fig. 3.7) is the only reinforced concrete structure now standing within the designated site, although there is a similar shelter on the farmland to the east. As discussed by Griffin and Tate [9], a roofed shelter was required at NMOF both to provide protection against the effect of a blast and the associated debris, and to resist the impact of a direct hit. The shelter is a Stanton shelter, so called because it was manufactured by the Stanton Ironworks Company Limited in Derbyshire [124]. This company 'promoted the ease of transportation and handling of their shelters, which made them suitable for sites which could not be accessed by lorry' [9]. The shelters were constructed from pre-cast reinforced concrete sections, which were erected on site by companies including Geo, Wimpey, Mowlem and Tarmac. The sections were assembled in pairs to form arches and bolted together at the apex of each arch, with further bolts and a bituminous sealing compound used to fix each section to those on either side of it [125]. A standard shelter was 18 sections long and housed 50 men. The floor could be concrete or earthen, and most Stanton shelters were at least partially buried.

Fig. 3.1. Aerial view showing NMOF site (RCAHMS 1984)

Fig. 3.2. The air control tower to the north of NMOF

Fig. 3.3. One of the buildings in the emergency hospital complex at Athelstaneford Mains

Fig. 3.4. One of the buildings to the west of the current NMOF site, since demolished

Fig. 3.5. Building 33 (on the right of the picture), demolished in 1992

Fig. 3.6. Building 36 (The Night Flying Equipment Store), built to drawing number 173831/40 produced by the Ministry of Defence

Fig. 3.7. The reinforced concrete air raid shelter, which is the only reinforced concrete building within the NMOF site

3.2 Construction of the buildings

The buildings investigated for this research were the cement-rendered brick masonry buildings and the reinforced concrete air raid shelter. The construction and conservation history of the metal-clad hangars are therefore not included in this chapter.

3.2.1 Cement-rendered brick masonry buildings

The cement-rendered brick masonry buildings are simple box-like structures, with brick walls built in stretcher bond, a half brick thick (approximately 120 mm). Brick piers are built into the walls at approximately 3.3 m intervals, protruding both internally and externally. The buildings stand upon levelling plinths, which have brick exteriors and a rubble and concrete infill. The plinths project approximately 50 mm from the main line of the wall and are finished with a 'solid mortar skew with a triangulated profile' [26]. A thin cement render has been applied to the exterior walls, including over the piers but not the plinth bricks. Joins between sections of render are sometimes visible. For example, in the bays on the north side of Building 25, the render was applied in four horizontal bands (Fig. 3.8). In areas where the render has been damaged it is evident that it was sometimes applied in two layers, with hatching on the lower layer to ensure a good bond (Fig. 3.9).

The buildings have low-pitched roofs consisting of corrugated asbestos sheeting supported by internally exposed steel trusses. Ferrous ties are visible at the top of the gable end walls and probably function to tie the buildings together. The

external walls are pierced by timber doors and single-glazed cast metal windows, with concrete lintels above them (Fig. 3.10), and there are water-shedding mortar skews rather than window sills. There were originally no gutters or downpipes on the buildings and no drains at ground level, although rainwater disposal goods have subsequently been added to some of the buildings. Bituminous damp proof courses were laid one brick course above the plinth, but they are usually bridged by the external render (Fig. 3.11). There were no damp proof courses laid underneath the floors. Internally, the bricks were generally left bare-faced, although they have sometimes been painted, as have the solid concrete floors. There was originally no internal panelling under the asbestos roof sheets but this has been added in some buildings.

The building materials would probably have been sourced locally as much as possible, due to the constraints of building during war time. The bricks are easily identifiable because they are stamped with the name of the brickworks, all of which were in the Edinburgh area. Bricks from Edinburgh, Niddrie, Prestongrange and Whitehill can be identified in the brick masonry buildings and the brick blast shelters (Fig. 3.12). Additionally, Wallyford bricks were found on a heap of rubble from dismantled buildings, and may or may not have been used during the Second World War. The cement must have come up from England because there was no cement works in Scotland at the time [127].

Fig. 3.8. Detail of join between two areas of render on Building 25, N side, E bay, S elevation

Fig. 3.9. Hatched layer under top layer of render on Building 22

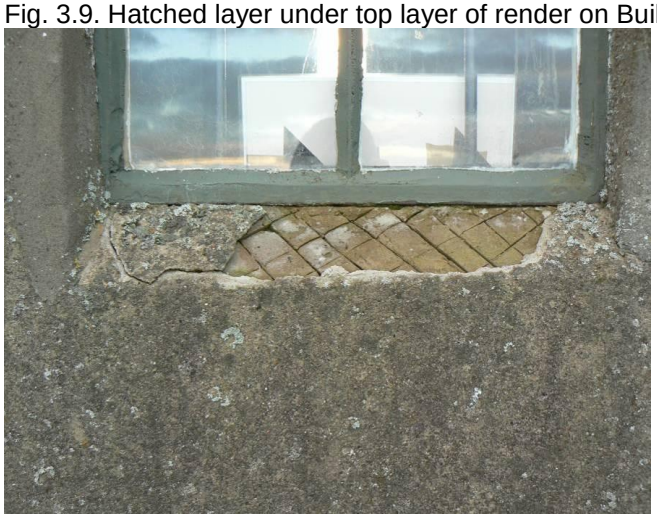

Fig. 3.10. Concrete lintel visible above window on Building 26, E elevation

Fig. 3.11. Visible damp proof course behind missing render on Building 22

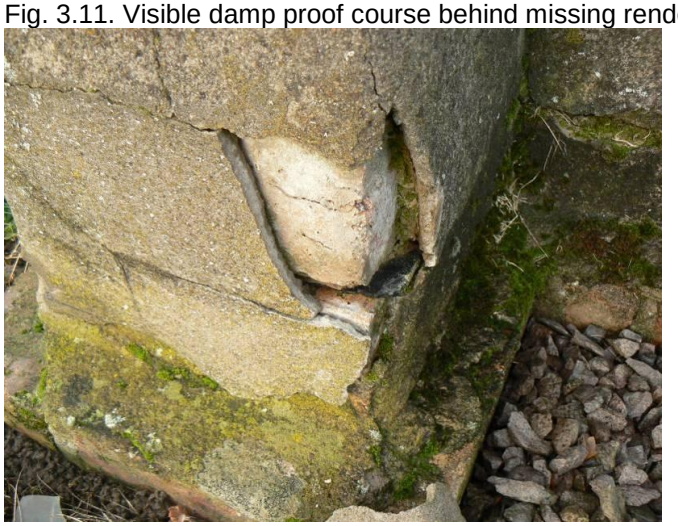

Fig. 3.12. Edinburgh and Niddrie bricks in a blast shelter

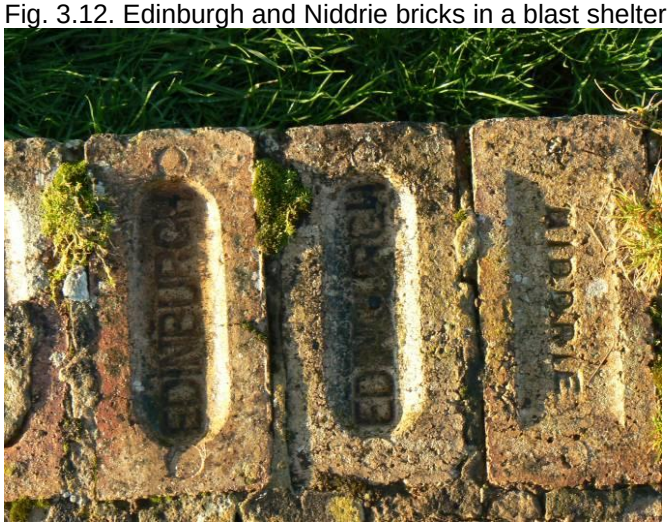

3.2.2 The air raid shelter

The shelter at the Museum of Flight is the standard 18 sections long (Fig. 3.13), and the floor plan is 8.7 m long and 1.8 m wide. Cementitious mortar is used to join the sections together, with bolts fixing the end walls to the long walls. The floor is not sunken, possibly because the site has a tendency towards flooding. There is an open doorway at each end, shielded by a section of brick walling, and the shelter is covered by a bank of earth which is approximately 0.1 m thick on top, widening to approximately 0.5 m thick at the base of the walls.

Fig. 3.13. The construction of the air raid shelter from curved concrete sections[1]

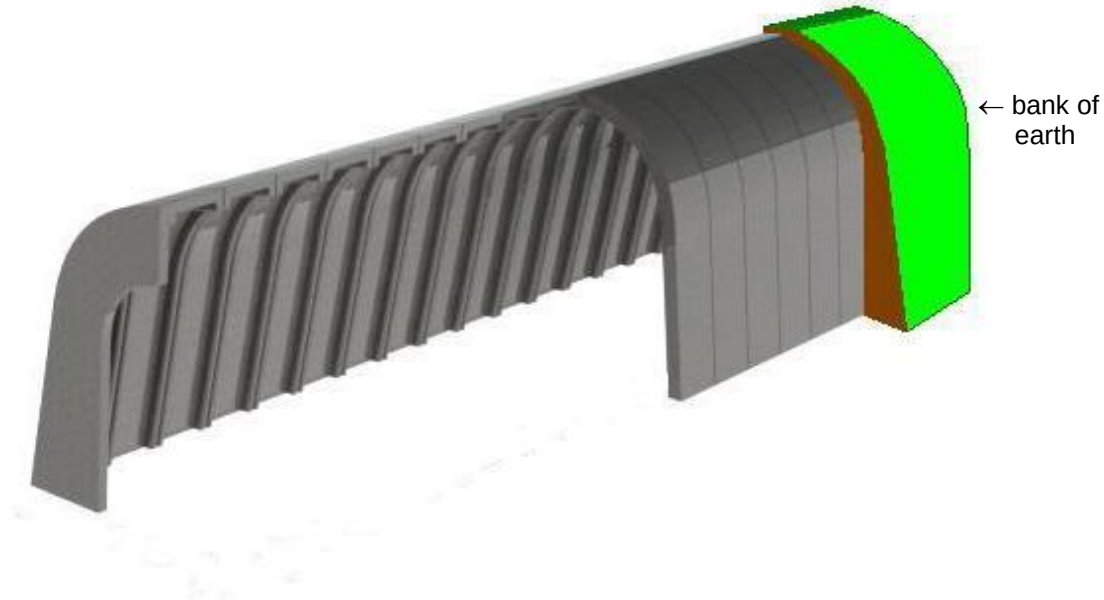

[1] This figure is adapted from Hercock [128].

3.3 Conservation history of the buildings

3.3.1 Conservation planning

The buildings were not part of a museum until 1975, and even then the site was not a Scheduled Historic Monument until 1991. Hence for the early life of the buildings the primary concern was to retain their functionality, and repair work was not documented in detail. This changed with the arrival of NMS, and information from the NMS archives from 1992 onwards was available for this research. The first major document obtained was the Buildings Development Strategy from 1992 [129]. It gave an overarching objective of developing the site 'around the theme of a World War II base', with proposals for how the buildings should be used and recommendations of the repairs required for each building, ranked from 'immediate priority for reasons of safety' to 'no later than 10 years'. The prioritisation also took into account the proposed uses of the buildings. Following on from this strategy Building 23 (the Electricity Sub Station) underwent extensive repairs, including the rebuilding of the upper half of the north east wall, for which the use of engineering bricks was specified; these are modern, low porosity bricks.

A key development in the history of NMOF was the introduction of a Concorde aeroplane into the museum in 2003. This involved modifications to Hangar 4 to accommodate Concorde, and was important because it increased interest and investment in NMOF.

In 2004 NMS commissioned Derek Carter Associates to write a detailed Conservation Plan, which assessed the condition of each building and gave it a conservation priority, based upon historical significance and state of repair [130]. It noted that many of the buildings had deteriorated since 1992, and suggested that a 'comprehensive programme of repair and consolidation' was needed. The aims of the conservation work were to repair previous and ongoing damage and deterioration, but also to upgrade the buildings to meet the requirements of current legislation and the uses intended by NMS. Specifications were given for the repairs required for each building, and typically included the repair of external roof and wall finishes and internal ceiling finishes, and the repair or replacement of windows and doors, with some extra works such as the installation of heating or dehumidification systems and security systems in order to make the buildings suitable for collections storage. There

was no mention of rainwater disposal goods. It was observed that the costs associated with conserving the airfield were massive, and that in order to consider applying to the Heritage Lottery Fund NMS would need to consider the 'heritage need...[of] the whole airfield', rather than focussing on the collections.

Following the writing of the Conservation Plan, Building 16 (Transport Building) and Building 25 (the Main Stores) underwent major programmes of repair and upgrading to prepare them for their new uses as a conservation workshop and a collections store. The work on Building 25 was informed by a report by the Scottish Lime Centre [126], consisting of a condition survey of the building and recommendations for how it should be repaired and subsequently maintained.

A strategic vision for NMOF was presented in the Development Plan in 2006 [131], which identified a wide range of objectives such as the creation of a 'world-class visitor attraction in East Lothian'. The objective relating to the buildings was to 'communicate the historical significance of the site through interpretation and ensure the long-term preservation of the buildings and the site'. The Development Plan recognised that many of the buildings had deteriorated due to inadequate maintenance, but that a programme to address the backlog had begun. It included detailed costs for repair works to Buildings 27, 28 and 45, and this work was completed by the end of 2009. Deteriorating road surfaces were upgraded in 2009 and site drainage was improved in 2010. The next priorities for major repairs have been identified as Buildings 31 and 32 (the Aero Instruments and Electronics Building and the Armoury), because they are large buildings which could potentially be opened to visitors[2].

3.3.2 Details of repair works on the brick masonry buildings

Early undocumented work on some of the brick masonry buildings included the fitting of internal roof panels inside some buildings and the installation of gutters and downpipes, which usually discharged onto the ground next to the buildings (Fig. 3.14). There are also numerous examples across the site of render patch repairs and crack fills, which would have been undertaken to keep the buildings watertight. The major programmes of repairs undertaken have included replacement of roofs;

[2] This was a personal comment from Stuart Baird in the Estates Department at NMS, 24 November 2009.

internal roof panelling; installation of heating and dehumidification; replacement of doors and windows; installation of rainwater goods; repointing of brickwork; and render repairs, including patch repairs, crack fills and grouting.

3.3.2.1 Roofs, environmental control, doors and windows and rainwater disposal goods

The approach for roof repairs set out in the Buildings Development Strategy was to replace the original corrugated asbestos roofs with a corrugated material of low asbestos content, to match details such as ridges and verges and to replace defective roof timbers. The strategy recommended a new roof for virtually every brick masonry building on the site, but in practice new roofs have only been given to buildings that have undergone major repairs (Fig. 3.15). The strategy also advocated lining the wall and roofs of the buildings with 'sheet insulation materials', and internal roof panels have been fitted to most buildings (Fig. 3.16), although wall linings were not permitted by Historic Scotland on the grounds that the painted brick appearance of the interior walls should be retained.

Improved environmental control was considered desirable to provide appropriate conditions for collections storage, although the Buildings Development Strategy suggested the building fabric might also benefit. The Conservation Plan noted the draughtiness and lack of insulation of the buildings and suggested installing dehumidifiers, whereas the Buildings Development Strategy recommended 'electrical frost protective heating' for each building. The possibility of air conditioning units for the main collections store (Building 25) was also considered, but in practice NMS has addressed environmental control on a case by case basis. Most of the buildings containing collections have heating, which is sometimes humidistatically controlled to aim for constant relative humidity, some of the buildings containing collections also have dehumidifiers, some buildings have heating primarily for human comfort and some buildings are completely unheated.

The presumption made in the Buildings Development Strategy was that doors and windows should be repaired where possible rather than replaced, but in practice as buildings have undergone major repairs all of their doors and windows have been replaced. The strategy also stated that gutters should preferably not be added to buildings which did not have them originally, although they might be considered by

Historic Scotland if it was ‘demonstrated that a lack of gutters is causing deterioration of the fabric’. In practice Historic Scotland has given permission for new cast iron gutters whenever a building has undergone major repairs, and downpipes, drains and gravel-filled drainage channels have also been added (Fig. 3.17).

Fig. 3.14. Downpipe on Building 26 discharging directly onto the ground

Fig. 3.15. New roof on Building 25, N elevation

Fig. 3.16. Internal roof panels inside Building 31

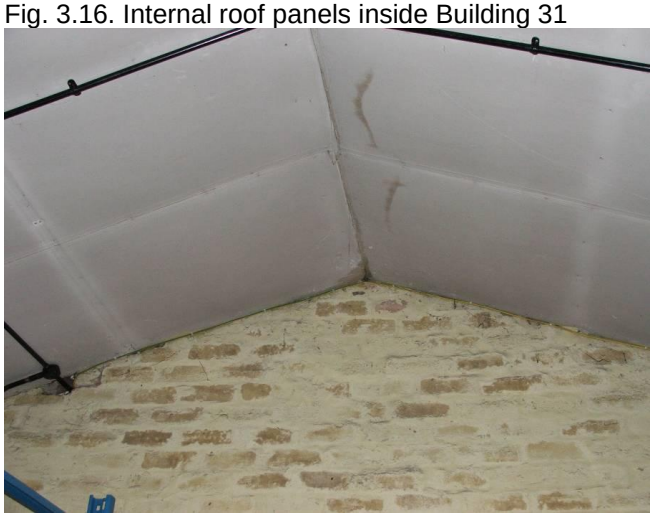

Fig. 3.17. Downpipe feeding into an underground drain and gravel drainage channel on Building 28, SE elevation

3.3.2.2 Render repairs

Early render repairs were generally roughly executed in cementitious mortar, and the crack fills often extend over the sound render on either side of the crack. The colour matching of the repairs is variable, but lichen growth has ensured that they now appear in reasonable harmony with the original render, and their performance otherwise has been good, although it is of course possible that some repairs have failed and been replaced. However, repairs to areas where the cement render is particularly prone to cracking, such as the corners of the window recesses and areas over the metal fixings, have often cracked again (Fig. 3.18). Some of the finer cracks have been filled with a dark grey material with a resinous appearance, and although this is quite unsightly, it has performed well and not cracked (Fig. 3.19).

The first documented render repairs were undertaken on Building 23 in 1992, following a rebuilding of the free-standing wall on the north east side of the building [129]. It was specified that the mix should 'match existing', but there is no record of the mix actually used or the application method. The Conservation Plan written in 2004 [130] gave more detailed specifications for render repairs, which were undertaken over the next few years as part of the major programmes of refurbishment to several buildings. The Conservation Plan presumed that it was desirable to preserve as much of the original render as possible through crack filling and grouting, applying patch repairs only where the render had been lost. The performance of the render repairs from 1992 onwards is discussed in Chapter 9.

Fig. 3.18. Early repair over a ferrous tie on the gable end of Building 22, now cracking

Fig. 3.19. Dark grey resinous material used for some early crack fills, Building 25, E bay, S elevation

3.3.2.3 Ongoing maintenance

The ongoing maintenance of the buildings at NMOF could potentially include regular painting of doors and window frames, clearance of leaves and repair of leaks in rainwater disposal goods, render patch repairs, crack fills and repointing of brick plinths.

In 2004 NMS applied for Scheduled Monument Consent to paint all the windows and doors across the site. The window frames were to be painted dark green to match traces of the original paint. The colour of the doors was not specified, but those painted since 2004 are either dark green or pale blue. In practice not all the buildings on the site were painted, as some still have white window frames and bright blue doors. There does not appear to have been any repainting since, and much of the paintwork at NMOF is consequently flaking (Fig. 3.20). There has also been inadequate maintenance of the rainwater disposal goods and the cement renders and pointing between the bricks (Figs. 3.21-3.22), and this is causing deterioration, as will be shown in subsequent chapters.

Fig. 3.20. Flaking paint on door, Building 25, W elevation

Fig. 3.21. Gutter blocked by plants, with damaged render on the pier head directly below, Building 26, W elevation

Fig. 3.22. Lack of pointing between bricks on Building 25, free-standing wall extending out from the E elevation

3.3.3 Details of repair works on the air raid shelter

The internal records from the Estates department at NMS recognise the ongoing deterioration of the air raid shelter. A detailed proposal was drawn up for works to ensure the 'short to medium term preservation of the structure' [132], including the removal of the earth over the shelter; repairs to the concrete sections, the metal fixings and the brick walls at the ends of the shelter; the application of a damp proof membrane to the outside of the shelter, followed by the reinstatement of the covering earth; and the installation of a perforated drain around the shelter. It was hoped that the complete refurbishment of the shelter would follow in due course, but recognised

that this would be specialised and expensive. One option proposed was that parts of the Stanton shelter which stands on the farmland to the east of NMOF could be used to replace the most damaged parts of the NMOF shelter. In practice no work has been undertaken on the shelter beyond the introduction of wooden boarding at the end and a secure perimeter fence to prevent access by members of the public. The condition and causes of deterioration of the air raid shelter are discussed in Chapter 11.

3.4 Sampling and testing strategy

A plan of the NMOF site is given in Fig. 3.23, and the buildings where research was undertaken have been highlighted.

Fig. 3.23 Plan of the NMOF site

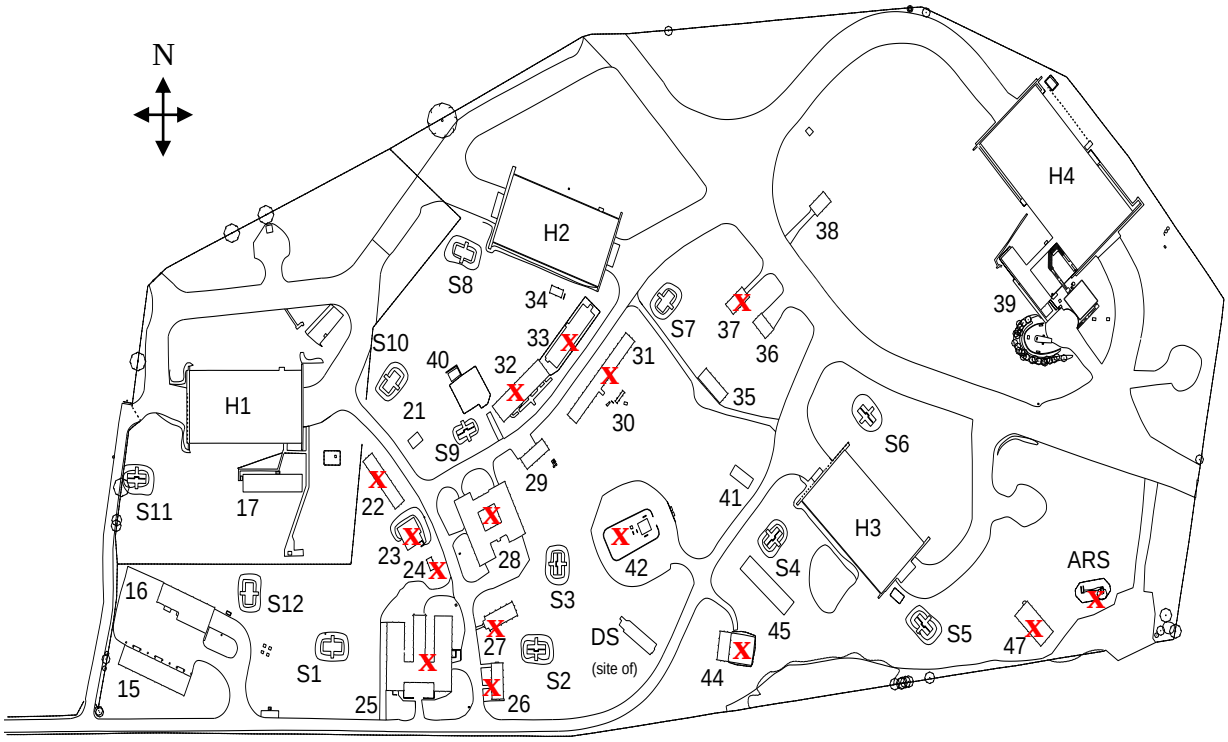

Approximate width of site is 580 m.

The selection of suitable buildings for surveys, monitoring and non-destructive testing was made to include a range of types of deterioration, and to compare repaired and unrepaired buildings. It was also necessary to choose areas which could

be accessed either from the ground or from a step ladder. The rationale for choosing particular buildings and monitoring locations is given in Tables 3.1 and 3.2.

Following the preliminary investigations, samples of building materials were taken for petrographic examination (Table 3.3) and other analysis (Table 3.4). These samples were chosen to answer specific questions and to make comparisons across a particular material type – for example, original renders from different buildings – and between different types of material, such as renders and bricks. Some of the tests were destructive, and where possible the samples underwent non-destructive testing before destructive testing. However, it was not always possible to use the same set of samples for each test or method of analysis.

The samples were taken from a small, representative group of buildings, but the choice of samples was often limited by availability. It was desirable to avoid sampling directly from the buildings at NMOF because it is a Scheduled Historic Monument, and Scheduled Monument consent for any destructive sampling was required from Historic Scotland. Instead, samples were obtained from the heap of bricks salvaged from buildings at NMOF (Fig. 3.24) and from pieces of detached render found on the ground next to buildings. Loose bricks and render were also taken from the emergency hospital complex, which is adjacent to the current NMOF site at Athelstaneford Mains (Fig. 3.25). The emergency hospital buildings were built at the same time and using the same materials as the buildings which now stand within NMOF, but as these buildings were not included when the site was scheduled as a Historic Monument, permission for sampling is not required. Additionally, several small pieces of partially detached render, brick and mortar were removed for direct measurement of moisture content, some blisters of render and aggregates which were thought to be related to the flaking of the render were picked out and four small core samples were drilled in the air raid shelter.

With regards to the testing and analysis of the historic renders, it had been observed during the petrographic examination that there appeared to be two distinct types of render at NMOF: smooth renders containing only fine sand aggregate, and rough renders containing well graded, mixed aggregate. Hence for the measurement of the physical properties such as tensile strength, density, porosity, sorptivity, pore size distribution and drying behaviour, it was assumed that the smooth renders were

broadly interchangeable, and that the same was true of the rough renders. The abbreviations used for the materials tested are given in Table 3.5.

Fig. 3.24. The rubble heap at NMOF containing examples of the historic bricks used for the buildings

Fig. 3.25. Bricks found at the emergency hospital complex at Athelstaneford Mains

3.4.1 Preparation of thin sections

The selection of small pieces of material to make into thin sections was undertaken to provide maximum information. The pieces of render encompassed the entire thickness of the render layer, with some of the brick substrate attached where possible, while the pieces of concrete extended down to and included part of the reinforcement, and the brick samples included the surface of the brick. Additionally, detached blisters of flaking render from Buildings 25 and 47 and some of the aggregate particles from Building 47 thought to be related to the flaking were

mounted. The samples were injected with blue resin prior to being cut, to allow internal pores, voids and cracks to be seen easily.

Table 3.1 Selection of buildings for surveys and non-destructive testing

property under investigation	buildings investigated/sampled from	specific reasons for choice
detailed condition survey	Buildings 27, 46, and 47	Chosen to represent a range of sizes and types of deterioration, and to include an extensively repaired building (Building 27)
	Air raid shelter	Chosen to inform detailed investigations in the air raid shelter
time lapse photography by comparing current photographs with historic photographs from NMS and RCAHMS	Buildings 23, 27, 28, 31, 32, 33, 34 and 46	Choice dictated by the buildings which NMS and RCAHMS had photographed previously
time lapse photography using photographs taken over the course of the project	Buildings 22 and 32	Buildings with extensive cracked render were chosen, as these were more likely to undergo changes within the monitoring period
strain measurement	Buildings 26, 31, 32, 42 and 46	Building 42 chosen because NMS had noted concerns over a specific large crack. Other buildings chosen to represent cracks which might be caused by structural movement or freeze-thaw damage, occurring in accessible locations
rebound hammer testing	Building 47	Chosen because this building had undergone a detailed condition survey and demonstrated render in various states of deterioration. Additional buildings were not tested because the technique was very time-consuming and gave limited information.
	Air raid shelter	Chosen to inform detailed investigations in the air raid shelter
Ultrasonic Pulse Velocity testing	Air raid shelter	only used in the air raid shelter because the renders were too rough to produce useful data
infrared thermography and electrical resistivity measurements	Buildings 23, 27, 28, 31, 46 and 47	Buildings chosen to give range of types of deterioration, and to

		compare repaired and unrepaired, and heated and unheated
	Air raid shelter	Chosen to inform detailed investigations in the air raid shelter

Table 3.2 Selection of locations for environmental monitoring

equipment	parameters monitored	monitoring location	specific reasons for choice
telemetric monitoring system	external and internal temperature and RH	external sensor adjacent to Building 39, and internal sensors in approximately 20 buildings across site	Locations chosen and system maintained by NMS
weather station	external temperature, RH, wind speed, wind direction and rainfall	between Buildings 17 and 22	Location was a fenced-off area providing good security, and at least 10 m from the nearest building
evaporimeter	evaporation rate		
soil moisture sensor	soil moisture content		
data loggers	external ambient temperature, surface temperature and RH, from which dew point temperature and the likelihood of condensation were calculated	Building 26	Chosen because N and S elevations could be compared, and there were building fixtures for attaching the loggers

Table 3.3 Selection of buildings for petrographic examination

sample type(s)	buildings investigated/sampled from	specific reasons for choice
original render	Buildings 24, 32 and 47	Chosen to cover a range of visually different original renders
blisters of detached original render	Building 47	Chosen because this phenomenon was being investigated and other investigations were being undertaken on this building
repair render	repairs applied to Building 23 in 1992 and Building 25 in 2005	Chosen because they were representative of the two documented phases of repairs, with samples taken from areas where the repairs were failing
bricks	taken from the rubble heap, and identified as coming from the Niddrie, Prestongrange and Wallyford brickworks (NB, PB and WaB)	Chosen to cover a range of different bricks
bricks	from underneath the repair renders on Buildings 23 and 25	Chosen to assist with investigating the causes of render failure
concrete	from the air raid shelter and a similar shelter at a different airfield (Cark airfield in Cumbria, England)	Chosen to inform detailed investigations in the air raid shelter

Table 3.4 Selection of buildings for other analysis

property under investigation and/or technique employed	sample type(s)	buildings investigated/sampled from	specific reasons for choice
direct measurement of moisture content	bricks, original render and concrete	Buildings 22, 31, 32 and 47	Chosen wherever partially or wholly detached samples were available
		Air raid shelter	Chosen to inform detailed investigations in the air raid shelter
binder:aggregate ratio by acid extraction	original render	Buildings 24 and 47	Chosen to include original renders with rough and smooth appearances, repair renders from both phases of work and original mortar for comparison with the renders
	repair render	Buildings 23 and 25	
	original mortar	Building 33	
	air raid shelter concrete and mortar	Air raid shelter	Chosen to inform detailed investigations in the air raid shelter
quantities of soluble	original render	Buildings 23, 24, 26, 46	Chosen to include

sulfate, chloride, nitrate, calcium, magnesium, potassium, sodium and aluminium ions, by ion chromatography and inductively coupled plasma – optical emission spectrometry		and 47	original renders with rough and smooth appearances, and from areas with and without flaking
	WWII render from a different site	Building at Cark Airfield	Chosen to make comparisons with similar buildings where no flaking was observed
	bricks	Edinburgh, Niddrie, Prestongrange, Wallyford and Whitehill bricks from the rubble heap, and deteriorated Wallyford brick from Building 25	Chosen to include all the types of bricks used at NMOF, and to compare a brick in good condition with a deteriorated brick
	original mortar	Buildings 33 and 44, and from incremental depths (0-1 cm, 1-3 cm, 3-5 cm and 5-7 cm) of the internal elevation of the east wall of Building 25	Chosen to make comparisons between the original mortars and renders, and to investigate the distribution of salts through the walls of Building 25
	concrete	Air raid shelter, air raid shelter at Cark Airfield and WWII defences on a beach near NMOF	Chosen to inform detailed investigations in the air raid shelter, and to make comparisons with other concrete from the same period
	salt efflorescences	from the internal walls of Buildings 25, 37 and the air raid shelter	Chosen because these were the three buildings where salt efflorescences were most evident
	ground water and sea water	ground water from near to Building 44 at NMOF, and sea water from the North Sea near NMOF	To investigate whether the ground water was likely to be a source for ions found within the building fabric, and to identify the ions which might be brought to NMOF from the sea in aerosol form
X-ray diffraction	salt	from the internal walls of	To identify the salt

	efflorescences	Buildings 25, 37 and the air raid shelter; and the external walls of Buildings 37 and 44	efflorescences, collaborating the results of the ions analysis
	bricks	Edinburgh, Niddrie, Prestongrange, Wallyford and Whitehill bricks from the rubble heap, and bricks from under the failed repair render on Building 25	To identify the bricks used in the free-standing wall on the south side of Building 25
	aggregate particles and shale	aggregate particles from the renders on Buildings 25, 26, 46 and 47 and shale from the quarry at Dunbar, near NMOF	To characterize the aggregate particles thought to be responsible for the flaking of the renders and the shale used experimentally to replace the aggregate particles
Scanning electron microscopy examination with Energy-dispersive X-ray spectroscopy	original render	Buildings 25, 32 and 47	To further investigate the causes of render flaking
	aggregate particles	aggregate particles from the render on Building 47	To characterize the aggregate particles thought to be responsible for the flaking of the renders
tensile strength testing	original render	Building 31 and hospital complex	To compare a smooth render containing only fine sand aggregate (B31 OR) to a rough render containing well graded, mixed aggregate (HC OR); these samples were considered representative of the two types of renders
	repair render	Buildings 23 and 25	To compare the original and repair renders
	bricks	Niddrie brick	To compare the bricks and renders; it was only possible to test one brick, and Niddrie bricks were widely used at

			NMOF
	composite samples of brick and render	Niddrie brick with hospital complex render	To investigate how brick and render performed in combination; this was the only sample of brick with attached render available
density, porosity and sorptivity	original render	Buildings 24, 31 and 47	Chosen to include original renders with rough and smooth appearances, repair renders from both phases of work and original mortar for comparison with the renders
	repair render	Buildings 23 and 25	
	original mortar	Building 33	
	bricks	Edinburgh, Niddrie, Prestongrange, Wallyford and Whitehill bricks from the rubble heap,	Chosen to include all the types of bricks used at NMOF
Pore size distribution	original and repair renders and bricks	as for density, porosity and sorptivity, except that Building 31 render and Building 33 mortar were omitted because they were considered of lesser importance, and the skin of the Prestongrange brick was tested as well as the interior	As for density, porosity and sorptivity. The skin of the Prestongrange brick was tested to compare it to the interior
drying behaviour	original render	Building 24	It was only possible to test one render, and B24 OR was considered representative of the smooth original render
	original mortar	Building 33	It was only possible to test one mortar, and B33 M was considered representative of the NMOF mortars
	brick	Niddrie brick	it was only possible to test one brick, and Niddrie bricks were widely used at NMOF

Table 3.5 Abbreviated names for the materials tested

abbreviated name	**material**
B33 M	original mortar from Building 33
B44 M	original mortar from Building 44
B23 OR	original render from Building 23
B24 OR	original render from Building 24
B47 OR	original render from Building 47
B31 OR	original render from Building 31
HC OR	original render from the hospital complex at Athelstaneford Mains
CA OR	original render from a building in Cark Airfield, Cumbria, England
B23 RR	1992 repair render from Building 23
B25 RR	2005 repair render from Building 25
ES B	Edinburgh brick, core drilled through stretcher face
EB B	Edinburgh brick, core drilled through bed face
NS B	Niddrie brick, core drilled through stretcher face
NB B	Niddrie brick, core drilled through bed face
PS B	Prestongrange brick, core drilled through stretcher face
PB B	Prestongrange brick, core drilled through bed face
WaS B	Wallyford brick, core drilled through stretcher face
WaB B	Wallyford brick, core drilled through bed face
WhS B	Whitehill brick, core drilled through stretcher face
WhB B	Whitehill brick, core drilled through bed face
ARS C	original concrete from the air raid shelter
ARS M	original mortar from the air raid shelter
B25 S	salt efflorescences from inside Building 25
B37 S	salt efflorescences from inside Building 37
ARS S	salt efflorescences from inside the air raid shelter

4.1 Introduction

This chapter describes the surveys and non-destructive testing undertaken as the first stage of the investigations at NMOF. The survey work comprised a visual inspection of all the buildings at NMOF to ascertain the overall condition of the site and the range of deterioration in evidence, followed by detailed graphic condition surveys on the interior of the air raid shelter and the exterior of three cement-rendered buildings. The rate of deterioration across the site was assessed by comparing current and historic photographs, and taking photographs at intervals over the course of the project. Additionally, strain measurement was undertaken to investigate whether existing cracks were getting wider.

The visual survey informed the approach to non-destructive testing, which included:

- Rebound hammer testing to assess the surface hardness of the render and concrete;
- Ultrasonic Pulse Velocity (UPV) testing to investigate the density, coherence and homogeneity of the render and concrete;
- Infrared thermography to identify areas of high moisture content and areas containing voids;
- Electrical resistivity measurements to collaborate the findings of the infrared thermography regarding moisture content.

Environmental monitoring was undertaken over the course of the project to investigate how key parameters vary over time, in order to relate the deterioration mechanisms to the environment. The parameters monitored were temperature and relative humidity with a telemetric monitoring system and dataloggers; wind speed, rainfall and other weather parameters with a weather station; internal and external evaporation rates with an evaporimeter; and soil moisture content with a soil moisture sensor.

4.2 Visual inspection and monitoring with time-lapse photography

4.2.1 Method

To identify the types of deterioration, preliminary surveys of the reinforced concrete air raid shelter, the exterior of all the cement-rendered buildings and the interior of a few of the cement-rendered buildings were undertaken. Examples of each type of deterioration were recorded with colour photographs. Detailed condition surveys were then undertaken on the interior of the air raid shelter and the exterior of three cement-rendered buildings: Buildings 27, 46 and 47. The condition surveys were undertaken by marking up scaled line drawings on site, and transferring the information into an electronic format using Adobe Illustrator. Additionally, the buildings were observed during and after periods of rainfall to identify wetting patterns, and the performance of the rainwater disposal goods was assessed visually.

The rate of deterioration of the buildings was assessed by comparing current photographs with historic photographs from the NMS archives and the Royal Commission on the Ancient and Historical Monuments of Scotland archives. Additionally, some of the buildings were photographed at frequent intervals over a period of 30 months, in places where the likelihood of rapid deterioration occurring was identified in advance.

4.2.2 Results and discussion

Additional results are given in Appendix 1, and the results for the air raid shelter are discussed in Chapter 11 and Appendix 6.

4.2.2.1 Preliminary condition survey

Render

The main type of deterioration of the cement render was cracking (Fig. 4.1 and Figs. A1.1-A1.3). The cracks had provided a place for mosses and other plants to grow and the delamination of pieces of render had eventually occurred, usually at the interface between the render and the brick. In some instances the exposed brick was sound, but elsewhere the render had pulled off the surface of the brick and the brick itself had cracked. The areas worst affected were the piers, particularly along their sloping edges, the skews underneath the windows and the render at the base of the walls, and

site observations showed that these parts of the buildings were wetted most frequently. Cracks in the render also occurred around the iron ties at the top of the gable end walls, and extending outwards from the corners of the door and window frames. It was noted in NMS internal documentation that many of the windows were pinned closed for security reasons during the Ministry of Agriculture, Fisheries and Food ownership of the site [133], and it was suggested that this caused the windows to distort and damage the surrounding building fabric. It was alternatively proposed that the cracking was due to the corrosion and subsequent expansion of the window frames [126]. Hard white efflorescences were visible along some cracks.

The render also deteriorated by blistering and flaking (Fig. 4.2), although this was only observed on some of the buildings, namely Buildings 22, 25, 26, 32, 44, 46 and 47. It occurred primarily, but not exclusively, on the south elevations. Small raised blisters were formed, which either detached individually or joined together causing the render surface to flake off in large sheets. Other damage to the render included mechanical damage resulting from accidental knocks and deliberate alterations to the buildings (Figs. A1.4-1.5). For example, the three evenly spaced areas of lost render on Building 34 probably corresponded to something having been fixed to the building previously.

Fig.4.1. Cracking at the top of a pier on Building 47

Fig. 4.2. Blistering and flaking render on Building 46

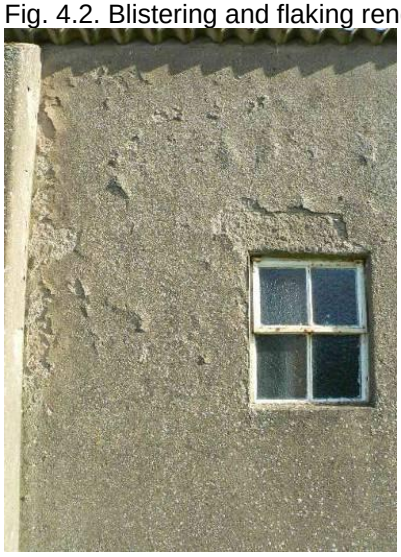

Bricks

The bricks in the most advanced state of deterioration were in the plinths (Fig. A1.6). They were in direct contact with the ground and were often visibly wet, and the pointing was frequently fragmentary or missing altogether, presumably because it had lost adhesion to the bricks or lost internal cohesion and fallen out. The deterioration of exposed bricks higher up the walls included cracking of bricks and the loss of the surface of bricks (Fig. A1.7). Some bricks were much worse affected than others, possibly due to differences arising during their production. There were some salt efflorescences visible on the bricks and mortar joints of un-rendered external walls, for example on Building 44 (Fig. A1.8).

Roofs, windows, doors and rainwater goods

The original roofs were generally in reasonable condition, but damage at their edges directed water down onto the render. They were also covered with thick layers of moss, which soaked up rainwater and caused dripping down the sides of the buildings. The window frames were wet frequently and were consequently prone to corrosion (Fig. A1.9), and both the windows and doors suffered from inadequate maintenance. This was also an issue for rainwater goods, where they existed, because they were not cleared often enough and consequently could become blocked by vegetation (Fig. A1.10).

Interiors

The main types of deterioration observed inside the buildings were staining of the internal ceiling panels, most probably due to water infiltration, and salt effloresences on the bricks and mortar joints, causing disruption of internal paint where it had been applied. The salt effloresences were most obvious in Building 25, particularly in the rooms with heating and/or dehumidification, and in Building 37, which was extremely well ventilated because the large external doors were frequently propped open. The effloresences were concentrated along the mortar joints, although they were also visible on the bricks (Fig. 4.3).

Fig.4.3. Salt effloresences on the internal wall of a heated room in Building 25

4.2.2.2 Detailed condition surveys

The graphic documentation undertaken on line drawings is given fully in Appendix 1, Section A1.2. This documentation confirmed the observations made in the preliminary condition survey regarding the location of render delamination and cracking, and showed that the blistering and flaking render was most prevalent on the south elevations. This is seen in Fig. 4.4, where the red areas are the surface loss of render due to flaking. The graphic documentation also demonstrated that most of the render on the buildings which had not been repaired extensively by NMS was original, and hence had survived for over 70 years, but that some 25% of the surface area of Building 27 was modern repair render.

Fig. 4.4. NE and SW elevations of Building 46, showing that flaking of the render (red) occurred predominantly on the SW elevation

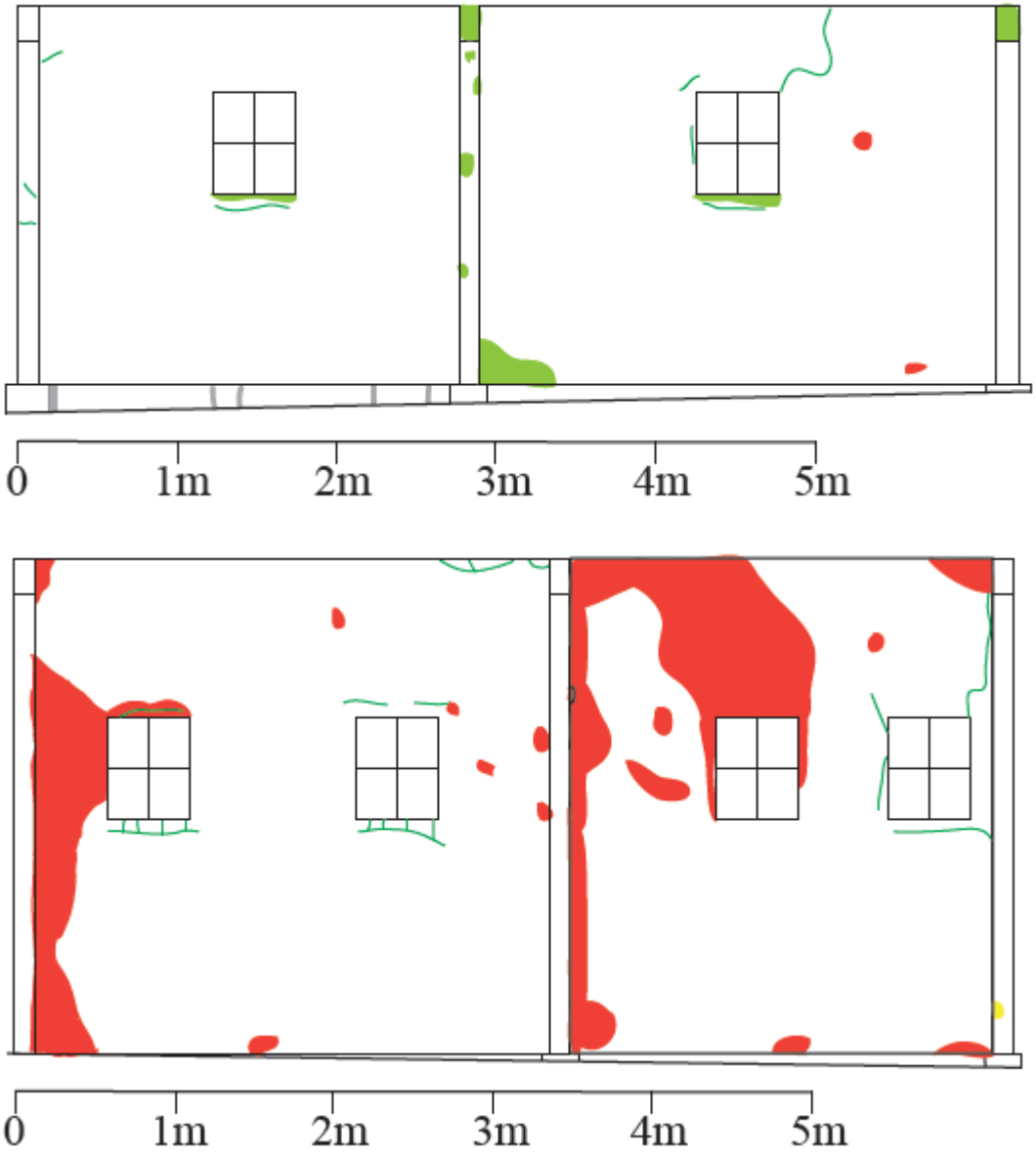

4.2.2.3 Observations of the buildings during rainfall

Observations of the buildings during or after rainfall showed that the parts of the buildings which were wet most severely were the piers, particularly along their sloping edges; the skews underneath the windows; the base of the walls due to splash back; and areas of render adjacent to broken roof panels or blocked gutters and downpipes (Fig. 4.5). Additionally, a discoloured zone which may have corresponded to a zone of rising damp was visible along the base of many of the

buildings even on dry days (Fig. 4.6). Where gutters were present they provided some protection for the upper walls and appeared to reduce the amount of water collecting on the ground, and hence the wetting of the base of the walls due to rising damp and splash back. The gravel-filled drainage channels around the repaired buildings seemed to assist with water disposal, but where there was gravel alongside the unrepaired buildings it was compacted into the ground rather than present in drainage channels, and may have hindered rainwater absorption by creating an impermeable surface.

Fig. 4.5. Wetting due to rainfall on Building 32

Fig. 4.6. Darkened zone along the base of the walls on Building 24, possibly caused by rising damp

4.2.2.4 Time lapse photography

Comparison of current and historic photographs

Comparisons with historic photographs were hampered by the lack of a comprehensive photographic archive at NMS, although some images are held by the Royal Commission on the Ancient and Historical Monuments of Scotland (RCAHMS). Comparison of current photographs with RCAHMS photographs dating from 1984 and NMS photographs dating from 1990 onwards showed that there had been some major changes to the buildings in the past 30 years. Only the plinth of Building 33 remained, the upper part of the building having been demolished in 1992 due to its poor condition (Figs. A1.27-A1.28). It was also noticeable that much of the repair render applied to Building 23 in 1992 had been lost between 2004 and 2010 (Figs. A1.29-A1.30). However, the photographs demonstrated that elsewhere the rate of deterioration had been slow, with areas of cracking that might have been considered active in 2004 appearing virtually identical in 2010 (Figs. A1.31-A1.32). It was also apparent that ongoing maintenance had been undertaken, for example to remove vegetation from around the buildings (Figs. A1.33-A1.34), and that the major programmes of repair had considerably changed the appearance of buildings (Figs. A1.35-A1.38).

Photographs taken over the project

From visual observations at NMOF it was clear that the delamination and loss of pieces of render was an ongoing process, which accelerated over the winter months, and monitoring with photographs over the course of the research project demonstrated the rapidity of the deterioration. For example, substantial chunks of render fell off the first pier from north west on the north east elevation of Building 22 between 11/11/2009 and 31/08/2011 (Fig. 4.7), and although there had been no further losses by 18/04/2012, the growth of cracks in the render adjacent to the area of loss indicated that further losses were likely at some point.

Photographs on a larger scale show how cracks develop and eventually lead to render delamination. From Figs. 4.8 and 4.9 of the third pier from south west on the north west elevation of Building 32 it can be seen that the cracks visible at A, B, C and D in October 2010 bordered the piece of render which was lost by February 2011. Fig. 4.9 also shows the existence of fine cracks at E, F and G which were

visible when the render was drying out after rain, but not visible in later photographs taken in dry weather. However, elsewhere the rate of deterioration was much slower, as the cracks in another area of this pier appeared unchanged from October 2010 to April 2012 (Figs. A1.39-A1.40).

Fig. 4.7. Building 22, delaminating render on the first pier from NW on the NE elevation

11/11/2009 13/10/2010 31/08/2011 18/04/2012

Fig. 4.8. Building 32, cracking render on the third pier from SW on the NW elevation (13/10/2010)

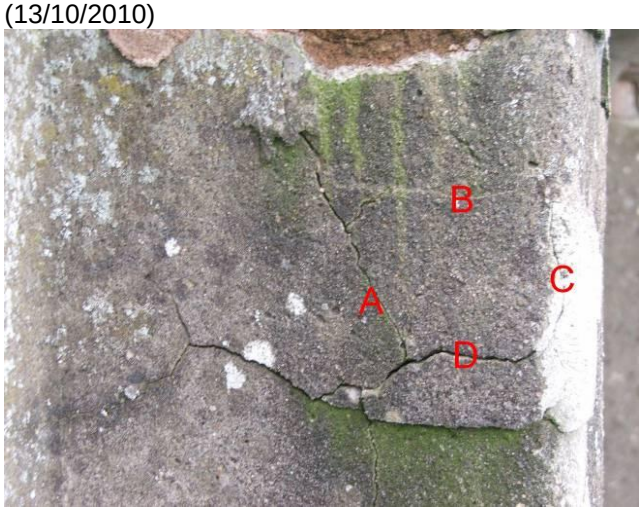

Fig. 4.9. Building 32, area of lost render (02/02/2011)

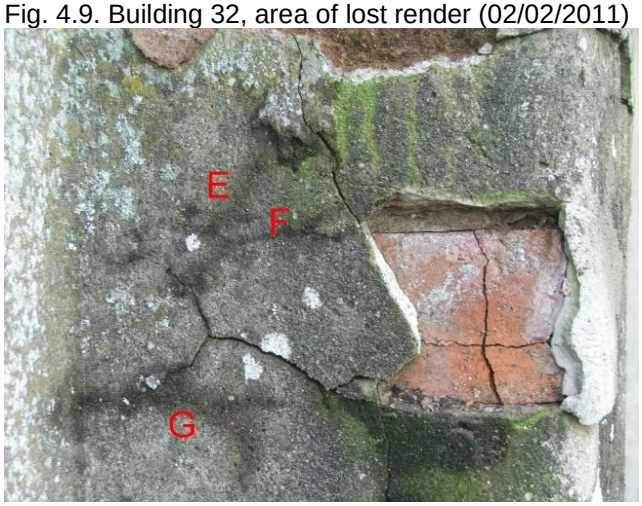

4.3 Strain measurement

4.3.1 Method

Strain measurement was undertaken primarily to investigate whether existing cracks were getting wider. Crack monitoring was considered desirable by NMS in order to establish whether cracks were structural, and in particular the monitoring of the cracks in the north east corner of Building 47 and above the door on the south east side of Building 42 had been described as 'urgent' [133].

The movement of cracks in five locations was measured: the east elevation of Building 26, above the middle window; the south west elevation of Building 31, on the south east side of the window; the south east elevation of Building 42, above the door; the south east elevation of Building 46, above and to the north east side of the door; and the north west elevation of Building 32, on the third pier from south west. The cracks in the first four locations were associated with doors and windows, whereas the cracks on Building 32 were typical of the cracking observed on piers. The cracks on Building 47 were not monitored because they were too high to be easily accessible.

Strain measurement was undertaken using 6 mm diameter stainless steel discs, with a hole drilled in the centre into which the jaws of measuring callipers were inserted. The horizontal movement of each crack was measured using pairs of datum points, which were fixed to the render on either side of the crack using epoxy resin so that the line of strain measurement was perpendicular to the length of the crack [134]. Between two and six pairs of datum points were fixed on each building, as shown in Fig. 4.10 and Appendix 1, Section A1.4. The distance between each pair of datum points was measured at four to eight weekly intervals, using digital calipers with a readability of 0.01 mm, and the length change Δl at each location was calculated using

$$\Delta l = l_n - l_o \qquad \textbf{(4.1)}$$

where l_n is the new length and l_o is the original length. Additionally, the strain between each pair of datum points ε was calculated as a percentage using

$$\varepsilon = \frac{\Delta l}{l_o} \times 100 \qquad \textbf{(4.2)}$$

and the seasonal movement of the crack was illustrated by plotting ε against time. There were several locations where a datum point fell off part way through the monitoring and had to be repositioned, and these locations have not been included in the results if there is sufficient continuous monitoring from other locations.

The monitoring was undertaken for approximately 21 months, from 10/03/2010 to 14/12/2012. Monitoring on Building 32 only began on 01/03/2011. The repeatability of the readings was investigated by taking the measurements on Building 46 on 14/12/2012 twice, with a few minutes between the first and second sets of readings.

To investigate the extent to which the un-cracked render expands and contracts, pairs of datum points were fixed on opposite elevations of Building 46, monitoring two horizontal and two vertical displacements on the south east elevation (H1, H2, V1 and V2) and two horizontal and two vertical displacements on the north west elevation (H3, H4, V3 and V4), and readings were taken as for the cracked render from 25/08/2010 to 14/12/2010.

Fig. 4.10. Location of datum points for strain measurement on Building 42

4.3.2 Results and discussion

4.3.2.1 Repeatability of results

The repeated readings taken on Building 42 on 14/12/2012 suggested that the measurements were repeatable to ±0.07 mm or less (Table 4.1), and the graphs were plotted with these error bars. It was acknowledged that the accuracy of the measurements was reduced because they were unavoidably taken at variable external temperatures rather than a fixed reference temperature. The external temperatures were usually below the 20 °C reference temperature of the digital calipers, which resulted in higher readings than would have been obtained at the reference temperature. Additionally, the steel datum points may have undergone some movement.

Table 4.1 Repeatability of measurements on Building 42

location	B46-1	B46-2	B46-4	B46-5	B46-6
reading 1	133.62	95.52	109.50	126.11	109.01
reading 2	133.55	95.54	109.48	126.07	109.05
reading 1 – reading 2	0.07	-0.02	0.02	0.04	-0.04

4.3.2.2 Movement of un-cracked render

The monitoring of the un-cracked render on Building 46 suggested that the strain between the datum points varied by a maximum of 0.48% over the course of an 18-month period (Fig. 4.11 and Figs. A.41-A.45). It was not possible to see a seasonal trend in the results, and there was no obvious difference between the south east and north west elevations. The variations were presumably due to some combination of thermal movement, movement due to water absorption and movement due to freeze-thaw cycles. More accurate linear variable displacement transducer (LVDT) measurements for the movement of un-cracked render are given in Chapter 8.

Fig. 4.11. Graph showing the strain measurement across the un-cracked render on Building 46, where the strain between datum points varied by a maximum of 0.27%

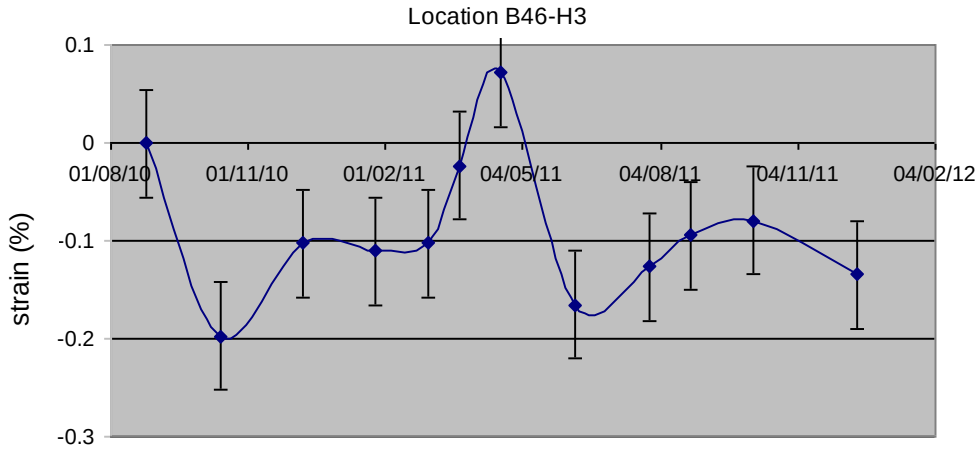

4.3.2.3 Movement of cracked render

Many of the strains between the datum points on the cracked render were below 0.48%, suggesting that they could simply have been due to render movement as measured on Building 46, and possibly caused by environmental changes. However, strains of up to 1.36% were also measured, which presumably were partially due to crack movement. The strains were not consistently higher in December 2012 than in March 2010, suggesting that although the cracks around the windows and doors were moving, they were not necessarily getting wider.

The graphs for Building 32, where cracks on a pier were monitored, indicate that if anything the width of the cracks measured decreased from March 2011 to December 2012. However, 01/03/2011 was an exceptionally warm day, with a maximum temperature of 14.26 °C recorded by the site weather station at 11.00, so it is possible that the first measurement was high due to render expansion. The cracks on the piers would generally be expected to be expanding, but changes may not have occurred within this relatively short time frame, and there were certainly no visual changes at any location during the monitoring period.

The graphs obtained for the two monitoring locations on Building 42 are very similar, and the graphs from Building 46 are also a good match for one another, but the other buildings monitored do not have a clear trend across the locations. Also, there are noticeable similarities in the graphs obtained for Buildings 42, 46, and 32, but not between any other buildings. It is not generally possible to relate the data to the external environment; for example, the weather in the days leading up to the high

readings obtained on Buildings 42 and 46 on 04/05/2010 was no warmer or sunnier than the weather prior to the low readings obtained on 02/06/2010. Some of the graphs for Buildings 42 and 46 are included below in Fig. 4.12, and a full set of graphs is given in Appendix 1, Section A1.4.

Fig. 4.12. Strain measurement across the cracking on Buildings 42 and 46, showing some similarities

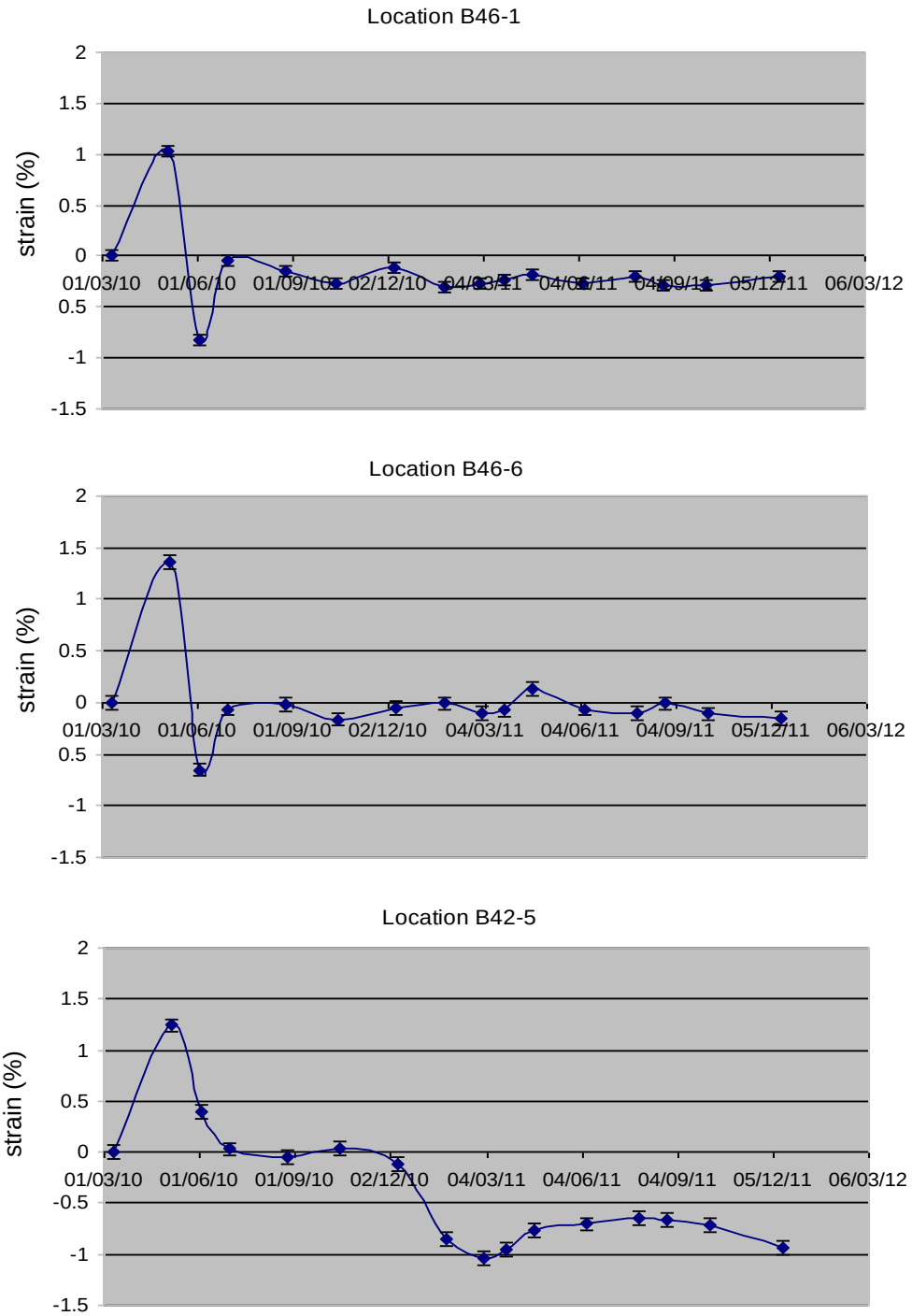

4.4 Non-destructive testing

4.4.1 Method

Non-destructive testing was undertaken using a rebound hammer (ELE International EL35-1480 Concrete Test Hammer) to assess the surface hardness of the render and concrete; an infrared camera (FLIR B400) to identify areas of high moisture content and areas containing voids; a hammer to check the presence of voids indicated by the infrared thermography; and a protimeter (Protimeter Surveymaster) to collaborate the findings of the infrared thermography regarding moisture content. Rebound hammer readings were taken on the south west wall of Building 47, at approximately 0.5 m intervals, with additional readings in areas exhibiting localised deterioration such as cracking. Infrared thermography was undertaken on the interior and exterior of several buildings on a cold but sunny day in February, when the conditions were around 7 °C and 80% relative humidity, and electrical resistivity measurements were taken alongside the infrared thermography and on other occasions in different weather conditions. Additionally, Ultrasonic Pulse Velocity testing was undertaken in the air raid shelter.

4.4.2 Results and discussion

The results for the air raid shelter are discussed in Chapter 11. The readings obtained with the rebound hammer on Building 47 varied from 16 to 34, averaging about 26 (Fig. 4.13). In general, the readings showed some correlation with the visual appearance of the render: smooth, well-compacted render gave high readings, and cracked or poorly compacted render gave lower readings. However, the readings were not lower in the areas where the surface of the render had flaked off, suggesting that the flaking had not affected the cohesion of the render below the surface. The readings were generally lower immediately below the windows and close to the ground, and these are areas which might be expected to be in poorer condition due to frequent wetting. However, lower readings were not obtained on the piers, which were also wet frequently. This suggests that the degree of weathering influenced by the render does not necessarily affect its hardness.

The infrared thermography showed surface temperature differences corresponding to the moisture content of the building fabric: areas with lower

temperatures generally had higher moisture contents, because the evaporation of moisture has a cooling effect. Used in combination with electrical resistivity measurements the thermography identified various localised damp areas which were probably caused by rainwater infiltration, and showed that the piers and the areas under the windows had significantly higher moisture contents than the surrounding fabric (Fig. 4.14). The brick plinths were all very wet, but a significant zone of rising damp above the plinths was not found, although the bottom 0.1 m of the render was generally slightly damper than the render further up the wall. This suggested that the damp proof course located one brick above the top of the plinth was reasonably effective in preventing the movement of water up the wall, despite being bridged by the render. The discoloured zone of render approximately 0.4 m high at the base of the walls may have been caused by splash back rather than rising damp, as the bottoms of the doors demonstrate the extent of splashback that occurs (Fig. 4.15). However, it is also possible that the zone of rising damp would be higher on a day with a lower evaporation rate, as demonstrated by Hall et al. [107].

The infrared thermography also showed that some early repairs had different moisture retention properties from the original fabric. For example, the infilled doorway on the south west wall of Building 23 had a considerably lower moisture content than the surrounding fabric. However, the post-2004 repairs generally appeared a good match for the historic fabric, because there was no obvious distinction between the moisture content of the different phases. This is illustrated in Chapter 9.

Finally, the infrared thermography helped to identify areas where the surface flaking of the render was at an early stage, and this is discussed further in Chapter 10.

Fig. 4.13. Building 47, SW wall, rebound hammer readings

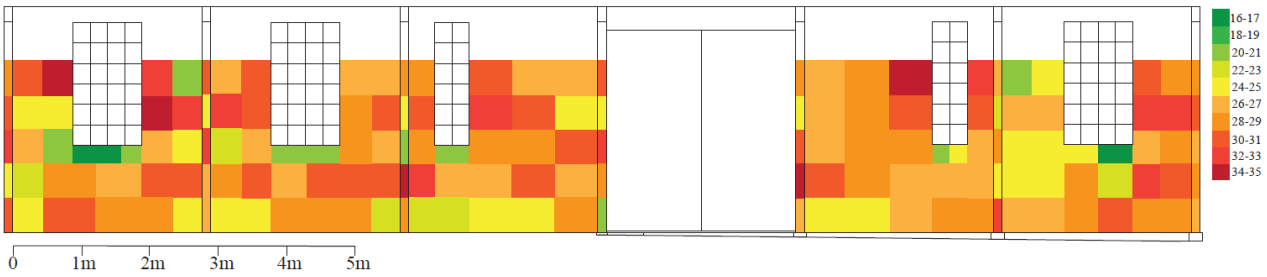

Fig. 4.14. Building 31, SE elevation, infrared thermograph showing cooler areas under the windows and on the piers, corresponding to higher moisture content. The infrared thermograph is a false colour image showing the surface temperature of surfaces in °C, where the red areas are warmest and the purple areas are coolest (Maureen Young, Historic Scotland)

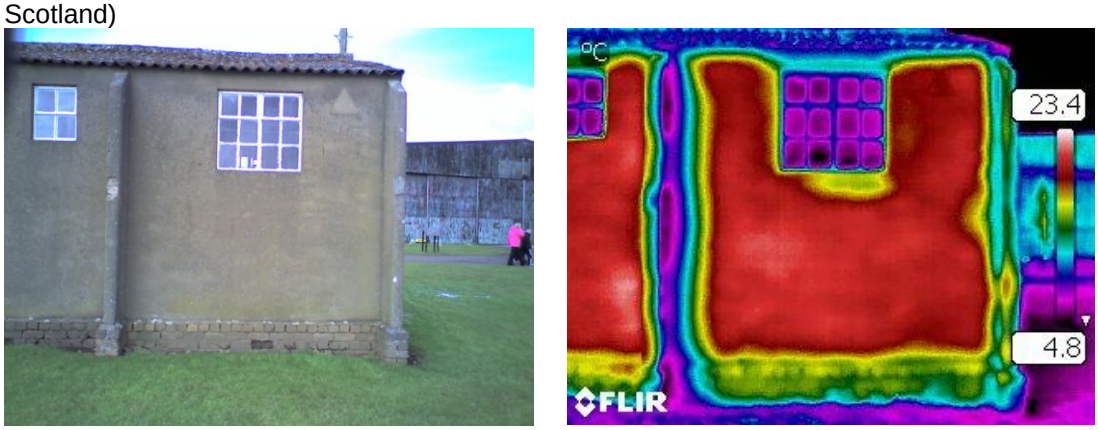

Fig. 4.15. Evidence of splash back on the door on the W elevation of Building 47

4.5 Direct measurement of moisture content

4.5.1 Method

Samples consisting of small partially detached pieces of bricks, render and mortar were taken from Buildings 22, 31, 32 and 47 , ensuring that they were in contact with the surrounding building fabric so as to have the same moisture content. The brick plinth in the area where samples were taken was approximately 0.28 m high. The samples were dried to constant mass and their percentage moisture contents were given by

$$\frac{m_w - m_d}{m_d} \times 100 \qquad \textbf{(4.3)}$$

where m_w is the wet mass and m_d is the dry mass.

4.5.2 Results and discussion

The moisture content data showed that even during dry weather the bricks and mortar close to the ground were very wet, and that the render adjacent to the brick plinth was also fairly wet (Table 4.2), suggesting some capillary rise of moisture. At a height of 1.5 m the render was slightly wet on the piers and fairly dry elsewhere. After rain the render on the piers was fairly wet, but still dryer than the render close to the ground. This suggests that at the time of sampling the ground had been wet for some time, supplying the base of the walls with a fairly constant supply of water.

Table 4.2 Moisture content of the bricks, render and mortar

	during dry weather					after rain
	bricks close to the ground	mortar from joint in bricks close to ground	render 0.3 m above ground (just above brick plinth)	render 1.5 m above ground	render on pier 1.5 m above ground	render on pier 1.5 m above ground
moisture content (% weight)	10.3 - 14.8	13.4	7.6 – 13.1	1.3 – 2.1	4.4	9.8
moisture content at saturation (% weight)	12.9 - 16.4 depending on type of brick	14.9	17.3	17.3	17.3	17.3

4.6 Environmental monitoring

4.6.1 Method

Environmental data from the site was collected using a telemetric monitoring system (Hanwell) which measured the temperature and relative humidity (RH) externally and inside some of the buildings, both heated and unheated; a site weather station (Signatrol WH 1090) which measured the temperature, RH, wind speed, wind direction and rainfall (Fig. 4.17); and data loggers (Signatrol SL52T and SL54TH button loggers) which measured the air temperature, RH and surface temperature on the exterior of Building 26. The purpose of the monitoring on Building 26 was to investigate the likelihood of condensation occurring on the render surface. The dew point temperature was calculated automatically by the data logger software using the air temperature and the RH. It was then subtracted from the measured surface temperature and plotted against time, and where the value approached zero, there was a strong likelihood of condensation.

An evaporimeter connected to a data logger (ETgage Company model E and Signatrol SL7003 logger) was used to monitor evaporation rates; this gave an electronic pulse for every 0.254 mm of evaporation, from which the evaporation rate in mm/hr or mm/day was calculated. It gathered approximately eight months of data at an external location, and several months of data from inside heated and unheated buildings (Buildings 26 and 31 respectively), but could not be used when temperatures were close to freezing. Additionally, a soil moisture sensor connected to a data logger (Delta-T Devices Ltd. ML2 sensor and GP1 logger) was buried approximately 1 m below the ground, and data was collected for almost 6 months. The probe measures the electrical capacitance of the soil, which is related to its moisture content. The fraction moisture content θ may be calculated from the output of the probe in V, V_1, using

$$\theta = \frac{(1.1 + 4.44V_1) - a}{b} \qquad \textbf{(4.4)}$$

where a and b are constants [135]. Standard values of a and b for mineral or organic soils may be used, or accurate values may be obtained through a calibration process. The soil at East Fortune is saline gley, which is 'generally rich in organic matter' if it is wet for much of the year [136]. As the data from NMOF showed that the soil was at least moderately wet throughout the monitoring period, it was assumed that the soil type was organic rather than mineral, and the standard values for a and b of 1.3 and 7.7 were used.

Where solar radiation data was required this was obtained from the Met Office [137], although daily readings were only available for Edinburgh, which is 20 miles from NMOF and may not have identical weather.

Fig. 4.17. Weather station at NMOF

4.6.2 Results

4.6.2.1 Weather data

Spreadsheets of weather data from June 2010 to September 2011 including data from inside Buildings 26 and 47, which were heated and unheated respectively, are included as electronic files. There are some gaps in the data due to equipment problems. Significant variations were observed between the external temperature and RH recorded by the weather station, the telemetric monitoring system and the data logger outside Building 26. These differences may have been due in part to the different locations of the equipment within the site. Spot readings were taken on several separate occasions using a recently calibrated hand-held thermohygrometer (Vaisala XO-37300-20) and compared to the live data from the monitoring equipment, and it was found that the data logger data gave the closest agreement with the thermohygrometer, followed by the weather station. The external temperature and RH data given in the spreadsheets are therefore from the data logger, but for periods of time when this data was not available, readings from the weather station have been given instead.

Where data was recorded at NMOF for the same month in two consecutive years, large variations were observed, particularly for rainfall and wind speed. For example, the total rainfall was 60.0 mm in June 2010, but 115.2 mm in June 2011, and the average wind speed was 139.7 knots in July 2010, but only 26.5 knots in July

2011. To obtain an accurate picture of the weather at NMOF it would be necessary to monitor for several years.

With reference to the 11 UK climatic regions defined by the Met Office [137], East Fortune lies within eastern Scotland. Detailed maps of each region are available, using a system of colour-coded zones to show the monthly averages for various climate variables. East Fortune is within the zone extending through Edinburgh and along the coast of East Lothian, which has the highest mean temperatures and lowest rainfall within eastern Scotland. When compared to the rest of the UK, temperatures along the East Lothian coast are around the national average, and it is among the driest places. The mean wind speed is above the national average.

The data collected at NMOF over 16 months was compared to the Met Office data for the coast of East Lothian averaged over the period 1971-2000 (Table 4.3 and Fig. 4.18). The Met Office data is plotted by the Met Office as a range, but the median value from each range was used to plot the histograms in Fig. 4.18. The temperatures at NMOF generally fell within the ranges given by the Met Office, although the average temperatures quoted for NMOF in November and December fell below the Met Office ranges, probably because the winter of 2010 was exceptionally cold. The rainfall at NMOF was sometimes within and sometimes above the Met Office ranges, suggesting that 2010-2011 was particularly wet, and possibly also because NMOF receives rain from the Lammermuir hills to the south. The wind speed at NMOF was considerably higher than that given by the Met Office, which is unsurprising because the flat, exposed nature of the NMOF site makes it particularly windy compared to the surrounding area.

The comparison of the conditions inside a heated and unheated building at NMOF with the external environment (Table 4.4 and Fig. 4.19) demonstrated that the heated building was warmer and drier than outside all year round, with the temperature difference varying from 1.8 °C in September to 10.2 °C in December. The conditions in the unheated building were very similar to the external conditions during the winter, but the unheated building was warmer and drier than outside from April-September, probably because it was warmed by solar gain.

Table 4.3 Comparison of the weather data from NMOF with Met Office data for the area containing NMOF

	NMOF data for 2010-2011			Met Office data for 1971-2000		
	mean temperature (°C)	mean total rainfall (mm)	mean wind speed (knots)	mean temperature (°C)	mean total rainfall (mm)	mean wind speed (knots)
January	3.2	14.8	33.8	3 - 5	20 - 80	15 - 20
February	5.0	134.4	39.2	3.5 - 5	20 - 60	10 - 15
March	6.6	82.8	38.4	5 - 7	20 - 80	10 - 15
April	10.9	16.8	42.6	6.5 - 8.5	20 - 50	10 - 15
May	12.0	98.4	52.6	9.5 - 11.5	30 - 60	8 - 10
June	14.6	87.6	52.6	12 - 14	30 - 60	8 - 10
July	15.7	160.2	83.1	14 - 16	30 - 60	8 - 10
August	14.7	200.4	62.5	14 - 16	30 - 70	8 - 10
September	13.4	50.9	31.6	11.5 - 13.5	40 - 80	10 - 15
October	10.2			9 - 10.5	40 - 80	10 - 15
November	4.8	231.7	47.7	5.5 - 7.5	20 - 80	10 - 15
December	0.0	31.0	28.4	4 - 6	20 - 80	10 - 15

Fig. 4.18. Comparison of the mean monthly weather data from NMOF with Met Office data for the area containing NMOF

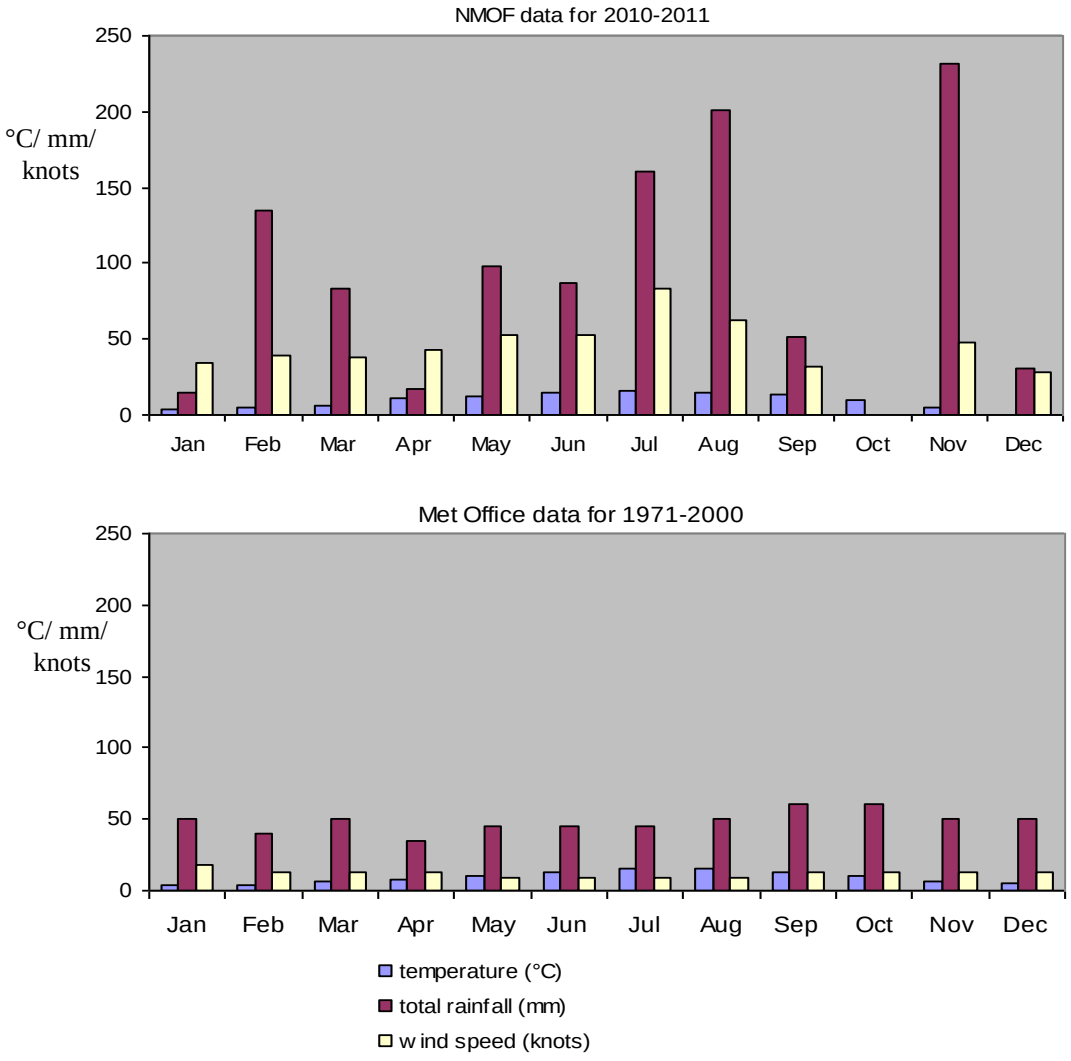

Table 4.4 Comparison of the conditions inside the buildings with the external environment at NMOF

	mean temp: external (°C)	mean RH: external (%)	mean temp: heated (°C)	mean RH: heated (%)	mean temp: unheated (°C)	mean RH: unheated (%)
January	3.2	92.2	12.4	52.4	2.8	94.8
February	5.0	93.3	13.9	54.6	4.5	95.7
March	6.6	84.6	16.0	49.0	6.6	87.0
April	10.9	78.6	20.5	45.5	12.6	71.6
May	12.0	74.4	21.1	43.5	13.9	63.9
June	14.6	77.9	22.5	48.9	17.3	57.0
July	15.7	80.1	20.9	58.5	18.7	64.3
August	14.7	81.3	17.8	67.5	16.6	68.0
September	13.4	82.3	15.2	72.4	13.9	75.0
October	10.2	88.2	17.4	59.4	9.2	86.1
November	4.8	88.3	14.1	52.3	4.4	91.1
December	0.0	94.2	10.2	49.2	-0.3	93.3

Fig. 4.19. Comparison of the conditions inside a heated and unheated building with the external environment at NMOF

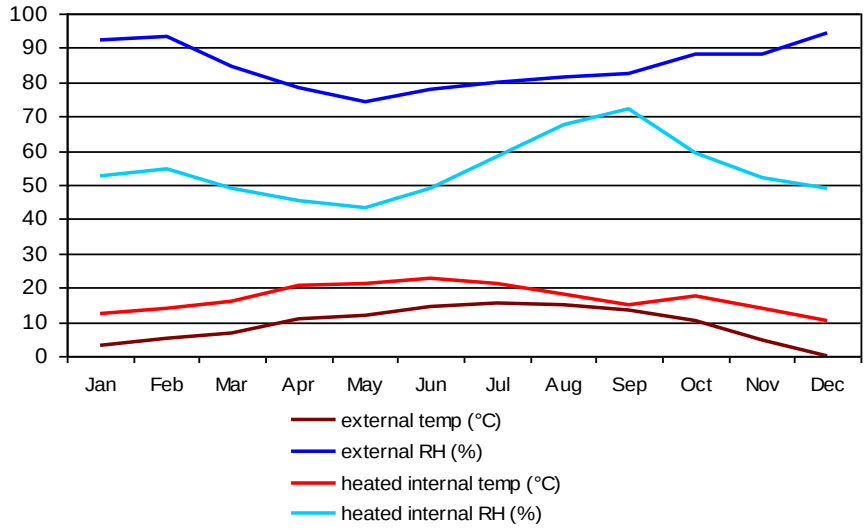

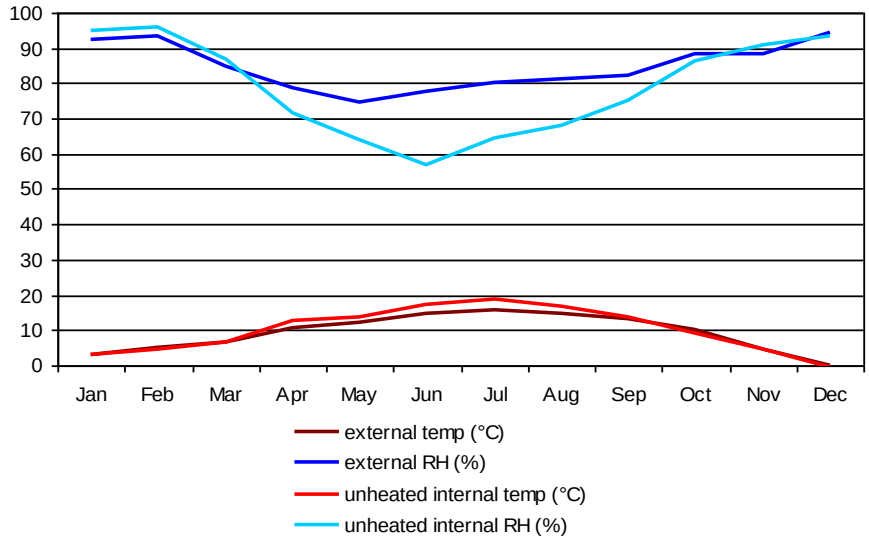

4.6.2.2 Surface temperature monitoring on Building 26

The surface temperature monitoring showed that condensation was likely to have occurred fairly frequently on both the north and south elevations of Building 26. There were generally more instances of potential condensation in the winter than in the summer, and more instances on the south elevation than on the north (Fig. 4.20). This was because the surface temperature was more variable and reached lower values on the south elevation.

Fig. 4.20. Graphs of surface temperature minus dew point temperature for February 2011, showing the likelihood of condensation events whenever ST-DPT≤0

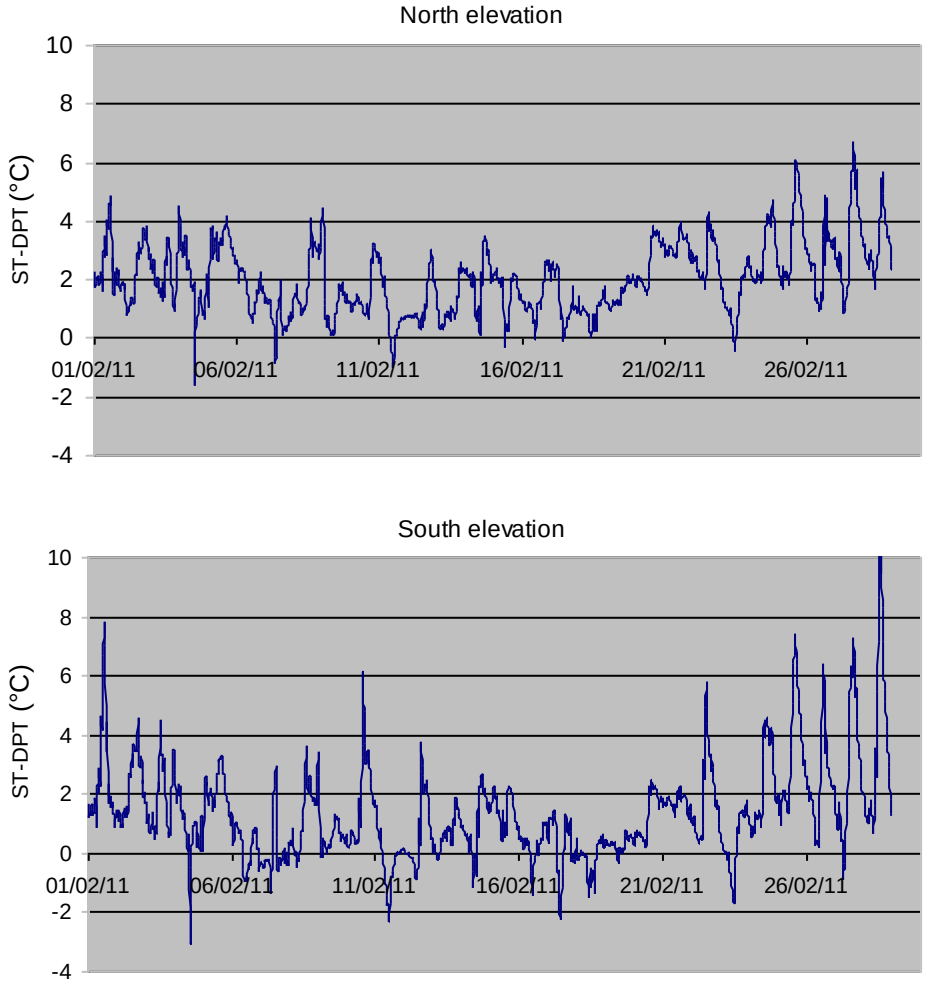

4.6.2.3 Evaporation rates

Evaporation data is included in the electronic files of weather data and is summarised in Table 4.5. This shows that the monthly mean of the daily external potential evaporation rate was highest in June and lowest in November, although data was not available for December-March. The maximum and minimum values recorded during the monitoring period were 4.32 mm/day on 14/07/2011 (day 195 within the year) and less than 0.25 mm/day on 1/12/2010 (day 335) and several other days in early December 2010. The minimum value was comparable to the minimum value for London over 1989-1994 of 0.21 mm/day on day 350, calculated from environmental data using the Penman equation [107], but the maximum value was considerably higher than the maximum calculated for London of 2.76 mm/day on day 180. This difference was probably due in part to the different methods used to obtain the evaporation rate, as discussed by Gavilán and Castillo-Llanque [116], but may also have been due to the high wind speeds experienced at East Fortune.

The potential evaporation rate in the heated building was higher than outside during March-April, when the heated building was typically 10 °C warmer than outside, and lower than outside during May-June, when the heated building was on average 5-6 °C warmer than outside, but with considerably less air movement. The potential evaporation rate in the unheated building was similar to the external potential evaporation rate during the winter and lower than the external potential evaporation rate during the summer, because there was less air movement inside.

Table 4.5 External and internal evaporation rates at NMOF

	mean evaporation rate: external (mm/day)	mean evaporation rate: internal heated (mm/day)	mean evaporation rate: internal unheated (mm/day)
January			0.52
February			0.51
March		2.54	
April	1.59	2.57	
May	1.93	1.29	
June	2.05	1.26	0.57
July	1.94		0.68
August	1.46		0.79
September	1.10		0.68
October	0.70		0.41
November	0.36		0.37
December			0.47

4.6.2.4 Soil moisture content

The soil moisture content data from the first few days of monitoring was discounted because it was suspected that the soil surrounding the probe might have dried out slightly when the probe was installed. Thereafter the fractional soil moisture content was around 0.39 for most of the time, which is moderately wet, but with occasional spikes of up to 0.56. Given that a moisture content of over 0.5 is considered very wet [135], the soil must have been approaching saturation on these occasions. The average daily soil moisture content was compared to the daily total rainfall in Edinburgh [137] (Fig. 4.21) and it was found that the soil moisture content was typically higher following periods of heavy rainfall. The values of near-saturation tie in with visual observations of water pooling on the surface of the ground.

Fig. 4.21. Relationship between rainfall and soil moisture content during April 2012

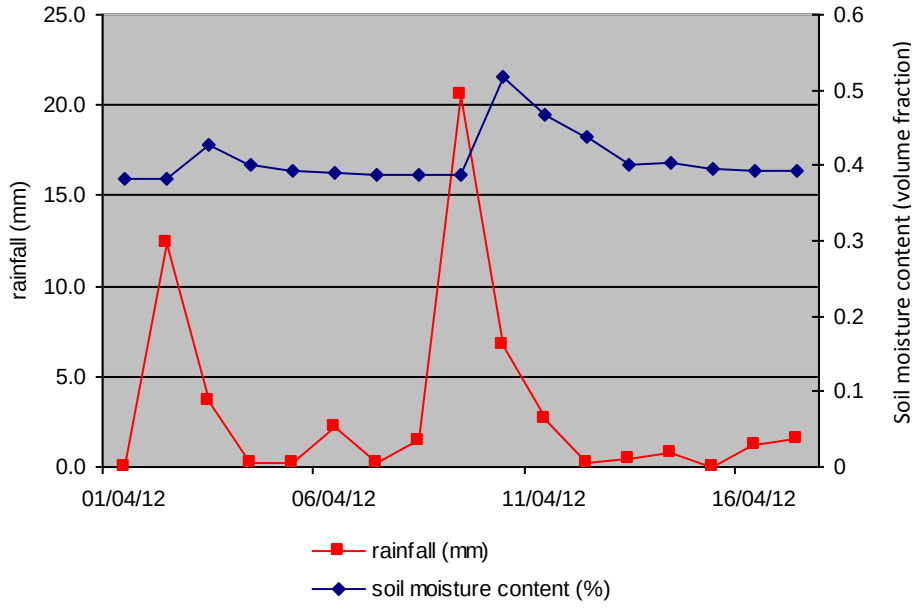

4.7 Conclusions

The detailed visual surveys showed that the main types of deterioration affecting the cement render were cracking and delamination from the brick substrate; and surface blistering and flaking. Cracking and delamination was found on all of the buildings on all elevations, and was more prevalent in areas which appeared to be wetted frequently, principally the piers protruding from the buildings. Blistering and flaking occurred on only some of the buildings, most commonly on the south elevations.

There was evidence that the buildings were being maintained, both with small-scale works such as the removal of damaging vegetation, and with major programmes of repair. These interventions were helping to prolong the lives of the buildings, for example by reducing the frequency and severity of wetting of the render. However, the level of maintenance was not always adequate, and there were localised areas of damaged render due to faulty rainwater goods and broken roof panels.

The time lapse photography demonstrated that cracking and delamination of the render could proceed extremely rapidly, particularly during periods of cold weather, but that cracks could also remain virtually unchanged for years. Minor movement of cracks was detected using strain measurements, but none of the cracks monitored were shown to be growing progressively wider over the 21 month monitoring period.

A combination of infrared thermography, electrical resistivity measurements and direct measurement of moisture content showed that the brick plinths and render just above the brick plinths were close to saturation, but that the zone of rising damp did not extend very far up the render. The render on the piers had a higher moisture content than the surrounding render even on a dry day, and was very wet after rain.

Surface temperature monitoring suggested that condensation may have been an additional source of moisture, as it appeared to occur fairly frequently. The infrared thermography was also useful to show that there was no discontinuity between the moisture content of the post-2004 repairs and the historic fabric, and to identify areas where sub-surface voids were forming within the render as a precursor to flaking. The rebound hammer readings generally gave some correlation with the visual appearance of the render, and demonstrated that in areas where the render surface had flaked off, the cohesion of the remaining render was unaffected.

Environmental monitoring data from NMOF showed that it was relatively dry, with temperatures around the UK average and wind speeds considerably exceeding the UK average, which is unsurprising given the flat and exposed nature of the site. The daily evaporation rate varied from close to zero in December to a maximum of 4.32 mm/day in July, which was higher than the maximum value calculated for London [107], possibly because of the high wind speeds at NMOF. Monitoring of the moisture content of the soil indicated that the soil was moderately

wet for most of the time, and approached saturation during periods of heavy rainfall. This tied in with visual observations of water pooling on the surface of the ground.

5.1 Introduction

The samples of building material taken were examined at low magnification and then mounted as thin sections for petrographic examination. Petrography is an invaluable technique for the investigation of buildings materials because it provides information about the composition of the materials and the workmanship, shows whether materials are deteriorating and assists with identifying the causes of deterioration. The petrographic examination was particularly useful to assess the quality of the original renders, demonstrate why some of the repair renders were failing and identify the type of bricks present underneath the failing repair render on Building 25.

5.2 Low magnification examination

5.2.1 Method

The hand samples available were examined to inform the petrographic examination and to assist with planning further analysis. They were initially examined with the naked eye and at 6.5 times magnification using a stereo microscope. The overall colour of each sample (or the colour of the binder only, for samples with large aggregate particles) was also assessed with the naked eye and assigned a colour using the Munsell colour system[3]. The features recorded were the colour and size of aggregate particles; the colour of the binder; the size and abundance of voids; and evidence of poor workmanship or deterioration. Additionally, the number of layers and their respective thicknesses were noted for the render samples, and the depth of cover was noted for the concrete. The hardness of the samples was graded using the classification system given by Ingham [63], which has five categories ranging from very soft to very hard.

The extent of carbonation of the cementitious renders and concrete samples was then investigated by spraying with phenolphthalein solution. The solution was prepared according to the method given by Belcher and Nutten [138], by dissolving 0.1 g of phenolphthalein powder in 60 g of ethanol and adding 40 g of deionised

[3] The reference chart used for the Munsell colour system was found at http://irtel.uni-mannheim.de/colsys/Munsell_A0.pdf, accessed 20 September 2012.

water. A freshly broken surface of the sample was then sprayed with the phenolphthalein solution. If the pH of the sample was above 9 it was stained bright purple by the phenolphthalein, but for pH values below 9 the phenolphthalein remained colourless. For cement-based materials, a pH above 9 indicates that the cement has not fully carbonated.

5.2.2 Results

Full results of the low magnification examination are given in Appendix 2, Section A2.1.

5.2.2.1 Renders

All of the renders were classified as hard. The original renders and B23 RR were light brown in colour, whereas B25 RR was light grey. The original renders were between 9 and 18 mm thick. B24 OR and B47 OR had been applied as a single layer, but there appeared to be two layers of roughly equal thicknesses in B32 OR, with large voids along the interface between the layers. The repair renders were between 8 and 12 mm thick and also appeared to have been applied in two layers, with a thick bottom layer and a thinner surface layer. B23 RR had a further layer of cement-rich material at the surface, but this layer was too thin to have been applied separately and was probably caused by over-working of the surface.

The aggregate in B24 OR and B23 RR was predominantly fine quartz, with a maximum particle size of 0.5 mm, whereas the aggregate in the other renders had a wider particle size distribution and was a mixture of quartz and other minerals (Fig. 5.1). In particular, the brown, grey, pink and orange particles measuring up to 4 mm in B47 OR gave it the appearance of concrete. The size and distribution of the air voids appeared to relate to the particle size distribution of the aggregates: B24 OR and B23 RR contained frequent air voids measuring below 1 mm, whereas the air voids in B32 OR, B47 OR and B25 RR were fewer in number but larger, measuring up to 3.5 mm.

B47 OR and B23 RR had carbonated completely, but although the surfaces and interfaces with the bricks in the other renders had carbonated, there were zones in the middle of these renders which remained un-carbonated or only partially carbonated. This zone was particularly evident in B25 RR, the most recently applied render, but B25 RR also had carbonated band along the interface between the layers,

as a consequence of the voids at the interface (Fig. 5.2). These voids suggested that the bonds between the layers might be poor, and were the only evidence of poor workmanship in the renders.

Fig. 5.1. Differing composition of the original renders viewed in section: B24 OR on the left and B47 OR on the right

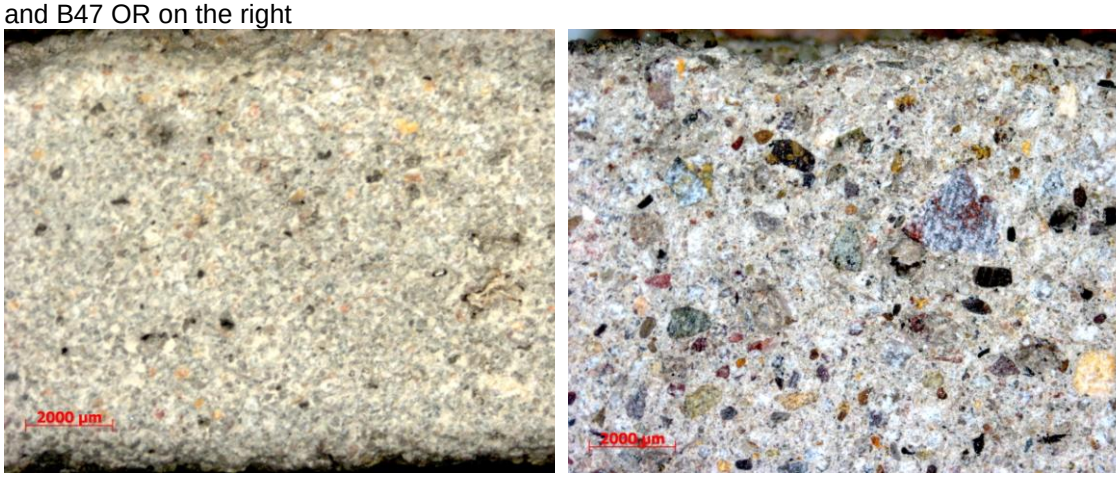

Fig. 5.2. Staining of B25 RR with phenolphthalein, showing carbonation of the surface, the interface with the bricks and the band along the interface between the layers

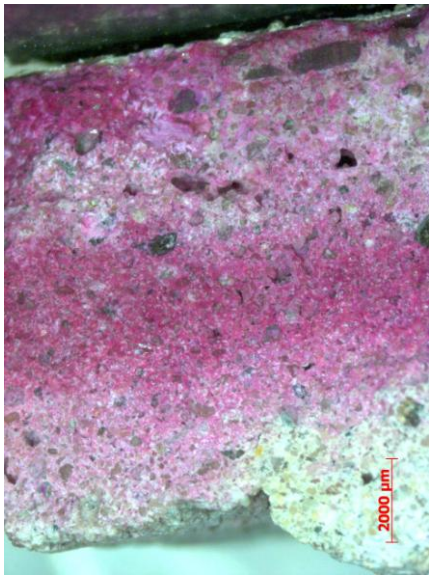

5.2.2.2 Bricks

The historic bricks were all machine-pressed, fired-clay bricks with frogs. Less was known about the modern bricks used to rebuild the wall on the north east side of Building 23, because only the stretcher faces of these bricks could be seen, but NMS had specified that they should be engineering bricks [129]. All of the bricks were classified as moderately hard. They varied in colour from light orange to mid-brown,

and were often different colours at the surface and in depth. The creamy orange colour of the Prestongrange brick suggested it might be a fireclay brick[4]. The historic Niddrie and Prestongrange bricks had rough, open surfaces, while the surfaces of the Wallyford brick and the Building 25 brick were moderately smooth, and the modern Building 23 brick was very smooth. Inside the bricks consisted of uniformly coloured matrices with inclusions of various colours measuring up to 3 mm, and the Wallyford and Building 25 bricks also contained black particles, possibly of coal, measuring up to 6 mm. The inclusions in the modern brick were fewer and smaller than those in the historic bricks (Fig. 5.3). There was fairly extensive cracking in the Niddrie and Prestongrange bricks, with the cracks generally aligned parallel to the bed face, whereas the Wallyford brick and the Building 25 brick had only fine cracking, and there was no cracking in the Building 23 brick.

Fig. 5.3. Bricks viewed in section, with historic Niddrie brick on the left and modern Building 23 brick on the right

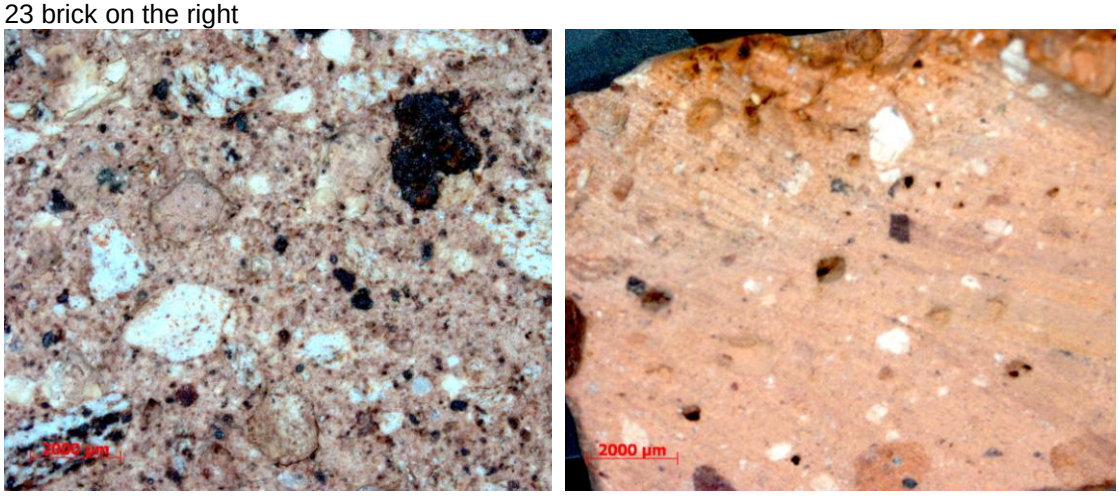

5.3 Petrographic examination

5.3.1 Method

The thin sections were examined in transmitted light, both plane polarized and cross polarized, at 50 to 500 times magnification. The features assessed for all the samples included the appearance of the surface and the presence of pores, voids and cracks; and the type, grading, size and abundance of the aggregates or inclusions. Other features investigated for the render and concrete samples were aspects of the

[4] This was a personal comment made by David Anderson of East Lothian Council Museums Service, January 2010.

workmanship, such as the number of layers visible and the finishing of the surface; the presence of portlandite, calcite and sulfates in the voids and around the aggregate particles; and the appearance of the cement matrix, with regards to the extent of carbonation and the size and abundance of relict cement grains, areas of hydrated cement and balled fines. Additionally, the render-brick interface was examined to assess the quality of the bond and to establish whether any portlandite, calcite, or sulfates were present along the contact surface or in the voids close to the surface.

The thin sections were used to estimate the mix proportions of the renders by point-counting. This was undertaken using an automated stage and specially designed software, which moved the stage in incremental steps so that the points examined formed a grid pattern across the thin section. 500 points were examined for a 2.5 × 5 cm thin section. The material visible at each point was categorized as cement paste, void or aggregate, and the aggregate was broken down into quartz, mudstone and other rock.

The relationship between the volumes of the various components in a cement mortar mix at the time of initial set and after hardening is given by Wong and Buenfeld [139] as

$$V_C + V_W = V_{AH} + V_{HP} + V_{CP} \quad \textbf{(5.1)}$$

where V_C, V_W, V_{AH}, V_{HP} and V_{CP} are the absolute volumes of the initial cement, initial free water, un-reacted (anhydrous) cement, hydration products and capillary pores. During point counting, the area categorized as cement paste consists of $V_{AH} + V_{HP} + V_{CP}$. Hence if it is assumed that the initial water/cement ratio is 0.5, so that $V_W = 0.5V_C$, the volume of the cement paste after hardening is equivalent to $1.5V_C$, and V_C can be calculated from the recorded volume of cement paste.

The aspects of render composition investigated with point counting were:

- The binder:aggregate ratios of the original and repair renders, for comparison with the ratios found using an acid extraction technique;
- The binder:aggregate ratios within the separate layers of B25 RR, to quantify the visual observation that the upper layer contained more binder than the lower layer;
- The proportion of voids in B23 RR, to quantify the observation that it appeared to contain more voids than the other renders;

- The type of aggregate, to quantify the difference between the predominantly quartz aggregate in B24 OR and the more varied aggregate in the other original renders.

5.3.2 Results

Additional images of the aggregates from the original and repair renders are given in Appendix 2, Section A2.2.

5.3.2.1 Original renders

Previous analysis had found the binders used to be predominantly or wholly cementitious [126], and it was therefore assumed that portlandite and calcite visible in the renders had originated from the Portland cement.

Building 24 original render

The original render from Building 24 (B24 OR) had been applied in two layers, with a cement-rich layer along the interface. The upper layer had probably been applied when the lower layer was still wet as the boundary was difficult to differentiate, and had been missed in the examination at low magnification. The render appeared fairly porous, with irregularly shaped entrapped air voids measuring up to 2000 μm (Fig. 5.4). There was a concentration of voids just below the surface, which had probably formed when the render was smoothed over as this process brings moisture to the surface.

There was evidence of skilled workmanship in that B24 OR was largely uncracked, with little calcite and portlandite on the surface or in the air voids, suggesting that the original mix had been quite dry and that there had not been much movement of water through the render subsequently. The render had a 'plucked' appearance where it had been in contact with the brick, indicating that some particles had been left attached to the brick, and there were calcite crystals and portlandite needles along the render-brick interface. This suggested that the bond between the render and brick was good, with the brick providing suction to draw in the cement hydrates.

Occurring frequently within the cement matrix of B24 OR were small to medium-sized, dark brown, opaque areas of fully hydrated cement and medium-sized relict cement grains (Fig. 5.5), again indicating that the initial mix was dry. Medium

to large lumps of balled fines also occurred frequently (Fig. 5.6), consisting of particles of quartz and cement, bound together with silt and clay. They may have formed when the cement and slightly damp sand were mixed together, before the water was added. As found using phenolphthalein indicator, the cement matrix was quite well carbonated at the surface and the interface with the brick, but only partially carbonated in the middle.

The aggregate in B24 OR was well sorted, and consisted predominantly of rounded quartz particles, ranging in size from 100-400 μm. It appeared to be from a single source and was probably quarry sand. Many of the quartz particles showed undulose extinction in cross polarized light, indicating 'strained' or distorted quartz from rocks that have been deformed (Figs. 5.7-5.8). This suggested that the quartz was derived from the southern uplands, although it might have been transported down to the East Lothian lowlands subsequently.

Building 32 original render

Despite the appearance of two layers in the examination of B32 OR at low magnification, only one layer was visible in the thin section. The render contained fewer voids than B24 OR (Fig. 5.9), but the presence of calcite and portlandite on the surface and in the voids suggested that the mix was wetter than the B24 OR mix. There were some micro cracks running perpendicular to the surface and parallel to the render-brick interface, which were probably caused by drying shrinkage (Fig. 5.10). Fine calcite crystals along the render-brick interface suggested that B32 OR had a good bond with the underlying bricks.

The cement matrix of B32 OR contained some large particles of balled fines, no relict cement grains and abundant large, dark brown, opaque areas of fully hydrated cement, again suggesting that there was more water present initially than in the B24 OR mix. The extent of carbonation was similar to that observed for B24 OR.

The aggregate used in B32 OR was distinctly different from the quarry sand in B24 OR. It was moderately sorted and appeared to be a mixture of two aggregate types from different sources. The first type was rounded fragments from a variety of rock types, measuring up to 4000 μm and including igneous rocks, sedimentary rocks, sporadic particles of metamorphic rocks, grains of pure feldspar, grains of carbonate minerals such as calcite, black particles of coal and sporadic particles of

mudstone. The mudstone had a strong organic content and some of the particles were layered, and had shrunk and cracked parallel to the layers. The mixed fragments included rocks local to East Lothian, rocks from the Pentland hills to the south of Edinburgh and rocks from the southern uplands, and such a mixture could plausibly have come from a gravel pit in East Lothian. The second aggregate type in B32 OR was angular quartz particles, approximately half of which by volume were smaller than 200 μm (Fig. 5.11). This suggested a deliberate addition of a fine, sharp sand, from a different source than the sand in B24 OR, although it might have been taken from a separate layer within the same quarry.

Building 47 original render

B47 OR was similar to B32 OR, but not identical. Again, there was only one layer visible in thin section and there were not many voids present. The surface had been smoothed down, resulting in a dense outer layer with some voids behind it. The presence of portlandite and calcite in the voids and around the aggregate particles suggested a wetter mix than for B24 OR, and there were again some micro cracks and fine cracks, probably due to drying shrinkage and possibly also resulting from the shrinkage or swelling of the layered mudstone particles. The bond with the brick appeared good, as there were no voids or cracking along the render-brick interface and the presence of calcite crystals suggested that moisture had been drawn from the render into the brick (Figs. 5.12-5.13).

Relict cement grains were rare in B47 OR, again suggesting a wetter mix than for B24 OR. Small to large dark brown, opaque areas of fully hydrated cement occured sporadically, and there were no balled fines evident. As in the other renders, the cement matrix appeared well carbonated at the surface and at the interface with the brick, but only partially carbonated in the middle. Staining with phenolphthalein had suggested that the render was fully carbonated throughout, and this demonstrates the inadequacy of phenolphthalein for detecting degrees of carbonation.

As in B32 OR, the aggregate in B47 OR was moderately sorted and was made of up two aggregate types: rounded rock fragments (Figs. 5.14 and 5.15) and angular quartz. This again suggested a deliberate addition of sharp quarry sand. The mixed rocks were similar to those found in B32 OR, and may have come from the same gravel pit, but the sand was coarser, with fewer than 25% by volume of the

particles below 200 µm (Fig. 5.16). If the sand came from the same quarry as that used for B24 OR and/or B32 OR, it must have come from a different layer.

Fig. 5.4. B24 OR, showing the join between the render layers and the presence of large voids, plane polarized light, field of view: 875 µm across

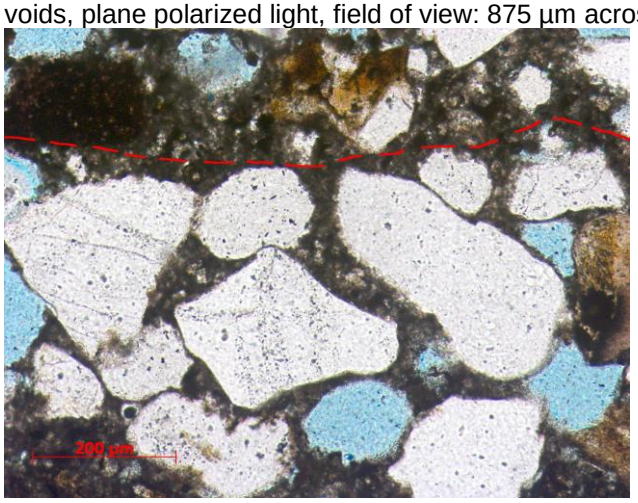

Fig. 5.5. Relict cement grain in B24 OR, seen in the centre of this image, plane polarized light, field of view: 440 µm across

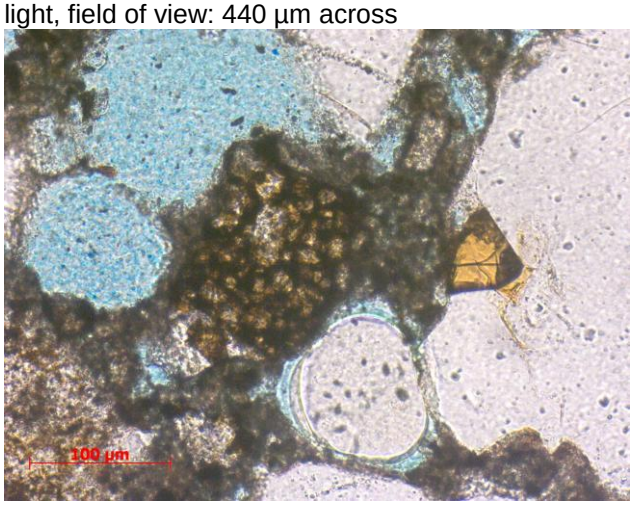

Fig. 5.6. Balled fines in B24 OR, plane polarized light, field of view: 1750 µm across

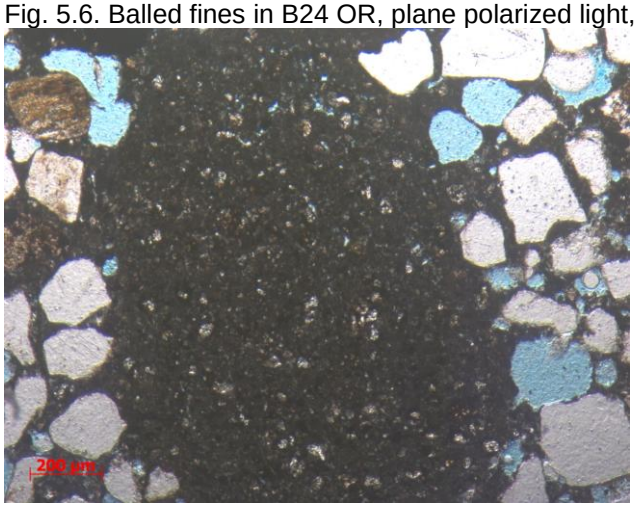

Fig. 5.7. Rounded quartz grains in B24 OR showing undulose extinction, plane polarized light, field of view: 875 µm across

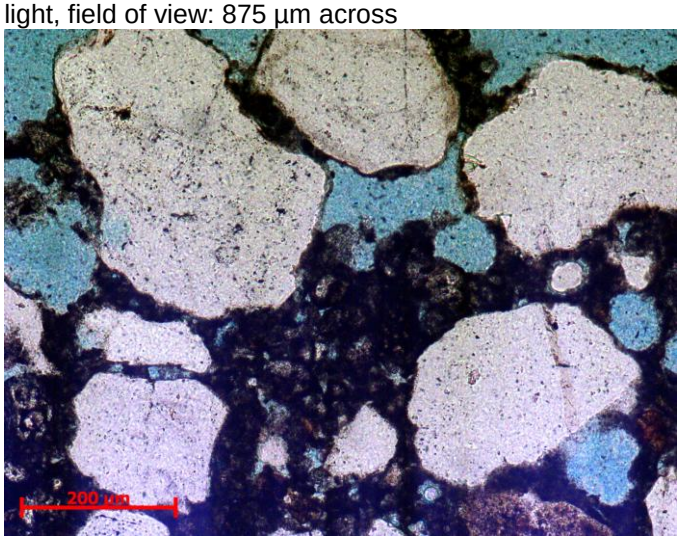

Fig. 5.8. As above, crossed polars

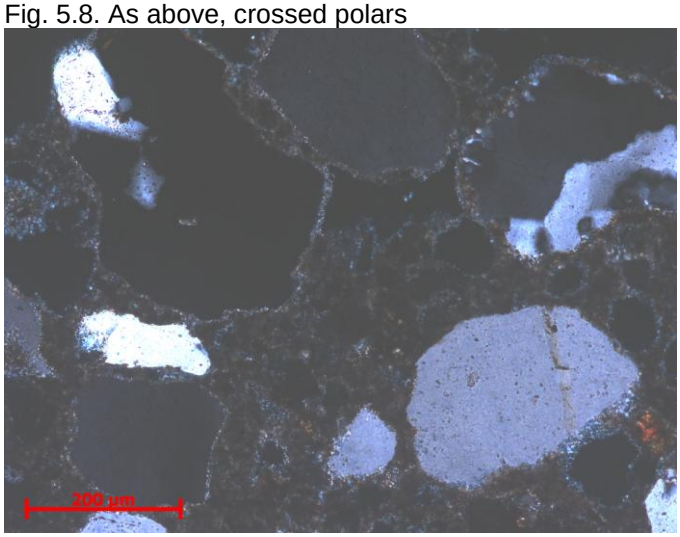

Fig. 5.9. Dense area of uncarbonated render from B32 OR with almost no voids, plane polarized light, field of view: 1750 µm across

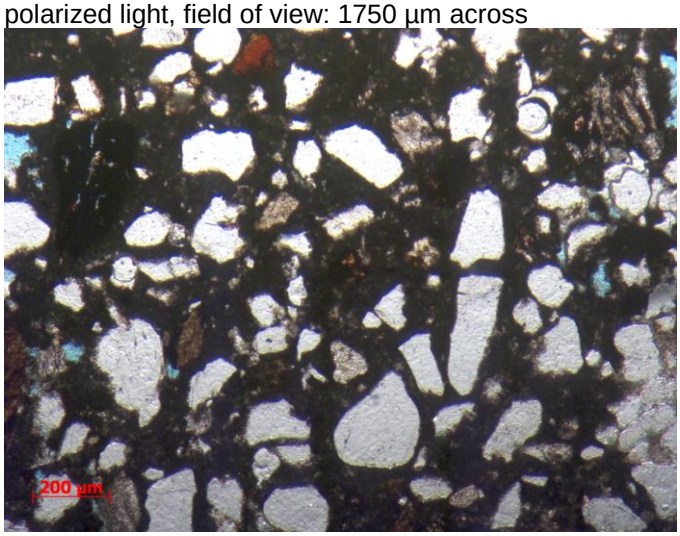

Fig. 5.10. A crack parallel to the brick interface in B32 OR, running through a weak aggregate particle (render in upper half of image, brick in lower half), plane polarized light, field of view: 875 µm across

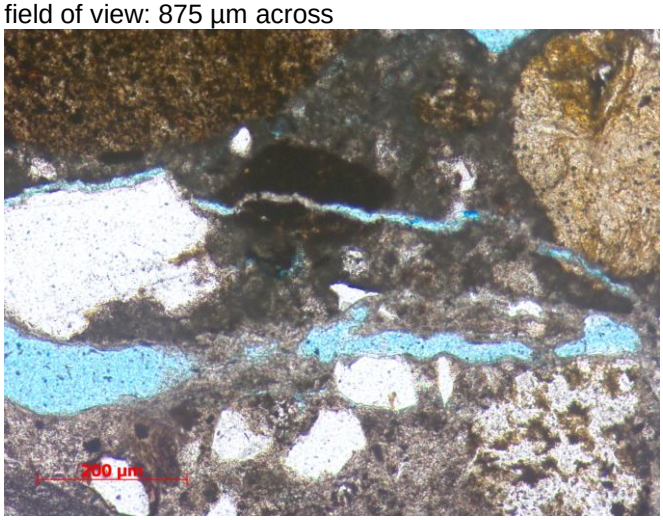

Fig. 5.11. Typical size range of the quartz grains in B32 OR, plane polarized light, field of view: 1750 µm across

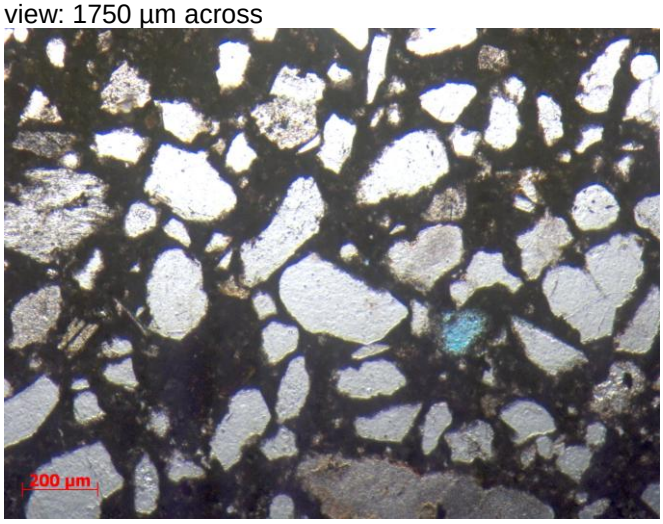

Fig. 5.12. Carbonated cement matrix and infill minerals in the voids close to the interface with the brick in B47 OR, plane polarized light, field of view: 440 µm across

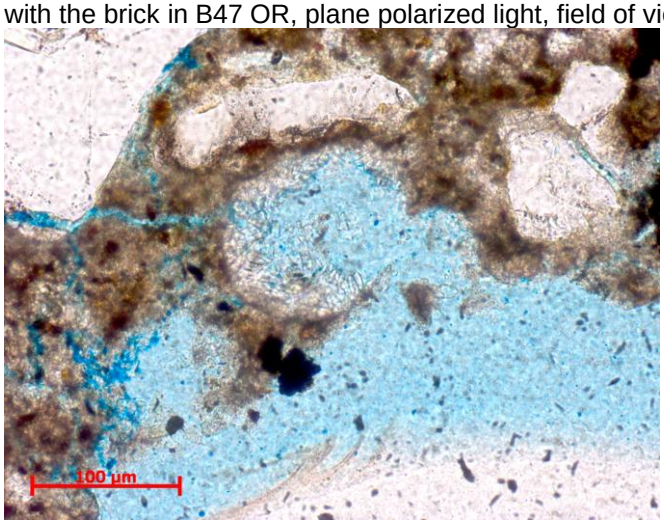

Fig. 5.13. As above, crossed polars

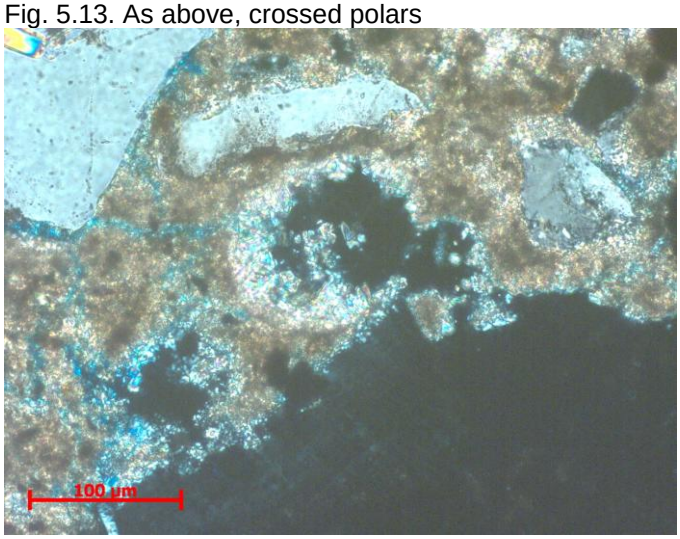

Fig. 5.14. Coal fragment in B47 OR, plane polarized light, field of view: 875 µm across

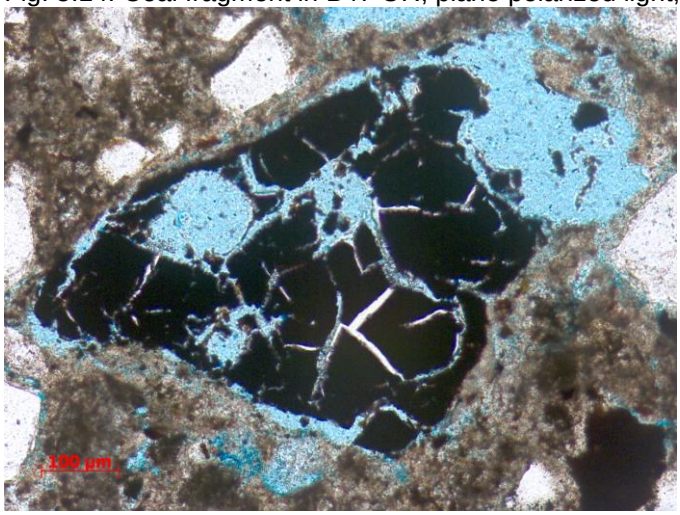

Fig. 5.15. Mudstone fragment in B47 OR, plane polarized light, field of view: 1750 µm across

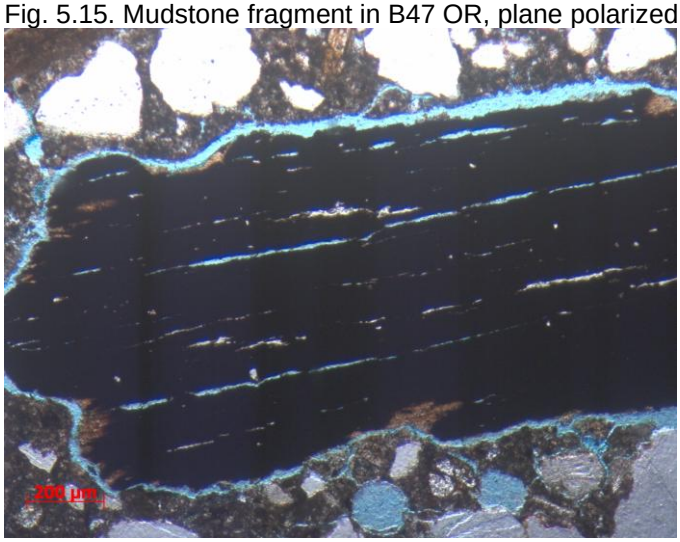

Fig. 5.16. Typical size range of the quartz grains in B47 OR, plane polarized light, field of view: 1750 µm across

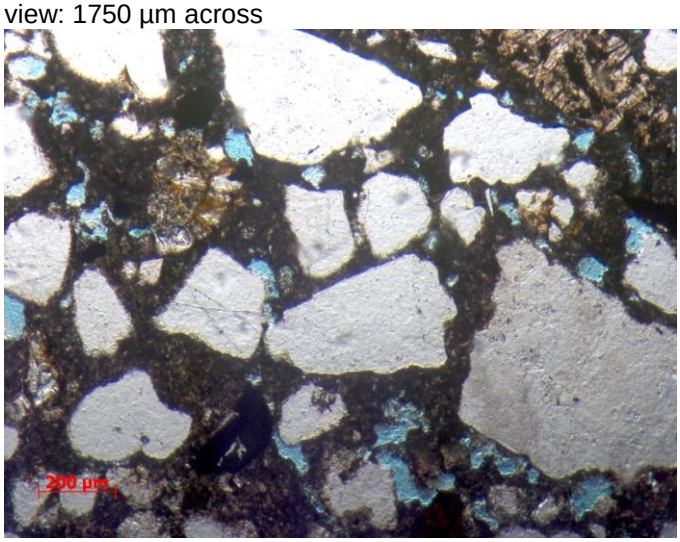

5.3.2.2 Repair renders

Building 23 repair render

The repair render applied to the rebuilt wall of Building 23 in 1992 (B23 RR) appeared to be a single layer, despite the conjectured appearance of two layers at low magnification. It contained numerous circular voids ranging in size from 50-1000 µm, suggesting the deliberate use of an air-entraining agent. The porosity was particularly high at the surface and the render-brick interface, and the surface had been worked to a very smooth finish. There were no crystallized sulfates visible but portlandite and calcite in the voids and around the aggregates indicated either that the mix was initially quite wet, or that there had been a lot of water percolating through the render. Despite this, there was very little cracking within the render. The render surface along the render-brick interface was very plain, indicating that the render had separated easily from the brick, and there was no evidence that cement fines had moved from the render to the brick.

The cement matrix in B23 RR contained abundant patches of dark brown hydrated cement, frequently occurring medium to large relict cement grains and sporadic lumps of balled fines. As staining with phenolphthalein staining had suggested, the cement matrix had carbonated all the way through. The aggregate consisted predominantly of well-rounded quartz grains, ranging in size from 50-400 µm, and characteristic of a fine building sand (Fig. 5.17). Sharp aggregates are preferable because they pack more efficiently [83].

Building 25 repair render

The render applied to the free-standing wall on the south side of Building 25 (B25 RR) as part of the major phase of repairs undertaken in 2005 had been applied in two layers (Fig. 5.18). There were some voids present in the render, particularly towards the bottom of each layer. Fine portlandite crystals in the voids indicated either that the original mix was wet or that water percolating through subsequently had leached portlandite out of the cement matrix. As with B23 RR, the surface had been heavily worked to achieve a smooth finish with no visible aggregates. The smoothing had created micro cracks running parallel to the surface and extending through some of the aggregate particles. Additionally, larger cracks up to 100 μm wide ran through the thickness of the render perpendicular to the surface, again breaking apart some of the aggregates. These were drying shrinkage cracks resulting from the use of an overly wet mixture.

There were almost continuous voids along the render-brick interface, containing abundant portlandite and calcite crystals. In this instance their formation was probably connected to the presence of large quantities of water, either from the high initial water content of the render, or because there had been a lot of water percolating through the render subsequently. Brown opaque areas of hydrated cement ranging in size from medium to very large occurred frequently in both render layers, again indicating that both mixes had high initial water contents. However, the lower layer contained only sporadic small to medium-sized cement grains, whereas these grains occurred commonly in the upper layer (Fig. 5.19). This suggested that the mix for the upper layer may have contained more cement. The render was fully carbonated at the surface and the interface with the brick, and partially carbonated elsewhere.

The aggregate was moderately sorted and appeared to have been the same in both layers. It contained quartz particles, mainly ranging in size from 20-600 μm, and fragments of other rocks, both igneous and sedimentary. These rock fragments were generally below 800 μm in diameter, although occasional large fragments measured up to 2500 μm. The aspects of workmanship visible from the thin sections of the repair renders are discussed more fully in Chapter 9.

Fig. 5.17. General view of aggregate fine fraction in B23 RR, showing abundant quartz grains, sandstone clasts (upper right and lower right) and altered fine-grained lava (lower left), plane polarized light, field of view: 1750 µm across

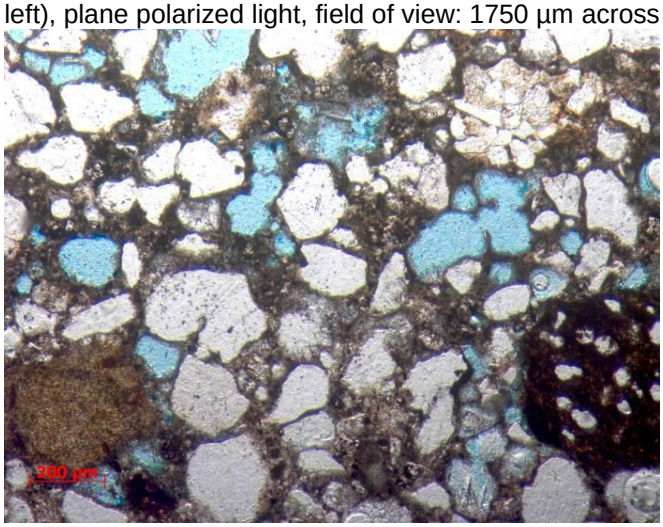

Fig. 5.18. Interface between layers in B25 RR (upper layer in upper half of image, lower layer below), plane polarized light, field of view: 875 µm across

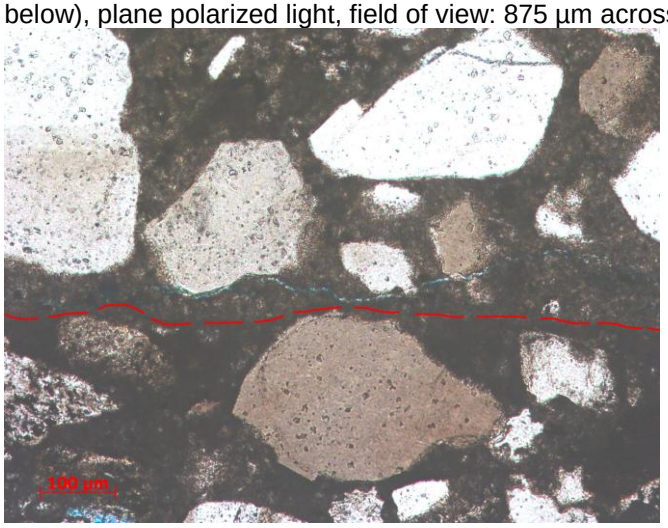

Fig. 5.19. Relict cement grains in the upper layer of B25 RR, plane polarized light, field of view: 440 µm across

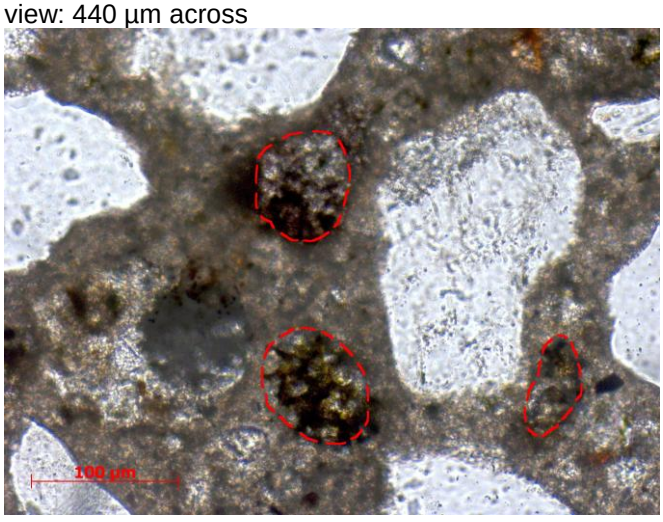

5.3.2.3. Detached blisters of render

At the bottom of each of the detached blisters was a rounded, brown, aggregate particle, measuring 4000 μm long in the blister from Building 25 and 1500 μm long in the blister from Building 47 (Fig. 5.20). The particles were identified as mudstone fragments with high organic contents. They had layered structures, with the layers aligned roughly parallel to the render surface, and cracking between the layers showed that there had been considerable laminar expansion. There were also occasional cracks up to 80 μm wide running diagonal to or perpendicular to the layers, and in both samples a continuous void 30-130 μm wide had formed between the aggregate particle and the surrounding render.

The expansion of the mudstone aggregates had caused considerable cracking within the cement render. This included cracks starting at the aggregate and running up through the render to the surface, measuring up to 50 μm wide and 1000 μm long, and micro cracks starting from the aggregate and radiating out through the render, measuring up to 10 μm wide and 400 μm long.

Of the six aggregate particles from Building 47 that were examined because they were thought to be related to the flaking, three were mudstone fragments with prominent cleavage similar to the aggregates observed in the detached blisters. The other three were fragments of sedimentary rocks consisting of crystalline particles held within a muddy matrix. None of the mudstone or other mud-rich particles were observed to contain pyrite, which is significant because pyrite may be a cause of swelling. Additional images of the detached blisters of render and aggregate particles are given in Chapter 10.

Fig. 5.20. The mudstone aggregate on the bottom of the Building 47 blister, plane polarized light, field of view: 1750 µm across

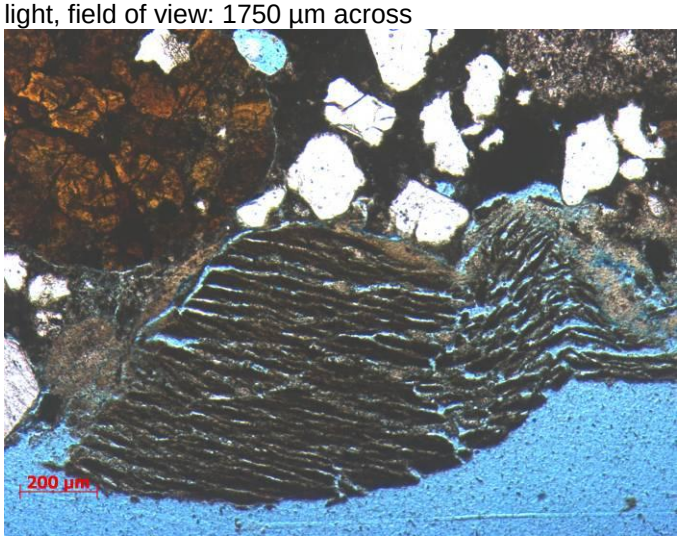

5.3.2.4. Bricks

All of the historic bricks contained large voids, of up to 4000 µm in diameter, and cracks measuring up to 70 µm wide and 1500 µm long, which may have been shrinkage cracks or may have been evidence of subsequent deterioration. Most of the bricks also contained networks of capillary pores, which in the Prestongrange bricks were channel-shaped and aligned parallel to the bed face, but small pores were less evident in the Wallyford bricks. Although the surfaces of the bricks appeared porous, they were relatively smooth (Fig. 5.21).

As observed at low magnification, the historic bricks consisted of uniformly coloured matrices with various inclusions, some measuring up to 5000 µm. Each brick had its own distinctive matrix colour and mix of inclusions: the Niddrie bricks had a mid-brown matrix and were characterized by burnt and unburnt coal particles, some of which were very porous, while the Wallyford bricks had a dark brown matrix and contained shrunken fragments of mudstone. The Prestongrange bricks had a light brown matrix with purplish inclusions of fireclay, and exhibited purple areas of high porosity (Fig. 5.22), which may have been fireclay inclusions that had not undergone full vitrification. Alternatively, they may have been areas of partially combusted fuel, which seems plausible given that coal particles were identified in the Niddrie bricks, and that the brickworks at Prestongrange was adjacent to the colliery.

The modern brick used to rebuild part of Building 23 in 1992 exhibited similar porosity and cracking to the historic bricks, and was therefore unlikely to be

engineering brick, despite this having been specified by NMS. However, the modern brick had a smoother and more compact surface than the historic brick, suggesting it had been well compacted during manufacturing (Fig. 5.23). The fine cracks parallel to the surface may have occurred when the brick was removed from its mould.

Fig. 5.21. Smooth but cracked surface of the Niddrie brick (surface at top of image), plane polarized light, field of view: 1750 µm across

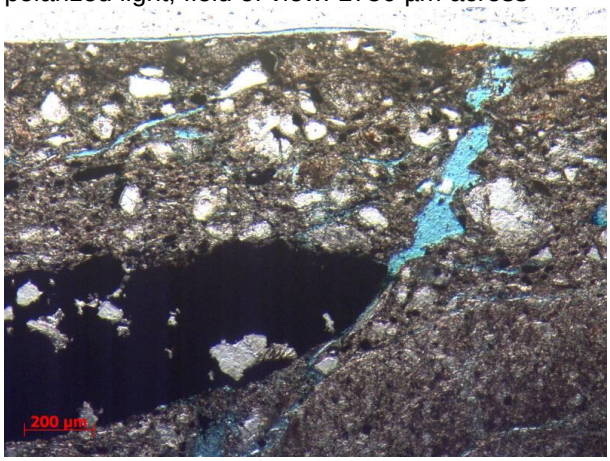

Fig. 5.22. Purple area of high porosity in the Prestongrange brick, plane polarized light, field of view: 1750 µm across

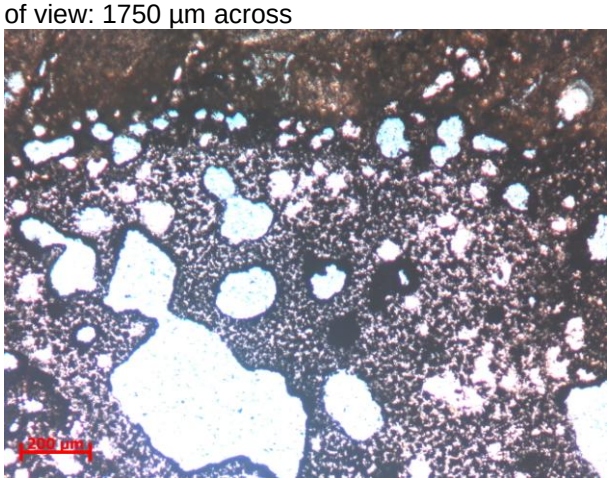

Fig. 5.23. Modern brick used to rebuild part of Building 23 in 1992, showing the smooth, compacted surface with fine cracking, plane polarized light, field of view: 1750 µm across

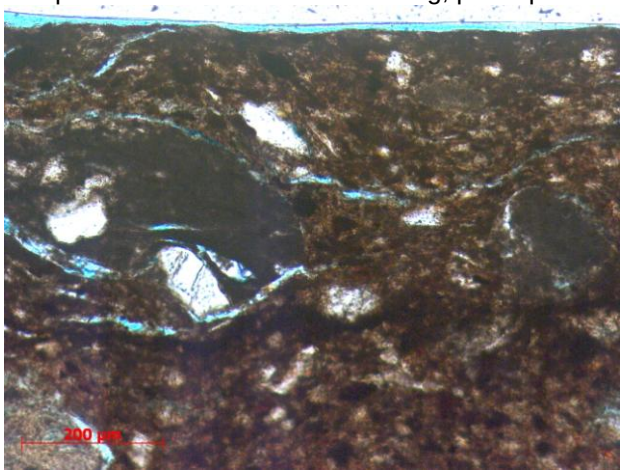

5.3.2.5 Point-counting

Errors may arise during point-counting if the number of points examined is insufficient to provide a representative sample. It was found by taking repeat readings that if 500 points were examined for a 2.5 x 5 cm thin section, the percentage of each of the main constituents by volume was repeatable to the nearest whole number, and consequently that the binder:aggregate ratio calculated was repeatable to one decimal place.

Point-counting was useful to demonstrate that:

- The binder:aggregate ratios for the original renders varied from approximately 1:2 to 1:3 (Table 5.1), while the ratio for the repair renders was around 1:1.8. The implications of this are discussed further in Chapters 6 and 9;
- The upper layer of B25 RR appeared to contain more cement than the lower layer, because the binder:aggregate ratio was 1:1.6 in the upper layer and 1:2.0 in the lower layer;
- The proportion of voids was highest in B24 OR, followed by B23 RR, and then the other original and repair renders;
- 91% of the aggregate in B24 OR was quartz, and it contained no mudstone, whereas the aggregates in B47 OR and B32 OR were composed of 44% and 56% quartz respectively, with various other rocks present including small quantities of mudstone (Table 5.2).

The full results of the point-counting are given in Appendix 2, Section A2.3.

Table 5. 1: Binder:aggregate ratios and proportions of voids in the original and repair renders (results are means from two samples of each render)

	B24 OR	B47 OR	B32 OR	B23 RR	B25 RR
binder:aggregate ratio	1:2.4	1:3.1	1:2.0	1:1.9	1:1.8
proportion of voids (%)	22	9	9	16	6

Table 5.2. Type of aggregate in the original renders (results are means from two samples of each render)

	B24 OR	B47 OR	B32 OR
quartz (% of aggregate)	91	44	56
mudstone (% of aggregate)	0	3	6
other rock (% of aggregate)	9	53	38

5.4 Conclusions

The examination of the renders at low and high magnification demonstrated that the choice of materials and quality of the workmanship for the original renders were generally good, resulting in dense renders with minimal cracking and strong adhesion to the brick substrate.

One of the original renders (B24 OR) appeared to contain only fine quartz aggregate, whereas the other original renders examined (B47 OR and B32 OR) contained two aggregate types: quartz and mixed rock fragments. Further differences between the aggregates in B47 OR and B32 OR showed that they were not from the exact same source, although the aggregates for all three renders could have come from quarries in East Lothian, and they could possibly all have come from different layers in the same quarry.

The original renders generally showed little evidence of deterioration. However, the detached blisters of render suggested that mudstone aggregates present in some of the renders had undergone expansion and caused cracking within the renders. Aggregate particles thought to be related to the flaking were found to be either mudstones or other mud-rich sedimentary rocks, and this type of deterioration is investigated in Chapter 10.

The materials and workmanship of the repair renders were not always appropriate or adequate. For example, the fine building sand used for the aggregate in B23 RR was an unsuitable choice for a render, and the high initial water content of B25 RR had resulted in extensive shrinkage cracking. The repair renders are discussed further in Chapter 9.

The historic bricks were similar to each other but not identical, as each brick had its own distinctive matrix colour and mix of inclusions. They contained large voids and cracks which could have been shrinkage cracks or could have been evidence of deterioration, but they were otherwise in reasonable condition. Research into the moisture absorption properties of the historic bricks is presented in Chapter 7. The modern brick from Building 23 was too porous to be an engineering brick, despite this having been specified, but had a noticeably smoother surface than the historic bricks.

6.1 Introduction

This chapter describes the experimental work undertaken to characterize the original and repair materials chemically and to obtain values for properties including strength, density, porosity, pore size distribution, sorptivity and drying behaviour. The purpose of the chemical analysis was to investigate the raw materials and mix proportions used for the renders and identify salt efflorescences, while the aims of measuring the physical properties of the materials were to:

- Establish whether the original and repair renders were likely to be durable, or whether they had weaknesses that could make them prone to deterioration;
- Demonstrate whether the visual differences between the original and repair renders observed at low and high magnification corresponded to variations in their physical properties;
- Understand the hydraulic properties of the bricks, in order to estimate the strength of the render-brick bonds.

As discussed in Chapter 2, a cement render is most likely to be durable if the bonding between the render and the substrate is good and there is no initial cracking in the render. Cracking can be avoided by specifying a mix with an appropriate binder:aggregate ratio, a well-graded aggregate and a low initial water content. The porosity and pore size distribution are also important: the use of an air-entraining agent may lead to high porosity, but it also creates a regularly spaced network of pores which can protect the render from freeze-thaw damage, whereas a render without air entrainment should ideally have low porosity to minimize the quantities of water available to cause damage. Low sorptivity and a rapid drying rate are desirable to avoid the frequent and prolonged saturation of the render, and to keep the substrate dry. The render should have slightly lower strength than the substrate, and the render should be flexible to tolerate some movement without cracking.

Some of the results are only given briefly in this chapter because they are discussed in more depth in subsequent chapters, and the abbreviations used for the materials tested are given in Table 6.1.

Table 6.1 Abbreviated names for the materials tested

abbreviated name	material
B33 M	original mortar from Building 33
B44 M	original mortar from Building 44
B23 OR	original render from Building 23
B24 OR	original render from Building 24
B47 OR	original render from Building 47
B31 OR	original render from Building 31
HC OR	original render from the hospital complex at Athelstaneford Mains
CA OR	original render from a building in Cark Airfield, Cumbria, England
B23 RR	1992 repair render from Building 23
B25 RR	2005 repair render from Building 25
ES B	Edinburgh brick, core drilled through stretcher face
EB B	Edinburgh brick, core drilled through bed face
NS B	Niddrie brick, core drilled through stretcher face
NB B	Niddrie brick, core drilled through bed face
PS B	Prestongrange brick, core drilled through stretcher face
PB B	Prestongrange brick, core drilled through bed face
WaS B	Wallyford brick, core drilled through stretcher face
WaB B	Wallyford brick, core drilled through bed face
WhS B	Whitehill brick, core drilled through stretcher face
WhB B	Whitehill brick, core drilled through bed face
ARS C	original concrete from the air raid shelter
ARS M	original mortar from the air raid shelter
B25 S	salt efflorescences from inside Building 25
B37 S	salt efflorescences from inside Building 37
ARS S	salt efflorescences from inside the air raid shelter

6.2 Binder:aggregate ratio of render and particle size distribution of aggregate

6.2.1 Method

The binder:aggregate ratio and particle size distribution of the aggregate are important because they influence the strength, resistance to cracking and hydraulic properties of the render. The binder:aggregate ratios of the renders were investigated using a simple acid extraction technique, and as previous analysis had found the binders used to be predominantly or wholly cementitious [126], it was assumed that this was the case for all of the renders and that analysis to determine the original content of lime was not necessary. Two or three samples of each type of render and mortar weighing approximately 1 g[5] were broken down gently with a pestle and mortar, to avoid crushing the aggregate, and dissolved in a mixture of 10 ml of

[5] Larger sample sizes were not used because breaking down the samples without crushing the aggregate was found to be extremely time-consuming.

concentrated hydrochloric acid (36% minimum) and 90 ml of deionised water. The concrete samples weighed approximately 2 g, because of the coarser aggregates in the concrete, and were dissolved in a mixture containing 20 ml of concentrated hydrochloric acid. The insoluble aggregate was separated out by filtration, dried to constant mass and weighed. It was assumed that every gram of powdered cement had reacted with 0.25 g of water, because 'the theoretical water/cement ratio (by weight) required for the complete hydration of…cement' is approximately 0.25' [140], and where M_a and M_{hc} were the masses of aggregate and hydrated cement in the hardened render, the original mass of powdered cement M_{pc} was given by $M_{hc}/1.25$. Taking standard values for the density of sand and powdered Portland cement of 1.602 g/cm^3 and 1.506 g/cm^3 respectively[6], the original volumes of aggregate and powdered cement V_a and V_{pc} were given by $M_a/1.602$ and $M_{pc}/1.506$.

The aggregate was passed through a series of sieves, with apertures ranging in size from 3 mm down to 0.053 mm. BS EN 933-2:1996 recommends that the aperture of the sieves should range from 125 mm down to 0.063 mm, but the samples tested did not contain aggregate above 3 mm in diameter, so the larger sieves were not necessary. The percentage by mass of material retained in each sieve was determined, and the results were plotted as bar charts, as recommended by Artiz-Young [83]. To investigate the reproducibility of the results the binder:aggregate ratio was measured on two samples of each material, and the particle size distribution were measured for two samples of B47 OR.

6.2.2 Results and discussion

The maximum variation between the pairs of binder:aggregate ratios obtained was 0.4 parts aggregate, and it was assumed that the averaged values were correct to 0.2 parts aggregate. The maximum variation within the particle size distribution results for the two samples of B47OR was 4% (Table 6.3), and it was therefore assumed that the results for the other samples were also accurate to ±4%. The errors were probably due to a combination of genuine variation between the samples and errors arising from the experimental techniques.

[6] The values for the density of sand and cement were taken from http://www.simetric.co.uk/si_materials.htm, accessed on 14 November 2012.

There is potential when using an acid extraction technique for some types of aggregate, such as calcite, to dissolve, resulting in an erroneously high binder:aggregate ratio. However, since no soluble aggregates had been observed during the petrographic examination, it was assumed that aggregate dissolution had not occurred. The average binder:aggregate ratios obtained by acid extraction were within 0.3 parts of aggregate of those obtained by point counting (Table 6.2). The results indicated that the binder:aggregate ratios varied from 1:2.2 to 1:2.9 for the original renders, and from 1:1.6 to 1:2.5 for the original mortar. The ratio obtained for the air raid shelter concrete was 1:30. The value of 1:2.9 obtained for B47 OR was similar to the value of 1:2.7 obtained previously for the original render from Building 25 [126], which was expected given that these renders are similar in appearance. The binder:aggregate ratio for both repair mixes was around 1:2, indicating a higher cement content than was used in the original renders.

Table 6.2 Binder:aggregate ratio obtained with acid extraction technique and point counting

sample	binder:aggregate ratio from acid extraction (mean from 2-3 samples)	binder:aggregate ratio from point counting (mean from 2 samples)	average binder:aggregate ratio
B33 OM	1:1.6		
B47 OR	1:2.9	1:3.1	1:3.0
B24 OR	1:2.2	1:2.4	1:2.3
B32 OR		1:2.0	
B23 RR	1:2.5	1:1.9	1:2.2
B25 RR	1:2.1	1:1.8	1:1.9
ARS C	1:3.0		
ARS M	1:2.5		

The particle size distribution of the original renders varied considerably (Table 6.4 and Figs. 6.1 and A3.1): none of the B24 OR aggregate was above 0.355 mm in diameter, compared to 52% of the aggregate from B47 OR, and this high content of coarse aggregate in B47 OR had been observed during the examination at low and high magnification. The aggregate used in B23 RR had a similar particle size distribution to B24 OR, and the aggregate in B25 RR contained more coarse particles than B24 OR, but fewer than B47 OR. The aggregates used in the mortars were quite fine, but still with more coarse aggregate than B24 OR. According to the criterion of Artiz-Young [83] that ‘a well graded sand will have no more than 30-35% retained in any one sieve’, the only well graded aggregate was present in B47 OR, while the other renders and mortars contained excessive amounts of aggregate in

the 0.106-0.212 mm band. Although the aggregate for ARS C appeared poorly graded due to an excessive amount of aggregate in the 0.841-3.000 mm band, if a larger sample were taken it would contain some larger aggregate particles, and the particle size distribution might then indicate a well graded aggregate.

Table 6.3 Particle size distribution of aggregates in B47 OR for an initial and repeated run, given as percentages by weight

	>3.000 mm	0.841-3.000 mm	0.355-0.841 mm	0.250-0.355 mm	0.212-0.250 mm	0.106 0.212 mm	0.053-0.106 mm	<0.053 mm	total
B47 OR run 1	0.0	28.2	24.8	9.1	5.0	15.9	8.6	8.4	100.0
B47 OR run 2	0.0	24.2	28.2	12.7	3.6	19.3	9.0	3.0	100.0

Table 6.4 Particle size distribution of aggregates in mortars, renders and concrete, given as percentages by weight (single values)

	>3.000 mm	0.841-3.000 mm	0.355-0.841 mm	0.250-0.355 mm	0.212-0.250 mm	0.106 0.212 mm	0.053-0.106 mm	<0.053 mm	total
B33 M	0	3	10	13	9	43	16	6	100
B47 OR	0	26	26	11	4	18	9	6	100
B24 OR	0	0	0	23	23	40	5	9	100
B23 RR	0	0	6	21	18	46	4	5	100
B25 RR	0	12	12	12	8	42	10	4	100
ARS C	0	45	24	11	4	11	3	2	100
ARS M	0	4	5	20	22	43	3	3	100

Fig. 6.1. Particle size distribution of the original renders, showing percentage by weight retained in each sieve size

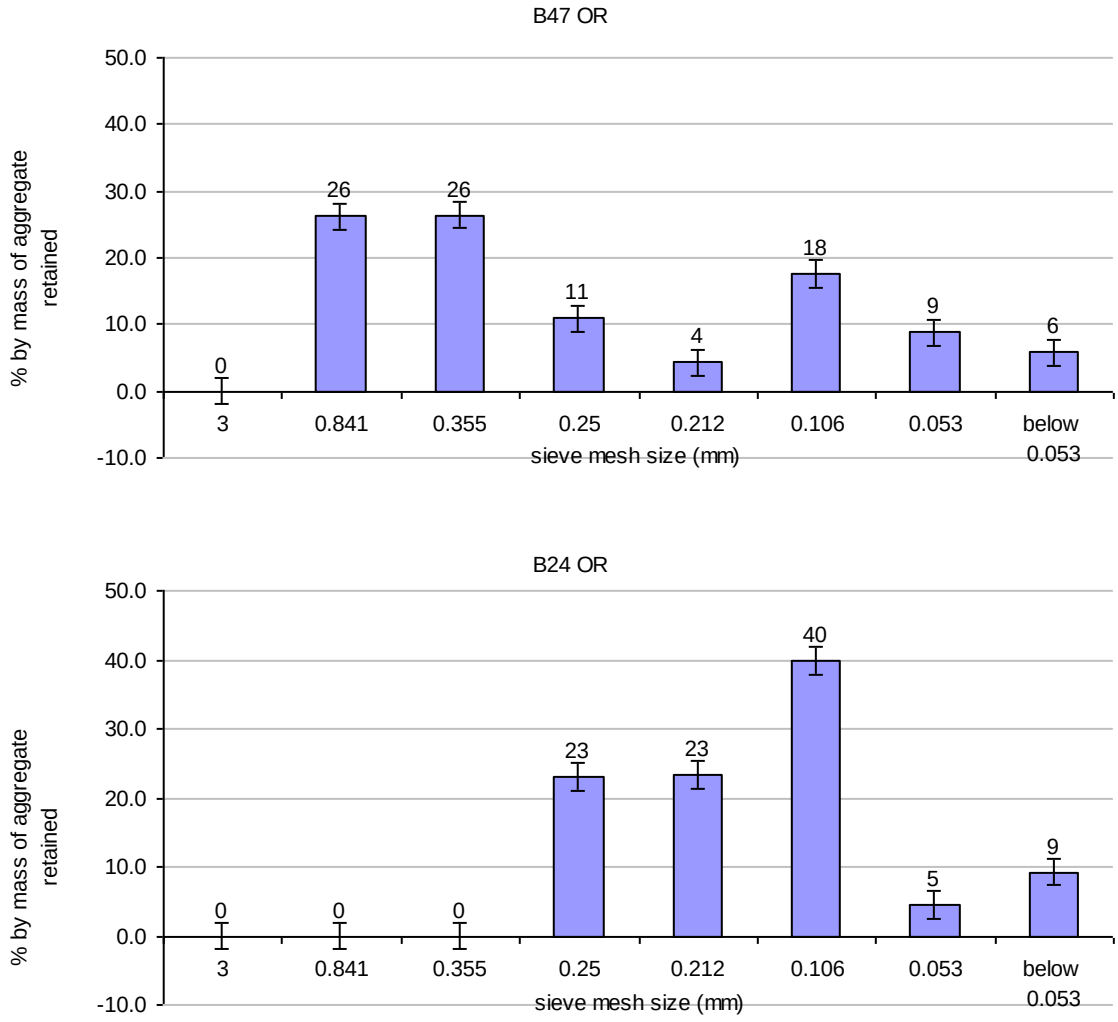

6.3 Ions analysis

6.3.1 Method

Ions analysis was undertaken to determine the quantities of soluble sulfate, chloride, nitrate, calcium, magnesium, potassium, sodium and aluminium ions present in samples, in order to:

- Investigate whether the flaking of the render might be due to the crystallization of salts;
- Identify the salts present as efflorescences on the interior of the buildings;
- Investigate whether the source of the salts found inside the buildings was likely to be the bricks or the mortar joints;

- Investigate the distribution of salts within the building walls by taking samples drilled through a mortar joint at different depths.

The locations from which samples were taken are given in Table 3.4.

The solutions required for the analytical procedure were prepared by taking approximately 1g of building material or 0.25 g of salt efflorescence (for samples B25 S1, B37 S1 and ARS S1), weighing the sample accurately and crushing it. Approximately 25 ml of water was weighed and added, and the mixture underwent 4 hours of warming at 60 °C with continual stirring, before standing at room temperature for seven days. The liquid was then removed by filtration and the pH was measured with a pH meter (AR 50 Dual channel pH/Ion/Conductivity Meter from Fisher Scientific). Separate portions of each solution were used for ion chromatography (IC) and inductively coupled plasma – optical emission spectrometry (ICP-OES).

IC was undertaken using a DX-500 ion chromatograph (DIONEX, Sunnyvale, CA, USA) to determine the concentrations of sulfate, chloride and nitrate ions in the solution[7], while ICP-OES[8] with a Perkin Elmer Optima 5300 DV was used for calcium, magnesium, potassium, sodium and aluminium ions, and the concentrations were given in parts per million (ppm). Full experimental details are given in Appendix 3, Section A3.1. Additionally, since the results obtained for the ions contents of the bricks were considerably lower than the values quoted elsewhere [142], further analysis of the Edinburgh and Niddrie bricks was undertaken with acid extractions, using the methods detailed in BS 3921:1985 and BS EN 772-5:2003[9]. It would generally be expected that more ions would be extracted if acid is used [45].

Hydroxide, hydrogen carbonate and carbonate ions were also likely to be present in the solutions. To calculate the charge balancing error for a specific solution, the concentration of each anion and cation in ppm was converted into molarity using $M = (0.001 \times c)/RMM$, where M is the molarity of the solution of a particular ion, c is its concentration in ppm and RMM is its relative molecular mass.

[7] The IC samples were run by other researchers: the first batch were run by Dr Peter Andersen at the University of Edinburgh and a further batch were run by Caledonian Laboratories Ltd, who were asked to test only for chlorides.
[8] The ICP-OES samples were run by the author at the University of Edinburgh, with assistance from Dr Lorna Eades.
[9] Additional analysis of the ions contents in the Edinburgh and Niddrie bricks was undertaken by William Revie of Construction Materials Consultants.

The sums of the positive and negative charges Σ_c and Σ_a were calculated, using $\Sigma = M_1v_1 + M_2v_2$ etc where M and v are the molarity and valence of each ion. As shown by Fritz [143], the percentage charge balancing error $\%CBE$ was then given by

$$\%CBE = \frac{100(\Sigma_c - \Sigma_a)}{\Sigma_c + \Sigma_a} \quad \textbf{(6.1)}$$

The error was usually positive because Σ_c was usually greater than Σ_a, due to the presence of hydroxide, hydrogen carbonate and carbonate ions which had not been measured.

A geochemical code, PHREEQC, was used to calculate the quantities of unmeasured ions such as hydroxide, hydrogen carbonate and carbonate from the known quantities of ions present [144]. To determine the closeness of fit the pH values calculated by PHREEQC were compared to the pH values measured.

The results were normalized by converting the concentration c of each ion in the solution in ppm to the percentage $\%e$ of the ion extracted from the sample by mass, using

$$\%e = \frac{cv_w}{10000M_s} \quad \textbf{(6.2)}$$

where v_w is the volume of water added to the sample in ml and M_s is the mass of the sample in g. It is useful to work with ion concentrations as percentages of sample mass, because they are referred to in standards such as the maximum sodium and potassium content in clay bricks (BS EN-771-1:2003) and the recommended maximum chloride content in concrete [19]. The reproducibility of the results was checked by testing one of the solutions three times, and by testing solutions prepared from two render samples taken from the same fragment, B47 OR NF2 and B47 OR NF3.

6.3.2 Results and discussion

6.3.2.1 Accuracy of results

The use of PHREEQC to estimate the individual concentrations of hydroxide, hydrogen carbonate and carbonate ions present in the solutions suggested that they were generally present in comparable quantities to the other anions. When the quantities of these ions were taken into account the percentage charge balancing

error was reduced for all samples, falling from previous values of up to 93% to new values of up to 53%. The pH values calculated by PHREEQC were generally accurate to ±1 if the measured pH was around 7-9, indicating a reasonable closeness of fit, but were less accurate for solutions with a measured PH of 9 or more. PHREEQC is unlikely to give very precise results because the measured ion contents used for the calculations have varying degrees of accuracy themselves, but it is nonetheless valuable to demonstrate the presence of species such as carbonate ions. The data obtained using PHREEQC is included in Appendix 3 (Tables A3.3-A3.8).

The ion concentrations measured were often below 10 ppm, meaning they were at the detection limits of the techniques. It was therefore not possible to use the results to make comparisons between samples for which very low ion concentrations were measured, as was the case for the two render samples taken from the same fragment, B47 OR NF2 and B47 OR NF3. A further issue was that it may be difficult to obtain reproducible results using an aqueous extraction method [19].

6.3.2.2 Flaking render (Table 6.5)

Some flaking had been observed on buildings 26, 46 and 47, whereas there was no flaking visible on Buildings 23 and 24. The levels of sulfates, chlorides and sodium were generally slightly higher on buildings where some flaking was evident, but there were various exceptions to this. Additionally, high values of chlorides and sulfates were found in the render sample from Cark airfield (CA OR NF1), where no flaking was observed on any of the buildings. No clear difference was found between the samples taken from areas with and without flaking on any one building, although the two samples with the highest sulfate contents were both from areas of flaking.

Table 6.5 Concentrations of selected ions in render samples taken from areas with and without flaking, expressed as a percentage of the solid sample (single values)

sample*	Cl^- %	NO_3^- %	SO_4^{2-} %	Ca^{2+} %	Mg^{2+} %	K^+ %	Na^+ %	Al^{3+} %
B26 OR NF1	0.001	0.000	0.034	0.056	0.000	0.009	0.001	0.022
B26 OR F1	0.004	0.001	0.025	0.158	0.001	0.014	0.003	0.059
B46 OR NF1	0.001	0.000	0.102	0.085	0.000	0.015	0.011	0.004
B46 OR NF2	0.005	0.001	0.092	0.137	0.000	0.009	0.002	0.010
B46 OR F1	0.008	0.002	0.049	0.147	0.000	0.010	0.009	0.000
B46 OR F2	0.006	0.002	0.520	0.215	0.000	0.011	0.021	0.010
B46 OR F3	0.016	0.006	0.488	0.211	0.001	0.019	0.004	0.018
B47 OR NF1	0.003	0.001	0.045	0.040	0.001	0.006	0.009	0.000
B47 OR NF2	0.002	0.000	0.061	0.082	0.000	0.010	0.009	0.000
B47 OR NF3	0.001	0.000	0.041	0.033	0.001	0.006	0.005	0.000
B47 OR F1	0.003	0.000	0.037	0.127	0.004	0.012	0.015	0.000
B47 OR F2	0.016	0.004	0.233	0.172	0.000	0.008	0.013	0.000
B24 OR NF1	0.002	0.002	0.056	0.161	0.000	0.004	0.003	0.000
B24 OR NF2	0.006	0.013	0.081	0.139	0.000	0.005	0.003	0.000
B24 OR NF3	0.002	0.003	0.183	0.143	0.009	0.012	0.006	0.000
B23 OR NF1	0.001	0.000	0.015	0.116	0.003	0.008	0.005	0.000
CA OR NF1	0.032	0.027	0.241	0.159	0.000	0.002	0.004	0.000

* NF samples were taken from areas without flaking, whereas F samples were from areas with flaking

6.3.2.3 Salts (Tables 6.6-6.8)

The data suggested that the salt efflorescences found on the internal walls in Buildings 37 and 25 and inside the air raid shelter were sodium sulfate. With regards to the source of salts inside the brick masonry buildings, the concentrations of sodium and sulfate ions in the bricks and mortar were considered low, given that bricks may contain 0.5% by weight or more of salts such as sodium sulfate and sodium chloride [142]. It is possible that the mortar was the source of sodium sulfate, given that the salts were most apparent along the mortar joints and that sodium sulfate efflorescences were found on other cementitious materials at the site, namely the concrete in the air raid shelter. However, sulfate efflorescences on bricks are also very common [100], and it is possible that the bricks initially contained more sulfates, which washed out when the bricks were stored outside. Additionally, the predominance of sodium sulfate along the mortar joints may have been related to the different moisture transport properties of the bricks and the mortar rather than the source of the salts.

The analysis of the mortar samples taken at varying depths starting from the inside of the east wall of Building 25 showed that the concentration of sulfates was up to six times higher than in mortar samples taken from areas without salt efflorescences. The concentration of sulfates increased with proximity to the internal surface, suggesting they were being transported through the wall by water evaporating out into the room.

Table 6.6 Concentrations of selected ions in salt samples taken from internal walls (single values)

sample	Cl^- %	NO_3^- %	SO_4^{2-} %	Ca^{2+} %	Mg^{2+} %	K^+ %	Na^+ %	Al^{3+} %
B37 S1	0.013	0.002	31.277	0.023	0.003	0.135	13.357	0.006
B25 S1	0.050	0.000	21.435	0.159	0.262	0.146	7.137	0.001
ARS S1	0.033	0.081	15.407	0.394	0.006	0.075	3.960	0.058

Table 6.7 Concentrations of selected ions in bricks and mortar (single values)

sample	Cl^- %	NO_3^- %	SO_4^{2-} %	Ca^{2+} %	Mg^{2+} %	K^+ %	Na^+ %	Al^{3+} %
EB1	0.000	0.000	0.002	0.026	0.000	0.000	0.005	0.000
EB2 (acid extraction)			0.030	0.088		0.092	0.008	
NB1	0.001	0.000	0.001	0.004	0.001	0.000	0.001	0.000
NB2 (acid extraction)			0.020	0.210		0.091	0.009	
PB1	0.001	0.000	0.002	0.009	0.001	0.000	0.009	0.000
WaB1	0.001	0.000	0.028	0.007	0.000	0.000	0.009	0.000
WaB2 (deteriorating brick near ground)	0.008	0.031	0.065	0.044	0.003	0.005	0.008	0.000
WhB1	0.000	0.000	0.002	0.026	0.000	0.000	0.011	0.000
B33 M1	0.002	0.003	0.079	0.176	0.010	0.008	0.006	0.000
B44 M1 (sampled near ground)	0.001	0.000	0.023	0.173	0.003	0.001	0.006	0.000

Table 6.8 Concentrations of sulfates in mortar samples drilled through the east wall of Building 25 (wall thickness was approximately 12 cm) (single values)

depth of sample (cm)	0-1	1-3	3-5	5-7
SO_4^{2-} %	0.136	0.123	0.107	0.081

6.3.2.4 Ground water (Table 6.9)

The ground water was compared to the analysis undertaken by the British Geological Survey of ground water from the Inverclyde group in the Midland valley [141][10], which is relatively close to NMOF. Most of the ion concentrations found in the ground water from NMOF matched the median values reported for the water from the Inverclyde group to within ±0.001 ppm. The exceptions were the concentrations

[10] Although NMOF is not actually within the Inverclyde group, it is approximately three miles from the perimeter of this group. Ground water analysis from the precise location of NMOF is not available from the British Geological Survey.

of chloride and potassium ions in the NMOF ground water, which were greater than the maxima found in the Inverclyde group. In particular, the concentration of chloride ions in the NMOF groundwater was approximately six times the Inverclyde maximum. NMOF is within five miles of the sea, so the source of chloride and potassium ions might have been windblown aerosols. However, given that the Inverclyde group includes some coastal areas, this does not fully explain the high chloride content of the NMOF ground water.

Table 6.9 Concentrations of ions in the ground water at NMOF (single values)

	Cl^- %	NO_3^- %	SO_4^{2-} %	Ca ppm	Mg ppm	K ppm	Na ppm	Al ppm
NMOF ground water	0.053	0.000	0.002	0.008	0.001	0.002	0.000	0.000
Inverclyde ground water (50^{th} percentile)	0.001		0.001	0.007	0.002	0.000	0.001	0.000
Inverclyde ground water (maximum)	0.009		0.013	0.008	0.005	0.001	0.010	0.002
seawater	2.007	0.000	0.252	0.023	0.075	0.021	1.183	0.000

6.4 X-ray diffraction

6.4.1 Method

X-ray powder diffraction (XRD) was undertaken in order to:

- Confirm the identification of the salts from inside the buildings, and identify the salt efflorescences present as hard white crusts along cracks in the external render and the salt efflorescences present on the bricks and mortar joints of un-rendered external walls, for example on Building 44;
- Identify the type of bricks used in the free-standing wall on the south side of Building 25, by comparing the minerals present in these bricks to the minerals in the other bricks from NMOF;
- Characterize the aggregate particles thought to be responsible for the flaking of the renders, characterize samples of quarried shale used experimentally to imitate the behaviour of the aggregate particles and characterize any clays present in the aggregate particles.

The diffractometer used was a Bruker D8 using fully monochromated CuKα radiation, and the diffraction patterns were analysed using DIFFRAC^{plus} evaluation

software from Bruker[11]. The samples were prepared by grinding the salt, aggregate or brick to a fine powder in a ball mill, and adhering approximately 20 mg of powder to a circular glass sample mount using petroleum jelly, creating a layer approximately 1 mm thick and 5-10 mm in diameter.

The aggregate particles analysed were those which had been identified petrographically as a sandstone with a silt or clay binder (a 'muddy' sandstone), and a layered siltstone or claystone (a shale). It was not possible to identify clay minerals conclusively within the whole rock aggregate samples, because the clays were only present in small quantities. The clay fraction (defined as particles below 2 μm in diameter) was therefore extracted from the shale aggregate, using a standard technique [145]. In this the sample was broken down into its constituent grains in a ball mill, and placed in a small beaker, with 50 ml of deionised water and four drops of Calgon solution[12]. The mixture was vibrated in an ultrasonic bath for 30 minutes to help to remove the clays from their substrates and break them up into single grains. It was then stirred, poured into a standard 100 ml glass measuring cylinder where the 100 ml mark was 163 mm above the bottom, topped up with water to the 100 ml mark and shaken vigorously.

The cylinder was left to settle on a vibration-free surface away from any sources of heat. Hardy and Tucker used Stoke's Law, which relates the terminal velocity of particles moving through a viscous fluid to their radius, to calculate that after seven hours only the particles below 2 μm in diameter would be left in suspension in the top 16 mm of the liquid column, corresponding to the top 10 ml of liquid. This portion was removed with a syringe and transferred into a 50 ml centrifuge tube, which was spun inside a centrifuge at 4500 rpm for 30 minutes. The action of the centrifuge created a clay 'plug' at the bottom of the tube, with clear liquid above it. The liquid was poured off and the clay was scraped out of the tube and placed upon a glass sample mount. It was allowed to air dry overnight, before being analysed with XRD.

The sample spectrum was compared to reference spectra for illite, kaolinite, smectite and chlorite. Additionally, a glycolation technique was used to differentiate between smectite and chlorite, which may both show peaks in the region of 12-15

[11] The XRD analysis was undertaken by the author at the University of Edinburgh.
[12] Calgon is the registered trade name for a water softening agent.

Angstroms, corresponding to values of 2θ between 7.33° and 5.84° [145]. The sample slide was placed in a dessicator jar with 0.25 l of ethylene glycol, and heated in an oven at 60 ºC for one hour. The sample was then removed and analysed with XRD immediately, before the glycol could evaporate. Glycolation fixes the basal d-spacing of smectite at 17 Angstroms, corresponding to 2θ = 5.19°, so through comparison with the initial spectrum, a peak should have shifted to this position if smectite is present.

6.4.2 Results and discussion

6.4.2.1 Salts

XRD confirmed that the salt efflorescences inside the buildings were sodium sulfate (thernadite) (Figs. A3.2-A3.3), and identified the salts present in cracks along the external render as calcium carbonate (Fig. A3.4), and the salts present on un-rendered external walls as calcium sulfate (Fig. A3.5).

6.4.2.2 Bricks

The spectrum produced by the XRD analysis of the historic bricks from the free-standing wall on the south side of Building 25 was most similar to the spectrum for the Wallyford bricks (Fig. A3.6), and this result is discussed in Chapter 9.

6.4.2.3 Aggregates and quarried shale

Analysis of the muddy sandstone aggregate gave a good match for quartz, as would be expected, and quartz was also identified in the quarried shale (Fig. A3.7). However, the analysis of the shale aggregate gave a very poor spectrum with no strong peaks. Identification of the clays extracted was challenging because the reference spectra for illite, kaolinite, smectite and chlorite had several peaks in common with each other and with the sample spectrum. However, the clay reference spectra also each had at least two strong peaks which they shared with the sample spectrum but not with the other clays. Kaolinite provided the strongest match for the sample, but it seemed likely that traces of illite, smectite and chlorite were also present (Figs. A3.8-A3.9).

Comparison of the sample spectrum before and after glycolation was difficult because the peaks in the crucial area (from 2θ = 5.19° to 2θ = 7.33°) were fairly

small. However, following glycolation the intensity of the peaks in the region 2θ = 7.00-7.33° had reduced and the intensity of the peaks in the region 2θ = 5.00-6.20° had increased, with a particularly strong peak at 2θ = 5.19° (Fig. A3.10). This again suggested the presence of some smectite.

6.5 Scanning electron microscopy

6.5.1 Method

Scanning electron microscopy examination (SEM) with Energy-dispersive X-ray spectroscopy (SEM-EDX) was undertaken in order to supplement the petrographic examination of the renders with images at higher magnification and give an indication of their chemical composition, thereby providing additional information about the surface flaking of the renders.

The instrument used was a Variable Pressure SEM (CamScan MX2500) in controlled pressure (Envac) mode, which did not require samples to be coated. The samples were embedded in resin and ground down to give a smooth surface, showing a cross-section through the render or an individual aggregate particle. Water was generally used during the final polishing, but as there were concerns that this might wash away friable particles within the renders, some samples were instead polished dry and wiped clean with methanol. The samples were imaged using the back-scattered electron detector, at up to 500 times magnification, and elemental analysis was provided using a Noran Vantage EDX system and Vista software, to estimate elemental compositions in specific user-defined areas. This technique cannot quantify carbon and oxygen directly, but it calculates their relative proportions stoichiometrically.

6.5.2 Results and discussion

The examination and analysis of an original render sample from Building 32 (B32 OR) showed a matrix rich in calcium, carbon, oxygen and silica, indicating a cementitious binder (Fig. 6.2). Most of the aggregate particles were identified as quartz by their high silica content. The smaller pale-coloured aggregate particles were rich in iron and oxygen but low in sulphur, and hence were deduced to be predominantly iron oxide rather than pyrite, and the small, dark-coloured aggregate particles were rich in carbon, and may have been coal, which had been observed

during the petrographic examination. There were various other aggregate particles present containing a range of elements.

The composition of the original render from Building 25 (B25 OR) was similar, with distinctive shrunken, cracked particles, as shown in Fig. 6.3 and layered particles, as shown in Fig. 6.4. These particles often appeared to have caused cracking within the render, sometimes extending through the grains of quartz. The cracked particles were rich in carbon, and as they had a similar appearance to the cracked particles identified as coal in the thin sections, they were probably also coal. The layered particles were composed primarily of carbon, oxygen and silicon, and contained small light-coloured particles composed of carbon, oxygen, silicon and iron, which may have been clays. The layered particles had been identified as mudstone during the petrographic examination, and the SEM-EDX analysis indicated that this identification was plausible.

The aggregate particles mounted individually were a brown, flaky particle and a soft yellow particle with a granular appearance, both picked out from the render of Building 47. The flaky particle was found to have a similar structure to the layered particles within B25 OR and also contained small iron-rich particles dispersed between the layers. The SEM-EDX analysis suggested that the granular particle was ‘muddy sandstone’, consisting of quartz grains in a clay matrix, and this again confirmed the findings from the petrographic examination.

Fig. 6.2. SEM micrograph of B32 OR, showing the cement matrix and mixed aggregates

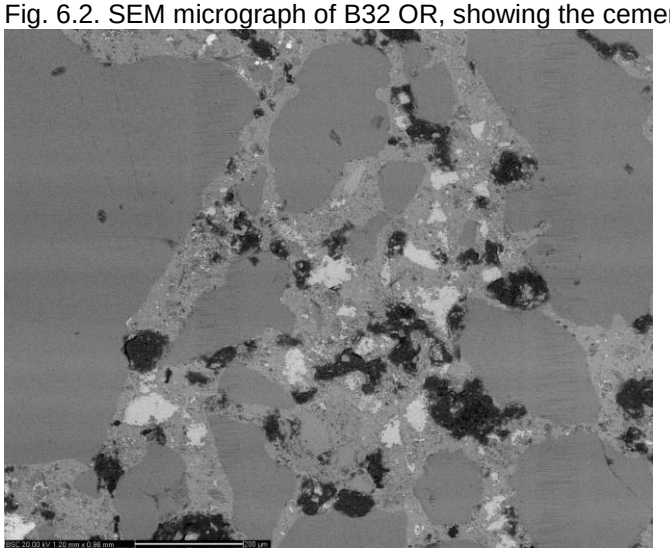

Fig. 6.3. SEM micrograph showing a shrunken, cracked particle in B25 OR, which may have caused cracking within the render

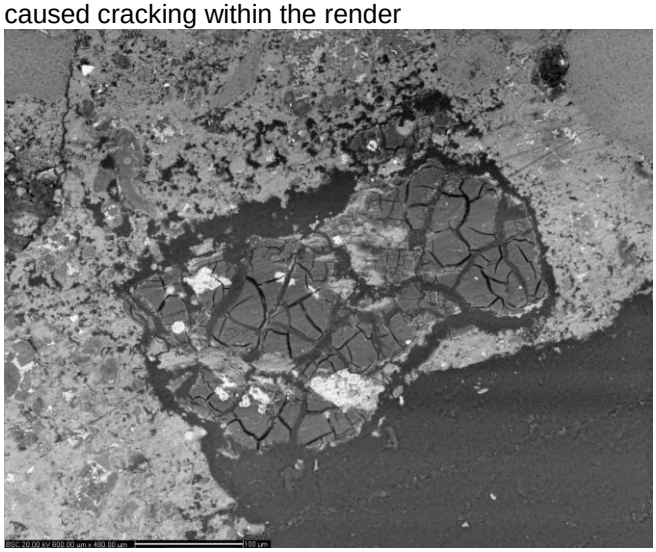

Fig. 6.4. SEM micrograph showing a layered particle in B25 OR, which appeared to have caused cracking within the render

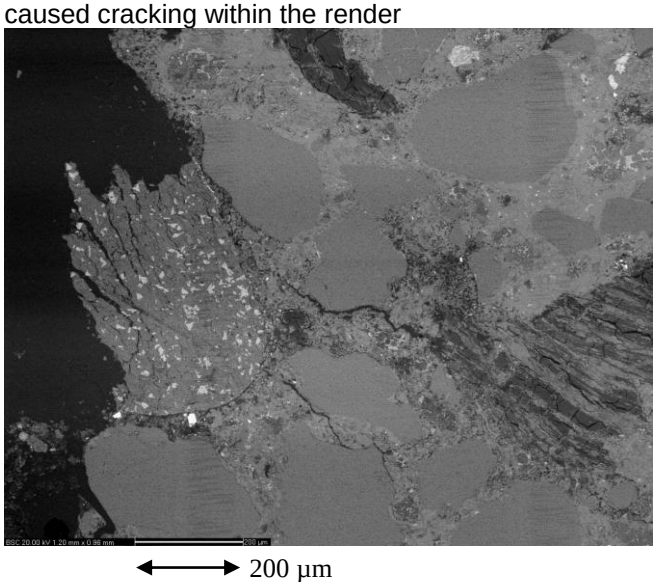

6.6 Strength testing

6.6.1 Method

Strength testing of brick and render samples was undertaken to compare the render and brick, as it has been suggested that a render should have lower strength than the substrate to accommodate movement [21]. It was also important to compare the original and repair renders, because repair renders should ideally have similar strength to the original renders they replace to ensure the compatibility of patch

repairs. However, this can be difficult to achieve using modern cements, which are generally stronger than earlier cements [4].

As it was not possible to obtain cores of the render, the samples used for strength testing were rectangular prisms of brick, render and brick-render composite, measuring approximately 50 × 20 × 15 mm (Fig. 6.6). The Niddrie bricks had developed cracks parallel to the bed face, probably from the manufacturing technique. They were cut into slices parallel to the head faces, and rectangular prisms were then cut with their long edges parallel to the bed face (NB B) or stretcher face (NS B), so that the cracks were orientated horizontally or vertically respectively during testing (Fig. 6.5). Some prisms (NEB B and NES B) were from the outer surface of the brick. The composite samples were cut with their long edges parallel to the stretcher face (Fig. 6.6). Up to three samples of each render and up to six samples from each part of the brick were tested, and a thin layer of gypsum capping plaster was applied to the underside of the prisms to create a flat surface.

Fig. 6.5. Brick samples used for the three-point bending test

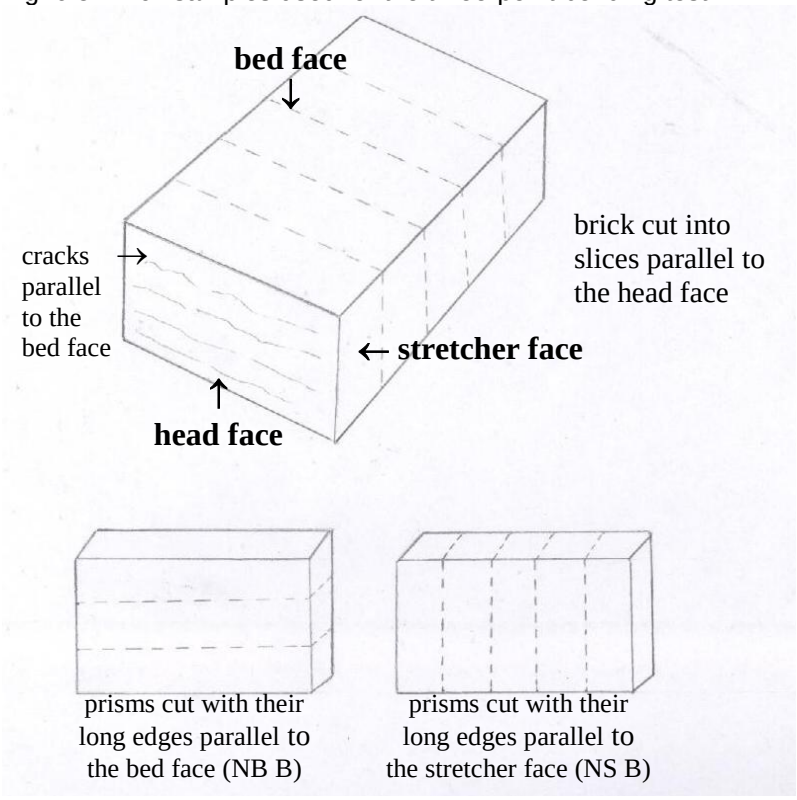

Fig. 6.6. Render, brick and composite samples for the three-point bending test

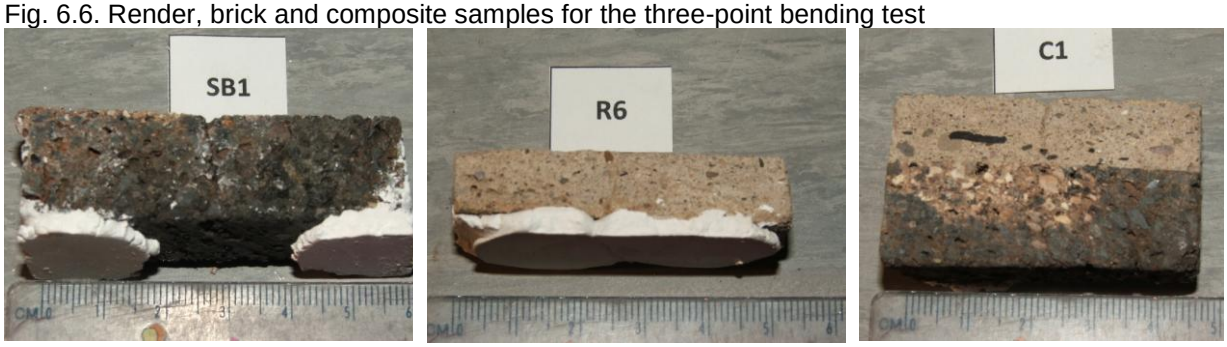

Tensile strength was measured by subjecting the samples to a three-point bending test, using an INSTRON 600 mechanical testing machine with a crosshead speed of 0.1 mm/min. The tensile strength f_{ct} was then calculated from the bending moment M and the second moment of area I using

$$M = \frac{wL}{2} \tag{6.3}$$

$$I = \frac{bd^3}{12} \tag{6.4}$$

$$f_{ct} = \frac{M\left(\frac{d}{2}\right)}{I} \tag{6.5}$$

where w is the load applied to the top edge of the sample, L is the distance between the two knife-edges on the bottom of the sample, b is the breadth of the sample and d is the depth of the sample [146]. The elastic modulus E was then calculated by substituting the gradient of the experimentally derived load-displacement curve w/v into the relationship

$$\frac{w}{v} = \frac{48EI}{L^3} \tag{6.6}$$

The compressive strength f_c was estimated from the tensile strength using

$$f_c = \left(\frac{f_{ct}}{0.3}\right)^{1.5} \tag{6.7}$$

as quoted by Raphael [84]. The experimental set-up is shown in Fig. 6.7.

Fig. 6.7. Experimental set-up for three-point bending tests

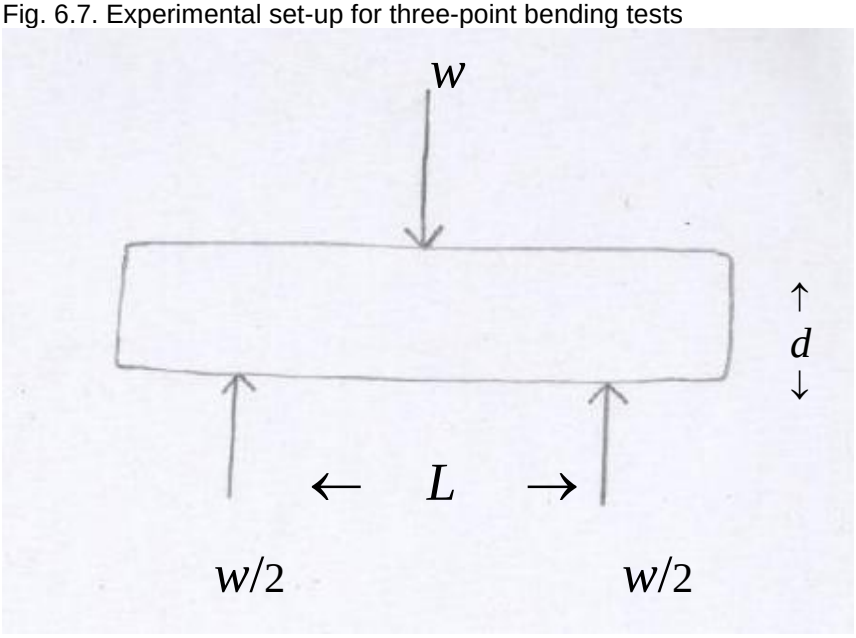

6.6.2 Results and discussion (Table 6.8)

The graphs of load against displacement for the renders and bricks typically showed a period of linear behaviour followed by sudden failure. This characterized them as brittle materials which fail soon after they have reached their elastic limit. The graphs of load against displacement for the brick samples often progressed in several stages, with the load increasing for some time and then falling slightly, before beginning to increase again (Fig. 6.8). This presumably corresponded to the sudden propagation of cracks through the bricks.

The full results for all the samples, included in Appendix 3, Table A3.10, show that there was a considerable spread in the strength measured for some of the samples. For example, the tensile strength measured for the three samples of HC OR varied from 2.8-5.8 MPa, and the tensile strength of the six NB B samples varied from 2.3-8.5 MPa. In general the samples which failed quickly had cracks which were observed prior to testing, whereas the samples for which higher strengths were measured were not visibly cracked.

The tensile strength of concrete made with modern Portland cement is typically around 3.7-4.5 MPa [90] and given that historic concrete would be expected to be weaker, the tensile strength values obtained here were rather high. The compressive strengths calculated were consequently also high, and have not been

included in this discussion. Conversely, the elastic moduli of 650 MPa and 270 MPa for the NMOF render and brick respectively (samples HC OR and NS B) were considerably lower than those reported elsewhere: for example, Azehnha et al. [94] found a modulus of elasticity of 6165 MPa for cement mortar, and Krakowiak et al. [91] reported a range of 2000-12700 MPa for clay bricks. The values obtained for the NMOF samples may be incomparable to those reported elsewhere because the test specimens were smaller than those recommended, but they are still useful to make comparisons between the materials tested.

The original render containing well graded aggregate (HC OR) was less strong than the original render containing poorly graded aggregate (B31 OR), and the same trend was observed with the repair renders. Angular and well-graded aggregates with a low average particle size typically result in higher strength mortars [83], and in this instance the effect of the low average particle size appears to have been most influential in increasing the strength of the render. The renders containing well graded aggregate had lower elastic moduli than the renders containing poorly graded aggregate, meaning that they were less stiff, and possibly also less brittle and prone to cracking.

The values of strength and elastic modulus obtained for the bricks were similar to the values for the renders containing well graded aggregate, but lower than the values for the poorly graded aggregate renders. The brick samples with cracks orientated vertically during testing failed quickly, because the stresses generated by three-point bending opened up the cracks. The samples cut from the surface of the brick (NEB B and NES B) were considerably stronger and had higher elastic modulus than those from inside the brick, possibly because the compacting of the brick surface reduces its porosity. The composite samples had similar strength and elastic modulus to the brick-only samples, and the sample with the lower tensile strength of 1.8 MPa failed due to the propagation of a pre-existing crack within the brick, whereas the crack responsible for the failure of the sample with tensile strength of 6.0 MPa extended through the brick and render.

Hence it was concluded that the bricks were reasonably compatible with the well graded aggregate render in terms of strength and elastic modulus, meaning that they would generally undergo similar distortion due to loading and fail at the same

point. However, the bricks could fail at low stresses if they contained pre-existing cracks. The renders containing poorly graded aggregate were generally stronger and more brittle than the bricks. The repair renders were stronger than the original renders with similar aggregate types, and this result is discussed further in Chapter 9.

Table 6.8. Average tensile strength and elastic modulus of renders and bricks

sample type	sample	tensile strength (MPa) (mean for 2-3 render samples, 3-6 brick samples and 2 composite samples)	elastic modulus (MPa) (mean for 2-3 render samples, 3-6 brick samples and 2 composite samples)
render	HC OR (well graded aggregate)	4.5	650
	B31 OR (poorly graded aggregate)	7.7	1180
	B23 RR (poorly graded aggregate)	9.5	1130
	B25 RR (well graded aggregate)	6.5	550
brick	NB B	5.1	390
	NS B	1.5	270
	NEB B	6.6	680
	NES B	5.8	1210
brick and render composite	C	3.9	480

Fig. 6.8. Load versus displacement for brick sample NEB B2. The load typically increased in stages, falling slightly at the end of each stage before beginning to increase again, and this presumably corresponded to the sudden propagation of cracks through the bricks.

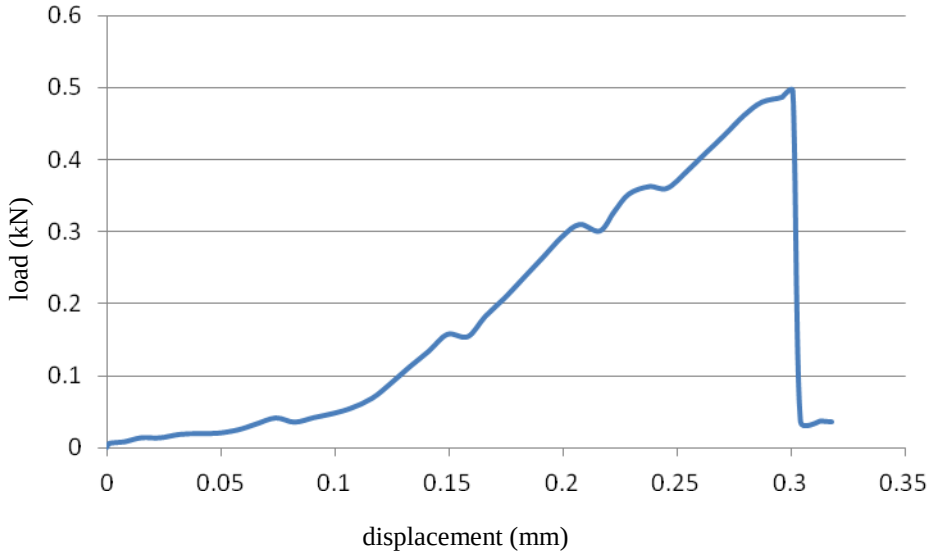

6.7 Density, porosity, sorptivity and pore size distribution

6.7.1 Method

The density, porosity, sorptivity and pore size distribution were measured because they determine the rates at which materials absorb water and dry out, and hence influence susceptibility to deterioration mechanisms such as freeze-thaw and external sulfate attack. Aggressive agents may enter the pore structure dissolved in water or in aerosol or gaseous form, and the ingress of carbon dioxide is a particular concern in reinforced concrete because it causes the concrete to carbonate, leading to a drop in pH levels and the corrosion of the steel reinforcements. The sorptivity of the brick substrate is important because it affects the extraction of water from the render, and hence the strength of the render-brick bond. It is also useful to compare the pore networks of the brick substrate and the render, because it has been suggested that the difference between them can create a resistance at the render-brick interface [18].

6.7.1.1 Density, porosity and sorptivity

The samples were regular cores or prisms, allowing their volumes to be calculated from their dimensions. The samples were weighed on a balance accurate to 0.001 g and the density ρ was calculated using

$$\rho = \frac{m}{V} \qquad \textbf{(6.8)}$$

where m is mass and V is volume. The samples were placed in a chamber from which the air was removed to create a vacuum, and water was then introduced into the chamber without releasing the vacuum. This forced water into the pores of the samples. After 12 hours they were removed, lightly patted dry and weighed immediately. The porosity ϕ was calculated as a percentage using

$$\phi = \frac{V_w}{100V_s} \qquad \textbf{(6.9)}$$

where $V_w = (m_2 - m_1)/\rho_w$, m_2 and m_1 are the masses of the sample when wet and dry, V_s is the volume of the sample and ρ_w is the density of water, taken as 1g/cm^3 at room temperature.

Sorptivity was measured using the technique described by Hall and Hoff [101]. A regular sample which had been oven dried and then cooled in a dessicator was placed in a dish of deionised water 1-2 mm deep, and weighed regularly as it absorbed water. The experiment finished when the rate of mass gain of the sample approached zero. The volume of water absorbed per unit cross cross-sectional area of the sample, *i*, was calculated using

$$i = \frac{\Delta m}{\rho_w \times A} \qquad \textbf{(6.10)}$$

where ρ_w is the density of water, A is the cross-sectional area of the sample and Δm is the mass gain. The sorptivity S was then given by the gradient of the straight line portion of a graph of i against $t^{1/2}$.

$$S = \frac{i}{t^{1/2}} \qquad \textbf{(6.11)}$$

For samples where the graph had more than one straight line portion the gradient of each portion was read off separately, to give a corresponding sorptivity value. The brick cores tested had been drilled from the bed and stretcher faces, and they were tested with the outer layer of the brick at the top and bottom of the core, 'skin up' and 'skin down'.

For the Wallyford bricks where the sorptivity measured was lower than for the other historic bricks by a factor of up to 25, and for B24 OR which had lower sorptivity than that obtained for a similar render, it was possible that the samples were repelling or reacting with the water used for the test. For these samples the sorptivity measurements were therefore repeated using n-decane; if this gave a much higher sorptivity value, it would indicate that the sorptivity measured with water was low due to the hydrophobic properties or reactivity of the sample.

The measured sorptivity S is related to the intrinsic sorptivity ζ, the surface tension σ and dynamic viscosity of the liquid η by

$$S = \left(\frac{\sigma}{\eta}\right)^{0.5} \varsigma \qquad \textbf{(6.12)}$$

and this gives

$$S_w\left(\frac{\eta_w}{\sigma_w}\right)^{0.5} = S_d\left(\frac{\eta_d}{\sigma_d}\right)^{0.5} \quad \textbf{(6.13)}$$

where S_w and S_d are the sorptivities measured using water and decane respectively, and σ_w, η_w, σ_d and η_d are the properties of water and decane respectively, taken as σ_w = 72.8, η_w = 1.00, σ_d = 23.8 and η_d = 0.88 [101]. Hence the ratio of to S_d to S_w should be 0.61, and a significantly different value suggests some kind of interaction between the material and one of the test liquids. Most commonly the ratio is higher, because the material is hydrophobic or prone to react with water, resulting in a lower value of S_w than would otherwise be obtained.

The density, porosity and sorptivity were usually measured for three samples of each type of material, although four samples of Building 33 mortar (B33 M) and Building 47 original render (B47 OR) were available, and only two samples of Building 31 original render (B31 OR), Building 25 repair render (B25 RR) and the air raid shelter concrete (ARS C) were available. The porosity and sorptivity tests were run twice on each sample.

6.7.1.2 Pore size distribution

For testing the materials were broken down into particles of 2-4 mm diameter using a pestle and mortar. The particles were packed into a glass cell and placed in a Mercury Intrusion Porosimeter (Autopore IV 9500 V1.07), initially in a low pressure chamber and then in a high pressure chamber. The porosimeter worked in incremental mode and recorded the intruded volume of mercury at each particular pressure, generating a pressurization curve. The software normalized the readings of intruded volume by dividing by the specimen mass or the specimen bulk volume, and converted the pressure volumes into equivalent pore sizes, as described in Chapter 2. The software also calculated values for the porosity and bulk density of the samples.

The data were presented as graphs plotting the cumulative intruded volume curve (CIV curve); the cumulative porosity curve (CP curve); and the differential pore size distribution (DPSD curve). It was assumed that any pores larger than 100 µm were gaps between particles. The values of porosity used to calculate the cumulative porosities from the values of cumulative intrusion were those obtained experimentally, using the relationship

$$\Phi_c = \frac{I_c}{I_{\max} \times \Phi_{\max}} \quad \textbf{(6.14)}$$

where Φ_c and Φ_{max} are the cumulative and maximum porosities, and I_c and I_{max} are the cumulative and maximum intruded volumes of mercury. However, for the PB skin sample the porosity was not obtained experimentally due to the small sample size, and so the value produced by the Mercury Intrusion Porosimetry (MIP) software was used instead, which seemed reasonable given that the MIP software had produced values close to those obtained experimentally for the other brick samples.

The bulk density and bulk porosity obtained experimentally were compared to those produced by the MIP software. The value for the median pore diameter produced by the MIP software was compared to the median pore diameter obtained from the cumulative porosity curve, and the mode pore diameter and threshold pore diameter were obtained from the cumulative porosity curve and differential pore size distribution plots. The mode pore diameter is given with the value occurring most frequently first, with other values that also occurred frequently in parantheses. The pore size distribution was calculated from the cumulative porosity curve using size classifications adapted from Aligizaki [97].

6.7.2 Results and discussion

The full results for all the measurements are given in Appendix 3, including graphs illustrating the MIP results, and the brick sorptivity results are discussed in depth in Chapter 7. The table summarizing the density, porosity and sorptivity results (Table 6.10) includes only the main sorptivities measured for the bricks and not any of the minor values measured due to the effect of the surface skin.

6.7.2.1 Accuracy of data

Porosity and sorptivity

For the renders, mortar and concrete, the range of the porosities measured for between two and four samples of each material was 2.8% at most (for B31 OR) and 1.5% on average, while for the bricks, the range of the porosities measured for three samples of each brick was 1.8% at most (for Wh B) and 1.0% on average. Some of these variations were probably due to genuine variations between samples, but some may also have been due to experimental errors, since the average difference between

the two values obtained from repeating the porosity test on the same sample was 0.5%. The average porosities in Table 6.10 have therefore been given to the nearest 0.5%.

For the renders, mortar and concrete, the sorptivities measured were generally identical across each material type to ±0.1 mm/min$^{1/2}$, and repeatable for each sample to ±0.1 mm/min$^{1/2}$. The exception was B23 RR, where although the result for each sample was repeatable to ±0.2 mm/min$^{1/2}$, the average sorptivity varied from 0.3 mm/min$^{1/2}$ for B23 RR2, to 1.4 mm/min$^{1/2}$ for B23 RR1. This was presumably due to variations between the samples.

The brick sorptivities were generally higher than the render sorptivities, and were generally repeatable for each sample to ±0.2 mm/min$^{1/2}$. The exception was the Wallyford brick sorptivities, which were very low, and hence were generally repeatable for each sample to ±0.05 mm/min$^{1/2}$. It was not possible to compare the sorptivities measured for different samples of each brick because the samples demonstrated variations depending on where they had been taken from and whether they were tested with the outer skin facing up or down. The sorptivity values have been quoted to the nearest 0.1 mm/min$^{1/2}$ for all samples except the Wallyford bricks, for which the values are quoted to the nearest 0.05 mm/min$^{1/2}$.

MIP

It is not possible to comment on the repeatability of the MIP results or the variations that may occur between different samples of the same material, because one sample of each material was tested once only. However, the bulk density and porosity obtained from MIP have been quoted to the nearest 0.1 g/cm^3 and 0.5%, as for the results obtained experimentally. The median and mode pore diameters and percentages of pore space within size classes have been given to one decimal place.

The porosity and bulk density obtained from MIP were generally quite close to those obtained experimentally, particularly for the brick samples. However, for B23 RR and B25 RR the experimental porosities were respectively 6.0% and 8.5% higher than the MIP porosities, and this may have been because these samples contained a significant number of small pores which were not penetrated by mercury.

The mode pore diameters obtained from the cumulative porosity curve and the differential pore size distribution were different because the mode pore diameter

read off the differential pore size distribution curve is a single peak value, whereas the mode pore diameter read off the cumulative porosity curve is the middle value between the two points at the steepest part of the graph (Fig. 6.9).

Fig. 6.9. Determination of the mode pore diameter for B24 OR, showing that different values are obtained from the cumulative porosity and differential pore size distribution curves

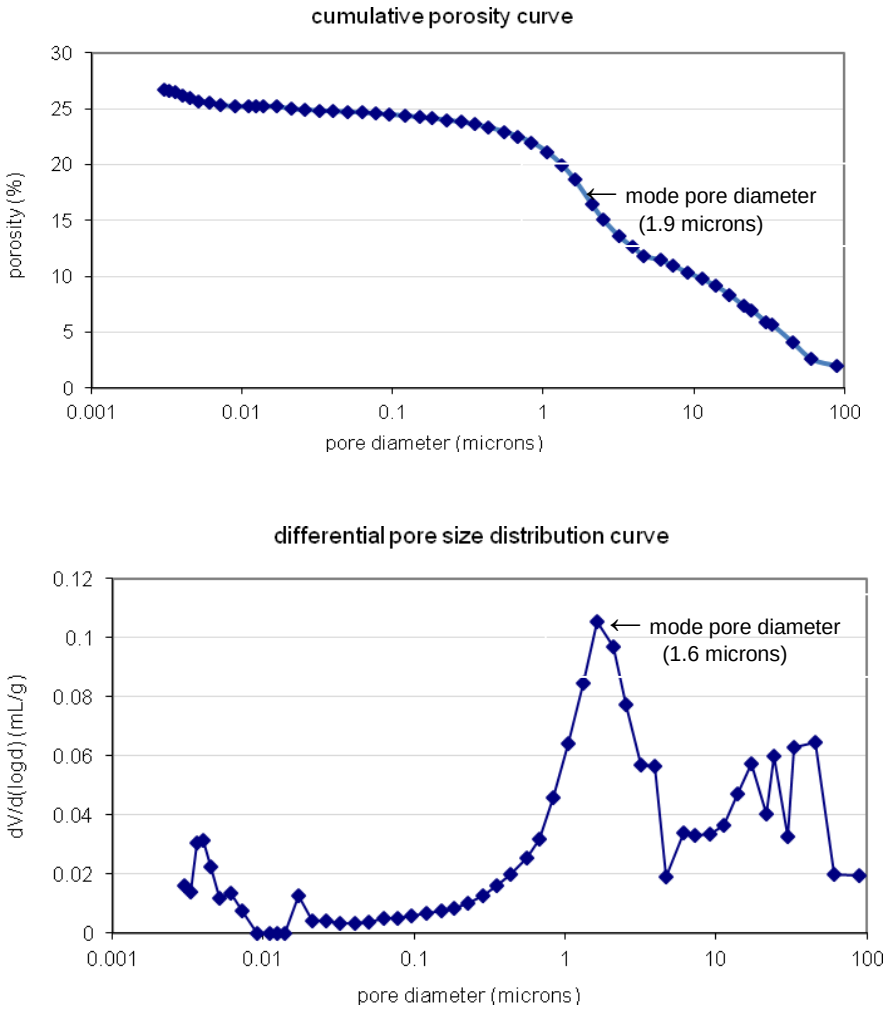

6.7.2.2 Results for renders (Tables 6.9-6.14)

Given that the MIP underestimated the porosity of B23 RR and B25 RR by 6.0% and 8.5% respectively, they may have contained up to this volume of small capillaries, and this has been indicated in tables 6.13 and 6.14.

B47 OR and B25 RR were ‘concrete-like’ renders containing well sorted, mixed aggregate, whereas the aggregate in B24 OR and B23 RR was poorly sorted, fine sand. B47 OR had the lowest porosity measured either experimentally or with MIP, and B24 OR and B23 RR had the highest porosities, which was probably at

least partly due to the fine aggregate in these renders. Additionally, the petrographic examination described in Chapter 5 had suggested that B23 RR contained an air-entraining agent, added deliberately to increase its porosity.

The median pore diameter was highest for B24 OR and B23 RR, and they also had similar pore size distributions, with at least 30% of the total pore space made up of air voids, as opposed to around 6% at most for B47 OR and 15% at most for B25 RR. Again, this may have been due to the particle size ranges and the presence of an air-entraining agent in B23 RR. However, B25 RR differed from the other renders in that it had a higher proportion of small and medium capillaries, and this may have indicated a higher initial water content, as it has been shown that the proportion of capillary pores increases with increasing water content [147]. The mode pore diameter was fairly similar for all the renders, averaging 1.5 μm. Secondary values of mode pore diameter at around 20 μm were obtained for B23 RR and B25 RR (Fig. 6.10), and three secondary values of mode pore diameter were obtained for B25 RR.

The repair renders both had higher sorptivity than the original renders. In particular, the sorptivity obtained for B23 RR was extremely variable and between two and four times greater than for the original renders. This may have been partly due to the high proportion of large capillaries and air voids in B23 RR, but B24 OR had a similar pore size distribution and much lower sorptivity. The results for the sorptivity of B23 RR and B24 OR with decane are given in Table 6.11, and show that although S_d/S_w was close to the predicted value of 0.61 for B23 RR, it was much higher than this for B24 OR. This was probably because S_w for B24 OR was anomalously low, due to the cement paste reacting with the water to reduce the effective permeability of the material. It has been observed that swelling and hydration may occur when hydrated and dried cement paste is re-wet [101].

Fig. 6.10. Determination of mode pore diameter for B23 RR

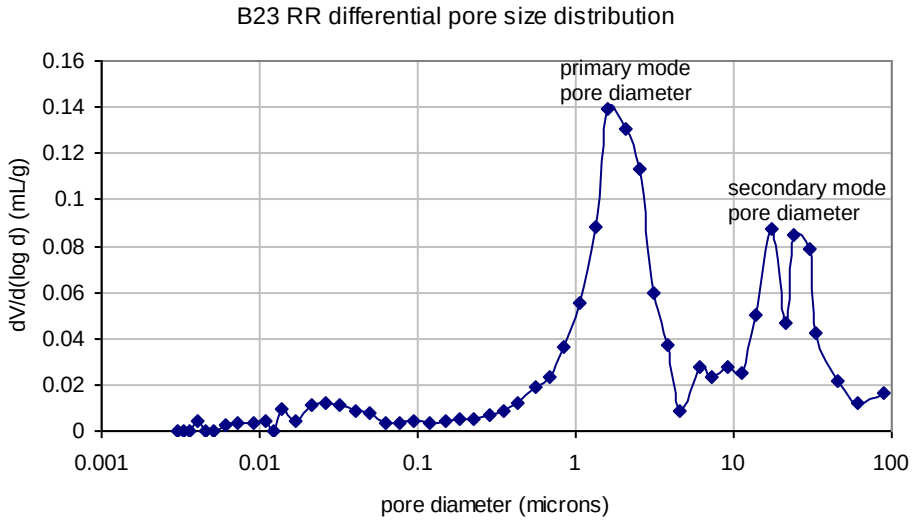

6.7.2.3 Results for bricks (Tables 6.9-6.10 and 6.12-6.14)

The bricks had very similar porosities, ranging from a minimum of 24.5% for the Niddrie bricks to a maximum of 27.5% for the Whitehill bricks. This similarity was unsurprising, because brick porosity depends upon the nature of the raw materials and the production technology [100], and the NMOF bricks were all produced in around 1940 in the Edinburgh area by machine pressing. However, they had very different pore size distributions, with the median pore diameter varying from 1.6 µm for the Whitehill bricks to 18.5 µm for the skin of the Prestongrange bricks. The Edinburgh, Niddrie and Whitehill bricks had mode pore diameters ranging from 0.5-5.5 µm, with secondary values at around 25 µm for the Niddrie and Whitehill bricks. The mode pore diameter for the Wallyford bricks was not well-defined but was around 17 µm, and the primary mode pore diameters for both for the interior and skin of the Prestongrange brick were high – around 25 µm for the interior and 38 µm for the skin – with lower secondary values at around 0.2-0.4 µm. A bimodal distribution for a traditionally produced brick has been found by other researchers [91].

The pore size distributions showed that the skin of the Prestongrange bricks had a higher proportion of air voids than the other bricks, and that the Edinburgh and Niddrie bricks had the lowest proportions of air voids. The skin of the Prestongrange bricks had fairly low sorptivity, while the Edinburgh and Niddrie bricks had average sorptivity amongst those tested, and the Wallyford bricks, which had a fairly high

proportion of air voids, had the lowest sorptivity of all the bricks. This demonstrates that for bricks a high proportion of air voids does not necessarily result in high sorptivity, possibly because air voids often occur alongside cracks which may inhibit moisture movement. The sorptivity measurements made on the Wallyford bricks using n-decane are discussed in Chapter 7.

Table 6.9 Density, porosity and sorptivity of mortar, render and brick samples (means for 3 samples of each material)

sample type	sample	density (g/cm^3)	porosity (%)	sorptivity ($mm/min^{1/2}$)
mortar	B33 M	1.8	27.0	0.2
render	B24 OR	1.7	29.5	0.1
	B47 OR	1.9	18.0	0.1
	B31 OR	1.9	24.0	not done
	B23 RR	1.7	31.0	0.5
	B25 RR	1.8	24.5	0.2
brick	ES B skin up	1.8	26.0	0.7
	ES B skin down	1.8	26.0	0.8
	EB B skin up	1.8	26.0	1.4
	EB B skin down	1.8	26.0	0.8
	NS B skin up	1.9	24.5	0.5
	NS B skin down	1.9	24.5	0.6
	NB B skin up	1.9	24.5	0.5
	NB B skin down	1.9	24.5	0.4
	PS B skin up	1.7	27.0	2.0
	PS B skin down	1.7	27.0	1.7
	PB B skin up	1.7	27.0	1.2
	PB B skin down	1.7	27.0	0.3
	WaS B skin up*	1.7	25.5	0.10
	WaS B skin down*	1.7	25.5	0.15
	WaB B skin up*	1.7	25.5	0.05
	WaB B skin down*	1.7	25.5	0.15
	WhS B skin up	1.7	27.5	1.0
	WhS B skin down	1.7	27.5	0.8
	WhB B skin up	1.7	27.5	1.0
	WhB B skin down	1.7	27.5	1.3

* The sorptivities for the Wallyford bricks have been given to the nearest 0.05 $mm/min^{1/2}$ because they are considerably lower than the values for the other bricks.

Table 6.10. Comparison of density and porosity measured with different techniques

sample	bulk density (experimental) (mean for 3 samples)	bulk density (MIP) (single value)	porosity (experimental) (mean for 3 samples)	porosity (MIP) (single value)
B24 OR	1.7	1.8	29.5	26.5
B47 OR	1.9	2.0	18.0	20.0
B23 RR	1.7	1.9	31.0	25.0
B25 RR	1.8	2.0	24.5	16.0
EB	1.8	not available	26.0	not available
NB	1.9	1.9	24.5	24.5
PB	1.7	1.9	27.0	25.5
PB (skin)	1.7	1.8	not measured	21.0
WaB	1.7	not available	25.5	not available
WhB	1.7	not available	27.5	not available

Table 6.11 Sorptivities measured with water and decane (S_w and S_d) for the renders containing fine sand aggregate (means for 3 samples of each material)

	S_w (mm/min$^{1/2}$)	S_d (mm/min$^{1/2}$)	S_d/S_w
B24 OR	0.1	0.5	5.0
B23 RR	0.5	0.5	1.0

Table 6.12. Median pore diameter, mode pore diameter and threshold pore diameter (single values)

sample	median pore diameter from CP curve* (µm)	mode pore diameter from CP curve* (µm)	mode pore diameter from DPSD curve* (µm)	threshold pore diameter from CP curve* (µm)
B24 OR	3.4	1.9	1.6	0.003
B47 OR	0.5	1.5	1.3	0.003
B23 RR	2.8	1.9 (and 19.3 – 27.2)	1.6 (and 17.3 - 24.2)	not available
B25 RR	0.3	1.9	0.6 (and 0.1 and 1.6 and 30.1)	not available
EB	4.0	5.5	8.1	not available
NB	2.8	2.3 (and 27.1)	2.1 (and 24.2)	
PB	6.2	25.0 (and 0.2)	24.2 (and 0.2 and 2.1)	0.006
PB (skin)	18.5	24.2 – 45.3 (and 0.35)	38.0 (and 0.4)	0.284
WaB	11.3	16.9	6.1-37.0	not available
WhB	1.6	0.5 (and 29.7)	0.6 (and 29.7)	not available

*The CP and DPSD curves are the cumulative porosity and differential pore size distribution curves.

Table 6.13. Percentage of pore space within size classes, as percentage of sample volume (single values)

sample	small capillaries 0.0025-0.01 µm	medium capillaries 0.01-0.05 µm	large capillaries 0.05-10 µm	small air voids 10 -50 µm upwards	large air voids 50 µm upwards	total (%)
B24 OR	1.5	0.5	14.6	6.6	3.5	26.7
B47 OR	1.3	3.0	14.2	0.5	0.8	19.8
B23 RR*	0.20 (possibly up to 6.0)	1.1	14.7	6.8	2.4	25.2 (up to 31.0)
B25 RR*	1.4 (possibly up to 9.9)	7.7	4.2	1.2	1.3	15.8 (up to 24.3)
EB	0.8	2.4	14.1	6.6	2.3	26.2
NB	0.0	0.2	17.4	4.7	2.4	24.7
PB	1.5	5.9	7.6	8.7	3.1	26.8
PB (skin)	0.0	2.1	5.9	8.2	4.8	21.0
WaB	0.6	3.9	7.5	10.2	3.20	25.4
WhB	0.3	1.6	10.1	13.9	1.5	27.4

* The values in parentheses for B23 RR and B25 RR indicate the maximum possible volume of small capillaries, which the MIP may have underestimated.

Table 6.14. Percentage of pore space within size classes, as percentage of all pore space (single values)

B24 OR	small capillaries 0.0025-0.01 µm	medium capillaries 0.01-0.05 µm	large capillaries 0.05-10 µm	small air voids 10 -50 µm upwards	large air voids 50 µm upwards	total (%)
B24 OR	5.6	1.8	54.8	24.7	13.1	100
B47 OR	6.8	15.1	71.8	2.4	3.9	100
B23 RR*	0.8 (19.2)	4.2 (3.4)	58.4 (47.5)	27.1 (22.1)	9.5 (7.8)	100
B25 RR*	9.1 (40.7)	48.5 (31.7)	26.9 (17.5)	7.6 (5.0)	7.9 (5.1)	100
EB	3.2	9.0	53.9	25.2	8.7	100
NB	0.0	0.8	70.5	19.0	9.7	100
PB	5.6	22.2	28.3	32.4	11.5	100
PB (skin)	0.0	10.0	28.1	39.0	22.9	100
WaB	2.4	15.3	29.5	40.2	12.6	100
WhB	1.1	5.7	36.9	50.8	5.5	100

* The values in parentheses for B23 RR and B25 RR indicate the revised distribution of the pores if the maximum possible volume of small capillaries is assumed to be accurate, rather than the value for the volume of small capillaries obtained by the MIP.

6.8 Drying behaviour

6.8.1 Method

The drying rate of the materials was investigated because it affects the likelihood of freeze-thaw damage. Materials which dry out quickly are less vulnerable to freeze-thaw because they quickly reach a moisture content below the threshold required for damage.

The method used to investigate the drying rate of the building materials was based on the method developed by Rousset-Tournier using stone cores [106]. The samples were saturated with water in a vacuum chamber for 16 hours and then tightly wrapped in plastic, leaving only their upper faces exposed. They were placed inside a plastic container approximately 300 mm high, with a small access hatch in the lid (Fig. 6.11). The RH inside the container was controlled by a small dish of saturated sodium chloride solution, which produces RH of 75% at 23 °C [148]. The dish was raised on a block so that its surface was on a level with the top of the samples. The container was placed inside an oven at 23 °C, and the environment was monitored using a button data logger (Signatrol SL54TH), positioned on the container wall half-way between the samples and the dish of salt solution, again level with the tops of the samples. There was no air movement within the container, and the samples were removed through the access hatch with minimal disturbance for weighing. They were weighed every few hours until the rate of mass loss approached zero.

The total water content of each sample at time t was calculated by subtracting the dry sample mass from the sample mass at time t. The water contents were normalized by dividing by the cross sectional areas of the samples. The water content in g/cm^2 was plotted against the time in hours for each sample, to give a drying curve. The initial rate of water loss in g/cm^2.h was given by the gradient of the initial, straight line portion of the graph. The turning point of the graph represented the critical saturation point, and the time taken to reach this point and the water content/area at this point were read off the graph. The times were normalized by dividing by the sample lengths, and the critical saturation levels (*CSL*) as percentages were determined using

$$CSL = \frac{w_{csl}}{w_i} \times 100 \qquad \textbf{(6.15)}$$

where w_{csl} is the water content at the critical saturation level and w_i is the initial water content.

In order to check the experimental set-up, two control experiments were undertaken. Firstly, the experiment was run with a core of Grès de Fontainebleau sandstone tested previously by Rousset-Tournier, to see if the earlier results could be

reproduced. Secondly, the drying rate from a dish of deionised water was measured, to investigate whether the drying kinetic of the container was linear. Following the control experiments, prismatic samples of Niddrie brick, original render from Building 24 and original mortar from Building 33 were tested, measuring approximately 50 mm high and 20 mm by 15 mm in cross section. Each sample was tested twice.

Fig. 6.11. Equipment for measuring the drying behaviour

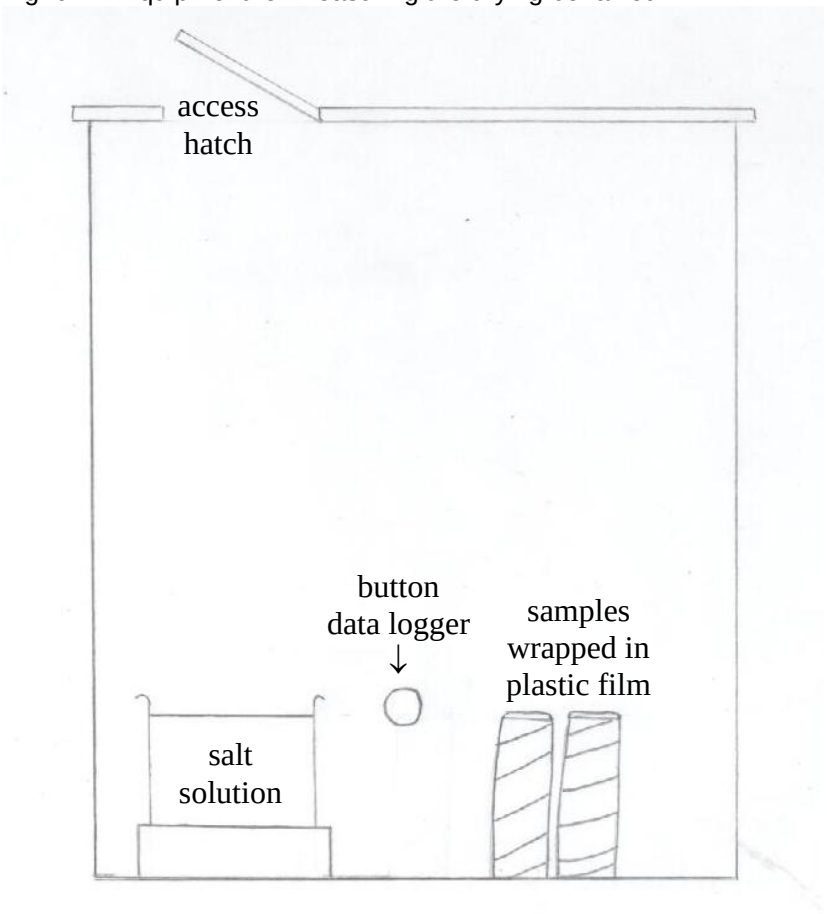

6.8.2 Results and discussion

6.8.2.1 Control experiments (Table 6.15)

The initial rate of water loss obtained for the sandstone core was within 7% of the value quoted by Rousset-Tournier. The time taken to reach the critical saturation level and the critical saturation level have been quoted as ranges, because reading them off the graph was quite subjective. The values obtained by Rousset-Tournier during a second run of the experiment fell within the ranges obtained here. The plot

of mass loss against time for the dish of deionised water showed that water evaporated from the dish at a steady rate of -0.0021 g/cm^2.h, and hence that the drying kinetic of the container was linear. The experimental set-up was therefore deemed satisfactory.

Table 6.15. Drying data for sandstone core tested previously by Rousset-Tournier

experiment	initial rate of water loss (g/cm^2.h)	time to reach critical saturation level (h)	time to reach critical saturation level per unit length of sample (h/cm)	critical saturation level (%)
Rousset-Tournier run 1	-0.0029	232	29	24.4
Rousset-Tournier run 2	-0.0029	211	26	30.8
Griffin run 1	-0.0027	200-225	25-28	30-35%

6.8.2.2 NMOF samples (Table 6.16 and A3.21-A3.23)

The determination of the time taken to reach the critical saturation level and the critical saturation level from a graph was again considered quite subjective. However, it was found that the time taken to reach the critical saturation level was repeatable to ±5 h, and that the critical saturation level was repeatable to ±5%. The initial rate of water loss was repeatable to ± 0.0005 g/cm^2.h. The results have therefore been given with this level of accuracy.

Unfortunately, the testing of the render samples was interrupted part-way through, and the results were therefore incomplete and of limited value. However, given that the original mortar had similar composition, it was anticipated that the render results would have been similar to the mortar results.

The results showed significant variations between samples of the same material. For example, the critical saturation levels measured for the brick samples were 35% and 45%, and for the mortar samples were 75% and 85%. These variations were presumably due to differences in the composition or condition of the samples.

Despite the variations between samples, there were still some general trends to be observed. The initial rate of water loss was lowest for the sandstone samples, higher for the brick samples and higher still for the mortar samples. The rates determined were considerably higher than the rate from the control dish of water (0.0021 g/cm^2.h). This is surprising given that the initial rate of water loss should be

the same for all porous materials and similar to that from a free water surface in the same conditions, and it is possible that some moisture escaped from the sides of the samples despite the plastic sealing.

The bricks had a lower critical saturation level than the mortar samples, and took longer to reach the critical saturation level (Fig. 6.12). For example, on average the bricks took 40 h/cm of sample to reach a critical saturation level of 40%, whereas the mortar took 10 h/cm of sample to reach a critical saturation level of 80%. By the end of the experiment the bricks had dried out completely, whereas although the drying rate for the mortar samples had slowed considerably, they had only lost around half of their total water content. The rate of water loss from the small and medium capillaries in cementitious materials depends upon the RH [18], and the loss of the remaining water may have been prohibited by the high RH.

As discussed in Chapter 2, drying generally occurs in two stages, often called the constant drying rate period (stage I) and the falling drying rate period (stage II). The bricks dried out much faster than the mortar, because they lost most of their water content during stage I drying when the rate of water loss was high, whereas the mortar had lots of water left to lose during stage II drying, when the rate of water loss slowed down. This suggests that if the mortar is wet fairly frequently, it will never fully dry out. The slow drying out of the mortar is likely to be due to the high proportion of small and medium capillaries in cementitious materials.

Table 6.16. Drying data for NMOF samples (single values)

Sample	initial rate of water loss ($g/cm^2.h$)	time to reach critical saturation level (h)	time to reach critical saturation level per unit length of sample (h/cm)	critical saturation level (%)
NB1	-0.0040	240	50	35
NB2	-0.0040	175	35	45
B33 M1	-0.0065	50	10	75
B33 M2	-0.0050	50	10	85

Fig. 6.12. Drying curves for Niddrie brick and original mortar

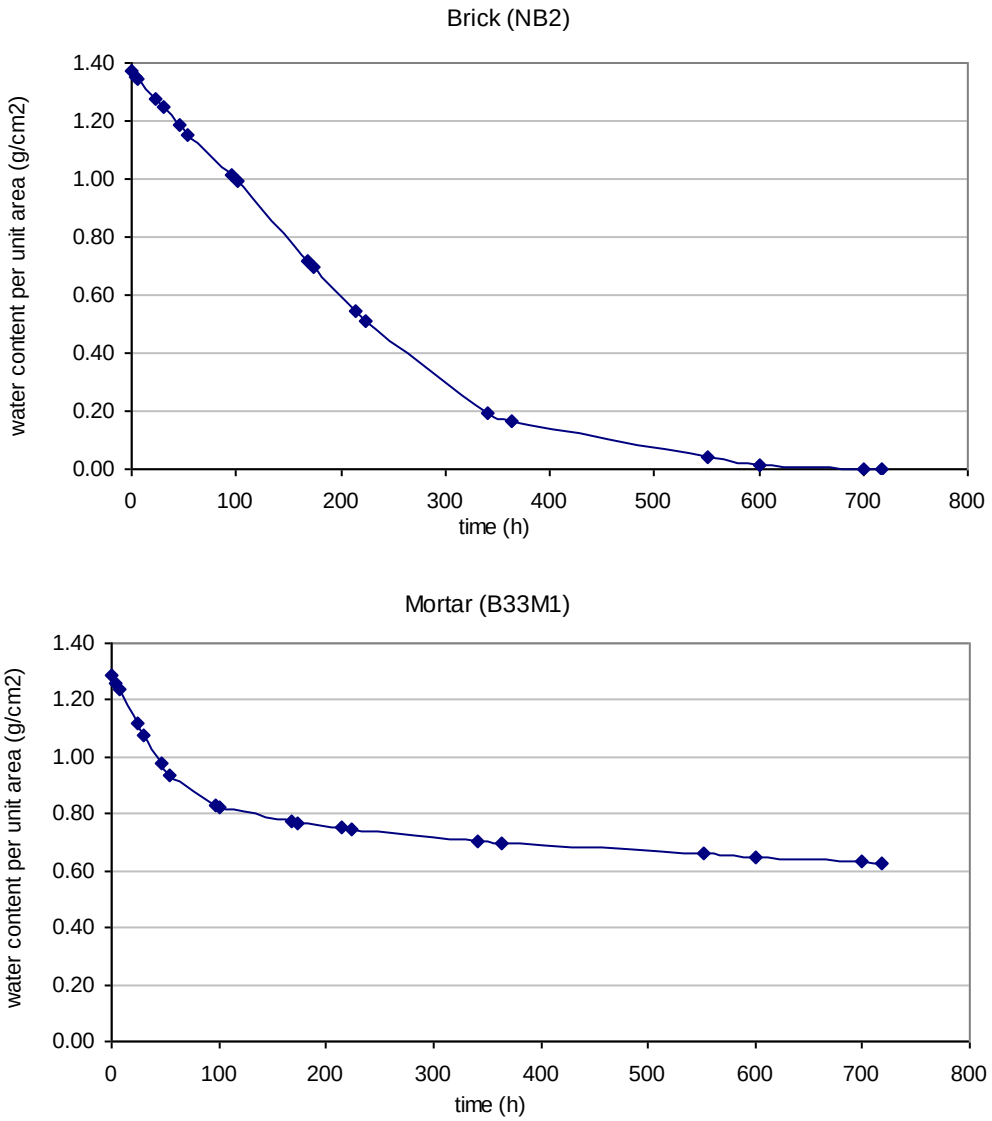

6.9 Conclusions

The determination of the particle size distribution of the aggregate from the renders confirmed the observation that the original renders fell into two categories: those with a fine, poorly graded, quartz aggregate (poorly graded aggregate renders) and those containing a coarser, well graded, mixed rock aggregate (well graded aggregate renders). The original mortars and B23 RR were similar to the poorly graded aggregate renders, whereas B25 RR more closely resembled the well graded aggregate renders. The binder:aggregate ratios were generally lower for the original renders than for the repair renders. The poorly graded aggregate renders typically had

higher porosity, higher sorptivity and a higher proportion of air voids than the well graded aggregate renders[13]. Hence for the renders tested it was concluded that the well graded aggregate original render was most likely to be durable, and that the others were vulnerable to freeze-thaw deterioration because the poorly graded aggregate or high cement contents had resulted in high porosity and sorptivity,

XRD and ion analysis identified the salts present in cracks along the external render as calcium carbonate, the salts present on un-rendered external walls as calcium sulfate and the salt efflorescences concentrated along the mortar joints inside the buildings as sodium sulfate (thernadite). The concentration of sodium sulfate increased with proximity to the surface of the wall, but it was not possible to establish conclusively whether the source of sulfates was the cement mortar or the bricks. The levels of sulfates, chlorides, sodium and aluminium in the renders were generally slightly higher on buildings where flaking was observed, but there were various exceptions to this. The increased levels of sulfates were not sufficient to suggest that the flaking was caused by sulfate salts.

SEM-EDX analysis demonstrated that the aggregate particles thought to be responsible for the flaking of the render were definitely causing cracking within the render. The particles were rich in clays, and often had layered structures. The clays were extracted and appeared to contain traces of kaolinite, illite, chlorite and smectite. The latter two have the potential to cause swelling, but it is doubtful whether they were present in sufficiently high concentrations.

The coarse aggregate original renders and B25 RR were reasonably compatible with the bricks in terms of strength and elastic modulus, meaning that they would generally undergo similar distortion due to loading and fail at the same point. However, the bricks sometimes failed prematurely if they contained pre-existing cracks. The renders containing fine sand aggregate were generally stronger and more brittle than the bricks, which could have made them prone to cracking.

The results from the testing of hydraulic properties showed that the densities of the materials were all very similar, ranging from 1.7 – 1.9 g/cm^3, and showing no clear relationship to the porosities measured. Sorptivity would generally be expected to increase with increasing porosity, but again the relationship was not clear,

[13] This is allowing for the fact that the sorptivity of B24 OR was unusually low when measured using water.

although the render with the highest porosity, B23 RR, also had the highest sorptivity. Sorptivity might also be expected to increase for higher median pore diameters, and this was found to be true for the renders, but less so for the bricks. The relationship between the porosity, sorptivity and pore size distribution of the bricks is discussed in more detail in Chapter 7.

Petrography had shown that B23 RR contained an air-entraining agent, and it was found to have high porosity and a high percentage of air voids. Mortars and renders without air-entraining agents should ideally have low porosity with few air voids to reduce the likelihood of freeze-thaw damage [18], and this was the case for the coarse aggregate original renders, and for B25 RR to a lesser extent. B25 RR had a particularly high proportion of small and medium capillaries, which may have been due to a high initial water content.

Besides being very porous, B23 RR had much higher sorptivity than the other renders, indicating that it would absorb water rapidly. The original renders and B25 RR had relatively low sorptivity, particularly in comparison to the historic bricks. However, it was demonstrated that the original cement mortar dried out more slowly than the historic bricks, and the original renders would be expected to behave similarly. Hence although the renders were generally not quick to reach saturation, they could then remain wet and vulnerable to moisture-related deterioration for relatively long periods of time.

The historic bricks were all fairly porous, with almost no small capillaries and a high percentage of air voids. As they generally had high sorptivity they would have exerted powerful suction when the render was applied, necessitating some pre-wetting of the brick to avoid drying the render out too rapidly, but potentially leading to the formation of a strong render-brick bond. This bond should facilitate the movement of moisture between the bricks and render, but the differences in the pore structures of the two materials and the greater sorptivity and drying rate of the bricks might cause the bricks to absorb and release moisture more rapidly than the render. The sorptivity of the Wallyford bricks was unusually low, particularly in depth, and this would have made a strong render-brick bond difficult to achieve.

7.1 Introduction

It has been found by other researchers that properties of bricks such as strength, porosity and sorptivity may be directionally dependent. For example, the sorptivity of bricks may vary depending on whether water is absorbed through the bed, header or stretcher face [102, 91] and whether water is required to pass through the outer surface of the brick [150]. This is important for moisture movement analysis because the stretcher face sorptivity is the parameter controlling rainwater absorption and evaporation, while the bed face sorptivity controls water uptake by capillary rise. There are also many practical applications, for example, the appropriate level of pre-wetting for bricks to which a lime or cement render is to be applied should be determined with reference to the stretcher face sorptivity.

Sorptivity was considered a key property for the bricks at NMOF because of its potential to influence the strength of the render-brick bond. Some evidence of anisotropy in the NMOF bricks was found during the experimental work described in Chapters 5 and 6, and additional sorptivity tests were undertaken to further investigate this phenomenon. The NMOF bricks were fired-clay, machine-pressed bricks with frogs, all produced in around 1940 in the Edinburgh area[14].

7.2 Method

The anisotropy of the historic bricks from NMOF was investigated using:

- Petrographic examination of thin sections of the bricks, to provide information about their composition and pore structures;
- X-ray diffraction analysis of the bricks to provide additional compositional information;
- Total Organic Carbon (TOC) analysis, using a Carlo Erba NA2500 Elemental Analyser. For analysis the bricks were ground to a fine powder in a ball mill and dried at 80 °C to constant mass. Three 0.02 mg samples of each brick were weighed and tested.
- Measurement of density, porosity, pore size distribution and sorptivity. For the sorptivity measurements, cores were drilled through the stretcher and bed faces,

[14] A date of manufacture for the Wallyford bricks is not known, but they must have been produced prior to the early 1970s when the Wallyford brickworks was closed [152].

and were tested with the outer surface of the brick facing downwards, 'skin down', and upwards, 'skin up'.

7.3 Results

The sorptivity values given in Chapter 6 were quoted to the nearest 0.1 mm/min$^{1/2}$. In this chapter sorptivity values have been quoted to the nearest 0.01 mm/min$^{1/2}$ in order to demonstrate small variations between samples, although it is accepted that the measurements were not necessarily repeatable to this level of accuracy.

7.3.1 Variations in sorptivity between the types of bricks

Comparing the samples drilled through the stretcher face and tested with the interior of the brick in the water ('skin up') the order of sorptivity from highest to lowest was Prestongrange, Whitehill, Edinburgh, Niddrie and finally Wallyford (Table 7.1). The Wallyford bricks had exceptionally low sorptivity of 0.08 mm/min$^{1/2}$. The sorptivities of the other bricks ranged from 0.51-2.00 mm/min$^{1/2}$, and these values are within the range of 0.32-2.72 mm/min$^{1/2}$ reported by other researchers for various types of clay bricks [102]. Sorptivity is generally expected to increase as porosity increases, and one researcher derived the empirical relation $S = 23.7\ \phi^{2.6}$ for a diverse range of around 60 types of clay bricks [152]. This relation held reasonably well for the Whitehill, Edinburgh and Niddrie bricks, depending on which of the measured sorptivities was considered, but was less applicable for the Prestongrange and Wallyford bricks (Table 7.2), which was unsurprising given that the NMOF bricks had very similar porosities, and showed no clear correlation between porosity and sorptivity.

Sorptivity is also expected to vary with pore size distribution, with fine pored materials having lower sorptivities than those with larger pores [101, 72], although it is suggested that the smallest pores, here defined as those below 10 μm in diameter, also 'have a major effect on transport processes' [97]. The pore size distributions of the bricks given in Fig. 7.1 showed some correlation between a high content of larger pores and high sorptivity. However the Niddrie bricks, with the lowest sorptivity, had almost no pores below 0.05 μm, whereas the Prestongrange bricks, with the highest sorptivity, had a fairly evenly spread pore size distribution, and it may be that the smaller pores contribute to the continuity of the pore network.

The differences in pore networks between the bricks may be attributed to differing methods of production, of which little is known, and differing composition, which was evident from the thin section analysis and X-ray diffraction. The NMOF bricks all contained quartz, mullite, cristobalite, hematite and cordierite. This indicates that they were well-fired at temperatures above 1000 °C, and that the starting material was carboniferous shale, which results in cordierite upon firing. The Wallyford bricks may have contained calcium-silicates (diopside-wollastonite), which generally indicate a higher firing temperature [153]. The inclusions of coal and sedimentary and igneous rock fragments varied significantly between the bricks, and although all of the bricks had a high TOC, this varied from 0.5 parts per thousand (ppt) for the Niddrie bricks in depth, to 103 ppt for the Wallyford bricks in depth (Table 7.1). The TOC was generally higher inside the bricks than at the surface, indicating incomplete combustion of organic matter during firing.

Table 7.1. Variations in sorptivity between the different bricks

	P	Wh	E	N	Wa
sorptivity ($mm/min^{1/2}$) (stretcher core, skin up)	2.00	0.99	0.72	0.51	0.08
porosity (%)	27.0	27.5	26.0	24.5	25.5
bulk density (g/cm^3)	1.735	1.685	1.790	1.895	1.665
median pore diameter (µm)	6.20	1.57	4.00	2.80	11.25
mode pore diameter (µm)	25.00 (and 0.23)	0.49 (and 29.69)	5.50	2.30 (and 27.10)	16.89
TOC (interior/surface) (ppt)*	17/3.9	1.6/1.1	4.4/1.0	0.5/4.3	103/3.4

* parts per thousand

Table 7.2. Comparison between the sorptivities measured and the values predicted using $S = 23.7\ \phi^{2.6}$

	P	Wh	E	N	Wa
predicted sorptivity ($mm/min^{1/2}$)	0.77	0.82	0.73	0.61	0.67
measured sorptivity ($mm/min^{1/2}$) (stretcher core, skin up)	2.00	0.99	0.72	0.51	0.08
measured sorptivity ($mm/min^{1/2}$) (stretcher core, skin down, 'main' sorptivity)	1.72	0.80	0.82	0.56	0.15

Fig. 7.1. Pore size distributions of the bricks, with sorptivities given for the stretcher cores, tested skin up

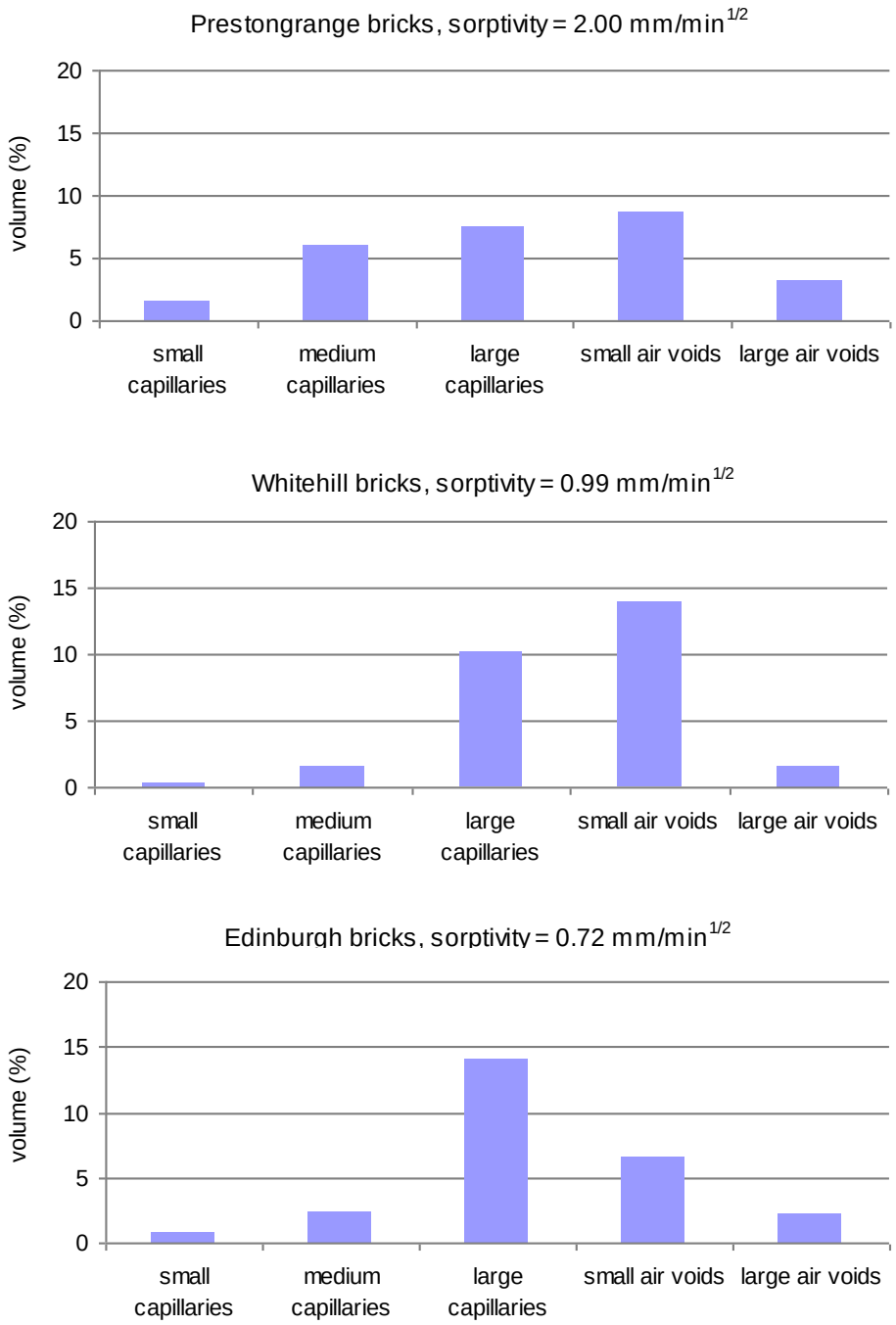

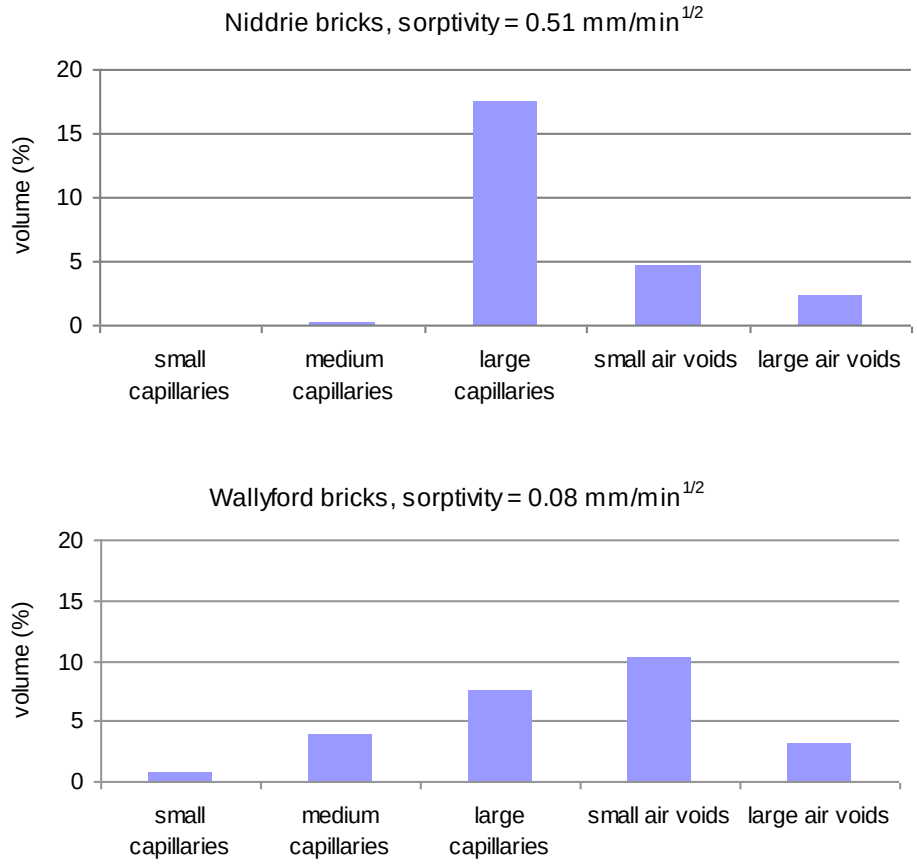

7.3.2 Variations between cores drilled through the bed face and the stretcher face

For some of the bricks, different sorptivities were measured depending on whether the core tested was drilled through the bed or stretcher face (Table 7.3). For the Niddrie, Prestongrange and Wallyford bricks, the sorptivity was higher for the stretcher face core than for the bed face core. The difference was greatest for the Prestongrange bricks, and the examination of these bricks without magnification showed cracks running parallel to the bed face (Fig. 7.2), while the thin sections showed the presence of capillary pores up to 70 μm long and 10 μm wide, again aligned parallel to the bed face (Fig. 7.3). It seems likely that during the sorptivity test water can move more upwards more easily if there are vertical cracks and pores available.

Higher sorptivities for brick samples cut parallel to the bed face have been reported elsewhere [102] and anisotropy in extruded bricks has also been observed [91]. Higher sorptivities were measured for samples cored along the direction of

extrusion, which was attributed to the aligned porosity of the bricks along this axis. A similar effect in limestone has been noted [154], whereby the sorptivity was higher if the direction of water movement was parallel to the bedding planes. Directional pores and cracks were not observed in the examination of the Edinburgh bricks, either without magnification or in thin section, and the sorptivity was actually found to be greater in the direction of the bed face core. Pores and cracks running parallel to the bed face might be expected in a pressed brick because a compressive force has been applied to it perpendicular to the bed face, but in the case of the Edinburgh brick it is possible that that the procedure for filling the mould was somehow different.

The role of cracks in increasing sorptivity has implications for potential changes in the sorptivity over time, because cracks are likely to develop as a brick ages. However, the effect will depend upon the size of the cracks. Fine cracks should draw water through the brick, but wider cracks may function as barriers and reduce sorptivity. The porosity of a brick may also change over time, but again, as the porosity might increase due to the dissolution of the certain components of the brick, for example in the presence of acidic pollutants, or decrease due to blocking of the pores by substances such as microbial biofilms, this could increase or reduce the sorptivity.

Table 7.3. Variations in sorptivity due to the brick orientation

	P	Wh	E	N	Wa
sorptivity mm/min$^{1/2}$ (stretcher core, skin up)	2.00	0.99	0.72	0.51	0.08
sorptivity mm/min$^{1/2}$ (bed core, skin up)	1.16	0.97	1.38	0.47	0.05

Fig. 7.2. Section through a Prestongrange brick, viewed with the bed faces at the top and bottom, showing large horizontal cracks

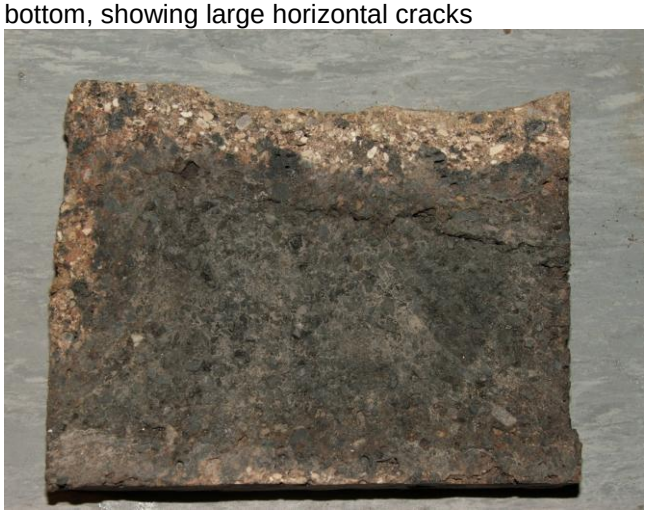

Fig. 7.3. Thin section cut from the stretcher face of a Prestongrange brick, showing pores parallel to the bed face, plane polarized light, field of view: 875 µm across

bed face

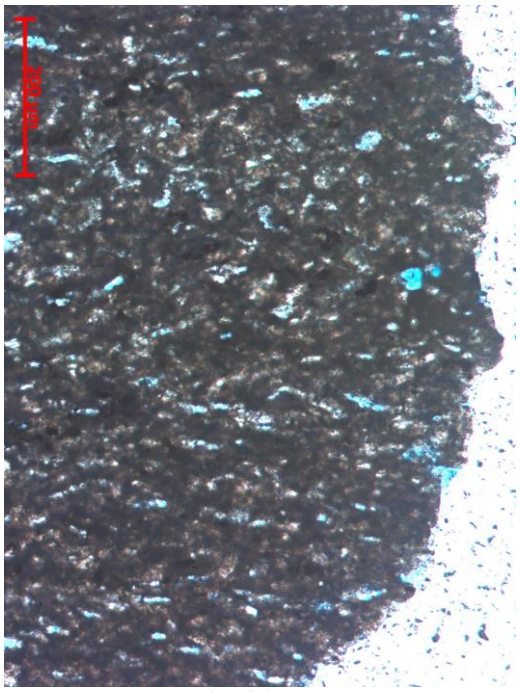

stretcher face

bed face

7.3.3 Effect of the surface skin on the sorptivity

For some samples the surface skin of the bricks was found to have a different sorptivity from the interior of the brick (Table 7.4). This effect was most evident for the bed cores, but was also observed for the stretcher cores of the Edinburgh brick. The Edinburgh, Prestongrange and Wallyford bed cores had lower sorptivity at the

surface than in depth, resulting in a graph of *i* against $t^{1/2}$ with a gradually increasing gradient, as water moved first through the surface skin and then through the inside of the brick (Fig. 7.4). The formation of a compact, low sorptivity surface layer during the firing process has been suggested previously [155] and such a layer was visible in some of the hand specimens, particularly along the upper bed face of the brick, which presumably undergoes the greatest compaction inside the mould when it is stamped with the manufacturer's name (Fig. 7.2). The MIP data for the outer skin of the Prestongrange brick showed that although the skin had a similar volume of large pores to the core of the brick, it had fewer small and medium capillaries (Fig. 7.5), resulting in a porosity of 21.0%, as opposed to 25.5%[15] for the material in depth. Hence the reduced sorptivity of the skin may in some instances be due to its reduced porosity.

The sorptivity close to the head face of the bricks was not measured in this study, but in other research pressed bricks were cut into slices parallel to the head faces [150], and it was found that the end slices had considerably higher sorptivity than the slices from the middle of the brick. It seems likely that the material close to the head faces is less thoroughly compacted than the material in the centre of the brick, since the centre of the brick is compressed when the frog is stamped.

Table 7.4. Variations in sorptivity in the bed cores due to the presence of a surface skin on the bricks, with the cores tested 'skin down'

	P	Wh	E	N	Wa1*	Wa2*
initial sorptivity ($mm/min^{1/2}$)	0.25	1.29	0.37	0.44	0.08	0.02
main sorptivity ($mm/min^{1/2}$)	0.32	1.32	0.78	0.44	0.17	0.09

*Values have been given for each of the Wallyford brick bed cores, because the variation between them was considered too great for the results to be averaged meaningfully.

[15] The value of 25.5% quoted here for the internal porosity of the Prestongrange brick was obtained with MIP. The value obtained using a vacuum saturation method was 27.0%.

Fig. 7.4. Capillary absorption of water through a stretcher core of Edinburgh brick, orientated with the skin down

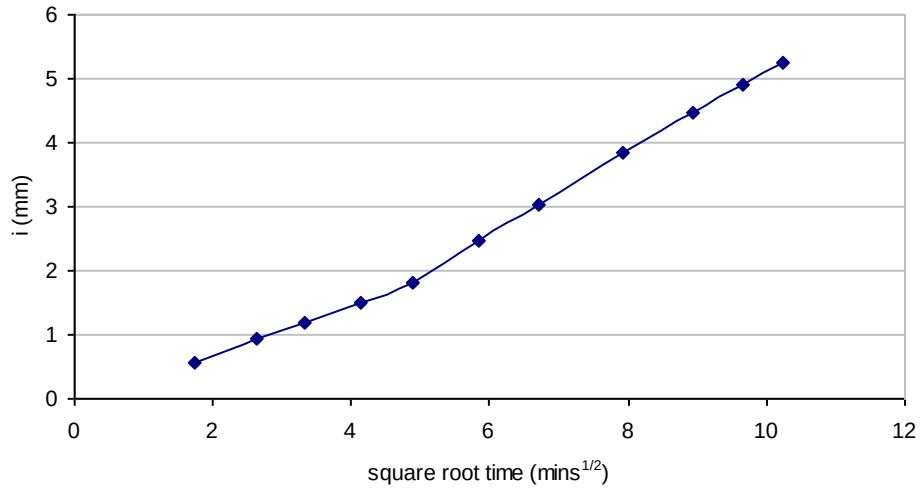

Fig. 7.5. Pore size distributions of the Prestongrange bricks, at the surface and in depth

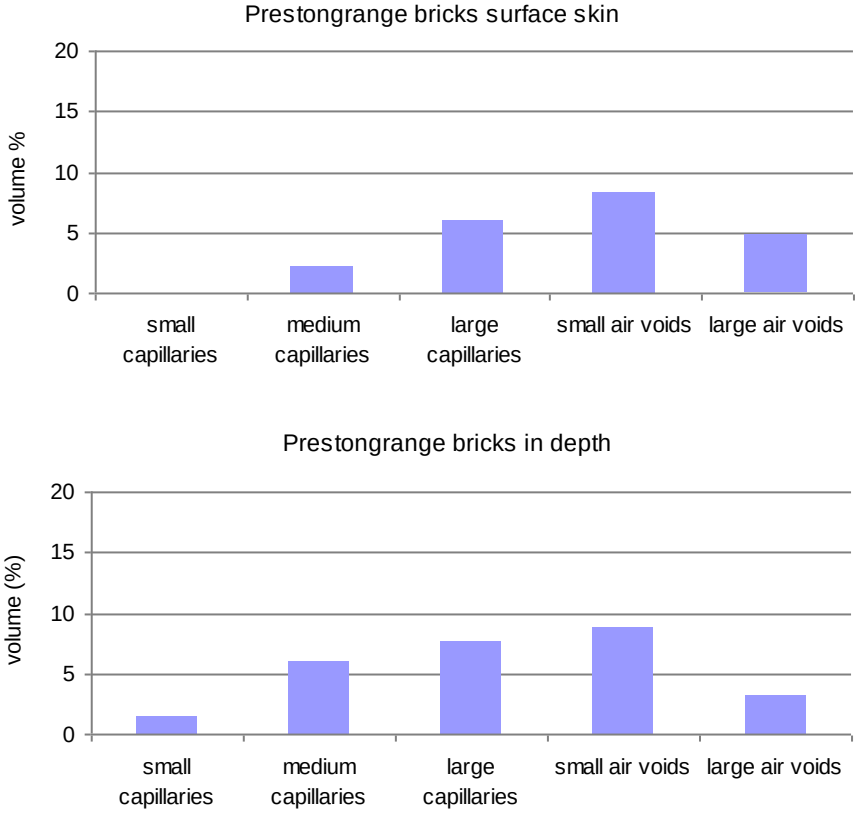

7.3.4 Low sorptivity of the Wallyford bricks

The unusually low sorptivity of the Wallyford bricks could not be attributed to the pore size distribution, because this was very similar to that of the Prestongrange

bricks. The sorptivity measurements on the Wallyford bricks were repeated using n-decane, as described in Chapter 6, and the results are given in Table 7.5. They show that although the predicted ratio of S_d to S_w is 0.61, the ratio obtained for the Wallyford bricks ranged from 7.0 to 25.0. This suggests that the sorptivity measured with water was low either because the Wallyford brick is hydrophobic or because it is prone to react with water. Sorptivity measurements with n-decane were also made on an Edinburgh stretcher core (ES1a), and the ratio obtained for S_d to S_w varied from 0.7 to 1.8 (Table 7.6), suggesting a lesser degree of hydrophobic behaviour in the Edinburgh brick.

The hydrophobic behaviour could have been due to the presence of an organic material, possibly a deliberately applied primer, but more probably microbiological growth, as the bricks used for testing were stored outside for several years without any protection. It has been found that compounds such as fatty acids, glycolipids and enzymes in a microbial biofilm may reduce the 'pore water tension', and hence alter the capillary water uptake of a porous material [156]. Additionally, it has been shown that stones containing significant quantities of minerals which weather easily, such as feldspars and clays, are particularly prone to microbiological growth [157], and the Wallyford bricks in particular had a high mudstone content (Fig. 7.6). Alternatively, the hydrophobic behaviour may have been due to the presence of coke inside the bricks, which is 'extremely hydrophobic' [158]. Common bricks in Scotland often contained colliery spoil [151, 159], which would have included pieces of coal, and the presence of fired coal or coke is evident in the bricks from NMOF, particularly the Niddrie bricks (Fig. 7.7). If the high TOC measured for the Wallyford bricks was because they contained more coke than the other bricks, this could explain why they demonstrated extreme hydrophobic behaviour.

Table 7.5. Sorptivity measurements for Wallyford bricks with water and n-decane

	WaS skin up	WaB2 skin up	WaS skin down	WaB2 skin down (initial)	WaB2 skin down (main)
sorptivity with water ($mm/min^{1/2}$)	0.08	0.04	0.15	0.02	0.09
sorptivity with decane ($mm/min^{1/2}$)	1.11	0.79	1.05	0.50	0.64
S_d/S_w	13.9	19.8	7.0	25.0	7.1

Table 7.6. Sorptivity measurements for Edinburgh bricks with water and n-decane

	ES1a skin up (initial)	ES1a skin up (final)	ES1a skin down (initial)	ES1a skin down (main)
sorptivity with water ($mm/min^{1/2}$)	0.95	0.416	0.3	1.4
sorptivity with decane ($mm/min^{1/2}$)	1.61	0.75	0.5	1
S_d/S_w	1.7	1.8	1.7	0.7

Fig. 7.6. Shrunken mudstone fragments in the Wallyford brick, plane polarized light, field of view: 1750 µm across

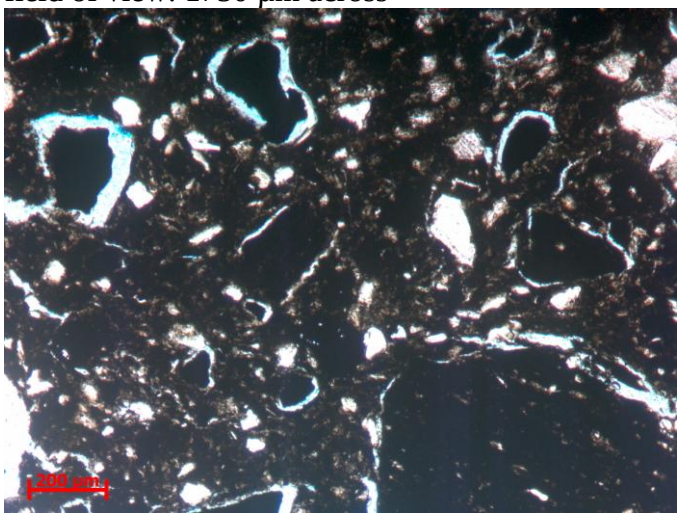

Fig. 7.7. Large, porous coal fragment in the Niddrie brick, plane polarized light, field of view: 1750 µm across

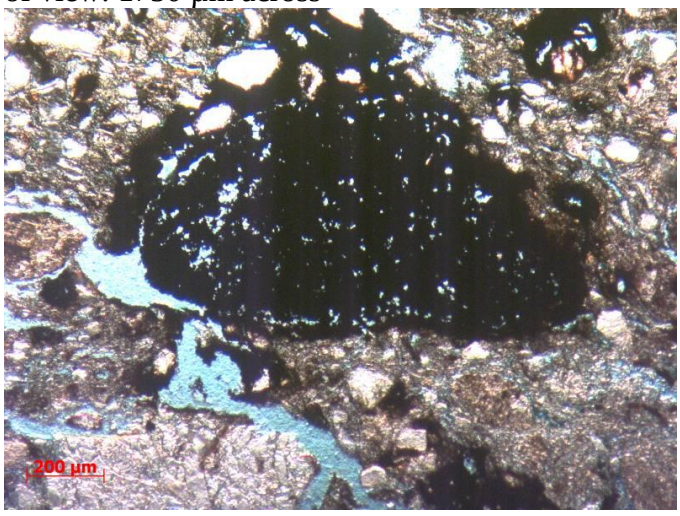

7.4 Conclusions

The sorptivity measurements undertaken on bricks from NMOF demonstrated that even though they were all pressed bricks produced at around the same time in the Edinburgh area, their sorptivities varied considerably. This appeared to be due to

differing pore size distributions rather than variations in porosity. For the Niddrie, Prestongrange and Wallyford bricks, the sorptivity was higher for the core drilled through the stretcher face than for the bed face core. These bricks contained fine cracks and channel-shaped pores running parallel to the bed face, probably created by the pressing process, and the cracks presumably assisted the movement of water through the bricks.

For some samples the surface skin of the bricks was found to have a lower sorptivity than the interior of the brick, particularly for the cores drilled through the bed face. This may partly have been because the porosity was lower at the surface, and may also have been due to the slightly hydrophobic properties of the bricks. The Edinburgh bricks were found to be slightly hydrophobic and the Wallyford bricks were extremely hydrophobic. The hydrophobic behaviour may have been caused by microbiological growth, particularly in the Wallyford bricks with their high mudstone content. Alternatively, it may have been due to the presence of hydrophobic coke inside the bricks, which was produced by the firing of the colliery spoil included in the brick raw materials.

Hence the experimental work confirmed the findings of other researchers that the properties of bricks may be directionally dependent and may be influenced by the presence of a surface skin. More research is required to understand why the surface skin may have reduced sorptivity, and to investigate why bricks may demonstrate hydrophobic behaviour.

8.1 Introduction

The aims of this chapter are to obtain a better understanding of why historic cementitious renders applied to brick substrates are prone to cracking, with particular reference to the buildings at NMOF. Cracking may be the first stage in a process which eventually leads to the delamination and loss of the render, and this may occur relatively quickly: in field studies of cement renders applied to building facades in Portugal the renders were typically found to have a service life of between 15 and 35 years [3].

There are several potential causes of cracking in cement and concrete, including structural movement, drying shrinkage, thermal movement, movement due to water absorption and movement due to freeze-thaw cycles [71], and these phenomena may be exacerbated by the differential movement of the substrate and the render, which places the render under tension. Since freeze-thaw cycling is a particular problem in countries with cold climates [18], this chapter begins with a review of the literature on the mechanism by which ice formation damages porous materials, and the experimental investigation of freeze-thaw cycling, particularly by dilation testing. The relevant results from Chapters 4, 5, and 6 are then summarized, and the additional experiments undertaken to investigate the strain response of brick and render samples due to freeze-thaw cycling are described. The results of these experiments are used to predict the likelihood of cracking occurring as a result of freeze-thaw cycling. This work is particularly valuable because although many researchers have undertaken dilation testing either with ceramic materials or with cement mortars, no single study has been found which tests both types of material by the same method, and this would be desirable to aid comparisons between material types. Finally, simple calculations are performed to predict the likelihood of the render at NMOF becoming saturated as a consequence of rising damp or driving rain.

8.2 Literature review

8.2.1 Mechanism of ice formation and associated damage in porous materials

Sun and Scherer [161] suggest that ice growth is dendritic and that the temperature between the dendrite branches is at the melting point of the crystals in the pores. They speculate that single crystals grow through the pore network, so that each crystal encompasses a group of pores. It has been shown that for an ice crystal to advance through a porous material, the driving force of undercooling 'must be sufficient for the crystal to pass through the breakthrough radius' [161]. This is the radius of the largest pore within an interconnecting system of pores, and is otherwise known as the critical pore size [97].

Early work to model the mechanisms by which ice formation damages porous materials was undertaken by Powers [162] and modified by Powers and Helmuth [163]. According to their hydraulic pressure theory, water freezes in the larger pores first and expands, pushing unfrozen water into the smaller pores and creating hydraulic pressure, which generates tensile stresses in the material and causes expansion and cracking. This theory is partially correct in that fully saturated cement paste certainly undergoes expansion upon freezing, but 'numerous experiments have shown that water tends to travel to, and not from, capillary pores when ice is forming' [18]. Other theories make use of the ice lens mechanism, whereby differences in free energy between unfrozen water and ice draw the water towards the ice in the larger pores, generating negative pressure [164, 165, 166]. If there is empty pore space the expansion effect is reduced and contraction dominates, in the phenomenon known as frost shrinkage.

Air entraining agents may be used in concrete and cement mortars to reduce frost damage. They create air voids 'with a typical diameter of ~50 μm spaced about 200 μm apart' [167]. Systems of air voids are usually characterized by the spacing factor, which is half the average distance between the periphery of voids, and hence the maximum distance displaced water needs to travel to freeze without causing damage. The critical spacing factor is the value beyond which the concrete deteriorates rapidly when subjected to freeze-thaw testing, and is usually quoted as 200 μm, although in practice higher values still often make for durable concretes

[18]. It was first assumed that the voids functioned by providing sinks for water displaced due to ice formation, and hence preventing the build-up of hydraulic pressure. However, it has since been shown that the primary role of the air voids is to provide space for the 'unconfined growth' of ice crystals [160], which suck in water by the ice lens mechanism. If undercooling is rapid when ice begins to grow, the concrete may be damaged by the stresses caused by hydraulic pressure despite the air voids present.

8.2.2 Methods for investigating freeze-thaw cycling of porous building materials

A lot of experimental work has been done to investigate the effect of freeze-thaw cycling on building materials such as stone, brick and concrete or cement mortar. Exposing materials to repeated freeze-thaw cycles is an effective method of assessing their freeze-thaw resistance, and methods are detailed in PD/CEN/TR 15177:2006 and DD/CEN/TS 12390-9:2006 for testing the freeze-thaw resistance of concrete due to internal structural damage and scaling respectively, and DD CEN/TS 772-22:2006 for clay masonry units. However, testing materials until damage is observed can be time-consuming if numerous cycles are required, and may not give much information about how the material behaves over each cycle. An alternative approach is dilation testing, which measures the length changes of building materials during freeze-thaw cycling and can give an early indication of the damage that may occur eventually [168]. Non-durable materials undergo a large dilation which increases significantly with repeated cycling, whereas durable materials only demonstrate a small dilation even after many cycles [18]. The building materials of interest at NMOF are bricks and cement render, and relevant literature exists for ceramic materials such as tiles and bricks [169, 170, 171,172) and Portland cement-based mortars, some containing fine sand aggregate and some with no aggregate [165, 166, 172, 174, 175]. A single study testing both ceramic materials and cement mortars by the same method does not appear to exist, and this would be desirable to aid comparisons between different material types.

The published literature on ceramics typically aims to compare materials from different provenances. The samples often undergo numerous freeze-thaw cycles causing visible deterioration. For cement mortars the factors investigated are the

cement:sand ratio, the water content, the addition of air-entraining agents such as synthetic detergents and Vinsol resin [174, 175], and the curing conditions [166, 175]. The samples typically only undergo a few cycles.

Some researchers of ceramic materials have adopted the temperature regime given in method E of the European standard EN539-2, with cycling from 15 °C to -15 °C and back in 2.5 hrs [169, 170, 171]. However a European standard for a dilation test for concrete does not exist, and ASTM C671-94, the 'Standard Test Method for Critical Dilation of Concrete Specimens Subjected to Freezing', was withdrawn in 2003 due to lack of use, and not replaced. Consequently the test methods employed for cement pastes and concrete vary widely, with cooling rates ranging from 3 °C/hr [175] to 2 °C/min [166] and minimum temperatures ranging from -20 °C [173] to -60 °C [166]. The effect of the cooling rate is generally not discussed, but when this was investigated with stone samples [168] it was found to affect 'the temperatures at which dilatation phenomena [take] place, the absolute length changes and the intensity of hysteresis'. Other drawbacks of common test methods are the brevity of the freezing period, meaning that the effect of longer freezing periods is not known; the limited number of cycles achievable within a reasonable time frame; and, for samples not submerged during freezing, the possibility that some water evaporates from the sample before freezing occurs.

Most researchers measure the freezer temperature and the temperature on or inside the sample, sometimes using a control sample with a hole drilled to accommodate a sensor [168]. Differential Scanning Calorimetry has also been used to investigate phase transitions and show the exothermic and endothermic response of ice crystallising and melting, respectively [18]. Samples may be vacuum-saturated [173], but capillary saturation techniques are more common, and Mačiulaitis and Kičaitė [172] consider this more representative of real life. Sun and Scherer saturated their samples and then dried them briefly to 'minimize ice extrusion' [174]. Some researchers also tested samples that were dry or at varying stages of saturation [168].

The sample movement can be measured using strain gauges [169, 170, 171, 173, 175], a dilatometer [166, 172], a linear variable displacement transducer (LVDT) [18] or a differential mechanical analyser (DMA) [174]. Strain gauges allow

the strain to be measured in several directions at once, which may be particularly useful for anisotropic ceramic samples [169].

A variety of other material properties may be measured and related to the freeze-thaw behaviour, including density, porosity, pore size distribution, permeability, water vapour diffusion resistance value, elastic modulus, dynamic modulus, compressive strength, tensile strength and flexural strength, from which the fracture energy can be calculated [173]. Some researchers take strength measurements before and after the freeze-thaw cycling [171].

The key parameter provided by the dilation test is the dilation accompanying ice formation during freezing. This is obtained 'by measuring the maximum difference between the contraction curve and the straight-line extrapolation of the pre-freezing curve', [18] as shown in Fig. 8.1. For a non-durable material the dilation increases significantly with progressive cycles, whereas for a durable material it remains roughly constant. According to ASTM C671-94, 'concrete is considered to be significantly damaged when the dilation increases by a factor of two or more between two successive cycles' [18]. The residual strain accumulated in the sample through successive cycles is also important, and for concrete is generally assumed to be significant when it exceeds 200 μm/m, or 0.02%.

Fig. 8.1. Determination of the dilation accompanying ice formation during freezing for a concrete specimen (redrawn from Pigeon and Pleau [18])

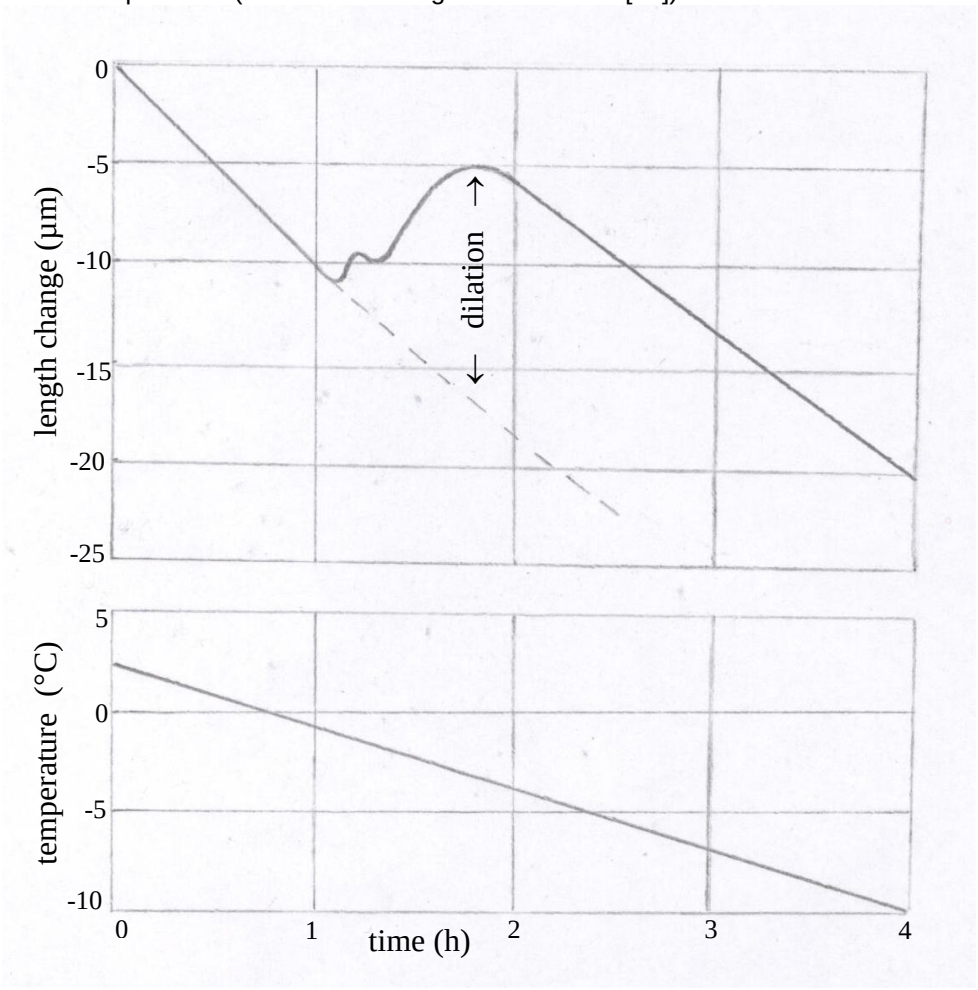

8.2.3 Findings from freeze-thaw cycling of porous building materials

The results obtained by Ruedrich [168] for dry sandstone samples showed a fairly linear contraction on cooling and expansion on heating, with no residual strain occurring. Wet sandstone samples underwent an initial contraction on cooling, followed by an expansion below 0 °C due to ice formation and then further contraction. No significant residual strain was observed for capillary saturated samples, but samples with higher degrees of saturation had large residual strains. Similarly, three periods of behaviour were generally observed when wet ceramics were frozen, with 'purely thermal' contraction to around –0.5 °C, followed by marked expansion, followed by further contraction or sometimes further slight expansion from around -9 °C onwards [171]. For some samples the residual strain

increased with each cycle, whereas for other samples the residual strain decreased with each cycle and eventually became negative. Mačiulaitis and Kičaitė [172] found that increasing the degree of saturation of bricks significantly increased the linear deformation. Perrin et al. [171] related the properties of the bricks to the damage observed, and concluded that frost durability was influenced partly by tensile strength and partly by porosity and pore size distribution, with large pores increasing durability.

Cement mortars have also been found to undergo an initial contraction upon cooling. Ice forms at the nucleation temperature, and samples containing air-entraining agents then contract further, whereas those without air-entraining agents generally expand. The effect of the initial water content and the curing conditions was investigated by Setzer and Liebrecht [166], who found that a lower original water content or storing specimens in water rather than at high RH resulted in smaller pores. Storing samples at 100% RH created some larger pores and caused them to behave similarly to the air-entrained mortars. Residual positive strains were measured for the samples without air-entraining agents and were found to increase with subsequent cycles [165, 173, 175].

Some researchers have also undertaken modelling to calculate the stresses and strains resulting from ice formation [169, 170], often using thermodynamic theory [165, 173]. Hörsch and Wittmann modelled crack patterns and predicted that the most damaged zones of the specimen should be close to the surface and near aggregates, which matched their real life observations. In particular, damage may occur near to porous aggregates, because if they become saturated and then freeze the water expelled creates damaging pressure within the surrounding cement paste [18].

8.2.4 Differential freezing in layered structures

A particular issue for renders is that wetting and freezing generally occur from the outer surface inwards. The phenomenon of single-sided freezing is often investigated during dilation tests on ceramic tiles, where a wet cloth is placed on one face of the tile to create a thermal gradient between the two faces [170]. It is generally found that the strain recorded due to cooling and the damage observed are greater for the face covered by the cloth, and it is suggested that ice forms at this face first, and

prevents water further inside the tile from moving towards the outside. The outer surface of a render is likely to have a higher water content than the interior and to respond more rapidly to a reduction in the external temperature, and this again could result in the preferential formation of ice at the surface, making the surface more vulnerable to cracking. It has been shown experimentally that the outer surface of a render is most likely to suffer deterioration [31]. Additionally, the render will typically have a higher water content than the brick substrate, as has been demonstrated by Hansen et al. [176]. If sub-zero temperatures occur, the render may undergo greater dilation due to ice formation than the brick, and this will create tension at the render-brick interface.

8.3 Investigation of the original cement render at NMOF

8.3.1 Method

8.3.1.1 Survey and non-destructive testing

As described in Chapter 4, the airfield buildings were surveyed in wet and dry weather in order to establish whether the cracking and delamination of the render was more prevalent in some areas than others. The rate of deterioration was assessed by comparing current and historic photographs, and several cracked areas of render on the piers were selected and photographed over a two-year period. Crack monitoring was undertaken over roughly the same period to investigate the movement of the cracks, using stainless steel discs as datum points and digital calipers. Additionally for this investigation, pieces of delaminated render were collected from the site and examined with the naked eye and at low magnification.

8.3.1.2 Render characterization

Of the materials characterization described in Chapters 5 and 6, the work considered relevant to the investigation of render cracking and delamination was:

- The petrographic examination of thin sections of the render and brick to obtain information about the pore structures;
- The measurement of the porosity of the render and brick using a vacuum saturation technique;

- The investigation of the pore size distribution of the render and brick using Mercury Intrusion Porosimetry (MIP) and size classifications adapted from Aligizaki [97];
- The measurement of the tensile strength, elastic modulus and strain at breaking point ε_{max} of render, brick and composite (render and brick) samples by undertaking three-point bending tests with an INSTRON testing machine.

8.3.1.3 Dilation testing

Dilation testing was undertaken to measure the length changes of brick and render samples due to water uptake at room temperature, temperature cycling of dry samples and freeze-thaw cycling. The materials tested were Niddrie brick; original render from Building 31 (B31 OR), which was characteristic of the smooth renders containing fine, quartz aggregate; and composite samples, consisting of a layer of Niddrie brick and a layer of render from the hospital complex at Athelstaneford Mains (HC OR).

The test samples were prisms measuring approximately 45 × 20 × 15 mm, which were orientated with their longest edges vertical. For the composite sample this resulted in a brick section on the bottom with a layer of render approximately 15 mm thick on top. The movement of the samples was measured using a linear variable displacement transducer (LVDT) (GT1000RA.L10 from RDP Electronics Limited) attached to a data logger (Signatrol SL7003 logger), and the ambient temperature and the surface temperature of the sample were monitored using thermocouples. The holder for the LVDT and the samples was made of stainless steel and underwent dimensional changes itself upon cooling and warming. This movement was measured by testing a sample of invar 36 rod, since the thermal coefficient of expansion of invar at 0 °C is approximately 5 x 10^{-7} °C^{-1} [177], small enough to be negligible, and so the dimensional change recorded was solely due to the holder. The movement of the holder was subsequently subtracted from the movement recorded for the samples. The experimental set-up is shown in Fig. 8.2.

To measure the length change resulting from water uptake at room temperature, the samples were stood in a shallow dish of water for 6 hr. For temperature cycling of dry samples, the samples underwent a 24 hr cycle comprising cooling from room temperature to -16 °C for 6 hr; warming from -16 °C to room

temperature for 4 hr and an isotherm at room temperature for 14 hr (Fig. 8.3). This temperature cycle was chosen because it was achievable with the freezer available, and although cooling rates occurring naturally are generally closer to 2 °C/hr, laboratory tests often use an accelerated cooling rate [18]. For freeze-thaw cycling of wet samples, the samples were vacuum saturated in a vacuum chamber or capillary saturated by standing in a dish of water for 48 hr, before undergoing the same 24 hr temperature cycle as the dry samples.

A fresh sample was used for each type of test, and the sample underwent three cycles of the test, to allow residual strains to develop. In between tests the samples were oven dried to constant mass at 110 °C and acclimatised at room temperature. For temperature cycling the length change of the sample against temperature was plotted. The length change at the minimum temperature and the residual length change at the end of the cycle were read off the graph, and for freeze-thaw cycles the dilation accompanying ice formation during freezing was determined, as shown in Fig. 8.1.

Additionally, the coefficient of linear thermal expansion for the dry samples α_l was calculated using

$$\alpha_l = \frac{\varepsilon_{mt}}{\Delta T} \qquad \textbf{(8.1)}$$

where ε_{mt} was the strain at the minimum temperature and ΔT was the difference between the maximum and minimum temperatures.

Fig. 8.2 Experimental set-up for LVDT measurements with brick, render and composite samples

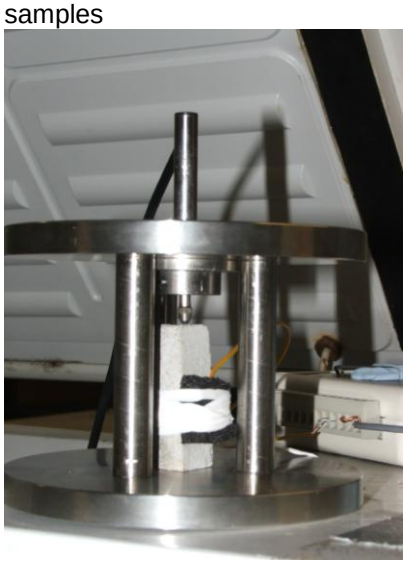

Fig. 8.3. Cooling and warming cycle used for the LVDT measurements

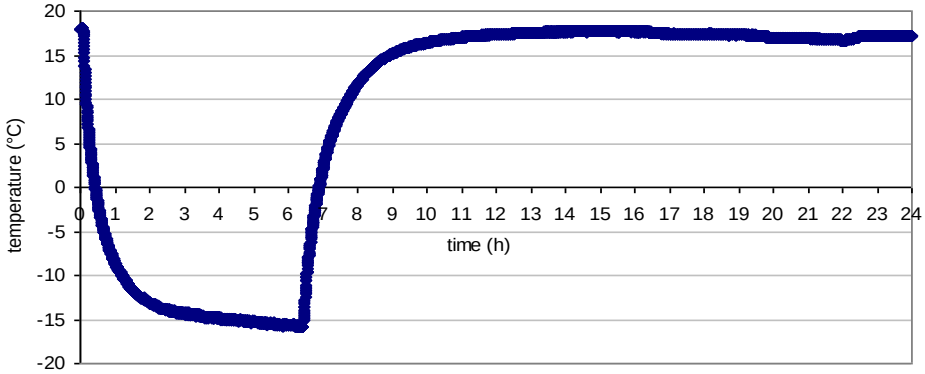

8.3.2 Results

8.3.2.1 Survey and non-destructive testing

It was clear from the visual inspection that the cement render on the raised piers was most prone to cracking and showed most evidence of previous losses (Fig. 8.4), but that some render losses had also occurred at the base of the walls, just above the brick plinths (Fig. 8.5). The piers were wet most frequently by rainfall, because most of the buildings did not have gutters, the roofs only had a small overhang, and the moss on the roofs soaked up water which dripped down onto the piers even when it was not raining. The render at the base of the walls was less exposed to rainfall, but may have had a high moisture content for some or all of the time due to rising damp,

as discussed in Chapter 4. The cracks in the render occasionally corresponded to cracks in the bricks themselves, but usually occurred above the mortar joints between the bricks. There was generally much less cracking in the bricks than in the render.

The comparison of photographs from 2004 and 2010 showed that while some areas of cracking had suffered render losses over the six-year period, others appeared unchanged. Similar variations were observed in the areas photographed frequently over a two-year period, but it was noticeable that most of the render losses within this period occurred over the severe winter of 2010-2011 (Fig. 8.6). The photographs also demonstrated that cracks in their early stages were not visible to the naked eye except after rain, when they appeared darker than the surrounding render. The low-magnification examination of pieces of detached render from NMOF showed that they had not undergone any visible loss of cohesion, and that delamination had usually but not always occurred at the render-brick interface (Fig. 8.7).

Crack monitoring suggested that the strain between two markers on an area of un-cracked render could vary up to 0.48% over the course of a year, and that the strain between two markers positioned on either side of a crack could vary by up to 1.30%. The stress associated with this amount of strain is calculated in Section 8.3.2.3.

Fig. 8.4. Cracking and render loss on a pier on the SE elevation of Building 38

Fig. 8.5. Render loss at the base of the SW elevation on Building 22

Fig. 8.6. Render losses on the second pier from SW, on the NW elevation of Building 32

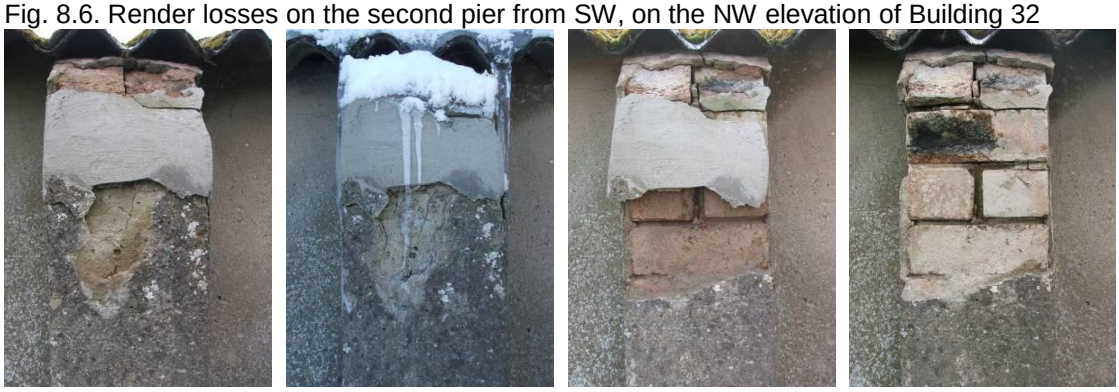

13/10/2010 08/12/2010 02/02/2011 12/08/2011

Fig. 8.7. Reverse side of a detached piece of render from Building 22, showing that delamination had occurred at the render-brick interface and only a few small fragments of brick had been removed

8.3.2.2 Render characterization

The tensile strength of each type of sample varied considerably (Table 8.1). This was because pre-existing cracks could cause premature failure, particularly for the brick and composite samples which contained cracks from the brick manufacturing process. However, the render and composite samples were on average stronger than the brick samples, and the average elastic modulus of the render was higher than for the brick, with the composite somewhere in between the two.

According to Sun and Scherer [160], an air-entrained mortar might typically contain 6% spherical air voids, regularly spaced and ranging from 10-1000 μm in size. It was observed from petrographic examination that the voids present in both the well sorted and poorly sorted aggregate renders (B47 OR and B24 OR) were irregularly spaced and irregular in shape (Fig. 8.8), and that the renders were therefore unlikely to have contained air-entraining agents. The pore size distribution obtained using MIP (Table 8.2) showed that B47 OR contained only 1.3% air voids, but that B24 OR contained 10.1% air voids. The presence of these irregular voids would increase the susceptibility of the renders to frost damage, because large, entrapped air voids 'increase the air content without offering any significant protection against freezing and thawing cycles' [18].

The Niddrie bricks contained 7.1% air voids, which the thin section examination showed to be irregularly spaced and irregular in shape (Fig. 8.9). Again, these might increase susceptibility to frost damage, but some researchers have found that large pores in ceramics increase durability [171], and this may be because the largest pores are rarely filled completely with water. Additionally, the bricks contained no small capillaries and almost no medium capillaries, which should assist in preventing frost damage because the water in the small capillaries remains liquid even at very low temperatures, and feeds the growth of ice crystals in larger pores, increasing the damage in these pores [162].

Table 8.1 Characterization of the brick and render samples

	vacuum porosity (%)	median pore diameter[4] (μm)	mode pore diameter[4] (μm)	tensile strength (N/mm^2)[5]	elastic modulus (N/mm^2)[5]	strain at breaking point (%)[5]
coarse aggregate render[1]	18.0	0.53	1.50	2.8-5.8	320-850	0.56-0.88
fine aggregate render[2]	24.0	3.40	1.90	7.7	1180	0.65
Niddrie brick[3]	24.5	2.80	2.30 (and 27.10)	0.7-2.0	200-460	0.31-1.01
composite (Niddrie brick and HC OR)				1.8-6.0	420-550	0.41-1.09

[1]The porosity and median and mode pore diameters quoted are for B47 OR, while the tensile strength, elastic modulus and strain at breaking point are for HC OR. These both contained well sorted aggregate.
[2]The porosity, tensile strength, elastic modulus and strain at breaking point quoted are for B31 OR, while the median and mode pore diameters are for B24 OR. These both contained fine, poorly sorted aggregate.
[3]The values of tensile strength and elastic modulus given for the Niddrie brick are for the samples cut with their long edges parallel to the stretcher face of the brick.
[4]The median and mode pore diameters have been taken from the MIP cumulative porosity curve. A secondary value for the mode pore diameter is given for the brick because it had a bimodial distribution.
[5]These values have been given as ranges to demonstrate the variations between samples where several samples were tested.

Table 8.2 Pore size distribution of the brick and render samples, showing the percentage of pore space within size classes, as percentage of sample volume

sample	small capillaries 0.0025-0.01 μm	medium capillaries 0.01-0.05 μm	large capillaries 0.05-10 μm	small air voids 10 -50 μm upwards	large air voids 50 μm upwards	total % (obtained by MIP)
coarse aggregate render (B47 OR)	1.3	3.0	14.2	0.5	0.8	19.8
fine aggregate render (B24 OR)	1.5	0.5	14.6	6.6	3.5	26.7
Niddrie brick	0.0	0.2	17.4	4.7	2.4	24.7

Fig. 8.8. Surface of B24 OR, showing the large, irregular air voids (blue), plane polarized light, field of view: 875 µm across

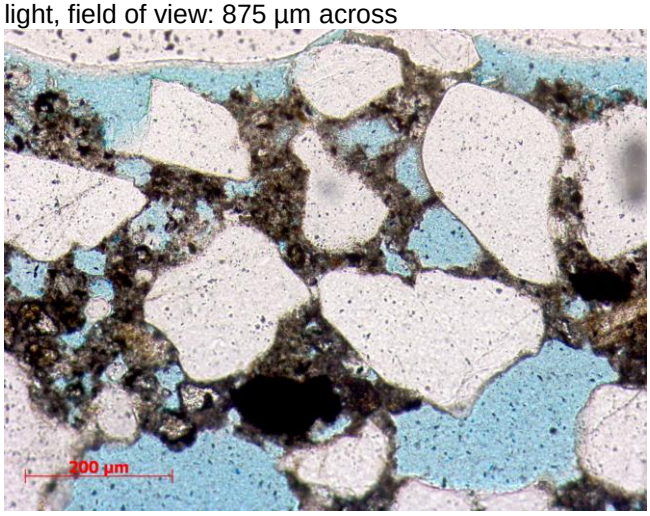

Fig. 8.9. Interior of Niddrie brick, showing the irregular cracks and air voids, plane polarized light, field of view: 1750 µm across

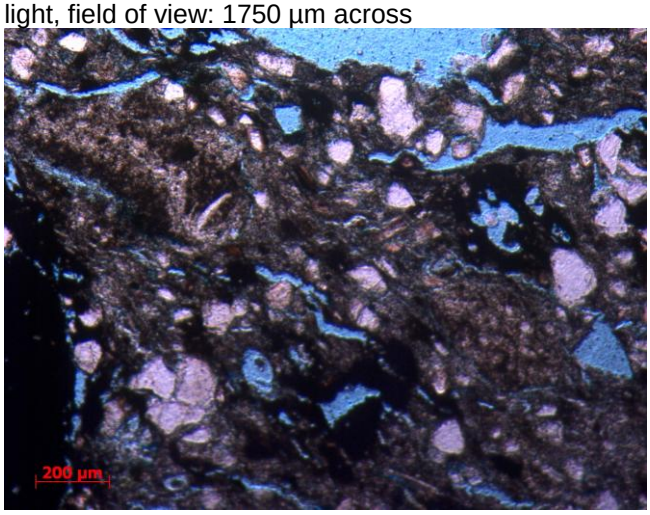

8.3.2.3 Dilation testing

Full results for the dilation testing are given in Appendix 4 and as electronic files.

Water uptake

The strain in the samples due to water uptake at room temperature was found to be below 0.0001%, and hence negligible.

Surface temperature monitoring during temperature cycling

The results from the surface temperature monitoring during temperature cycling illustrated in Fig. 8.10 showed that the surface temperature measured on the samples lagged behind the freezer temperature. At a freezer temperature of around -8 °C, the surface temperature of the capillary- and vacuum-saturated samples rose by approximately 2 °C, in response to the exothermic formation of ice. At this point the

surface temperature of the samples was around 0 °C. It has been found that the temperature rise due to ice formation can increase with progressive cycling, particularly for cementitous materials where the drying between cycles can cause microcracking and alter the structure of the cement paste [18], and minor increases in peak size with progressive cycles were found for the render and brick samples (Table 8.3).

Table 8.3 Surface temperature (ST) increase at point of ice formation over progressive freeze-thaw cycles of capillary-saturated samples

	cycle 1 ST increase (°C)	cycle 2 ST increase (°C)	cycle 3 ST increase (°C)	change in ST increase from cycle 1 to cycle 3 (°C)
render	2.18	3.44	3.65	1.47
brick	1.23	1.89	2.17	0.94

Fig. 8.10. Surface temperature and freezer temperature for the third freeze-thaw cycle of capillary-saturated render

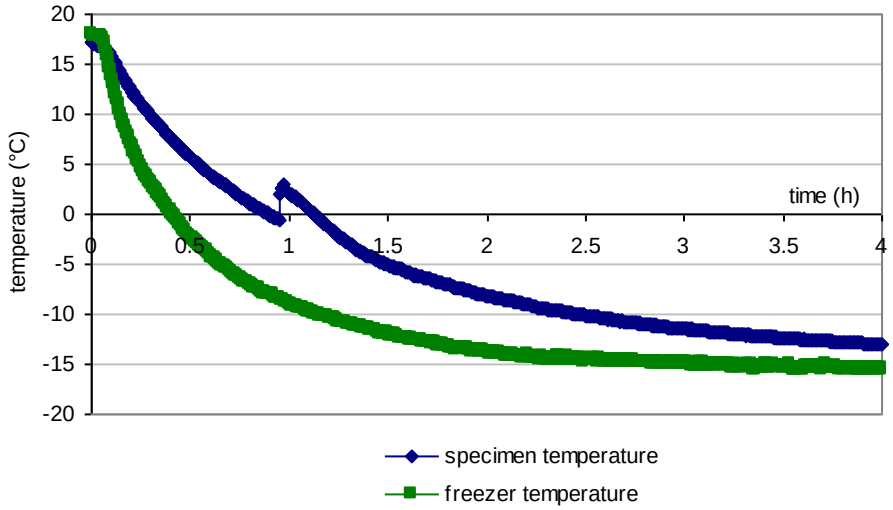

Accuracy and repeatability of LVDT measurements

The repeatability of the LVDT measurements could not be investigated because it was impossible to take readings at the exact same location on a sample, plus the samples were altered by each cycle. The strains in Tables 8.5 and 8.7 have been given to four decimal places to allow small changes to be seen. The data contained some artifacts from movement of the sample holder which have been omitted from the data presented.

Temperature cycling of dry samples

The strain in the dry samples at the minimum temperature and the end of each cycle are given in Table 8.5. The dry render samples contracted more upon freezing than the brick and composite samples, which was expected because concrete typically has a higher coefficient of linear thermal expansion than brick [178], and the composite samples were approximately 70% brick. The coefficients of linear thermal expansion obtained for the render and brick are given in Table 8.4, and show that the values measured decreased with progressive cycles, possibly because the samples were permanently deformed after the first cycle. Using the values from the first cycle, the coefficient of linear thermal expansion of the brick was 8.0 x 10^{-6} mm/mm/°C, which is in good agreement with the 6.5 x 10^{-6} mm/mm/°C reported by Allen and Iano [178]. However the coefficient of linear thermal expansion of the render was 1.94 × 10^{-5} mm/mm/°C, which was considerably higher than the 9.9 × 10^{-6} mm/mm/°C reported by Allen and Iano for normal-weight concrete.

Table 8.4 Coefficients of linear thermal expansion for dry render and brick samples

sample	measured coefficient of linear expansion x 10^{-6} (mm/mm/°C)			coefficient of linear expansion x 10^{-6} from Allen and Iano [178] (mm/mm/°C)
	cycle 1	cycle 2	cycle 3	
render	19.4	14.1	14.0	9.9 (value for normal-weight concrete)
brick	8.0	4.1	2.6	6.5
composite	5.1	4.0	3.2	

At the end of the first cycle the render showed a residual negative strain, meaning that it had contracted slightly. However for the other render cycles and all of the brick and composite cycles positive values of residual strain were measured, suggesting that plastic deformation had occurred. The average maximum strain in the dry render due to freezing was 0.054%, which was over 10 times smaller than the strain measured at breaking point for the same render (B31 OR), as given in Table 8.1. The environmental data from NMOF discussed in Chapter 4 indicated that the experimental temperature change of 34 °C was around the maximum experienced by the render in situ. Hence although temperature cycling may cause some permanent deformation of the render, it is probably insufficient to cause failure, even when the render is restrained by the bricks. The change in length of the dry render sample during temperature cycling is shown in Fig. 8.11.

Table 8.5 Length changes of the samples due to temperature cycling of dry samples

sample	cycle	strain at minimum temperature (%)	strain at end of cycle (%)	cumulative strain at end of cycle (%)
render	1	-0.0661	-0.0029	-0.0029
	2	-0.0480	0.0017	-0.0012
	3	-0.0477	0.0064	0.0052
brick	1	-0.0274	0.0002	0.0002
	2	-0.0141	0.0059	0.0062
	3	-0.0090	0.0125	0.0187
composite	1	-0.0173	0.0064	0.0064
	2	-0.0138	0.0159	0.0222
	3	-0.0110	0.0095	0.0317

Fig. 8.11. Strain in the dry render sample during temperature cycling, cycle 3. The sample contracts upon cooling and then expands upon warming

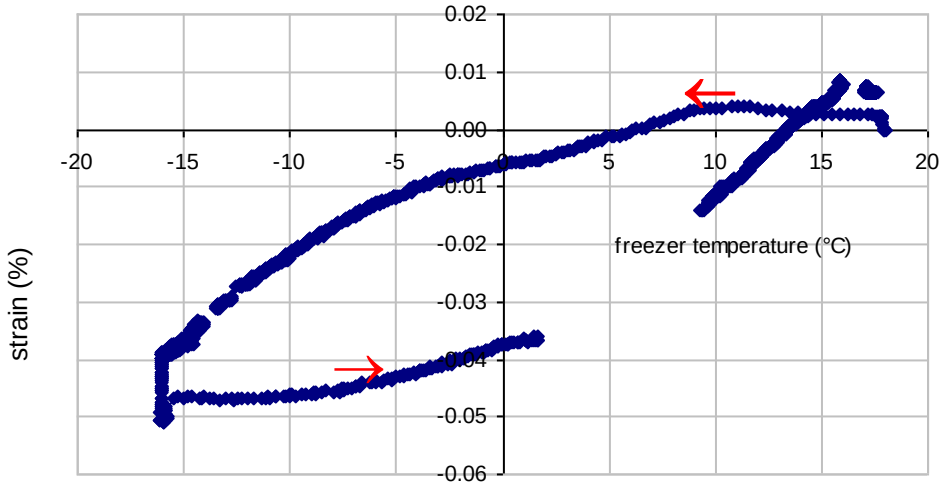

Temperature cycling of capillary- and vacuum-saturated samples (freeze-thaw)

The porosities obtained from capillary and vacuum saturation were generally repeatable to ±0.5%, and they have therefore been quoted with this level of accuracy (Table 8.6). The average vacuum porosity of the render samples was 25.5%, which was slightly higher than the 24.0% measured previously for B31 OR. However, the average vacuum porosity of the brick samples was 28.5%, which was 4.0% higher than the 24.5% measured previously for the Niddrie bricks, suggesting that the samples may have had a high content of voids and cracks. The water contents of the capillary-saturated render, brick and composite samples averaged 71%, 58% and 60% respectively of the vacuum-saturated water contents. According to Hall and Hoff [117] a value of around 85% may generally be assumed for this quantity, suggesting that the samples had not reached their maximum capillary saturation. The

brick may have absorbed less water than the render when it was capillary-saturated because the brick contained large air voids which were only partially filled with water.

Table 8.6 Porosity of samples due to capillary and vacuum saturation

sample	previous measurement	measurement during LVDT experiments		% of total pore space filled by capillary saturation
	porosity by vacuum saturation	porosity by vacuum saturation	porosity by capillary saturation	
render	24.0	25.5	18.0	71
brick	24.5	28.5	16.5	58
composite	not done	28.5	17.0	60

All of the saturated samples expanded at the point of ice formation (Fig. 8.12 and Table 8.7), but the strains were greater for the vacuum-saturated samples than for the capillary-saturated samples by factors of up to 56. This was presumably because the capillary-saturated samples had empty pores to accommodate some of the water displaced during freezing, whereas every pore in the vacuum-saturated samples was full, leading to greater expansion when freezing occurred. The strain due to ice formation did not increase significantly with successive cycles for the brick and composite vacuum-saturated samples, but for the vacuum-saturated render it roughly doubled with each cycle, reaching 0.0950% in the third cycle. According to the criterion in the previous ASTM standard for critical dilation, concrete is 'significantly damaged when the dilation increases by a factor of two or more between two successive cycles' [18], meaning that the vacuum-saturated render was significantly damaged by freezing. The strain at failure calculated for this render type from tensile strength testing was 0.65%, suggesting that if the length change experienced by the render upon freezing continued to increase, the render would eventually fail.

Referring back to Section 8.3.2.1, the maximum strain measured across an expanse of un-cracked render at NMOF over the course of a year was 0.48%.This was only slightly below the minimum strains at breaking point for the render given in Table 8.1, suggesting that the render at NMOF could be subjected to sufficient strain for cracking to occur, as had been verified from field observations.

The capillary-saturated bricks and composite samples sustained a small net expansion after each cycle, but the capillary-saturated render sustained a small net

contraction. The values of residual strain were similar to the values for the dry samples, suggesting the strain was caused by thermal contraction and expansion rather than damage from ice crystallization. However, the vacuum-saturated samples demonstrated residual strains which were 2-10 times higher than those measured for the dry and capillary saturated samples, suggesting this strain was partly due to damage from ice crystallization. The cumulative strain increased with each cycle, as found by other researchers for cement mortars without air-entraining agents [165, 173, 175] and for some but not all ceramics [171]. Subtracting the cumulative residual strain in the dry samples after three temperature cycles from the cumulative residual strain in the vacuum saturated samples after three temperature cycles, the cumulative residual strain due purely to freeze-thaw damage was 0.029% in the render and 0.043% in the brick.

Pigeon and Pleau [18] consider a strain of 0.01% or more sustained after 300 freeze-thaw cycles to be indicative of a non-durable cement mortar. If this criterion is applied to the render tested it was certainly non-durable, as after only three freeze-thaw cycles of a vacuum-saturated sample the cumulative residual strain was 0.035%.

Fig. 8.12. Strain in the vacuum-saturated render sample during temperature cycling, cycle 3. During cooling the sample contracts slightly, and then expands from around –8°C due to ice formation

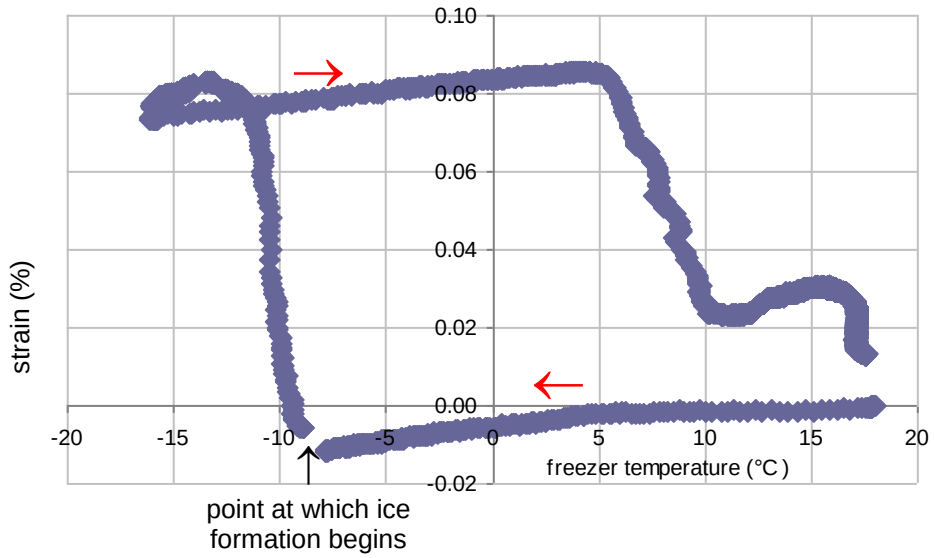

Table 8.7 Strain in the samples due to temperature cycling of capillary- and vacuum-saturated samples

sample	cycle	strain due to ice formation (%)	strain at minimum temperature (%)	strain at end of cycle (%)	cumulative strain at end of cycle (%)
render capillary saturated	1	0.0025	-0.0357	-0.0054	-0.0054
	2	0.0043	-0.0392	-0.0078	-0.0132
	3	0.0037	-0.0249	-0.0017	-0.0149
brick capillary saturated	1	0.0027	-0.0009	0.0109	0.0109
	2	0.0043	-0.0059	0.0068	0.0177
	3	0.0086	0.0031	0.0039	0.0216
composite capillary saturated	1	0.0018	-0.0149	0.0076	0.0076
	2	0.0049	-0.0092	0.0034	0.0110
	3	0.0047	-0.0061	0.0059	0.0169
render vacuum saturated	1	0.0199	0.0071	-0.0010	-0.0010
	2	0.0518	0.0317	0.0174	0.0164
	3	0.0950	0.0914	0.0187	0.0351
brick vacuum saturated	1	0.0544	0.0514	0.0276	0.0276
	2	0.0552	0.0554	0.0180	0.0456
	3	0.0558	0.0611	0.0156	0.0612
composite vacuum saturated	1	0.1023	0.0875	0.0273	0.0273
	2	0.0913	0.1023	0.0089	0.0362
	3	0.1366	0.1278	0.0334	0.0696

8.4 Calculations to predict the frequency of saturation of the original cement render at NMOF

8.4.1 Wetting of the bottom of the render due to rising damp

To estimate the height of capillary rise in the walls of the brick masonry buildings at NMOF, two representative buildings were considered, one with a plinth 0.4 m high, and one without a plinth. Both of these buildings are simplifications of the real buildings at NMOF, because plinths were used to even out variations in the topography of the ground, and hence the height of the plinth varied across each building. The plinths were constructed from a single layer of bricks on the outside with a concrete and rubble infill, as seen in the remains of Building 33 (Fig. 8.12). Above the plinths the walls of the buildings were half a brick thick (110 mm), with a render approximately 10 mm thick on the outside, and no render on the inside. One brick course (85 mm) above the plinth there was a bitumen damp proof course, extending across the brick wall but bridged by the render, as shown in Fig. 8.13. It

was assumed that the base of the plinth and the base of the walls in the building without a plinth were in contact with the water table, and hence exposed to an unlimited supply of water. This seemed reasonable given that the monitoring of soil moisture content described in Chapter 4 had shown that the soil was always moderately wet.

Fig. 8.12. Plinth of Building 33, showing concrete infill with brick exterior. This building was a Nissen hut with curved, corrugated iron walls rather than brick masonry walls, and so was unusual in that the damp proof course was one brick course below the top of the plinth rather than one brick course above the plinth.

Fig. 8.13. Typical construction of a brick masonry building used for rising damp calculations

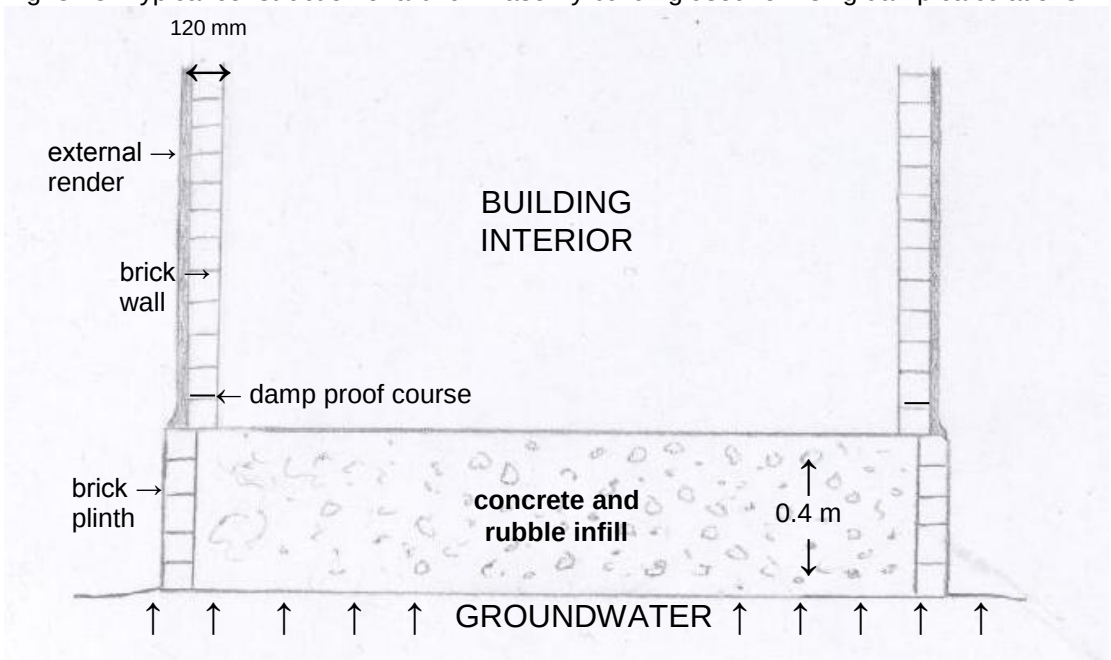

8.4.1.1 Building with plinth

It was assumed that the plinth infill consisted of a layer of solid concrete 0.15 m high with rubble underneath, and that the rubble was permanently saturated. The rate of capillary flow u of water upwards through the concrete layer was calculated using

$$u = \frac{S^2}{2\theta_w h} \qquad \textbf{(8.2)}$$

where the height of the plinth h=150, the sorptivity S=0.10 and the volume fraction water content θ_w=0.13[16], which were the average values obtained for the concrete from the air raid shelter. This gave the rate of capillary flow as 0.00026 mm/min. The minimum average potential evaporation rate at NMOF was 0.0003 mm/min, and as the rate of capillary flow was less, this suggested that water moving up through the concrete would not reach the upper surface of the plinth, and hence that the render would not be affected by rising damp.

8.4.1.2 Building without plinth

As described in Section 2.16, Hall et al. [107] have shown that in a wall where rising damp has stabilized, the height of rise $h_{ss\ may}$ be given by

$$h_{ss} = S\left(\frac{b}{Ne\theta_w}\right)^{1/2} \qquad \textbf{(2.11)}$$

where S is the sorptivity of the building material, b is the thickness of the wall, N is the number of surfaces through which evaporation occurs, e is the evaporation rate and θ_w is the volume fraction water content of the wetted region. This equation was used to estimate the height of rise in the building without a plinth at different times of the year, although in practice there is a time lag between a change in the evaporation rate and the corresponding change in the height of rise.

The different properties of the surface layer of render were ignored[17], and the walls were treated as solid brick 120 mm thick. The porosity and sorptivity for Niddrie bricks were used, with sorptivity measured through the bed face for a core

[16] The volume fraction porosity f for the air raid shelter concrete was 0.155, but, as discussed in Chapter 2, a value for θ_w of 0.85f was assumed.

[17] It was found that the values of porosity and sorptivity obtained if the values for the render and brick were averaged were virtually the same as the values for just the brick, because the brick layer was much thicker than the render layer.

orientated 'skin down', so that S=0.40 and θ_w=0.21[18]. It was assumed that the internal evaporation rate was the same as the external rate, although in practice this depended on the time of year and whether the building was heated. Using Equation 2.11, it was calculated that for the months when the evaporation rate was the minimum of 0.0003 mm/min, the predicted height of rise would be 390 mm, while in June when the evaporation rate was the maximum of 0.0014 mm/min, the predicted height of rise would be 180 mm. This meant that water would rise up the first brick course (85 mm) to the damp proof course, and would then move through the render past the damp proof course, before moving upwards inside the render and bricks. Assuming that the damp course was in good condition, the effect of it would be to reduce the height of rise from the value predicted, because it would reduce the rate of water flow upwards. However, there would be a permanently wet zone at the very base of the walls.

Table 8.7 Predicted heights of rise in a brick masonry building without a plinth at NMOF

month	average potential evaporation rate at NMOF in mm/min	predicted height of rise through walls in building without plinth (mm)
January	0.0003	390
February	0.0003	390
March	0.0003	390
April	0.0011	200
May	0.0013	190
June	0.0014	180
July	0.0013	190
August	0.0010	210
September	0.0008	240
October	0.0005	300
November	0.0003	390
December	0.0003	390

8.4.2 Wetting of the render on the piers due to driving rain

To calculate the time taken for the render on the pier heads to reach capillary saturation due to driving rain, it was assumed that the pier heads were exposed to an unlimited supply of water whenever it was raining. Since the pier heads were sloping and protruded past the overhang of the roofs, they were wet even by rain with no horizontal component, and were also wet by the run-off from the roofs.

Equations 6.10 and 6.11 for sorptivity were rearranged to give

[18] The volume fraction porosity f for the Niddrie bricks was 0.245, and hence θ_w was 0.21.

$$t = \left(\frac{\Delta m}{\rho_w \times A \times S} \right)^2 \quad \textbf{(8.3)}$$

where t is the time taken for the water to move a distance d through the sample, Δm is the mass gain of the sample, ρ_w is the density of water, A is the cross-sectional area of the sample and S is its sorptivity. Additionally

$$\Delta m = \theta_w \times d \times A \times \rho_w \quad \textbf{(8.4)}$$

where θ_w is the volume fraction water content of the render due to water absorption by capillarity, again taken as 0.85f, d is the thickness of the render and A is the area of the render. Hence

$$t = \left(\frac{\theta_w \times d}{S} \right)^2 \quad \textbf{(8.5)}$$

Taking d to be the average render thickness of 10 mm, the maximum time taken for the render to become fully capillary saturated when starting from dry was calculated to range from 30 minutes for B23 RR to 630 minutes for B24 OR (Table 8.8). This suggests that all of the render types on the pier heads may reach full capillary saturation on occasion, and that the repair renders may reach full capillary saturation after a relatively short period of rain. Once the renders are fully saturated, the high sorptivity of the bricks would ensure that water then moves into the brick substrates, as has been shown by Hansen et al. [176].

Table 8.8 Time taken for render of thickness 10 mm to be fully capillary saturated by rain

	B24 OR	B47 OR	B23 RR	B25 RR
time taken (minutes)	630	230	30	110

An experiment to measure the drying rates of brick and mortar from NMOF is described in Section 6.8, and cementitious render would behave similarly to the mortar tested. A render thickness of 1 cm may be considered equivalent to a mortar sample 1 cm high. At 75% RH, the time taken for the mortar sample to reach its critical saturation level (the point at which the rate of drying ceases to be linear and begins to fall) would be approximately 10 hr. After approximately 140 hr the water content of this sample would still be around half the absolute moisture content. Although the evaporation rate at NMOF would generally be higher than the experimental evaporation rate due to air movement, this demonstrates how slowly

the render dries out, and suggests that it may never dry out fully between rainfall events.

8.5 Conclusions

8.5.1 Experimental work

The LVDT measurements suggested that the cracking of the cement render observed at NMOF was not caused by the thermal or hygral movement. However, it was noted that major deterioration of the render occurred during a particularly cold winter, and critical dilation testing showed that according to the criterion in the previous ASTM standard for concrete, the vacuum-saturated render was significantly damaged after only three freeze-thaw cycles. If the length change experienced upon freezing continued to increase, the render would eventually have failed. Furthermore, the render would be classified as non-durable by modern standards, because of the residual strain accumulated through progressive freeze-thaw cycles. The cracking of the render was therefore most probably due to freeze-thaw cycling.

The bricks underneath the cement render at NMOF had not cracked as extensively as the render, and the dilation testing showed that the expansion of vacuum-saturated brick samples upon freezing did not increase significantly with progressive cycling, and hence that the bricks were not sustaining significant damage. The bricks may have been less prone to freeze-thaw damage than the render either because the very large pores were rarely filled completely with water, or because the absence of small pores limited the water supply to feed the ice crystals in the larger pores.

It is generally agreed that concrete needs to be close to full saturation for frost damage to occur. The threshold value was found by MacInnis and Beaudoin [179] to be 90% for non-air-entrained 0.40-0.50 water/cement ratio concretes. The render at NMOF had generally survived in good condition, and this may be because it rarely reached 90% saturation. However, it was observed that render on the piers and at the base of the walls appeared to be wetted more frequently than render elsewhere, and calculations demonstrated that there was likely to be a permanently wet zone at the base of the walls in parts of the buildings where the plinths were very low, and that the render on the piers could become capillary saturated quite quickly when it rained.

Hence the moisture content in these areas was likely to reach 90% saturation for at least some of the time.

The dilation testing also showed that the cement render from East Fortune could potentially undergo greater expansion upon freezing than the bricks. Hence besides causing the formation of cracks, freeze-thaw cycling might also cause the differential movement of the render and bricks, particularly if the render was critically saturated and the bricks were only partially wet. This movement could lead to buckling of the render and tearing at the render-brick interface, creating voids which could be filled by water penetrating through the cracks. If freezing then occurred, the pressure of the ice in the voids might be sufficient to push the render off the bricks altogether.

8.5.2 Evaluation of experimental procedure

The dilation test has a number of limitations as observed by Pigeon and Pleau [18]. The rate of cooling used is often more rapid than a natural cooling rate, which can cause materials to appear less durable than is true in practice; the freezing period is quite short, meaning that the effect of longer freezing periods is not known; and it is only possible to undertake a relatively small number of cycles within a reasonable time frame. Additionally, for the test method used for this research, where saturated samples are not submerged during freezing, it is possible that some water will evaporate from the sample before freezing occurs. However, in this research dilation testing provided an early indication of the freeze-thaw susceptibility of the render, information which could not have been obtained from three cycles of a standard freeze-thaw test. Furthermore, the testing proved useful for making comparisons between bricks and render and hence in understanding how they behave when they are used together.

8.5.3 Conservation implications

The potential for rising damp at NMOF might be reduced if the ground were less wet. This could be achieved by improving the drainage around the buildings, for example by preventing downpipes from discharging directly onto the ground and by installing gravel-filled drainage channels. Water run-off across the site as a whole could also be improved. Additionally, although the design of the buildings makes the

piers prone to wetting by rainfall, adding gutters, removing moss from the roofs and increasing the overhang of the roof panels where possible would reduce the severity and frequency of wetting.

As a case study with wider implications, this research shows that historic cement renders without air-entraining agents may be prone to cracking due to freeze-thaw cycling, particularly if they are wet frequently by rising damp or driving rain. Hence in specifying repair mixes, it may not be appropriate to specify a mix that matches the chemical composition of the original. A cementitious mix containing an air-entraining agent or a more flexible mix based on hydraulic lime may be more resistant to cracking.

9.1 Introduction

The previous chapter demonstrated that the cracking and delamination of the render is likely to be caused by freeze-thaw cycling. This chapter uses the monitoring and experimental data from Chapters 4, 5 and 6 to investigate why the render applied to the rebuilt wall on the north east side of Building 23 in 1992 and the render applied to the free-standing wall on the south side of Building 25 in 2005 have failed very rapidly, whereas the other render patch repairs undertaken recently have performed well to date. This work is of particular interest to building conservation specialists and has been published [24].

9.2 Execution of the repairs

As described in Chapter 3, the first documented render repairs were undertaken on Building 23. The Buildings Development Strategy written by NMS in 1992 [129] had proposed that part of Building 23 should be rebuilt using engineering bricks, and it can be seen that the free-standing wall extending along the north east side of the building was rebuilt from a height of 0.8 m upwards with new bricks, and was re-rendered on both sides, the new render extending over the historic bricks at the base of the wall (Fig. 9.1). The old bricks were keyed but the new bricks were not, possibly because they already had a ridged surface. The Buildings Development Strategy had noted that repairs of the cement render were ‘easily affected’, and had given the instruction to ‘hack off defective render to pier heads and general areas’ and re-render with a mix to ‘match existing’. There is no record of the mix actually used or the application method.

Fig. 9.1. The rebuilt wall in the Electricity Sub-Station, showing the boundary between the old and new bricks

Following the work on Building 23 there was a lull in activity until 2004, when a Conservation Plan was written for NMOF, proposing a phased programme of conservation [130]. As part of this extensive render repairs were undertaken on Buildings 25, 28 and 27, and were completed in 2005, 2008 and 2009 respectively. The Conservation Plan repeated the instruction that render repairs should 'match existing', and also suggested that the removal of the defective render should be 'careful'.

Additionally, the Scottish Lime Centre wrote a brief for the repairs [126], which stated that render in poor condition should be consolidated through crack filling and grouting, and that only missing render should be replaced with patch repairs. The recommendations given to ensure good workmanship included:

- Prior to undertaking repairs, cracks should be flushed out and the brick substrate should be cleaned;
- Prior to filling cracks, algae, moss and lichen should be selectively removed, although with advice sought to avoid damaging any protected species;
- For patch repairs the brick substrate should be pre-wetted but not saturated;
- The water content of the grout should be minimised to avoid creating a low strength, high porosity material;
- The water content of the render should be sufficient to create a workable render, but not enough to cause slumping;
- Repairs should be cured by covering them with damp hessian.

The original render had been sampled from Building 25 and found to have proportions of approximately 1 part cement to 2.7 parts aggregate by volume. The mix specified for patch repairs was 1 part ordinary Portland cement (OPC) to 3 parts Lomond building sand by volume, in order to match the composition of the original fairly closely. In specifying OPC the Lime Centre cautioned that 'the nature of the cement used in the construction may be considerably different than modern OPC, in terms of composition, colour characteristics and holistic performance'. It was noted in particular that colour integration of the patch repairs might be problematic due to the iron component in OPC (tetracalcium alumino ferrite (C_4AF)), which gives it a characteristic grey colour. However, it was hoped that the reddish colour of the sand might alleviate the greyness. The mix specified for crack fills and grouting was a cement-based grout containing 1-2% casein to improve flow, with the addition of fine aggregate for grouting large voids. Given that some of the early cement-based crack fills had cracked, it was suggested that the casein might also improve the flexibility of the fills.

The Scottish Lime Centre also proposed various alterations to the buildings which would assist indirectly with the conservation of the render by keeping it dryer. These alterations would inevitably alter the original appearance of the buildings, and while some, such as the installation of new gutters and downpipes, were considered acceptable, others were rejected because they were too invasive. For example, it was observed that the mortar skew underneath the windows did not shed water effectively, and that it would perform better if it was capped with 'purpose made flashing' or if a new sill was installed altogether. However, neither option received approval, and the decision was taken to repair the mortar skew to its existing detailing. The application of a coating of hydraulic lime wash or masonry paint to the exterior of the buildings was rejected on similar grounds.

9.3 Visual assessment of the repairs

Despite being smoother than the original render and with less exposed aggregate, the repair render applied to Building 23 (B23 RR) was a fairly good colour match for the original, due to the brownish colour of the cement and lichen growth. However, B23 RR had cracked and detached from the brick substrate in large pieces, leaving large expanses of exposed brick. The cracks had often formed over the mortar joints within the brick wall, and there were hard white salt efflorescences along the lines of the cracks, and darkened render to either side of the cracks (Fig. 9.2). It was observed that the render losses increased during periods of freezing weather. Where the repair render had been applied over historic bricks at the bottom of the wall it had also begun to fail, but less dramatically, suggesting that the modern bricks were partly but not wholly responsible for the failure.

Fig. 9.2. Cracking and delamination of the repair render applied to Building 23

In areas where grouting and crack-filling had been undertaken since 2005 the render appeared sound and there was no new cracking. However, the appearance of the treated areas was unsatisfactory because grout had stained the render (Fig. 9.3), and the cleaning undertaken around the cracks prior to filling had removed the lichen and created a very patchy appearance (Fig. 9.4). As predicted, appearance was also an issue for the patch repairs undertaken from 2005 onwards (B25 RR), which had a smoother finish with less aggregate visible than the original render, and looked very grey. It was anticipated that the repairs would become rougher after weathering and

browner as lichen growth accumulated, as had already occurred in frequently wetted areas (Fig. 9.5). Despite the instruction that only failed render should be removed, photographs of the buildings before the work suggested that the repairs had sometimes been more extensive than was strictly necessary, as on the south east face of Building 27 where three of the five bays had been re-rendered entirely (Fig. 9.6).

Appearance aside, the post-2000 patch repairs had performed fairly well, with only some minor cracking visible by 2012 (Fig. 9.7). The exception was the free-standing wall running around the loading bay on the south side of Building 25, which had been re-rendered almost entirely in 2005. Here the new render (B25 RR) had cracked extensively (Fig. 9.8), and tapping surveys suggested that it had largely delaminated from the bricks underneath.

Fig. 9.3. Staining caused by grouting on Building 25

Fig. 9.4. Patchy appearance caused by cleaning around cracks prior to filling them, again on Building 25

Fig. 9.5. Colour change due to lichen growth on the post-2000 repairs on Building 25

Fig. 9.6. New render on Building 27, showing the extent of the repairs undertaken and also the contrast between old and new

Fig. 9.7. Minor cracking of the new repairs

Fig. 9.8. Cracking of the repair render on the free-standing wall behind Building 25

9.4 Method for investigating why the repairs had failed

9.4.1 Original and repair renders

Of the materials characterization described in Chapters 4, 5 and 6, the work considered relevant to understanding why the repairs had failed was:

- The determination of the binder:aggregate ratios and particle size distribution of the aggregates in the renders, to determine whether the repairs had similar composition to the original render;
- The investigation of moisture transport properties using infrared thermography and electrical resistivity measurements, to assess whether the repairs were less permeable to moisture than the original render;
- The measurement of physical properties such as tensile strength, density, porosity, pore size distribution and sorptivity, to determine whether the repairs were otherwise physically compatible with the original render;
- The petrographic examination of thin sections of the original and repair renders, to provide information about the materials, the workmanship and the deterioration mechanisms, and to check the mix proportions by point counting.
- The XRD analysis of the salts found along the cracks in B23 RR.

9.4.2 Bricks underneath the repairs

The bricks underneath the repair renders were also important because their hydraulic properties would have influenced the strength of the render-brick bonds. The smooth, reddish appearance of the exposed modern bricks underneath B23 RR suggested they might be engineering bricks as specified, but the bricks underneath B25 RR were not visible except in a small patch where the render had delaminated off. It was only possible to obtain small samples of these two brick types, which were characterized and compared to the other bricks from NMOF using petrography and X-ray diffraction.

The historic bricks known to have been used at NMOF were from Edinburgh, Niddrie, Prestongrange and Whitehill. They were found extensively around the site incorporated into the buildings, and large samples were available from the rubble heap at NMOF, which had built up over time as buildings were repaired or demolished. Additionally, Wallyford bricks were found on the rubble heap, although they were not observed within the buildings. They were included in the investigations, given that they were not modern in appearance and dated from prior to the early 1970s when the Wallyford brickworks closed [151]. A modern engineering brick was also tested in case the wall where B25 RR had failed had been rebuilt with modern bricks.

The identification of the mineral phases present in bricks can be difficult, because they may only be present in small quantities and because the XRD spectra are complicated by the presence of amorphous material which is not identifiable by XRD. The key minerals used to differentiate between the bricks were:

- Diopside-wollastonite (calcium silicates) which forms in clay fired above 1000 °C and hence is not found in low-fired bricks;
- Albite (a feldspar);
- Calcite, which decomposes at approximately 600-850 °C in fired natural clay [153] and hence is not found in modern bricks fired at high temperatures. The calcite results were used with caution because it was possible the samples were contaminated with calcite from the cementitious renders and mortars.

The hydraulic properties of all the historic bricks from NMOF had been measured, as described in Chapter 6. It was therefore anticipated that once the brick

from underneath B25 RR had been matched to one of the historic brick types, the properties of the brick might be related to the failure of B25 RR.

9.5 Results

9.5.1 Chemical composition of the original and repair renders

The particle size distribution of the original renders varied considerably (Fig. 9.9). The original render from Building 24 (B24 OR), which was smooth in appearance, contained only fine aggregate below 0.255 mm in diameter, while the original render from Building 47 (B47 OR), which appeared much rougher, contained more coarse particles. The aggregate used in B23 RR had a similar particle size distribution to B24 OR, and the aggregate in B25 RR contained more coarse aggregate than B24 OR, but less than B47 OR. Hence each repair render was a reasonable match for one of the original renders from the site. However, B23 RR was poorly graded because the particle sizes were concentrated within a small range, whereas B25 RR was better graded because it contained a good range of particle sizes. A well graded render is likely to be stronger and more resistant to cracking [83].

Fig. 9.9. Particle size distribution curves for the original and repair renders

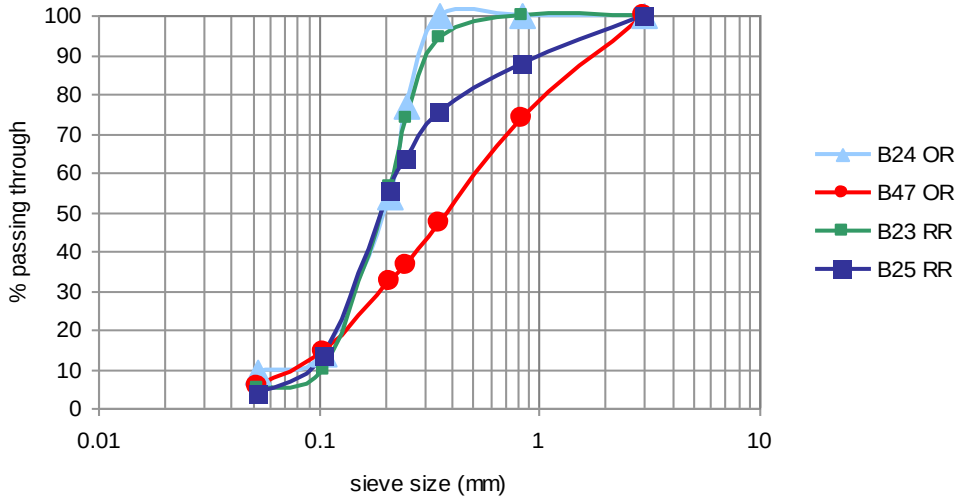

Besides having a similarly graded aggregate to B24 OR, B23 RR also had a similar binder:aggregate ratio (Table 9.1), and it seems likely that B23 RR was mixed to obtain the smooth, cement-rich finish found on B24 OR and also on the original render from Building 23. The original render on Building 25 was rougher and was found by the Scottish Lime Centre to have a binder:aggregate ratio of 1:2.7.

However, although a 1:3 binder:aggregate ratio was then specified for B25 RR, the ratio obtained experimentally for the repairs was 1:1.9, suggesting that too much cement was added to the mix. This may partly explain why B25 RR appeared much smoother than the original render on Building 25.

Table 9.1. Binder:aggregate ratios of the original and repair renders

	binder:aggregate ratio from acid extraction (by volume)	binder:aggregate ratio from point counting (by volume)	average binder:aggregate ratio
B24 OR	1:2.2	1:2.4	1:2.3
B47 OR	1:2.9	1:3.1	1:3.0
B23 RR	1:2.5	1:1.9	1:2.2
B25 RR	1:2.1	1:1.8	1:1.9

9.5.2 Hydraulic properties of the repair renders

Infrared thermography and electrical resistivity measurements indicated that the moisture content in adjacent areas of original render and post-2000 repair render was very similar, and that there was no build-up of moisture around the edges of the repairs (Fig. 9.10). This suggested that B25 RR had similar hydraulic properties to the original render. It was not possible to compare B23 RR to the original render because they were not applied in adjacent areas.

Fig. 9.10. Infrared thermography in an area on Building 27 with post-2000 repairs, showing no obvious demarcation between the old and new render. The infrared thermograph is a false colour image showing the surface temperature of surfaces in °C, where the red areas are warmest and the purple areas are coolest. The edge of the new repairs has been marked on the infrared thermograph (Original images: Maureen Young, Historic Scotland).

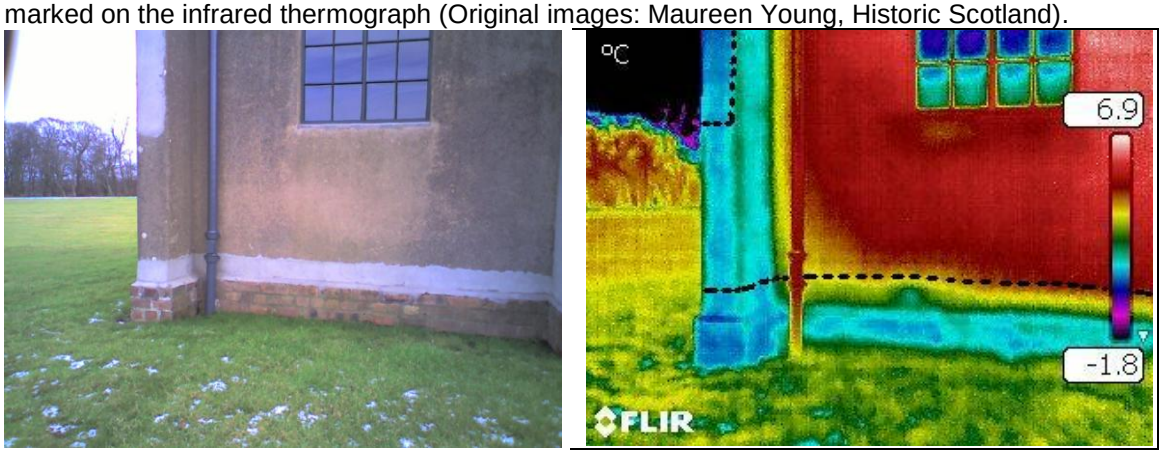

9.5.3 Other physical properties of the original and repair renders (Tables 9.2 and 9.3)

The original render containing well sorted aggregate (HC OR) had lower tensile strength than the render containing poorly sorted aggregate (B31 OR), and the same trend was observed with the repair renders, meaning that B25 RR was less strong than B23 RR. For each aggregate type (well or poorly sorted) the repair render was slightly stronger than the historic equivalent, probably because of the increased strength of modern cement. Given that modern cement is typically three times stronger than the cement that would have been used originally at NMOF [30], a greater difference in strength was anticipated, particularly since the binder:aggregate ratios of the repair renders were around that required to give maximum strength [181]. The renders containing poorly sorted aggregate had considerably higher elastic modulus than the renders containing well sorted aggregate, demonstrating that they were stiffer, and possibly also more brittle.

The most porous renders were B24 OR and B23 RR, which contained fine, poorly sorted aggregate. The lower porosity of B47 OR may have related to the well graded aggregate and the relatively low binder:aggregate ratio. Despite having a similar aggregate mix to B47 OR, B25 RR was considerably more porous, possibly because its high cement content necessitated a high initial water content. B25 RR also had higher sorptivity than both original renders and B23 RR had extremely high sorptivity, demonstrating its ability to absorb water rapidly.

The MIP data showed that B24 OR and B23 RR had similar median and critical pore diameters and similar pore size distributions, with at least 30% of the total pore space made up of air voids. B23 RR had a second critical pore size at around 23.2 μm, indicating a concentration of pores this size, which may have contributed to its particularly high sorptivity. The pore size distributions of B47 OR and B25 RR were fairly similar, with far fewer air voids than the smooth renders. However, B25 RR differed from the other renders in that it had a higher proportion of small and medium capillaries, and this may again have indicated a higher initial water content.

Table 9.2. Tensile strength, density, porosity, sorptivity and median and mode pore diameter of the original and repair renders

	tensile strength (MPa)	elastic modulus (GPa)	density (g/cm^3)	porosity (%)	sorptivity ($mm/min^{1/2}$)	median pore diameter (µm)	mode pore diameter (µm)
B24 OR (B31 OR)*	7.7	1.18	1.8	29.5	0.1	3.3	1.9
B47 OR (HC OR)*	4.5	0.65	1.9	18.0	0.1	0.5	1.5
B23 RR	9.5	1.13	1.7	31.0	0.5	2.9	1.9 (and 19.3 - 27.2)
B25 RR	6.5	0.55	1.8	24.5	0.2	0.3	1.9

* The sample names in parentheses correspond to the samples used for tensile strength testing, as suitable samples of the other original renders were not available.

Table 9.3. Pore size distribution of the render samples, showing the percentage of pore space within size classes, as percentage of sample volume

sample	small (gel) capillaries 0.0025-0.01 µm	medium capillaries 0.01-0.05 µm	large capillaries 0.05-10 µm	small air voids 10 -50 µm upwards	large air voids 50 µm upwards	total % (obtained by MIP)
B24 OR	1.5	0.5	14.6	6.6	3.5	26.7
B47 OR	1.3	3.0	14.2	0.5	0.8	19.8
B23 RR*	0.20 (possibly up to 6.0)	1.1	14.7	6.8	2.4	25.2 (up to 31.0)
B25 RR*	1.4 (possibly up to 9.9)	7.7	4.2	1.2	1.3	15.8 (up to 24.3)

* The values in parentheses for B23 RR and B25 RR indicate the revised distribution of the pores if the maximum possible volume of small capillaries is assumed to be accurate, rather than the value for the volume of small capillaries obtained by the MIP.

9.5.4 Petrographic examination of the original and repair renders

9.5.4.1 B23 RR

The high porosity of B23 RR was evident in the thin section, and the regular spacing and round shape of the pores suggested the deliberate use of an air-entraining agent (Fig. 9.11). However, the distribution of the voids was too irregular to increase the freeze-thaw durability of the render: the critical spacing factor for air voids in concrete is usually quoted as 200 µm, meaning that the maximum distance between two adjacent voids should be 400 µm [18], but distances of up to 800 µm were measured between adjacent voids in B23 RR. It seemed unlikely that the initial water content had been high because there was very little shrinkage cracking, but the presence of portlandite and calcite in the voids and around the aggregates indicated that there had been a lot of water percolating through the render (Figs. 9.12 and

9.13). The render surface along the render-brick interface was plain rather than plucked, indicating that the render had separated easily from the brick. At the only point where a fragment of brick had remained attached to the render there were no portlandite or calcite crystals evident on the brick surface, showing that cement fines had not moved from the render to the brick (Fig. 9.14). This suggested that the brick had not exerted much suction on the render, either because it was over-wetted or of low sorptivity, and that the render-brick bond was poor.

Fig. 9.11. Extreme porosity near the surface of B23 RR (surface at top of image), with rounded pores suggesting the use of an air-entraining agent, plane polarized light, field of view: 1750 µm across

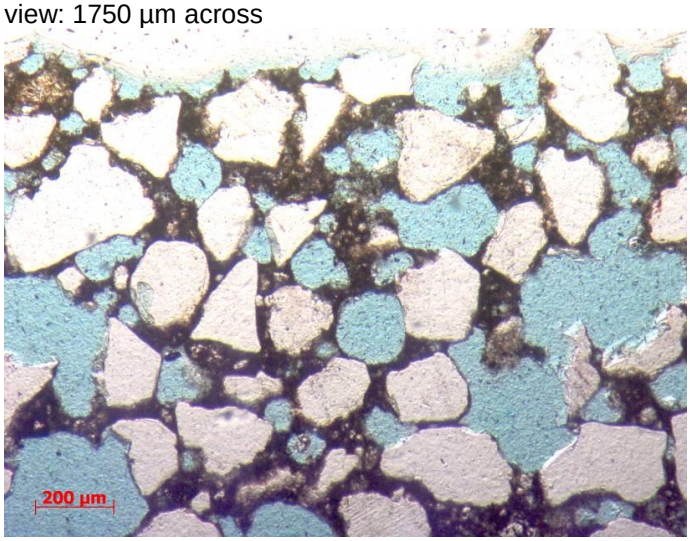

Fig. 9.12. Portlandite and calcite growing in the pores and around the aggregate particles in B23 RR, plane polarized light, field of view: 440 µm across

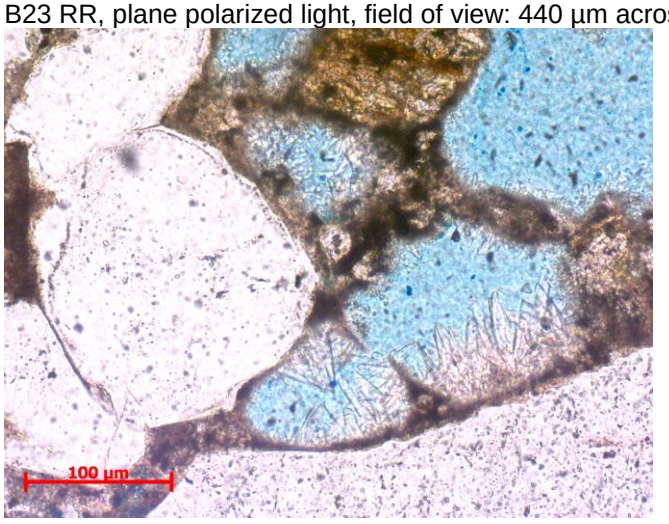

Fig. 9.13. As above, crossed polars

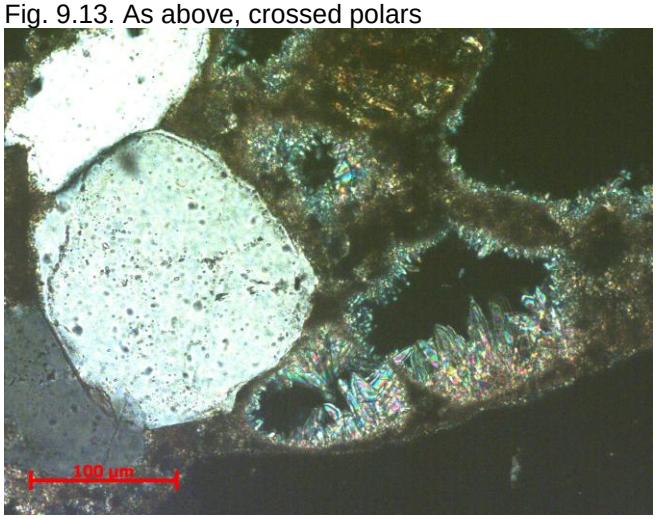

Fig. 9.14. Interface between B23 RR and the brick (render in upper half of image, brick in lower half), showing that there was no portlandite or calcite on either the surface of the brick or inside the brick's pores (lower left), plane polarized light, field of view: 440 µm across

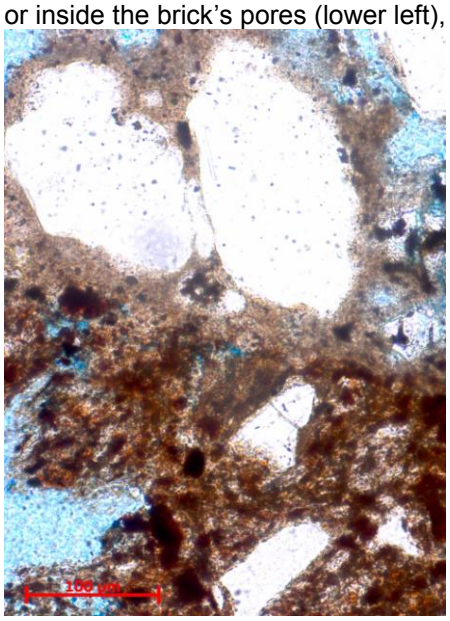

9.5.4.2 B25 RR

The thin section of B25 RR showed that the initial mix had been overly wet, because it contained drying shrinkage cracks up to 100 µm wide, running through the thickness of the render perpendicular to the surface and breaking apart some of the aggregates (Fig. 9.15). Additionally, the smoothing of the wet surface had created small tears just below the surface (Fig. 9.16), and portlandite had been leached out of the cement matrix and deposited in the voids, either due to the initial wetness of the mix or because water had percolated through subsequently.

The brick surface appeared smooth and non-porous, suggesting it would have been difficult to bond to, and there were almost continuous voids along the render-brick interface, joined together by cracks. These voids were again filled with portlandite and calcite (Figs. 9.17 and 9.18). Cracks in the bricks adjacent to the render-brick interface suggested that water had penetrated through to the bricks and promoted their deterioration (Fig. 9.19).

Two separate layers were visible within the render. The upper layer had been applied when the lower layer was dry, and the lower layer was not keyed. The bond between the layers appeared weak, because there were large voids running along the interface, extending for up to 4500 μm, and micro cracks in the upper layer running parallel to the interface. Both layers contained brown opaque areas of hydrated cement which again indicated a high initial water content. However, the lower layer contained only sporadic small to medium-sized cement grains, whereas these grains occurred commonly in the upper layer, suggesting that the mix for the upper layer may have been richer in cement. This was confirmed by point-counting: the binder:aggregate ratio was 1:1.61 for the upper layer, compared to 1:1.99 for the lower layer. This would have resulted in interfacial tensile stress and may have contributed to the render detachment and cracking.

Fig. 9.15. Drying shrinkage crack running perpendicular to the surface of B25 RR (surface at top of image), plane polarized light, field of view: 1750 μm across

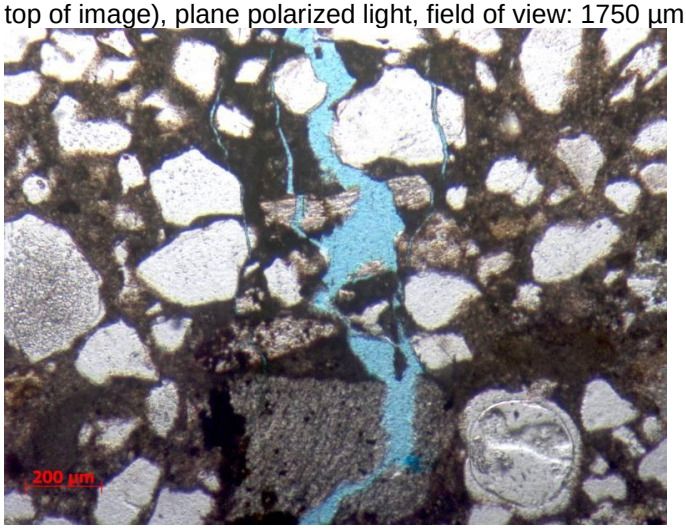

Fig. 9.16. Smoothed surface finish of B25 RR (surface at top of image), with cracks running parallel to the surface, plane polarized light, field of view: 875 µm across

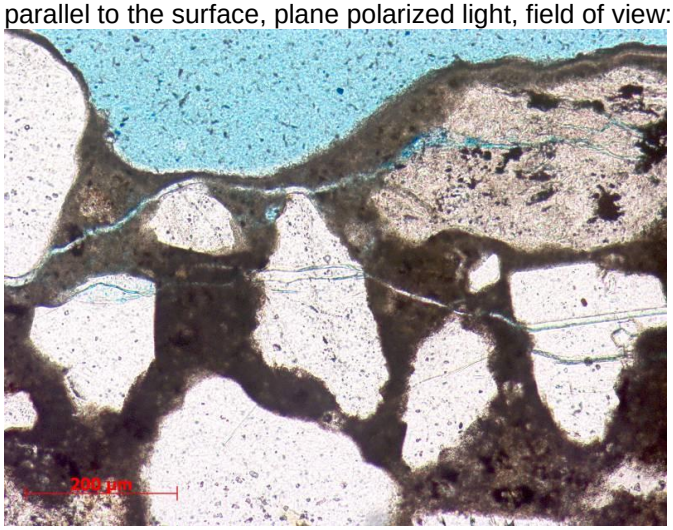

Fig. 9.17. Voids filled with portlandite and calcite crystals along the interface between B25 RR and the brick (render in upper part of image, brick in lower part), plane polarized light, field of view: 440 µm across

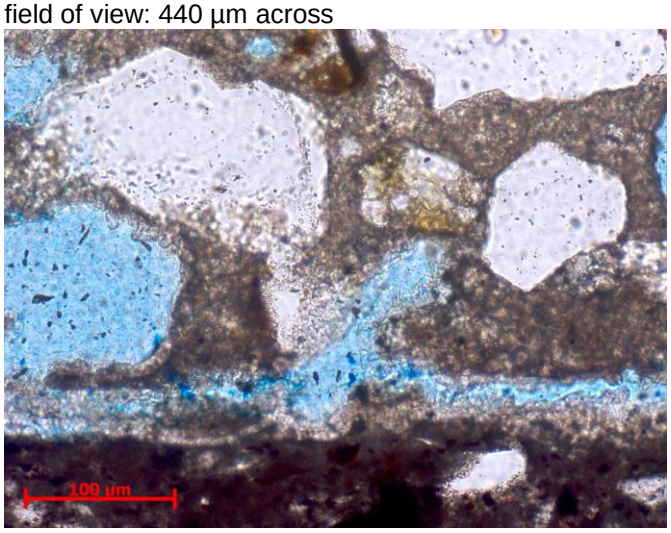

Fig. 9.18. As above, crossed polars

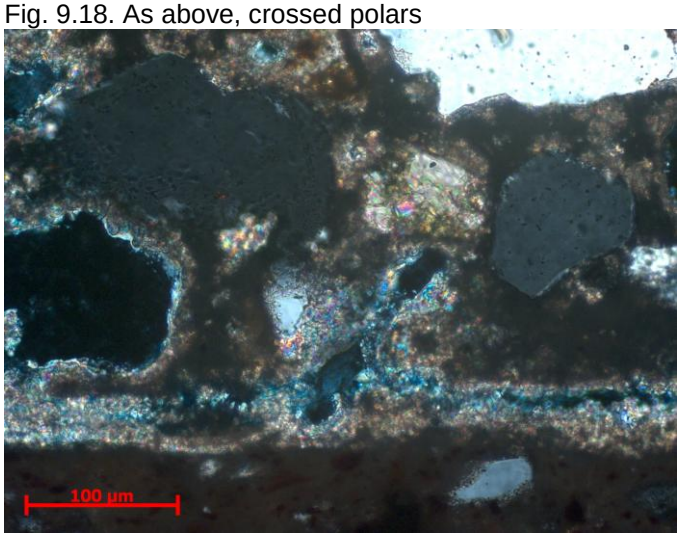

Fig. 9.19. Cracking in the brick close to the interface with B25 RR, plane polarized light, field of view: 1750 µm across

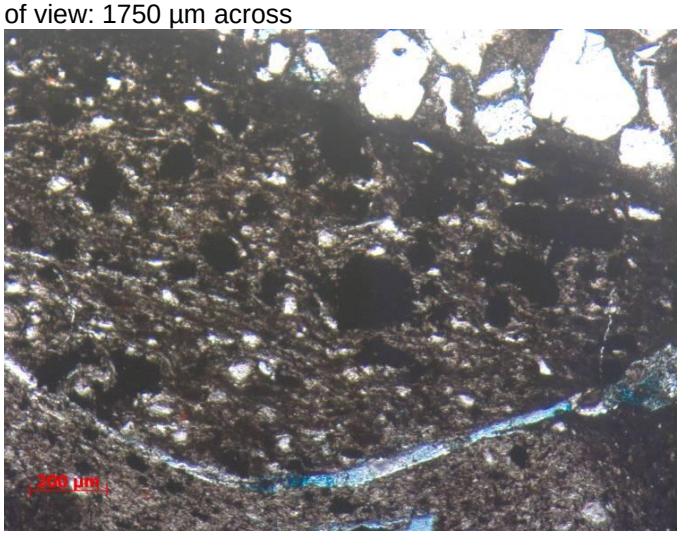

9.5.5 XRD analysis of salt efflorescences on B23 RR

XRD indicated that the salt visible along the cracks in B23 RR was calcite. The petrographic examination had shown that there was calcite and portlandite present in the pores of B23 RR, and portlandite was probably being transported to the surface by water moving through the render, and then reacting with carbon dioxide from the air to form calcite.

9.5.6 Characterization of the bricks underneath the repairs

Petrography showed that the modern brick used to rebuild the wall to which B23 RR was applied exhibited similar porosity and cracking to the historic bricks, and was therefore unlikely to be a type of engineering brick. The sample of Building 23 brick was too small to measure its hydraulic properties, but the thin section showed that its surface was smooth and compact, suggesting that it might have low surface sorptivity (Fig. 9.20).

The brick from underneath the failing render on Building 25 was compared in thin section to the other bricks from NMOF. It appeared very similar to the Wallyford brick, with a mid-brown matrix containing inclusions of quartz and characteristic shrunken mudstone particles (Fig. 9.21). XRD confirmed that from the trace minerals present, Wallyford brick was the best match (Table 9.4). It seems reasonable to conclude that the wall behind Building 25 was rebuilt at some point, since the bricks used were not found in the other buildings at NMOF. The rebuilding

probably occurred prior to the early 1970s when the Wallyford brickworks was closed [151].

Although the Wallyford bricks were found to have similar porosity to the other historic bricks, they had very low sorptivity (Table 9.5). They would have provided very little suction for the applied render, which would have resulted in a poor render-brick bond.

Table 9.4. Identification of the minerals present in the bricks from underneath the failing render on Building 25 using XRD

	quartz	diopside-wollastonite
brick underneath B23 RR	●	●
brick underneath B25 RR	●	○
Edinburgh brick	●	
Niddrie brick	●	
Prestongrange brick	●	
Wallyford brick	●	○
Whitehill brick	●	
modern engineering brick	●	●

● = strongly present
○ = weakly present

Table 9.5. Hydraulic properties of the historic bricks from NMOF

	porosity (%)	main sorptivity through stretcher face ($mm/min^{1/2}$)**
Edinburgh	26.0	0.7
Niddrie	24.5	0.5
Prestongrange	27.0	2.1
Wallyford*	25.5	0.05
Whitehill	27.5	0.9

* The sorptivities for the Wallyford bricks have been given to the nearest 0.05 $mm/min^{1/2}$ because they are considerably lower than the values for the other bricks.
** The sorptivites quoted are from experiment run 1 only.

Fig. 9.20 Smooth surface of the modern brick from Building 23 with fine cracks parallel to the surface (at the top of the image), plane polarized light, field of view: 875 µm across

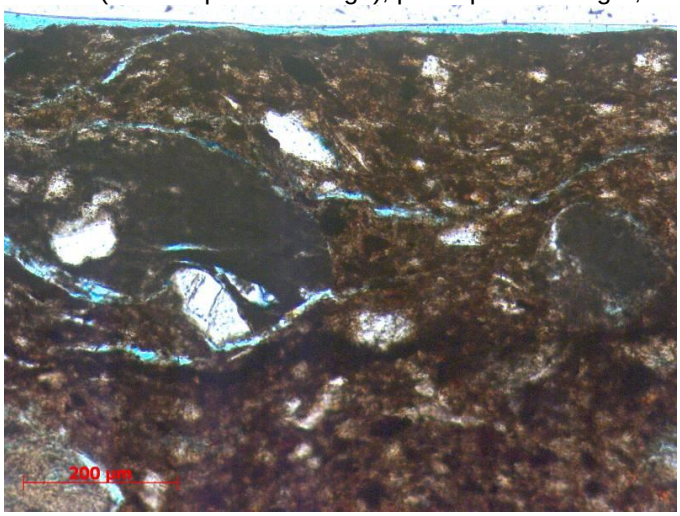

Fig. 9.21. Shrunken mudstone fragments in the Wallyford bricks (left) and the bricks from underneath B25 RR (right), plane polarized light, field of view of each image: 1750 µm across

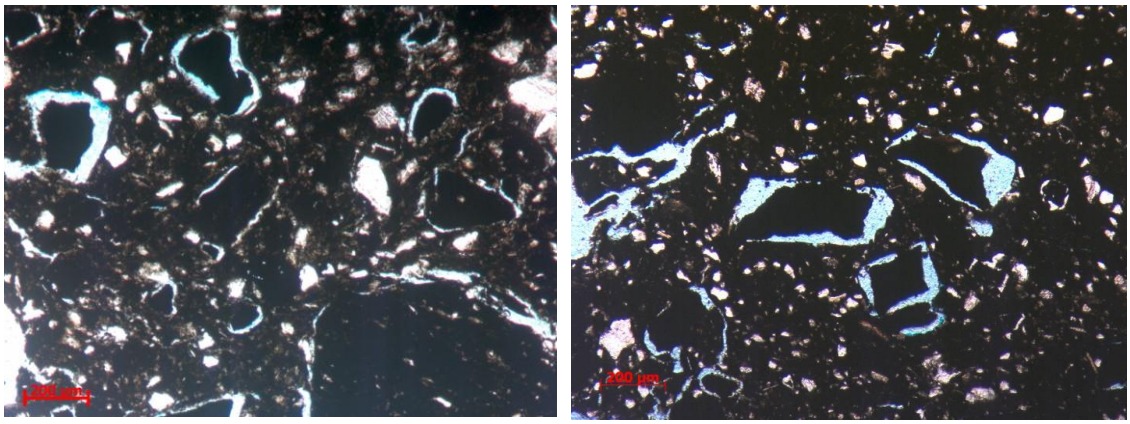

9.6 Conclusions

9.6.1 Building 23 repair render

The investigations undertaken demonstrate that B23 RR had similar composition to the original renders made with fine sand aggregate, such as B24 OR and B31 OR, although B23 RR also appeared to contain an air-entraining agent. B23 RR had similar porosity to B24 OR but much higher sorptivity, which MIP suggested might be due to a low number of small capillaries and high concentration of air voids. Petrography showed that B23 RR was particularly porous at the surface. The high porosity and sorptivity would have allowed water to percolate through the render, as evidenced by the abundance of portlandite and calcite in the voids and around the aggregates. The render would have reached saturation quickly, particularly as the

wall was very exposed, and if freezing conditions were then experienced, cracking would have ensued.

The cracks were very widely spaced: micro-cracking was generally not evident in the thin sections, suggesting that the only cracks formed were those observed visually above the mortar joints in the wall. The differential movement of the bricks and mortar would have resulted in stress concentrations along the mortar joints, and presumably the energy released when the render cracked along these fault lines was sufficient to restore equilibrium.

It was evident from the thin section that the initial bond between the bricks and the render was poor, probably because the modern bricks used to rebuild the wall had a smooth and relatively impermeable finish, which would have prevented them from providing much suction for the render. Once cracks had formed through the thickness of the render they would have provided an easy route in for water, which leached portlandite out of the cement render and deposited it as calcite on the surface. The extraction of portlandite resulted in the observed darkening of the render at the sides of the cracks. The water would have penetrated to the render-brick interface, filling the voids there and creating further damage if freezing occurred. Over time the render-brick bond would be weakened to the point where a final freezing event was sufficient to push a section of render off altogether.

9.6.2 Building 25 repair render

B25 RR contained a similar well-graded heterogeneous aggregate to the original renders made with coarse aggregate, such as B47 OR and B32 OR. Its porosity, density and sorptivity were similar to those of the original renders, and despite being made with modern cement, it had a similar elastic modulus to the well graded aggregate original renders, and only slightly higher tensile strength. Hence the attempt to match the composition of the original render had produced a repair render with similar physical properties to the original, which has generally performed well. However, the mix had a higher cement content than was specified, and this, possibly in combination with modern styles of workmanship, resulted in the addition of excessive amounts of water. This caused shrinkage cracking at a microscopic and sometimes macroscopic level, and made the repairs susceptible to moisture-related deterioration.

The repair render applied to the free-standing wall on the south side of Building 25 began to fail soon after it was applied, and this was because the wall was rebuilt at some point with Wallyford bricks of low sorptivity. The failure of the bricks to absorb sufficient moisture from the render resulted in a poor render-brick bond and the formation of large shrinkage cracks, which provided a route in for water. As occurred with B23 RR, the render could then become saturated and crack due to freeze-thaw damage, and the same characteristic pattern of cracks above the mortar joints in the wall formed. Additionally, the differing cement contents of the two layers of the render made the upper layer stronger, creating tensions which increased the likelihood of the render fracturing.

9.6.3 Conservation implications

The repair mix introduced in 2005 has performed reasonably well, and could feasibly be used for future repairs. It would be desirable to reduce the binder:aggregate ratio to the 1:3 specified by the Scottish Lime Centre and this would give the repairs a rougher finish to match the original render more closely. The water content should be kept as low as possible to avoid the formation of shrinkage cracks, and if it is strictly necessary for the render to be applied in two layers, the cement content should be slightly lower in the upper layer.

A major drawback of a repair mix based on modern cement is the grey colour, although this could possibly be addressed by tinting the mix, and a further drawback is the brittle nature of cement renders, making them prone to cracking. The use of hydraulic lime as a binder could be considered instead, as this would allow for better colour matching of the original render, and produce a more flexible render [182]. The strength and hydraulic properties of a hydraulic lime render would need to be measured to ensure it was compatible with the original render.

As a case study with wider implications, the repair work at NMOF shows the importance of having a good understanding of the properties of the materials involved, particularly the hydraulic properties of the substrate; and the need for good workmanship and the careful management of contractors to ensure that specifications are followed.

10.1 Introduction

The previous two chapters investigated the mechanism by which the render at NMOF cracks and delaminates from the brick substrate, and the reasons why this has occurred very rapidly for some of the repair renders. This chapter describes the investigations undertaken to identify the causes and mechanisms of the surface flaking and blistering of the cementitious render observed on some of the buildings at NMOF. It begins with a review of the literature on the behaviour of expansive aggregates within concrete. The relevant results from Chapters 4, 5, and 6 are summarized, and additional experiments undertaken to test the hypothesis that the flaking was caused by the presence of expansive shale aggregates are described. Finally, a simple model from the literature on the cracking caused by corroding reinforcements in concrete is used to investigate whether the forces generated by the expanding aggregates were sufficient to crack the concrete, and a more complex model is also used to calculate the two dimensional stress distribution around the cavity containing the shale particle and along the render surface.

10.2 Literature review

10.2.1 Expansive aggregates in concrete

It is widely known that the expansion of certain aggregates within concrete can cause the formation of 'three-legged cracks radiating out from a point', and the break out of small pieces of the concrete surface, commonly known as pop outs [183]. The pop outs have a characteristic cone shape, with a weathered aggregate particle at the apex of the cone. The aggregates responsible may expand due to alkali aggregate reaction (AAR) or simply due to wetting, possibly in combination with freezing.

Aggregates which swell on wetting include shale, coal and chert. The swelling properties of shales have been studied extensively because the movement of shale-rich rocks and soils can cause massive damage to buildings, tunnels and pavements [184]. Literature on the swelling of shales was reviewed by Huang et al. [185] who concluded that the extent of swelling depends upon several factors, including the presence of swelling clay minerals. The principal swelling clay minerals are from the smectite group, which has a silicate-gibbsite-silicate structure, with variable amounts of water molecules lying in between the mineral layers. In a

study of swelling rocks in Switzerland, the three types of rocks identified as being particularly susceptible to swelling contained montmorillonite or corrensite, which is an interstratification of chlorite and vermiculite or smectite [186].

Research on clay-bearing sandstones has shown that they may undergo dimensional changes upon wetting and drying, due to the swelling pressure generated by the wetting of the clays [187, 188]. The two modes of swelling in clays are intracrystalline swelling and long-range, osmotic swelling, and the predominant mechanism operating within clay-bearing sandstones was found by Wangler and Scherer [189] to be intracrystalline swelling from the 'hydration of the counterbalancing cations' within the clay. The primary clay present in the sandstones was chlorite, which is non-swelling, but it can weather to form swelling layers of smectite interspersed with non-swelling layers [149].

Jimenez Gonzalez et al. [190] demonstrated that the maximum stress that could develop in a stone block during drying or wetting is

$$\sigma_{d/w} = \pm \frac{E_{d/w}}{1-\nu_{d/w}} \varepsilon_s \qquad \textbf{(10.1)}$$

where $\sigma_{d/w}$ is the drying or wetting stress in the stone, $E_{d/w}$ is the Young's modulus of the dry or wet stone, ε_s is the free swelling strain and $v_{d/w}$ is the Poisson's ratio of the dry or wet stone, usually estimated to be 0.25. The strain measured increases over time, and this was attributed to damage because wet-dry cycling reduces the material's stiffness and its ability to withstand pressure [188]. The work on flaw propagation and buckling in clay-bearing sandstones by Wangler et al. [191] suggested that non uniform wetting patterns cause small flaws to grow and coalesce, generating large flaws with a sufficiently high critical aspect ratio to cause buckling. Anisotropic stones are more susceptible to damage, because natural flaws are likely to occur along the bedding planes.

Wangler et al. calculated that sandstones could be damaged by wetting alone, but suggested that the 'synergetic interaction' of the swelling mechanism with other mechanisms such as salt crystallization and freezing was likely. The effect of freeze-thaw cycles upon rocks has been researched extensively, and shales have been found to be affected particularly severely [192]. Potts observed that mudstones are much more resilient despite having a similar grain-size distribution to shales, and he

speculated that the layered structure of shales provides 'planes of weakness' which act as cracks for ice to grow along.

Early work on pop-outs in concrete includes field observations made by Idorn in Denmark [32]. He noted that pop-outs were more likely to occur with gravel pit aggregates than with aggregates dredged from the sea, and suggested this was because the gravel pit aggregates were more porous. He also observed that although pop-outs could form without freezing conditions, their formation was accelerated by freezing, and they were found more frequently on the exposed parts of structures.

Experimental work was undertaken by Schuster and McLaughlin [193], showing that chert and shale both caused pop-outs when they occurred close to the concrete surface. They concluded that the durability of aggregate particles depended on a 'complicated interrelationship' between porosity, pore size distribution, water absorption properties and degree of saturation, and that particles needed to be above a certain critical size to cause deterioration. They also found that chert particles reduced the dynamic modulus of elasticity of concrete beams but shale did not, and speculated that shale was weaker than the surrounding mortar, tending to fail internally rather than damage the mortar. This was demonstrated when pieces of concrete which had undergone freeze-thaw cycling were broken open: the shales had disintegrated but had caused 'no deep-seated deterioration'.

The most detailed early study was undertaken by Verbeck and Landgren [194]. They discussed the mechanism of freezing and suggested that if the water content of the aggregate is high enough, ice formation inside the aggregate will push water out into the paste surrounding the aggregate particle, allowing potentially destructive hydraulic pressures to develop in the paste as well as in the aggregate. They defined three stages of freezing and suggested that the most damaging stage of freezing, when the highest hydraulic pressures develop, is not the freezing of the aggregate itself but rather the freezing of the saturated paste adjacent to the aggregate.

Verbeck and Landgren demonstrated experimentally that the likelihood of pop-outs occurring increases as the size and porosity of the aggregate particle increase, and that aggregates with low permeability due to fine pores are more likely to rupture than those of higher permeability. They speculated that an aggregate with

high porosity but low permeability would be inclined to shatter due to high internal pressures, whereas an aggregate with high porosity and high permeability would be more likely to cause failure in the surrounding mortar. For aggregates undergoing unconfined freezing they defined a maximum critical particle size, $L_{max,}$ above which the particle was likely to rupture. This was calculated using

$$L_{\max} = \frac{1.133\times10^{5}(K_1 T)}{dW_f / dt} \qquad \textbf{(10.2)}$$

where K_1 is the permeability coefficient of the aggregate in cm/s, T is the tensile strength of the aggregate in MPa and dW_f/dt is the freezing rate in cm/s, which is equivalent to the aggregate porosity multiplied by the rate of linear propagation of the freezing zone in cm/s. It was observed that the thickness and permeability of the surrounding cement paste are also important, and demonstrated experimentally that the time taken for pop-outs to develop increases with increasing depth of cover and decreasing water-cement ratio.

More recently, the occurrence of pop-outs due to the expansion of EAF (electric arc furnace) slag was investigated by Lee and Lee [195] who developed a non-linear finite element analysis to relate the size and depth of the aggregate particle to the strength of the overlying concrete, and hence calculated the strength and thickness of repair mortar required to avoid further pop-outs, a result which they verified experimentally. However, to the best of the author's knowledge there are no other recent studies which model or calculate the stress generated by expansive aggregates within concrete.

10.2.2 Fracture mechanics in concrete

Early work on fracture mechanics in brittle materials was done by Griffith [196]. He treated the development of cracks as an equilibrium problem, in which the reduction in strain energy of a body due to crack formation could be equated to the gain in surface energy resulting from the increased surface area, and he derived the relationship that

$$G = 2\gamma = \frac{\pi\sigma^{2}a}{E} \qquad \textbf{(10.3)}$$

where G is the energy dissipated, σ is the applied stress, a is the crack length, 2γ is the surface energy generated by the cracking process and E is the elastic modulus of

the material [197]. However, Griffith's theory did not take into account the role of plasticity in the fracture of ductile materials, and was expanded by Irwin to give

$$G = 2\gamma + G_p \quad \textbf{(10.4)}$$

where G_p is the energy dissipated as heat by the plastic zone at the tip of the crack [198]. This plastic zone has become known as the fracture process zone.

More recent models proposed for the fracture of quasi-brittle materials such as concrete are summarized by Wang and Zheng [199], Elices and Planas [200] and Reda Taha et al. [201]. According to Raghu Prasad et al. [202] the simple approach of linear elastic fracture mechanics does not take into account 'the existence of slow crack growth, formation of a nonlinear fracture process zone and softening of concrete', and Reda Taha et al. argued that non-linear quasi-brittle fracture mechanics are most appropriate because concrete is a quasi-brittle material, behaving differently from brittle materials such as glass and ductile materials such as steel, and in particular having a different shape and size of fracture process zone. Both the energy consumed in fracturing the concrete and the energy consumed to overcome the toughening mechanisms in the fracture process zone need to be considered, and the models developed can be divided into two groups: the fictitious crack model developed by Hillerborg et al. [203], also known as the cohesive crack model; and the equivalent elastic crack models, including the model proposed by Karihaloo et al. [204], the crack band model by Bazant and Oh [205] and the two-parameter crack model by Jeng and Shah [206]. The fictitious or cohesive crack model is frequently used to model type 1 fractures, where the crack surfaces move directly apart in tensile mode [199, 200].

The fracturing of a concrete specimen subjected to uniaxial tension was described simply by Tixier and Mobasher [207]. They divided the resulting stress-strain curve into three regions (Fig. 10.1):

1. 0 to A, the linear-elastic region, where the elastic modulus is E_0 and the material is undamaged (the scalar damage parameter ω=0);
2. A to B, the pre-peak region, where microcracking has begun. The elastic modulus decreases linearly from E_0, showing a reduction in stiffness due to damage, and ω increases;

3. From B to C, the post-peak or softening region, where the microcracks join together, and 'the deformation is represented as the opening of a single main crack'. ω continues to increase, reaching a maximum value at C. The strain at C may be identified as the critical crack opening w_c, at which the tensile stress is zero [200]. The area under the curve is equivalent to the specific fracture energy of the material G_F, which is the work needed to completely separate the two faces of the crack, per unit length.

Fig. 10.1. Stress-strain curve for concrete subjected to unixial tension, showing the linear-elastic region from 0 to A, where the material is undamaged; the pre-peak region from A to B, where microcracking has begun; and the post-peak region from B to C, where the microcracks join together to form a single main crack (redrawn from Tixier and Mobasher [207])

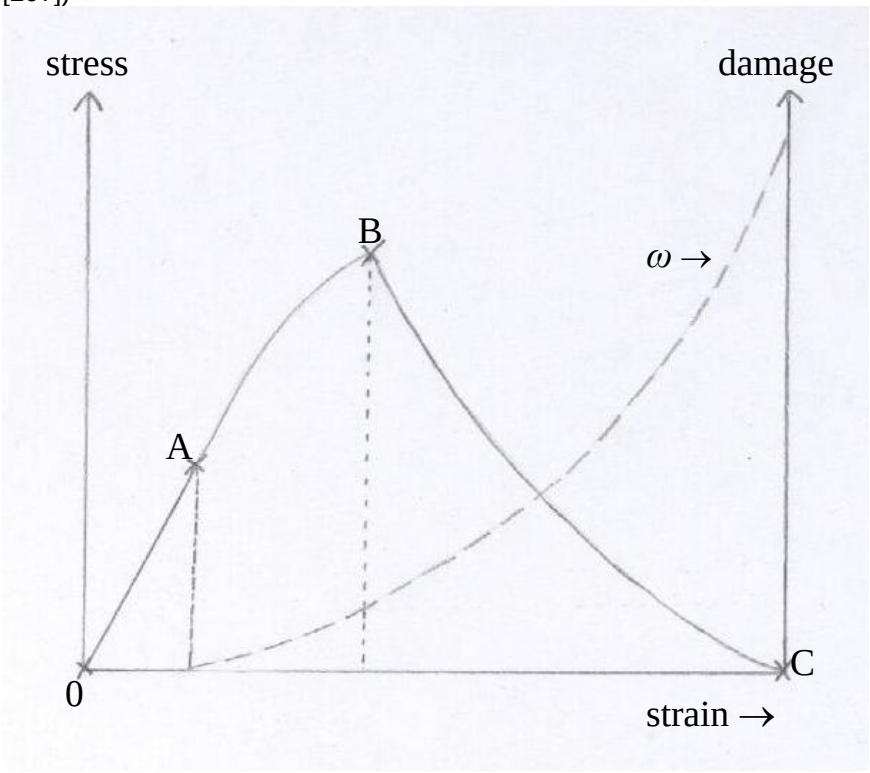

Some researchers have also identified a fourth region of 'ultimate cracking', where additional cracks develop through the concrete cover, until 'no further development of concrete cracks occurs' [208] and this additional cracking after the first main crack is formed has been demonstrated experimentally and through modelling [209].

Tixier and Mobasher [207] assumed that the unloading in the post-peak region is elastic and the elastic modulus E is given by

$$E = \frac{\sigma}{\varepsilon - \varepsilon_0} \quad \textbf{(10.5)}$$

with

$$\varepsilon_0 = \varepsilon_p - \frac{f_t}{E_0} \quad \textbf{(10.6)}$$

where σ is tensile stress, ε_p is the strain at the peak and f_t is the tensile strength of the concrete. However, in a cohesive crack model the unloading is generally not assumed to be elastic and some models take into account the complex mechanisms of 'ligament formation, bridging and fracture' and 'crack trapping and crack face pinning' [210]. This makes computations more complicated because a nonlinear structural analysis is required, which has sometimes been tackled using finite element analysis [199].

The role of heterogeneities in the fracturing of concrete was discussed by Pandermarakis and Sotiropoulou [210]. Flaws, pores and the interfacial zone around the cement-aggregate interface cause a reduction in the modulus, toughness and tensile strength of the concrete, and enhanced microcracking and fracture initiation consequently tend to occur in these areas. Also, cracks can become tortuous as they propagate either because they interact or because they meet large aggregates. Wittman [211] observed that cracks in pure cement paste or fine mortar can develop along a plane, because the small particles only impose 'minor deviations', but in a mortar or concrete with larger aggregates, most of the aggregates are stronger than the cement matrix, and so cracks are forced to run around them. The fracture energy G_f increases with the maximum aggregate size ϕ_{max} providing the size distribution remains similar, and the relationship given by Wittmann was

$$G_f = a \times \phi_{\max}^n \quad \textbf{(10.7)}$$

where a and n are constants determined experimentally. Some researchers have referred to the characteristic crack length, which also depends on aggregate size and is calculated from 'size effect formulas' [210].

10.2.3 Application of fracture mechanics to behaviour of expansive aggregates in concrete

The source of uniaxial tension to which concrete is subjected may be external or internal. Examples of internal sources include the expansive pressures generated by

the growth of crystals of ice or salts. There is an extensive literature on ice crystallization in cement paste, but the expressions derived for the stress or strain imposed upon the cement matrix typically involve properties of liquid water and ice. For example, Coussy et al. [212] derived an equation for the volumetric dilation ε of cement paste during freezing

$$\varepsilon = \frac{bp_L + (b_C \Sigma_m - 3\alpha_C K)\Delta T}{K} \quad \textbf{(10.8)}$$

where b is the Biot coefficient, p_L is the pressure exerted by the liquid in the pores, b_C is the Biot coefficient of the crystals, Σm is the melting entropy, K is the bulk modulus, and ΔT is the temperature change due to cooling. Similarly, the expressions derived for the pressure generated by the crystallization of ettringite, due either to external sulfate attack or to delayed ettringite formation, typically involve parameters such as the concentration and solubility of sulfates [207].

Another possible source of internal pressure in concrete is the expansion of steel reinforcements due to corrosion, and this is a comparable process to the expansion of aggregates due to swelling. It has been modelled with a cylindrical steel bar running through a thick-walled concrete cylinder under uniform internal pressure [213, 214]. The expansion of the reinforcement generates hoop stresses, which are tensile and decrease as the distance from the reinforcement increases. Smeared cracks are assumed to form in the radial direction as the hoop stresses exceed the tensile strength of the concrete. The cracks initially form on the inside of the cylinder, creating 'an inner cracked zone where the tangential stresses are zero' and an outer uncracked zone. Some researchers then identify a phase of crack formation on the external surface of the concrete 'at the location where the concrete cover is smallest' [208], and the final propagation of cracking through to the outside of the cylinder occurs when the strain energy released as the crack reaches the surface is greater than the fracture energy of the new crack surfaces formed [214]. With a simple model the time taken for the crack to reach the outside of the cylinder may be less than that observed experimentally. More complex models take into account processes such as the filling of the cracks around the reinforcement with corrosion products, and result in complex relationships which are often solved using finite element analysis [213].

It is generally accepted that the principle factors affecting the time taken for cracking to occur are the tensile strength of the concrete f_{ct}, the diameter of the steel bar d and the depth of cover of the concrete c. The relationship between these factors was defined by Rasheeduzzafar et al. [215] using a corrosion-cracking resistance factor, R_c, given by

$$R_c = \frac{cf_{ct}}{d} \qquad \textbf{(10.9)}$$

Expressions for the critical pressure $q_{r,c}$ required for cracks to propagate to the outside of the cylinder were given by Lu et al. [216] as

$$q_{r,c} = \frac{2cf_{ct}}{d} \qquad \textbf{(10.10)}$$

for a thin-walled cylinder where the tensile stress is assumed to be uniform, and

$$q_{r,c} = \left(0.3 + 0.6\frac{c}{d}\right) f_{ct} \qquad \textbf{(10.11)}$$

for a thick-walled cylinder where the tensile stress is non-uniform.

Some researchers have investigated the cracking patterns caused by corroding reinforcements, either experimentally or using finite element modelling. Noghabai [209] compared crack patterns obtained experimentally with patterns obtained using an inner softening band model. The two techniques gave good agreement for cylindrical bars within concrete cylinders, and showed that numerous small cracks formed initially, but that as the pressure increased between one and three cracks propagated more rapidly than the others and eventually lead to the splitting of the concrete cover. The patterns derived using this model on cylindrical reinforcements within a concrete beam with a rectangular cross section showed that final crack propagation occurred across the shortest distance possible, normal to the concrete surface, and a similar result was obtained by Kotes et al. [217], who modelled a cylindrical bar in a concrete beam with a cubic cross section. This type of model is shown in Fig. 10.2.

Fig. 10.2. Model of a concrete beam containing a cylindrical bar (redrawn from Xia et al. [218])

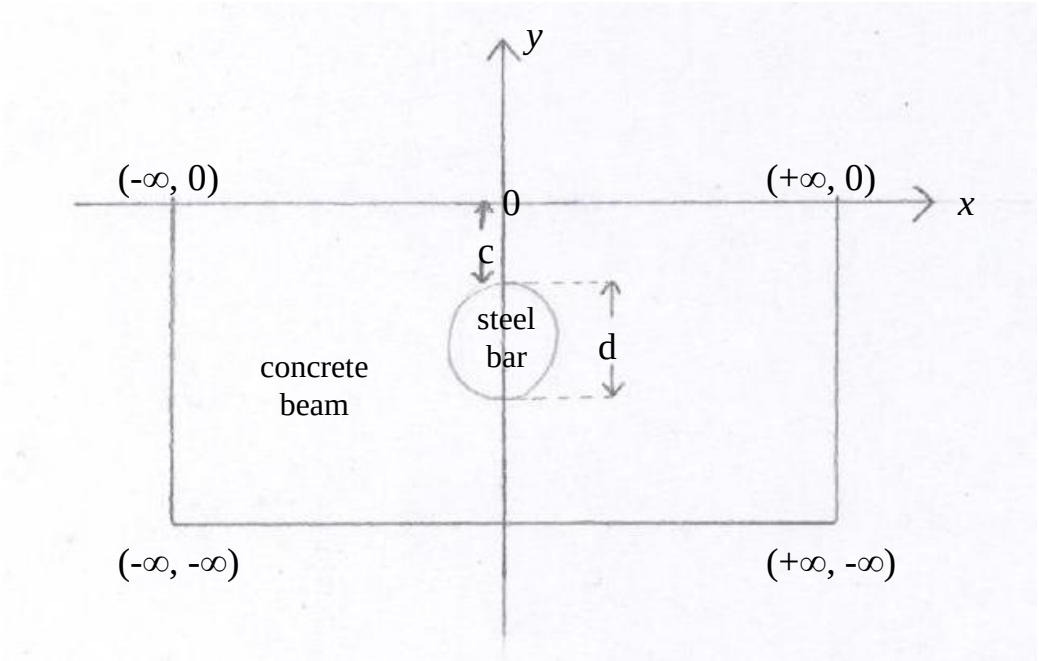

However, a slightly different crack pattern for a cylindrical reinforcement in a beam with a cubic cross section was obtained experimentally by Williamson and Clark [219]. They found that provided the ratio of concrete cover to reinforcement diameter was low, final crack propagation occurred with cracks inclined to the concrete surface as well as normal to it. This resulted in two parallel cracks running along the surface, above and below the location of the reinforcement below the surface. A similar crack pattern was proposed by Maaddawy et al. [220] after Liu and Weyers [221]. As observed by the Concrete Society [183] the critical cracks generated by an expansive aggregate particle also tend to occur inclined to the concrete surface, forming a circular crack on the surface with the buried aggregate at the centre. The detaching fragment is consequently a cone shape.

It has been shown mathematically that the formation of inclined cracks results from the stress variations occurring within a beam with a cubic cross section. For example, Jeffery [222] used bipolar coordinates to derive complex solutions for the stress distribution in scenarios including a ‘semi-infinite plate with a circular hole subject to a uniform normal pressure’. He demonstrated that final crack propagation either began at the concrete surface and ran in perpendicular to the surface, or began at the edges of the hole and radiated outwards, meeting the surface at an inclined

angle. The route taken was dependent upon the ratio of the radius of the hole to its distance from the concrete surface. Later work by Verruijt [223] using a combination of analytical and numerical analysis confirmed Jeffery's results, and produced expressions for the stress and displacement at any point within the plate.

An alternative explanation for the formation of inclined cracks was given by Xia et al. [218], who suggested the cracks were caused by the non uniform thickness of the layer of corrosion around the reinforcement, which typically follows an elliptical distribution with the thickest layer on the side of the reinforcement closest to the concrete surface. They calculated the hoop and radial stresses within the two-dimensional plane obtained by taking a cross section through the beam, where the x axis (θ=0°) runs parallel to the concrete surface and the y axis (θ=90°) runs from the centre of the reinforcement to the concrete surface. This method demonstrated that the radial stress acting on the concrete between the reinforcement and the surface is 'compressive in most areas except for low-level tensile stress in small zones close to the left and right ends of the bar', leading to inclined cracking.

10.3 Investigation of the original render at NMOF

10.3.1 Method

10.3.1.1 Survey and non-destructive testing

As described in Chapter 4, the airfield buildings were surveyed in wet and dry weather in order to identify which buildings had flaking render and which elevations on those buildings were worst affected. The results of the surveys were recorded photographically and on line drawings, and infrared thermography was undertaken to investigate the extent of the areas affected by flaking. It can detect the presence of sub-surface voids and cracks because the surface of these areas warms up more quickly upon heating than surrounding areas, resulting in a higher surface temperature. The surface of the flaking render was examined in situ with a portable digital microscope.

10.3.1.2 Render characterization

Of the materials characterization described in Chapters 5 and 6, the work considered relevant to the investigation of render flaking was:

- The petrographic examination of thin sections of original render, to calculate their mix proportions by point counting and to compare the aggregates in the renders from a building with flaking (Building 47) and a building with no visible flaking (Building 24);
- The petrographic examination of thin sections made from detached blisters of render, to look for potential causes of flaking;
- The petrographic examination of the aggregate particles thought to be related to the flaking, to identify them mineralogically;
- The acid extraction undertaken to estimate the mix proportions of the renders;
- The investigation of the ions content of the renders by analysing aqueous extractions with IC and ICP-OES;
- The examination and semi-quantitative analysis of the aggregate particles thought to be related to the flaking with SEM-EDX;
- The characterization of the aggregate particles thought to be related to the flaking with XRD.

10.3.2 Results

10.3.2.1 Survey and non-destructive testing

Flaking was observed on approximately one third of the cement-rendered airfield buildings, and was more prevalent on the south elevations and adjacent to the raised piers. Infrared thermography undertaken on a cold but sunny day showed that the surface of the flaking render was warmer than the surrounding render because the cracks below the surface had created a surface skin (Fig. 10.3). It also suggested that the extent of the deterioration was greater than was visually apparent, because some of the warmer areas appeared in good condition but were found by tapping to be hollow, suggesting they were beginning to deteriorate.

In its early stages the deterioration appeared as small, raised blisters, sometimes with layered aggregate particles visible below the cement-rich surface (Figs. 10.4-10.5), and as it progressed the blisters joined together, causing substantial areas of the render surface to distort and detach. In some places the surface skin had been lost altogether, exposing friable plaster underneath with small holes left by aggregate particles and some exposed aggregates, including flaky grey and yellow

particles. When the blisters of render were removed they were typically cone shaped, with a flaky grey or yellow particle at the base of the cone (Fig. 10.6). It was observed that after rain the areas of detaching render appeared much wetter than the surrounding render, and speculated that this might be because the aggregate particles just below the surface absorbed water (Fig. 10.7).

Fig. 10.3. Infrared thermography on Building 46 showing that the surface of the flaking render was warmer than the surrounding render. The infrared thermograph is a false colour image showing the surface temperature of surfaces in °C, where the red areas are warmest and the purple areas are coolest (Maureen Young, Historic Scotland)

Fig. 10.4. Raised blister of render on Building 46

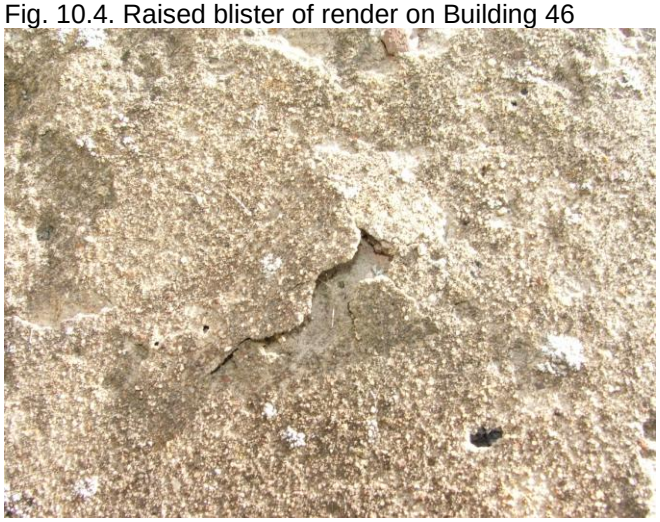

Fig. 10.5. Aggregate particle visible just below the render surface on Building 47, viewed with a portable digital microscope,15 times magnification

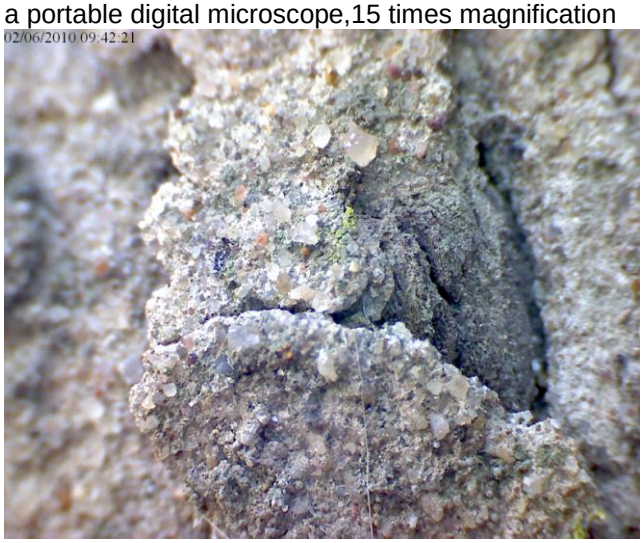

Fig. 10.6. Detached blister of render on Building 25, with fractured grey aggregate particles visible inside

Fig. 10.7. Visibly wet areas of flaking render on Building 47, following rain

10.3.2.2 Render characterization

The renders from buildings with and without deterioration were found to be significantly different (Table 10.1). The render that did not appear to flake from Building 24 had an average binder:aggregate ratio of 1:2.3 and a fine, quartz-rich aggregate, whereas the flaking render from Building 47 had a lower binder:aggregate ratio and a well graded, mixed rock aggregate. 53% of this aggregate consisted of rocks other than quartz, and 3% was mudstone. Significant differences in the soluble ions present in the renders were not found, although the flaking renders were generally slightly higher in sulfates, chlorides, sodium and aluminium. It is possible this was because the flaking renders had a higher content of non-quartz aggregates.

Thin section examination of the aggregate particles from Building 47 that were thought to be related to the flaking showed that they were similar to the mudstone identified in the Building 47 render. They all had layered structures and a significant silt or clay content, and some were rich in quartz (Figs. 10.8-10.10). They were therefore classified as shale, which is defined as a 'fissile and laminated' type of mudstone [224]. The particle analysed using SEM-EDX consisted of layers of quartz-rich material, with tiny particles of iron-rich material between the layers, which were probably clays (Fig. 10.11). XRD analysis of the clays extracted from the aggregates indicated the presence of kaolinite, with traces of illite, smectite and chlorite. Smectite is a swelling clay and chlorite can weather to form swelling layers of smectite interspersed with non-swelling layers [149], although it is doubtful whether the clay concentrations were sufficient to cause significant swelling.

Both the thin sections and the SEM micrographs showed cracks in the render emanating from the layered aggregate particles, suggesting that the particles might be causing the macroscopic cracking and flaking observed (Fig. 10.12).

Table 10.1 Chemical composition of renders from buildings with and without flaking

	render from building with flaking	render from building with no visible flaking
binder:aggregate ratio from acid extraction	1: 2.9	1: 2.2
binder:aggregate ratio from point counting	1:3.1	1:2.4
aggregate composition from point-counting	44% quartz, 3% mudstone, 53% other rocks	91% quartz, 0% mudstone, 9% other rocks

Fig. 10.8. Aggregate particle from B47 OR thought to be related to the flaking: mudstone with aligned, compacted carbonate clasts, plane polarized light, field of view: 440 µm across

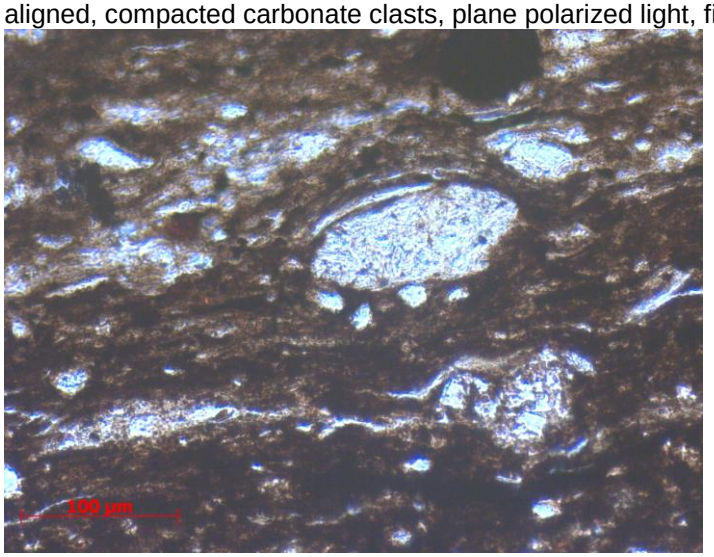

Fig. 10.9. Aggregate particle from B47 OR thought to be related to the flaking: well-cemented sandstone clast with a mud-rich matrix, plane polarized light, field of view: 875 µm across

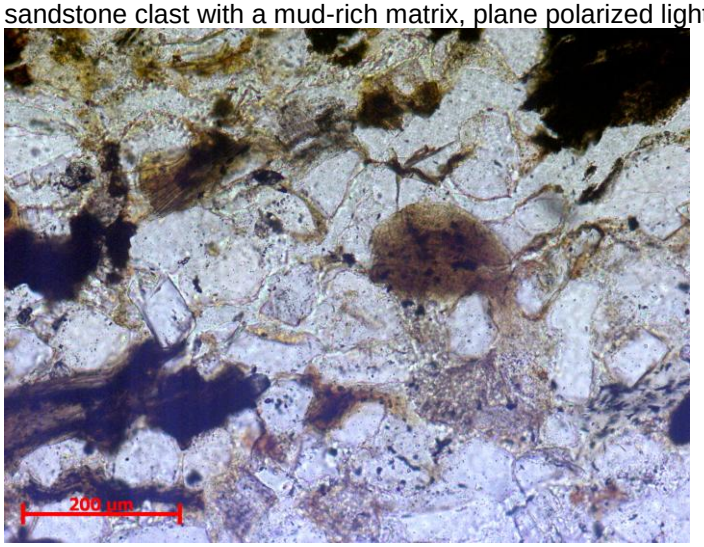

Fig. 10.10. As above, crossed polars

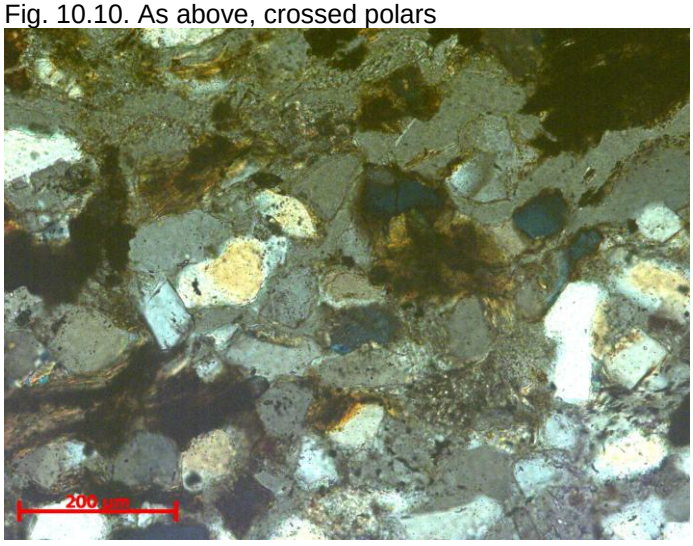

Fig. 10.11. SEM micrograph showing an aggregate particle picked out from B47 OR. The tiny pale-coloured particles visible between the layers were iron-rich and may have been clays.

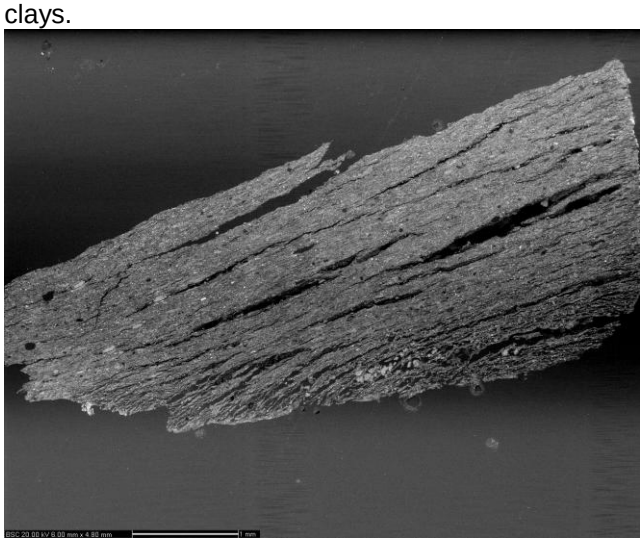

Fig. 10.12. Crack going from the mudstone aggregate particle in the Building 25 blister to the render surface, plane polarized light, field of view: 875 µm across

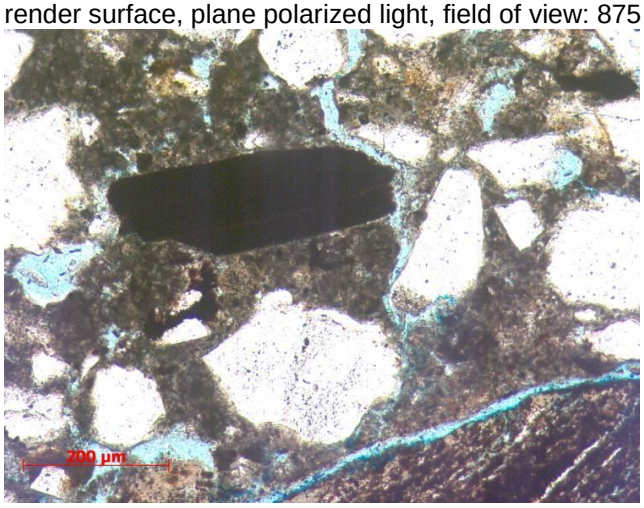

10.4 Further investigation of the aggregate particles

10.4.1 Method

10.4.1.1 Durability of the shale aggregate

The ability of the shale aggregate to withstand cycles of wetting-drying and freeze-thaw was investigated using a modified version of BS EN 1367-1. Samples weighing 0.01-0.02 g and composed of aggregate particles measuring 3-4 mm were subjected to wetting-drying or freeze-thaw cycling. For both types of cycling the sample was initially immersed in 50 ml of deionised water for 24 hr. For wetting-drying the excess water was then poured off and the sample was left to dry out at room

temperature for a further 24 hr, while for freeze-thaw the sample was placed in a freezer at -16 °C for 6 hr, before being returned to room temperature to thaw out for a further 18 hr. Each cycle was repeated three times before the residue was dried at room temperature. The samples were then placed within a sieve with a mesh size of 1 mm, and the mass percentage of each sample reduced to particles below 1 mm was calculated.

10.4.1.2 Selection and characterization of similar shale for experimental purposes

As only very small quantities of the shale aggregate could be extracted from the original render, a similar shale was required for experimental purposes. Several pieces of freshly quarried shale were obtained from the cement works in Dunbar, East Lothian, which is about 15 miles from East Fortune airfield. This shale was examined in thin section and analysed using powder XRD.

10.4.1.3 Strains in the aggregates from wetting-drying and freeze-thaw

The strains in the aggregates from the capillary uptake of water and n-decane were investigated. Three shale particles and one particle of sandstone with a mud component were tested, alongside a quartz pebble of similar dimensions and two pieces of the quarried shale for comparison. For the test the particle was placed with its layers orientated horizontally on a glass petri dish. A linear variable displacement transducer (LVDT)(GT1000RA.L10 from RDP Electronics Limited) was positioned above just touching the particle, so that it measured the expansion or contraction of the particle in the direction perpendicular to the layers. The movement of the LVDT over time was recorded by a data logger (Signatrol SL7003 logger). The experimental set-up is shown in Fig. 10.13.

A layer of water 1-2 mm deep was introduced into the petri dish with a pipette, and the particle absorbed water by capillary suction. The experiment was stopped after 6 hr, by which time any movement of the particle had ceased. The particle was allowed to dry out at room temperature, and the experiment was repeated using n-decane, a non-polar solvent. The n-decane absorption experiment was repeated for one of the aggregate particles, to investigate the repeatability of the results.

Additional variations undertaken with the quarried shale particle were:

- Absorption of water and n-decane by the particle positioned with its layers orientated vertically;
- Absorption of water and n-decane after artificial weathering with 14 freeze-thaw cycles (freezing at -16 °C for 6 hr followed by thawing at room temperature for 18 hr);
- Strain during ice formation, when the particle was capillary-saturated before being placed in a freezer at-16 °C for 6 hr.

Fig. 10.13. Equipment for measuring the strains in the aggregates from water uptake

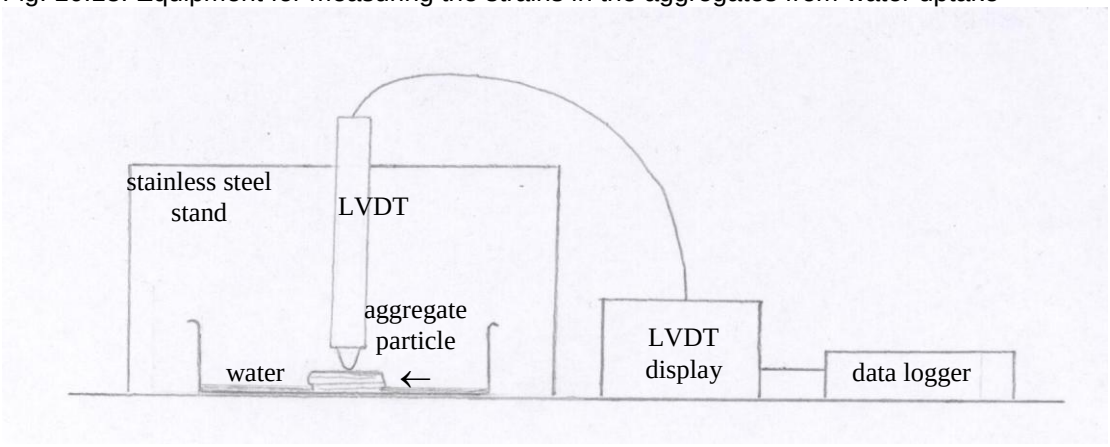

10.4.2 Results

10.4.2.1 Durability of the shale aggregate

The wetting-drying and freeze-thaw cycling undertaken on shale aggregate showed that three cycles of freeze-thaw caused 63% of the sample to disintegrate from an initial size of 3-4 mm to below 1 mm, but that three cycles of wetting-drying had no discernible effect on the aggregate (Table 10.2). This susceptibility to damage caused by freeze-thaw suggested that the shale must be at least moderately water absorbent.

Table 10.2 Disintegration of shale aggregate due to wetting-drying and freeze-thaw cycling

test	initial mass retained in 1mm mesh sieve	final mass retained in 1 mm sieve	% mass loss
wetting-drying	0.0096	0.0096	0
freeze-thaw	0.0174	0.0065	63

10.4.2.2 Selection and characterization of similar shale for experimental purposes

Quartz was the only mineral in the freshly quarried shale identified by XRD, and the thin section showed layers of quartz interspersed with layers of silt or clay (Fig. 10.14). As the quarried shale had a similar appearance to the shale aggregate in thin section, it was considered suitable for use in experiments.

Fig. 10.14. Freshly quarried shale from Dunbar cement works, plane polarized light, field of view: 875 µm across

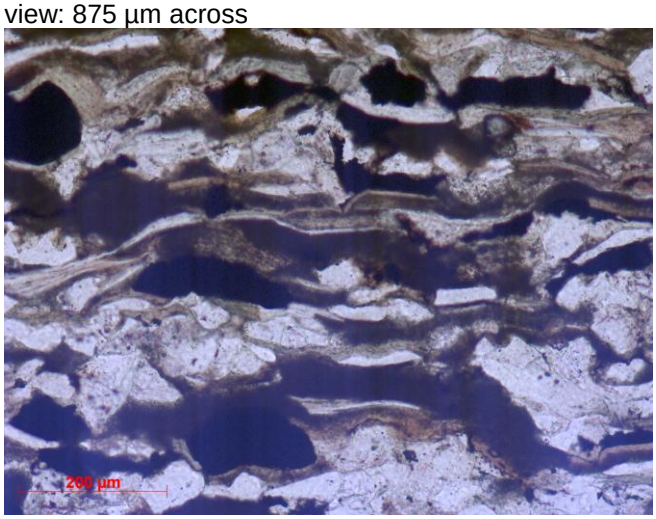

10.4.2.3 Strains in the aggregates from wetting-drying and freeze-thaw

The results of the LVDT measurements for the absorption of water and n-decane are given in Table 10.3. As in Chapter 8, the convention adopted has been that negative strains represent contraction and positive strains represent expansion. When the n-decane absorption experiment was repeated for one of the samples (aggregate particle 2), the strain measured was -0.27% on the first run and -0.29% on the second run, suggesting that the results were repeatable to ±0.02%. The strains in Table 10.3 are quoted to two decimal places in order for even the small length changes measured for the quarried shale to be shown.

No strain was measured in the quartz pebble from wetting with water and n-decane, as would be expected given that it did not contain clays. All of the aggregate particles contracted when they were exposed to water, the mudstones by around 3% and the sandstone with a mud component by 0.74%. They had been expected to expand, but the weathering they had undergone may have created cracks in between

the layers, which contracted due to capillary forces when water was absorbed, in the same way that soils with a capillary zone undergo compression when they absorb water [225]. The contraction observed from wetting with n-decane was smaller by a factor of at least 2.5. This again suggests the action of capillary forces, which would be reduced for n-decane because it has lower surface tension[19].

The maximum strain measured for the quarried shale from wetting with water was 0.59%, presumably due to the hydration and expansion of some of the clay particles. However the strain from wetting when a sample was positioned with the layers orientated vertically was only 0.01%, demonstrating the directional nature of the swelling. Decane uptake did not cause swelling of the quarried shale, presumably because n-decane does not undergo a hydration reaction with clays. After 14 freeze-thaw cycles the strain from wetting reduced to 0.04%. This was presumably because the shale had weathered to the point where the expansion of the clays was offset by the contraction caused by capillary forces.

An overall strain of 1.24 % was measured for the quarried shale when it was capillary saturated and then frozen, demonstrating that the strain from wetting and freezing was greater than that from wetting alone. Furthermore the shale undergoing both wetting and freezing showed some residual strain, indicating that it had been extended beyond its elastic limit, whereas the shale undergoing wetting only returned to its original length. The full results of this experiment are given in Appendix 5.

Table 10.3 Strains measured due to wetting of particles with water and n-decane

	strain with water (%)	strain with n-decane (%)
quartz pebble	0.00	0.00
aggregate particle 1 (shale)	-2.92	-1.06
aggregate particle 2 (shale)	-3.11	-0.28
aggregate particle 3 (shale)	-3.25	-0.05
aggregate particle 4 (sandstone with mud component)	-0.74	-0.03
quarried shale sample 1	0.32	0.00
quarried shale sample 2	0.59	0.00
quarried shale with layers orientated vertically	0.01	0.00
quarried shale after artificial weathering	0.04	0.00

[19]Where σ_w and σ_d are the surface tensions of water and decane respectively, taken as σ_w = 72.8 and σ_d = 23.8 [101], the ratio of σ_w/σ_d is 3.1.

10.5 Preliminary conclusions

The hypothesis formed from the investigation of the original cement render at NMOF and the further investigations of shale aggregate particles and quarried shale was that the expansion and contraction of the shale particles was causing the surrounding render to crack, and that this was the cause of the macro-cracking and flaking observed in the original cement renders. Further experiments as detailed in Section 10.6 were devised to test this hypothesis, and the calculations described in Section 10.7 were undertaken to investigate whether the force generated by the shale particles was sufficient to cause cracking.

It was speculated that the deterioration was more severe on the south elevations of the buildings because they undergo the greatest temperature variations, as demonstrated by the surface temperature monitoring in Chapter 4. Hence the aggregates on the south elevations are likely to undergo more freeze-thaw cycles than the aggregates on the north elevations. It was also speculated that the deterioration was prevalent adjacent to the raised piers because the larger aggregate particles are concentrated there, due to the technique of render application. However, this could not be proven without taking large render samples, which was deemed unacceptable.

10.6 Experimental work with replicas

10.6.1 Method

It is widely accepted that the best way of investigating the performance of a particular aggregate within concrete is to apply freeze-thaw tests to samples of the concrete made with the mix proposed [226]. A dilation method as detailed in ASTM C682-94 (now withdrawn due to lack of use) was used to further investigate the effect of shale upon cement renders, by preparing replica renders with ordinary Portland cement (OPC), coarse washed sand and the quarried shale from Dunbar.

As shown in Table 10.1, the mix proportions of the original renders which underwent flaking were approximately 1 part cement to 3 parts aggregate, with mudstone constituting around 3% of the aggregate by volume. Three render mixes were therefore prepared, a control (C) consisting of 1 OPC:3 sand, a low shale mix (LS) consisting of 1 OPC:0.5 shale:2.5 washed sand and a high shale mix (HS)

consisting of 1 OPC:1 shale:2 washed sand. The proportions of shale were higher than in the original renders in order to exaggerate its effect. The water:cement ratio of 0.9 was the same for each mix. The mixes were compacted into plastic tubes measuring approximately 16 x 50 mm. They were cured for 4 weeks at 100% relative humidity, before being removed from the tubes and trimmed. Additionally, patches of the mixes measuring approximately 60 x 60 mm were applied to historic Niddrie bricks from NMOF, which had been pre-wet to ensure a good bond, and they underwent the same curing regime. A brick with render applied is shown in Fig. 10.15.

The porosity of the cylindrical samples by capillary and vacuum saturation was calculated, as described in Chapter 6. Their length changes due to the capillary uptake of water at room temperature and the freeze-thaw cycling of capillary saturated samples were measured using the LVDT. For wetting only the samples were stood in a shallow dish of water for 6 hr, while for wetting with freeze-thaw the samples were capillary saturated by immersion in water for 24 hr, followed by a 24 hr cycle comprising cooling for 6 hr from room temperature to -16 °C, warming for 4 hr from -16 °C to room temperature and an isotherm at room temperature for 14 hr, as shown in Fig. 8.3.

For the freezing experiments the internal temperature of the freezer and the surface temperature of the sample were measured using thermocouples. The test was repeated on each sample four times, and in between tests the samples were oven dried at 110 °C and acclimatised at room temperature. The holder for the LVDT and the samples was made of stainless steel and underwent dimensional changes itself upon cooling and warming. As described in Chapter 8, this movement was measured by testing a sample of invar 36 rod, and was subsequently subtracted from the movement recorded for the samples.

The deterioration of the renders due to 14 cycles of wetting-drying or freeze-thaw was investigated using the renders applied to the bricks. For wetting-drying the bricks were stood render face down in a shallow dish of water for 12 hr, followed by render face up in ambient conditions for 12 hr, while for freeze-thaw the wetting period was followed by 12 hr in a freezer at -16 °C. The renders were photographed

periodically to record any visual signs of deterioration, and thin sections of the renders at the beginning and end of the cycling were examined.

Fig. 10.15. Rendered bricks prepared for wetting-drying and freeze-thaw testing. Each brick has patches of all three render types, with the control (C) render on the left, the low shale (LS) render on the right, and the high shale (HS) render in the middle

10.6.2 Results

10.6.2.1 LVDT measurements on renders containing shale

The renders containing shale had higher porosity than the control render (Table 10.4), although the LS render sample was more porous than the HS, possibly as a result of variations between samples resulting from uneven distribution of the shale. The strains measured for the control, LS and HS renders from wetting varied from 0.011-0.037%. There was no clear relationship between the render type and the degree of expansion, nor was there any particular trend with increasing cycle number. When the samples were capillary saturated and then placed in the freezer, all three renders contracted initially, and then expanded at around -7 °C due to ice crystallization. The expansive strains in the samples due to ice formation were slightly higher for the shale renders than for the control render, possibly because they were more porous and expanded more when ice was formed (Table 10.4). The samples contracted again when they were cooled further, and then expanded upon warming. The residual strains were negative, indicating an overall contraction. There was no relationship between the number of cycles and the residual strain, although this might have been observed if more cycles had been undertaken. The full results of this experiment are given in Appendix 5.

Table 10.4 Porosity of the replica render samples and length changes due to cooling and ice formation

	Control	LS	HS
porosity by vacuum saturation (%)	22.0	29.0	26.0
porosity by capillary saturation (%)	17.0	25.0	21.5
average strain due to ice formation (%)	0.0017	0.0021	0.0020
average strain at minimum temperature (%)	-0.0330	-0.0219	-0.0215
average strain at end of cycle (%)	-0.0311	-0.0203	-0.0272

10.6.2.2 Examination of renders containing shale

There was no visual deterioration of any of the renders due to wetting alone. However, surface pitting of the LS render was observed after only four freeze-thaw cycles, and had worsened by the end of the experiment (Fig. 10.16). No deterioration was observed in the HS render due to freeze-thaw, possibly because the mixing process had broken down the shale particles to below the size needed to cause surface cracking.

Petrographic examination showed there were cracks inside the shale particles and running along their edges even before weathering, presumably because the particles absorbed water when the mix was wet and shrank as they dried out (Fig. 10.17). Areas of high microporosity and larger pores tended to occur along the interfacial zone, and this would have created regions of reduced modulus and tensile strength, where fracture initiation was likely to occur [210]. The shale particles were notably more disaggregated in the samples which had undergone wetting cycles, and there was some microcracking of the cement paste. Further microcracking was evident after freeze-thaw cycling, with the cracks generally beginning at the aggregate and propagating through the cement in a direction perpendicular to the aggregate surface. The thin section examination of the LS render where surface pitting occurred showed that the surface had largely disintegrated and the pressure generated had been sufficient to crack some quartz particles (Fig. 10.18).

Fig. 10.16. Surface pitting of the LS render after 14 freeze–thaw cycles

Fig. 10.17. Area of high porosity around a shale particle (upper left) in the HS render before weathering, plane polarized light, width of image 1750 μm

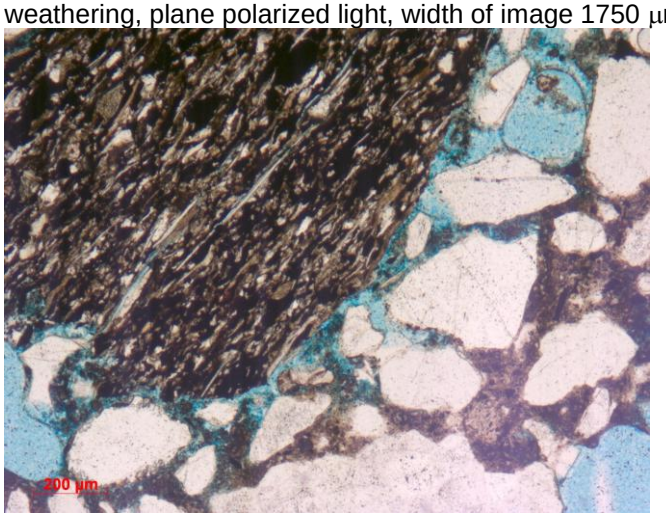

Fig. 10.18. Surface disintegration of the LS render after freeze-thaw cycling, plane polarized light, width of image 875 μm

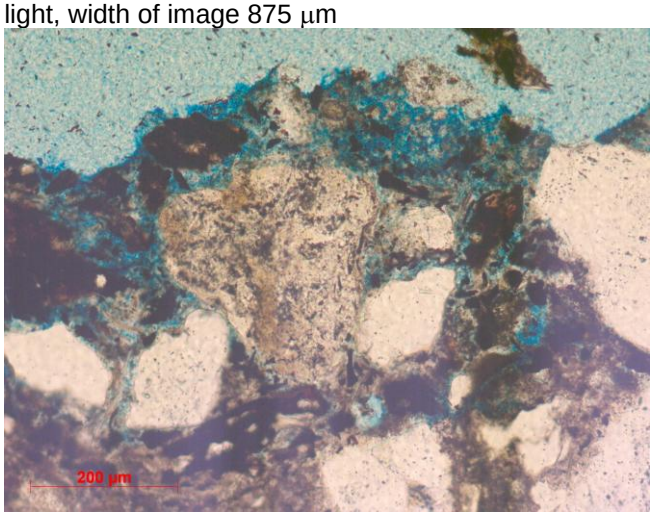

10.6.3 Conclusions from experiments with replica renders

The experimental work with replica renders showed that shale aggregate increased the porosity of the cement render, and from thin section analysis it was evident that this was due to the high porosity of the shale itself and enhanced porosity in the cement paste in the interfacial zone around the shale particles. The expansive strains in the samples due to ice formation were slightly higher for the shale renders than for the control render. The wetting-drying and freeze-thaw cycling of the renders showed that wetting alone did not cause visual deterioration of the render, whereas wetting with freeze-thaw caused pitting of the LS render after only four cycles, and was shown in thin section to have generated considerable pressure.

10.7 Calculation of the expansive pressure generated by the shale particles

10.7.1 Simple method

It is suggested in Section 10.2 that the expansion of steel reinforcements in concrete due to corrosion is a comparable process to the expansion of aggregates due to water uptake, either alone or followed by freezing. Using the model of a cylindrical steel bar running through a thick-walled concrete cyclinder under uniform internal pressure, the critical pressure $q_{r,c}$ required for cracks to propagate to the outside of the cylinder has been given by Lu et al. [216] as

$$q_{r,c} = \left(0.3 + 0.6\frac{c}{d}\right) f_{ct} \qquad \textbf{(10.11)}$$

where f_{ct} is the tensile strength of the concrete, d is the diameter of the steel bar and c is the depth of cover of the concrete. Hence if the pressure generated by the expansion of the steel bar or the expansion of the aggregate particle is greater than $q_{r,c}$, cracks will appear at the surface, and, in the case of the expansive aggregate, a pop-out may result.

The internal stresses generated within the aggregate particle upon wetting only and wetting and freezing σ_{wo} and σ_{wf}, may be calculated from the strains measured ε_{wo} and ε_{wf}, and the elastic modulus of the aggregate E, using the relationship

$$E = \frac{\sigma}{\varepsilon} \quad \textbf{(10.12)}$$

where ε_{wo}=0.59% and ε_{wf}=1.24%, as obtained in section 10.4.2.3. It is assumed that the internal stress is transferred to the surrounding cement matrix. The particle will expand in two opposite but parallel directions, towards and away from the concrete surface, and the pressure exerted on the concrete in each direction is $\sigma_{w.}$

In order to calculate $q_{r,c}$, σ_{wo} and σ_{wf}, the tensile strength of the cement render and the elastic modulus of the aggregate particles were required. It was not possible to test the aggregate particles taken from the render because they were too small and heavily weathered, and the quarried shale was substituted because the thin section analysis had showed that its composition was similar. The measurement of the tensile strength and elastic modulus of the cement render is described in Section 6.5, and rectangular prisms of quarried shale measuring approximately 50 × 20 × 10 mm were tested in the same way.

10.7.2 Results from simple method

The tensile strength f_{ct} used for the render was the value of 4.5 MPa obtained for HC OR, which was an original render containing well graded, mixed aggregate rather than just fine sand. The stress-strain curves obtained for the quarried shale typically showed an initial period of low elastic modulus E_i, averaging 0.12 GPa, followed by a period with higher elastic modulus E_f, averaging 0.92 GPa, before the sample failed suddenly (Fig. 10.19). These values are lower than those reported elsewhere of 4.5 GPa for a rich oil shale (high organic matter content) and 16 GPa for a lean oil shale (low organic matter content) [227], but the quarried shale was probably much more friable than any shale that would be investigated for commercial purposes. It is noted in section 10.4.2.3 that shale undergoing wetting only returned to its original length, whereas shale undergoing both wetting and freezing showed some residual strain, indicating that it had been extended beyond its elastic limit. Hence the lower value of the elastic modulus was used for calculations of the stress due to wetting only, while the higher value was used for calculations of the stress due to wetting and freezing.

Substituting the values of ε_{wo}, ε_{wf}, E_i and E_f into equation 10.12 gave values for σ_{wo} and σ_{wf} of 0.7 MPa and 11.4 MPa. Typical values of c and d obtained from measuring a pop-out were 5 mm and 2 mm respectively. Substitution of these values

and f_{ct} into equation 10.11 gave a critical pressure $q_{r,c}$ of 8.1 MPa. Cracking may occur if the stress generated by the wetting or wetting and freezing of the particle exceeds the critical pressure. For these values of c and d, $\sigma_{wo} < q_{r,c}$, but $\sigma_{wf} > q_{r,c}$, suggesting that the quarried shale might not generate enough pressure simply by swelling to crack the render, but might cause cracking by absorbing water and then freezing. This result was in agreement with the damage produced experimentally, described in Section 10.6. Substitution of other values of c and d into equation 10.11 showed that if c was increased (say to 10 mm) or d was reduced (say to 1 mm), the critical pressure required to crack the concrete increased, such that $\sigma_{wf} < q_{r,c}$, suggesting that in these cases cracking would not occur. Again, this result is in agreement with the field observations that very small aggregate particles or aggregate particles at depths of around 10 mm or more below the surface did not cause cracking. The values of $q_{r,c}$ obtained for various values of c and d are given in Table 10.5.

Table 10.5 Values of critical pressure generated by aggregates of varying size and depth

	ε_{wo} (%)	ε_{wf} (%)	E_i (MPa)	E_f (MPa)	σ_{wo} (MPa)	σ_{wf} (MPa)	c (mm)	d (mm)	f_{ct} (MPa)	$q_{r,c}$ (MPa)
scenario 1	0.59	1.24	0.12	0.92	0.7	11.4	5	2	4.5	8.1
scenario 2	0.59	1.24	0.12	0.92	0.7	11.4	2	2	4.5	4.1
scenario 3	0.59	1.24	0.12	0.92	0.7	11.4	10	2	4.5	14.9
scenario 4	0.59	1.24	0.12	0.92	0.7	11.4	5	1	4.5	14.9

Fig. 10.19. Load against displacement for the quarried shale undergoing bending during three-point loading

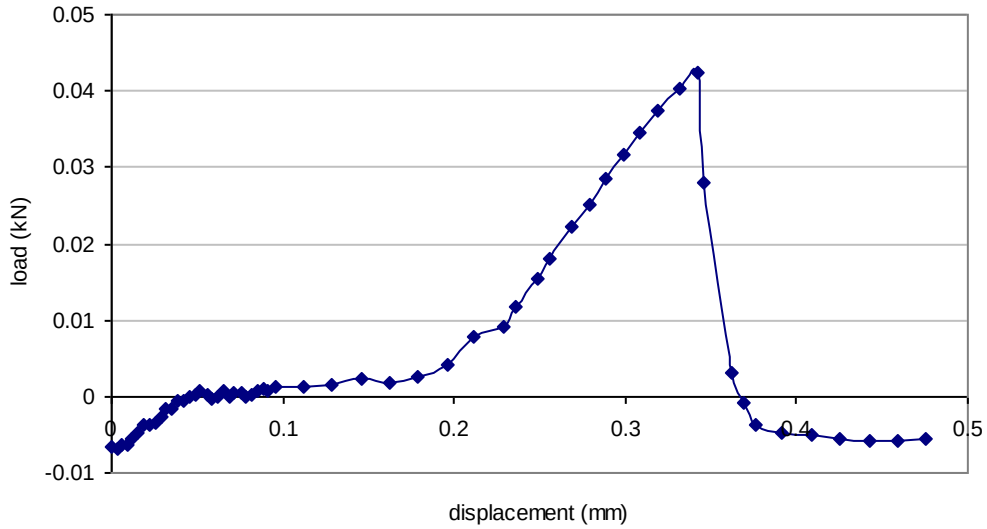

10.7.3 Complex method

A more complex method was developed using the two dimensional model of Jeffery [222] for plane stress and plane strain within a semi-infinite plate with a circular hole subject to a uniform normal pressure, in order to model the stress placed on the render surface during expansion[20]. The shale aggregate was considered as sitting in a spherical cavity, and the expansion of the aggregate during wetting or freezing was assumed to be isotropic, producing a tensile hoop stress on the cavity wall.

The bipolar co-ordinate system of Jeffery was adopted. He defined the curvilinear co-ordinate system by the conjugate functions

$$\alpha + i\beta = \log \frac{x + i(y + a)}{x + i(y - a)} \qquad \textbf{(10.13)}$$

where x and y are Cartesian co-ordinates and a is a positive real length. The general scheme of co-ordinates was then defined as shown in Fig. 10.20. O_1 and O_2 are the points (0, -a) and (0, a) respectively. P is any point in the plane, if the radii r_1 and r_2 are inclined to the x-axis by angles θ_1 and θ_2. The curves with α = constant are a set of co-axial circles, with O_1 and O_2 as the limiting points. Circles with positive values of α lie above the x-axis while those with negative values of α sit below it. The x-axis is given by $\alpha = 0$. The curves for β = constant are arcs of circles passing through O_1 and O_2 and cutting the set of circles associated with α = constant at right angles. $\beta = 0$ corresponds to the y-axis; β is positive to the right of the y-axis and negative to the left of it, while on the y-axis $\beta = 0$ except on the segment O_1O_2 where $\beta = \pm\pi$.

The primary interest was in understanding the stress distribution round the hole and the corresponding effect on the straight edge, the render surface. The stress fields were defined with respect to an angle, θ, which sweeps clockwise round the cavity circle, with $\theta = 0°$ and 360° at the perpendicular from the circle centre to the straight edge (Fig. 10.21). r is the radius of the circles and d is the distance from the centre of the circle to the straight edge. The x and y co-ordinates of the circle with respect to θ, the angle between the perpendicular and any radii position are given by

$$x = 2r(\sin\frac{\theta}{2}\cos\frac{\theta}{2}) \qquad \textbf{(10.14)}$$

[20] This work was undertaken by Dr Andrea Hamilton at the University of Edinburgh.

$$y = 2r((\sin\frac{\theta}{2})^2 + d - r) \quad \textbf{(10.15)}$$

and α and β are calculated from the real and imaginary components of equation 10.13, respectively.

According to Jeffery, the stress around the hole *HS* is given by

$$HS = -P + 2P\text{cosech}^2\alpha(\cosh^2\alpha - \cos^2\beta) \quad \textbf{(10.16)}$$

and the stress along the straight edge *ES* is given by

$$ES = -4P\frac{r^2(x^2 - d^2 + r^2)}{(x^2 + d^2 - r^2)^2} \quad \textbf{(10.17)}$$

where *P* is the applied pressure inside the hole, in this case the pressure placed on the cavity wall by the expanding shale particle. *x* and *y* are the circle co-ordinates but *x* is extended to values greater than the circle diameter to model the effect of stress at distance along the render surface. The results are normalised by the pressure inside the hole.

Fig. 10.20. Bipolar co-ordinate system defined by Jeffery [222] (redrawn from Jeffery)

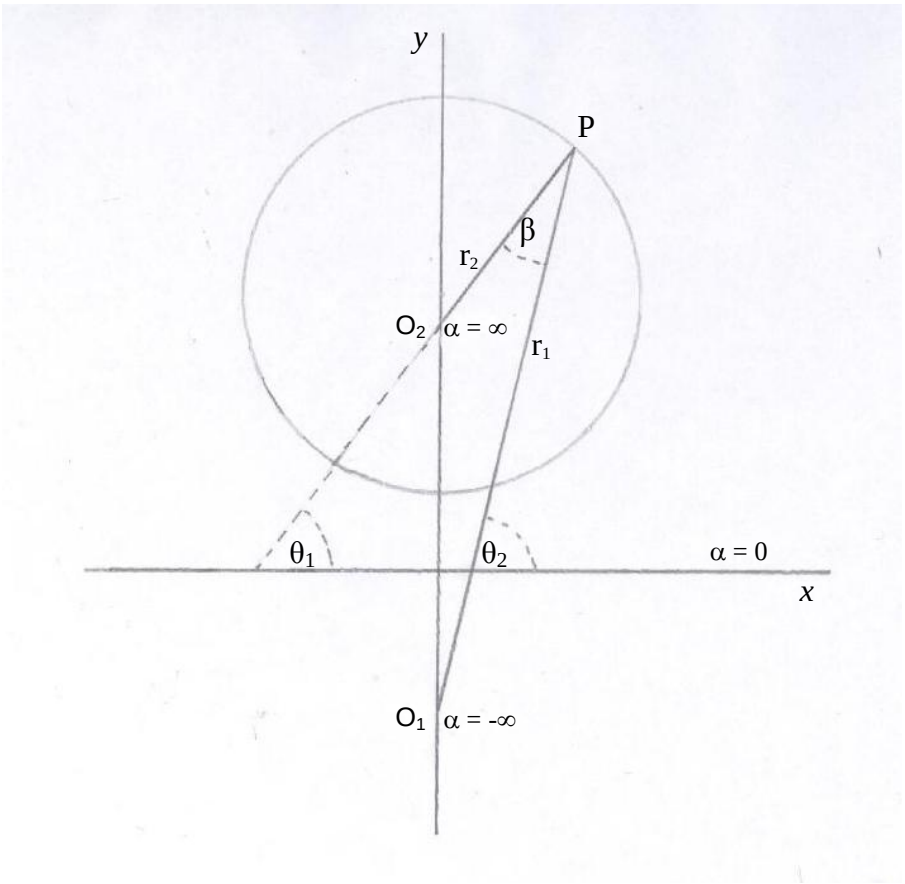

Fig. 10.21. Co-ordinate system describing the circle co-ordinated in terms of θ

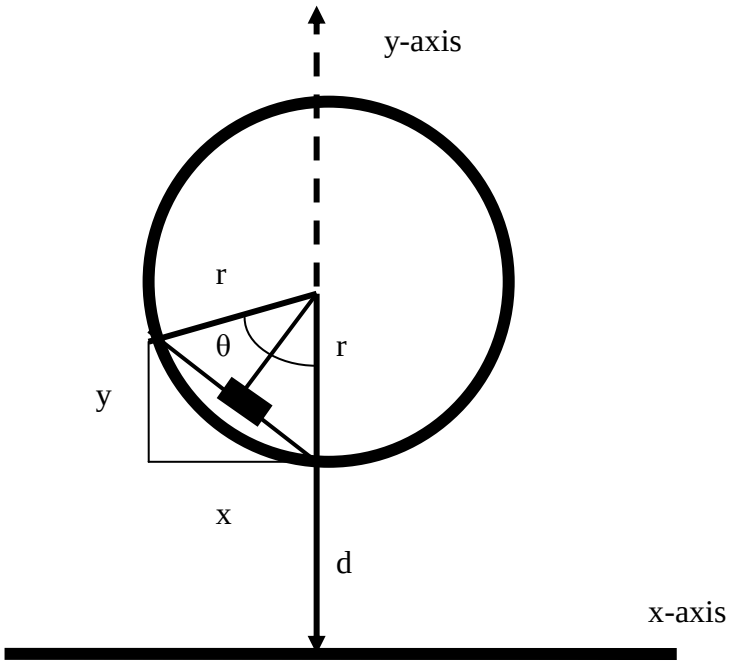

10.7.4 Results from complex method

d and *r* were varied in accordance with the observed values for the render thickness where pop-outs occur (*d*-*r*) and the radius of the popout cavity *r*, and θ was varied to determine the point of greatest stress around the cavity. The aims were to explain the conical shape of the pop outs by determining where fracture initiates in the cavity and to establish the conditions under which fracture can initiate at the render surface. The stress along the edge and hole resulting from the swelling pressure of the aggregate was normalised to minimise the number of variables in any one calculation and to show more clearly the impact of varying *d*. The depth of cover (*d*-*r*) was varied from 1 to 5 mm, θ was varied from 1° to 360°, *r* was initially fixed at 1 mm and *P* was taken as 1 MPa. For each set of values of *P, d, r* and θ the stress distribution around the hole *HS* and the stress along the straight edge *ES* were calculated.

The variation of *HS* for different values of *d* and θ is shown in Fig. 10.22. This demonstrates that fracture will initiate at well defined angles, which move according to the render thickness, and that the stress on the hole is up to 1.66 times greater than the isotropic applied stress inside it. The θ values corresponding to the maximum tensile hoop stress on the edge of the hole are 60° and 300° for *d* = 2 mm,

moving to 80° and 280° as *d* approaches 6 mm. This means that the angle of the pop out increases from 120° to 160° as the render covering gets thicker, which explains the observed conical shape of the pop outs.

Fig. 10.22. Stress distribution around the hole, with each plot corresponding to a different value of *d*. Blue is *d* = 2 mm, green is *d* = 3 mm, red is *d* = 4 mm, cyan is *d* = 5 mm and purple is *d* = 6 mm; *r* = 1 mm.

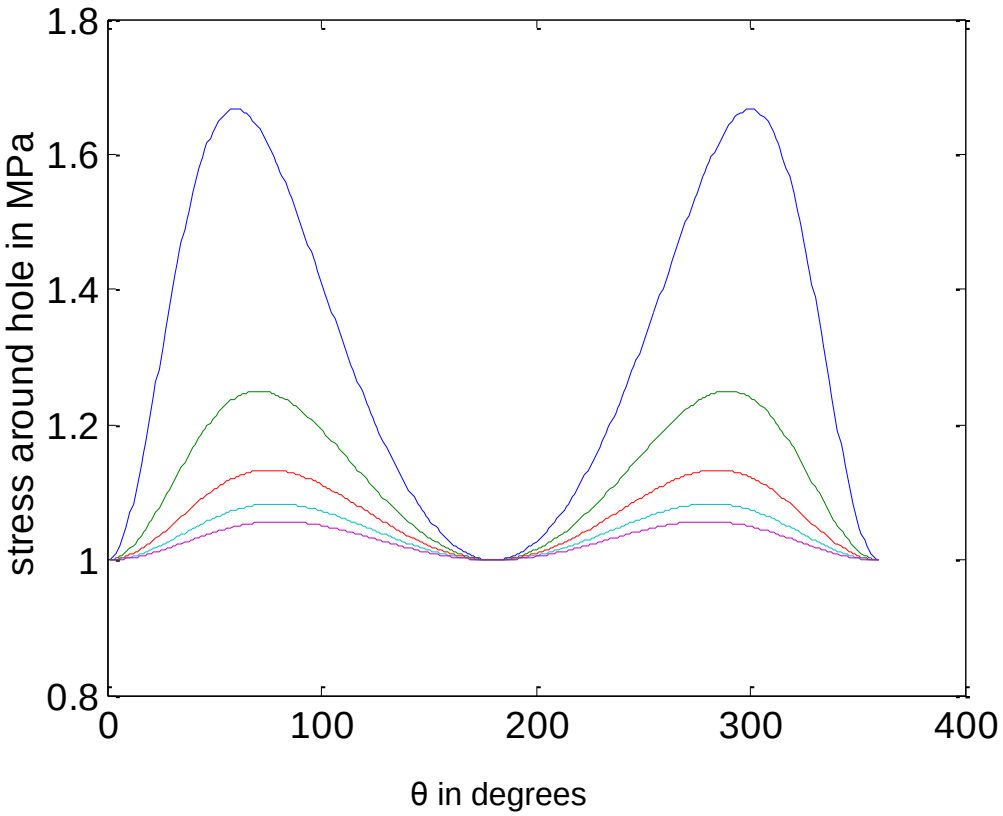

The stress on the straight edge is both tensile and compressive, as shown in Fig. 10.23. The point of maximum tension is at *x* = 0 mm, directly perpendicular to the shale particle. However, when *r* is 1 mm the stress around the hole is always greater than the stress along the edge, indicating that fracture will initiate from the hole rather than at the point of maximum tension. The likelihood of warping or buckling increases with decreasing *d*, therefore thin render layers are most vulnerable to warping and damage.

Fig. 10.23. The stress along the edge, showing compressive stress (negative values) and tensile stress (positive values). As before, blue is *d* = 2 mm, green is *d* = 3 mm, red is *d* = 4 mm, cyan is *d* = 5 mm and purple is *d* = 6 mm; *r* = 1 mm.

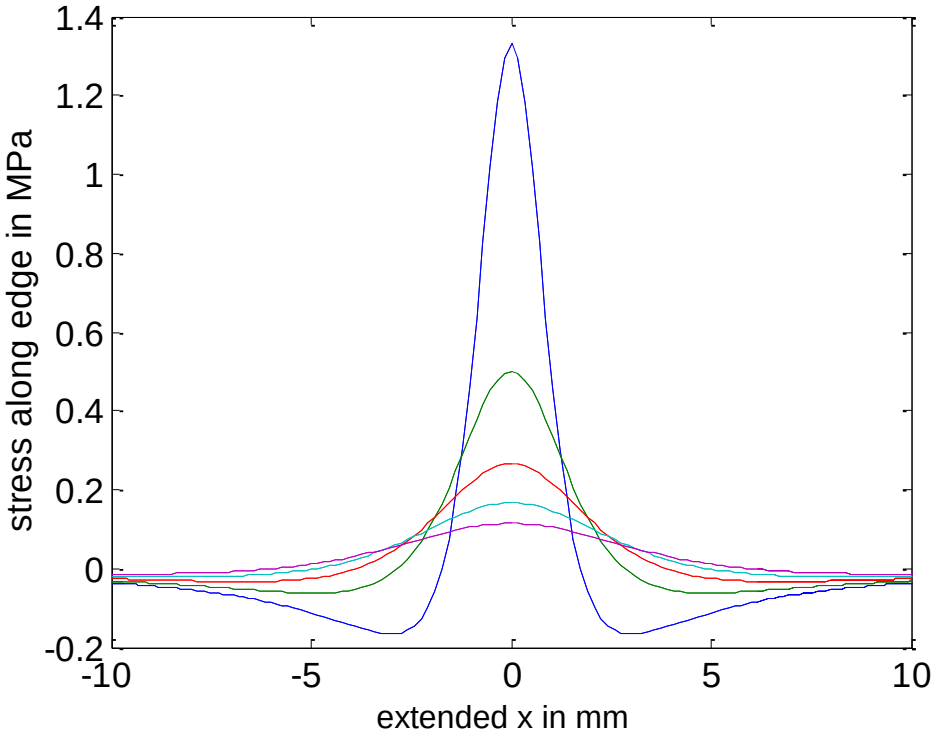

Increasing the size of the cavity while maintaining the same applied pressure will generate greater pressure on the cavity wall and change the angle of the conical pop out. Normalising all lengths in the calculation by dividing *d* by *r*, where *r* varies from 1 to 3 mm, shows the minimum and maximum stresses experienced with these defined parameters of *r*, *d* and *P* (Fig. 10.24). The highest stresses on the cavity wall are produced by the lowest values of *d/r*, ranging from 4/3 to 6. The angle of maximum stress varies from around 41° to 69°, and correspondingly also from (360 – 69)° and (360 – 41)°, with the shallowest angles resulting from the lowest values of *d/r* and the highest stress on the cavity wall. The maximum tensile stress along the straight edge exceeds the stress around the hole for *d/r* = 1.33 – 1.73. This means that for large cavities with a thin covering of render, the crack initiates on the render surface rather than at the cavity.

Fig. 10.24. The stress on the cavity wall calculated using *d/r* and plotted against *θ*. The highest stresses result from the lowest values of *d/r*, as shown in the uppermost blue curve, where the stress is approximately 3.5 times the applied pressure

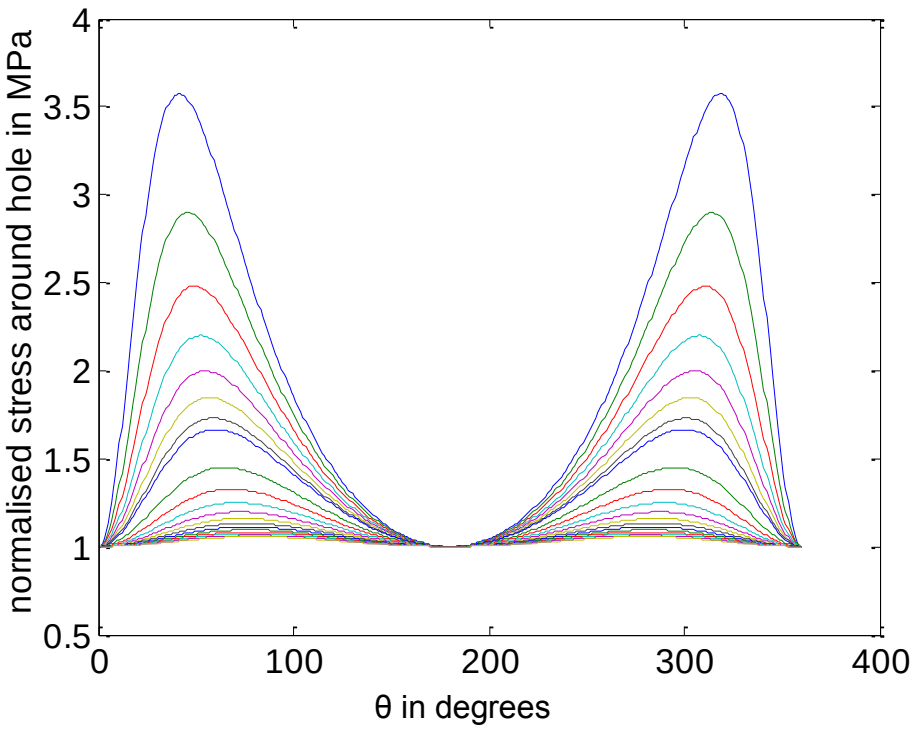

10.7.5 Comparison between methods

Both the simple and complex methods demonstrate that cracking becomes more likely to occur as the ratio of the depth of concrete cover to the size of the shale particle (measured as the radius or diameter) is reduced. However, the methods do not agree on the values for the depth of concrete cover and the radius of the shale particle required to cause cracking. For example, the simple model suggests that cracking is likely to occur when the depth of concrete cover *c* is 5 mm, and the diameter of the shale particle *d* is *2* mm. In the complex model, this equates to a particle radius *r* of 1 mm, and a value for the distance from the centre of the particle to the render surface *d* of 6 mm. This scenario is shown in the purple curve in Fig. 10.22, which indicates that the stress varies very little around the hole, rather than being higher at the 'cone' angles, suggesting that crack formation would be unlikely. Fig. 10.22 shows that lower values of *d/r* result in much higher values of stress at θ=60° and 300°. The values for the stress around the hole calculated by the complex model suggest that the assumption made in the simple model that the pressure

exerted on the concrete by the swelling particle is equal to the stress due to wetting or wetting and freezing is inaccurate. However, the results obtained by the simple model still appear to agree with experimental observations.

10.8 Final conclusions

The survey work in combination with petrography and SEM suggested that the blistering and flaking of the cementitous renders at NMOF was due to pop-outs. This is a reasonably well known type of concrete deterioration, whereby cone-shaped pieces of concrete scale off due to the presence of expansive aggregate particles just below the surface. In this case the aggregates responsible were shale and mud-rich sandstone. LVDT measurements showed that weathered aggregate particles from the original render contracted due to capillary forces, but that freshly quarried shale from a local source underwent significant expansion due to water absorption, and even greater expansion due to water absorption followed by freezing.

It was found from experiments with replica renders that shale increased the porosity of the render and increased the expansion of the saturated render due to ice formation. The replica render containing shale was not visually deteriorated by wetting-drying cycling, but appeared pitted after only a few freeze-thaw cycles, and it was shown in thin section that the surface had largely disintegrated and some quartz particles had cracked.

The pressure generated by the expansion of the shale was calculated with reference to the uniform expansion of corroding steel reinforcements in concrete, which is a comparable process, modelled simply using a cylindrical steel bar running through a thick-walled concrete cylinder. This model suggested that the shale was unlikely to generate enough pressure to crack the render by swelling alone, but might cause cracking by absorbing water and then freezing. Hence the model demonstrated what had been observed experimentally. A more complex model based on the work of Jeffery [222] was then used to calculate the two dimensional stress distribution around the cavity containing the shale particle and along the render surface. This showed that the conical shape of the pop-outs is due to the variations in the tensile hoop stress around the cavity.

The flaking of the original render at East Fortune is largely unavoidable, since the expansive aggregates were part of the original mix, and nothing can be

done to alleviate the Scottish climate. However, it may be possible to slow down the deterioration by reducing the frequency or severity of wetting. The buildings did not originally have gutters, allowing rainwater to pour off the roofs and down the walls, but where gutters have been added at a later date the wetting of the walls has been reduced, and this intervention could be considered for all the airfield buildings.

11.1 Introduction

The previous four chapters reported on the research undertaken on the cement-rendered brick masonry buildings at NMOF, to understand how the properties of the historic bricks affect the render-brick bond, and to define the causes and mechanisms of render cracking and render blistering and flaking. This final investigative chapter describes the research undertaken in the air raid shelter, which was the only reinforced concrete building at NMOF (Fig. 11.1). The aims of the research were to:

- Record the method of construction of the shelter and establish the materials used, both to allow the shelter to be compared to similar shelters at other sites, and to identify any weaknesses in its design;
- Record the condition of the shelter, in order to define the types of deterioration;
- Understand how moisture moved through the structure, since moisture was highly likely to be involved in the deterioration mechanisms;
- Define the physical and chemical properties of the concrete, to identify potential causes of deterioration;
- Combine the results of the survey work and analytical testing to understand the causes and mechanisms of deterioration, and suggest how it would proceed in the future;
- Consider the treatment options available.

Like the investigations of the render repairs described in the previous chapter, this work is of interest to building conservation specialists and has been published [9].

Fig. 11.1 Interior of the air raid shelter at NMOF

11.2 Method

11.2.1 Visual assessment

Visual observations of the design and construction of the shelter were made and the dimensions were measured. The condition of the shelter was assessed and the results were recorded with photographs and on line drawings, using the numbering system shown in Fig. 11.2. Visual observations were also made to understand how moisture moved through the shelter in different weather conditions.

Fig. 11.2. Floor plan of the air raid shelter, showing the numbering system used for documentation purposes

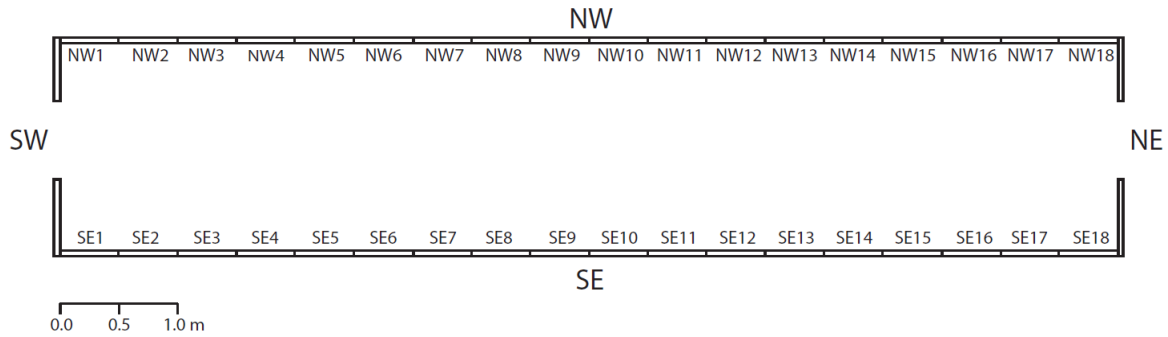

11.2.2 Testing to investigate patterns of moisture movement within the shelter

The moisture content of the concrete was investigated non-destructively using a combination of infrared thermography and electrical resistivity measurements. The equipment used is described in Chapter 4. The shelter was heated inside with an electric heater to assist with creating temperature differences in the concrete for the infrared camera to detect, and it was anticipated that areas with high moisture content would show up as cooler, because water evaporating from the wall surface would lower the surface temperature. Additionally, the moisture content of the concrete at various locations was measured directly by sampling small delaminating pieces and drying them to constant mass. The samples were taken shortly after rain, when some areas of the shelter were visibly wet.

11.2.3 Petrography

The visual condition survey was complimented by the petrographic examination of thin sections, as described in Chapter 5, in order to obtain information about the materials used, the workmanship and the causes and mechanisms of deterioration. The thin sections were made from delaminated fragments of the raised 'ribs' at the sides of the concrete sections, and they extended from the concrete surface down to the steel reinforcements which ran through the ribs. A thin section of the concrete from the Stanton shelter at Cark airfield was also examined for comparison. Cark Airfield is a Second World War airfield in Cumbria, England, with similar buildings to those at NMOF.

11.2.4 Physical properties

The physical properties of the concrete were investigated to provide more information about the quality of the concrete and the variation within the shelter. Non-destructive-testing was undertaken to identify variations in the surface properties of the concrete, using a rebound hammer, as described in Chapter 4 and Ultrasonic Pulse Velocity (UPV) testing. The UPV test machine was a C.N.S. Electronics Portable Ultrasonic Non-Destructive Digital Indicating Tester (PUNDIT) with 54 kHz transducers.

The rebound hammer readings were taken on each of the concrete sections within the long walls of the shelter, at heights of 0.5 m, 1.0 m, 1.5 m and 2.0 m above ground level. Three readings were taken at each height: one on the central flat panel and one from the ribs at either side, giving a total of 12 readings per section (Fig. 11.3). The readings were taken with the rebound hammer positioned perpendicular to the wall, which for the readings at 2.0 m resulted in the hammer being inclined at 8.1 ° to the horizontal, because of the curvature of the wall. According to the manufacturer's label, this should incur negligible skew. In places on the ribs where the concrete surface was lost or where the render was so badly cracked that the pressure of the hammer could have caused the delamination of a piece of concrete, a reading was not taken. One reading per panel was repeated a few weeks after the first set of readings, to investigate the repeatability of the readings.

Five locations with low, high and intermediate rebound hammer readings were selected for UPV testing, and the surface appearance of the concrete at each location was noted. The transducer arrangement was indirect, since the presence of the covering bank of earth over the outside of the shelter made it impossible to measure pulse transmission times through the thickness of the walls. However, a linear transducer arrangement was used as this may help to overcome uncertainties in measurements [48]. At each location the transmitter was held at a fixed position, and the receiver was moved vertically upwards to take readings 0.1 m, 0.2 m and 0.3 m above the transmitter (Fig. 11.4). The pulse velocity for each pairing was calculated, and if the concrete is reasonably homogeneous, the pulse velocity for each pairing should be roughly the same.

A 30 mm diameter core sample was then drilled from each of the five locations where UPV testing had been undertaken. There were some limitations in obtaining representative and good quality cores:

- Cores could only be drilled at heights of 1-1.5 m to allow the operator to exert sufficient force on the drill;
- It was found necessary to use a masonry bit to bite the concrete at the beginning of each core, and this left a small hole in the top of the sample;
- Some cores broke during the drilling process; the separate pieces were then treated as individual samples.

A further five 25 mm cores were drilled off-site from a large piece of delaminated concrete, which had come from the rib on the north east side of section NW17.

The concrete cores were initially used to measure porosity and sorptivity, as described in Chapter 6. They were then capped with gypsum plaster, to obtain parallel surfaces at each end, and their compressive strength was measured using an INSTRON 600 mechanical testing machine with a crosshead speed of 0.25 mm/min.

Fig. 11.3. Location of rebound hammer readings

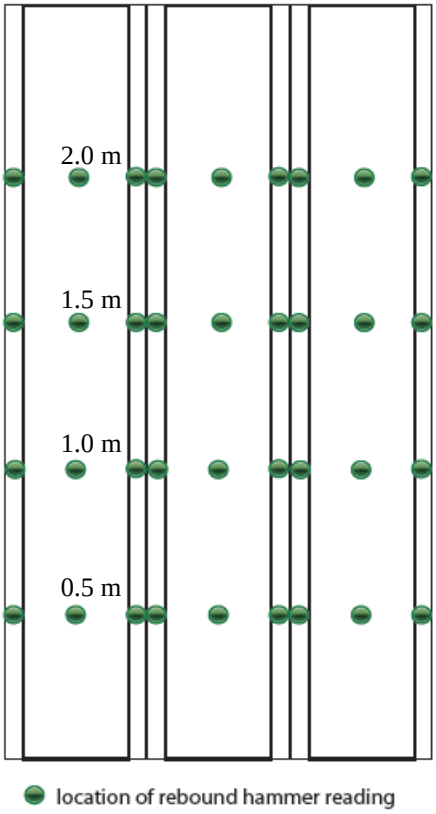

Fig. 11.4. A linear transducer arrangement for indirect UPV measurements (redrawn from Bungey and Millard [48])

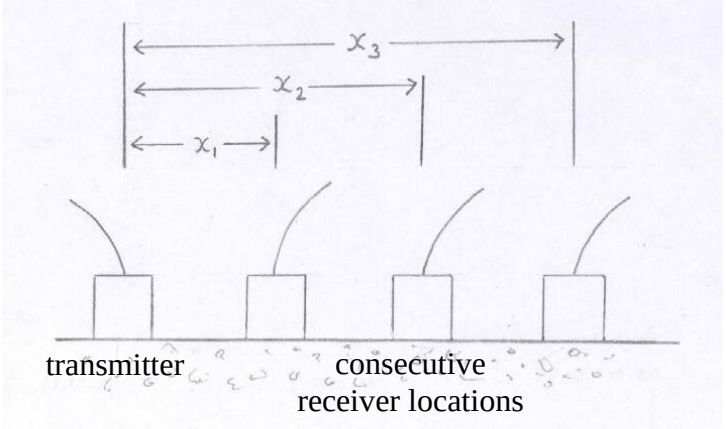

11.2.5 Chemical properties

The chemical properties of the concrete were investigated in order to establish why the steel reinforcements were corroding. As discussed in Chapter 2, there are two factors influencing the corrosion reaction: carbonation of the surrounding concrete and chloride attack [45]. Freshly made concrete has a pH of 12-13.5, due to the presence of alkaline calcium, sodium and potassium hydroxides, and the high pH causes a thin, protective layer of oxide to form on the surface of the steel, in a process known as passivation. However, over time the calcium hydroxide in the concrete reacts with carbon dioxide from the air to form calcium carbonate, which reduces the pH of the concrete to around 8-9. The carbonation front moves in from the surface, and when it reaches the concrete surrounding the reinforcements the passive layer breaks down and the steel corrodes. A high level of chlorides in the concrete – typically around 0.4% by weight of cement – will also cause the passive layer to break down, again allowing the steel to corrode.

Carbonation is more common, and is particularly rapid in wet/dry cycling environments, as found in the shelter. Carbonation is also very likely to lead to corrosion when the depth of the concrete cover is shallow, since the carbonation front can reach the steel reinforcements within a few years. The extent of carbonation of the concrete was assessed petrographically and was additionally investigated by spraying a freshly broken concrete surface with phenolphthalein indicator, prepared as described in Chapter 5. If the pH of the sample was above 9 it was stained bright purple by the phenolphthalein.

Analysis was also undertaken to look for chlorides in the concrete. Aqueous extractions from the cementitious fraction of concrete samples and the mortar joining the concrete sections together were prepared, and analysed with IC to determine concentrations of sulfate, chloride and nitrate ions, and ICP-OES for calcium, magnesium, potassium, sodium and aluminium ions, as described in Chapter 6. Extractions from a concrete Stanton shelter at Cark airfield in Cumbria, England, which also has a maritime environment, and from Second World War concrete defences on a beach near NMOF were also analysed for comparison.

11.3 Results

11.3.1 Design and construction of the air raid shelter

The shelter at the Museum of Flight was 18 sections long, with cementitious mortar used to join the sections together and bolts fixing the end walls to the long walls. The sections making up the long walls had a rebar running up the vertical rib on each side and around 20 thinner horizontal rebars running across the central panel (Fig. 11.5). The horizontal rebars were spaced irregularly and often placed at quite an angle to the horizontal. They may have helped to reduce cracking when the concrete was made, and would also have increased the ability of the concrete to withstand a blast. The vertical rebars had iron bolt-like protrusions spaced along them, probably intended to enhance the bond between the rebar and the concrete. Each end wall was constructed from four pre-cast reinforced concrete sections with ribs down the sides, fixed together with iron bolts to make a shape like an upended horseshoe.

Fig. 11.5. The placement of reinforcements within a concrete section

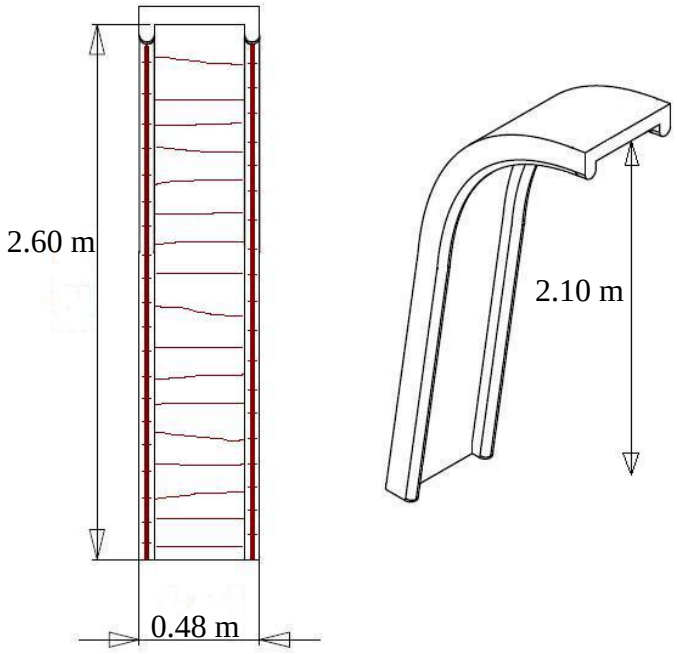

Air raid shelters were clearly only intended as temporary structures, and there were some obvious design faults making the shelter at NMOF prone to deterioration:

- The concrete cover over the horizontal rebars was only 1-3 mm, whereas much deeper cover would generally be recommended in order to protect the reinforcements from corrosion;
- The sections for the long walls were joined together with cementitious mortar rather than bolted and sealed with bitumen as recommended by the manufacturer, and these joints had the potential to fail and allow water penetration;
- There was no waterproofing barrier between the earth surrounding the shelter and the concrete sections, meaning that liquid water could move directly into the concrete.

11.3.2 Condition of the air raid shelter

The graphic condition survey for the north west interior elevation is given in Fig. 11.6, and the full graphic documentation recording the condition of the shelter is included in Appendix 1. The surface appearance of the concrete was found to vary considerably: it was sometimes smooth and compact, but elsewhere full of small voids, either because the original mix was too dry or because it was inadequately compacted (Fig. 11.7). The voids were particularly common in the curved sections at the top of the panels and in the ribs at the sides of the panels, where they often corresponded to areas of cracking and delamination, possibly because the voids permitted the easier passage of contaminants through the concrete. Hence although the appearance of the voids was not really an issue, their possible role in contributing to the deterioration of the concrete was important.

The most common type of deterioration was the corrosion of the rebars, which had generated significant expansive forces causing the concrete to crack and delaminate. As the horizontal rebars were close to the surface, they were often exposed with the loss of only a few millimetres of concrete. However, the corrosion had led to more substantial losses of concrete on the ribs where the bars were buried deeper (Fig. 11.8). The losses on the ribs were particularly severe at either end of the air raid shelter.

In addition, some of the mortar joints between the sections were disintegrating and some pieces of mortar had fallen out altogether. This may have contributed to the overall deterioration of the shelter by providing a route in for water. Evidence that the shelter was damp was seen in the black staining on the

surface of the concrete (Fig. 11.9), which was probably biological growth. Fluffy salt efflorescences were also sometimes present, mainly at the base of the walls (Fig. 11.10).

The problems experienced by the shelter at NMOF were clearly not unique, because the Stanton shelter at Cark airfield in Cumbria was observed to be in similar condition. From photographs some other Stanton shelters appeared to be in much better condition inside, and although this may have been because they had been extensively repaired, the shelters in good condition also had the sections bolted together throughout rather than joined with mortar. The bolting may be beneficial in reducing moisture ingress (Fig. 11.11).

Fig. 11.6. Graphic survey showing the condition of the NW interior elevation

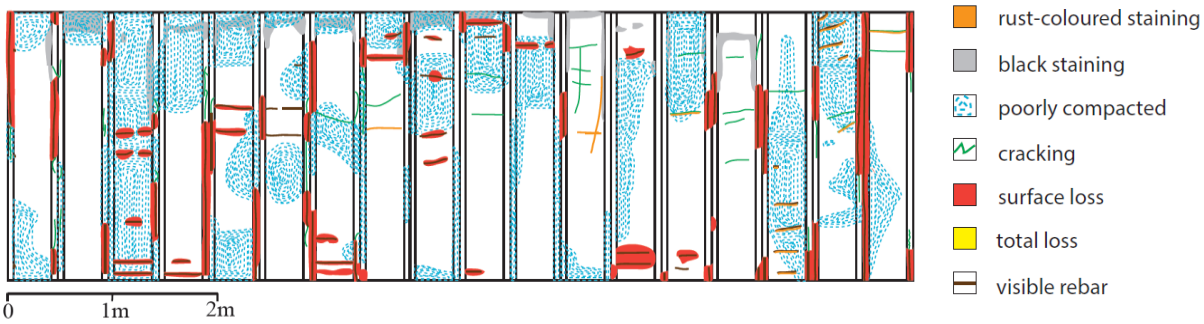

Fig. 11.7 Voids visible at the surface of the concrete

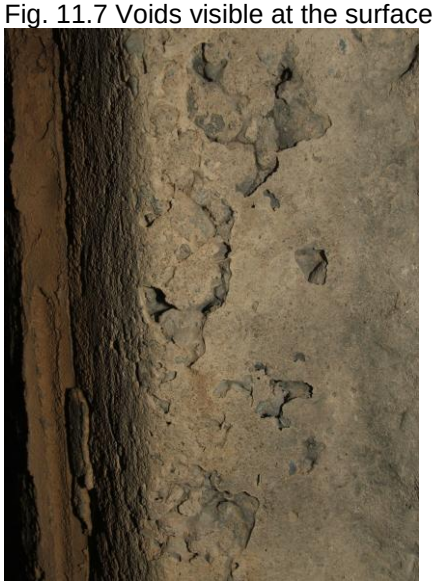

Fig. 11.8. The cracking and delamination of the concrete due to corrosion of the rebars

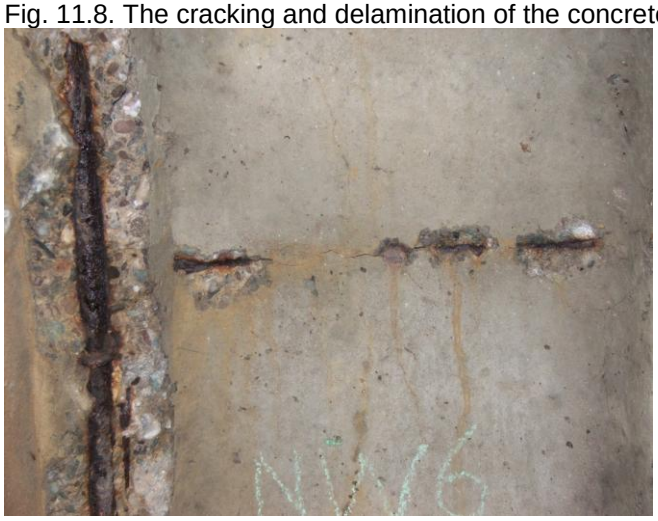

Fig. 11.9 Black staining on the surface of the concrete

Fig. 11.10 Salt efflorescences on the surface of the concrete

Fig. 11.11 The interior of the Stanton shelter at RAF Chilbolton, Hampshire, showing how the concrete sections have been bolted together along the ribs (Richard Hall).

11.3.3 Patterns of moisture movement within the shelter

11.3.3.1 Non-destructive investigations

Despite the fact that the concrete was in direct contact with the earthen floor, on dry days there was only a very thin strip of obviously wet concrete at the base of the walls, with a height of approximately 10 mm. After rain the concrete and the mortar joints between sections were visibly wet at the upper parts of the walls, in particular along the ribs (Fig. 11.12). This was caused by water from the soil outside moving through the concrete by capillary suction, and also by water leaking directly in through the gaps in the mortar joints and pouring over the surface of the concrete.

On a dry day the infrared thermography showed a colder zone around the base of the walls (Fig. 11.13), and while this was partly attributed to heat rising, due to the heater used to exaggerate temperature differences, it may also have been due to evaporative cooling. The electrical resistivity measurements were higher for a zone at the base of the walls, extending up to around 0.6 m, and so when considered together the two sets of readings appeared to indicate a zone of rising damp.

Fig. 11.12. Localised damp patches after rain

Fig. 11.13. Infrared thermograph, showing a cooler zone at the base of the walls (Maureen Young, Historic Scotland), with internal photograph for reference. The infrared thermograph is a false colour image showing the surface temperature of surfaces in °C, where the red areas are warmest and the purple areas are coolest

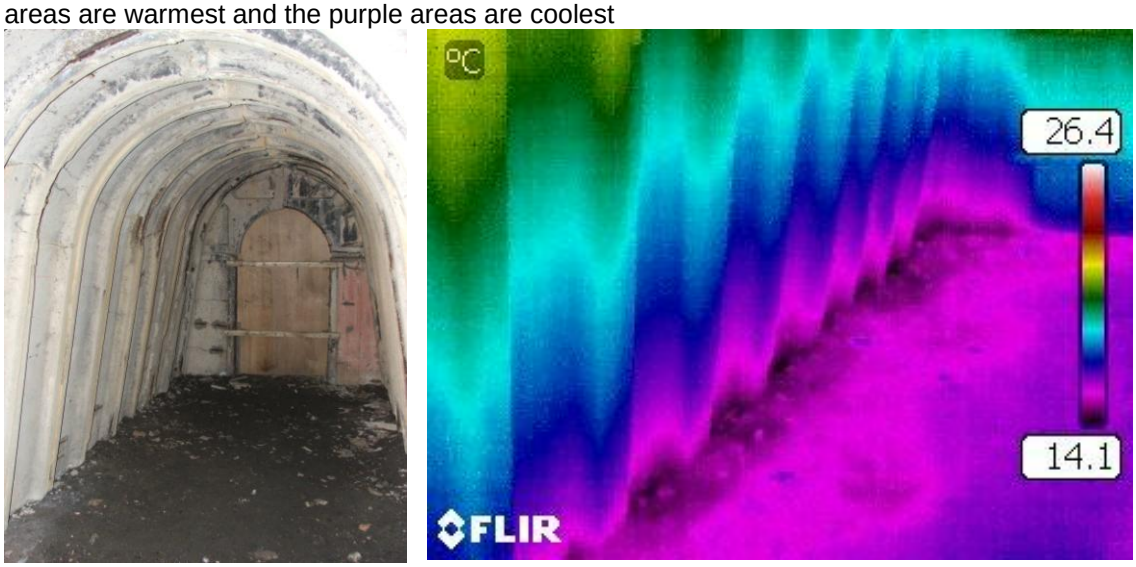

11.3.3.2 Direct measurement of moisture content

The results for the direct measurement of moisture content by drying samples to constant mass are given in Table 11.1, and show that concrete which was visibly wet had a moisture content of around 65% of the moisture content at saturation, while concrete that was from within the suspected zone of rising damp but appeared dry had a moisture content of only around 41% of the moisture content at saturation. This suggested that although there was a slight zone of rising damp at the base of the walls, this contributed less to the moisture content of the concrete than rainwater

moving in from above. Once moisture had entered the concrete the only way for it to leave was through the front surface of the walls, and because evaporation was likely to be slow due to the low temperatures and lack of air circulation, the concrete could potentially remain damp for most of the time.

Table 11.1 Moisture contents of concrete samples from different locations in the air raid shelter

location of sample	appearance	% moisture content	moisture content as a % of the moisture content at saturation
rib between NW5 and NW6, 0.39 m from ground	visibly wet	4.84	67.0
rib between NW10 and NW11, 1.55 m from ground	visibly wet	4.59	63.5
rib between NW10 and NW11, 1.56 m from ground	visibly slightly wet	4.23	58.5
SE9 central panel, 0.26 m from ground	dry	2.94	40.6

11.3.4 Petrographic examination of the concrete

The concrete used for the shelter appeared to be fairly good quality. It was generally dense and only partially carbonated, and there was no evidence of cracking. Crystallised calcite and portlandite were not visible on the surface or in the pores, suggesting that the initial water content of the mix was low and there had not been much water percolating through subsequently. The frequent occurrence of relict cement grains (pieces of the original cement clinker which had not been hydrated) again suggested a low initial water content. The aggregate was moderately sorted, and consisted predominantly of quartz particles and fragments of igneous rocks, in particular dolorites. Interestingly, although the concrete from the shelter at Cark airfield was of similar quality, it had a completely different aggregate mix, consisting mainly of limestone fragments. This would suggest that Stanton Ironworks was sourcing aggregates from more than one quarry, which seems likely given the number of shelters manufactured.

Fig. 11.14.Concrete from the shelter at NMOF, with coarse dolerite fragments visible on the left and the upper right, plane polarised light, field of view: 875 µm across

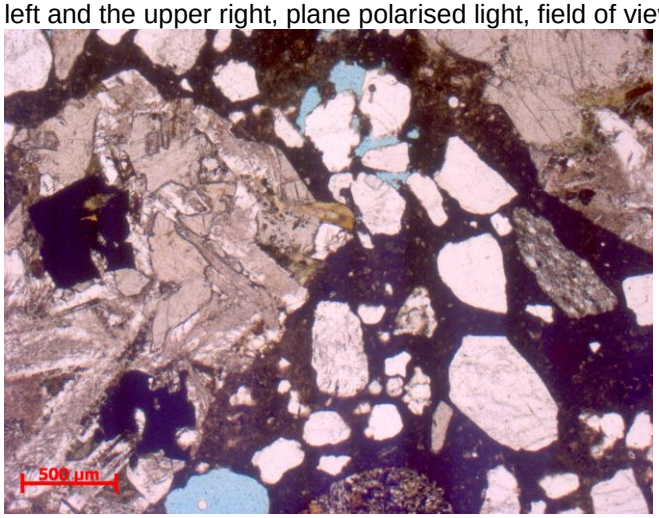

Fig. 11.15. Concrete from the shelter at Cark airfield, containing a large fossiliferous limestone fragment, plane polarised light, field of view: 875 µm across

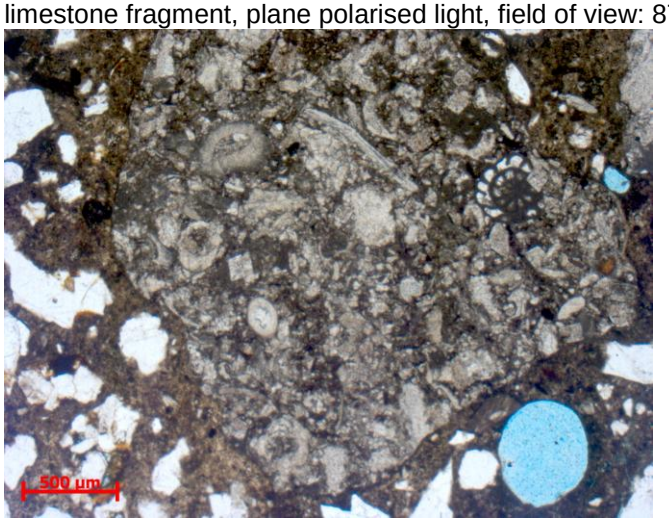

11.3.5 Physical properties of the concrete

As shown in Table 11.2, the compressive strength values obtained for the core samples varied from 20.9 MPa to 51.8 MPa, averaging 34.6 MPa, and these values are fairly high for a historic concrete [30, 85]. The compressive strength values did not correlate with the UPV readings, possibly because the UPV readings were affected by the small voids within the concrete, but they showed some correlation with the rebound hammer readings. For example, at NW11 the lowest average rebound hammer reading of 19 corresponded with the second lowest average compressive strength of 28.5 MPa, and at SE16 the highest average rebound hammer reading of 37 corresponded with the highest average compressive strength of 51.8 MPa. There was some correlation between the appearance of the concrete and the

compressive strength measured, with well compacted areas of concrete generally having higher compressive strength.

The porosity and sorptivity values are given in Table 11.3, with some comparative values for concrete samples made with a cement:sand:aggregate ratio of 1:2:4 [228], and although the porosities were slightly higher than those found by Hall, the sorptivities were at the bottom end of Hall's range. Hence overall the results suggest a good quality concrete with low moisture absorption properties. However, it has been noted that some of the concrete surfaces contained small voids, and it is possible that these areas would have been more permeable. The full results for the compressive strength, porosity and sorptivity values are given in Appendix 3.

Table 11.2 Physical properties of the concrete

location	height (m)	appearance of concrete	rebound hammer readings (rebound number)	UPV readings (pulse velocity in m/s)	compressive strength (MPa)
NW2	1.0	poorly compacted	31, 29, 25 average: 28	1.7, 2.0, 2.1 average: 1.9	32.4, 30.9 average: 31.7
NW11	1.0	poorly compacted	21, 19, 17 average: 19	2.6, 2.9, 2.7 average: 2.7	28.5 average: 28.5
NW17	1.5	fairly well compacted	not available	not available	28.7, 37.7, 20.9 average: 29.1
SE2	1.5	well compacted, but some cracking	31, 40, 33 average: 35	3.3, 2.7, 2.9 average: 3.0	36.4, 48.3 average: 42.4
SE6	1.0	fairly well compacted	19, 34, 34 average: 29	1.7, 2.0, 2.0 average: 1.9	30.1 average: 30.1
SE16	1.5	very well compacted	42, 37, 32 average: 37	2.6, 2.7, 2.2 average: 2.5	51.8 average: 51.8

Table 11.3 Porosity and sorptivity of the concrete

	porosity (%)	sorptivity ($mm/min^{1/2}$)
shelter concrete 1	15.0	0.1
shelter concrete 2	16.5	0.1
comparative concretes tested by Hall [228]	11.3-14.1*	0.09-0.35*

* The ranges of values quoted for the comparative concretes depend on the water:cement ratio (ranging from 0.40-0.80) and the degree of tamping.

11.3.6 Chemical properties of the concrete

From the petrography the concrete was found to be carbonated at the surface but only partially carbonated in depth. The staining with phenolphthalein indicator also showed the concrete to be carbonated at the surface but largely uncarbonated at depths past around 10 mm, presumably because of its density and low porosity (Fig.

11.16). This suggested that the corrosion of the reinforcements had not occurred due to carbonation of the concrete.

Fig. 11.16. Staining of concrete from the NMOF shelter with phenolphthalein indicator. The pH of the purple areas is above 9, and these areas have therefore not carbonated.

The results of the ions analysis of aqueous extracts from the concrete, given in Table 11.4 and fully in Appendix 3, showed that several of the concrete samples were high in chlorides. The maximum chloride content of 0.475 % obtained for the 'concrete 4' sample was significantly higher than that recorded for the other concrete and cement samples, and only slightly lower than for the sample of Second World War concrete from a beach close to NMOF. As discussed in Chapter 2, chloride content is often measured using an acid extraction technique, where levels of over 0.4% are considered to carry 'moderate corrosion risk in damp conditions' [45]. If an aqueous extraction technique is used, as in this research, fewer chloride ions will be extracted and the threshold value for moderate risk will be lower. Hence the value of 0.475% was definitely high enough to indicate a significant risk of corrosion, and the values ranging from 0.171% - 0.209% for some of the other samples also indicated some level of risk.

The source of the chlorides was unlikely to be the aggregate, since the petrography undertaken indicated that a marine aggregate was not used. Furthermore, since the high chloride levels did not correlate with high levels of sodium ions, airborne sodium chloride from the sea was also probably not the source of the chlorides. The groundwater was a possible source, and it was reported in Chapter 6

that the concentration of chlorides in the NMOF groundwater was very high[21]. However, in this case there should have been high concentrations of chlorides in the mortar joints and they were not found. This suggested that the chlorides were cast into the concrete, and since the sodium levels were low, it is possible that the source of chlorides was calcium chloride added as a set accelerator, as was common throughout the twentieth century until the 1970s [11].

The ions analysis indicated that the chlorides were concentrated slightly below the surface, and this result was verified by SEM-EDX of a concrete thin section, which showed that the chloride content varied from 0.14-0.24% at the surface of the concrete, and reached up to 0.78% at a depth of approximately 10 mm. The accuracy of the SEM-EDX analysis was checked with cement standards of known chloride content, as described in Appendix 6, and it was found that for standards containing 0.2% chloride or more, the average values obtained for analysis of three or more samples were accurate to ±0.11%.

The chloride distribution suggested that evaporation occurred below the surface, and Hall et al. [107] have shown that a sub-surface evaporation zone is characteristic of a section of wall with a varying moisture content, like the shelter walls.

[21] The concentration of chlorides in the groundwater from NMOF was approximately six times the maximum obtained by the British Geological Survey for ground water from the Inverclyde group in the Midland valley, which is approximately three miles from NMOF [141].

Table 11.4 Concentrations of some soluble ions in the concrete

sample*	% chloride	% nitrate	% sulfate	% Ca	% K	% Na	% Al
concrete 1	0.171	0.016	0.000	0.825	0.031	0.021	0.000
concrete 2	0.203	0.021	0.013	0.372	0.012	0.013	0.004
concrete 3	0.042	0.021	0.099	0.422	0.076	0.027	0.020
concrete 4	0.475	0.062	0.050	1.899	0.009	0.000	0.005
concrete 5	0.001	0.001	0.250	0.071	0.045	0.010	0.009
concrete 6	0.209	0.057	0.024	0.297	0.008	0.010	0.003
mortar 1	0.002	0.002	0.035	0.030	0.005	0.003	0.000
mortar 2	0.004	0.008	0.008	0.051	0.007	0.004	0.021
comparison 1	0.002	0.003	0.183	0.143	0.012	0.006	0.000
comparison 2	0.009	0.023	0.037	0.042	0.007	0.007	0.001
comparison 3	0.523	0.000	0.200	0.103	0.051	0.431	0.000

*Samples were as follows:
Concrete 1: flat panel of section NW3, 1 m from ground, sampled at surface
Concrete 2: flat panel of section NW3, 1 m from ground, sampled 50 mm below surface
Concrete 3: flat panel of section SE2, 1.5 m from ground, sampled at surface
Concrete 4: flat panel of section SE2, 1.5 m from ground, sampled 100 mm below surface
Concrete 5: rib of section NW17, 2 m from ground, sampled at surface
Concrete 6: rib of section NW17, 2 m from ground, sampled 100 mm below surface, adjacent to reinforcement
Mortar 1: mortar joint from 2 m from ground, sampled at surface
Mortar 2: mortar joint from 2 m from ground, sampled 100 mm below surface
Comparison 1: cement render from Building 24 (sample B24 OR NF3)
Comparison 2: Second World War concrete from Stanton shelter at Cark airfield
Comparison 3: Second World War concrete from beach near NMOF

11.4 Conservation options

If the corrosion of the reinforcements continues, the delamination of chunks of concrete will also continue and much of the surface concrete will eventually be lost. The appearance of the air raid shelter would then be significantly altered and it might also be structurally unstable. The aims of a conservation strategy are to slow down or stop the corrosion of the reinforcements and to repair the damage to the concrete. Concrete conservation needs to be approached with reference to the new European standard for concrete repair BS EN 1504, published in ten parts between 2003 and 2008. BS EN1504 gives 11 principles for ‘repair and protection of damages to the concrete and damages induced by reinforcement corrosion’ [13], but it should be applied judiciously because it has been developed for general repair situations rather than the conservation of historic structures, and it may therefore suggest inappropriate solutions in some situations. As many options as possible are listed in Table 11.5, even though they may not all be realistic for the shelter at NMOF.

Table 11.5 Conservation options for the air raid shelter at NMOF

option	relevant principle from BS EN 1504	appropriate treatment	advantages and disadvantages
1. Do nothing for a certain period of time	Not covered by a principle, but listed as an option in BS EN 1504-9	1. Do nothing	Would allow for further researching and testing of treatments, but in the meantime further concrete delamination would probably occur
2. Reduce the moisture content of the concrete	Principle 1: Protection against ingress	2a. Introduce physical barriers to limit water ingress (e.g. a waterproof membrane covering the shelter and sealing of the gaps between the concrete sections)	Simple, low-cost and would not alter the appearance of the shelter
	Principle 8: Increasing resistivity	2b. Limit moisture content by surface treatments	Some alteration of the surface appearance of the concrete, though this could be minimized if the coating were colourless
	No relevant principle	2c. Improve ventilation	A slight improvement could easily be achieved and would assist with drying out the concrete
			Options 2a–2c might slow down the corrosion reaction, but would be unlikely to stop it altogether
3. Remove chloride ions from the concrete	Principle 7: Preserving or restoring passivity	3. Electrochemical desalination	Expensive and time-consuming, but only minor disruption of the concrete. Might not stop the corrosion in areas where it has already begun
4. Reverse the polarity of the reinforcement to stop the corrosion reaction	Principle 10: Cathodic protection	4. Install cathodic protection system	Expensive and it would be necessary to try to conceal the anodes to avoid altering the surface appearance of the concrete, but potentially the most effective way of halting the corrosion reaction

5. Protect the surface of the reinforcement to stop the corrosion reaction	Principle 11: Control of anodic areas	5a. Paint reinforcements with suitable coatings	Major disruption of the concrete would be required to access the reinforcements, although the corrosion reaction would then be stopped
		5b. Apply a migratory corrosion inhibitor	Simple and would not alter the appearance of the concrete but might be ineffective
6. Remove the reinforcements altogether	Not covered by BS EN 1504 since it is assumed that the reinforcements are required for structural reasons, but this is probably not the case in the shelter	6. Remove reinforcements	Major disruption of the concrete would be required to access the reinforcements, but the corrosion reaction would then be stopped forever
7. Repair concrete losses	Principle 3: Concrete restoration	7. Undertake patch repairs where the concrete has delaminated off	Might help to slow down the corrosion of exposed rebars, but would alter the appearance of the shelter

A combination of the options listed in Table 11.5 is probably required to preserve the shelter. Given that water is undoubtedly contributing to the deterioration processes, treatments to reduce moisture ingress should be a priority, particularly since they are simple and minimally disruptive. BS EN 1504 should be used to evaluate potential materials for sealing the joints such as mortars, bitumen and modern sealants. The subsequent installation of a waterproof membrane would necessitate the removal of the overlying earth and the selection of a suitable material before the earth was replaced, with some thought given to landscaping to increase rainwater run-off. Improving the ventilation in the shelter would also help to dry out the concrete.

These strategies alone are unlikely to stop the corrosion altogether and so other options should be considered as well. The electrochemical techniques available (options 3 and 4) might be effective in halting the corrosion reaction without altering the appearance of the concrete, and advice should be sought from a concrete repair specialist. Painting the reinforcements with anti-corrosion coatings or removing them altogether should probably be considered the last resort because of the ensuing damage. Whatever else is done, extensive patch repairs will be required to make good the concrete.

11.5 Conclusions

The concrete used for the air raid shelter at NMOF appeared to be fairly good quality, with a low initial water content resulting in low sorptivity, high strength for a concrete of this age and very little cracking. The main type of deterioration observed was the corrosion of the steel reinforcements, which was causing the delamination of the overlying concrete. This appeared to be due to the localized presence of chloride ions rather than the carbonation of the concrete. Since high concentrations of chlorides were not found in the mortar used to join the concrete sections together, it was likely that the source of the chlorides was in the raw materials used in the concrete mix. The chloride levels were not matched by high levels of sodium ions and so the source may have been calcium chloride added as a set accelerator. The deterioration was probably promoted by the frequent wetting and drying of the concrete.

The conservation of the shelter is clearly necessary to prevent further loss of concrete and it is proposed that simple measures to reduce moisture ingress and improve ventilation should be implemented as soon as possible. The specification of further conservation interventions should now be undertaken with advice from a concrete repair specialist. Electrochemical techniques such as electrochemical desalination or the installation of a cathodic protection system appear promising ways of stopping the corrosion reaction while retaining the appearance of the shelter. BS EN 1504 has proved useful in providing a framework for assessing the structure and developing treatment options, but it needs to be applied judiciously because it has not been developed specifically for historic structures.

12.1 Introduction

This chapter summarises the main findings of the research undertaken. The conservation implications for the buildings at NMOF are discussed, followed by the implications for other historic cement-rendered and concrete buildings. The research methodology is reviewed, and suggestions are made for topics worthy of further research.

12.2 Research findings

Investigations into the history of East Fortune airfield and NMOF illustrated that the cement-rendered brick masonry buildings and reinforced concrete air raid shelter at NMOF were similar to Second World War buildings from across the UK, and that findings regarding the deterioration and conservation of the NMOF buildings were therefore likely to be relevant to many other sites. NMOF was particularly significant due to its completeness and the good state of preservation of the buildings. It was acknowledged that the conservation of wartime buildings is challenging because they were erected hurriedly and only intended as temporary structures, resulting in some poor detailing and a lack of features such as rainwater disposal goods. A review of the conservation history of the buildings at NMOF demonstrated that the buildings had been maintained throughout their lives, although early repairs had been fairly rudimentary. The approach to repairs undertaken more recently by NMS had been carefully planned, bearing good conservation practice in mind, but a lack of ongoing maintenance was contributing to the deterioration of some buildings.

The detailed visual surveys of the buildings at NMOF showed that the main types of deterioration affecting the cement render were cracking and delamination from the brick substrate; and surface blistering and flaking. Time lapse photography demonstrated that the cracking and delamination could proceed extremely rapidly, particularly during periods of cold weather, but that cracks could also remain virtually unchanged for years. Minor movement of cracks was detected using strain measurements. Infrared thermography identified areas where sub-surface voids were forming within the render as a precursor to flaking, and rebound hammer readings demonstrated that in areas where the render surface had flaked off, the cohesion of the remaining render was unaffected.

A combination of infrared thermography, electrical resistivity measurements and direct measurement of moisture content showed that the brick plinths on the cement-rendered buildings and the render just above the plinths were close to saturation, but that the zone of rising damp did not extend very far up the render. Surface temperature monitoring suggested that condensation occurred fairly frequently, contributing to the moisture content of the render, and rainfall was found to be an important source of moisture, particularly for the exposed piers on the buildings. Fortunately the weather station data showed that NMOF was relatively dry but very windy, with high evaporation rates during the summer. Despite the climate, the soil was found to be moderately wet for most of the time and approaching saturation during periods of heavy rainfall, which tied in with visual observations of water pooling on the surface of the ground.

Following on from the survey work and non-destructive testing, a strategy for sampling the building materials from NMOF was devised. The samples were examined at low and high magnification and characterized chemically and physically, and this provided information about the original and repair materials used at NMOF and assisted with identifying the causes and mechanisms of deterioration. It was found that the choice of materials and quality of the workmanship for the original renders were generally good, resulting in dense renders with minimal cracking and strong adhesion to the brick substrate. The aggregate mixes varied from building to building but there were two main types: fine, poorly graded, quartz aggregate and coarser, well graded, mixed rock aggregate. The poorly graded aggregate renders typically had higher porosity, higher sorptivity and a higher proportion of air voids than the well graded aggregate renders. The binder:aggregate ratio of the original renders varied from around 1:2 to 1:3, and it was concluded that the renders with poorly graded aggregate and low binder:aggregate ratios were most vulnerable to cracking. The poorly graded aggregate renders also tended to be stronger and more brittle than the bricks, whereas the well graded aggregate renders were reasonably compatible with the bricks in terms of strength and elastic modulus, meaning that they would generally undergo similar distortion due to loading and fail at the same point.

The cracking of the renders was investigated further with a dilation test that used LVDT measurements. It was found that cracking was unlikely to be caused by thermal or hygral movement, but that it could potentially result from freeze-thaw cycling, as visual observations had indicated. Vacuum-saturated render was significantly damaged after only three freeze-thaw cycles, and it was calculated that there was likely to be a permanently wet zone at the base of the walls, and that the render on the piers could become capillary saturated quite quickly when it rained. This suggested that the render in these areas probably reached the threshold value of 90% needed for frost damage to occur [179] for at least some of the time.

The dilation test showed that the expansion of vacuum-saturated brick samples upon freezing did not increase significantly with progressive cycling, and hence that the bricks were not significantly damaged by freeze-thaw cycling. It had been found that the original bricks were all fairly porous, with almost no small capillaries and a high percentage of air voids, and it was suggested that they were less prone to freeze-thaw damage than the render either because the very large pores were rarely filled completely with water, or because the absence of small pores limited the water supply to feed the ice crystals in the larger pores. It was also found that the bricks dried out much more rapidly from a saturated state than the render, which again would have reduced their vulnerability to freeze-thaw damage.

The strength of the bonds between the original renders and bricks were attributed largely to the high sorptivity of the bricks, generating powerful suction when the render was applied. The sorptivity of the bricks was investigated in a series of experiments, and it was suggested that variations in sorptivity between the different brick types were due to differing pore size distributions rather than variations in porosity. For some of the bricks the sorptivity was higher for a core drilled through the stretcher face than for a bed face core, and this appeared to be due to the presence of fine cracks and channel-shaped pores running parallel to the bed face, which were probably created by the pressing process. Additionally, for some samples the surface skin of the bricks was found to have a lower sorptivity than the interior of the brick, particularly for cores drilled through the bed face. This may partly have been because the porosity was lower at the surface, and may also have been due to the slightly hydrophobic properties of the bricks. The Wallyford bricks

had much lower sorptivity than the other bricks and were extremely hydrophobic, and it was suggested that the hydrophobic properties were either due to microbiological growth or to the presence of hydrophobic coke, produced by the firing of the colliery spoil included in the brick raw materials.

The low sorptivity of the Wallyford bricks played a key role in the failure of the render repairs applied to the free-standing wall on the south side of Building 25 in 2005. The repair mix had been specified carefully, resulting in a render with similar physical properties to the original, and it performed well in most areas. However, the thin section examination showed that the render applied to the free-standing wall behind Building 25 had an excessively high initial water content, and it was found that the free-standing wall had been rebuilt at some point with Wallyford bricks. Their failure to absorb sufficient moisture from the render resulted in a poor render-brick bond and the formation of shrinkage cracks at a microscopic and sometimes macroscopic level, which provided a route in for water.

The repair render applied to Building 23 in 1992 also failed rapidly. It had similar porosity to the poorly graded aggregate original renders but much higher sorptivity, which MIP suggested might be due to a low number of small capillaries and high concentration of air voids. It appeared from the thin section that the render contained an air-entraining agent, but the distribution of the voids was too irregular to provide protection against freeze-thaw damage. It was also evident from the thin section that the initial bond between the bricks and the render was poor, again probably because the modern bricks used to rebuild the wall did not provide adequate suction when the render was applied. Water entering the render through the pore structure or cracks would have filled the voids at the render-brick interface, creating damage if freezing occurred. Over time the render-brick bond would have weakened to the point where further freezing events could push sections of render off altogether.

The blistering and flaking of the original render was due to a different mechanism entirely. It was initially suspected that the flaking might be caused by sulfate salts such as ettringite, but ions analysis of the render indicated this was unlikely, and it was observed during the building survey that the flaking might be related to the presence of flaky grey and yellow aggregate particles. The thin section

examination of detached blisters of render suggested that mudstone aggregates had expanded and caused cracking within the renders, and this was confirmed by examination of render samples in a SEM. The blisters appeared to be pop-outs, which are a relatively well known type of concrete deterioration, whereby cone-shaped pieces of concrete scale off due to the presence of expansive aggregate particles just below the surface. In this case the particles causing the cracking had layered structures and were identified petrographically as shale and mud-rich sandstone. They were rich in clays, which XRD analysis suggested included traces of kaolinite, illite, chlorite and smectite. The latter two were the most significant, because smectite is a swelling clay and chlorite can be converted into smectite [149].

It was found from experiments with replica renders that shale from a local source increased the porosity of the render, increased the expansion of the saturated render due to ice formation and caused pitting after only a few freeze-thaw cycles. LVDT measurements showed that this shale underwent significant expansion due to water absorption, and even greater expansion due to water absorption followed by freezing. The strains measured were used to calculate whether the swelling shale could generate sufficient force to crack the render, using the model of the uniform expansion of steel reinforcements in concrete. The model suggested that the shale was unlikely to generate enough pressure to crack the render by swelling alone, but might cause cracking by absorbing water and then freezing, verifying what had been observed experimentally. A more complex model of a semi-infinite plate with a circular hole was used to demonstrate why cracking occurs at an inclined angle to the render surface, resulting in conical shaped pop outs.

The final area of research was the reinforced concrete air raid shelter. This was a mass-produced Stanton shelter, assembled on site from precast sections, and the concrete used appeared to be fairly good quality, with low sorptivity, high strength for a concrete of this age and very little micro-cracking. However, extensive delamination of the concrete had occurred, due to the corrosion of the underlying rebars. The corrosion was found to be caused by the localized presence of chloride ions rather than the carbonation of the concrete, and since high concentrations of chlorides were not detected in the mortar used to join the concrete sections together, it was likely that the source of the chlorides was in the raw materials used in the

concrete mix. The chloride levels were not matched by high levels of sodium ions, suggesting that the source might have been calcium chloride, added as a set accelerator. The frequent wetting and drying of the concrete that was observed probably accelerated the deterioration.

12.3 Conservation implications for the buildings at NMOF

The deterioration of the cement renders and concrete at NMOF was largely due to problems with the original materials and design of the buildings, which arose because the buildings were erected hurriedly and were only intended to be temporary. It would not generally be possible to address inadequacies in the materials retrospectively. For example, the shale aggregates causing flaking could not be removed from the renders, and nor could an air-entraining agent be introduced to protect them from freeze-thaw damage, although it might be possible to reduce the chloride content of the concrete in the air raid shelter using an electrochemical technique. Similarly, certain aspects of the building design such as the protruding piers and the inadequate window sills could not be altered without compromising the appearance of the buildings to an unacceptable level.

However, given that the main types of deterioration encountered at NMOF involved water, it might be possible to at least slow down the deterioration processes by reducing the availability of water. Appropriate measures could include adding rainwater disposal goods to buildings and increasing the overhang of the roofs to direct water away from the walls, as has already been done on buildings that have undergone major repairs. A physical barrier such as a waterproof membrane could be introduced to prevent the movement of water into the air raid shelter concrete, and the ventilation in the shelter could be improved.

Given that wetting of the render is often caused by poor maintenance, such as the failure to repair faulty rainwater disposal goods, an ongoing programme of regular maintenance would also help to ensure the longevity of the buildings. This should include repairing missing areas of render promptly, as they otherwise provide a route in for water and lead to further render losses.

12.4 Implications for other historic cement-rendered and concrete buildings

The types of deterioration found at NMOF are highly likely to be found in other historic cement-rendered and concrete buildings, particularly those of a similar age, and this research should therefore assist with the diagnosis of deterioration elsewhere. The cracking and delamination of cement renders is a common problem, and this research suggests that a good understanding of the moisture absorption properties of the substrate is necessary in order to achieve a good bond, and that cracking may be extremely difficult to avoid in cement renders which do not contain air-entraining agents or additives to improve flexibility. It also highlights the need for good workmanship and careful management of contractors, to ensure that specifications are followed when repairs are undertaken.

The diagnosis of pop-outs in cement renders is valuable because this phenomenon does not appear to have been reported elsewhere, even though the occurrence of pop-outs in mass concrete is relatively well known.

12.5 Methodology

This research demonstrates the variety of information which may be relevant to investigations of historic buildings. Visual surveys, non-destructive testing, environmental monitoring, petrographic examination, chemical analysis and the determination of a wide range of physical properties all contributed to understanding why and how the concrete and cement-rendered buildings at NMOF were deteriorating. Additionally, particular hypotheses were tested by devising appropriate experiments and by using simple models to quantify the phenomena observed.

Aspects of the methodology particularly worthy of mention are as follows:

- Detailed visual surveys of the buildings in a variety of weather conditions provided valuable clues about the deterioration mechanisms and reduced the risk of data being misinterpreted. For example, the role of soft, layered aggregate particles in contributing to the flaking and blistering of the render was realized from visual observations. Similarly, observations of the buildings during rainfall showed that the piers were wet most frequently, and thus helped to explain why the render on the piers was most prone to cracking.

- The use of historical information contributed to the understanding of the site. For example, the comparison of historic and current photographs gave an indication of the rate of deterioration, and reference to documentation about the Stanton Ironworks Company provided information about the construction of the air raid shelter.
- The thin section examination generated information which could not have been easily obtained by other means. This included observations of the appearance of the render-brick interface and the key finding that one of the repair renders had been applied in two separate layers with different cement contents, resulting in interfacial tensile stress.
- The use of replica render samples to investigate the behaviour of shale aggregates in a render subjected to freeze-thaw cycling, as described in Chapter 10, illustrates the value of replicas to test a particular hypothesis.
- The dilation test used to assess the ability of the brick and render to withstand freeze-thaw cycling had various limitations, as discussed in Chapter 8. However, it was extremely valuable in providing an indication of the freeze-thaw susceptibility of the original render after only three cycles, and this information could not have been obtained from three cycles of a standard freeze-thaw test. The test also proved useful for making comparisons between brick and render and hence in understanding how they behave when they are used together. Previous researchers had tested either brick or cement mortar, but not both.
- The model of a corroding reinforcement bar in a concrete cylinder used to calculate whether the strain due to the swelling aggregate was sufficient to crack the render, as described in Chapter 10, produced results which verified experimental observations. This suggested that the model was appropriate. The more complex model was also very useful to demonstrate why cracks occur at an inclined angle to the render surface, resulting in cone-shaped pop outs.

The approach described for this research yielded useful results and would be appropriate for other investigations on a similar scale, but it was too time-consuming to be used in its entirety for the investigations which typically precede a programme

of conservation work. Such investigations should always begin with a review of the documentary evidence and a detailed visual survey, but the non-destructive testing and analytical work undertaken will then depend on the specific questions that need to be answered.

12.6 Further research

As this research is very wide-ranging it offers many opportunities for further research. The differing sorptivities found in original bricks due to the presence of a surface skin could be fitted to a two-layer or n-layer model, which would calculate the variation of sorptivity with distance from the surface. Experiments could also be devised to investigate the reasons why the sorptivity of the surface skin tended to be lower than the sorptivity in depth, and the reasons for the slightly hydrophobic behaviour of the Edinburgh bricks, and the extremely hydrophobic behaviour of the Wallyford bricks.

In performing the LVDT experiments described in Chapters 8 and 10, it was found that some movement upon freezing was recorded even when the holder for the LVDT and the samples was made from invar alloy and the sample was also invar alloy. This may have been because the LVDT itself was made from stainless steel. Additionally, the data obtained contained artifacts, which were probably caused by slip in the screws fixing the LVDT within the holder. These problems were not insurmountable, but it would be desirable to eliminate them from the experimental method. A further constraint was that the experiment was very time-consuming because only one sample could be tested at once. Consequently only three freeze-thaw cycles were undertaken for each sample, and although these suggested that the length change experienced by the render upon freezing would increase until the render eventually failed, this could be stated more conclusively if further cycles were undertaken. Variations on the experiment with different freeze-thaw cycles could also be undertaken using a programmable instrument, such as a differential mechanical analyzer suitable for samples immersed in liquid.

The aim of the calculations undertaken in Chapter 8 using a simple sharp front model was to demonstrate that there was a zone of rising damp at the base of the rendered walls. The model could be developed to quantify the effect of the damp proof course on the height of rise of water in the walls. Additionally, the model

simply estimated the height of rise on a monthly basis using the average evaporation rate for each month. In practice the evaporation rate varies from hour to hour, and more accurate results could be obtained using a sharp front capillary rise model with time-dependent evaporation conditions or a finite-element unsaturated flow model, as described by Hall et al. [107].

More research could be done into conservation treatments for the buildings at NMOF and other historic cement-rendered and concrete buildings. As observed in Chapter 9, render repairs undertaken using modern cements are likely to be grey in colour and prone to cracking, particularly if they do not contain air-entraining agents. Modifications and alternatives include tinting repairs to reduce the grey colour, using polymer-modified mixes to improve flexibility, using air-entraining agents to reduce the risk of freeze-thaw damage and substituting hydraulic limes for cement. Appropriate mixes could be designed and evaluated with regards to whether they match the physical properties of original renders and how they perform in the long-term.

With regards to the conservation of the air raid shelter, trials could be undertaken to test some of the options discussed in Chapter 11 to arrest or retard the corrosion of the reinforcements, and repair the damage that has already occurred. The use of electrochemical techniques is a highly specialist area and would require input from a professional practitioner.

1. Lea, F.M. and Desch, C.H., *The chemistry of cement and concrete*, Edward Arnold & Co., London, UK (1935).

2. Mitchell, D.S. *The use of lime and cement in traditional buildings*, Inform guide, Historic Scotland, Edinburgh, UK (2007).

3. Gaspar, P.L. and de Brito, J., 'Limit States and Service Life of Cement Renders on Façades', *Journal of Materials in Civil Engineering*, Vol. 23, 2011, pp. 1396-1404.

4. Ellis, P., 'The Analysis of Mortar: the Past 20 Years', *Historic Churches*, 2002 (accessed online at http://www.buildingconservation.com/articles/mortar/mortar.htm, 24 October 2012).

5. Grattan-Bellew, P.E., 'Microstructural investigation of deteriorated Portland cement concretes', *Construction and Building Materials*, Vol. 10, No. 1, 1996, pp. 3-16.

6. Park, D., Kutter, B.L. and DeJong, J.T., 'Centrifuge modeling of a sensitive clay slope for simulation of strain softening' in *Seventh International Conference on Physical Modeling in Geotechnics*, 2010, pp. 159-164.

7. Broomfield, J., 'The Repair of Reinforced Concrete', *The Building Conservation Directory*, 1996 (accessed online at http://www.buildingconservation.com/articles/concrete/concrete.htm, 24 October 2012).

8. Addis, B. and Bussell, M., 'Key Developments in the History of Concrete Construction and the Implications for Remediation and Repair', in *Concrete Building Pathology*, ed. S. Macdonald, Blackwell, Oxford, UK (2003), pp. 15-105.

9. Griffin, I. and Tate, J., 'Conserving our Wartime Heritage: a Reinforced Concrete Air Raid Shelter in East Lothian, Scotland', *Journal of Architectural Conservation*, Vol. 18, No. 1, March 2012, pp. 81-100.

10. Hamilton, S.B., *A Note on the History of Reinforced Concrete in Buildings*, National Building Studies Special Report No. 24, London, UK (1956).

11. Ramachandran, V.S., 'Calcium chloride in concrete – applications and ambiguities', *Canadian Journal of Civil Engineering*, Vol. 5, No. 2, June 1978, pp. 213-221.

12. Clarke, J.L., *Historical approaches to the design of concrete buildings and structures*, Technical Report No. 70, The Concrete Society, Surrey, UK (2009).

13. Raupach, M., 'Concrete Repair According to the new European Standard EN 1504', in *Proceedings of the International Conference on Concrete Repair, Rehabilitation and Retrofitting (ICCRRR), 21-23 November 2005, Cape Town, South Africa*, eds. M. Alexander et al., Leiden, The Netherlands (2006), pp. 6-8.

14. Wittman, F.H., 'Deterioration Mechanisms Active in Reinforced Concrete Structures', *Restoration of Buildings and Monuments,* No. 7, 2001, pp. 263-270.

15. Skalny, J., Marchand, J. and Odler, I., *Sulfate attack on concrete,* Spon Press, London and New York (2002).

16. Corinaldesi, V., Moriconi, G. and Tittarelli, F., 'Thaumasite: evidence for incorrect intervention in masonry restoration', *Cement and Concrete Composites*, No. 25, 2003, pp. 1157-1160.

17. West, G., *Alkali-aggregate reaction in concrete roads and bridges,* Thomas Telford Publications, London, UK (1996).

18. Pigeon, M. and Pleau, R., *Durability of Concrete in Cold Climates,* E & FN Spon, London, UK (1995).

19. Broomfield, J., *Corrosion of steel in concrete*, Taylor and Francis, Oxford, UK (2007).

20. Sheehan, T. and Marsh, B., 'Concrete in the Future', in *Concrete Building Pathology*, ed. S. Macdonald, Blackwell, Oxford, UK (2003), pp. 241-260.

21. Rosário Veiga, M., Fragata, A., Velosa, A.L., Magalhães, A.C. and Margalha G., 'Lime-based Mortars: Viability for Use as Substitution Renders in Historical Buildings', *International Journal of Architectural Heritage: Conservation, Analysis, and Restoration*, Vol. 4, No. 2, 2010, pp. 177-195.

22. Farrell, D.M., Davies, K. and McCaig, I., 'Cathodic Protection of Iron and Steel, recent applications to heritage buildings', *The Building Conservation Directory*, 2001, (accessed online at http://www.buildingconservation.com/articles/cathodic/cathodic.htm, 27 July 2012).

23. Matthews, S., Murray, M., Boxall, J., Bassi, R. and Morlidge, J., 'Maintenance of Concrete Buildings and Structures', in *Concrete Building Pathology*, ed. S. Macdonald, Blackwell, Oxford, UK (2003), pp. 191-240.

24. Griffin, I., Hamilton, A. and Tate, J., 'The repair of historic cement renders, with reference to the buildings at a World War II airfield in East Lothian, Scotland', *Journal of the Building Limes Forum*, Vol. 19, 2012, pp. 57-65.

25. Banfill, P., ‘Options for the rehabilitation of buildings suffering from corrosion in reinforced concrete’, online article from Cobra 1995, RICS Research, London, UK, 1995 (accessed online at http://www.rics.org/site/scripts/downloads.aspx?categoryID=729, 21 March 2012).

26. British Geological Survey, *Natural Hydraulic Limes*, online fact sheet, (accessed online at www.bgs.ac.uk/downloads/start.cfm?id=1365, 21 March 2012).

27. Williamson, G., ‘Achieving successful repairs’, *CONCRETE*, Vol. 42, No. 2, March 2008, pp. 10–11.

28. Farrell, D.M., ‘Concrete repairs to Tynemouth Coastal Battery’, unpublished report for Rowan Technologies Limited, 2009 (accessed online at http://www.rowantechnologies.co.uk/tynmouth_battery_report_2009.pdf, 27 July 2012).

29. Broomfield, J. and Macdonald, S., ‘Repairing Damaged Concrete’, in *Concrete Building Pathology*, ed. S. Macdonald, Blackwell, Oxford, UK (2003), pp. 161-188.

30. Wright, A. and Kendall, P., ‘The Listening Mirrors. A Conservation Approach to Concrete Repair Techniques’, *Journal of Architectural Conservation*, March 2008, pp. 33-54.

31. Arizzi, A., Viles, H. and Cultrone, G., ‘Experimental testing of the durability of lime-based mortars used for rendering historic buildings’, *Construction and Building Materials*, Vol. 28, 2012, pp. 807-818.

32. Idorn, G.M., *Durability of Concrete Structures in Denmark, A Study of Field Behaviour and Microscopic Features*, Technical University of Denmark, Copenhagen, (1967).

33. Katzer, J., ‘An example of durability of concrete’, *Restoration of Buildings and Monuments*, Vol. 12, No 1, 2006, pp. 81-86.

34. Onton, H., ‘Estimation of residual carrying capacity and restoration of the historic reinforced concrete shells and frames erected in Estonia’, in *Structural Studies, Repairs and Maintenance of Heritage Architecture X*, ed. C.A. Brebbia, Prague, Czech Republic (2007), pp. 407-417.

35. Thomasen, S.E. and Searls, C.L., ‘Durability of concrete ornaments on historic structures’ in *Durability of Building Materials and Components, Proceedings of the Fifth International Conference held in Brighton, UK, 7-9 November 1990*, eds. J.M. Baker, P.J. Nixon, A.J. Majumdar and H. Davies (1990), pp. 433-444.

36. Brown, J.H., 'Carbonation. The effect of exposure and concrete quality: field survey results from some 400 structures', in *Durability of Building Materials and Components, Proceedings of the Fifth International Conference held in Brighton, UK, 7-9 November 1990*, eds. J.M. Baker, P.J. Nixon, A.J. Majumdar and H. Davies (1990), pp. 249-258.

37. Young, M., 'Thermal survey at Hill House, Helensburgh', *Focus*, Historic Scotland, 2011, pp. 20-21.

38. Wiles, A., 'St John and St Mary Magdalene, Goldthorpe: the conservation of an early concrete building', *ASCHB Transactions*, Vol. 32, 2009, pp. 40-50.

39. Letellier, R., *Recording, Documentation and Information Management for the Conservation of Heritage Places, Guiding Principles*, the Getty Conservation Institute, Los Angeles (2007) (accessed online at http://www.getty.edu/conservation/publications_resources/pdf_publications/guiding_principles.pdf, 31 July 2012).

40. ICOMOS, *Principles for the recording of monuments, groups of buildings and sites*, ICOMOS, Paris, France (1996) (accessed online at http://www.international.icomos.org/charters/archives-e.pdf, 31 July 2012).

41. Cooper, N., *Guide to Recording Historic Buildings*, Butterworth Architecture, London and Boston (1990).

42. English Heritage, *Understanding Historic Buildings, A guide to good recording practice*, English Heritage Publishing, London, UK (2006) (accessed online at http://www.english-heritage.org.uk/publications/understanding-historic-buildings/, 31 July 2012).

43. Historic Scotland, *Measured Survey and Building Recording*, ed. R. Dallas, Historic Scotland, Edinburgh, UK (2003).

44. Institute for Archaeologists, *Standard and guidance for the archaeological investigation and recording of standing buildings or structures*, Institute for Archaeologists, Reading, UK (2008) (accessed online at http://www.archaeologists.net/sites/default/files/node-files/ifa_standards_buildings.pdf, 31 July 2012).

45. Broomfield, J., 'The Identification and Assessment of Defects, Damage and Decay', in *Concrete Building Pathology*, ed. S. Macdonald, Blackwell Science Ltd., Oxford, UK (2003), pp. 140-160.

46. BS EN 1504, British Standards Institution, London, UK (2003-2009).

47. English Heritage, *Concrete*, part of the Practical Building Conservation series, to be published in 2013, English Heritage, London, UK (preview accessed online at http://www.english-

heritage.org.uk/content/publications/publicationsNew/concrete-conservation/concrete-marketing-spreads.pdf, 24 October 2012).

48. Bungey, J. and Millard, S., *Testing of Concrete in Structures*, Blackie Academic & Professional, Glasgow, UK (1996).

49. G B Geotechnics Ltd., *Non-destructive investigation of standing structures*, Technical Advice Note 23, Historic Scotland, Edinburgh, UK (2001).

50. Breyss, D., *Non-Destructive Assessment of Concrete Structures: Reliability and Limits of Single and Combined Techniques*, State-of-the-Art Report of the RILEM Technical Committee 207-INR, Springer (2012).

51. International Concrete Repair Institute, *Nondestructive evaluation (NDE) methods for condition assessment, repair, and performance monitoring of concrete structures*, ICRI Guideline, Rosemont, IL, USA (2009).

52. Meneely, J., Smith, B., Curran, J. and Ruffell, A., 'Developing a 'Non-destructive scientific toolkit to monitor monuments and sites', in *ICOMOS Scientific Symposium: Changing World, Changing Views of Heritage, Valletta, Malta* (2009)
(accessed online at
http://www.international.icomos.org/adcom/malta2009/pdf/ADCOM_200910_SYMP_1_Documentation_John_Meneely.pdf, 24 October 2012).

53. Spodek, J. and Rosina, E., 'Application of Infrared Thermography to Historic Building Investigation', *Journal of Architectural Conservation*, Vol. 15, No. 1, March 2009, pp. 65-81.

54. Avdelidis, N.P. and Moropoulou, A., 'Applications of infrared thermography for the investigation of historic structures', *Journal of Cultural Heritage*, No. 5, 2004, pp. 119-127.

55. Pinchin, S.E., 'Techniques for monitoring moisture in walls', *Reviews in Conservation*, No. 9, 2008, pp. 33-45.

56. Sirieux, C., Lataste, J.F., Breysse, D., Naar, S. and Dérobet, X., 'Comparison of non-destructive testing: Infrared thermography, electrical resistivity and capacity methods for assessing a reinforced concrete structure', *Journal of Building Appraisal*, Vol. 3, No. 1, 2007, pp. 77-88.

57. Sass, O. and Viles, H., 'Wetting and drying of masonry walls: 2D-resistivity monitoring of driving rain experiments on historic stonework in Oxford, UK', *Journal of Applied Geophysics*, 70, 2010, pp. 72-83.

58. Institution of Structural Engineers, *Appraisal of existing structures*, third edition, The Institution of Structural Engineers, London, UK (2010).

59. Basu, A. and Aydin, A., 'A method for normalization of Schmidt hammer rebound values', *International Journal of Rock Mechanics and Mining Sciences*, 41, 2004, pp. 1211-1214.

60. Pucinotti, R. and De Lorenzo, R.A., 'In situ non-destructive testing: the steel and concrete resistance assessment of ancient r/c structures', in *Structural studies, repairs and maintenance of heritage architecture IX*, Wit Press, Southampton, UK (2005), pp. 355-364.

61. Tay, D.C.K. and Tam, C.T., 'In situ investigation of the strength of deteriorated concrete', *Construction and Building Materials*, Vol. 10, No. 1, 1996, pp. 17-26.

62. Munsell, A.H., *Color balance illustrated, an introduction to the Munsell system (1913),* Kessinger Legacy Reprints, Whitefish, MT, USA (2010).

63. Ingham, J., *Geomaterials under the microscope,* Manson Publishing, London, UK (2011).

64. St.John, D.A., Poole, A.B. and Sims, I., *Concrete petrography: a handbook of investigative techniques,* Arnold, London, UK (1998).

65. The Concrete Society, *Concrete petrography: an introductory guide for the non-specialist,* Technical Report No.71, The Concrete Society, Surrey, UK (2010).

66. Fookes, P.G., Lay, J., Sims, I. and West, G., *Aggregates: Sand, Gravel and Crushed Rock Aggregates for Construction Purposes,* third edition, Engineering Geology Special Publication 17, Geological Society, London, UK (2001).

67. Adams, A.E., MacKenzie, W.S. and Guilford, C., *Atlas of sedimentary rocks under the microscope,* Pearson Education Limited, Essex, UK (1984).

68. MacKenzie, W.S., Donaldson, C.H. and Guilford, C., *Atlas of igneous rocks and their textures,* Pearson Education Limited, Essex, UK (1982).

69. Yardley, B.W.D., MacKenzie, W.S. and Guilford, C., *Atlas of metamorphic rocks and their textures,* Longman Scientific and Technical, Essex, UK (1990).

70. The Concrete Society, *Concrete core testing for strength,* Technical Report No.11, The Concrete Society, Surrey, UK (1987).

71. The Concrete Society, *Non-structural cracks in concrete*, Technical Report No.22, fourth edition, The Concrete Society, Surrey, UK (2010).

72. Derluyn, H., Janssen, H. and Carmeliet, J. 'Influence of the nature of interfaces on the capillary transport in layered materials', *Construction and Building Materials*, No. 25, 2011, pp. 3685–3693.

73. Brocken, H.J.P., Adan, O.C.G. and Pel, L., 'Moisture transport properties of mortar and mortar joint: a NMR study', *Heron*, No. 42, 1997, pp. 55-69.

74. Hughes, J. and Válek, J., *Mortars in Historic Buildings: A review of the Conservation, Technical and Scientific Literature*, Historic Scotland, Edinburgh, UK (2003).

75. Parrott, L.J., 'Assessing carbonation in concrete structures', in *Durability of Building Materials and Components, Proceedings of the Fifth International Conference held in Brighton, UK, 7-9 November 1990,* eds. J.M. Baker, P.J. Nixon, A.J. Majumdar and H. Davies (1990), pp. 575-586.

76. Stewart, J. and Moore, J., 'Chemical Techniques of Historic Mortar Analysis', in *Mortars, Cements, and Grouts Used in the Conservation of Historic Buildings,* ICCROM, Rome, Italy (1981), pp. 297-310.

77. Schnabel, L., 'Mortar Analysis', *Building Renovation*, September/October 1993, pp. 25-28.

78. Schnabel, L., 'Mortar Analysis Part 2: Analytical Methods', *APT Bulletin*, Vol. 40, No. 2, 2009, pp. 1-7.

79. Blaine Cliver, E., 'Tests for the Analysis of Mortar Samples', *APT Bulletin*, Vol. 6, No. 1, 1974, pp. 68-73.

80. Walsh, J.J., 'Distinguishing natural cement from other binders in historical masonry construction using forensic microscopy techniques', in *Second American Natural Cement Conference, Washington DC, March 2006,* American Society for Testing and Materials Special Technical Publication, Vol. 1494, 2008, pp. 20-31.

81. Jedrzejewska, H., 'Old Mortars in Poland: A New Method of Investigation', *Studies in Conservation*, Vol. 5, No. 4, 1960, pp. 132-138.

82. Fritz, S.J., 'A survey of charge-balance errors on published analyses of potable ground and surface waters', *Ground Water*, Vol. 32, No. 4, July-August 1994, pp. 539-546.

83. Artiz-Young, R., 'Sands for use in lime mortars and renders in new-build construction', *Journal of the Building Limes Forum*, Vol. 17, 2010, pp. 54-60.

84. Raphael, J.M., 'Tensile strength of concrete', *Journal of the American Concrete Institute*, Vol. 81, No. 2, 1984, pp. 158-165.

85. Neville, A. M., *Properties of Concrete*, third edition, Pittman, London, UK (1981).

86. Bartojay, K. and Joy, W., 'Long-term properties of Hoover Dam mass concrete', in *Hoover Dam : 75th Anniversary History Symposium, Proceedings of a conference held in Las Vegas, October 21-22, 2010,* eds. R.L. Wiltshire, D.R. Gilbert and J.R. Rogers (2010), pp. 74-84.

87. Somerville, G., 'Cement and concrete as materials: changes in properties, production and performance', in *Historic Concrete: Background to Appraisal,* eds. R.J.M. Sutherland, D. Humm and M. Chrimes, Thomas Telford, London, UK (2001), pp. 105-116.

88. Moropoulou, A., Tsiourva, Th., Bisbikou, K., Biscontin, G., Bakolas, A. and Zendri, E., 'Hot lime technology imparting high strength to historic mortars', *Construction and Building Materials,* Vol. 10, No. 2, March 1996, pp. 151-159.

89. Vintzileou, E. N. and Adami, C., 'The bond mechanism in stone- or brick-to-grout interfaces', *Strain,* Vol. 45, No. 5, October 2009, pp. 400-409.

90. Naik, T.R., Kraus, R.N. and Rakesh, K., 'Influence of types of coarse aggregates on the coefficient of thermal expansion of concrete', *Journal of Materials in Civil Engineering*, Vol. 23, No. 4, April 2011, pp. 467-472.

91. Krakowiak, K.J., Lourenço, P.B. and Ulm, F.J., 'Multitechnique investigation of extruded clay brick microstructure', *Journal of the American Ceramic Society*, Vol. 94, pp. 3012-3022.

92. Zsembery, S., Adams, G. and McNeilly, T., 'Determining the compressive strength of clay bricks', in *Proceedings of the Sixth International Brick Masonry Conference, Rome, May 1982* (1982), pp. 308-320.

93. Fernandes, F. and Lourenço, P.B., 'Evaluation of the compressive strength of ancient clay bricks using microdrilling', *Journal of Materials in Civil Engineering,* No. 19, 2007, pp. 791-800.

94. Azehnha, M., Faria, R., Magalhães, F., Ramos, L. and Cunha, A., 'Measurement of the E-modulus of cement pastes and mortars since casting, using a vibration based technique', *Materials and Structures,* Vol. 45, Nos. 1-2, 2012, pp. 81-92.

95. Klingner, R.E., 'Using autoclaved aerated concrete correctly', *The Masonry Magazine,* June 2008 (accessed online at http://www.masonrymagazine.com/6-08/autoclaved.html, 4 September 2012).

96. Zhang, F., Rougelot, T. and Burlion, N., 'Porosity of concrete: influence of test conditions and material variability', *European Journal of Environmental and Civil Engineering*, Vol. 16, Nos. 3-4, March-April 2012, pp. 311-321.

97. Aligizaki, K.K., *Pore structure of cement-based materials*, Taylor and Francis, London and New York (2006).

98. Hall, C. and Tse, T.K., 'Water movement in porous building materials – VII. The Sorptivity of Mortars', *Building and Environment*, Vol. 12, No. 2, 1986, pp. 113-118.

99. Lian, C., Zhuge, Y. and Beecham, S., 'The relationship between porosity and strength for porous concrete', *Construction and Building Materials*, Vol. 25, 2011, pp. 4294-4298.

100. Pavía, S. and Bolton, J., *Stone, brick and mortar: historical use, decay and conservation of building materials in Ireland*, Wordwell Ltd., Co.Wicklow, Ireland (2000).

101. Hall, C. and Hoff, W.D., *Water transport in brick, stone and concrete*, second edition, Taylor & Francis, London and New York (2011).

102. Gummerson, R.J., Hall, C. and Hoff, W.D., 'Water movement in porous building materials – II. Hydraulic suction and sorptivity of brick and other masonry materials', *Building and Environment*, Vol. 15, 1980, pp. 101-108.

103. Winslow, D.N., Cohen, M.D., Bentz, D.P., Snyder, K.A. and Garboczi, E.J., 'Percolation and pore structure in mortars and concrete', *Cement and Concrete Research*, Vol. 24, No. 1, 1994, pp. 25-37.

104. Mindess, S., Young, J.F. and Darwin, D., *Concrete*, second edition, Prentice Hall, Englewood Cliffs, New Jersey, USA (2002).

105. Bläuer, C., Häberli, H., Löffel, A. and Rousset, B., 'Repair mortars for the sandstones of the Cathedral of Berne', *Proceedings of the Second Historic Mortars Conference, 22-24 September 2010, Prague, Czech Republic*, eds. J. Válek, C. Groot and J.J. Hughes, Rilem Proceedings Pro 78 (2010), pp. 909-916.

106. Rousset-Tournier, B., *Transferts par capillarité et évaporation dans des roches – rôle des structures de porosité*, doctoral thesis, Louis Pasteur University, Strasbourg, Switzerland (2001) (accessed online at http://www.csc-sarl.ch//files/theserousset2001.pdf?11,16, 13 November 2012).

107. Hall, C., Hamilton, A., Hoff, W.D., Viles, H.A. and Eklund, J.A., 'Moisture dynamics in walls: response to micro-environment and climate change', *Proceedings of the Royal Society*, Vol. 467, 2011, pp. 194-211.

108. Blocken, B. and Carmeliet, J., ‘A review of wind-driven rain research in building science’, *Journal of Wind Engineering and Industrial Aerodynamics,* Vol. 92, 2004, pp. 1079-1130.

109. Cutler, N. and Viles, H., ‘Eukaryotic microorganisms and stone biodeterioration’, *Geomicrobiology Journal*, Vol. 27, 2010, pp. 630–646.

110. Curteis, T., ‘The survey and identification of environmental deterioration’, *The Building Conservation Directory*, London (2008) (accessed online at http://www.buildingconservation.com/articles/envdet/environment.html, 13 November 2012).

111. Norberg, P., ‘Monitoring of surface moisture by miniature moisture sensors’, in *Durability of Building Materials and Components, Proceedings of the Fifth International Conference held in Brighton, UK, 7-9 November 1990*, eds. J.M. Baker, P.J. Nixon, A.J. Majumdar and H. Davies (1990), pp. 539-550.

112. Pender, R., 'Monitoring the surface temperature of wall paintings', in *Non-destructive Testing to Evaluate Damage due to Environmental Effects on Historic Monuments, preprints of the EC Workshop at Trieste, 1996* (1996).

113. Sensirion, *Application Note, Dew-point Calculation*, on-line factsheet (accessed online at http://irtfweb.ifa.hawaii.edu/~tcs3/tcs3/Misc/Dewpoint_Calculation_Humidity_Sensor_E.pdf, 13 November 2012).

114. Chun, K.P., Wheater, H.S. and Onof, C., ‘Projecting and hindcasting potential evaporation for the UK between 1950 and 2099’, *Climatic Change,* Vol. 113, 2012, pp. 639-661.

115. Monteith, J.L. and Unsworth, M.H., *Principles of Environmental Physics,* second edition, Hodder and Stoughton, London, New York, Melbourne and Auckland (1990).

116. Gavilán, P. and Castillo-Llanque, F., ‘Estimating reference evapotranspiration with atmometers in a semiarid environment’, *Agricultural Water Management*, Vol. 96, 2009, pp. 465-472.

117. Hall, C. and Hoff, W.D., ‘Rising damp: capillary rise dynamics in walls’, *Proceedings of the Royal Society,* Vol. 463, 2007, pp. 1871-1884.

118. Renshaw, J., *East Fortune Airfield Conservation Plan*, unpublished report for National Museums Scotland, Edinburgh, UK (2004).

119. Lake, J., ‘Conserving military airfields’, *Context,* No. 66, June 2000, pp. 20-24.

120. Bunyan, I., Storer, J. and Thompson, C., *East Fortune, Museum of Flight and History of the Airfield*, Royal Scottish Museum, Edinburgh, UK (1983).

121. Newman, G., *From Airships to Airshows, a brief history of East Fortune Airfield*, unpublished report for National Museums Scotland, Edinburgh, UK (undated).

122. Francis, P., *British Military Airfield Architecture*, Patrick Stephens Ltd, Yeovil, UK (1996).

123. Air Ministry, *The Royal Air Force Builds for War, A History of Design and Construction in the RAF: 1935-1945*, HMSO, London, UK (1997).

124. Stanton Ironworks Company Limited, *Stanton at War*, Derbyshire, UK (undated). (Accessed online at www.stantonironworks.co.uk, 26 September 2011).

125. Stanton Ironworks Company Limited, 'A hundred shelters a week', *The Stantonian*, date unknown, pp.3.

126. Forster, A., *Report on Building No. 25*, unpublished report undertaken by the Scottish Lime Centre for Smith Scott Mullan Associates on behalf of National Museums Scotland, Edinburgh, UK (2004).

127. Lafarge, *Dunbar Works Internet Edition*, online publication (accessed online at http://www.lafarge.co.uk/pdf/dunbar.pdf?xtmc=historycementworks&xtcr=2, 15 November 2012).

128. Hercock, H., *Conservation of buildings at East Fortune military airfield*, unpublished report for BEng Individual Project, University of Edinburgh, UK (2010).

129. National Museums Scotland, *Buildings Development Strategy*, unpublished internal report, Edinburgh, UK (1992).

130. Renshaw, J., *East Fortune Airfield Conservation Plan*, unpublished report for National Museums Scotland, Edinburgh, UK (2004).

131. Gareth Hoskins Architects, *The National Museum of Flight Development Plan*, unpublished report for National Museums Scotland, Edinburgh, UK (2006).

132. National Museums Scotland, *List of works for refurbishment of Air Raid Shelter at Museum of Flight, East Fortune*, unpublished internal report, Edinburgh, UK (2004).

133. National Museums Scotland, *Completed survey summer 2004*, unpublished internal report, National Museums Scotland, Edinburgh, 2004.

134. Johnson, R.W., 'The significance of cracks in low-rise buildings', web publication, 2001 (http://www.humboldtmfg.com/pdf/cracks-low-rise-buildings.pdf, accessed 1 August 2012).

135. Delta-T Devices Ltd., *ThetaProbe Soil Moisture Sensor Type ML2x, User Manual*, Delta-T Devices Ltd., Cambridge, UK (1999).

136. Macaulay Institute website,
(Accessed online at http://www.macaulay.ac.uk/explorescotland/gleys.html, 28 August 2012).

137. Met Office website,
(Accessed online at www.metoffice.gov.uk, 28 August 2012).

138. Belcher, R. and Nutten, A.J., *Quantitative inorganic analysis*, third edition, written in association with A.M.G. Macdonald, Butterworths, London, UK (1970).

139. Wong, H.S. and Buenfeld, N.R., ' Determining the water-cement ratio, cement content, water content and degree of hydration of hardened cement paste: method development and validation on paste samples', *Cement and Concrete Research*, Vol. 39, 2009, pp. 957-965.

140. Gani, M.S.J., *Cement and Concrete*, Chapman and Hall, London, UK (1997).

141. British Geological Survey, Midland Valley groundwater chemistry analyses, online information (accessed online at http://www.bgs.ac.uk/research/groundwater/quality/baselineScotland/MidlandValleyData.html, 15 November 2012).

142. Abu Bakar, B.H., Wan Ibrahim, M.H. and Megat Johari, M.A., 'A Review: Durability of Fired Clay Brick Masonry Wall due to Salt Attack', *International Journal of Integrated Engineering*, Vol. 1, No. 2, 2009, pp. 111-127.

143. Fritz, S.J., 'A survey of charge-balance errors on published analyses of potable ground and surface waters', *Ground Water*, Vol. 32, No. 4, July-August 1994, pp. 539-546.

144. Tiruta-Barna, L., 'Using PHREEQC for modelling and simulation of dynamic leaching tests and scenarios', *Journal of Hazardous Materials*, Vol. 157, Issues 2-3, September 2008, pp. 525-533.

145. Hardy, R. and Tucker, M.E., 'X-ray powder diffraction of sediments', in *Techniques in Sedimentology*, ed. M.Tucker, Blackwell Scientific Publications, Oxford, UK (1988), pp. 191-288.

146. Gere, J.M. and Timoshenko, S.P., *Mechanics of Materials*, fourth edition, PWS Publishing Company, Boston, MA (1996).

147. Punurai, W., Jarzynski, J., Jianmin, Q., Kim, J., Jacobs, L.J. and Kurtis, K., Characterization of multi-scale porosity in cement paste by advanced ultrasonic techniques, *Cement and Concrete Research*, Vol. 37, 2007, pp. 38-46.

148. Omega website, *Equilibrium Relative Humidity of saturated salt solutions*, online fact sheet (accessed online at http://www.omega.com/temperature/z/pdf/z103.pdf, 10 December 2012).

149. Senkayi, A.L., Dixon, J.B. and Hossner, L.R., 'Transformation of chlorite to smectite through regularly interstratified intermediates', *Soil Science Society of America Journal*, Vol. 45, 1981, pp. 650-656.

150. Ince, C., Carter, M.A., Wilson, M.A., El-Turki, A., Ball, R.J., Allen, G.C. and Collier, N.C., 'Analysis of the abstraction of water from freshly mixed jointing mortars in masonry construction', *Materials and Structures*, Vol. 43, 2010, pp. 985-992.

151. Sallery, D. 'Old bricks – history at your feet', website (accessed online at http://www.penmorfa.com/bricks/scotland2.html#Letter%20W, 23 November 2012).

152. Hall, C., Hoff, W.D. and Prout, W., 'Sorptivity-porosity relations in clay brick ceramic', *American Ceramic Society Bulletin*, Vol. 71, No.7, 1992, pp. 1112-1116.

153. Pavía, S. 'An investigation into Irish historical ceramics: the brick of Arch Hall, Wilkinstown, Co.Meath', *Proceedings of the Royal Irish Academy*, 105C (6), 2005, pp. 221-242.

154. Roels, S., Carmeliet, J. and Hens, H., 'Microscopic analysis of imbibition processes in oolitic limestone', *Geophysical Research Letters*, Vol. 27, No. 21, November 1 2000, pp. 3533-3536.

155. Gummerson, R.J., Hall, C. and Hoff, W.D., 'Capillary water transport in masonry structures: building construction applications of Darcy's Law', *Construction Papers*, Vol.1, 1980, pp. 17-27.

156. Warscheid, Th. and Braams, J. 'Biodeterioration of stone: a review', *International Biodeterioration and Biodegradation*, Vol. 46, Issue 4, 2000, pp. 343-368.

157. Warscheid, Th., Becker, Th., Baams, J., Brüggerhoff, S., Gehrmann, C., Krumbein, W.E. and Petersen, K. 'Studies on the temporal development of microbial infection of different types of sedimentary rocks and its effect on the alteration of the physico-chemical properties in building materials', in *Conservation of stone and other materials, Vol.1*, ed. M.J. Thiel, E & FN Spon, London, UK (1993), pp. 303-310.

158. Bennett, R.P., Blevins, H.J. and Cuevas, H.J., 'New chemical reduces coke dust emissions at Mississippi refinery', *Oil and Gas Journal*, Vol. 92, Issue 52, December 1994, pp. 74-77.

159. Gutt, W. and Nixon, P.J., 'Use of waste materials in the construction industry, analysis of the RILEM Symposium by Correspondence', *Materials and Structures*, Vol. l2, No. 70, l979, pp. 255 – 306.

160. Sun, Z. and Scherer, G.W., 'Measurement and simulation of dendritic growth of ice in cement paste', *Cement and Concrete Research*, Vol. 40, 2010, pp. 1393-1402.

161. Scherer, G., 'Crystallization in pores', *Cement and Concrete Research*, Vol. 29, 1999, pp. 1347-1358.

162. Powers, R.C. 'The Air Requirement of Frost-Resistant Concrete', *Highway Research Board Proceedings*, Vol. 29, 1949, Highway Research Board, pp. 184-211.

163. Powers, T.C. and Helmuth, R.A., 'Theory of Volume Changes in Hardened Portland-Cement Paste During Freezing', *Highway Research Board Proceedings*, Vol. 32, 1953, Highway Research Board, pp. 285-297.

164. Litvan, G.G., 'Freeze-Thaw Durability of Porous Building Materials', in *Durability of Building Materials and Components, ASTM STP 691*, eds. P.J. Sereda and G.G. Litvan, American Society for Testing and Materials (1980), pp. 455-463.

165. Hörsch, T. and Wittmann, F.H., 'Simulation of damage and crack formation in the composite structure of concrete under freeze-thaw cycles', in *Proceedings of the Second International Rilem Workshop on Frost Resistance of Concrete*, eds. M.J. Setzer, R. Auberg and H.J. Keck, RILEM, Bagneux, France (2002), pp. 225-234.

166. Setzer, M.J. and Liebrecht, A. 'Frost dilatation and pore system of hardened cement paste under different storage conditions', in *Proceedings of the Second International Rilem Workshop on Frost Resistance of Concrete*, eds. M.J. Setzer, R. Auberg and H.J. Keck, RILEM, Bagneux, France (2002), pp. 169-178.

167. Scherer, G.W., 'Modeling damage from ice and salt', in *Proceedings of the International RILEM Symposium on Concrete Modelling – CONMOD'08, 26-28 May 2008, Delft, The Netherlands*, RILEM, Bagneux, France (2008), pp. 13-23.

168. Ruedrich, J. and Siegesmund, S., 'Salt and ice crystallisation in porous sandstones', *Environmental Geology*, Vol. 52, 2007, pp. 225-249.

169. Wardeh, G. and Perrin, B., 'Analysis of strains in baked clay based materials during freezing and thawing cycles', *Journal of Building Physics*, Vol. 29, No. 3, January 2006, pp. 201-217.

170. Wardeh, G. and Perrin, B., 'Freezing-thawing phenomena in fired clay materials and consequences on their durability', *Construction and Building Materials*, Vol. 22, 2008, pp. 820-828.

171. Perrin, B., Vu, N.A., Multon, S., Voland, T. and Ducroquetz, C., 'Mechanical behaviour of fired clay materials subjected to freeze-thaw cycles', *Construction and Building Materials*, Vol. 25, 2011, pp. 1056-1064.

172. Mačiulaitis, R. and Kičaitė, 'Peculiarities of destruction mechanism in ceramic products under simulated exploitation conditions', *Materials Science*, Vol. 12, No. 4, 2006, pp. 341-345.

173. Mihashi, M., Zhou, Z.Y. and Tada, S., 'Micromechanics model to predict macroscopic behaviour of concrete under frost action', in *Proceedings of the Second International Rilem Workshop on Frost Resistance of Concrete*, eds. M.J. Setzer, R. Auberg and H.J. Keck, RILEM, Bagneux, France (2002), pp. 235-241.

174. Sun, Z. and Scherer, G.W., 'Kinetics of ice growth in cement and concrete', in *Proceedings of the International RILEM Symposium on Concrete Modelling – CONMOD'08, 26-28 May 2008, Delft, The Netherlands*, RILEM, Bagneux, France (2008), pp. 183-190.

175. Penttala, V., 'From freezing and thawing pore water pressures to concrete stresses', in *Proceedings of the Second International Rilem Workshop on Frost Resistance of Concrete*, eds. M.J. Setzer, R. Auberg and H.J. Keck, RILEM, Bagneux, France (2002), pp. 147-160.

176. Hansen, K.K., Munch, T.A., Thorsen, P.S. and Villumsen, C., 'Moisture movements in render on brick wall', in *Second International Conference on Building Physics, Antwerp, Belgium, 14-18 September 2003*, eds. J. Carmeliet, H. Hens and G. Vermeir (2003), pp. 471-478.

177. Berthold, J.W., Jacobs, S.F. and Norton, M.A., 'Dimensional stability of fused silica, invar and several ultralow thermal expansion materials', *Applied Optics*, Vol. 15, No. 8, 1976, pp. 1898-1899.

178. Allen, E. and Iano, J., *Fundamentals of Building Construction: Materials and Methods*, fifth edition, John Wiley and Sons, Hoboken, New Jersey (2009).

179. MacInnis, C. and Beaudoin, J.J., 'Effect of the degree of saturation on the frost resistance of mortar mixes', *Journal of the American Concrete Institute*, Vol. 65, 1968, pp. 203-207.

180. Ballato, P., Cruciani, G., Dalconi, M.C., Fabri, B. and Macchiarola, M., 'Mineralogical study of historical bricks from the Great Palace of Byzantine Emperors in Istanbul based on powder X-ray diffraction data', *European Journal of Mineralogy*, Vol. 17, pp. 777-784.

181. Chee Ban, C. and Ramli, M., 'Optimization of Mix Proportion of High Performance Mortar for Structural Applications', *American Journal of Engineering and Applied Sciences*, Vol. 3, No. 4, 2010, pp. 643-649.

182. Ashurst, J., 'The technology and use of hydraulic lime', *The Building Conservation Directory*, 1997 (accessed online at http://www.buildingconservation.com/articles/hydraulic/hydraulic.htm, 12 December 2012).

183. The Concrete Society, *Diagnosis of deterioration in concrete structures*, Technical Report No.54, The Concrete Society, Surrey, UK (2000).

184. Al-Mhaidib, A., 'Swelling behaviour of expansive shales from the middle region of Saudi Arabia', *Geotechnical and Geological Engineering*, Vol. 16, 1999, pp. 291-307.

185. Huang, S.L., Aughenbaugh, N.B. and Rockaway, J.D., 'Characterization of swelling potential of shale strata', in *Proceedings of the 27th U.S. Symposium on Rock Mechanics (USRMS), June 23-25, 1986, Tuscaloosa*, AL (1986), pp. 68-76.

186. Madsen, F. T. and Müller-Vonmoos, M., 'Swelling pressure calculated from mineralogical properties of a Jurassic opalinum shale, Switzerland', *Clays and Clay Minerals*, Vol. 33, No. 6, 1985, pp. 501-509.

187. Wendler, E., Charola, A.E. and Fitzner, B. 'Easter Island tuff: laboratory studies for its consolidation', in *Eighth International Congress on Deterioration and Conservation of Stone*, ed. J. Riederer, Moller Druck und Verlag, Berlin, Germany (1996), pp. 1159–1170.

188. Jiménez González, I. and Scherer, G.W., 'Evaluating the potential damage to stones from wetting and drying cycles', in *Measuring, Monitoring and Modeling concrete Properties*, ed. M.S. Konsta-Gdoutos, Springer, Netherlands (2006), pp. 685-693.

189. Wangler, T. and Scherer, G.W., 'Clay swelling mechanism in clay-bearing sandstones', *Environmental Geology*, Vol. 56, 2008, pp. 529-534.

190. Jiménez González, I., Rodríguez-Navarro, C. and Scherer, G.W., 'Role of clay minerals in the physicomechanical deterioration of sandstone', *Journal of Geophysical Research,* Vol. 113, 2008, F02021.

191 Wangler, T.P., Stratulat, A., Duffus, P., Prévost, J.H. and Scherer, G.W., 'Flaw propagation and buckling in clay-bearing sandstones', *Environmental Earth Sciences*, Vol. 63, 2011, pp. 1656-1572.

192. Potts, A.S., 'Frost action in rocks: some experimental data', *Transactions of the Institute of British Geographers*, Wiley-Blackwell, No. 49, 1970, pp. 109-124.

193. Schuster, R.L. and Mclaughlin, J.F., 'A study of chert and shale gravel in concrete: Technical Paper', a Joint Highway Research Paper, No. 2, Purdue University, January 1961 (accessed online at http://ia700402.us.archive.org/28/items/studyofchertshal00schu/studyofchertshal00schu.pdf, 21 November 2012).

194. Verbeck, G. and Landgren, R., 'Influence of physical characteristics of aggregates on frost resistance of concrete', *Proceedings of the American Society for Testing Materials*, Vol. 60, 1960, pp. 1063-1079.

195. Lee, M. and Lee, J., 'Study on the cause of pop-out defects on the concrete wall and repair method', *Construction and Building Materials*, Vol. 23, 2009, pp. 482-490.

196. Griffith, A.A., 'The phenomena of rupture and flow in solids', *Philosophical Transactions of the Royal Society of London,* A.221, 1921, pp. 163-198 (accessed online at http://www.cmse.ed.ac.uk/AdvMat45/Griffith20.pdf, 1 June 2012).

197. Ceriolo, L. and Tommaso, A.Di., 'Fracture mechanics of brittle materials: a historical point of view', in *Second International PhD Symposium in Civil Engineering*, 1998, Budapest.

198. Irwin, G.R., 'Analysis of stresses and strains near the end of a crack traversing a plate', *Journal of Applied Mechanics*, Vol. 24, 1957, pp. 361-364.

199. Wang, C. and Zheng, C., 'Semi-analytical finite element method for fictitious crack model in fracture mechanics of concrete', *Applied Mathematics and Mechanics*, Vol. 25, No. 11, November 2004, pp. 1265-1270.

200. Elices, M. and Planas, J., 'Fracture mechanics parameters of concrete, an overview', *Advanced Cement Based Materials*, Vol. 4, 1996, pp. 116-127.

201. Reda Taha, M.M., Xiao, X., Yi, J. and Shrive, N.G., 'Evaluation of flexural fracture toughness for quasi-brittle structural materials using a simple test method', *Canadian Journal of Civil Engineering*, Vol. 29, 2002, pp. 567-575.

202. Raghu Prasad, B.K., Bharatkumar, B.H., Ramachandra Murthy, D.S., Narayanan, R. and Gopalakrishnan, S., 'Fracture mechanics model for analysis of plain and reinforced high-performance concrete beams', *Journal of Engineering Mechanics*, Vol. 131, No. 8, August 2005, pp. 831-838.

203. Hillerborg, A., Modéer, M. and Petersson, P.E., 'Analysis of crack formation and crack growth in concrete by means of fracture mechanics and finite elements', *Cement and Concrete Research*, Vol. 6, 1976, pp. 773-782.

204. Karihaloo, B.L., Carpinteri, A. and Elices, M., '*Fracture mechanics of cement mortar and plain concrete', Advanced Cement Based Materials*, Vol. 1, 1993, pp. 92-105.

205. Bazant, Z.P. and Oh, B.H., 'Crack band theory for fracture of concrete, *Materials and Structures*, Vol. 16, 1983, pp. 155-177.

206. Jeng, Y.S. and Shah, S.P., 1985, 'A two parameter fracture model for concrete', *ASCE Journal of Engineering Mechanics*, Vol. 111, No. 4, 1985, pp. 1227-1241.

207. Tixier, R. and Mobasher, B., 'Modeling of damage in cement-based materials subjected to external sulfate attack. I: formulation', *Journal of Materials in Civil Engineering*, Vol. 15, No. 4, July/August 2003, pp. 305-313.

208. Du, Y.G., Chan, A.H.C. and Clark, L.A., 'Finite element analysis of the effects of radial expansion of corroded reinforcement', *Computers and Structures*, Vol. 84, 2006, pp. 917-929.

209. Noghabai, K., 'FE-modelling of cover splitting due to corrosion by use of inner softening band', *Materials and Structures*, Vol. 32, August-September 1999, pp. 486-491.

210. Pandermarakis, Z.G. and Sotiropoulou, A.B., 'The identification of a hidden long-term plastic damage stage during splitting tensile loading of concrete: a fracture mechanics approach', *Strain*, Vol. 46, 2010, pp. 538-549.

211. Wittmann, F.H., 'Crack formation and fracture energy of normal and high strength concrete', *Sadhana*, Vol. 27, Part 4, August 2002, pp. 413-423.

212. Coussy, O. and Monteiro, P.J.M., 'Poroelastic model for concrete exposed to freezing temperatures', *Cement and Concrete Research*, Vol. 38, 2008, pp. 40-48.

213. Pantazopoulou, S.J. and Papoulia, K.D., 'Modeling cover-cracking due to reinforcement corrosion in RC structures', *Journal of Engineering Mechanics,* April 2001, pp. 342-351.

214. Balafas, I. and Burgoyne, C.J., 'Environmental effects on cover cracking due to corrosion', *Cement and Concrete Research,* Vol. 40, 2010, pp. 1429-1440.

215. Rasheeduzzafar, Al-Saadoun, S.S. and Gahtani, A.S., 'Corrosion cracking in relation to bar diameter, cover and concrete quality', *Journal of Materials in Civil Engineering,* Vol. 4, No. 4, November 1992, pp. 327-342.

216. Lu, C., Jin, W. and Liu, R., 'Reinforcement corrosion-induced cover cracking and its time prediction for reinforced concrete structures', *Corrosion Science,* Vol. 53, 2011, pp. 1337-1347.

217. Koteš, P., Brodňan, M. and Slopková. K., 'Simulation of corrosion of reinforcement in reinforced concrete', in *Proceedings of the International RILEM Symposium on Concrete Modelling – CONMOD'08, 26-28 May 2008, Delft, The Netherlands*, RILEM, Bagneux, France (2008), pp. 761-766.

218. Xia, N., Ren, Q., Liang, R.Y., Payer, J. and Patnaik, A., 'Nonuniform corrosion-induced stresses in steel-reinforced concrete', *Journal of Engineering Mechanics,* Vol. 138, No. 4, April 2012, pp. 338-346.

219. Williamson, S.J. and Clark, L.A., 'Pressure required to cause cover cracking of concrete due to reinforcement corrosion', *Magazine of Concrete Research,* Vol. 52, No. 6, December 2000, pp. 455-467.

220. Maaddawy, T.E. and Soudki, K., 'A model for prediction of time from corrosion initiation to corrosion cracking', *Cement and Concrete Composites,* Vol. 29, 2007, pp. 168-175.

221. Liu, Y. and Weyers, R., 'Modeling of the time to corrosion cracking in chloride contaminated reinforced concrete structures', *ACI Materials Journal,* Vol. 95, 1998, pp. 675-681.

222. Jeffery, G.B., 'Plane stress and plane strain in bipolar co-ordinates', *Philosophical Transactions of the Royal Society of London. Series A, Containing Papers of a Mathematical or Physical Character,* Vol. 221, 1921, pp. 265-293.

223. Verruijt, A., 'Deformations of an elastic half plane with a circular cavity', *Journal of Solids Structures,* Vol. 35, No. 1, pp. 2795-2804.

224. geology.com, 'Shale' web page (accessed online at http://geology.com/rocks/shale.shtml, 20 November 2012).

225. Fredlund, D.G. and Rahardjo, H., *Soil mechanics for unsaturated soils*, John Wiley, New York (1993).

226. Forster, S.W., 'Soundness, Deleterious Substances and Coatings', in *Significance of Tests and Properties of Concrete and Concrete-Making Materials*, eds. J.F. Lamond and J.H. Pielert, ASTM International, 2006.

227. Eseme, E., Urai, J.L. Krooss, B.M. and Littke, R., 'Review of mechanical properties of oil shales: implications for exploitation and basin modelling', *Oil Shale*, Vol. 24, No. 2, 2007, pp. 159-174.

228. Hall, C., 'Water sorptivity of mortars and concretes: A review', *Magazine of Concrete Research*, No. 41, 1989, pp. 51–61.

A1.1 Condition survey photographs

Fig. A1.1. Cracked brick underneath the delaminating render on Building 32

Fig. A1.2. Cracking around windows on Building 31

Fig. A1.3. Hard white efflorescences along the cracks on Building 38

Fig. A1.4. Chipped render on Building 25

Fig. A1.5. Lost render on Building 34, possibly due to previous fixtures

Fig. A1.6. Damp and deteriorating bricks at ground level with missing pointing on Building 31

Fig. A1.7. Cracking and surface loss of bricks approximately 1.5 m from the ground on Building 42

Fig. A1.8. Salt efflorescences on the bricks and mortar joints of an un-rendered external wall on Building 44

Fig. A1.9. Corroding window frame and damaged roof panelling on Building 32

Fig. A1.10. Leaking gutter on Building 25

A1.2 Graphic Condition Surveys

Legend for cement-rendered buildings

Legend for air raid shelter

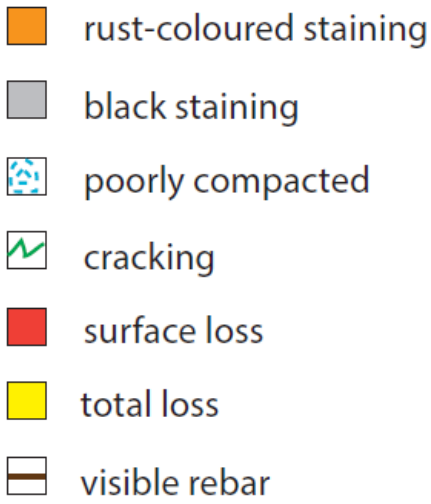

Fig. A1.11. Building 27: N elevation

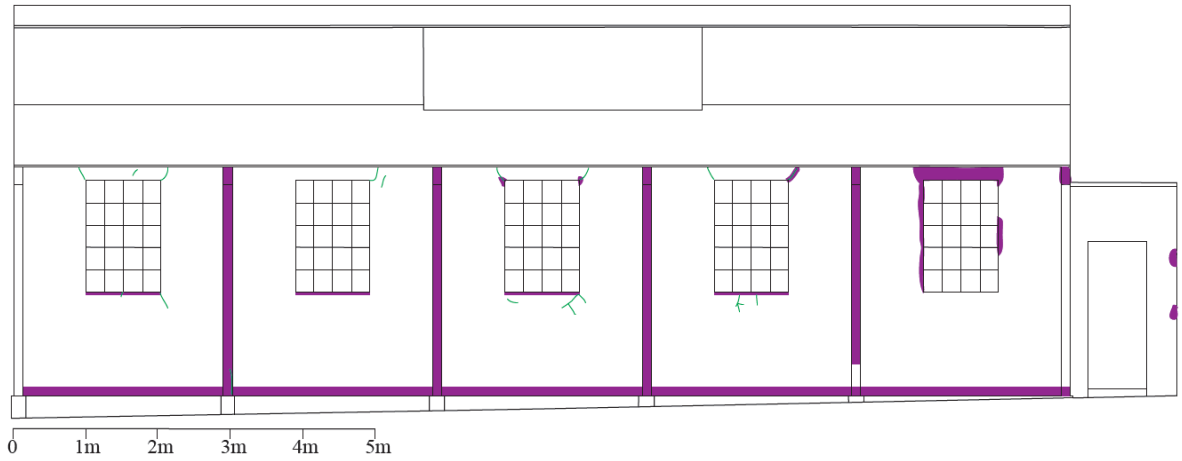

Fig. A1.12. Building 27: S elevation

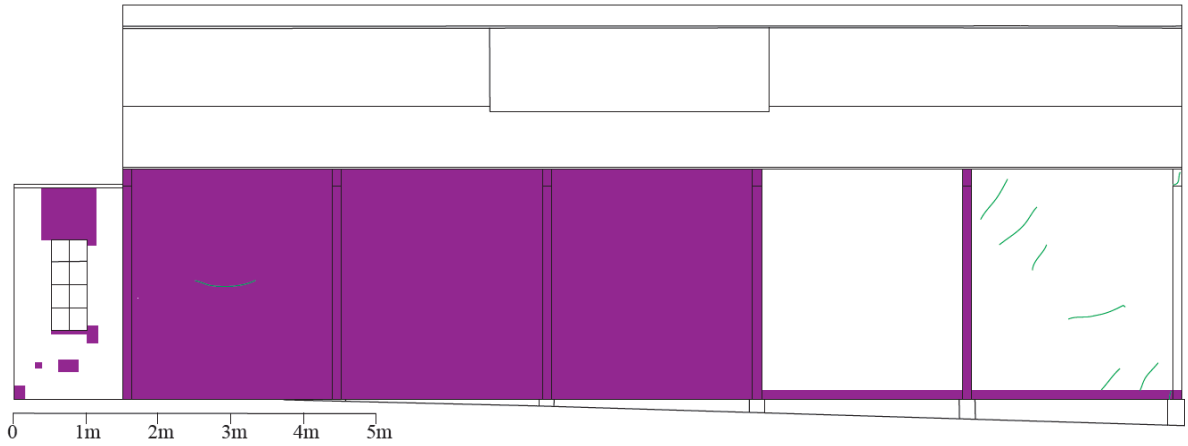

Fig. A1.13. Building 27: W elevation

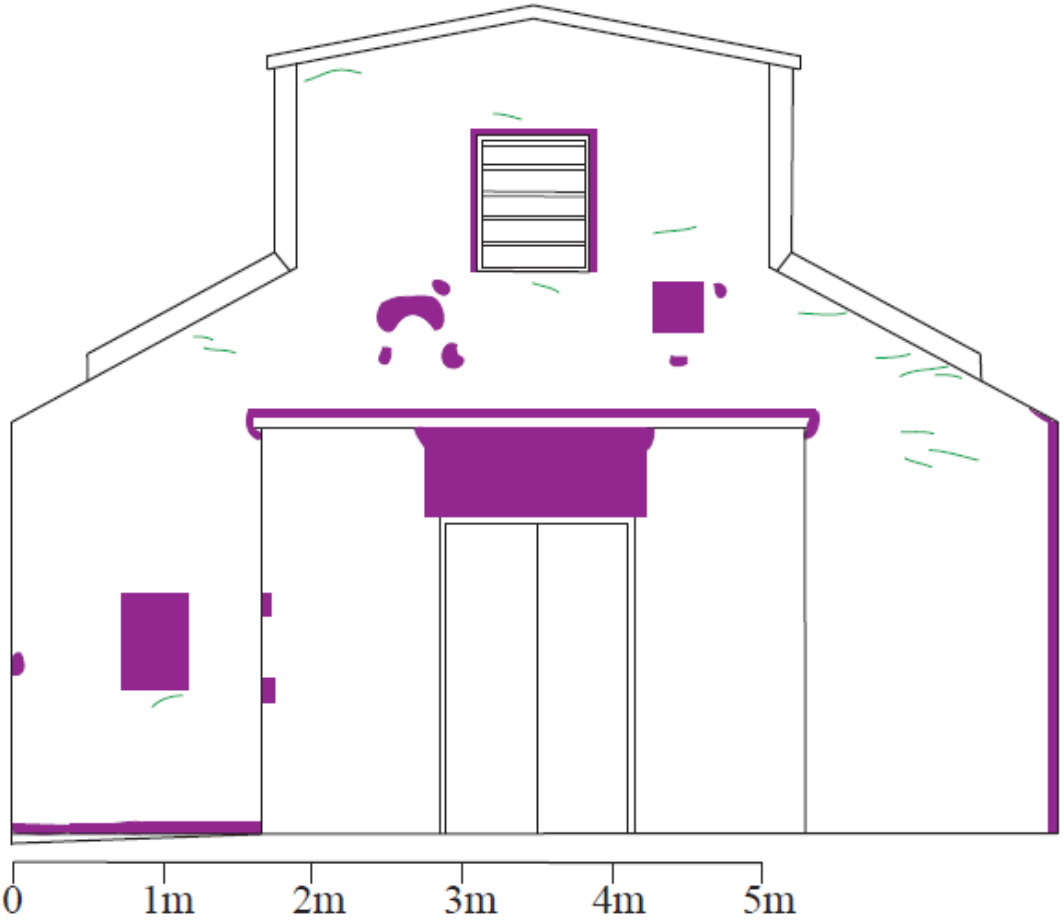

Fig. A1.14. Building 27: E elevation

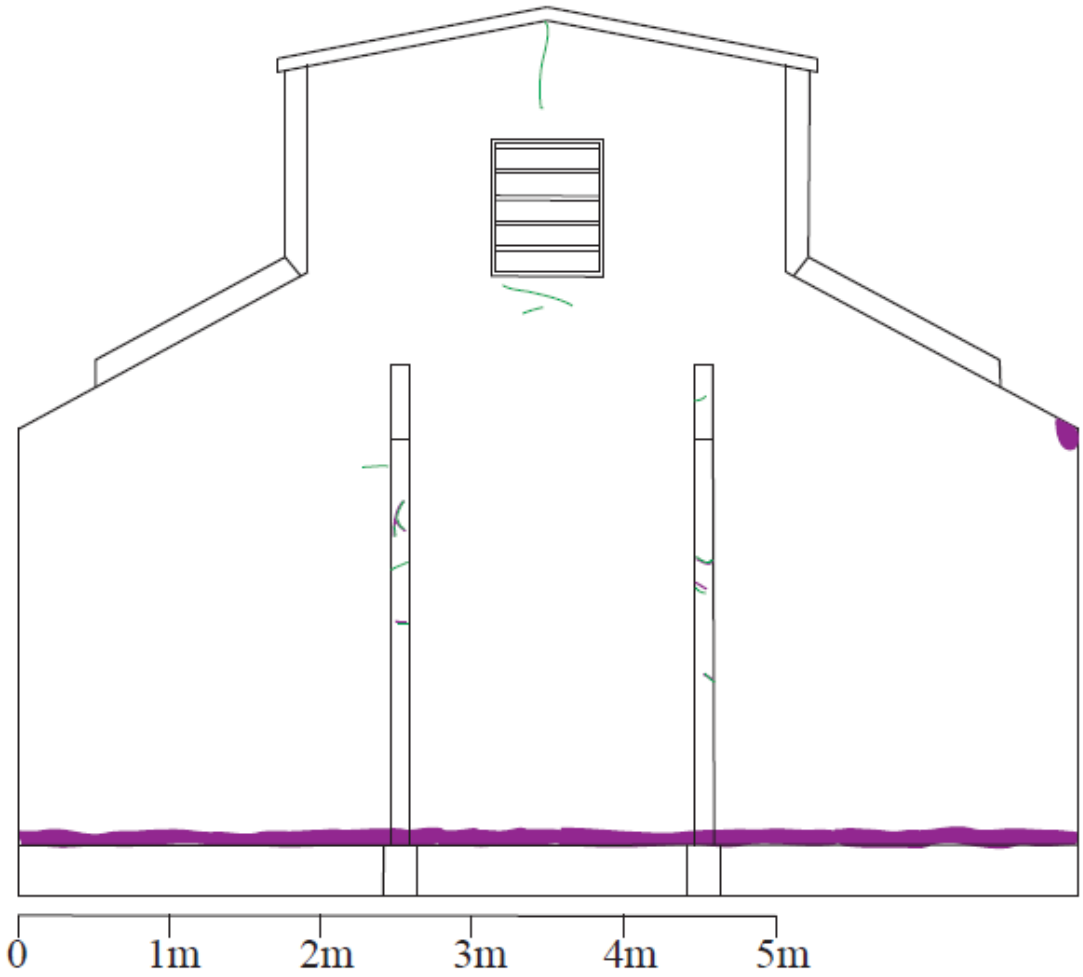

Fig. A1.15. Building 46: NW elevation

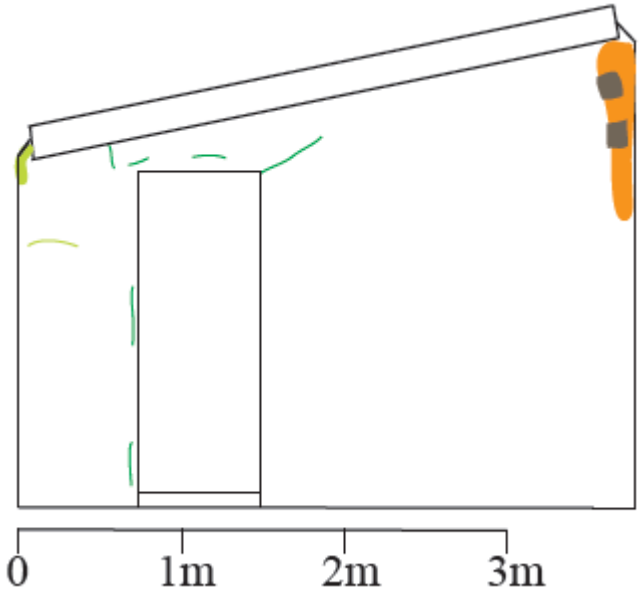

Fig. A1.16. Building 46: SE elevation

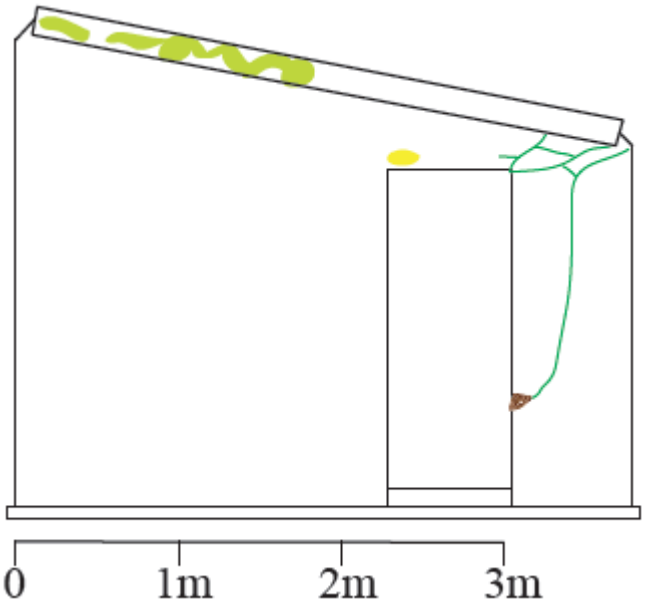

Fig. A1.17. Building 46: NE elevation

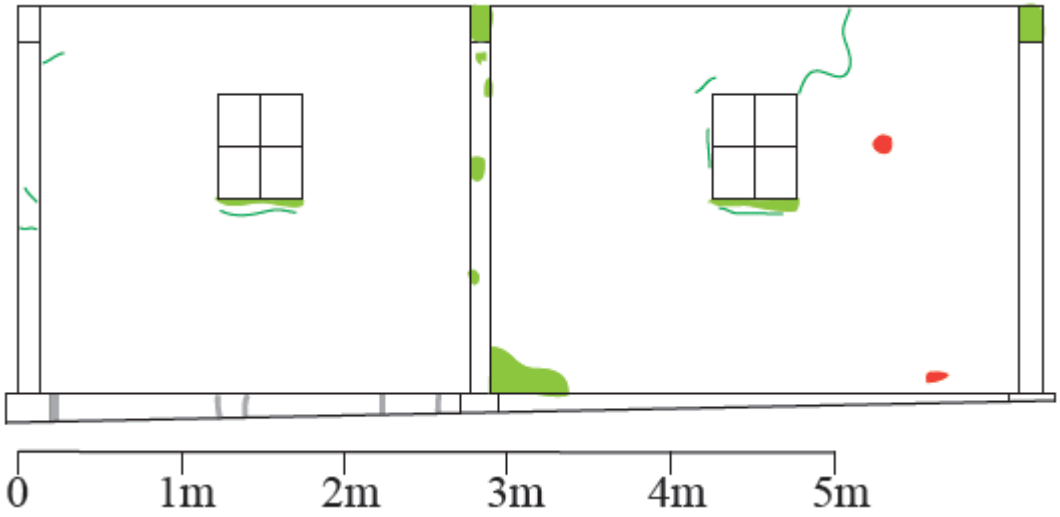

Fig. A1.18. Building 46: SW elevation

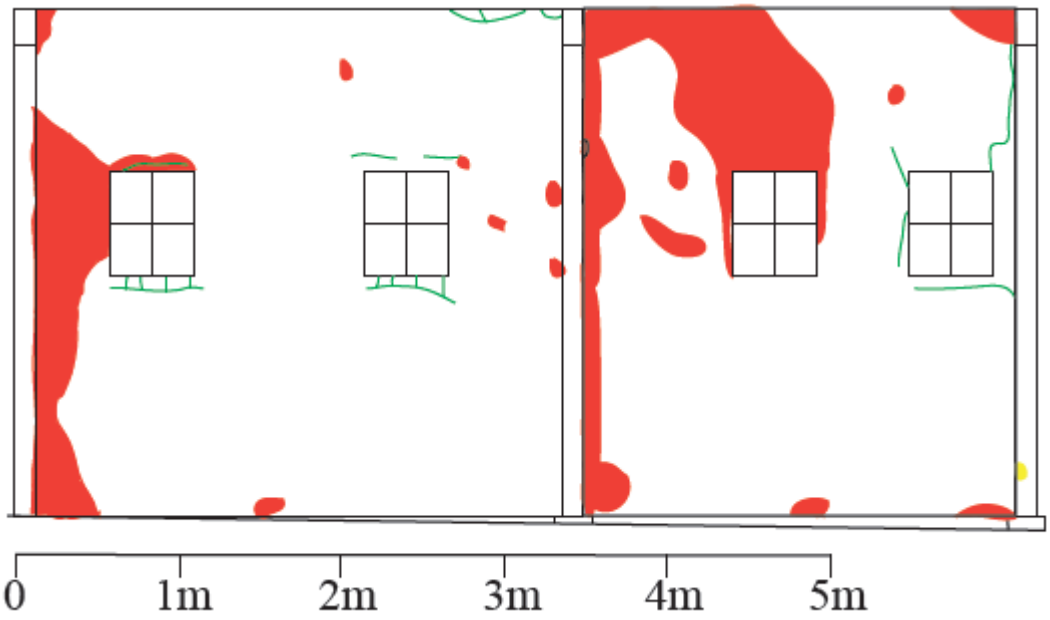

Fig. A1.19. Building 47: NE elevation

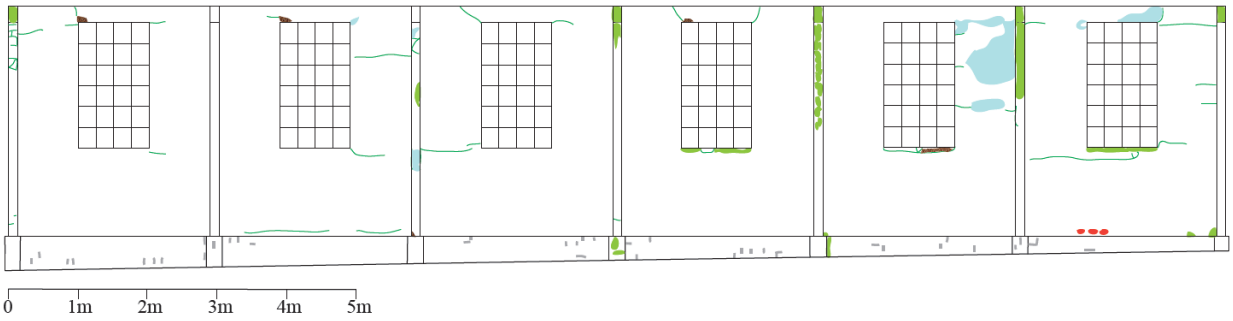

Fig. A1.20. Building 47: SW elevation

Fig. A1.21. Building 47: NW elevation

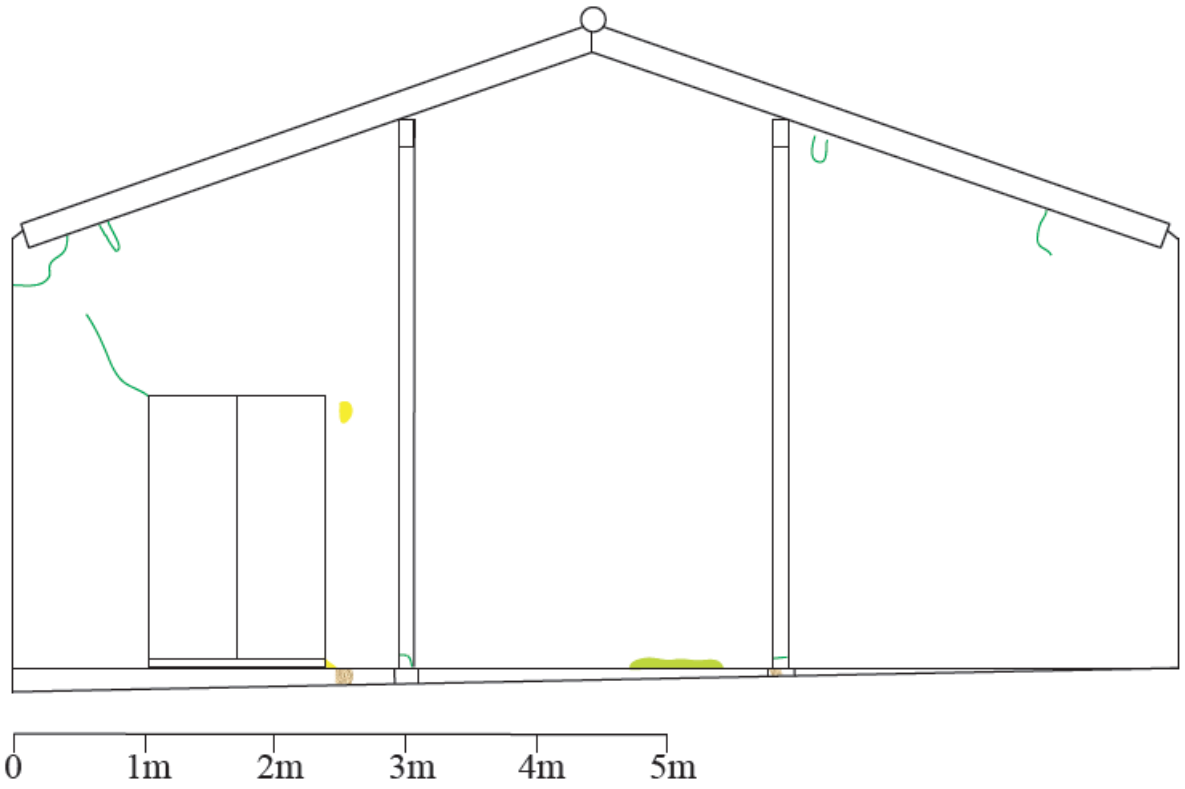

Fig. A1.22. Building 47: SE elevation

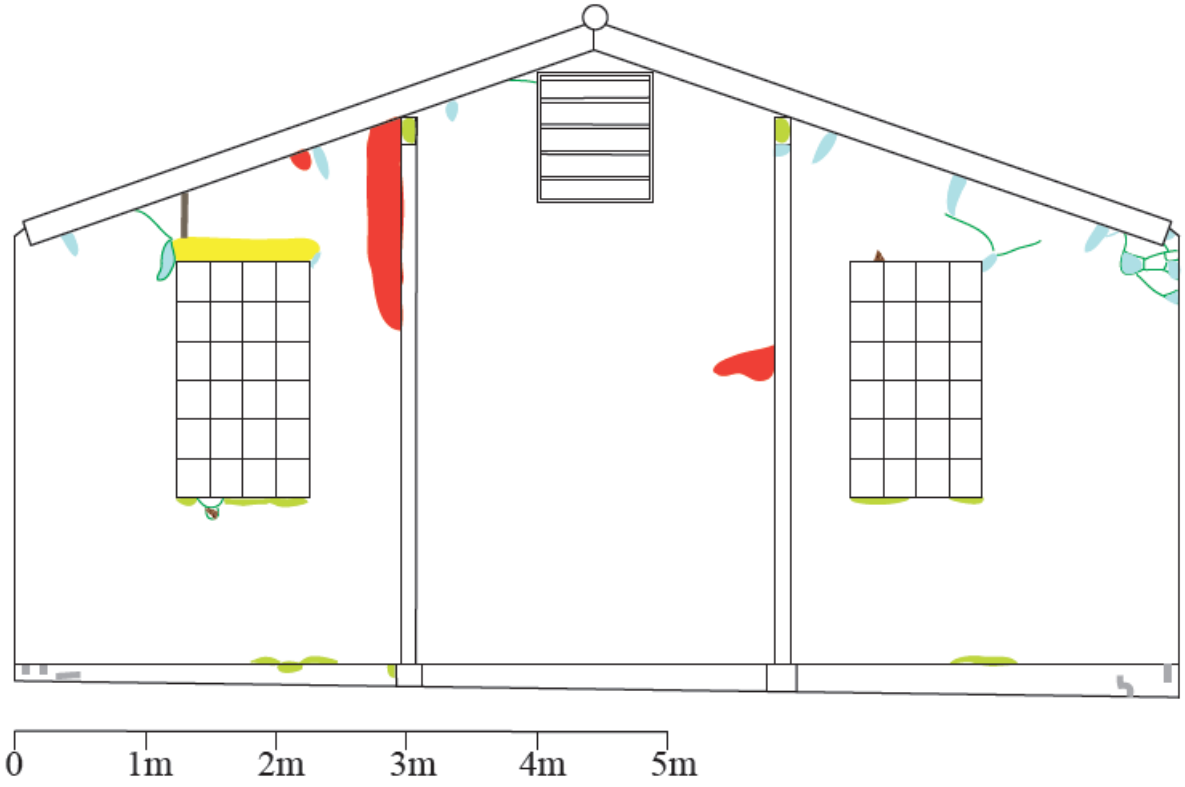

Fig. A1.23. Air raid shelter: NE interior elevation

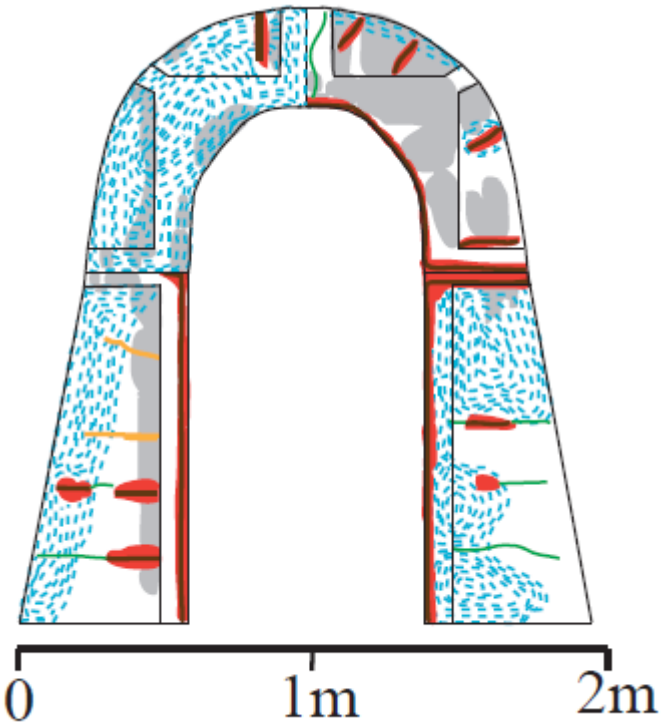

Fig. A1.24. Air raid shelter: SW interior elevation

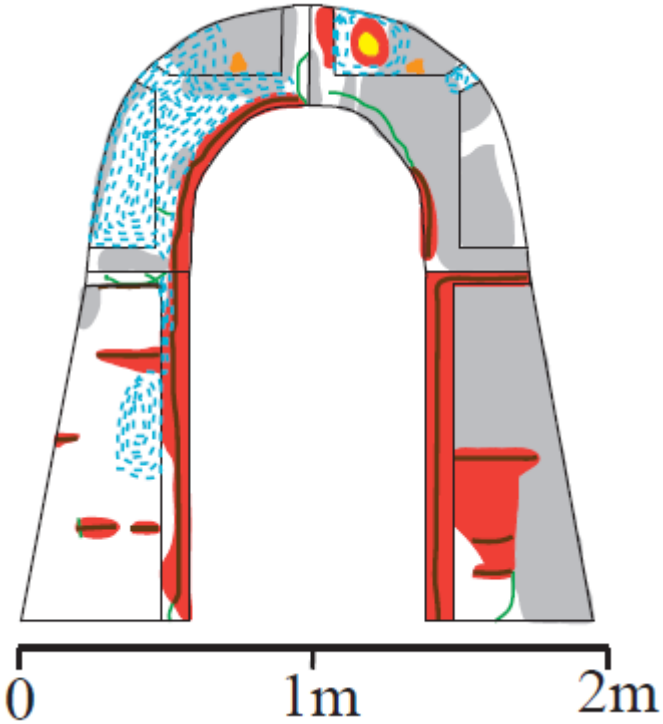

Fig. A1.25. Air raid shelter: NW interior elevation

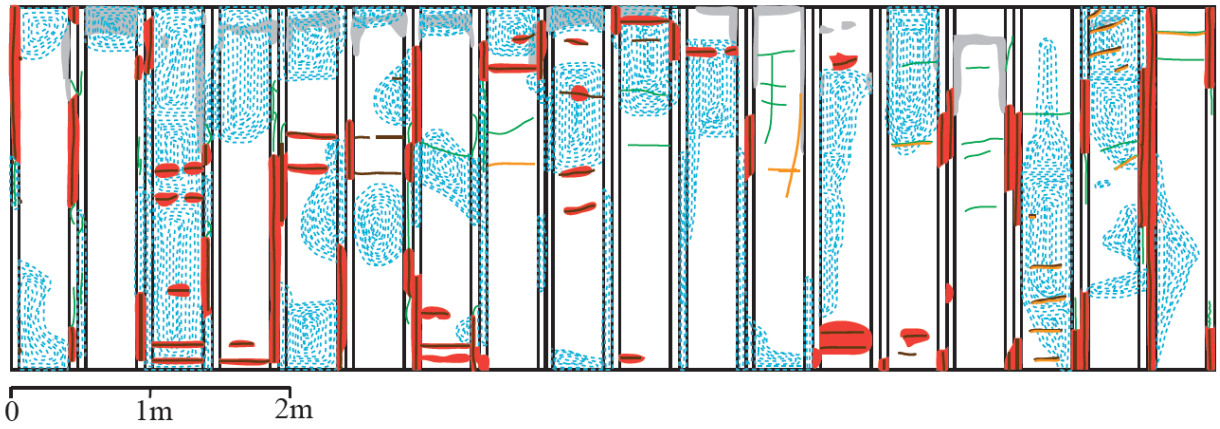

Fig. A1.26. Air raid shelter: SE interior elevation

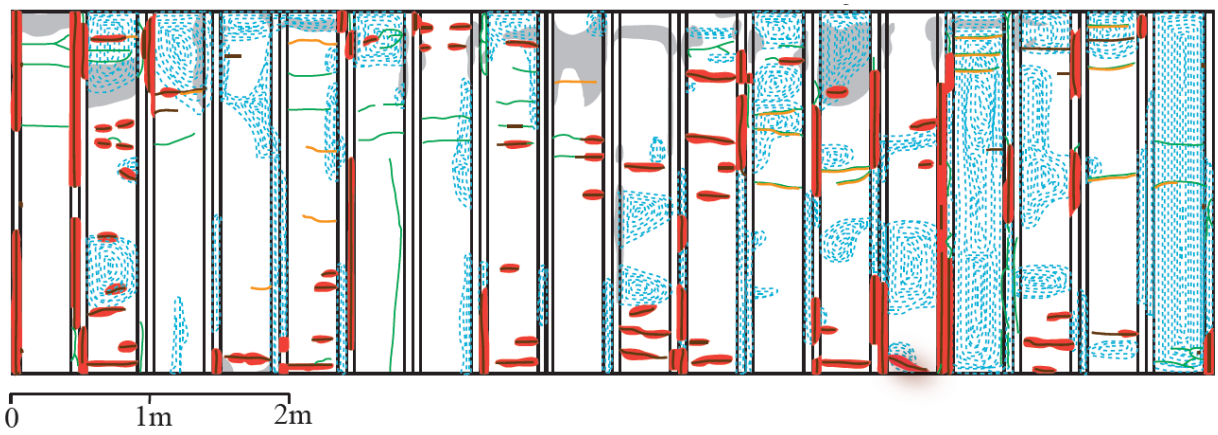

A1.3 Time lapse photography

Fig. A1.27. Building 32, with Building 33 visible prior to its demolition (NMS 1990)

Fig. A1.28. Building 32, with only the plinth of Building 33 remaining (2010)

Fig. A1.29. Building 23, with most of the 1992 repair render intact (NMS 2004)

Fig. A1.30. Building 23, with much of the 1992 repair render lost (2010)

Fig. A1.31. Building 46, area of cracking adjacent to the door on the SE elevation (NMS 2004)

Fig. A1.32. Building 46, visually unchanged area of cracking (2010)

Fig. A1.33. Building 34 in need of some maintenance (NMS 2004)

Fig. A1.34. Building 34 with the broken window boarded up and the vegetation removed (2010)

Fig. A1.35. Building 27 prior to major repair works (RCAHMS 1984)

Fig. A1.36. Building 27 following major repair works undertaken by NMS (2010)

Fig. A1.37. Building 28 prior to major repair works (NMS 2004)

Fig. A1.38. Building 28 following major repair works undertaken by NMS (2010)

Fig. A1.39. Building 32, cracked render on the second pier from SW, on the NW elevation of the building (13/10/2010)

Fig. A1.40. Building 32, visibly unchanged area of cracked render (18/04/2012)

A1.4 Strain measurement

A1.4.1 Monitoring of the un-cracked render on the SE and NW elevations of Building 46

Fig. A1.41. Location of datum points on Building 46

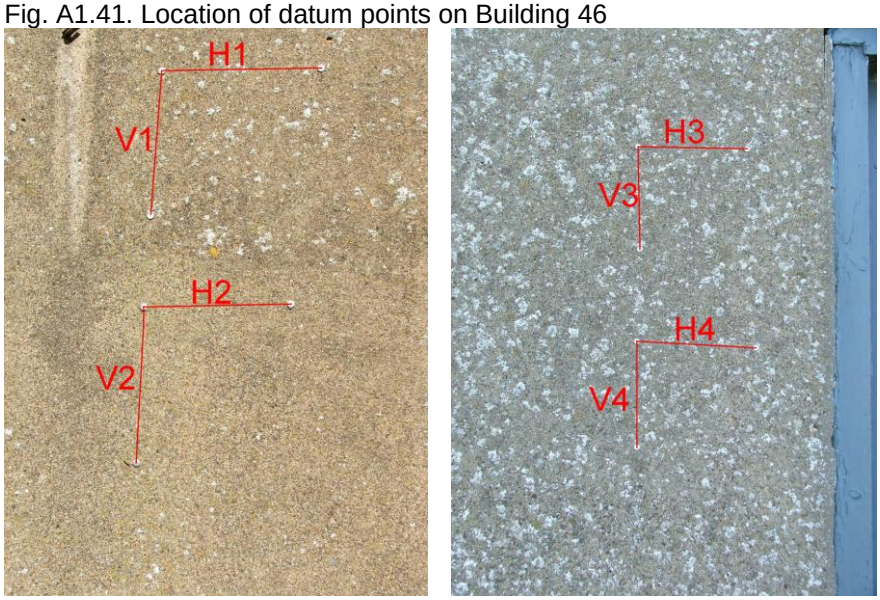

Figs. A1.42.-A1.45. Strain measurement across the un-cracked render on Building 46

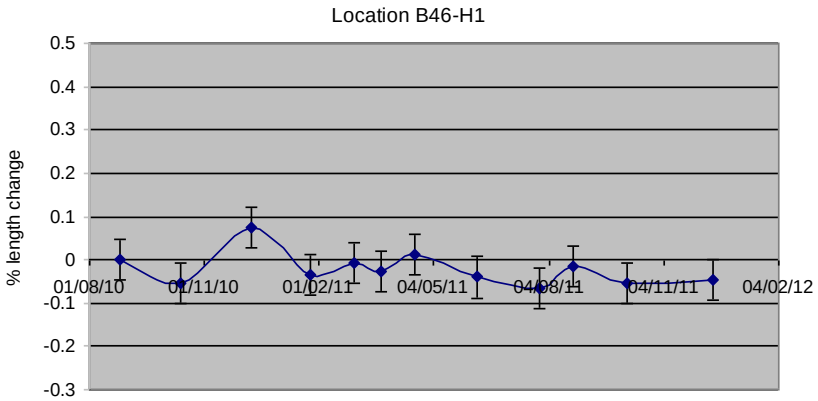

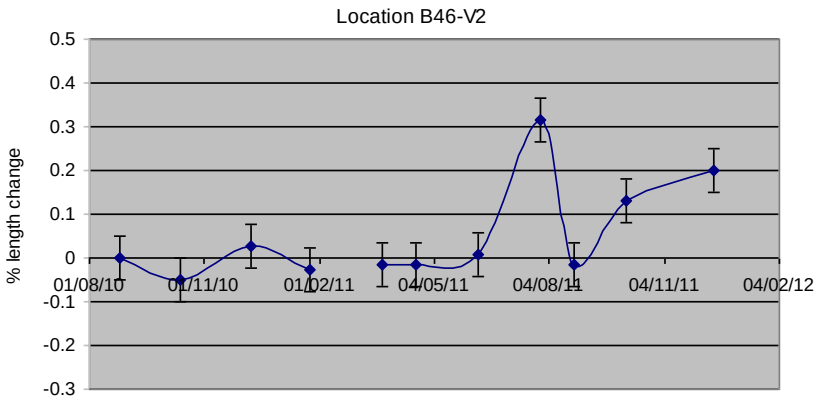

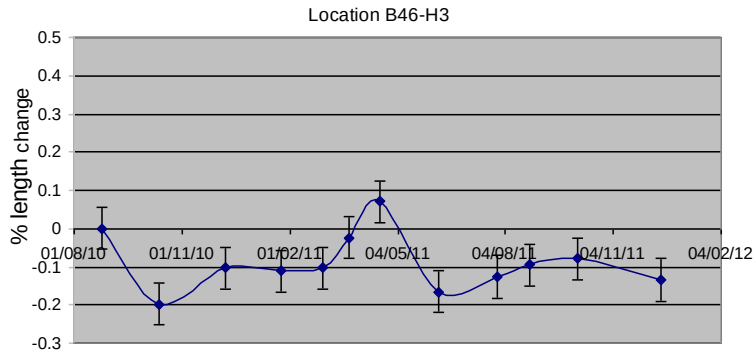
Location B46-H3
% length change
0.5
0.4
0.3
0.2
0.1
0
-0.1
-0.2
-0.3
01/08/10
01/11/10
01/02/11
04/05/11
04/08/11
04/11/11
04/02/12

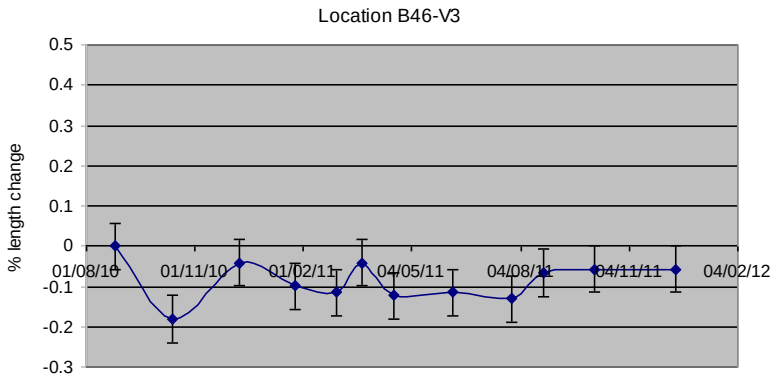
Location B46-V3
% length change
0.5
0.4
0.3
0.2
0.1
0
-0.1
-0.2
-0.3
01/08/10
01/11/10
01/02/11
04/05/11
04/08/11
04/11/11
04/02/12

A1.4.2 Strain measurement across the cracking above a window on the E elevation of Building 26

Fig. A1.46. Location of datum points on Building 26

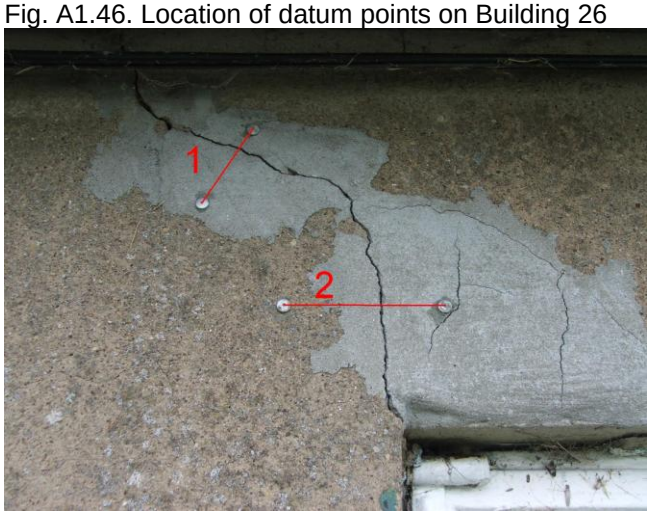

Figs. A1.47.-A1.48. Strain measurement across the cracking on Building 26

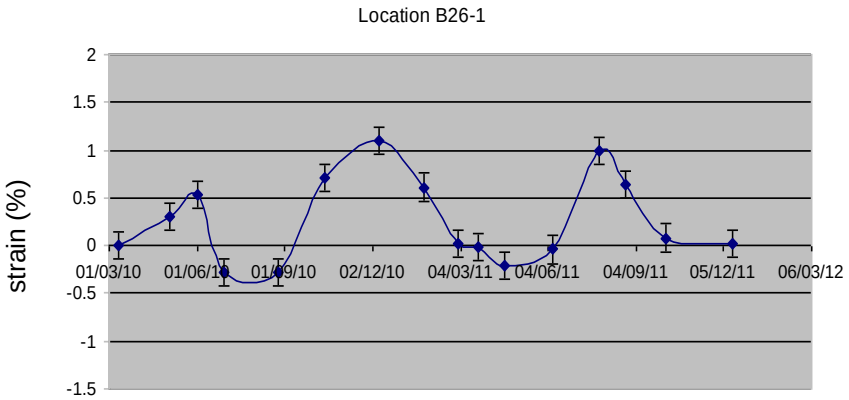

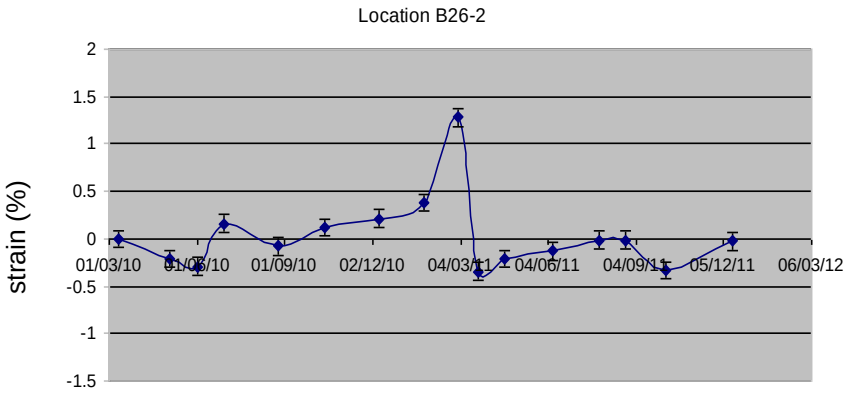

A1.4.3 Strain measurement across the cracking above a window on the SW elevation of Building 31

Fig. A1.49. Location of datum points on Building 31

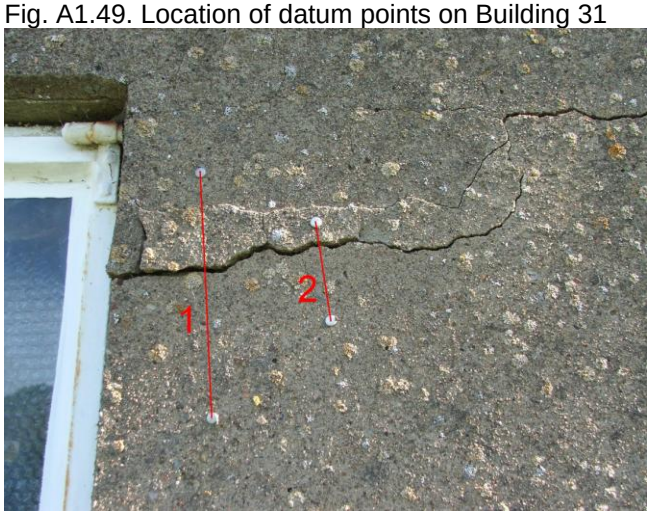

Fig. A1.50. Strain measurement across the cracking on Building 31

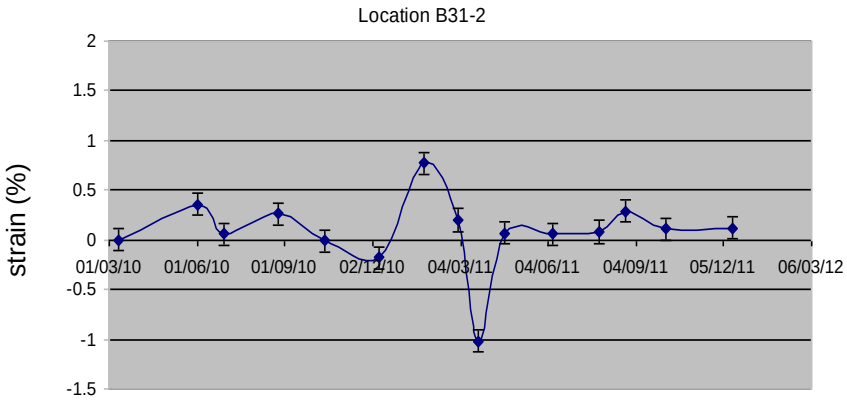

A1.4.4 Strain measurement across the cracking on a pier on the NW elevation of Building 32

Fig. A1.51. Location of datum points on Building 32

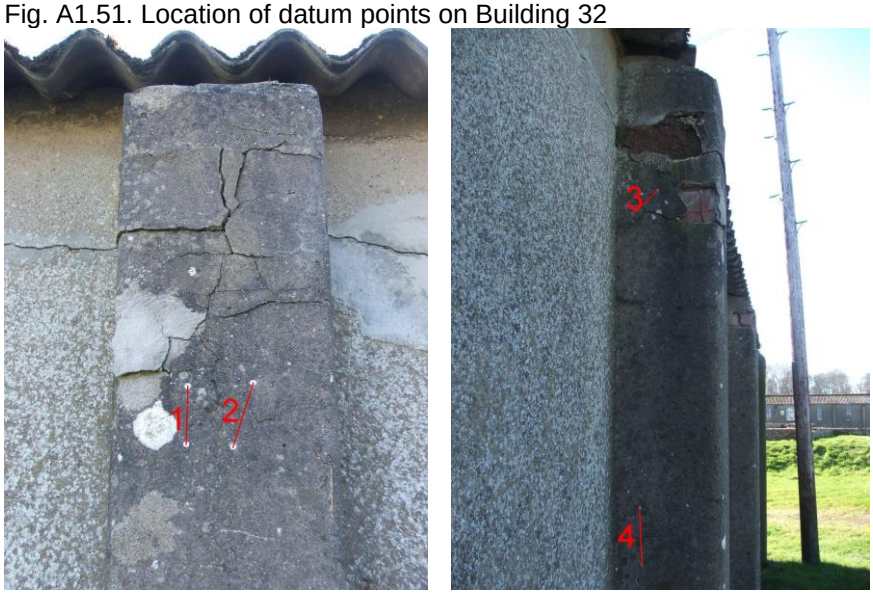

Figs. A1.52.-A1.53. Strain measurement across the cracking on Building 32

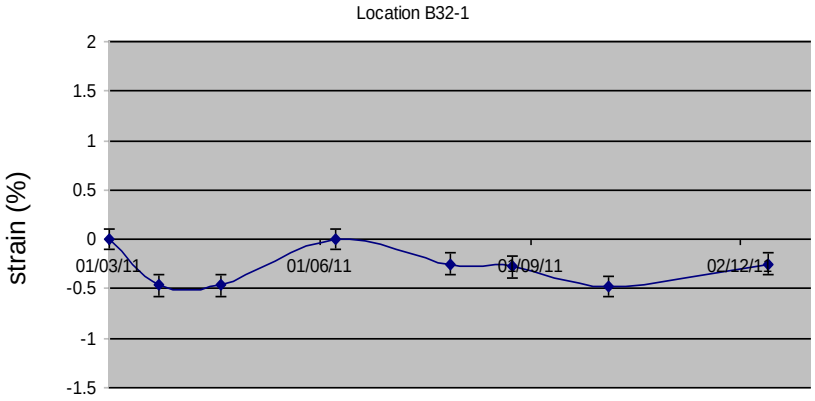

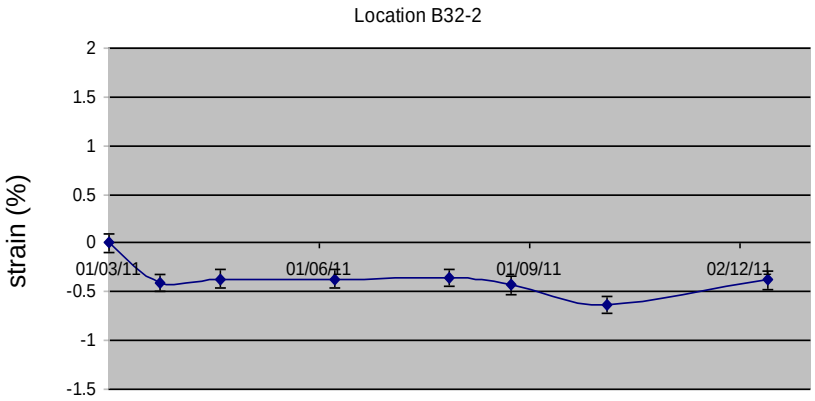

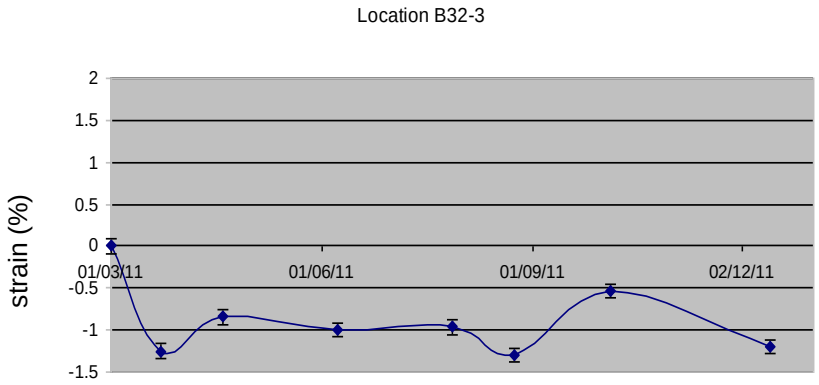
Location B32-3
strain (%)
2
1.5
1
0.5
0
-0.5
-1
-1.5
01/03/11
01/06/11
01/09/11
02/12/11

A1.4.5 Strain measurement across the cracking above the door on the SE elevation of Building 42

Fig. A1.54. Location of datum points on Building 42

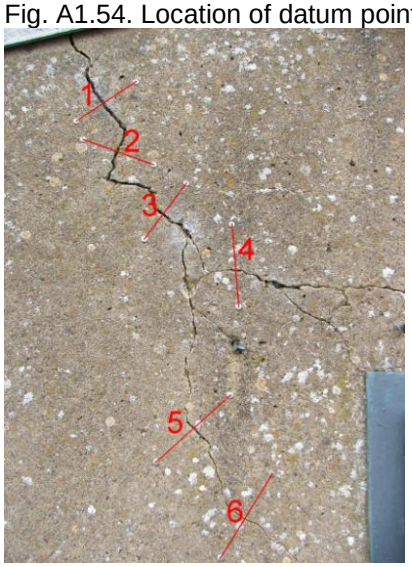

Figs. A1.55.-A1.56. Strain measurement across the cracking on Building 42

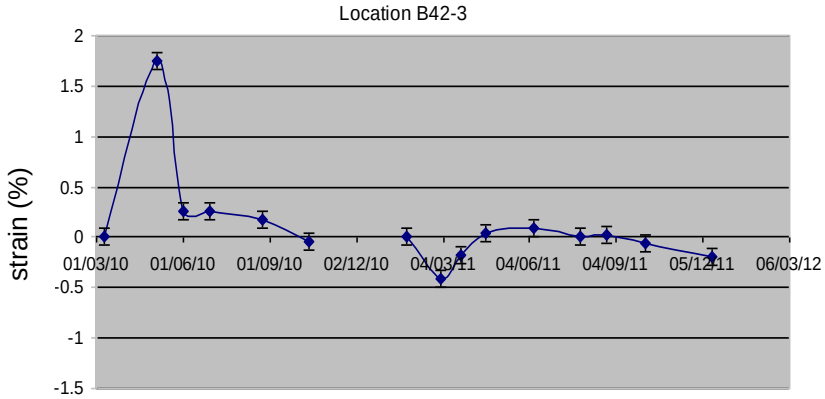

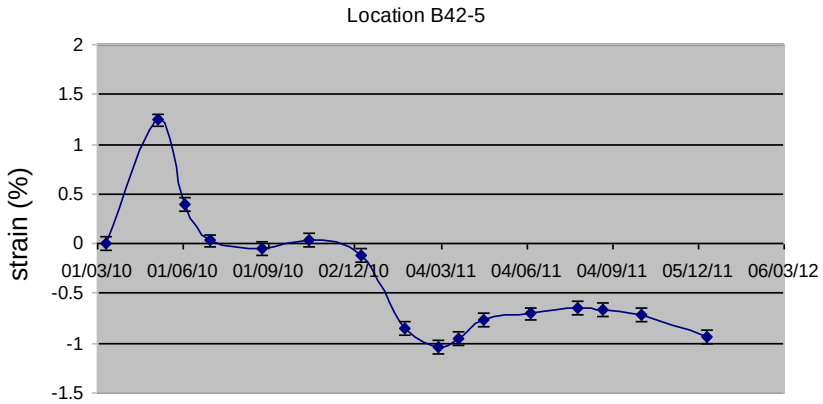

A1.4.6 Strain measurement across the cracking beside the door on the SE elevation of Building 46

Fig. A1.57. Location of datum points on Building 46

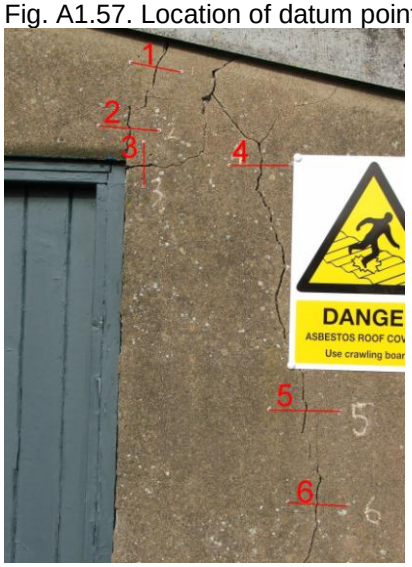

Figs. A1.58.-A1.59. Strain measurement across the cracking on Building 46

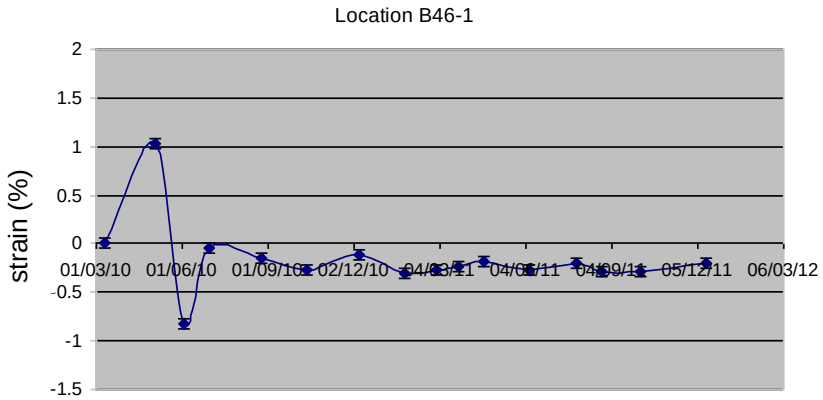

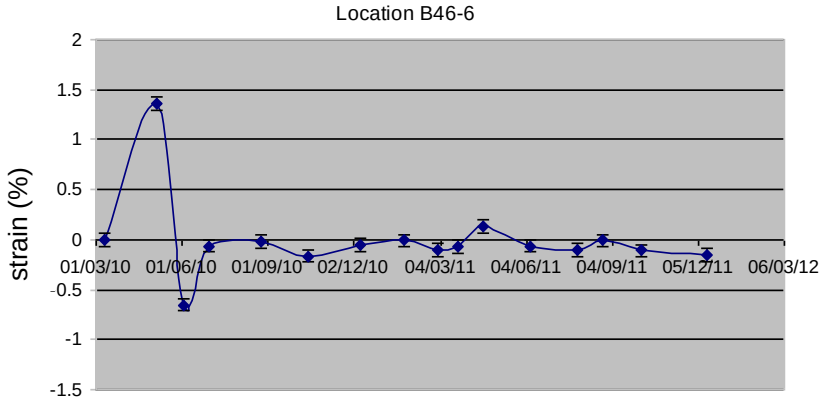

A2.1 Low magnification examination of hand samples

Table A2.1 Surface appearance and layer structures of hand samples

sample	photomicrograph	surface appearance	number of layers and their thicknesses
B24 OR		close, floated surface, with lichen present	1 layer visible: 9-14 mm thick
B32 OR		fairly rough surface, with lichen present	possibly 2 layers, separated by voids: top layer: 7-9 mm thick, bottom layer: 6-9 mm thick
B47 OR		fairly rough surface, with lichen present	1 layer visible: 15-18 mm thick

B23 RR		close, floated surface, with some lichen present	2 layers visible: top layer: 4-5 mm thick, bottom layer: 5-6 mm thick. Surface 0.5 mm appears as a compacted, laitance-rich layer, although it is too thin to have been applied separately.
B25 RR		close, floated surface, without much lichen present	2 layers visible: top layer: 3-4 mm thick, bottom layer: 5-8 mm thick.
ARS C		smooth, pre-cast surface, with no lichen visible	depth of cover: 5-55 mm thick from the surface to the steel reinforcement

NB	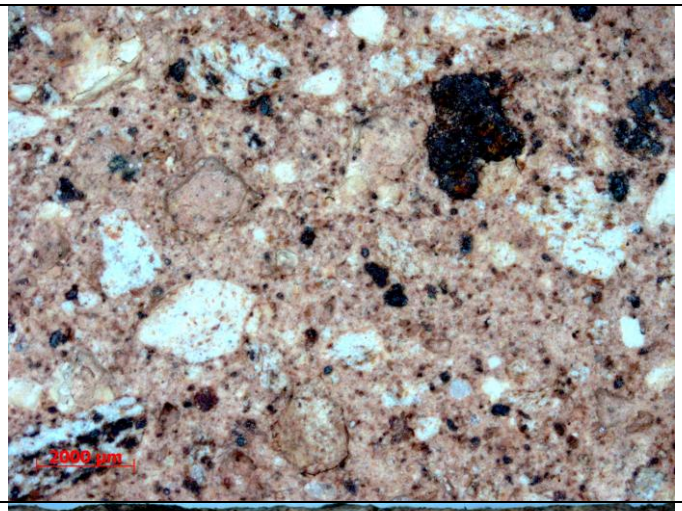	fairly rough, open surface
PB	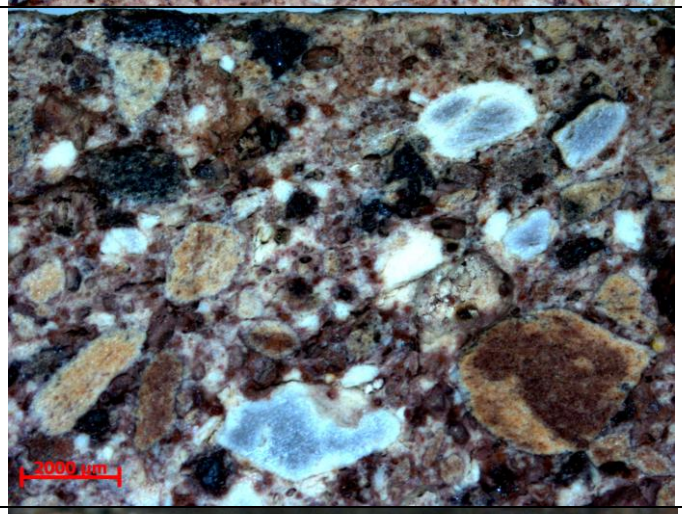	fairly rough, open surface
WaB		moderately smooth surface

B25 B	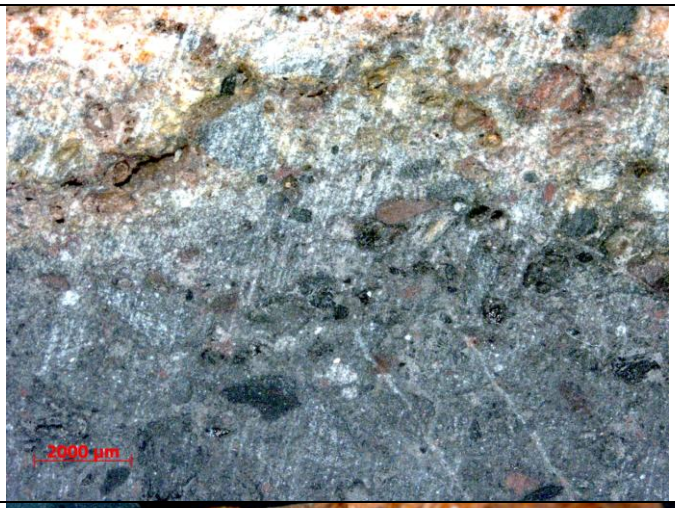	moderately smooth surface
B23 B	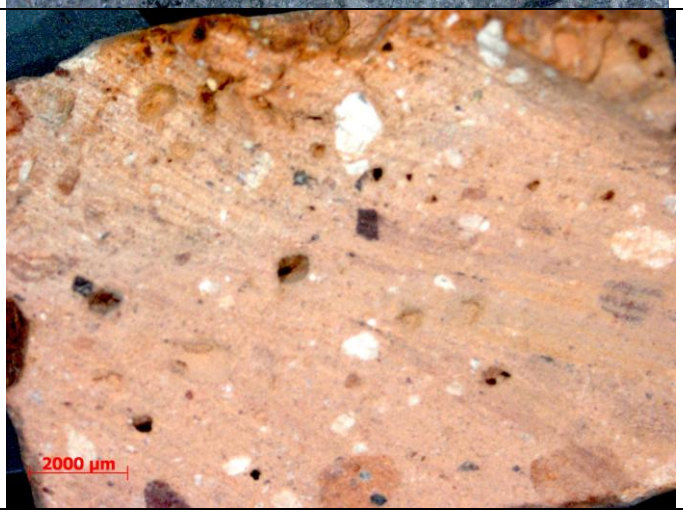	very smooth surface

Table A2.2 Colour and composition of hand samples

sample	colour and size of aggregates	colour of binder	overall or binder colour using the Munsell colour system	size and abundance of voids	evidence of distress or deterioration	hardness
B24 OR	mainly grey quartz, with some orange and brown particles up to 0.5 mm diameter	light brown	10Y 4/2	frequent air voids up to 1 mm diameter	none	hard
B32 OR	grey quartz, with brown, grey, pink and orange particles up to 2 mm diameter	light brown	2.5Y 7/4	occasional large voids, up to 3.5 mm diameter	the elongated voids visible in the middle of the section suggest poor compaction	hard
B47 OR	grey quartz, with brown, grey, pink and orange particles up to 4 mm diameter	light brown	2.5Y 6/4	occasional large voids, up to 2 mm diameter	none	hard
B23 RR	mainly grey quartz, with some orange, yellow and black particles up to 0.3 mm diameter	light brown	7.5Y 2/2	frequent air voids up to 0.5 mm diameter	none	hard
B25 RR	grey quartz, with brown, grey, pink and orange particles up to 1 mm diameter	light brown	5Y 8/6	occasional large voids, up to 2 mm diameter, particularly at the interface between layers	the voids visible at the interface between the layers suggest poor compaction	hard
ARS C	grey quartz, with brown, grey, pink and orange particles up to 11 mm diameter	light grey	5Y 7/2	occasional large voids up to 7 mm long, in areas of honeycombing	none	very hard
N B	white, black, brown and grey particles, up to 3 mm diameter	light orange at surface and darker orange in depth	surface: 2.5Y 8/6 10 mm below surface: 2.5Y 7/6	voids generally not visible, except possibly where aggregate particles have been lost	cracks through the matrix and around the aggregate particles, up to 0.7 mm wide	moderately hard
P B	white, brown and black particles, up to 3 mm diameter	yellow-brown at the surface and mid brown	surface: 7.5YR 4/6 10 mm below surface:	voids generally not visible	cracks through the matrix and around the	moderately hard

		in depth	2.5YR 2/4		aggregate particles, up to 0.7 mm wide	
Wa B	orange, black and brown particles, up to 2 mm, with black coal-like particles up to 5 mm diameter	reddish-brown at the surface and dark brown/ black in depth	surface: 5YR 5/8 10 mm below surface: 10YR 1/2	occasional voids, up to 0.5 mm diameter	cracks through the matrix up to 0.3 mm wide	moderately hard
B25 B	orange, black and brown particles, up to 1.5 mm, and black coal-like particles, particularly at the surface, up to 6 mm diameter	mid brown at surface and dark brown/ black in depth	surface: 10YR 5/6 10 mm below surface: 2.5Y 1/2	occasional voids, up to 0.5 mm diameter	cracks on surface	moderately hard
B23 B	white, black, red and orange particles, up to 2 mm diameter	mid orange-red at surface and light orange in depth	surface: 2.5YR 4/8 10 mm below surface: 7.5YR 6/8	some voids up to 1 mm diameter	none	moderately hard

Table A2.3 Staining with phenolphthalein solution

sample	photomicrograph	description
B24 OR	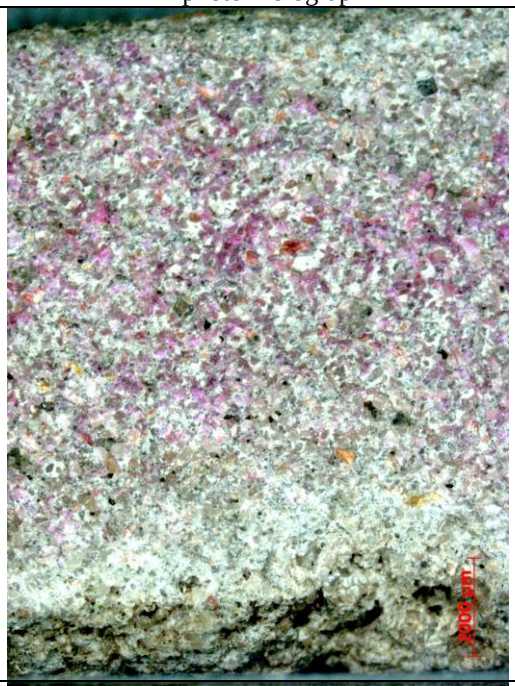	Slight staining of the middle of the section, suggesting that the surface and the interface with the bricks had carbonated, and that the middle section was carbonated in places.
B32 OR	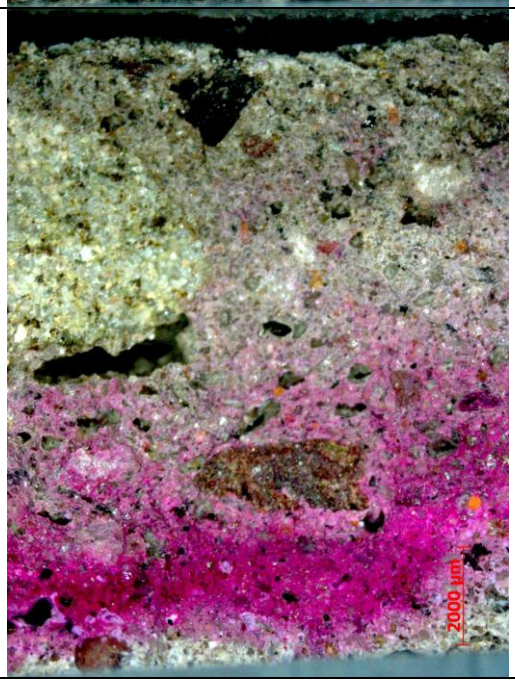	Deep staining towards the bottom of the section, suggesting that this zone was not carbonated, but that the surface and interface with the bricks had carbonated. .
B47 OR		No staining, suggesting that the sample was at least partially and possibly fully carbonated.
B23 RR		No staining, suggesting that the sample was at least partially and possibly fully carbonated.

B25 RR	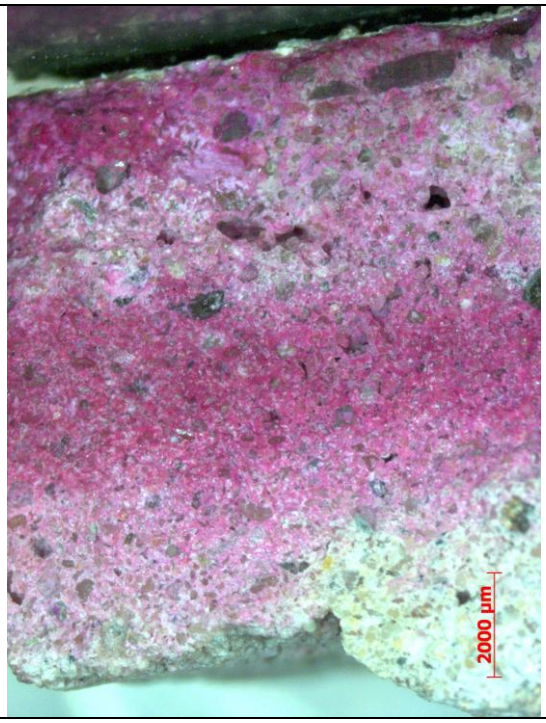	Deep staining of the middle of the sample and the top 2 mm just below the surface, suggesting that these areas had not carbonated. The interface with the bricks had carbonated and the area around the voids approximately 3 mm below the surface had begun to carbonate.
ARSC	Surface of the concrete section 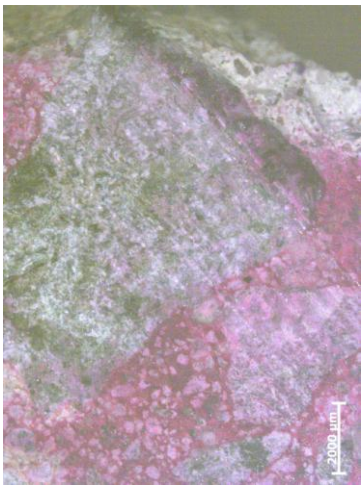 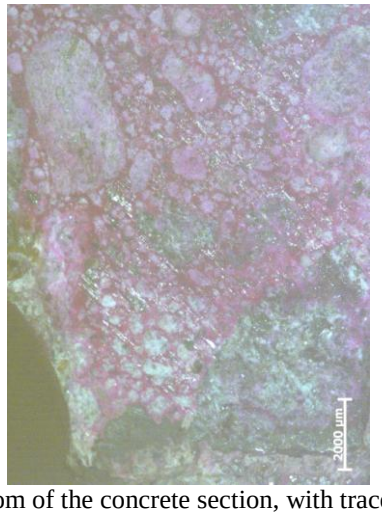 Bottom of the concrete section, with traces of corroded steel on the lower left	Deep staining through most of the sample, suggested that it had not carbonated. The surface and bottom of the sample were only partially stained and had probably begun to carbonate.

A2.2 Aggregates from the original and repair renders

Fig. A2.1. Calcite crystal fragment in B32 OR, plane polarized light, field of view: 1750 µm across

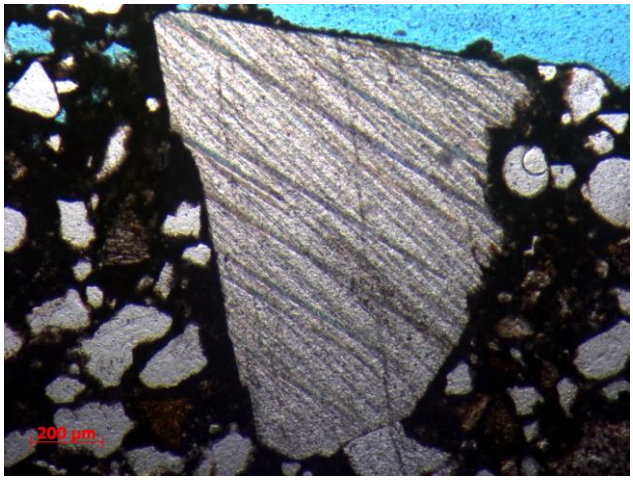

Fig. A2.2. Mud flake in B32 OR, plane polarized light, field of view: 875 µm across

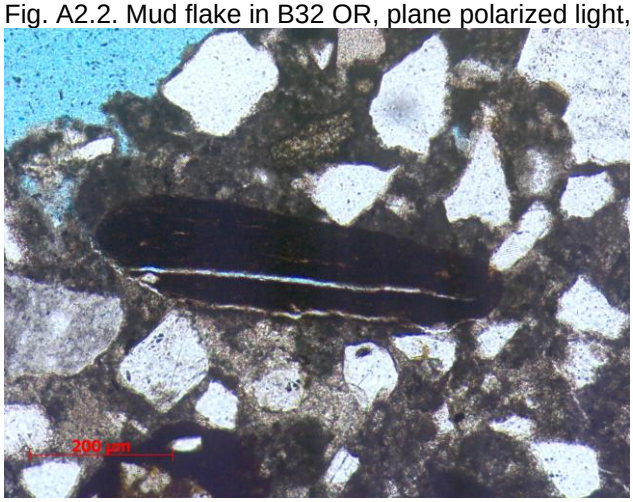

Fig. A2.3. Fine-grained probable silicic lava fragment (upper left) and coal particle (lower right) in B32 OR, plane polarized light, field of view: 875 µm across

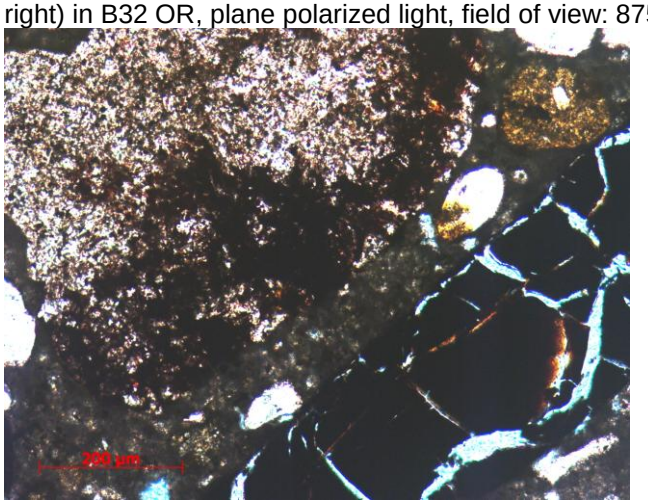

Fig. A2.4. Basaltic or hawaiitic lava fragment in B32 OR, showing plagioclase microphenocrysts in an unresolvable opaque matrix, plane polarized light, field of view 875 µm across

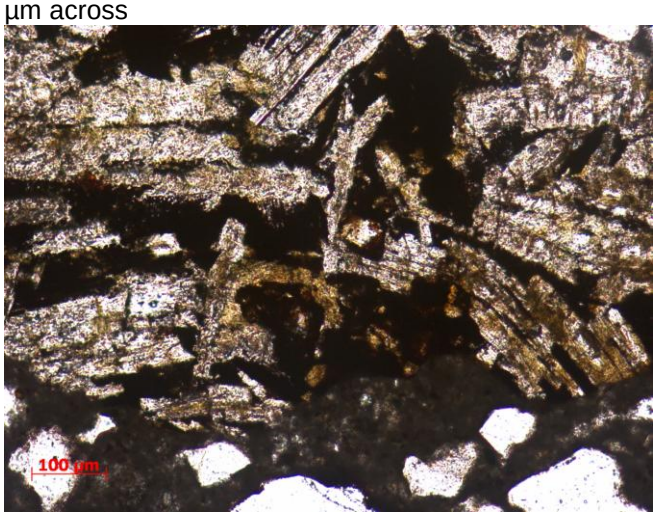

Fig. A2.5. Feldspar-rich lava fragment in B32 OR, plane polarized light, field of view: 875 µm across

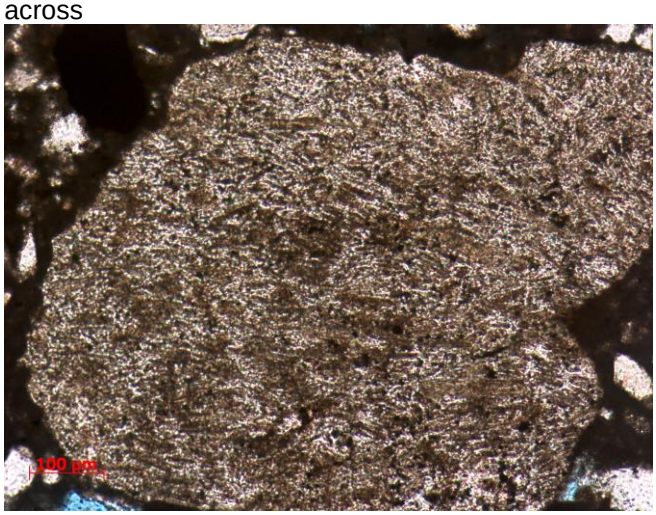

Fig. A2.6. Fragment of medium grained dolerite in B47 OR, with unaltered pyroxene and plagioclase feldspar, plane polarized light, field of view: 1750 µm across

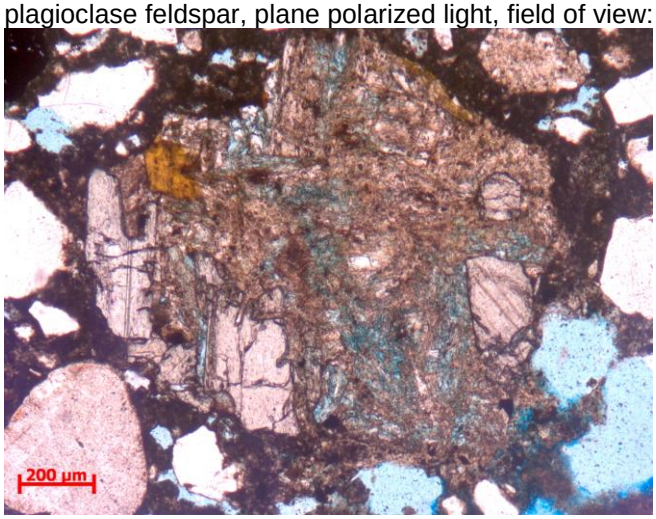

Fig. A2.7. As above, crossed polars

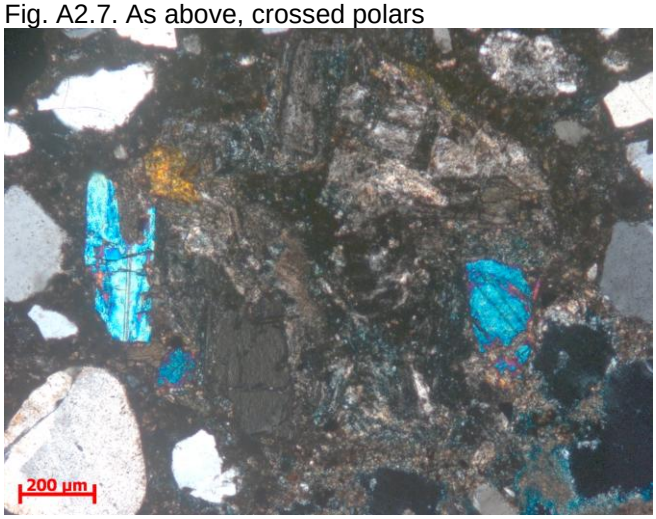

Fig. A2.8. Part of poorly-sorted polymict sandstone clast in B47 OR, plane polarized light, field of view: 1750 µm across

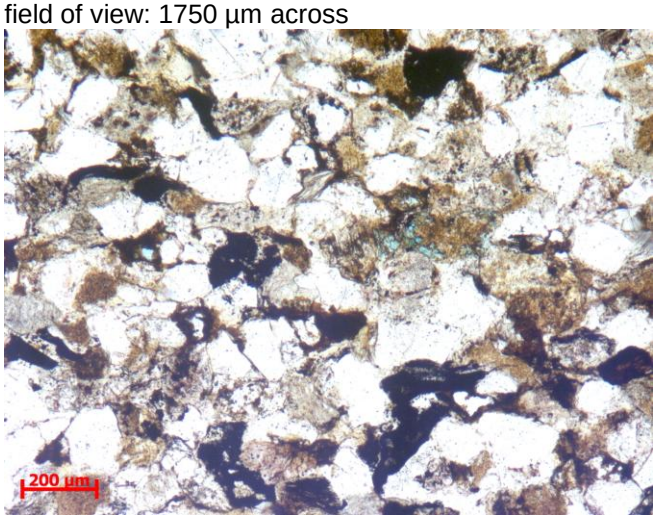

Fig. A2.9. As above, crossed polars

Fig. A2.10. Quartzite in B25 RR, plane polarized light, field of view: 440 µm across

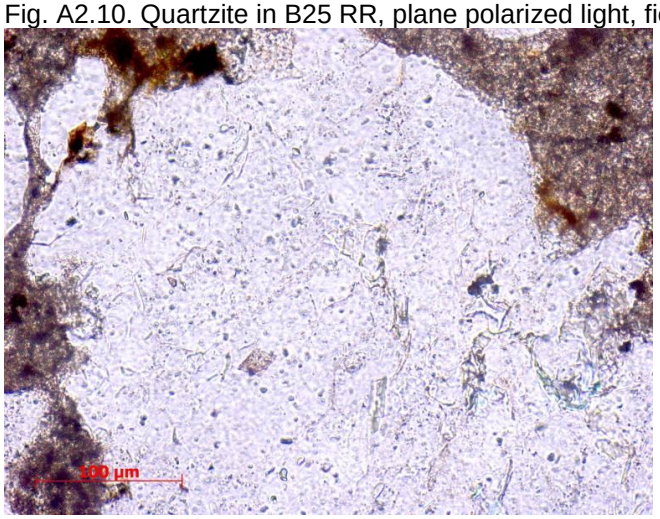

Fig. A2.11. As above, crossed polars

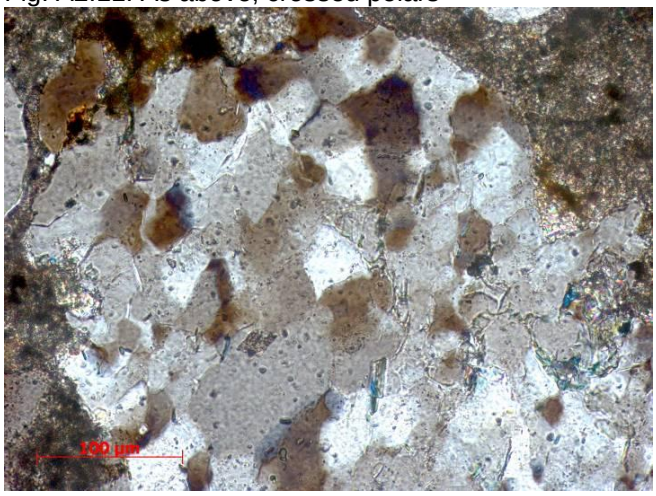

Fig. A2.12. Basaltic lava fragment with euhedral micro-phenocrysts of plagioclase feldspar in an opaque, altered groundmass, from B25 RR, plane polarized light, field of view: 875 µm across

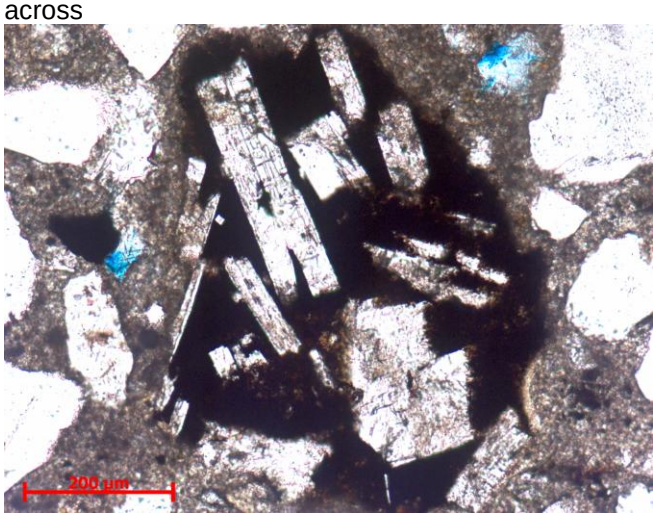

Fig. A2.13. As above, crossed polars

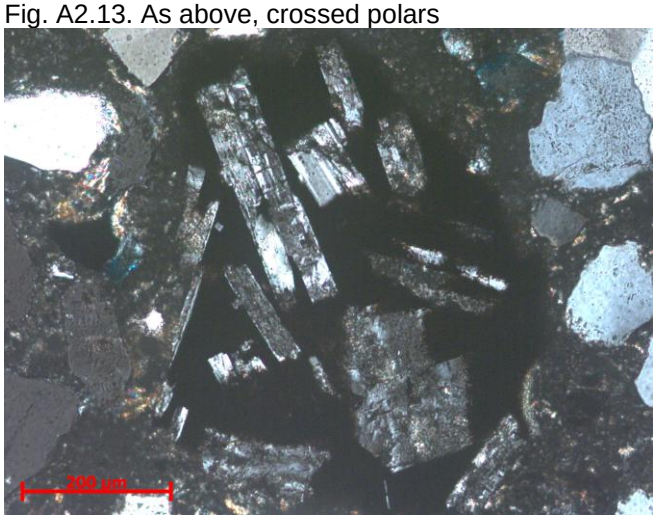

Fig. A2.14. Carbonate-cemented sandstone clast in B25 RR, plane polarized light, field of view: 875 µm across

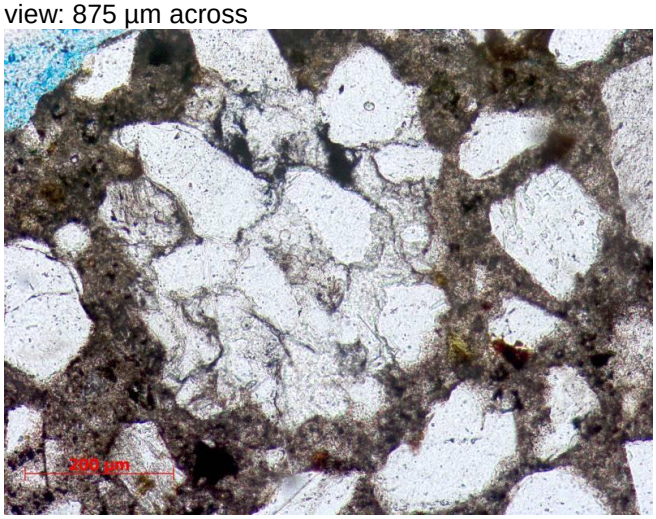

Fig. A2.15. As above, crossed polars

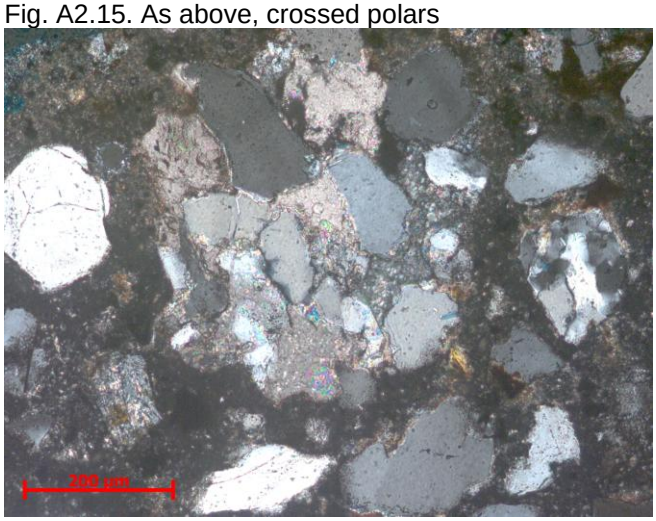

Fig. A2.16. Mica-rich siltstone clast in B25 RR, plane polarized light, field of view: 875 µm across

Fig. A2.17. As above, crossed polars

Fig. A2.18. Feldspar-rich doleritic rock fragment in B25 RR, plane polarized light, field of view: 1750 µm across

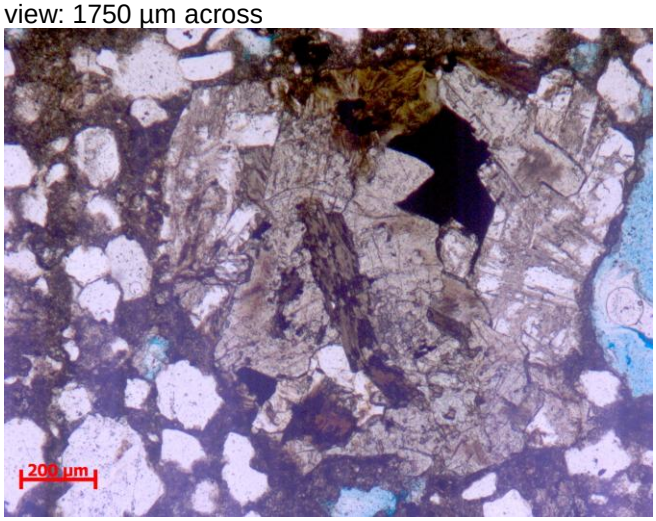

Fig. A2.19. As above, crossed polars

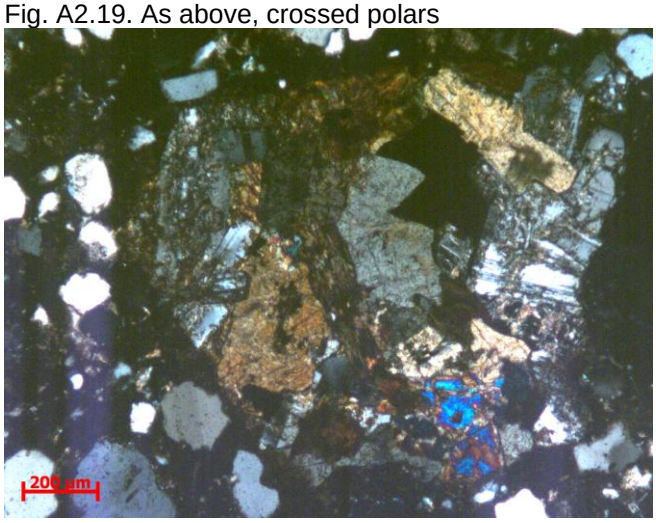

Fig. A2.20. Aggregate particle thought to be related to the blistering: mudstone fragment with prominent cleavage, plane polarized light, field of view: 875 µm across

Fig. A2.21. Aggregate particle thought to be related to the blistering: a mud-rich particle with some crystalline material, plane polarized light, field of view: 875 µm across

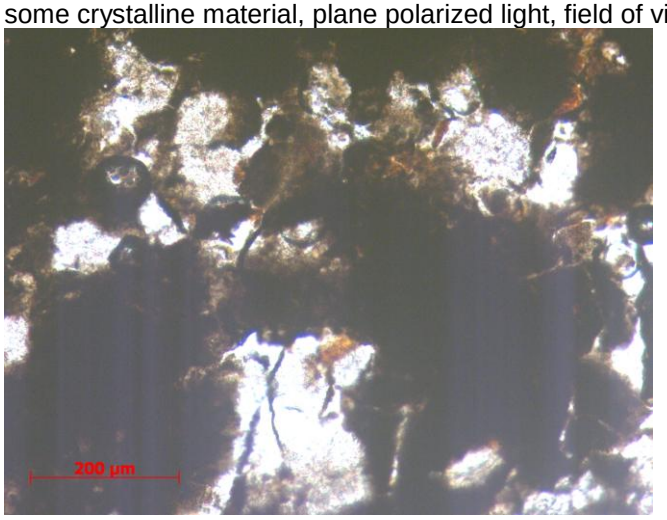

A2.3 Full results of point-counting

Table A2.4 Results of point-counting for the historic renders

sample	voids (%)	cement paste (%)	cement clinker (%)	hydrated cement (%)	quartz below 200 µm (%)	quartz above 200 µm (%)	feldspar (%)	mudstone (%)	other aggregate (%)
B24 OR1	21.33	30.67	1.33	0.00	8.09	33.91	0.00	0.00	4.67
B24 OR2	22.59	26.58	1.66	0.00	12.70	32.16	0.66	0.00	3.65
B32 OR1	8.31	37.87	0.00	1.66	13.69	13.56	0.66	3.65	20.60
B32 OR2	9.63	35.22	0.00	2.33	17.02	14.87	0.00	1.99	18.94
B47 OR1	8.97	25.58	0.00	0.33	8.38	20.53	0.33	0.66	35.22
B47 OR2	9.33	33.3	0.00	0.67	4.77	19.58	0.00	3.02	29.33

Table A2.5 Results of point-counting for the repair renders

sample	voids (%)	cement paste (%)	cement clinker (%)	hydrated cement (%)	quartz (%)	feldspar (%)	mudstone (%)	other aggregate (%)
B23 OR1	16.60	30.60	0.40	6.20	36.80	1.00	0.20	8.20
B23 OR2	15.20	28.54	0.20	8.40	36.76	1.00	0.40	9.50
B25 RR upper layer 1	2.60	45.60	0.00	1.40	33.40	1.60	0.00	15.40
B25 RR upper layer 2	4.17	45.54	0.20	0.59	30.89	1.98	0.00	16.63
B25 RR bottom layer 1	7.80	36.80	0.20	0.80	41.80	3.00	0.00	9.60
B25 RR bottom layer 2	8.60	40.00	0.00	1.20	37.40	2.20	0.60	10.00

A3.1 Detailed method for ions analysis

A3.1.1 Ion Chromatography

Water samples were analysed for nitrate, chloride, sulphate and phosphate ions using a DX-500 ion chromatograph (DIONEX, Sunnyvale, CA, USA). Separation was achieved using an IonPac AS22A analytical column and a mobile phase composed of 4.5 mM sodium bicarbonate/1.4 mM sodium carbonate, delivered at a flow rate of 1.2 ml/min. Post-column eluent suppression was achieved using an anion self-regenerating suppressor (ASRS-1) operated at a current of 50 mA. Detection was via a ED40 electrochemical detector set at an output range of 30 μS. Instrument control and data collection were accomplished using PeakNet software.

A3.1.2 ICP-OES

Water samples were analysed for calcium, magnesium, potassium, sodium and aluminium ions using a Perkin Elmer Optima 5300 DV, employing an RF forward power of 1400 W, with argon gas flows of 15, 0.2 and 0.75 L min^{-1} for plasma, auxiliary, and nebuliser flows, respectively. Using a peristaltic pump, sample solutions were taken up into a Gem Tip cross-Flow nebuliser and Scotts spray chamber at a rate of 1.50 mL min^{-1}. The instrument was operated in axial mode.

A range of calibration standards were prepared using single element 1000 mg l^{-1} stock solutions (Fisher Scientific UK Ltd.) diluted with deionised water (18Ω, Elga USF). A Merck multi element standard (ICP-multielement solution VI, part number 1.10580.0100) was employed as an external reference standard. This was analysed neat and was also diluted 50 and 100 fold to give concentrations of 100, 5 and 1 mg/l. With all of the calibration lines the correlation coefficients for the linear regression were 0.9992 or better.

Initially four wavelengths were selected and three replicate runs per sample were employed. The selected wavelengths for each element were analysed in fully quantitative mode, with three points per unit wavelength. After the analysis was completed the wavelengths giving the best resolution were selected for reporting results.

A3.2 Full results of chemical and physical characterization

Table A3.1 Abbreviated names for the materials tested

abbreviated name	**material**
B33 M	mortar from Building 33
B24 OR	original render from Building 24
B47 OR	original render from Building 47
B31 OR	original render from Building 31
HC OR	original render from the hospital complex buildings at Athelstaneford Mains
B23 RR	1992 repair render from Building 23
B25 RR	2005 repair render from Building 25
ARS C	concrete from the air raid shelter (section NW17, rib on NE side)
ARS M	mortar from the air raid shelter (between sections SE5 and SE6)
ES B	Edinburgh brick, core drilled through stretcher face
EB B	Edinburgh brick, core drilled through bed face
NS B	Niddrie brick, core drilled through stretcher face
NB B	Niddrie brick, core drilled through bed face
PS B	Prestongrange brick, core drilled through stretcher face
PB B	Prestongrange brick, core drilled through bed face
WaS B	Wallyford brick, core drilled through stretcher face
WaB B	Wallyford brick, core drilled through bed face
WhS B	Whitehill brick, core drilled through stretcher face
WhB B	Whitehill brick, core drilled through bed face
C	Composite of Niddrie brick and hospital complex render

Fig. A3.1. Particle size distribution of aggregates for all samples tested, showing percentage by weight retained in each sieve size

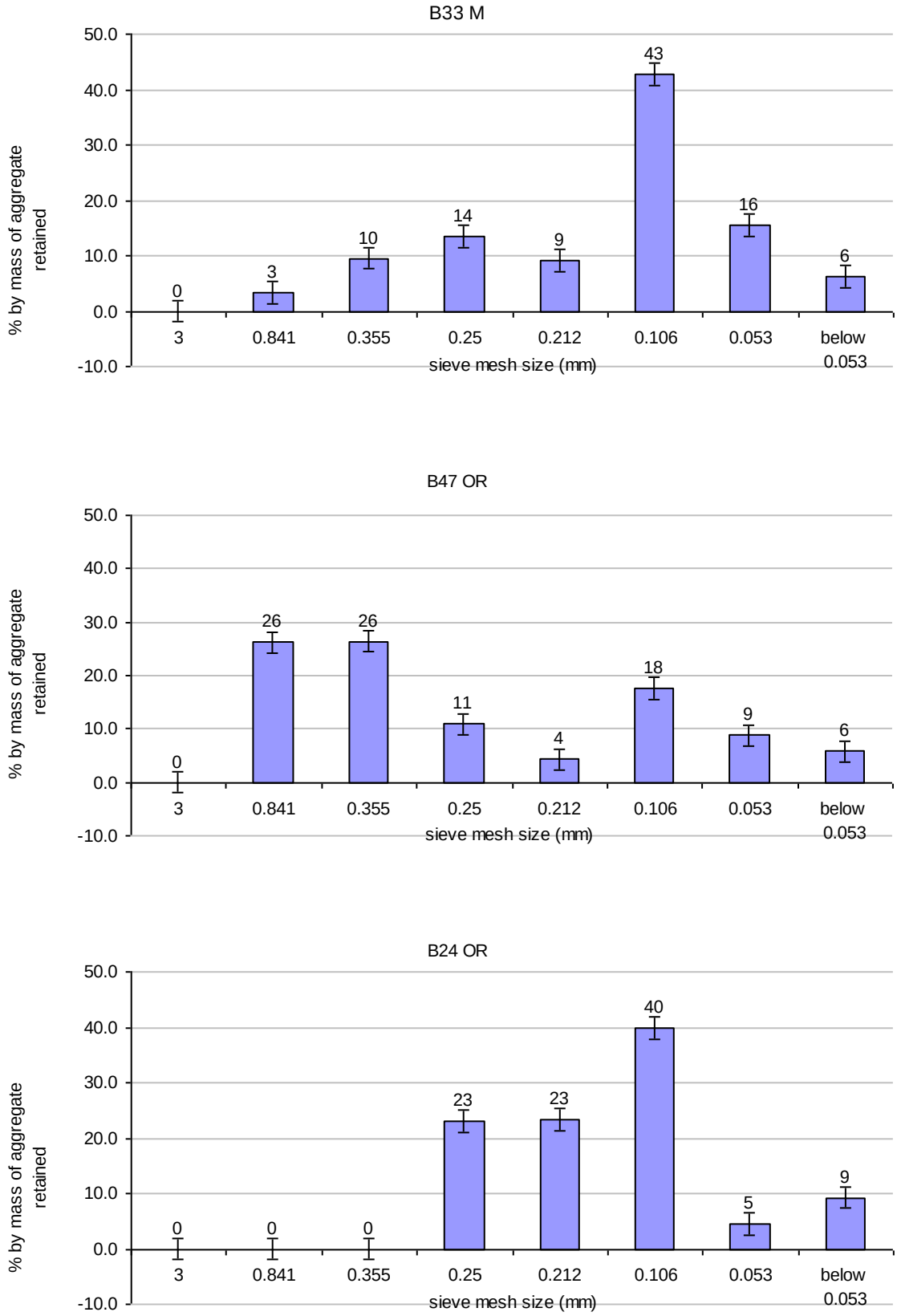

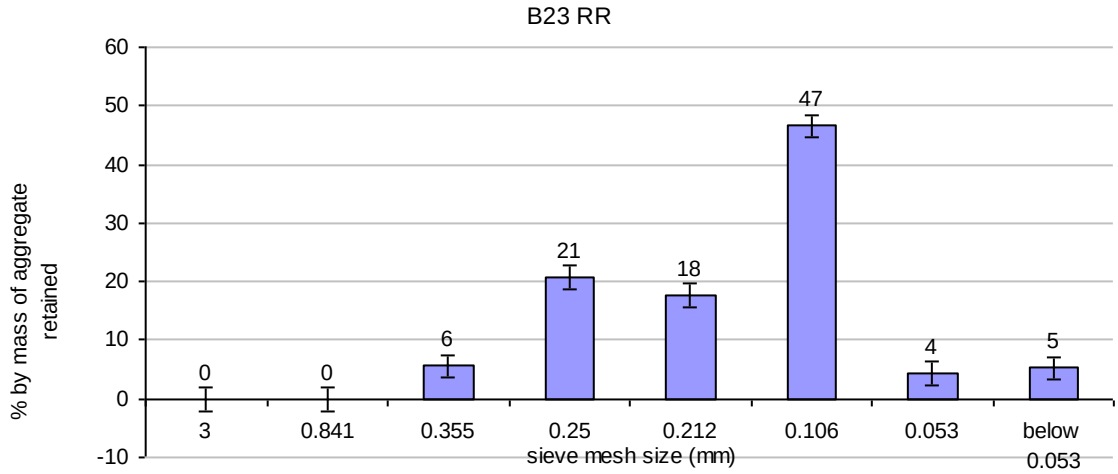
B23 RR
% by mass of aggregate retained
60
50
40
30
20
10
0
-10
0
0
6
21
18
47
4
5
3
0.841
0.355
0.25
0.212
0.106
0.053
below 0.053
sieve mesh size (mm)

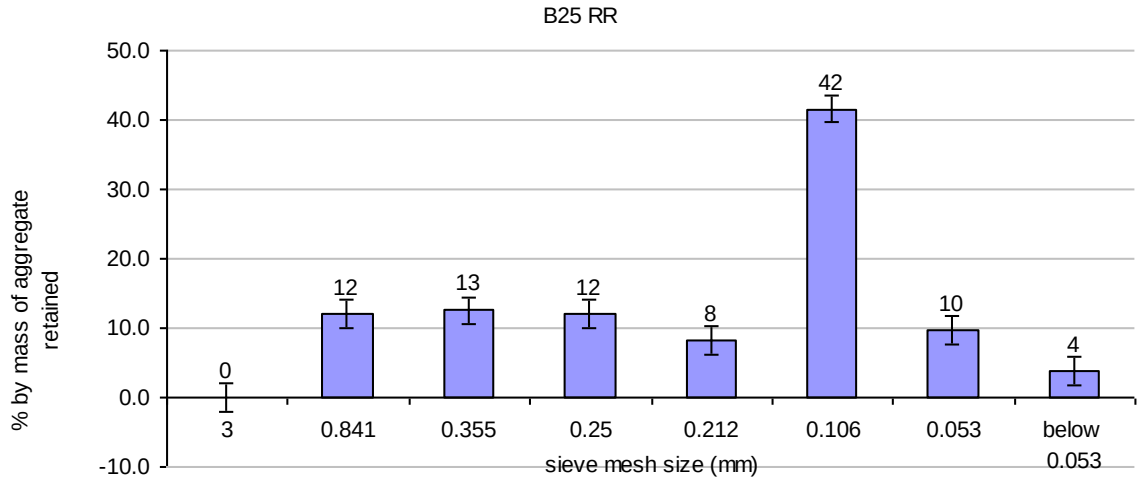
B25 RR
% by mass of aggregate retained
50.0
40.0
30.0
20.0
10.0
0.0
-10.0
0
12
13
12
8
42
10
4
3
0.841
0.355
0.25
0.212
0.106
0.053
below 0.053
sieve mesh size (mm)

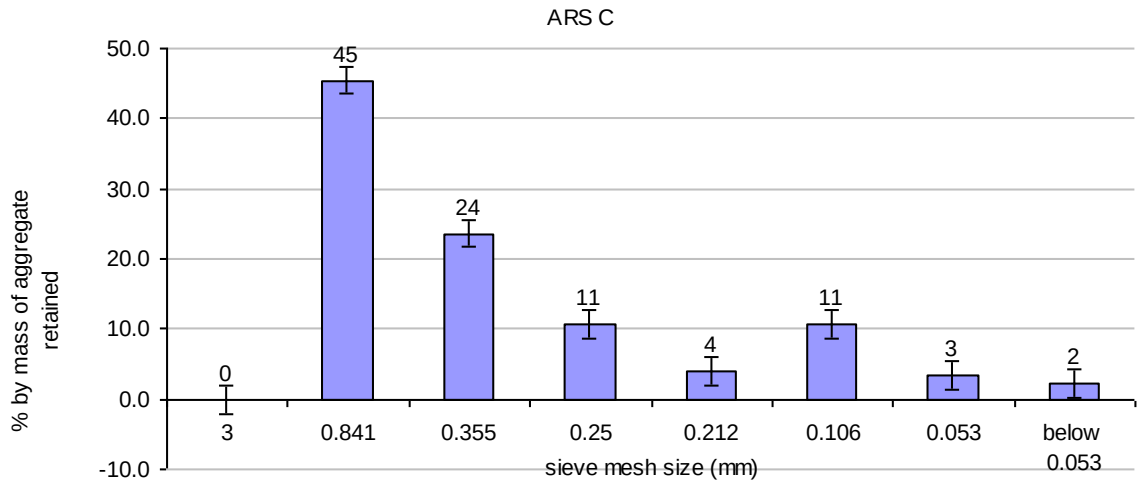
ARS C
% by mass of aggregate retained
50.0
40.0
30.0
20.0
10.0
0.0
-10.0
0
45
24
11
4
11
3
2
3
0.841
0.355
0.25
0.212
0.106
0.053
below 0.053
sieve mesh size (mm)

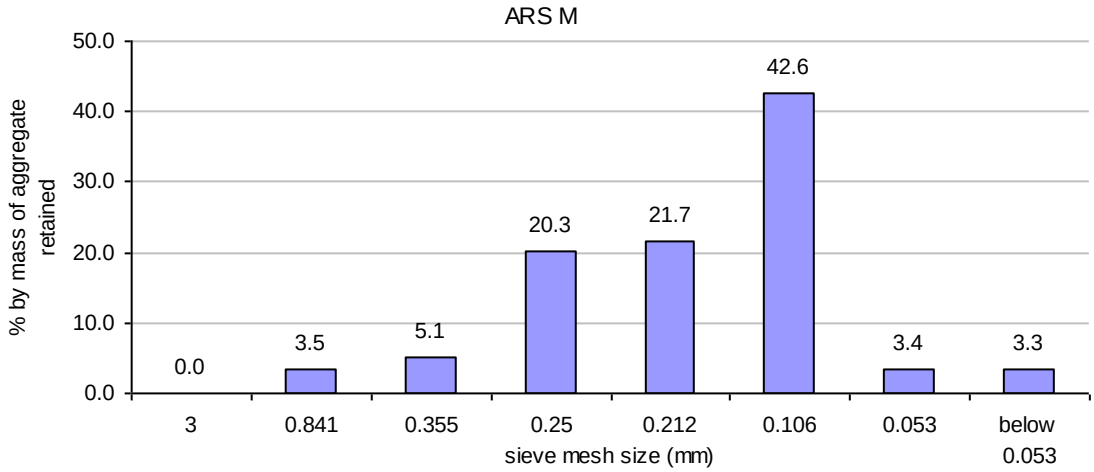

Table A3.2 Full results for binder:aggregate ratio by acid extraction technique

sample	sample mass (g)	mass aggregate (g)	mass cement paste (g)	original mass cement powder (g)	original volume aggregate (g)	original volume cement (g)	binder: aggregate ratio
B33 Ma	1.0845	0.6290	0.4555	0.3644	0.3926	0.2420	1:1.6
B33 Mb	1.1262	0.6430	0.4832	0.3866	0.4014	0.2567	1:1.6
B47 ORa	0.9987	0.6508	0.3479	0.2783	0.4062	0.1848	1:2.2
B47 ORb	1.1756	0.8365	0.3391	0.2713	0.5222	0.1801	1:2.9
B47 ORc	1.2585	0.9475	0.3110	0.2488	0.5914	0.1652	1:3.6
B24 ORa	1.0065	0.6536	0.3529	0.2823	0.4080	0.1875	1:2.2
B24 ORb	1.0579	0.6902	0.3677	0.2942	0.4308	0.1953	1:2.2
B23 RRa	1.1135	0.7324	0.3811	0.3049	0.4572	0.2024	1:2.3
B23 RRb	1.1837	0.8204	0.3633	0.2906	0.5121	0.1930	1:2.7
B25 RRa	1.0640	0.6803	0.3837	0.3070	0.4247	0.2038	1:2.1
B25 RRb	1.3513	0.8612	0.4901	0.3921	0.5376	0.2603	1:2.1
ARS Ca	2.0628	1.4843	0.5785	0.4628	0.9265	0.3073	1:3.0
ARS Cb	2.1339	1.5266	0.6073	0.4858	0.9529	0.3226	1:3.0
ARS Ma	1.0844	0.7322	0.3522	0.2818	0.4571	0.1871	1:2.4
ARS Mb	1.3803	0.9400	0.4403	0.3522	0.5868	0.2339	1:2.5

Table A3.3 Preparation of aqueous extractions for ions analysis

sample	sample description	sample mass (g)	mass of water (g)
EB	Edinburgh brick from salvage heap	0.51	24.48
NB	Niddrie brick from salvage heap	0.51	24.10
PB	Prestongrange brick from salvage heap	0.51	23.25
WaB1	Wallyford brick from salvage heap	0.51	38.74
WaB2	Wallyford brick from near ground in Building 25	0.49	23.73
WhB	Whitehill brick from salvage heap	0.52	24.10
B26 OR NF1	Building 26 original render from area without flaking	0.52	24.99
B26 OR F1	Building 26 original render from area with flaking	0.49	29.59
B46 OR NF1	Building 46 original render from area without flaking	2.04	27.04
B46 OR NF2	Building 46 original render from area without flaking	0.57	24.64
B46 OR F1	Building 46 original render from area with flaking	1.96	24.86
B46 OR F2	Building 46 original render from area with flaking	1.96	27.51
B46 OR F3	Building 46 original render from area with flaking	0.50	27.93
B47 OR NF1	Building 47 original render from area without flaking	2.02	36.76
B47 OR NF2	Building 47 original render from area without flaking	1.97	25.35
B47 OR NF3	Building 47 original render from area without flaking	2.02	27.39
B47 OR F1	Building 47 original render from area with flaking	1.97	26.45
B47 OR F2	Building 47 original render from area with flaking	2.06	24.34
B24 OR NF1	Building 24 original render, no flaking on building	2.02	36.76
B24 OR NF2	Building 24 original render, no flaking on building	1.95	27.42
B24 OR NF3	Building 24 original render, no flaking on building	0.50	42.28
B23 OR NF1	Building 23 original render, no flaking on building	0.52	24.50
CA OR NF1	Cark Airfield original render, no flaking on building	2.06	24.07
B33 OM1	Building 33 original render	0.5	27.40
B44 OM1	Building 44 original render, sampled from near ground	0.51	25.60
B37 S1	salt efflorescence from inside the N wall on Building 37	0.20	28.88
B25 S1	salt efflorescence from inside the E wall on Building 25	0.21	25.36
ARS C1	air raid shelter concrete, 1 m from ground, surface	2.00	25.39
ARS C2	air raid shelter concrete, 1 m from ground, 0.05 m below surface	1.54	24.69
ARS C3	air raid shelter concrete, 1.5 m from ground, surface	0.5	25.92
ARS C4	air raid shelter concrete, 1.5 m from ground, 0.10 m below surface	0.55	33.07
ARS C5	air raid shelter concrete, 2 m from ground, surface	0.53	31.15
ARS C6	air raid shelter concrete, 2 m from ground, 0.10 m below surface	1.92	26.37
CA ARS C1	Cark airfield concrete from air raid shelter	2.00	25.51
B C1	Second World War concrete from beach near NMOF	0.30	27.54
ARS M1	air raid shelter mortar joint between sections, exterior surface	2.01	24.48
ARS M2	air raid shelter mortar joint between sections, interior surface	2.03	26.59
ARS S1	salt efflorescence from inside the air raid shelter	0.04	45.57
GW	ground water from NMOF		
SW	sea water		

Table A3.4 Measured concentrations of anions

sample	chloride ppm	nitrate ppm	sulfate ppm	chloride molarity	nitrate molarity	sulfate molarity	sum of anion charges
EB	0.05	0.05	0.45	0.0000013	0.0000008	0.0000047	0.0000125
NB	0.18	0.05	0.18	0.0000050	0.0000008	0.0000018	0.0000215
PB	0.14	0.05	0.50	0.0000039	0.0000008	0.0000052	0.0000161
WaB1	0.09	0.05	3.72	0.0000026	0.0000008	0.0000387	0.0000819
WaB2	1.64	6.29	13.40	0.0000462	0.0001014	0.0001394	0.0004319
WhB	0.04	0.05	0.14	0.0000012	0.0000008	0.0000014	0.0000058
B26 OR NF1	0.19	0.05	7.09	0.0000054	0.0000008	0.0000739	0.0001550
B26 OR F1	0.65	0.14	4.06	0.0000182	0.0000022	0.0000423	0.0001061
B46 OR NF1	0.51	0.14	76.56	0.0000142	0.0000023	0.0007974	0.0016133
B46 OR NF2	1.04	0.21	21.20	0.0000294	0.0000034	0.0002206	0.0004751
B46 OR F1	5.95	1.21	38.22	0.0001675	0.0000195	0.0003981	0.0009851
B46 OR F2	3.99	1.33	370.22	0.0001123	0.0000215	0.0038565	0.0078488
B46 OR F3	2.83	1.00	87.30	0.0000797	0.0000161	0.0009093	0.0019155
B47 OR NF1	1.48	0.44	24.45	0.0000418	0.0000071	0.0002547	0.0005602
B47 OR NF2	1.30	0.10	47.50	0.0000366	0.0000017	0.0004948	0.0010306
B47 OR NF3	0.41	0.06	30.35	0.0000116	0.0000010	0.0003162	0.0006469
B47 OR F1	2.37	0.05	27.87	0.0000667	0.0000008	0.0002904	0.0006693
B47 OR F2	13.76	3.18	197.47	0.0003876	0.0000513	0.0020570	0.0045548
B24 OR NF1	0.85	1.14	30.58	0.0000238	0.0000184	0.0003186	0.0006814
B24 OR NF2	4.45	9.50	57.38	0.0001253	0.0001533	0.0005977	0.0014760
B24 OR NF3	0.18	0.31	21.70	0.0000051	0.0000049	0.0002256	0.0004622
B23 OR NF1	0.12	0.05	3.28	0.0000034	0.0000008	0.0000341	0.0000734
CA OR NF1	26.96	22.91	206.18	0.0007594	0.0003695	0.0021477	0.0054262
B33 OM1	0.27	0.57	14.40	0.0000077	0.0000093	0.0001499	0.0003176
B44 OM1	0.15	0.05	4.59	0.0000043	0.0000008	0.0000478	0.0001017
B37 S1	0.87	0.10	2166	0.0000246	0.0000017	0.0225625	0.0451522
B25 S1	4.10	0.05	17750	0.0001154	0.0000008	0.0184896	0.0370963
ARS C1	134.50	12.42	0.04	0.0037888	0.0002003	0.0000004	0.0039918
ARS C2	126.44	13.01	7.79	0.0035618	0.0002098	0.0000812	0.0039358
ARS C3	8.05	4.09	19.10	0.0002267	0.0000660	0.0001991	0.0006917
ARS C4	79.00	10.29	8.37	0.0022250	0.0001659	0.0000872	0.0025663
ARS C5	0.23	0.19	42.60	0.0000065	0.0000031	0.0004438	0.0008983
ARS C6	152.35	41.40	17.58	0.0042916	0.0006677	0.0001831	0.0053274
CA ARS C1	7.07	18.11	28.59	0.0001991	0.0002921	0.0002978	0.0010887
B C1	56.97	0.05	21.75	0.0016048	0.0000008	0.0002266	0.0020606
ARS M1	1.83	1.97	28.68	0.0000515	0.0000318	0.0002988	0.0006827
ARS M2	3.14	5.85	5.77	0.0000884	0.0000944	0.0000601	0.0003049
ARS S1	0.30	0.74	142.00	0.0000084	0.0000120	0.0014792	0.0029797
GW1	77.00	0.05	17.40	0.0021696	0.0000008	0.0001816	0.0025346
GW2	68.10	0.05	18.40	0.0019190	0.0000008	0.0001919	0.0023047
SW1	20065.03	0.05	2514.64	0.5652122	0.0000008	0.0261942	0.6176032

Table A3.5 Measured concentrations of cations

sample	Ca^{2+} (ppm)	Mg^{2+} (ppm)	K^{+} (ppm)	Na^{+} (ppm)	Al^{3+} (ppm)
EB	5.45	0.09	0.00	0.97	0.06
NB	0.88	0.12	0.00	0.24	0.02
PB	1.91	0.10	0.00	1.99	0.00
WaB1	0.91	0.05	0.00	1.16	0.00
WaB2	8.98	0.56	1.00	1.73	0.02
WhB	0.01	0.04	0.00	2.35	0.00
B26 OR NF1	11.64	0.06	0.15	1.81	4.56
B26 OR F1	26.17	0.08	0.54	2.23	9.83
B46 OR NF1	64.41	0.01	11.14	8.63	2.61
B46 OR NF2	31.76	0.03	0.35	2.13	2.38
B46 OR F1	115.84	0.04	7.79	7.36	0.08
B46 OR F2	153.06	0.23	8.03	14.69	7.25
B46 OR F3	37.70	0.20	0.70	3.38	3.21
B47 OR NF1	22.21	0.38	3.09	4.94	0.05
B47 OR NF2	63.32	0.06	7.45	6.93	0.02
B47 OR NF3	24.33	0.35	4.14	3.74	0.02
B47 OR F1	94.92	2.63	9.08	11.33	0.04
B47 OR F2	145.72	0.04	6.83	10.55	0.17
B24 OR NF1	88.27	0.01	2.40	1.37	0.13
B24 OR NF2	99.03	0.02	3.18	2.03	0.06
B24 OR NF3	16.95	1.09	0.71	1.39	0.03
B23 OR NF1	24.58	0.62	1.09	1.74	0.05
CA OR NF1	136.09	0.08	1.35	3.37	0.15
B33 OM1	32.12	1.77	1.52	1.07	0.02
B44 OM1	34.41	0.49	0.28	1.12	0.05
B37 S1	1.59	0.18	9.32	925.00	0.42
B25 S1	13.14	21.70	12.10	591.00	0.06
ARS C1	650.01	0.02	24.76	16.24	0.22
ARS C2	231.79	0.01	7.35	8.24	2.67
ARS C3	81.49	0.01	5.17	14.65	3.88
ARS C4	315.90	0.01	0.00	1.53	0.83
ARS C5	12.12	0.13	1.70	7.62	1.59
ARS C6	216.34	0.01	5.94	7.28	2.35
CA ARS C1	32.83	0.42	5.34	5.19	0.80
B C1	11.24	6.79	5.54	46.98	0.07
ARS M1	24.27	0.55	3.79	2.12	0.07
ARS M2	38.86	0.01	5.06	2.94	16.34
ARS S1	3.63	0.05	0.69	36.50	0.53
GW1	68.51	9.34	0.21	23.00	0.00
GW2	82.11	9.22	0.14	19.06	0.00
SW1	233.93	747.68	5.38	11829.73	0.02

Table A3.6 Molarity of cations

sample	Ca^{2+} molarity	Mg^{2+} molarity	K^{+} molarity	Na^{+} molarity	Al^{3+} molarity	sum of cation charges
EB	0.0001363	0.0000037	0.0000000	0.0000420	0.0000022	0.0003287
NB	0.0000219	0.0000048	0.0000000	0.0000103	0.0000007	0.0000659
PB	0.0000477	0.0000043	0.0000000	0.0000866	0.0000000	0.0001906
WaB1	0.0000227	0.0000020	0.0000000	0.0000505	0.0000000	0.0001000
WaB2	0.0002246	0.0000232	0.0000257	0.0000750	0.0000006	0.0005979
WhB	0.0000004	0.0000016	0.0000000	0.0001023	0.0000000	0.0001061
B26 OR NF1	0.0002910	0.0000023	0.0000038	0.0000788	0.0001688	0.0011755
B26 OR F1	0.0006543	0.0000033	0.0000138	0.0000971	0.0003639	0.0025178
B46 OR NF1	0.0016103	0.0000005	0.0002857	0.0003751	0.0000968	0.0041729
B46 OR NF2	0.0007940	0.0000012	0.0000090	0.0000927	0.0000880	0.0019560
B46 OR F1	0.0028961	0.0000018	0.0001997	0.0003198	0.0000031	0.0063247
B46 OR F2	0.0038264	0.0000095	0.0002058	0.0006386	0.0002683	0.0093212
B46 OR F3	0.0009425	0.0000081	0.0000179	0.0001468	0.0001187	0.0024222
B47 OR NF1	0.0005554	0.0000158	0.0000792	0.0002147	0.0000018	0.0014415
B47 OR NF2	0.0015829	0.0000026	0.0001911	0.0003012	0.0000008	0.0036658
B47 OR NF3	0.0006083	0.0000147	0.0001063	0.0001628	0.0000009	0.0015177
B47 OR F1	0.0023730	0.0001095	0.0002329	0.0004926	0.0000016	0.0056954
B47 OR F2	0.0036430	0.0000015	0.0001752	0.0004588	0.0000064	0.0079422
B24 OR NF1	0.0022068	0.0000004	0.0000617	0.0000594	0.0000049	0.0045501
B24 OR NF2	0.0024757	0.0000009	0.0000816	0.0000881	0.0000023	0.0051297
B24 OR NF3	0.0004238	0.0000447	0.0000183	0.0000606	0.0000010	0.0010188
B23 OR NF1	0.0006145	0.0000254	0.0000279	0.0000757	0.0000017	0.0013886
CA OR NF1	0.0034021	0.0000034	0.0000347	0.0001467	0.0000056	0.0070093
B33 OM1	0.0008030	0.0000727	0.0000389	0.0000463	0.0000009	0.0018393
B44 OM1	0.0008603	0.0000202	0.0000073	0.0000485	0.0000020	0.0018226
B37 S1	0.0000397	0.0000072	0.0002389	0.0402174	0.0000154	0.0405964
B25 S1	0.0003285	0.0008930	0.0003103	0.0256957	0.0000021	0.0284553
ARS C1	0.0162502	0.0000010	0.0006348	0.0007063	0.0000080	0.0338672
ARS C2	0.0057948	0.0000005	0.0001886	0.0003581	0.0000989	0.0124339
ARS C3	0.0020373	0.0000002	0.0001324	0.0006370	0.0001436	0.0052752
ARS C4	0.0078975	0.0000002	0.0000000	0.0000667	0.0000307	0.0159544
ARS C5	0.0003030	0.0000053	0.0000435	0.0003313	0.0000590	0.0011687
ARS C6	0.0054086	0.0000005	0.0001524	0.0003167	0.0000872	0.0115488
CA ARS C1	0.0008207	0.0000175	0.0001370	0.0002257	0.0000295	0.0021274
B C1	0.0002811	0.0002831	0.0001420	0.0020425	0.0000026	0.0033207
ARS M1	0.0006067	0.0000231	0.0000971	0.0000920	0.0000024	0.0014560
ARS M2	0.0009716	0.0000006	0.0001297	0.0001278	0.0006051	0.0040174
ARS S1	0.0000908	0.0000021	0.0000176	0.0015870	0.0000197	0.0018495
GW1	0.0017128	0.0003844	0.0000053	0.0010000	0.0000000	0.0051996
GW2	0.0020528	0.0003793	0.0000036	0.0008287	0.0000000	0.0056964
SW1	0.0058484	0.0311531	0.0001380	0.5143360	0.0000006	0.5884787

Table A3.7 Calculation of original charge balancing error and prediction of concentrations of hydroxide, hydrogen carbonate and carbonate ions using PHREEQC

sample	original charge balancing error (%)	OH^- molality	HCO_3^- molality	CO_3^{2-} molality
EB	92.65	0.0000006	0.0002969	0.0000008
NB	50.79	0.0000000	0.0000107	0.0000000
PB	84.40	0.0000003	0.0001666	0.0000003
WaB1	9.97	0.0000000	0.0000135	0.0000000
WaB2	16.12	0.0000000	0.0000000	0.0000000
WhB	89.58	0.0000002	0.0000938	0.0000001
B26 OR NF1	76.70	0.0000006	0.0003344	0.0000010
B26 OR F1	91.92	0.0000017	0.0009067	0.0000079
B46 OR NF1	44.23	0.0000036	0.0019470	0.0000387
B46 OR NF2	60.92	0.0000020	0.0010600	0.0000109
B46 OR F1	73.05	0.0000077	0.0041120	0.0001774
B46 OR F2	8.58	0.0000006	0.0003006	0.0000010
B46 OR F3	11.68	0.0000000	0.0000231	0.0000000
B47 OR NF1	44.02	0.0000015	0.0008168	0.0000064
B47 OR NF2	56.11	0.0000043	0.0023260	0.0000549
B47 OR NF3	40.23	0.0000015	0.0008287	0.0000067
B47 OR F1	78.97	0.0000068	0.0036290	0.0001372
B47 OR F2	27.11	0.0000049	0.0026280	0.0000744
B24 OR NF1	73.95	0.0000059	0.0031610	0.0001027
B24 OR NF2	55.31	0.0000049	0.0026400	0.0000725
B24 OR NF3	37.59	0.0000010	0.0005174	0.0000026
B23 OR NF1	89.96	0.0000023	0.0012380	0.0000147
CA OR NF1	12.73	0.0000005	0.0002670	0.0000008
B33 OM1	70.55	0.0000026	0.0013930	0.0000190
B44 OM1	89.43	0.0000030	0.0015920	0.0000247
B37 S1	-5.31	0.0000428	0.0225500	0.0063720
B25 S1	-13.18	0.0000000	0.0000000	0.0000000
ARS C1	78.91	0.0000219	0.0116000	0.0016040
ARS C2	51.91	0.0000093	0.0049490	0.0002713
ARS C3	76.81	0.0000059	0.0031780	0.0001040
ARS C4	72.29	0.0000136	0.0072080	0.0005841
ARS C5	13.08	0.0000001	0.0000345	0.0000000
ARS C6	36.87	0.0000052	0.0027420	0.0000835
CA ARS C1	32.30	0.0000047	0.0000013	0.0000000
B C1	23.42	0.0000022	0.0011830	0.0000140
ARS M1	36.16	0.0000012	0.0006300	0.0000038
ARS M2	85.89	0.0000017	0.0009181	0.0000083
ARS S1	-23.40	0.0000000	0.0000000	0.0000000
GW1	34.46	0.0000043	0.0023220	0.0000559
GW2	42.39	0.0000053	0.0028550	0.0000850
SW1	-2.41	0.0000000	0.0000000	0.0000000

Table A3.8 Calculation of new charge balancing error and prediction of pH using PHREEQC

sample	new sum of anion charges	new charge balancing error (%)	measured pH	predicted pH
EB	0.0003116	2.67	7.01	7.73
NB	0.0000322	34.32	6.72	6.29
PB	0.0001835	1.88	6.68	7.48
WaB1	0.0000953	2.38	6.66	6.39
WaB2	0.0004320	16.12	6.89	3.73
WhB	0.0001000	2.97	7.93	7.24
B26 OR NF1	0.0004921	40.98	7.90	7.78
B26 OR F1	0.0010303	41.92	9.66	8.21
B46 OR NF1	0.0036414	6.80	10.91	8.53
B46 OR NF2	0.0015589	11.30	8.37	8.27
B46 OR F1	0.0054596	7.34	10.54	8.84
B46 OR F2	0.0081519	6.69	9.1	7.70
B46 OR F3	0.0019386	11.09	8.33	6.61
B47 OR NF1	0.0013915	1.77	8.09	8.16
B47 OR NF2	0.0034707	2.73	10.1	8.60
B47 OR NF3	0.0014904	0.91	9.41	8.17
B47 OR F1	0.0045795	10.86	7.85	8.79
B47 OR F2	0.0073366	3.96	10.85	8.64
B24 OR NF1	0.0040537	5.77	11.23	8.73
B24 OR NF2	0.0042658	9.19	10.9	8.65
B24 OR NF3	0.0009856	1.66	7.66	7.96
B23 OR NF1	0.0013432	1.66	7.87	8.34
CA OR NF1	0.0056952	10.34	10.49	7.65
B33 OM1	0.0017511	2.45	9.18	8.39
B44 OM1	0.0017461	2.14	7.93	8.45
B37 S1	0.0804890	-32.95	10.16	9.55
B25 S1	0.0370963	-13.18	7.54	2.44
ARS C1	0.0188217	28.56	12.54	9.27
ARS C2	0.0094367	13.70	11.92	8.91
ARS C3	0.0040837	12.73	11.68	8.74
ARS C4	0.0109560	18.57	12.38	9.07
ARS C5	0.0009329	11.22	8.57	6.79
ARS C6	0.0082415	16.71	11.77	8.66
CA ARS C1	0.0010947	32.05	8.4	5.35
B C1	0.0032737	0.71	8.8	8.31
ARS M1	0.0013216	4.84	7.95	8.05
ARS M2	0.0012413	52.79	10.34	8.22
ARS S1	0.0029797	-23.40	7.53	3.00
GW1	0.0049727	2.23	7.63	8.60
GW2	0.0053351	3.28	7.68	8.69
SW1	0.6176032	-2.41	8.04	1.71

Fig. A3.2. Salt efflorescences from inside Building 25

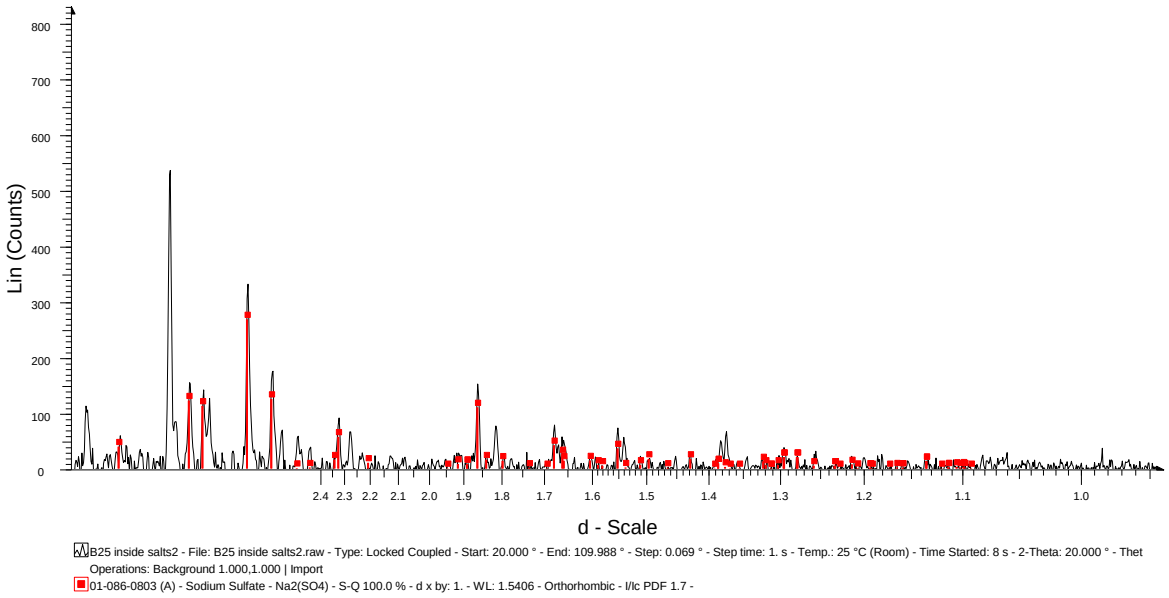

Fig. A3.3. Salt efflorescences from inside Building 37

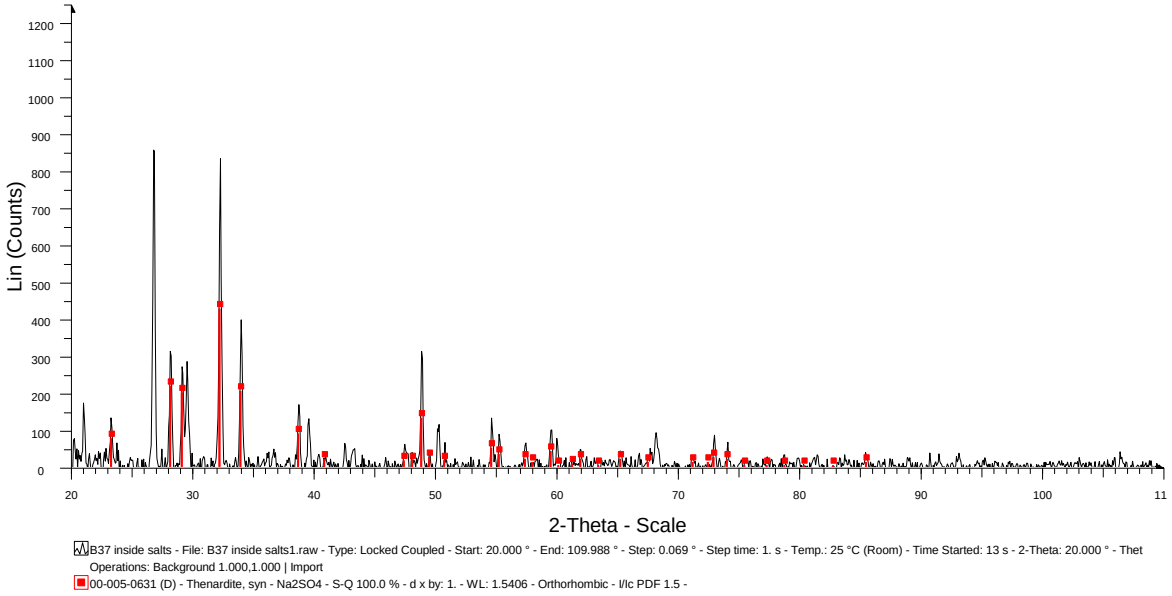

Fig. A3.4. Salt efflorescences from the cracks in the external render on Building 23

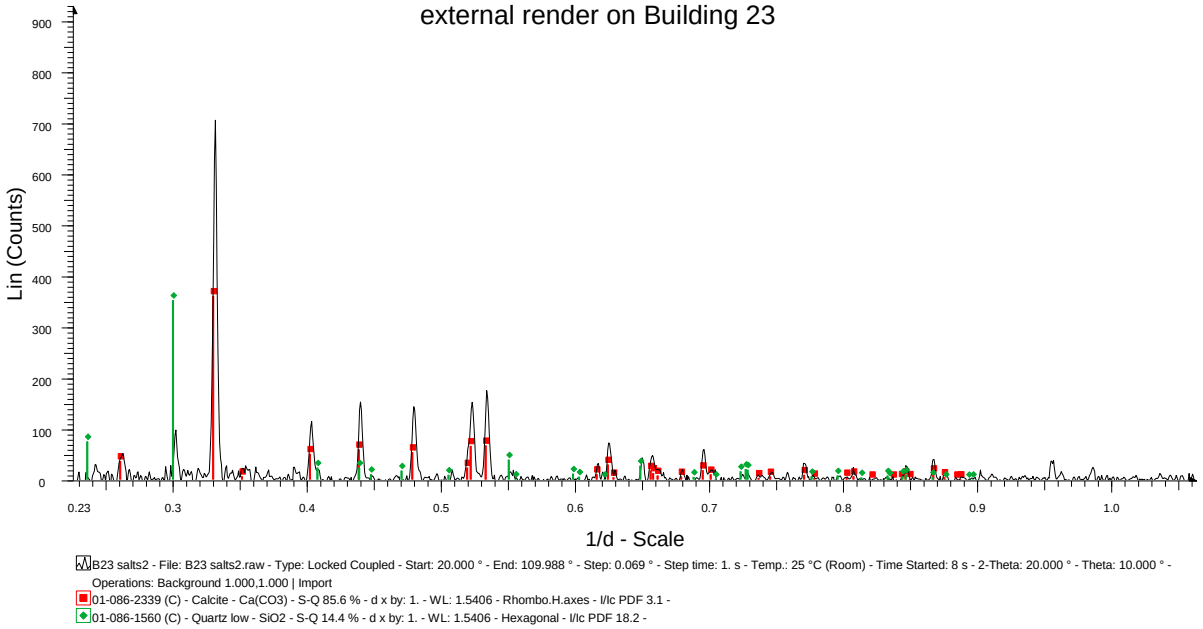

Fig. A3.5. Salt efflorescences on the un-rendered bricks on the exterior of Building 44

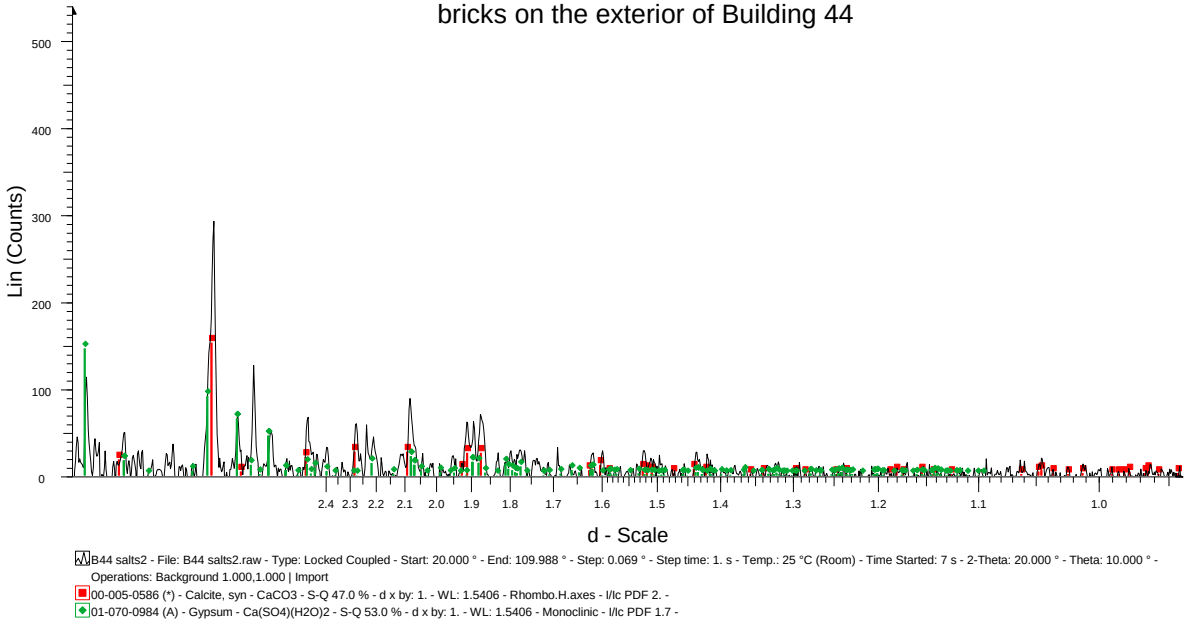

Fig. A3.6. Brick below B25 RR and Wallyford brick

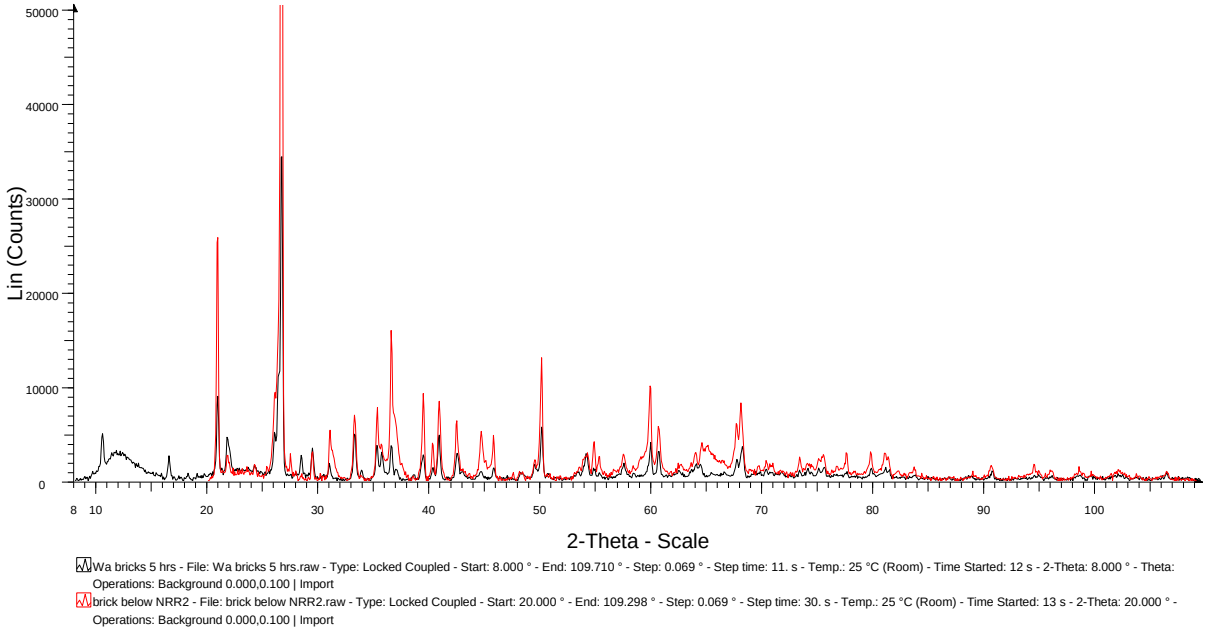

.

Fig. A3.7. Quarried shale with spectrum for quartz

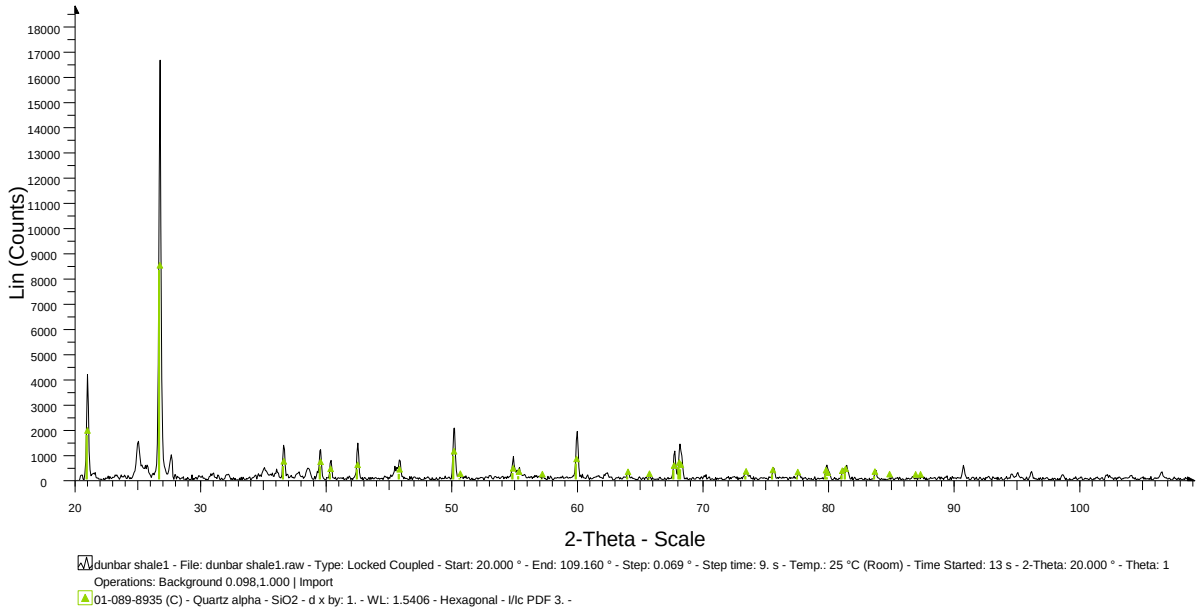

Fig. A3.8. Clay extracted from the shale aggregate with spectra for quartz and calcite

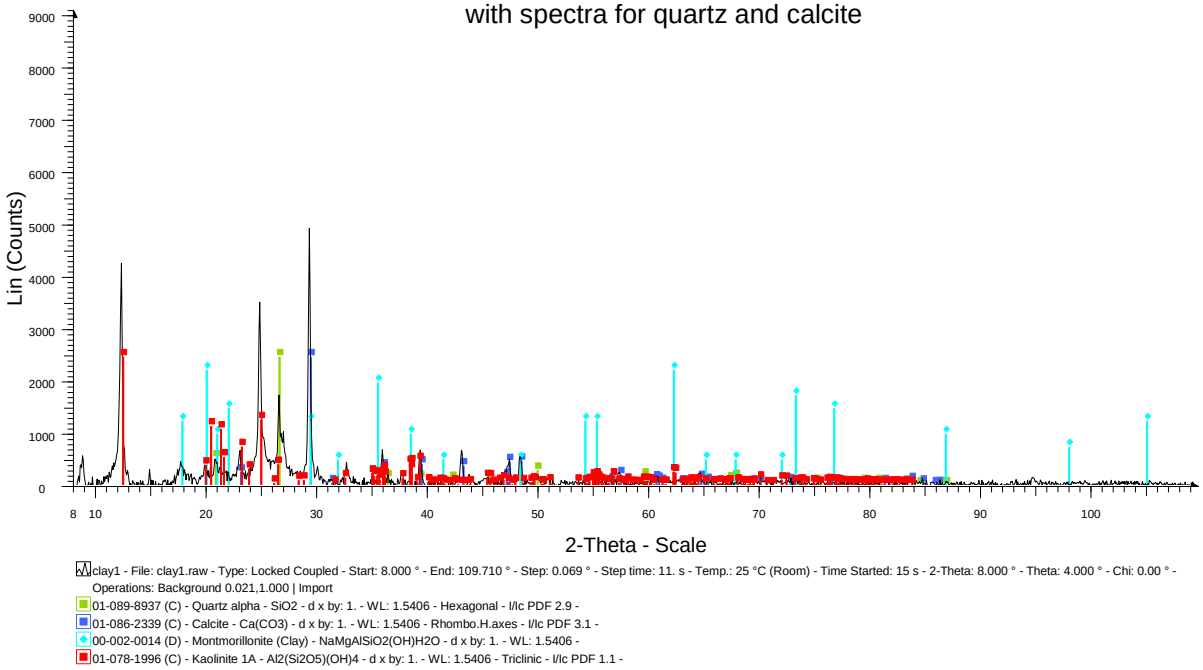

Fig. A3.9. Clay extracted from the shale aggregate, with spectra for various clay standards

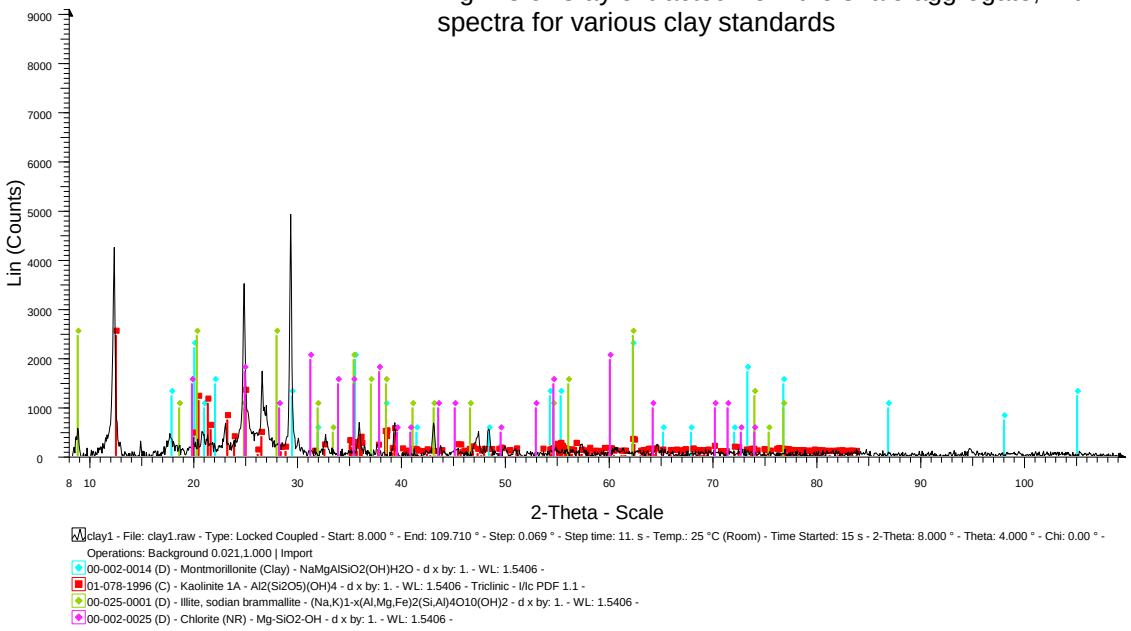

Fig. A3.10. Clay extracted from the shale aggregate before and after glycolation

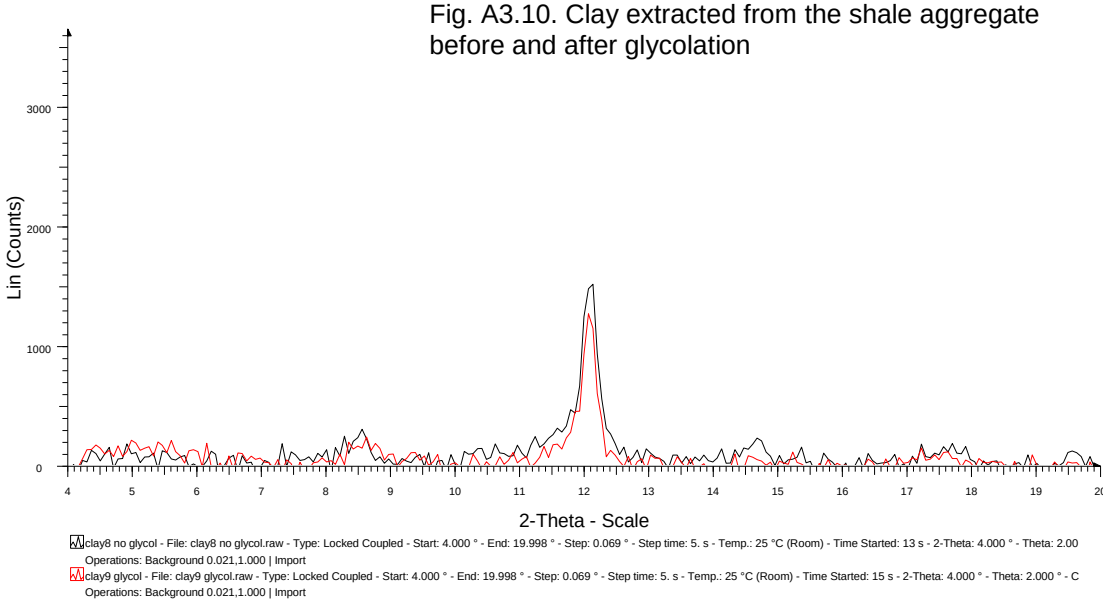

Table A3.9 Dimensions of render and brick samples for strength testing

sample	breadth 1 (mm)	breadth 2 (mm)	breadth 3 (mm)	average breadth (mm)	depth 1 (mm)	depth 2 (mm)	depth 3 (mm)	average depth (mm)
HC OR1	17.85	18.50	19.32	18.56	9.71	11.02	10.54	10.42
HC OR2	21.06	19.46	20.24	20.25	8.34	8.82	9.46	8.87
HC OR3	22.18	21.22	20.03	21.14	12.59	12.22	12.34	12.38
B31 OR	13.66	13.80	13.85	13.77	10.74	11.08	10.25	10.69
B23 RR1	14.85	15.98	14.30	15.04	12.70	12.35	13.63	12.89
B23 RR2	12.62	12.71	12.59	12.64	12.44	12.47	12.49	12.47
B25 RR1	14.95	15.19	15.67	15.27	10.84	10.85	11.62	11.10
B25 RR2	16.04	15.94	15.93	15.97	11.68	11.85	11.80	11.78
NB B1	19.07	18.79	19.17	19.01	17.99	17.57	17.91	17.82
NB B2	19.12	18.97	19.42	19.17	16.80	16.90	17.46	17.05
NB B3	19.87	19.22	18.48	19.19	18.90	18.64	20.29	19.28
NB B4	23.09	22.82	22.65	22.85	19.12	19.10	17.63	18.62
NB B5	22.39	22.21	22.35	22.32	17.60	18.80	18.00	18.13
NB B6	18.64	19.31	19.06	19.00	16.94	16.95	16.33	16.74
NS B1	18.41	16.30	17.32	17.34	17.64	17.56	17.65	17.62
NS B2	20.87	19.66	18.98	19.84	18.71	18.57	18.55	18.61
NS B3	21.35	21.33	19.44	20.71	18.28	17.41	17.32	17.67
NS B4	17.18	18.61	16.61	17.47	17.37	17.31	17.39	17.36
NEB B1	18.14	17.87	17.50	17.84	16.05	15.55	16.16	15.92
NEB B2	15.61	15.91	16.62	16.05	14.42	14.06	14.89	14.46
NEB B3	13.96	14.61	13.91	14.16	17.92	17.07	16.88	17.29
NEB B4	19.68	19.04	17.77	18.83	15.52	15.11	14.84	15.16
NES B1	17.38	19.10	16.21	17.56	18.33	18.35	18.43	18.37
NES B2	16.94	17.75	19.10	17.93	19.07	19.36	18.92	19.12
C1	27.70	27.53	27.30	27.51	11.46	13.15	12.78	12.46
C2	29.59	28.84	28.51	28.98	13.90	15.59	14.27	14.59

Table A3.10 Full results for tensile strength and elastic modulus of render and brick samples

sample	b (mm)	d (mm)	y (mm)	L (mm)	I (mm^4)	w (N)	M (N.mm)	f_{ct} (MPa)	w/v (N/mm)	E (N/mm^2)
HC OR1	18.56	10.42	5.21	30	1751	213.2	1599	4.76	2.65	850
HC OR2	20.25	8.87	4.44	30	1179	203.7	1527	5.75	1.63	775
HC OR3	21.14	12.38	6.19	30	3346	204.8	1536	2.84	1.92	323
B31 OR	13.77	10.69	5.35	30	1402	267.6	2007	7.65	2.93	1175
B23 RR1	15.04	12.89	6.45	30	2687	557.8	4183	10.04	5.33	1117
B23 RR2	12.64	12.47	6.23	30	2041	393.0	2947	9.00	4.17	1149
B25 RR1	15.27	11.10	5.55	30	1742	289.2	2169	6.91	2.05	661
B25 RR2	15.97	11.78	5.89	30	2174	289.1	2168	5.87	1.67	431
NB B1	19.01	17.82	8.91	30	8969	670.3	5027	4.99	3.63	228
NB B2	19.17	17.05	8.53	30	7923	731.5	5487	5.90	7.45	529
NB B3	19.19	19.28	9.64	30	11455	1344.0	10080	8.48	10.99	539
NB B4	22.85	18.62	9.31	30	12288	644.1	4831	3.66	2.44	112
NB B5	22.32	18.13	9.07	30	11089	378.0	2835	2.32	4.72	239
NB B6	19.00	16.74	8.37	30	7429	647.7	4858	5.47	8.97	679
NS B1	17.34	17.62	8.81	45	7902	121.9	1371	1.53	1.91	458
NS B2	19.84	18.61	9.31	45	10654	74.2	835	0.73	1.32	236
NS B3	17.47	17.36	8.68	30	7611	182.5	1369	1.56	2.40	178
NS B4	18.11	19.04	9.52	30	10420	298.1	2236	2.04	3.76	203
NEB B1	17.84	15.92	7.96	30	5997	783.0	5872	7.79	7.75	727
NEB B2	16.05	14.46	7.23	30	4040	495.2	3714	6.64	3.33	463
NEB B3	14.16	17.29	8.65	30	6099	633.4	4751	6.73	8.91	822
NEB B4	18.83	15.16	7.58	30	5464	500.1	3751	5.20	6.89	710
NES B1	17.56	18.37	9.19	45	9073	555.2	6246	6.32	6.90	1444
NES B2	17.93	19.12	9.56	45	10438	509.9	5737	5.25	5.38	978
C1	27.51	12.46	6.23	30	4438	166.2	1246	1.75	3.33	422
C2	28.98	14.59	7.29	30	7495	816.2	6122	5.96	7.28	546

Table A3.11 Dimensions of mortar and render samples for density, porosity and sorptivity, part 1

sample	length 1 (mm)	length 2 (mm)	length 3 (mm)	average length (mm)	breadth 1 (mm)	breadth 2 (mm)	breadth 3 (mm)	average breadth (mm)
B33 M1	79.81	79.34	79.85	79.67	16.48	16.45	16.52	16.48
B33 M2	70.15	70.13	69.88	70.05	23.19	23.09	23.03	23.10
B33 M3	61.36	61.69	61.02	61.36	23.60	23.29	23.56	23.48
B33 M4	60.31	61.31	60.78	60.80	19.72	19.54	19.18	19.48
B24 OR1	119.48	119.29	119.34	119.37	26.60	26.00	28.30	26.97
B24 OR2	118.3	118.57	118.40	118.42	25.66	26.02	24.88	25.52
B24 OR3	64.57	64.38	64.50	64.48	30.31	30.17	30.07	30.18
B47 OR1	111.80	112.62	111.94	112.12	30.18	30.46	29.57	30.07
B47 OR2	76.71	77.17	76.89	76.92	31.28	30.60	31.37	31.08
B47 OR3	82.01	82.21	82.23	82.15	30.98	29.23	30.22	30.14
B47 OR4	66.51	67.03	67.09	66.88	30.69	30.80	30.94	30.81
B31 OR1	48.20	47.87	48.15	48.07	16.48	15.53	17.50	16.50
B31 OR2	45.04	45.37	45.57	45.33	15.19	14.70	15.00	14.96
B23 RR1	94.37	94.29	94.01	94.22	18.64	18.76	18.66	18.69
B23 RR2	65.85	65.95	65.60	65.80	29.69	29.53	29.71	29.64
B23 RR3	58.62	58.97	58.84	58.81	22.35	22.44	22.33	22.37
B25 RR1	51.98	51.99	51.68	51.88	15.41	15.68	15.06	15.38
B25 RR2	46.42	46.17	45.75	46.11	15.97	15.90	15.93	15.93

Table A3.12 Dimensions of mortar and render samples for density, porosity and sorptivity, part 2

sample	depth 1 (mm)	depth 2 (mm)	depth 3 (mm)	average depth (mm)	volume (cm^3)
B33 M1	10.79	11.12	10.12	10.67	14.02
B33 M2	12.17	11.88	12.01	12.02	19.45
B33 M3	12.70	13.51	13.44	13.22	19.04
B33 M4	17.22	17.02	16.20	16.81	19.91
B24 OR1	13.38	13.89	13.38	13.55	43.62
B24 OR2	13.49	13.75	13.41	13.55	40.95
B24 OR3	13.10	13.49	12.76	13.12	25.53
B47 OR1	15.53	16.63	15.43	15.86	53.48
B47 OR2	13.56	13.00	13.98	13.51	32.31
B47 OR3	17.75	16.20	15.98	16.64	41.21
B47 OR4	15.80	15.14	15.00	15.31	31.55
B31 OR1	10.15	10.31	10.52	10.33	8.19
B31 OR2	13.13	13.24	12.70	13.02	8.83
B23 RR1	11.18	10.74	10.83	10.92	19.22
B23 RR2	7.72	7.91	8.09	7.91	15.42
B23 RR3	10.52	10.82	10.90	10.75	14.14
B25 RR1	10.93	10.86	11.53	11.11	8.86
B25 RR2	11.85	11.82	12.08	11.92	8.76

Table A3.13 Dimensions of concrete and brick samples for density, porosity and sorptivity

sample	length 1 (mm)	length 2 (mm)	length 3 (mm)	average length (mm)	diameter 1 (mm)	diameter 2 (mm)	diameter 3 (mm)	average diameter (mm)	volume (cm^3)
ARS C1	38.19	38.09	38.28	38.19	24.05	24.08	24.01	24.05	17.33
ARS C2	32.30	31.70	31.41	31.80	24.16	24.09	24.10	24.12	14.52
ES B1a	60.90	60.70	60.89	60.84	24.42	24.43	24.39	24.41	28.48
ES B1b	45.38	45.29	45.24	45.30	24.36	24.23	24.28	24.29	21.00
EB B1	55.21	55.01	54.93	55.05	24.37	24.40	24.48	24.42	25.78
NS B1	79.68	80.07	79.79	79.85	24.27	24.30	24.25	24.27	36.95
NB B1	57.43	57.12	57.36	57.30	24.51	24.48	24.52	24.50	27.03
NB B2	54.79	54.94	55.18	54.97	24.53	24.46	24.50	24.50	25.91
PS B1	72.39	72.22	72.19	72.27	24.38	24.37	24.30	24.35	33.66
PB B1	61.92	62.40	62.10	62.14	24.45	24.49	24.46	24.47	29.22
PB B2	59.20	59.10	58.60	58.97	24.05	24.04	24.19	24.09	26.89
WaS B1	76.18	76.34	76.27	76.26	24.10	24.11	24.09	24.10	34.79
WaB B1	53.13	53.66	53.00	53.26	24.63	24.50	24.65	24.59	25.31
WaB B2	53.73	53.55	53.23	53.50	24.41	24.68	24.48	24.52	25.27
WhS B1	66.45	66.84	66.60	66.63	24.21	24.44	24.19	24.28	30.85
WhB B1	61.59	61.99	61.80	61.79	24.21	24.14	24.20	24.18	28.39
WhB B2	62.07	61.89	61.65	61.87	24.56	24.41	24.51	24.49	29.16

Table A3.14 Full results for mortar, render and concrete samples: density and porosity

sample	dry mass (g)	volume (cm^3)	bulk density (g/cm^3)	wet mass 1 (g)	porosity 1 (%)	wet mass 2 (g)	porosity 2 (%)
B33 M1	25.40	14.02	1.812	29.29	27.75	29.32	27.96
B33 M2	37.54	19.45	1.930	42.71	26.58	42.71	26.58
B33 M3	33.07	19.04	1.737	38.52	28.62	38.49	28.46
B33 M4	37.04	19.91	1.860	42.10	25.41	42.26	26.21
B24 OR1	73.83	43.62	1.693	86.55	29.16	86.52	29.09
B24 OR2	70.04	40.95	1.710	82.51	30.45	82.28	29.89
B24 OR3	44.03	25.53	1.725	51.45	29.06	51.50	29.26
B47 OR1	103.29	53.48	1.931	112.67	17.54	112.79	17.76
B47 OR2	62.95	32.31	1.948	69.15	19.19	68.75	17.95
B47 OR3	76.00	41.21	1.844	83.73	18.76	83.63	18.51
B47 OR4	59.89	31.55	1.898	65.36	17.34	65.28	17.08
B31 OR1	15.01	8.19	1.830	17.12	25.71	17.08	25.30
B31 OR2	16.46	8.83	1.860	18.47	22.81	18.45	22.57
B23 RR1	31.57	19.22	1.642	37.42	30.44	37.49	30.80
B23 RR2	28.01	15.42	1.816	32.85	31.38	32.72	30.54
B23 RR3	24.31	14.14	1.719	28.75	31.40	28.71	31.12
B25 RR1	16.02	8.86	1.807	18.11	23.58	18.25	25.16
B25 RR2	16.31	8.76	1.863	18.35	23.30	18.50	25.01
ARS C1	38.04	17.33	2.195	40.60	14.77	40.65	15.06
ARS C2	31.08	14.52	2.140	33.42	16.12	33.50	16.67

Table A3.15 Full results for mortar, render and concrete samples: sorptivity

sample	dry mass (g)	plot of mass gain (g) v time$^{1/2}$ (min$^{1/2}$) – gradient run 1	plot of mass gain (g) v time$^{1/2}$ (min$^{1/2}$) – gradient run 2	area (mm^2)	sorptivity run 1 (mm/min$^{1/2}$)	sorptivity run 2 (mm/min$^{1/2}$)
B33 M1	25.40	0.0397	0.0307	175.99	0.226	0.174
B33 M2	37.54	0.0458	0.0610	277.70	0.165	0.220
B33 M3	33.07	0.0594	0.0631	310.37	0.191	0.203
B33 M4	37.04	0.0425	0.0634	327.52	0.130	0.194
B24 OR1	73.83	0.0431	0.0329	365.40	0.118	0.090
B24 OR2	70.04	0.0428	0.0317	345.80	0.124	0.092
B24 OR3	44.03	0.0435	0.0384	395.90	0.110	0.097
B47 OR1	103.29	0.0547	0.0474	477.01	0.115	0.099
B47 OR2	62.95	0.0788	0.0567	420.04	0.188	0.135
B47 OR3	76.00	0.0502	0.0537	501.69	0.100	0.107
B47 OR4	59.89	0.0646	0.0714	471.80	0.137	0.151
B23 RR1	31.57	0.3115	0.2662	204.00	1.527	1.305
B23 RR2	28.01	0.0741	0.0661	234.38	0.316	0.282
B23 RR3	24.31	0.1784	0.1522	240.44	0.742	0.633
B25 RR1	16.02	0.0311	0.0305	170.86	0.182	0.179
B25 RR2	16.31	0.0372	0.0432	189.87	0.196	0.228
ARS C1	38.04	0.0496	0.0476	453.92	0.109	0.105
ARS C2	31.08	0.0409	0.0378	456.57	0.090	0.083

Table A3.16 Full results for brick samples: density and porosity

sample	dry mass (g)	volume (cm^3)	bulk density (g/cm^3)	wet mass 1 (g)	porosity 1 (%)	wet mass 2 (g)	porosity 2 (%)
ES B1a	50.89	28.48	1.787	58.57	26.96	58.45	26.54
ES B1b	37.40	21.00	1.781	42.82	25.81	42.81	25.77
EB B1	46.48	25.78	1.803	53.25	26.26	53.20	26.07
NS B1	70.67	36.95	1.912	79.54	24.00	79.62	24.23
NB B1	51.09	27.03	1.890	57.79	24.79	57.72	24.53
NB B2	48.89	25.91	1.887	55.32	24.82	55.26	24.58
PS B1	58.77	33.66	1.746	68.06	27.60	68.20	28.02
PB B1	50.86	29.22	1.741	58.62	26.56	58.80	27.17
PB B2	46.05	26.89	1.713	52.78	25.03	53.19	26.56
WaS B1	58.47	34.80	1.680	67.69	26.50	67.19	25.06
WaB B1	41.74	25.31	1.649	48.21	25.57	48.03	24.86
WaB B2	42.11	25.27	1.666	48.52	25.36	48.37	24.77
WhS B1	53.01	30.85	1.718	61.18	26.48	61.17	26.45
WhB B1	47.28	28.39	1.666	55.20	27.90	54.90	26.84
WhB B2	48.83	29.16	1.675	57.08	28.30	57.05	28.19

Table A3.17 Full results for brick samples: sorptivity run 1, part 1

sample	sample orientation	dry mass (g)	plot of mass gain (g) v time$^{1/2}$ (min$^{1/2}$) initial gradient	plot of mass gain (g) v time$^{1/2}$ (min$^{1/2}$) main gradient	plot of mass gain (g) v time$^{1/2}$ (min$^{1/2}$) final gradient
ES B1a	skin up	50.89		0.4424	
ES B1a	skin down	50.89	0.1898	0.3121	
ES B1b	skin up	37.40		0.2502	
ES B1b	skin down	37.40		0.2865	
EB B1	skin up	46.48		0.6986	
EB B1	skin down	46.48	0.1677	0.2424	
NS B1	skin up	70.67		0.2352	
NS B1	skin down	70.67		0.2567	
NB B1	skin up	51.09		0.2112	
NB B1	skin down	51.09		0.1674	
NB B2	skin up	48.89		0.2318	
NB B2	skin down	48.89		0.2463	
PS B1	skin up	58.77		0.9959	
PS B1	skin down	58.77		0.8976	
PB B1	skin up	50.86	0.3940	0.5658	
PB B1	skin down	50.86		0.1006	
PB B2	skin up	46.05	0.4268	0.4775	
PB B2	skin down	46.05	0.0822	0.1580	
WaS B1	skin up	58.47		0.0331	0.0155
WaS B1	skin down	58.47		0.0796	
WaB B1	skin up	41.74		0.0306	0.0188
WaB B1	skin down	41.74	0.0394	0.0855	
WaB B2	skin up	42.11		0.0172	0.0159
WaB B2	skin down	42.11	0.0079	0.0456	
WhS B1	skin up	53.01		0.4162	
WhS B1	skin down	53.01		0.3277	
WhB B1	skin up	47.28		0.4393	
WhB B1	skin down	47.28		0.4333	
WhB B2	skin up	48.83		0.4195	
WhB B2	skin down	48.83		0.6181	

Table A3.18 Full results for brick samples: sorptivity run 1, part 2

sample	sample orientation	area (mm^2)	initial sorptivity ($mm/min^{1/2}$)	main sorptivity ($mm/min^{1/2}$)	final sorptivity ($mm/min^{1/2}$)
ES B1a	skin up	467.87		0.946	
ES B1a	skin down	467.87	0.406	0.667	
ES B1b	skin up	463.15		0.540	
ES B1b	skin down	463.15		0.619	
EB B1	skin up	468.00		1.493	
EB B1	skin down	468.00	0.358	0.518	
NS B1	skin up	462.52		0.509	
NS B1	skin down	462.52		0.555	
NB B1	skin up	471.32		0.448	
NB B1	skin down	471.32		0.355	
NB B2	skin up	471.07		0.492	
NB B2	skin down	471.07		0.523	
PS B1	skin up	465.44		2.140	
PS B1	skin down	465.44		1.928	
PB B1	skin up	469.92	0.838	1.204	
PB B1	skin down	469.92		0.214	
PB B2	skin up	455.68	0.937	1.048	
PB B2	skin down	455.68	0.180	0.347	
WaS B1	skin up	455.94		0.073	0.034
WaS B1	skin down	455.94		0.175	
WaB B1	skin up	474.79		0.064	0.040
WaB B1	skin down	474.79	0.083	0.180	
WaB B2	skin up	472.09		0.036	0.034
WaB B2	skin down	472.09	0.017	0.097	
WhS B1	skin up	462.77		0.899	
WhS B1	skin down	462.77		0.708	
WhB B1	skin up	459.09		0.957	
WhB B1	skin down	459.09		0.944	
WhB B2	skin up	470.94		0.891	
WhB B2	skin down	470.94		1.312	

Table A3.19 Full results for brick samples: sorptivity run 2, part 1

sample	sample orientation	dry mass (g)	plot of mass gain (g) v time$^{1/2}$ (min$^{1/2}$) initial gradient	plot of mass gain (g) v time$^{1/2}$ (min$^{1/2}$) main gradient
ES B1a	skin up	50.89		0.4800
ES B1a	skin down	50.89		0.4319
ES B1b	skin up	37.40		0.1779
ES B1b	skin down	37.40		0.4902
EB B1	skin up	46.48		0.5906
EB B1	skin down	46.48	0.1802	0.4855
NS B1	skin up	70.67		0.2352
NS B1	skin down	70.67		0.2567
NB B1	skin up	51.09		0.2112
NB B1	skin down	51.09		0.1674
NB B2	skin up	48.89		0.2318
NB B2	skin down	48.89		0.2463
PS B1	skin up	58.77		0.8639
PS B1	skin down	58.77		0.7018
PB B1	skin up	50.86	0.5772	0.6000
PB B1	skin down	50.86	0.1178	0.1537
PB B2	skin up	46.05		0.5073
PB B2	skin down	46.05	0.1488	0.1743
WaS B1	skin up	58.47		0.0374
WaS B1	skin down	58.47		0.0562
WaB B1	skin up	41.74		0.0301
WaB B1	skin down	41.74		0.0728
WaB B2	skin up	42.11		0.0202
WaB B2	skin down	42.11		0.0418
WhS B1	skin up	53.01		0.4951
WhS B1	skin down	53.01		0.4146
WhB B1	skin up	47.28		0.4215
WhB B1	skin down	47.28	0.5929	0.6018
WhB B2	skin up	48.83		0.5166
WhB B2	skin down	48.83		0.8057

Table A3.20 Full results for brick samples: sorptivity run 2, part 2

sample	sample orientation	area (mm^2)	initial sorptivity ($mm/min^{1/2}$)	main sorptivity ($mm/min^{1/2}$)
ES B1a	skin up	467.87		1.026
ES B1a	skin down	467.87		0.923
ES B1b	skin up	463.15		0.384
ES B1b	skin down	463.15		1.058
EB B1	skin up	468.00		1.262
EB B1	skin down	468.00	0.385	1.037
NS B1	skin up	465.44		0.509
NS B1	skin down	465.44		0.555
NB B1	skin up	469.92		0.448
NB B1	skin down	469.92		0.355
NB B2	skin up	455.68		0.492
NB B2	skin down	455.68		0.523
PS B1	skin up	455.94		1.856
PS B1	skin down	455.94		1.508
PB B1	skin up	474.79	1.228	1.277
PB B1	skin down	474.79	0.251	0.327
PB B2	skin up	472.09		1.113
PB B2	skin down	472.09	0.327	0.383
WaS B1	skin up	462.77		0.082
WaS B1	skin down	462.77		0.123
WaB B1	skin up	459.09		0.063
WaB B1	skin down	459.09		0.153
WaB B2	skin up	470.94		0.043
WaB B2	skin down	470.94		0.089
WhS B1	skin up	467.87		1.070
WhS B1	skin down	467.87		0.896
WhB B1	skin up	463.15		0.918
WhB B1	skin down	463.15	1.291	1.311
WhB B2	skin up	468.00		1.097
WhB B2	skin down	468.00		1.711

Fig. 3.2. Graphs illustrating the Mercury Intrusion Porosimetry results

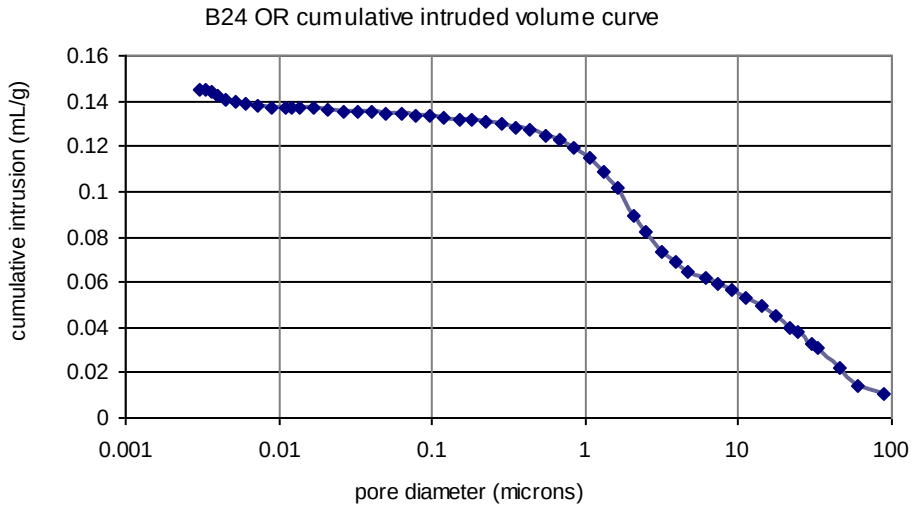

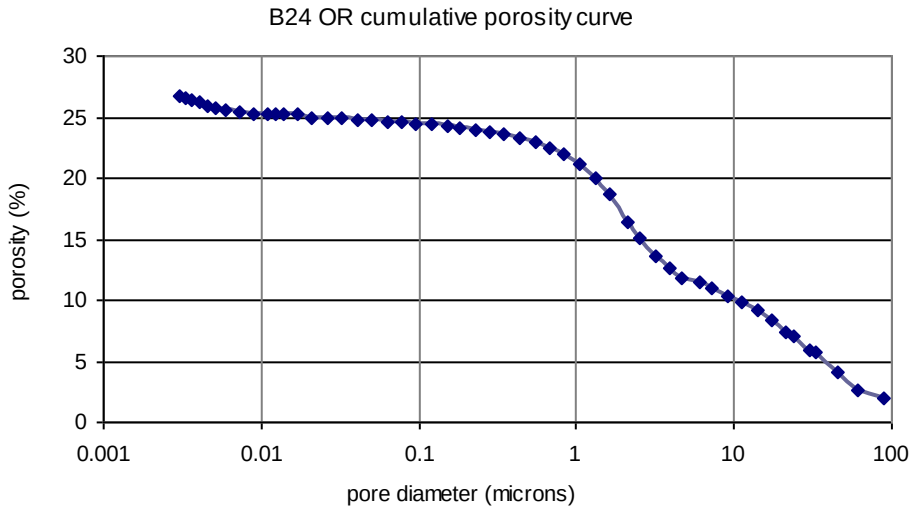

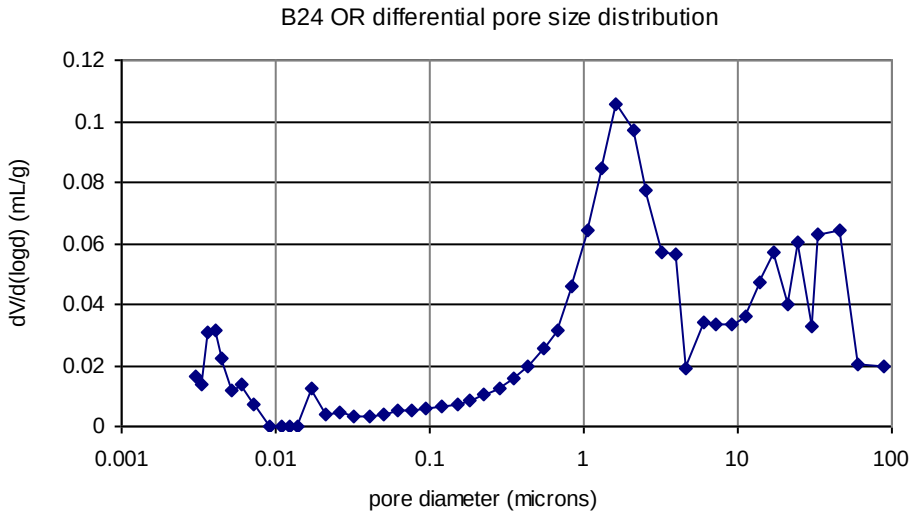

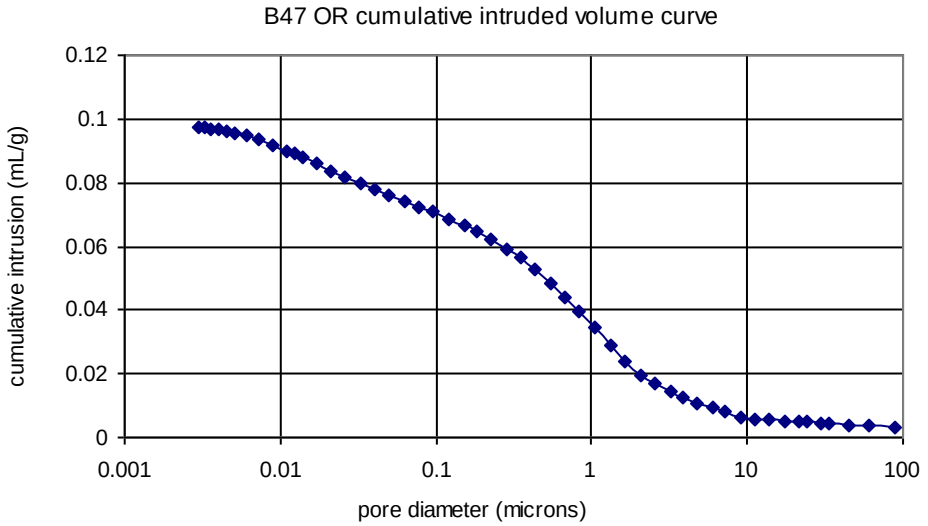
B47 OR cumulative intruded volume curve
cumulative intrusion (mL/g)
0.12
0.1
0.08
0.06
0.04
0.02
0
0.001
0.01
0.1
1
10
100
pore diameter (microns)

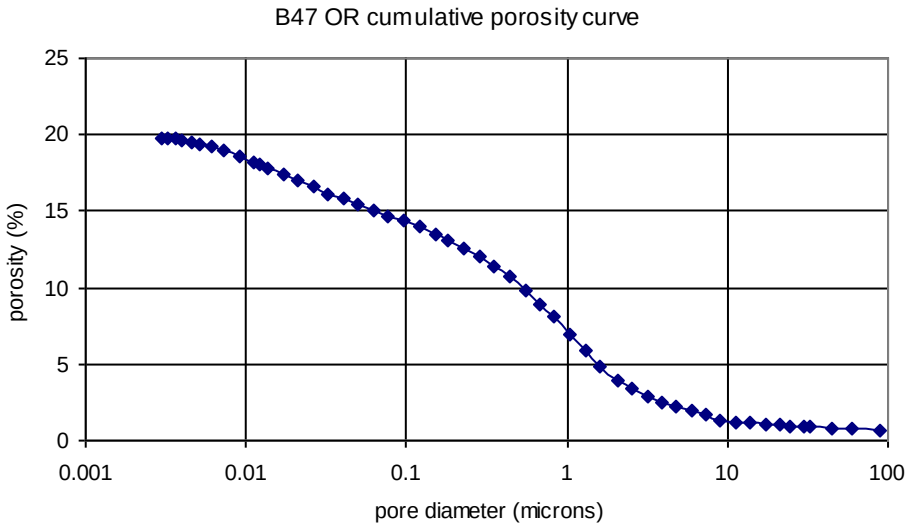
B47 OR cumulative porosity curve
porosity (%)
25
20
15
10
5
0
0.001
0.01
0.1
1
10
100
pore diameter (microns)

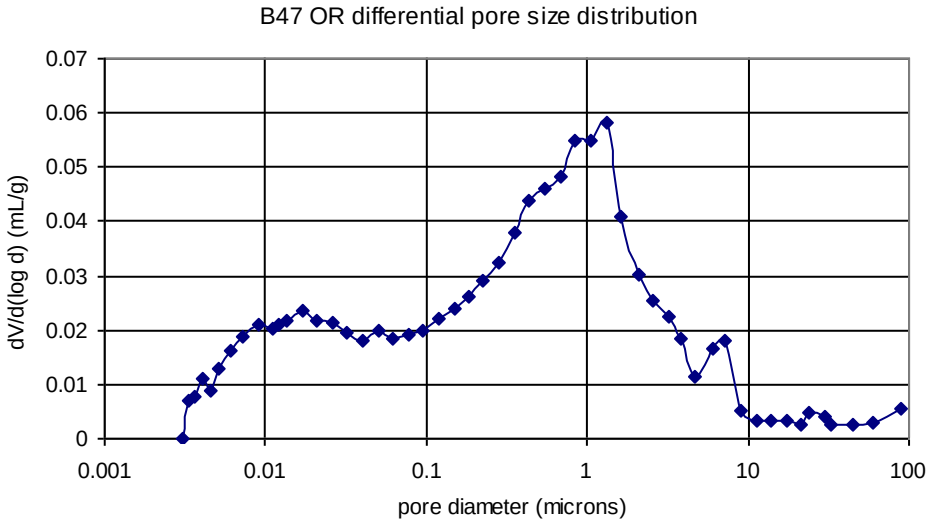
B47 OR differential pore size distribution
dV/d(log d) (mL/g)
0.07
0.06
0.05
0.04
0.03
0.02
0.01
0
0.001
0.01
0.1
1
10
100
pore diameter (microns)

B23 RR cumulative intruded volume curve

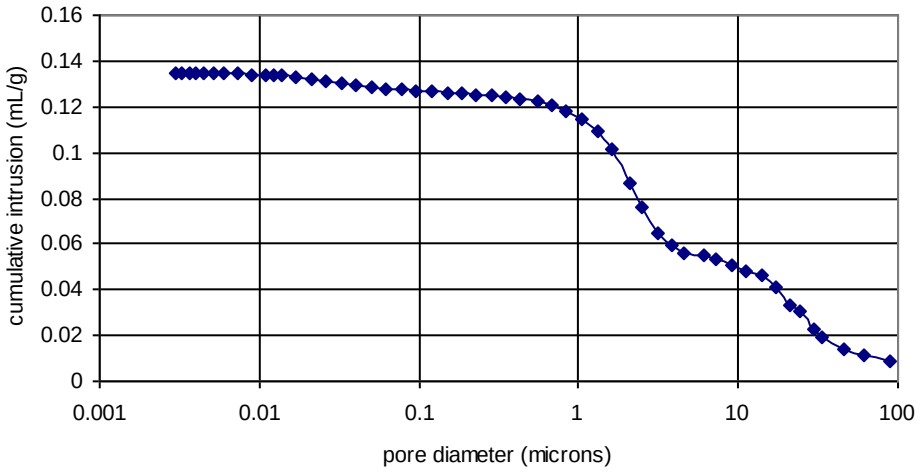

B23 RR cumulative porosity curve

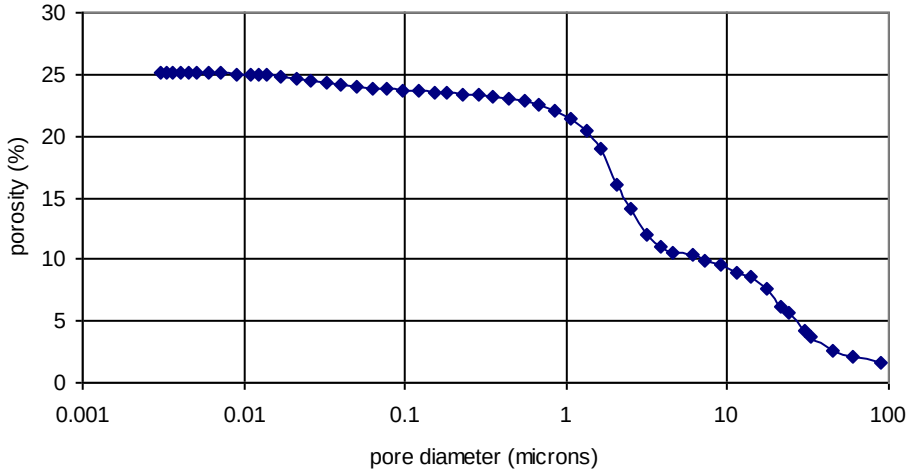

B23 RR differential pore size distribution

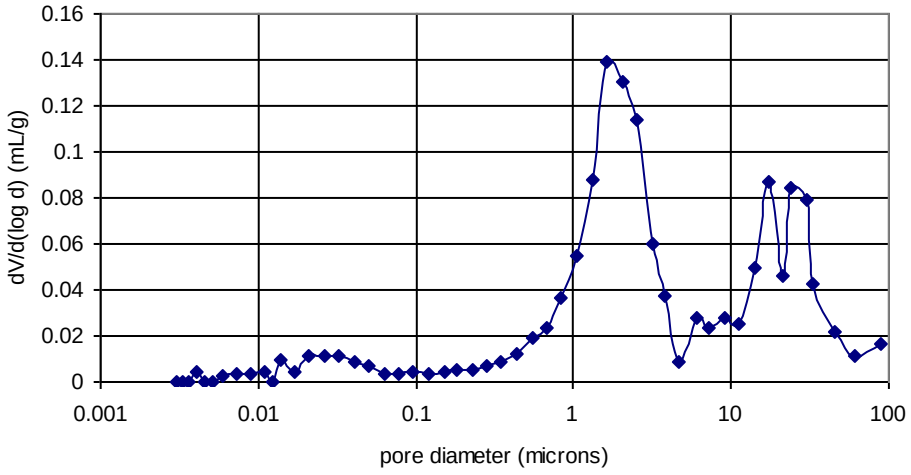

B25 RR cumulative intruded volume curve

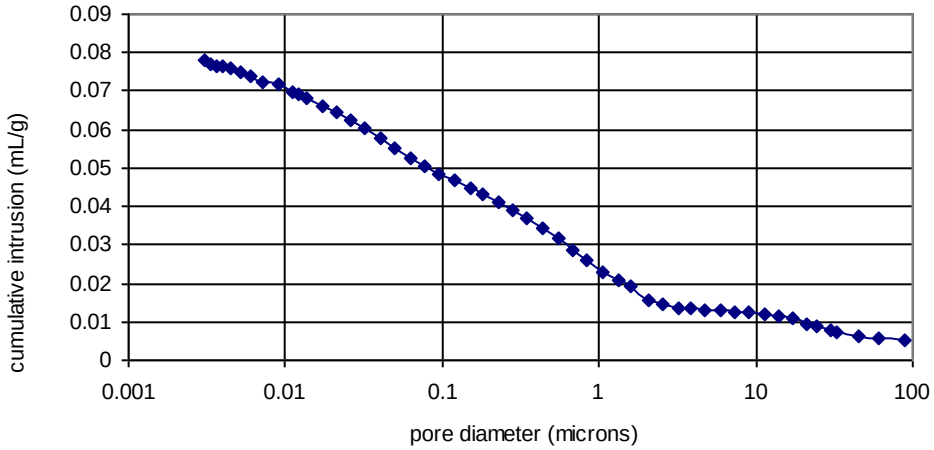

B25 RR cumulative porosity curve

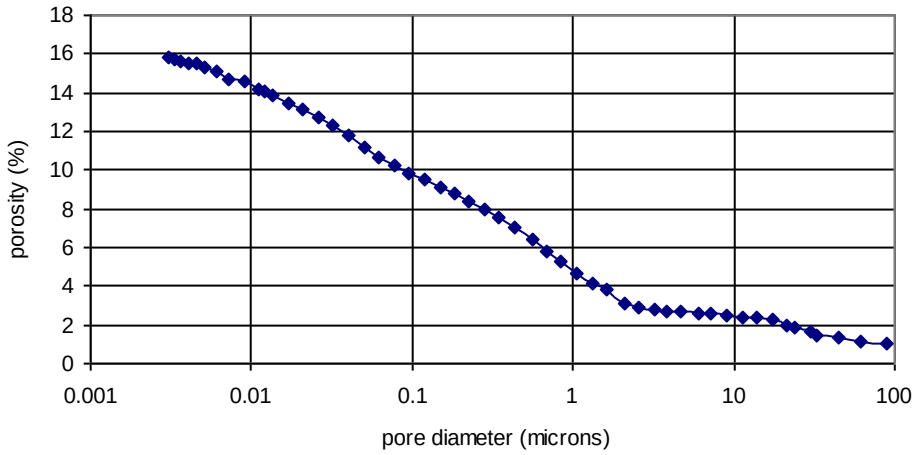

B25 RR differential pore size distribution

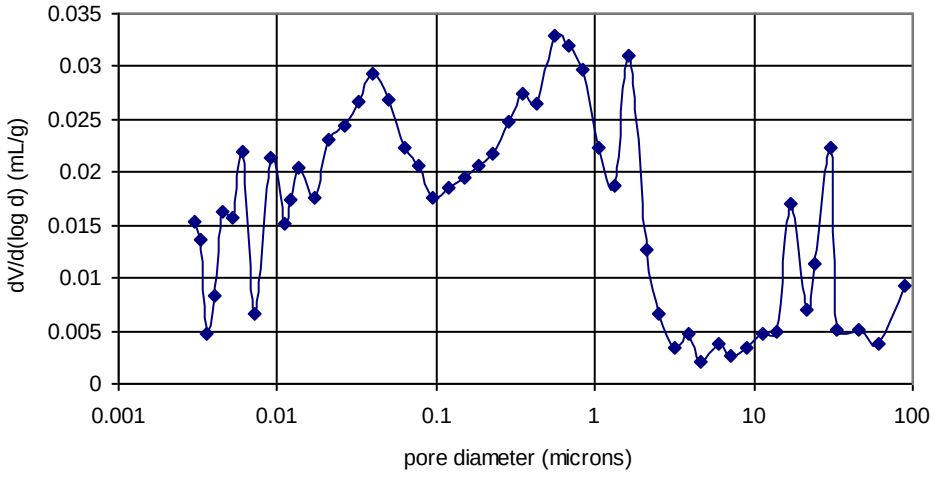

EB cumulative intruded volume curve

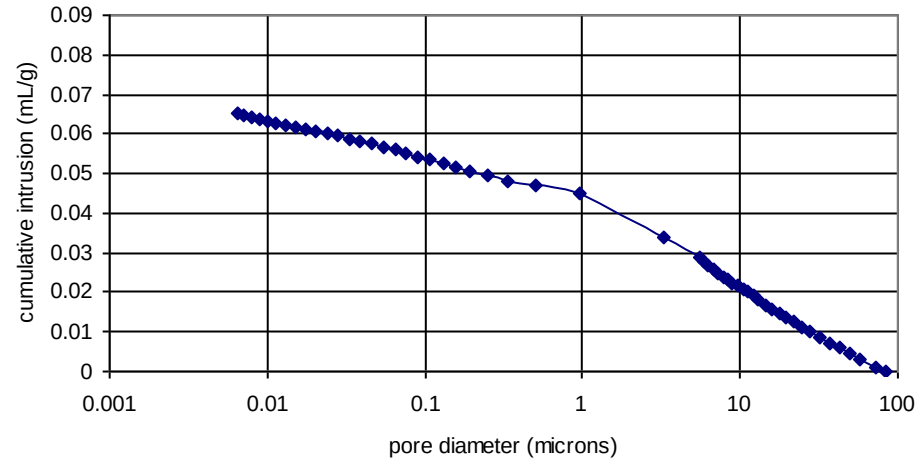

EB cumulative porosity curve

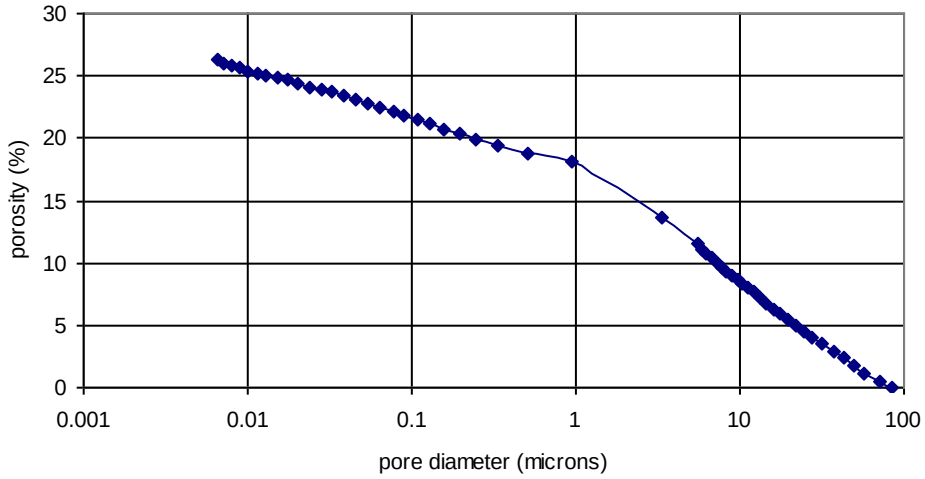

EB differential pore size distribution

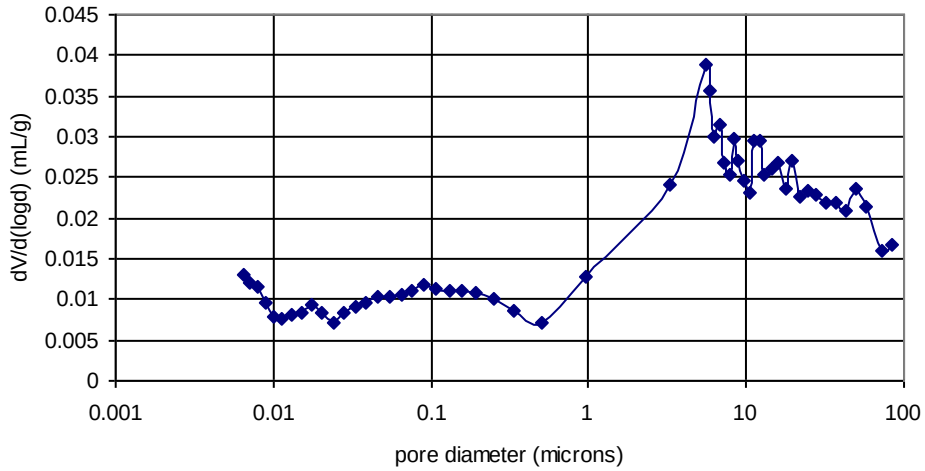

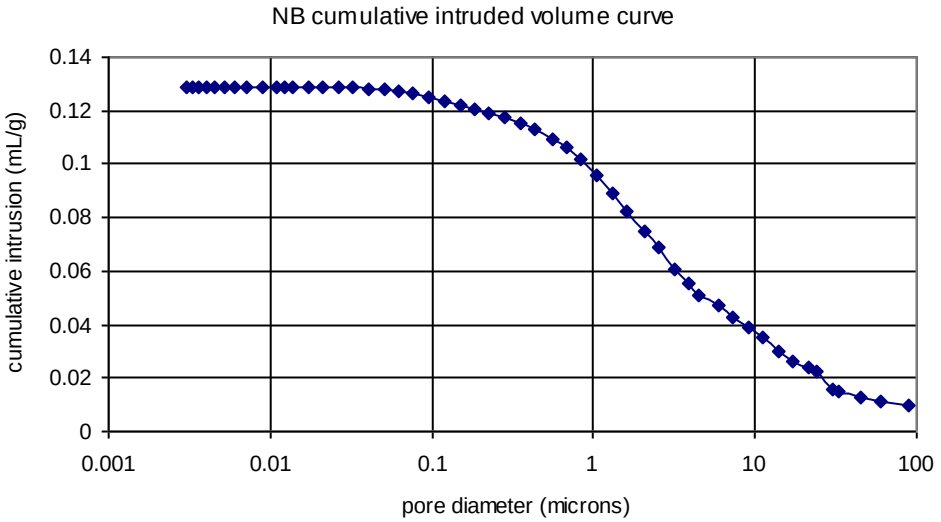
NB cumulative intruded volume curve
cumulative intrusion (mL/g)
0.14
0.12
0.1
0.08
0.06
0.04
0.02
0
0.001
0.01
0.1
1
10
100
pore diameter (microns)

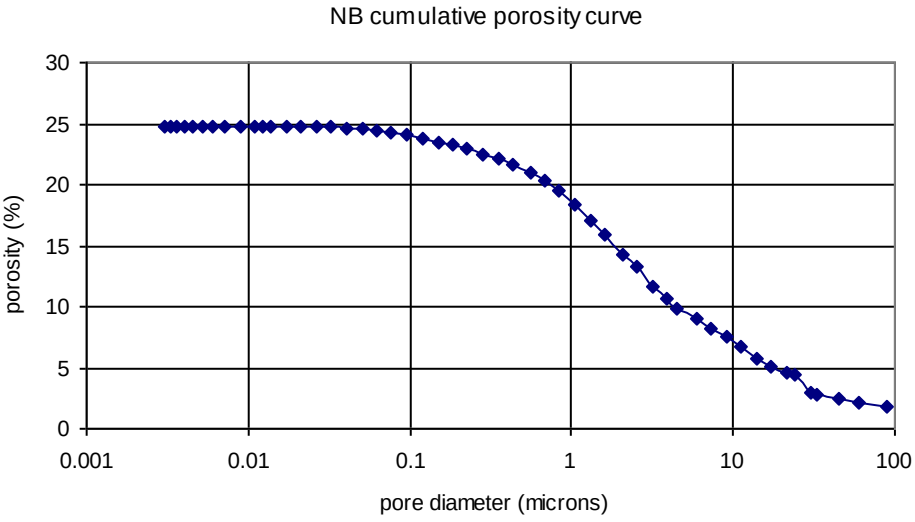
NB cumulative porosity curve
porosity (%)
30
25
20
15
10
5
0
0.001
0.01
0.1
1
10
100
pore diameter (microns)

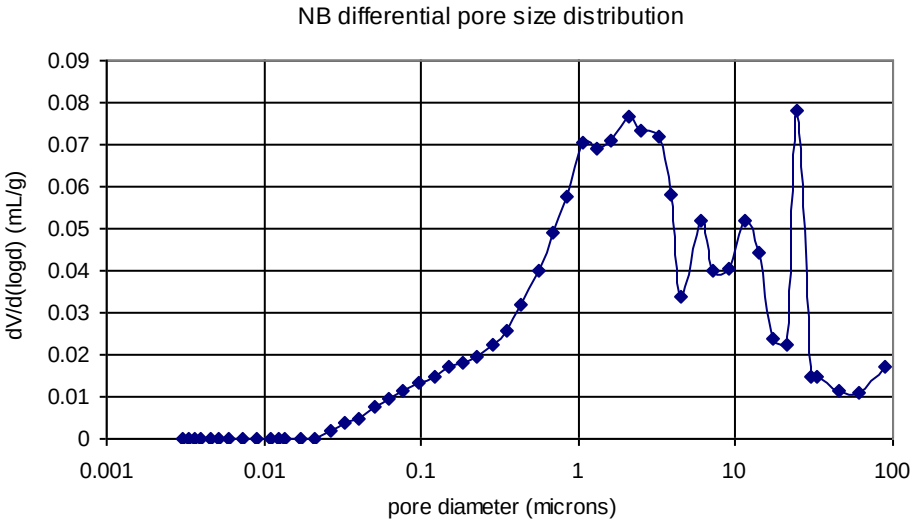
NB differential pore size distribution
dV/d(logd) (mL/g)
0.09
0.08
0.07
0.06
0.05
0.04
0.03
0.02
0.01
0
0.001
0.01
0.1
1
10
100
pore diameter (microns)

PB cumulative intruded volume curve

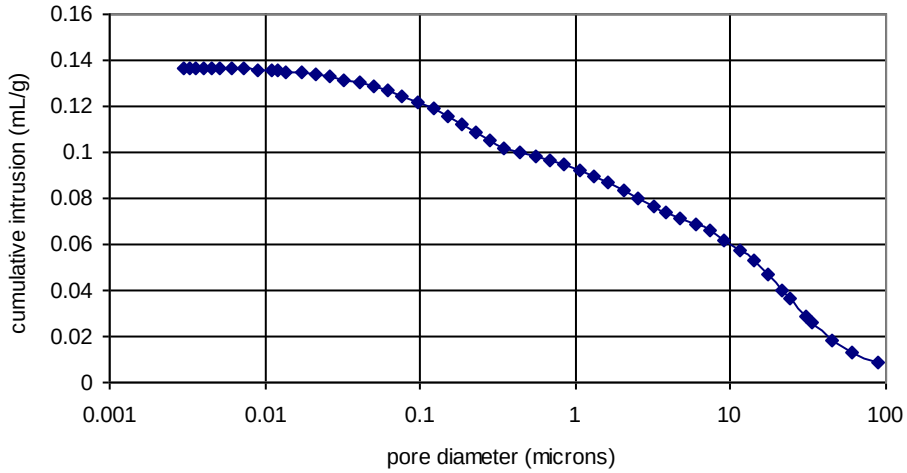

PB cumulative porosity curve

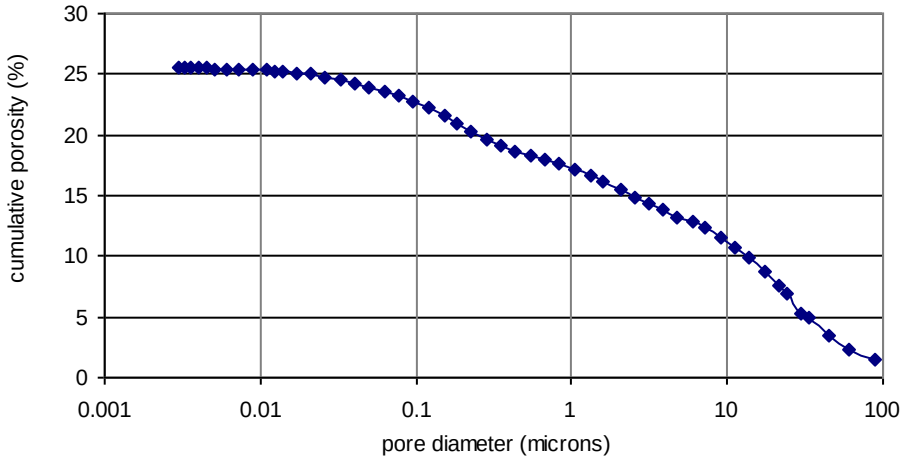

PB differential pore size distribution

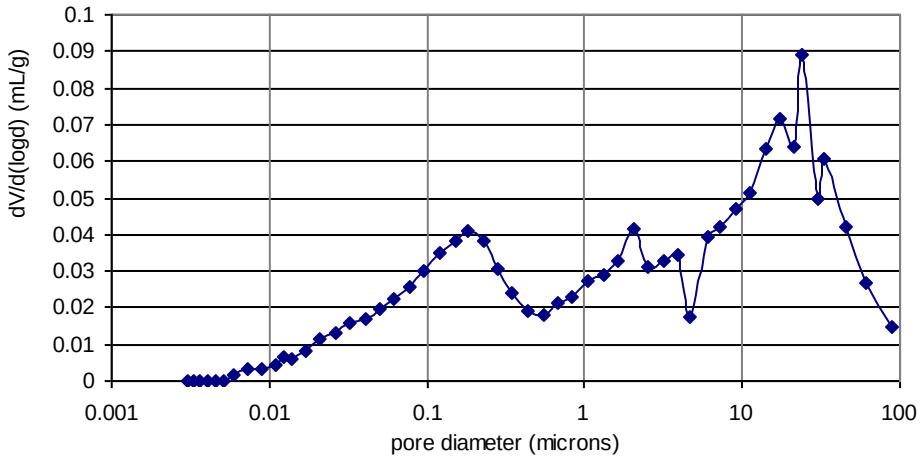

PB skin cumulative intruded volume curve

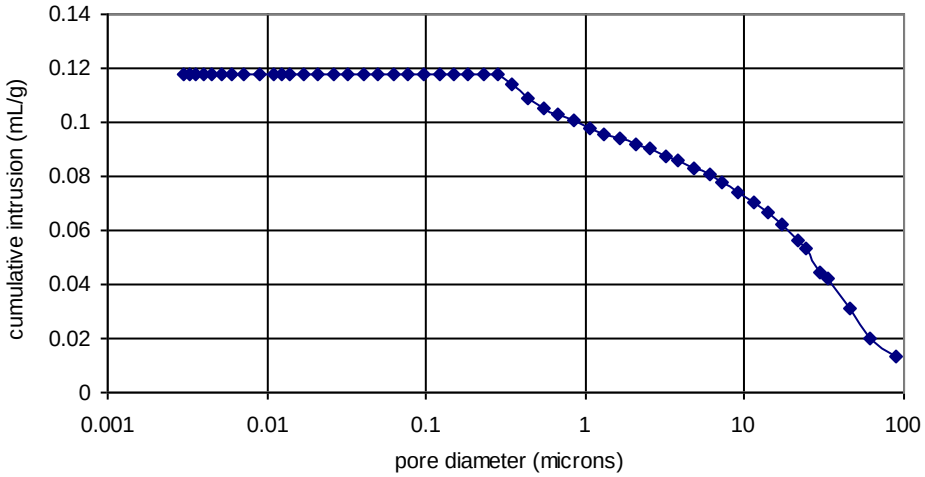

PB skin cumulative porosity curve

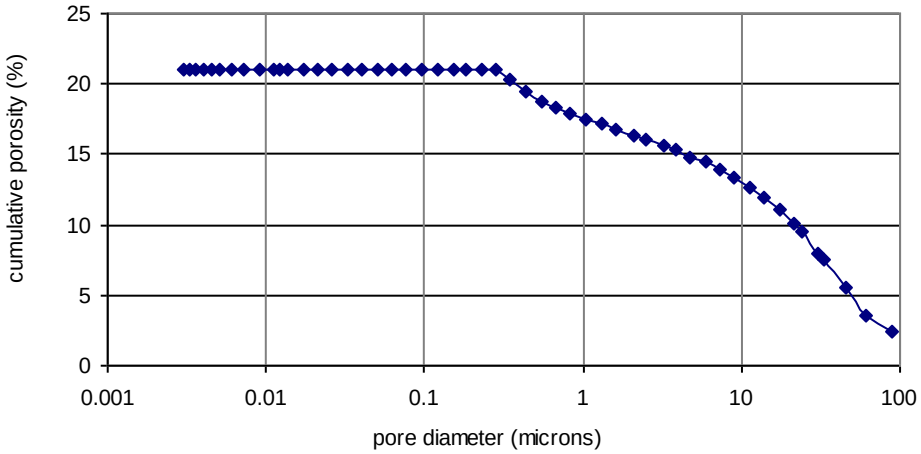

PB skin differential pore size distribution

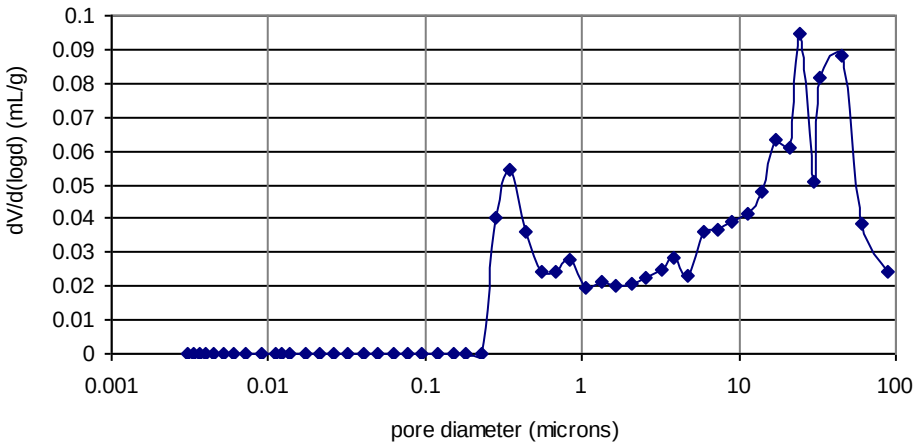

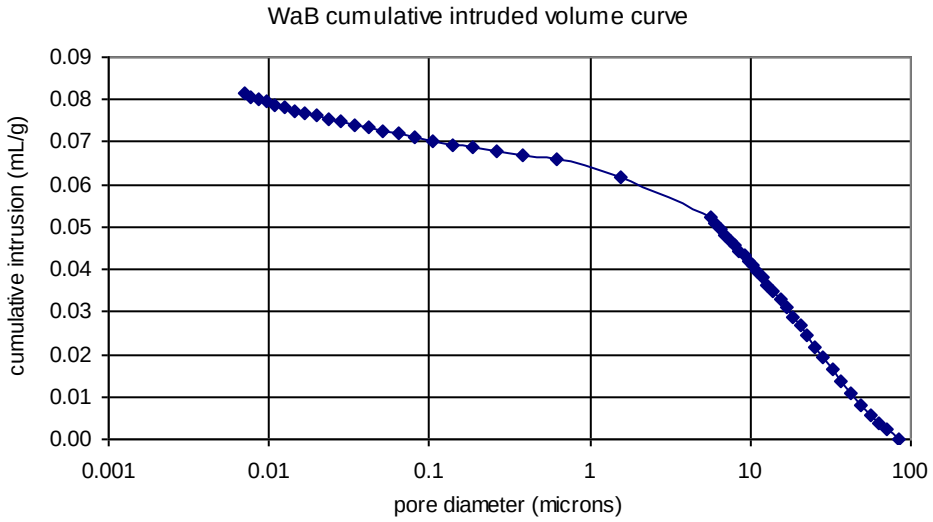
WaB cumulative intruded volume curve
cumulative intrusion (mL/g)
0.09
0.08
0.07
0.06
0.05
0.04
0.03
0.02
0.01
0.00
0.001
0.01
0.1
1
10
100
pore diameter (microns)

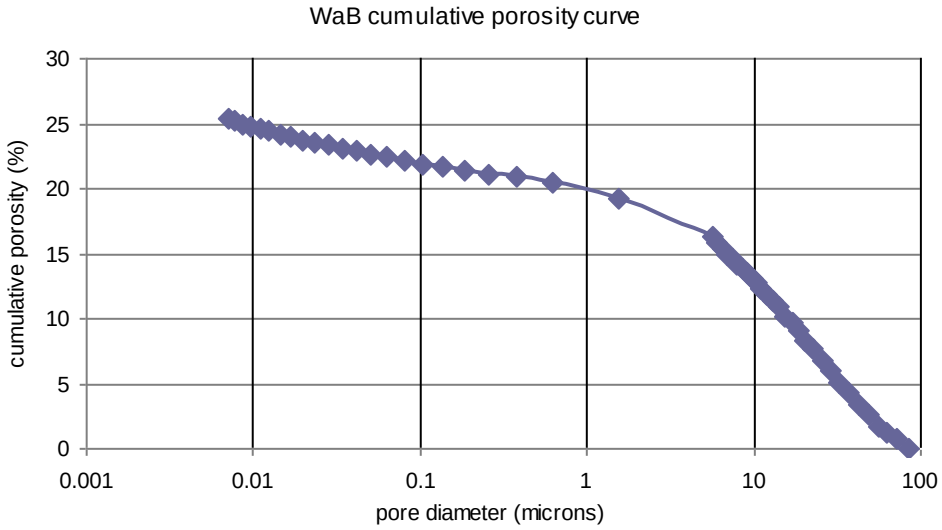
WaB cumulative porosity curve
cumulative porosity (%)
30
25
20
15
10
5
0
0.001
0.01
0.1
1
10
100
pore diameter (microns)

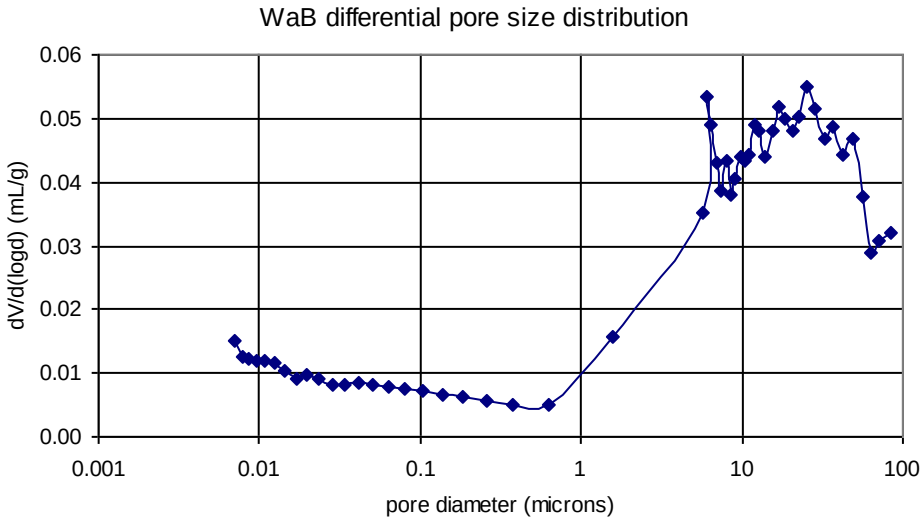
WaB differential pore size distribution
dV/d(logd) (mL/g)
0.06
0.05
0.04
0.03
0.02
0.01
0.00
0.001
0.01
0.1
1
10
100
pore diameter (microns)

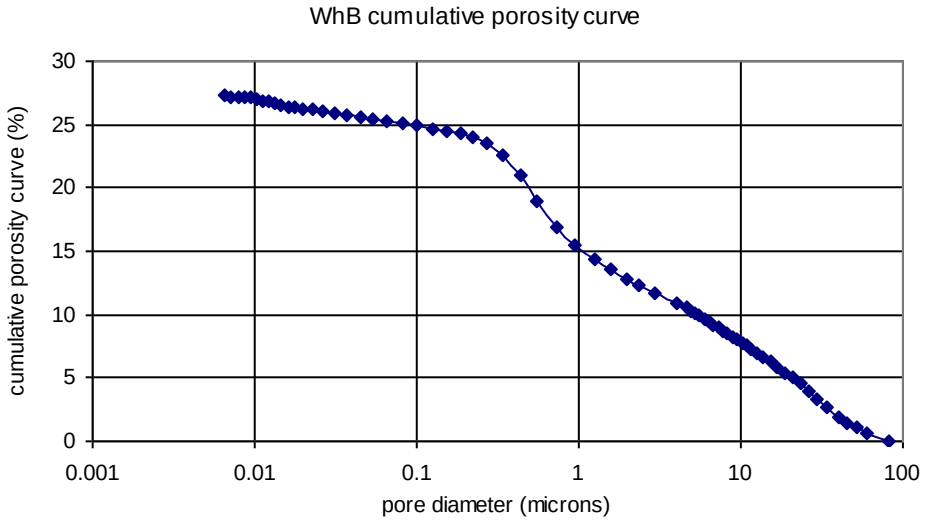
WhB cumulative porosity curve
cumulative porosity curve (%)
30
25
20
15
10
5
0
0.001
0.01
0.1
1
10
100
pore diameter (microns)

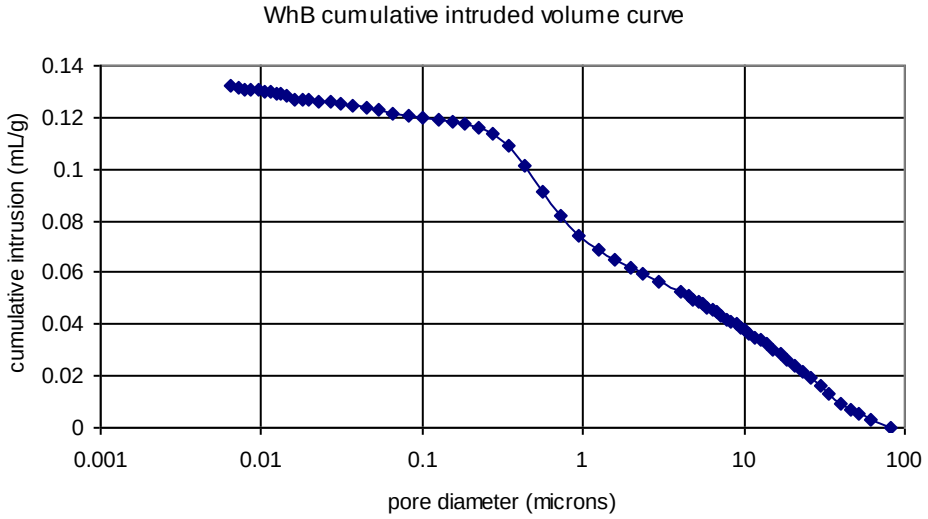
WhB cumulative intruded volume curve
cumulative intrusion (mL/g)
0.14
0.12
0.1
0.08
0.06
0.04
0.02
0
0.001
0.01
0.1
1
10
100
pore diameter (microns)

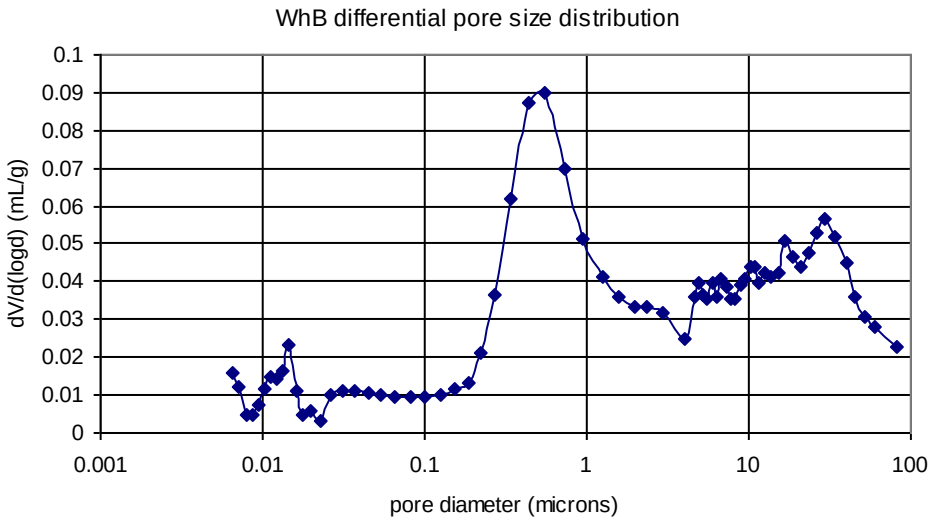
WhB differential pore size distribution
dV/d(logd) (mL/g)
0.1
0.09
0.08
0.07
0.06
0.05
0.04
0.03
0.02
0.01
0
0.001
0.01
0.1
1
10
100
pore diameter (microns)

Table A3.21 Full results of drying data for brick samples

time (h)	mass NB1 (g)	water content NB1 (g)	water content/area NB1 (g/cm^2)	mass NB2 (g)	water content NB2 (g)	water content/area NB2 (g/cm^2)
0.0	23.07	3.30	1.38	25.55	3.36	1.31
3.7	23.02	3.25	1.35	25.51	3.32	1.30
6.7	22.99	3.22	1.34	25.47	3.28	1.28
23.8	22.83	3.06	1.28	25.27	3.08	1.20
29.8	22.76	2.99	1.25	25.22	3.03	1.18
45.9	22.62	2.85	1.19	25.05	2.86	1.12
53.8	22.54	2.77	1.15	24.97	2.78	1.08
96.3	22.20	2.43	1.01	24.56	2.37	0.92
101.3	22.15	2.38	0.99	24.51	2.32	0.91
167.8	21.49	1.72	0.72	23.9	1.71	0.67
173.6	21.44	1.67	0.70	23.86	1.67	0.65
213.9	21.07	1.30	0.54	23.62	1.43	0.56
223.0	20.99	1.22	0.51	23.58	1.39	0.54
340.3	20.23	0.46	0.19	23.2	1.01	0.39
364.2	20.17	0.40	0.17	23.13	0.94	0.37
552.0	19.87	0.10	0.04	22.6	0.41	0.16
601.0	19.81	0.04	0.02	22.45	0.26	0.10
700.0	19.77	0.00	0.00	22.22	0.03	0.01
718.6	19.77	0.00	0.00	22.19	0.00	0.00

Table A3.22 Full results of drying data for mortar samples

time (h)	mass B33 M1 (g)	water content B33 M1 (g)	water content/area B33 M1 (g/cm^2)	mass B33 M2 (g)	water content B33 M2 (g)	water content/area B33 M2 (g/cm^2)
0.0	26.21	3.29	1.29	27.96	3.61	1.39
3.7	26.15	3.23	1.26	27.91	3.56	1.37
6.7	26.09	3.17	1.24	27.87	3.52	1.36
23.8	25.78	2.86	1.12	27.60	3.25	1.25
29.8	25.68	2.76	1.08	27.54	3.19	1.23
45.9	25.43	2.51	0.98	27.38	3.03	1.17
53.8	25.32	2.4	0.94	27.31	2.96	1.14
96.3	25.05	2.13	0.83	27.04	2.69	1.04
101.3	25.03	2.11	0.82	27.02	2.67	1.03
167.8	24.90	1.98	0.77	26.83	2.48	0.96
173.6	24.89	1.97	0.77	26.82	2.47	0.95
213.9	24.84	1.92	0.75	26.74	2.39	0.92
223.0	24.82	1.90	0.74	26.71	2.36	0.91
340.3	24.72	1.80	0.70	26.56	2.21	0.85
364.2	24.70	1.78	0.70	26.53	2.18	0.84
552.0	24.61	1.69	0.66	26.38	2.03	0.78
601.0	24.58	1.66	0.65	26.35	2.00	0.77
700.0	24.54	1.62	0.63	26.30	1.95	0.75
718.6	24.53	1.61	0.63	26.30	1.95	0.75

Table A3.23 Results summary from drying experiments

sample	initial rate of water loss ($g/cm^2/h$)	time to reach critical saturation level (h)	sample length (cm)	time to reach critical saturation level per unit length sample (h/cm)	water content per unit area at critical saturation level (g/cm^2)	initial water content per unit area (g/cm^2)	critical saturation level (%)
NB1	0.0039	240	4.93	48.7	0.45	1.38	32.7
NB2	0.0038	175	4.93	35.5	0.62	1.31	47.3
B33 M1	0.0067	50	4.76	10.5	0.95	1.29	73.6
B33 M2	0.0050	50	5.15	9.7	1.15	1.39	82.7

A4.1 Full results for LVDT experiments with brick, render and composite samples

Table A4.1 Dimensions of LVDT samples, part 1

sample	height 1 (mm)	height 2 (mm)	height 3 (mm)	average height (mm)	breadth 1 (mm)	breadth 2 (mm)	breadth 3 (mm)	average breadth (mm)
R1	48.20	47.87	48.15	48.07	16.48	15.53	17.50	16.50
R2	48.68	48.37	48.25	48.43	18.76	18.37	18.45	18.53
R3	45.04	45.37	45.57	45.33	15.19	14.70	15.00	14.96
R4	46.55	46.62	46.82	46.66	14.26	14.09	14.17	14.17
R5	47.14	47.00	46.59	46.91	13.77	13.57	13.80	13.71
B1	41.53	42.08	42.01	41.87	19.03	18.85	19.40	19.09
B2	42.43	42.99	42.47	42.63	19.44	19.31	19.53	19.43
B3	41.21	40.53	40.74	40.83	20.49	19.86	20.22	20.19
B4	41.84	41.44	41.97	41.75	19.42	19.23	19.62	19.42
B5	43.77	42.52	42.67	42.99	19.73	20.27	19.73	19.91
C1	43.93	43.98	44.16	44.02	24.12	24.13	23.20	23.82
C2	41.47	42.56	41.92	41.98	21.64	21.84	21.35	21.61
C4	42.62	42.94	42.79	42.78	19.08	19.18	18.73	19.00
C5	42.60	42.35	42.83	42.59	21.57	22.20	21.28	21.68

Table A4.2 Dimensions of LVDT samples, part 2

sample	depth 1 (mm)	depth 2 (mm)	depth 3 (mm)	average depth (mm)	volume (cm^3)
R1	10.15	10.31	10.52	10.33	8.19
R2	10.36	11.16	11.51	11.01	9.88
R3	13.13	13.24	12.70	13.02	8.83
R4	11.95	11.17	10.71	11.28	7.46
R5	11.13	10.73	10.48	10.78	6.93
B1	19.70	19.97	19.79	19.82	15.85
B2	20.40	20.95	21.00	20.78	17.21
B3	20.64	21.23	21.16	21.01	17.32
B4	19.60	19.50	19.49	19.53	15.84
B5	21.21	21.43	21.63	21.42	18.34
C1	20.06	19.90	19.85	19.94	20.90
C2	18.65	18.72	18.75	18.71	16.97
C4	20.27	20.08	20.38	20.24	16.45
C5	18.67	18.50	18.38	18.52	17.10

Table A4.3 Determination of porosity of LVDT samples due to capillary saturation

sample	dry mass (g)	wet mass (g)			mass gain (g)			volume (cm^3)	porosity (%)		
		1	2	3	1	2	3		1	2	3
render	16.00	17.57	17.57	17.59	1.57	1.57	1.59	8.83	17.79	17.81	17.96
brick	27.02	29.88	29.84	29.84	2.85	2.82	2.82	17.21	16.58	16.39	16.36
composite	34.75	38.31	38.35	38.28	3.55	3.60	3.53	20.90	17.00	17.21	16.86

Table A4.4 Determination of porosity of LVDT samples due to vacuum saturation

sample	dry mass (g)	wet mass (g)			mass gain (g)			volume (cm^3)	porosity (%)		
		1	2	3	1	2	3		1	2	3
render	17.16	19.69	19.67	19.69	2.53	2.51	2.53	9.88	25.58	25.44	25.63
brick	28.67	33.89	33.85	33.94	5.22	5.18	5.27	18.34	28.48	28.25	28.75
composite	28.55	33.37	33.42	33.46	4.83	4.88	4.91	17.10	28.22	28.51	28.73

Fig. A4.1 Graphs illustrating the sample length changes due to temperature cycling

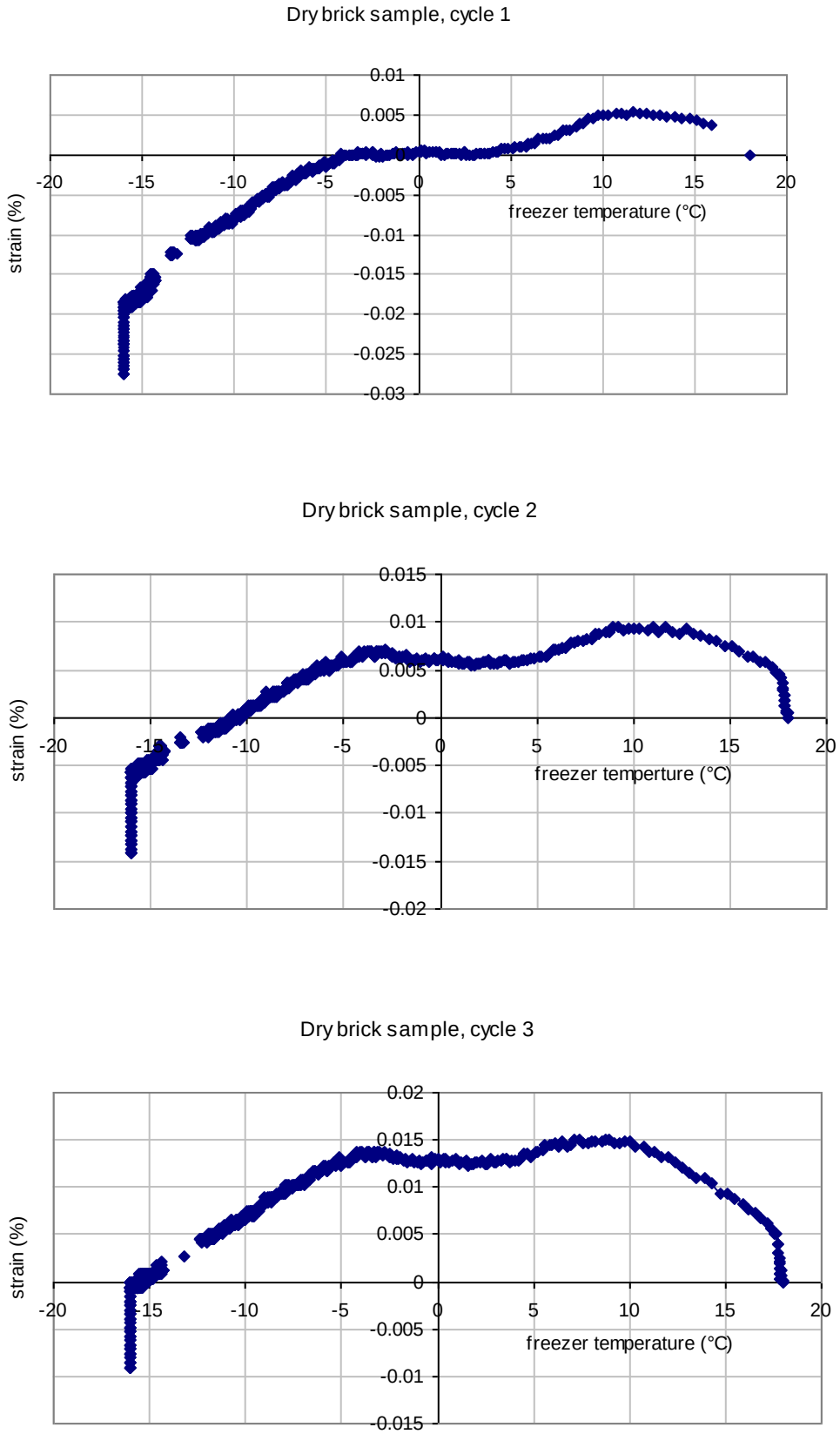

Dry render sample, cycle 1

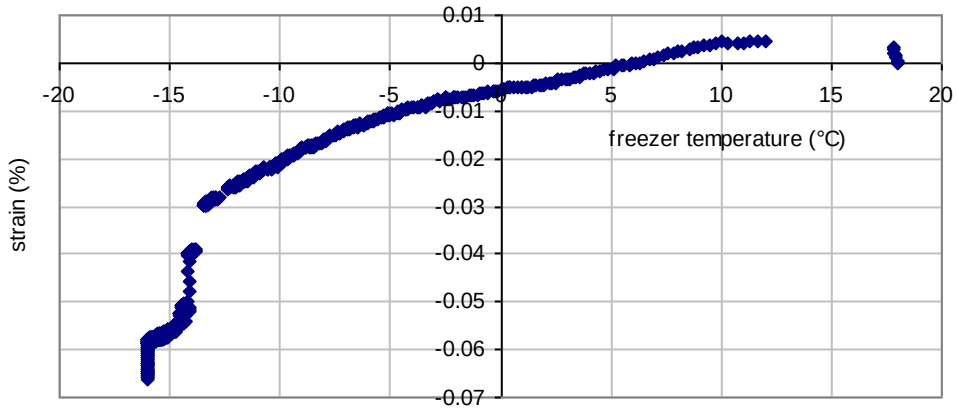

Dry render sample, cycle 2

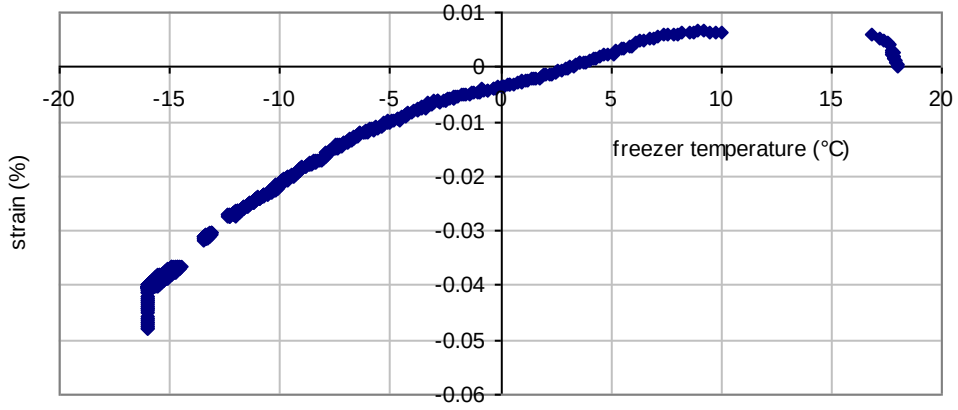

Dry render sample, cycle 3

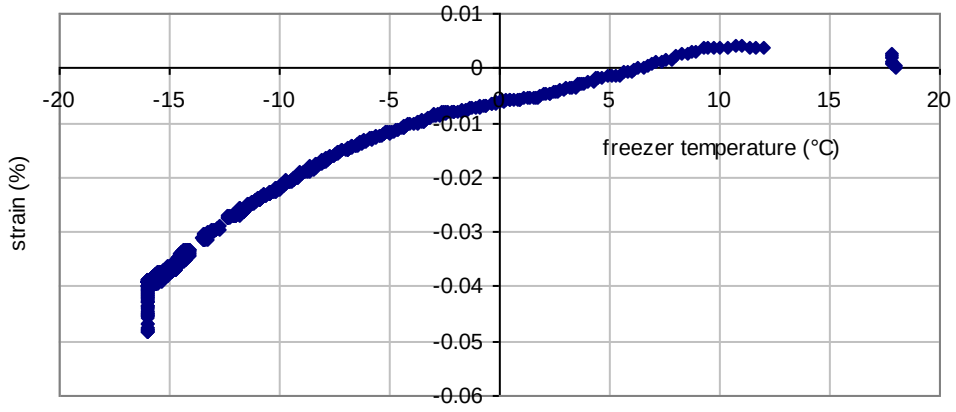

Dry composite sample, cycle 1

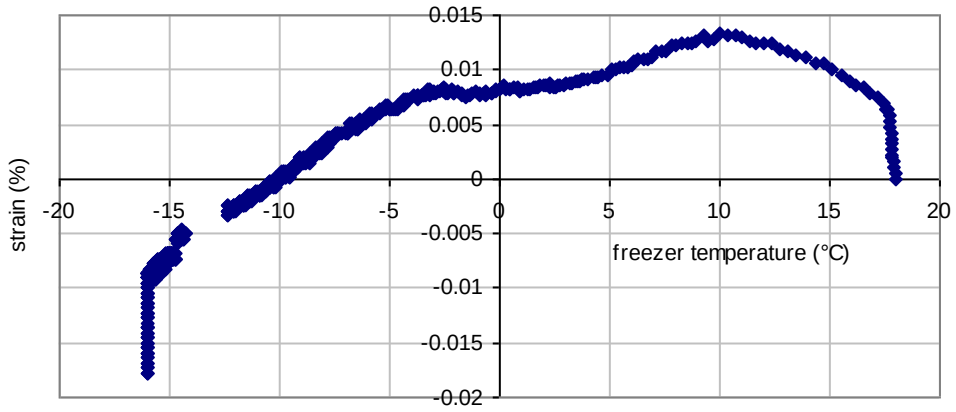

Dry composite sample, cycle 2

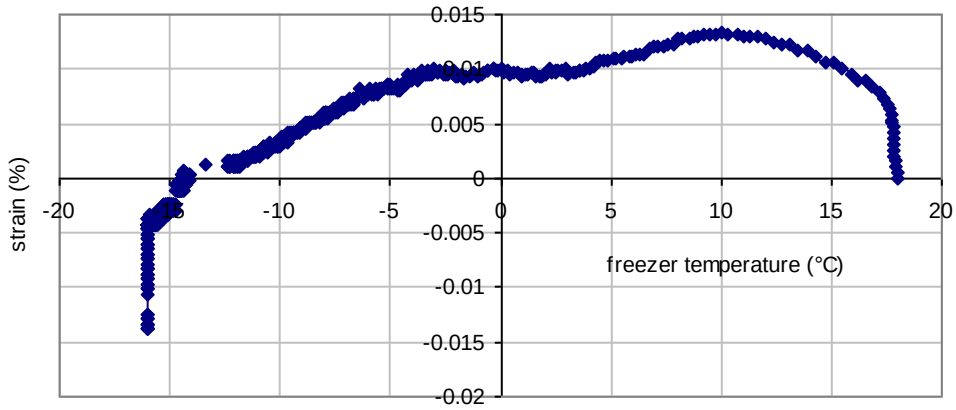

Dry composite sample, cycle 3

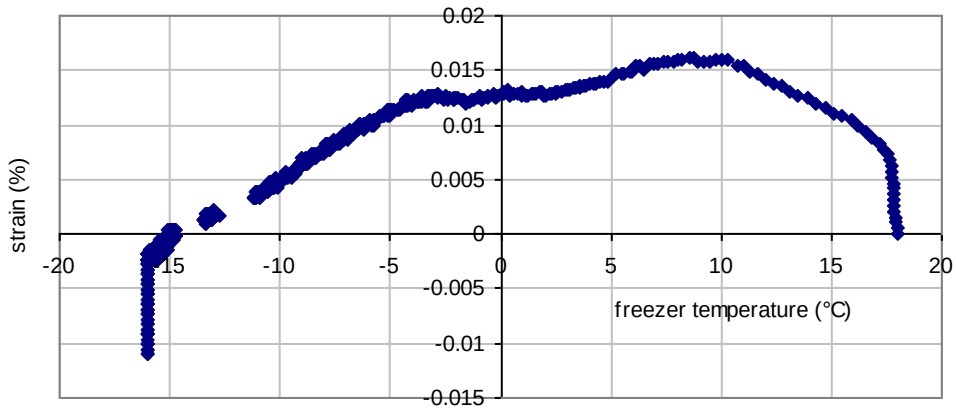

Capillary saturated brick sample, cycle 1

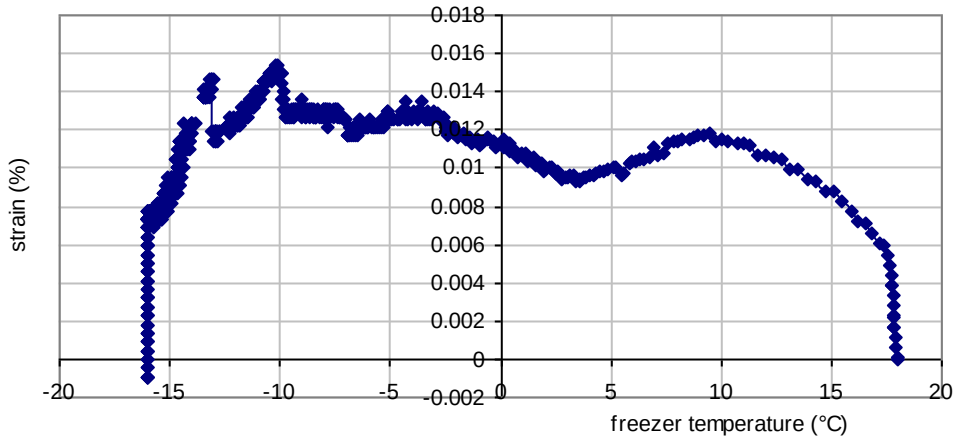

Capillary saturated brick sample, cycle 2

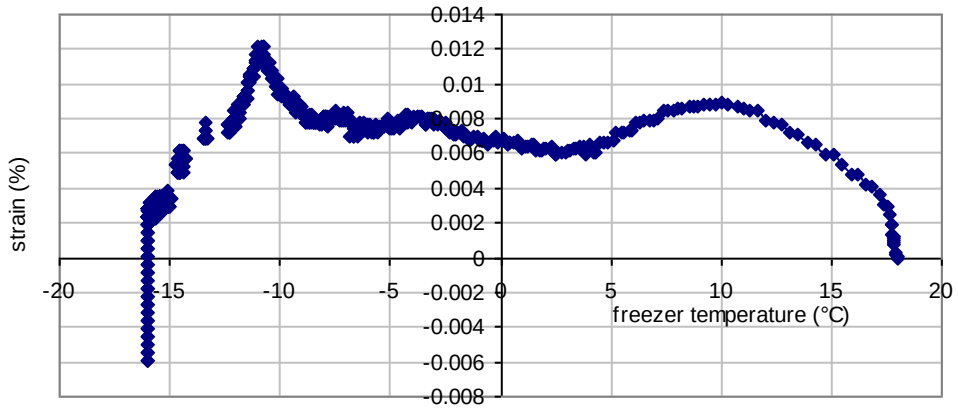

Capillary saturated brick sample, cycle 3

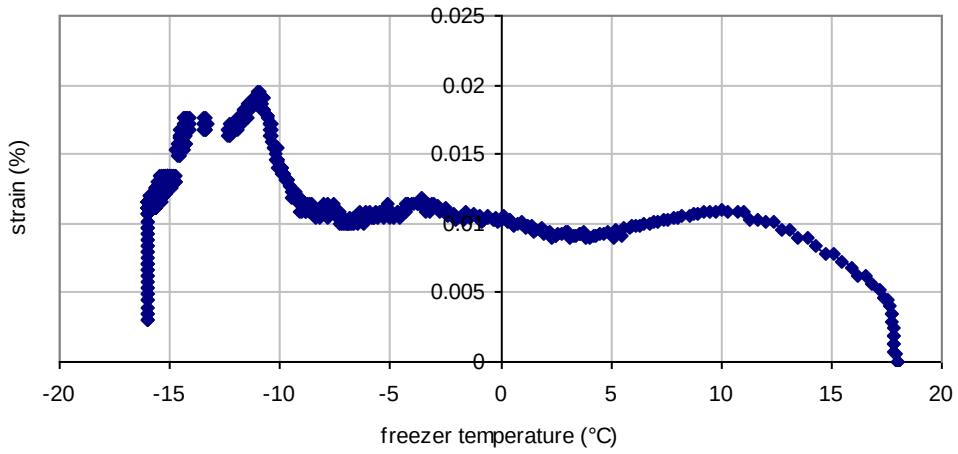

Capillary saturated render sample, cycle 1

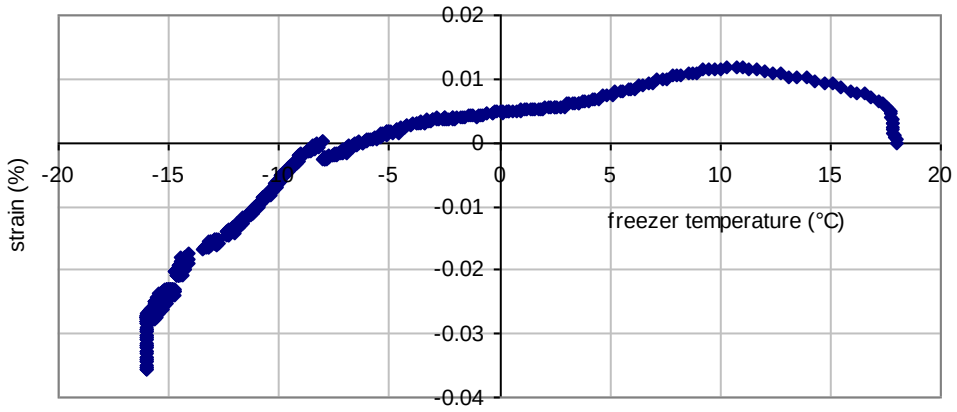

Capillary saturated render sample, cycle 2

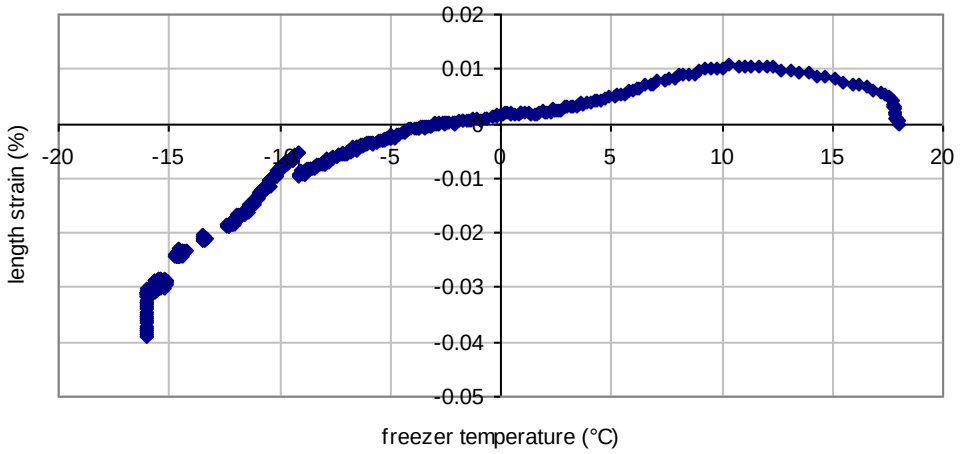

Capillary saturated render sample, cycle 3

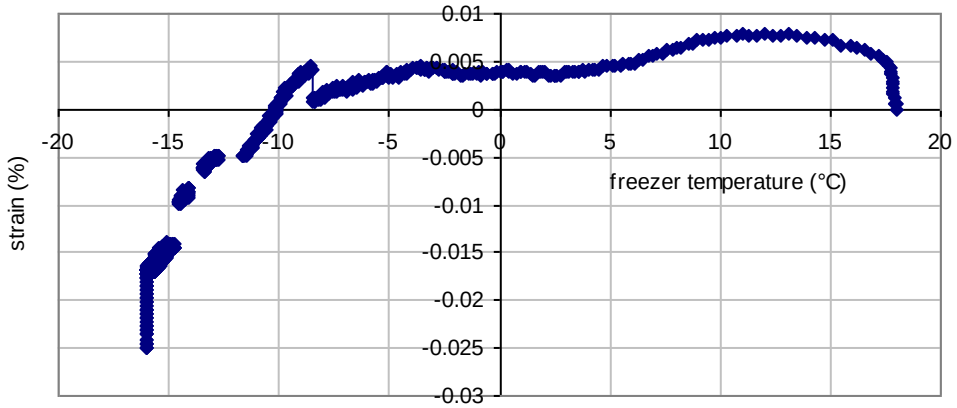

Capillary saturated composite sample, cycle 1

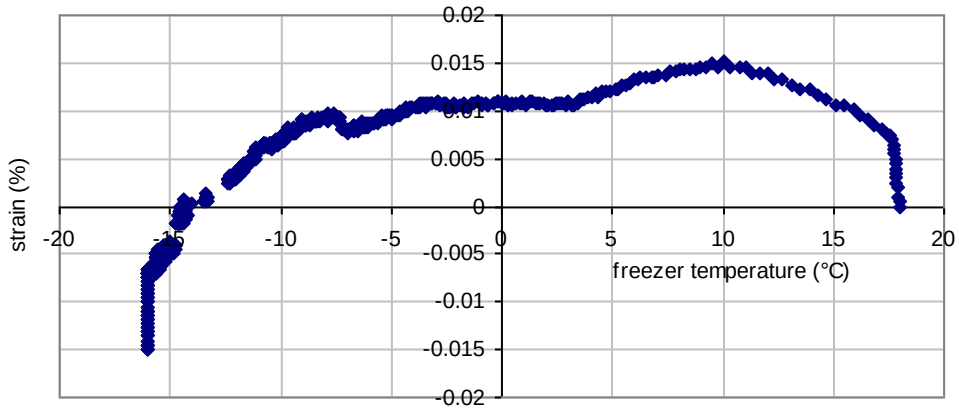

Capillary saturated composite sample, cycle 2

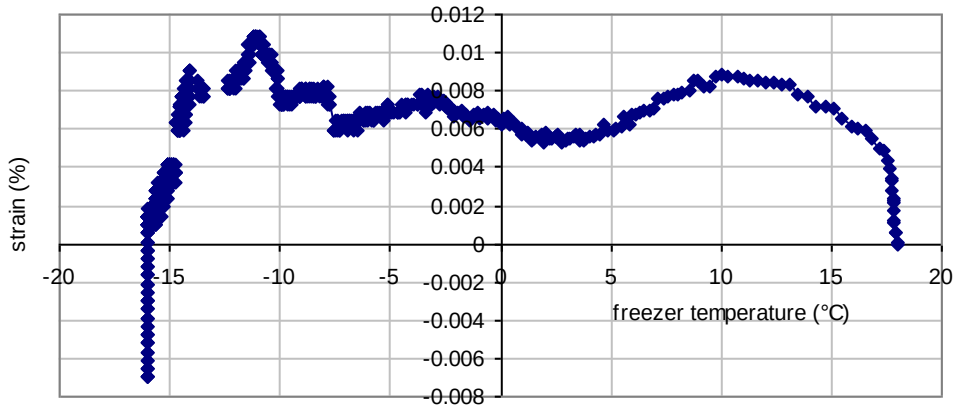

Capillary saturated composite sample, cycle 3

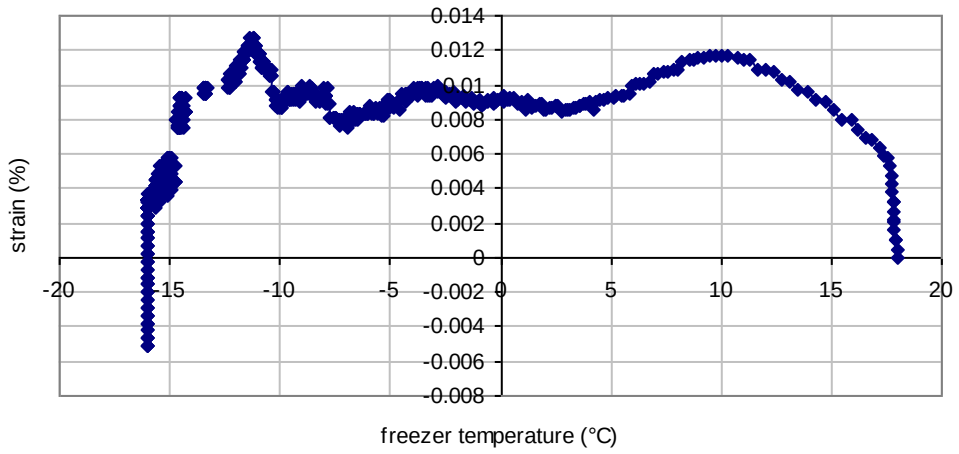

Vacuum saturated brick sample, cycle 1

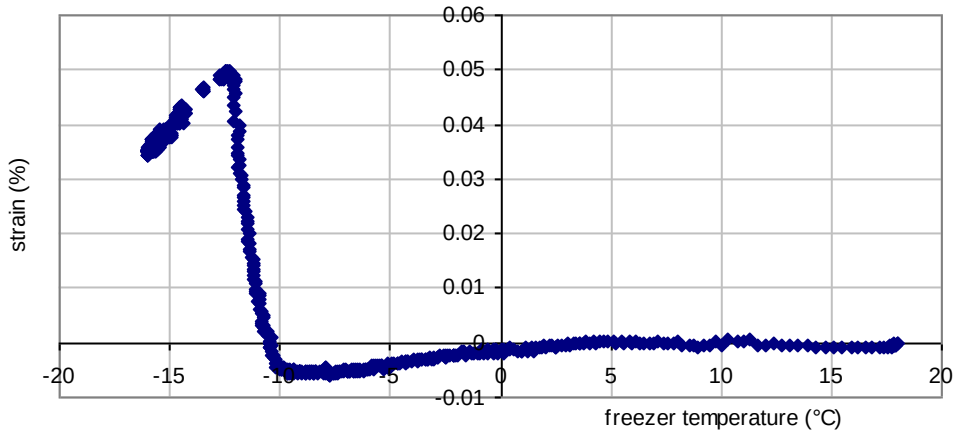

Vacuum saturated brick sample, cycle 2

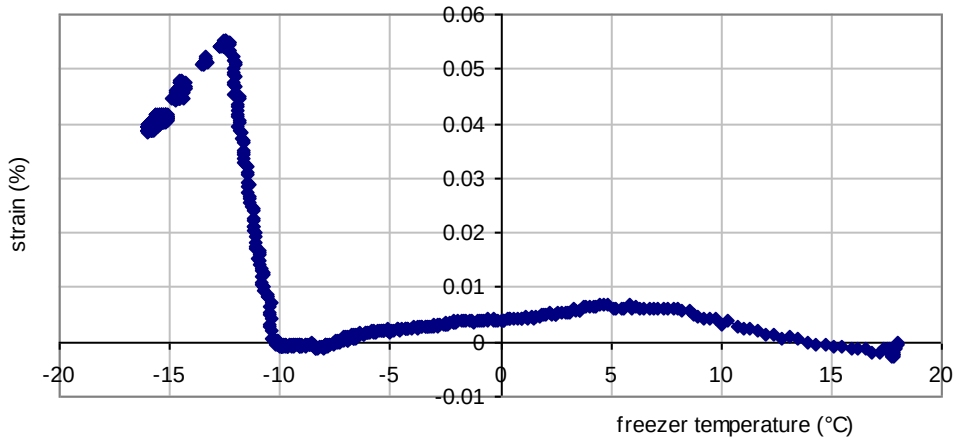

Vacuum saturated brick sample, cycle 3

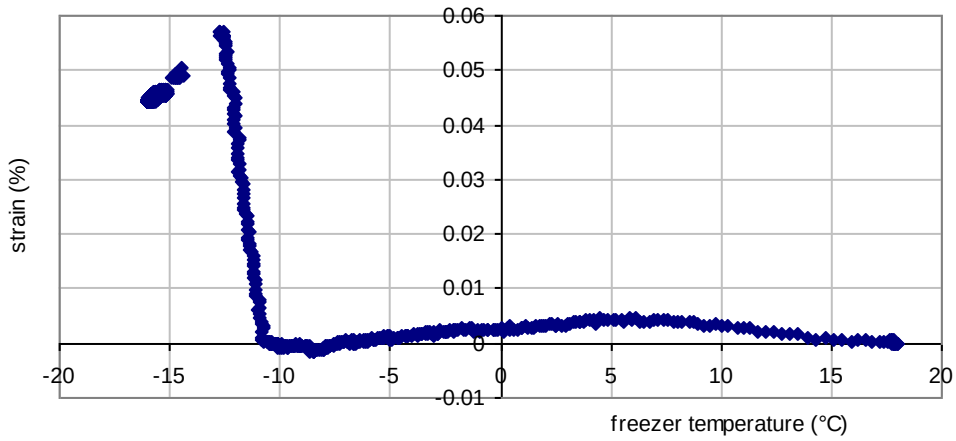

Vacuum saturated render sample, cycle 1

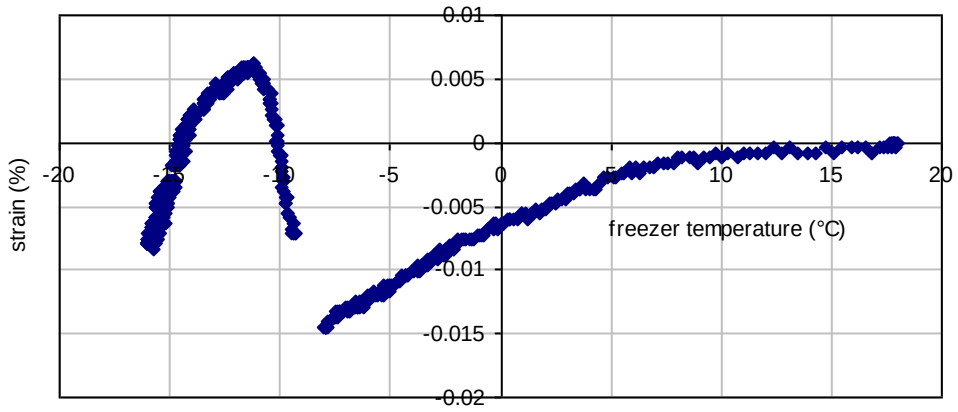

Vaccum saturated render sample, cycle 2

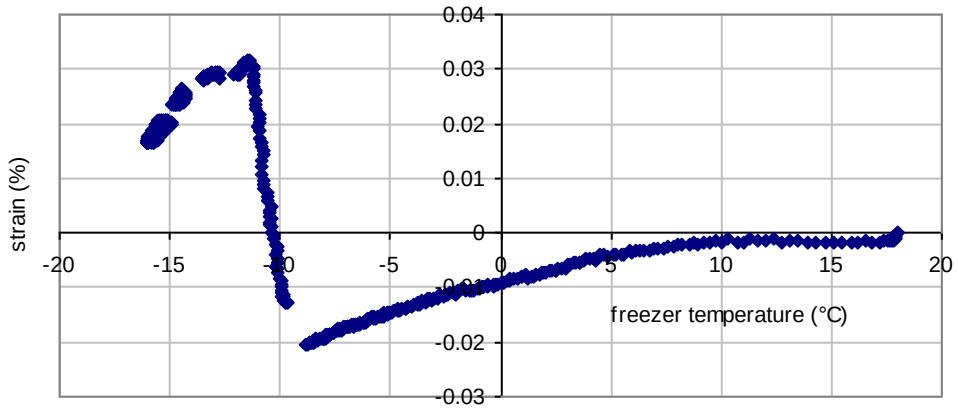

Vacuum saturated render sample, cycle 3

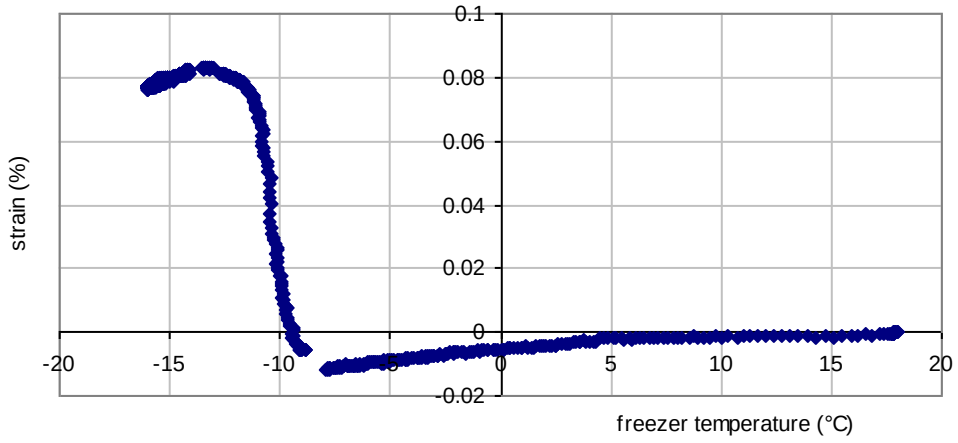

Vacuum saturated composite sample, cycle 1

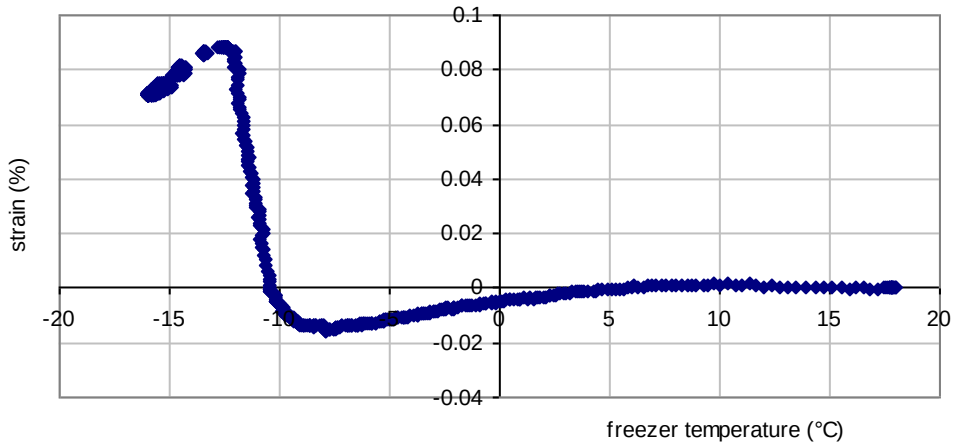

Vacuum saturated composite sample, cycle 2

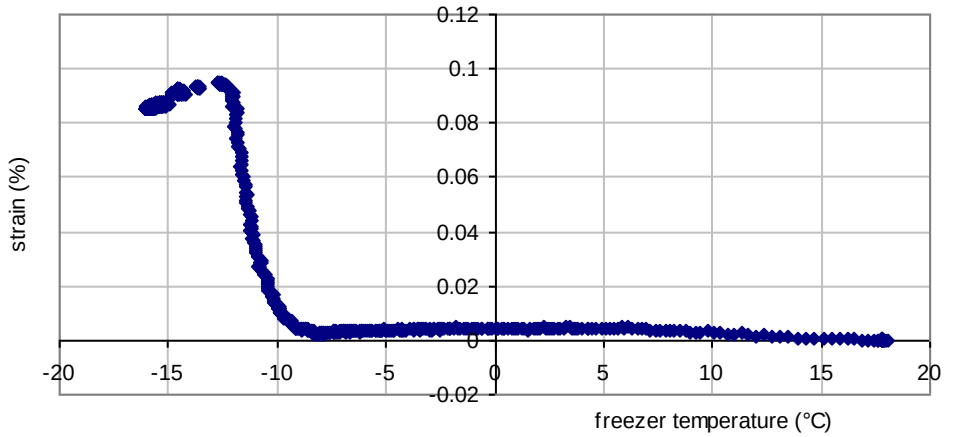

Vacuum saturated composite sample, cycle 3

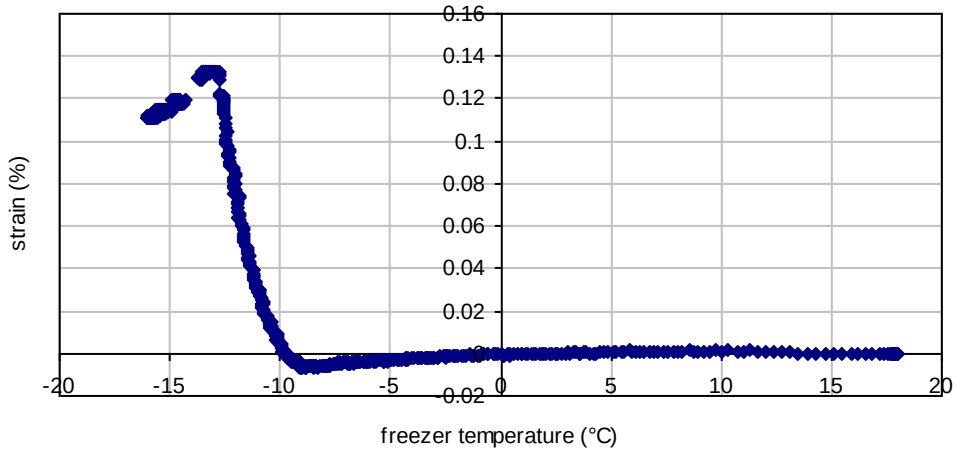

A5.1 Full results of experiments with expansive aggregates and replica renders

Table A5.1 Dimensional changes of particles due to uptake of water and n-decane

sample	test regime	original thickness (ηm)	length change (ηm)	length change (%)
quartz pebble	water absorption	3900	0.0	0.00
quartz pebble	decane absorption	3900	0.0	0.00
aggregate particle 1 (shale)	water absorption	1550	-45.3	-2.92
aggregate particle 1 (shale)	decane absorption	1550	-16.5	-1.06
aggregate particle 2 (shale)	water absorption	1320	-41.2	-3.11
aggregate particle 2 (shale)	decane absorption (run 1)	1320	-3.5	-0.27
aggregate particle 2 (shale)	decane absorption (run 2)	1320	-3.8	-0.29
aggregate particle 3 (shale)	water absorption	1210	-39.4	-3.25
aggregate particle 3 (shale)	decane absorption	1210	-0.6	-0.05
aggregate particle 4 (sandstone with mud component)	water absorption	1840	-13.6	-0.74
aggregate particle 4 (sandstone with mud component)	decane absorption	1840	-0.6	-0.03
quarried shale sample 1	water absorption	3630	11.5	0.32
quarried shale sample 1	decane absorption	3630	0.0	0.00
quarried shale sample 2	water absorption	12620	75.0	0.59
quarried shale sample 1 with layers orientated vertically	water absorption	4560	0.5	0.01
quarried shale sample 1 with layers orientated vertically	decane absorption	4560	0.0	0.00
quarried shale sample 3 after artificial weathering	water absorption	2720	1.0	0.04
quarried shale sample 3 after artificial weathering	decane absorption	2720	0.0	0.00
quarried shale sample 2	capillary saturation with water followed by freezing	12620	156	1.24

Table A5.2. Water uptake of replica renders due to capillary saturation

sample	sample reference	dry mass (g)	wet mass cycle 1 (g)	wet mass cycle 2 (g)	wet mass cycle 3 (g)	porosity cycle 1 (g)	porosity cycle 2 (g)	porosity cycle 3 (g)
control render	C2	19.24	20.68	20.86	21.02	14.37	16.12	17.71
low shale render	LS1	16.76	18.54	18.64	18.65	20.32	21.37	21.59
high shale render	HS4	18.57	20.68	20.76	20.88	23.29	24.07	25.40

Table A5.3 Dimensional changes of replica renders due to uptake of water

sample	sample reference	length change (%) cycle 1	length change (%) cycle 2	length change (%) cycle 3
control render	C1	0.0372	0.0139	0.0157
low shale render	LS2	0.0273	0.0362	0.0105
high shale render	HS2	0.0124	0.0282	0.0234

Table A5.4 Dimensional changes of control replica render C1 due to capillary saturation and freezing

cycle	length change at point of ice formation (%)	freezer temperature at point of ice formation (%)	length change at minimum temperature (%)	length change at end of cycle (%)
cycle 1	-0.0076	-6.78	-0.0294	-0.0246
cycle 2	-0.0085	-5.27	-0.0326	-0.0306
cycle 3	0.0000	-7.44	-0.0225	-0.0275
cycle 4	-0.0250	-7.44	-0.0477	-0.0415

Table A5.5 Dimensional changes of low shale replica render LS1 due to capillary saturation and freezing

cycle	length change at point of ice formation (%)	freezer temperature at point of ice formation (%)	length change at minimum temperature (%)	length change at end of cycle (%)
cycle 1	0.0000	-6.07	-0.0254	-0.0164
cycle 2	-0.0010	-7.34	-0.0237	-0.0258
cycle 3	-0.0008	-7.58	-0.0193	-0.0138
cycle 4	0.0000	-7.72	-0.0193	-0.0251

Table A5.6 Dimensional changes of high shale replica render HS4 due to capillary saturation and freezing

cycle	length change at point of ice formation (%)	freezer temperature at point of ice formation (%)	length change at minimum temperature (%)	length change at end of cycle (%)
cycle 1	-0.0035	-7.34	-0.0301	-0.0371
cycle 2	0.0010	-7.44	-0.0214	-0.0218
cycle 3	-0.0004	-8.11	-0.0172	-0.0220
cycle 4	0.0036	-7.34	-0.0172	-0.0278

A6.1 Estimation of chloride levels inside concrete from the air raid shelter using SEM-EDX

A6.1.1 Chloride levels in the concrete thin section

Table A6.1 Chloride mapping within the air raid shelter concrete thin section

sample number	location	calcium (%)*	chloride (%)	comments
1	3 cm below surface, close to reinforcement	30.04	0.13	
2	3 cm below surface, close to reinforcement	23.07	0.34	
3	3 cm below surface, close to reinforcement	22.65	0.26	
4	3 cm below surface, close to reinforcement	25.70	0.38	
5	3 cm below surface, close to reinforcement	25.96	0.51	
6	very close to surface	28.70	0.16	
7	very close to surface	27.99	0.18	
8	very close to surface	29.18	0.24	
9	very close to surface	15.06	0.30	Ca surprisingly low, therefore this result was discounted
10	close to surface	31.65	0.14	
11	2 cm below surface	20.54	0.57	
12	2 cm below surface	23.18	0.52	
13	2 cm below surface	18.74	0.51	
14	2 cm below surface	24.22	0.42	
15	2 cm below surface	21.57	0.58	
16	1 cm below surface	24.56	0.78	
17	1 cm below surface	21.40	0.54	
18	1 cm below surface	29.57	0.31	
19	1 cm below surface	22.18	0.49	

* Calcium was mapped as well as chloride because it was anticipated that the calcium content of the cement matrix in the concrete should be reasonably constant, and that a particularly high or low value might indicate a problematic measurement.

Table A6.2 Average values for chloride mapping within air raid shelter concrete thin section

location	average chloride (%)
surface	0.18
1 cm below surface	0.53
2 cm below surface	0.52
3 cm below surface, close to reinforcement	0.32

A6.1.2 Evaluation of accuracy of SEM-EDX analysis using chloride standards

From experimenting with different scan times and different detector positions, as shown in Table A6.3, it was decided that the best configuration was a scan time of 90 s, with the detector in its usual position.

From the analysis of the cement standards it was concluded that the values obtained for the polished surfaces were generally more accurate than the values obtained for the smooth but unpolished surfaces, and that the analysis was able to differentiate between 0.2%, 0.5% and 1.0% chloride, although possibly not between 0.1% and 0.2% chloride. Referring only to the values obtained for the polished surfaces, the average values obtained for the 0.2%, 0.5% and 0.1% standards were correct to ±0.11% or less.

Table A6.3 Results of analysis of 0.1% chloride standard

location	run 1 chloride (%)	run 2 chloride (%)	run 3 chloride (%)	run 4 chloride (%)	average chloride (%)
smooth but unpolished surface	0.17	0.15	0.15		0.16
polished surface, area 1	0.22	0.22			0.22
polished surface, area 2	0.14 (60s)	0.21 (90s)	0.22 (120s)	0.22 (60s but with detector moved to get more counts/sec)	0.22 (discounting run 1 result)

Table A6.4 Results of analysis of 0.2% chloride standard

location	run 1 chloride (%)	run 2 chloride (%)	run 3 chloride (%)	average chloride (%)
smooth but unpolished surface	0.28	0.26	0.31	0.28
roughly polished surface	0.12	0.09	0.11	0.11
highly polished surface	0.20	0.28	0.16	0.20

Table A6.5 Results of analysis of 0.5% chloride standard

location	chloride (%)	average
smooth but unpolished surface	0.8, 0.85, 0.82, 0.96, 0.83, 0.84, 0.94, 0.69, 0.67, 0.72	0.81
polished surface	0.30, 0.31, 0.44, 0.49, 0.39	0.39

Table A6.6 Results of analysis of 1.0% chloride standard

location	chloride (%)	average
smooth but unpolished surface	1.47, 1.18, 1.51, 1.31, 1.40	1.37
polished surface	1.12, 1.23, 1.04, 1.06	1.11